

PERFORMANCE ANALYSIS OF AIR-COOLED PHOTOVOLTAIC/THERMAL SYSTEMS

By

Moustafa Adil Abdulrahem Al-Damook

The University of Leeds

School of Mechanical Engineering

November 2019

The candidate confirms that the work submitted is his own, except where work formed jointly-authored publication has been included. The contribution of the candidate and other authors to this work has been explicitly indicated overleaf. The candidate confirms that appropriate credit has been given within the thesis where reference has been made to the work of others. This copy has been supplied on the understanding that it is copyright material and that no quotation from the thesis may be published without proper acknowledgement.

© 2019 The University of Leeds, Moustafa Al-Damook.

This work is dedicated to:

My beloved parents

Adil and Widad

My beloved wife, sons and daughters

Ridhab Al-Halboosi

Othman, Zaid, Shahd and Widad

My beloved brothers and sisters;

My friends who encourage and support me, especially, Sheikh
Mahmood, Sheikh Muhammad, Osama, Khalid and Bashar

WORK APPEARING IN JOINTLY AUTHORED PUBLICATIONS

Journal Article:

1. Al-Damook M, Obaid ZH, Al Qubeissi M, Dixon-Hardy D, Cottom J, Heggs PJ. CFD modelling and performance evaluation of multi-pass solar air heaters. Numerical Heat Transfer; Part A: Applications. 2019 June 25.

Peer Reviewed Conference Proceedings and Poster

1. M. Al Hamdani, M. Al Qubeissi, M. Al-Damook, D. Dixon-Hardy, and P. J. Heggs, "Thermal Optimisation of Fin Clusters for Heat Sink Purposes," in 11th ICTEA: International Conference on Thermal Engineering, in Doha Qatar in collaboration with Texas A&M Doha campus and Hamad Bin Khalifa University, 2018.
2. M. Al-Damook, D. Dixon-Hardy, P. J. Heggs, M. Al Qubeissi, K. Al-Ghaithi, P. E. Mason, "CFD analysis of a one-pass photovoltaic/thermal air system with and without offset strip fins," in MATEC Web of Conferences, Cracow, Poland, May 21-24 2018.
3. M. Al-Damook, M. Al Qubeissi, D. Dixon-Hardy, P. J. Heggs, K. Al-Ghaithi, "Comparative investigation of multi-pass flow for air photovoltaic/thermal collectors," in UK FLUIDS CONFERENCE 2018, University of Manchester, UK, September 04-06 2018. (Poster)
4. M. Al-Damook, M. Al Qubeissi, D. Dixon-Hardy, Zinedine Khatir, P. J. Heggs, "Thermal and electrical performance evaluation and design optimization of hybrid PV/T systems," in 16th UK Heat Transfer Conference 2019, University of Nottingham, UK, September 8-10 2019.
5. Moustafa Al-Damook, Darron Dixon-Hardy, Peter J. Heggs, Mansour Al Qubeissi, Zinedine Khatir, "CFD analysis of PV/T air systems," in International Conference on Sustainable Materials and Energy Technologies, Coventry University, UK, September 12-13 2019

ACKNOWLEDGEMENTS

All the praises be to Allah, the Most Beneficent, the Most Merciful.

I would first like to thank my supervisors Dr Darron Dixon-Hardy, Professor Peter Heggs, Dr Mansour Qubeissi and Dr Zinedine Khatir for their continuous guidance and support. They consistently allowed this thesis to be my own work but steered me in the right direction whenever they thought I needed it.

I am most thankful to my mother and father, wife, children, brothers and all my family members for their help, support, encouragement and patience during the years of my study.

I would like to thank the Higher Committee for Education Development in Iraq (HCED) for financial support of this work, as well as Iraqi Ministry of Higher Education and Scientific Research (MOHE), and Renewable Energy Research Center University of Anbar, Iraq.

I would also like to express my gratitude to Zaid Al-Damook, Dr Josh Cottom, Dr Saad Wasmi, Dr Mushtaq Al-Asadi, Haithem Aburebaiya, Khaled Al-Ghaithi, Richard Birley, Iram Razaq, Nicola Wood, Dr Patrick Mason Dr Yasser Al-Jubouri and Dr Mohamed Al-Khateeb for their guidance and support during the years of my study.

I would also thank the University of Warwick to offer experimental results for chapter 5 for validation purpose specifically Dr Asim Mumtaz and Dr Roger Thorpe.

Finally, many thanks for Mrs Vicky Master for her support and guidance during my PhD program

ABSTRACT

Photovoltaic (PV) systems have witnessed exceptional development in the last two decades, where it has been shown that PVs may absorb more than 75% of the insolation, however, only limited percentage can be transformed into electricity (7-24%). The remaining energy is released mostly as waste heat in the cells. Overheating may also cause damage to adhesive seals, delamination and non-homogeneous temperatures. Therefore, PV/Thermal (PV/T) systems are a mechanism that can address these issues by keeping the PV cell temperature at the operating range improving efficiency to acceptable levels, as well as producing heat and electricity simultaneously. In this study, PV/T air systems are considered.

There are three main challenges to overcome with PV/T air systems; 1) the fan power requirement, 2) extreme weather temperature, 3), and the poor heat capacity of air, which leads to poor thermal performance, compared to other coolants such as water. The aim of this research is to address these challenges developing an efficient and affordable PV/T air system. To achieve this, eleven objectives have been suggested where appropriate several different solution methods are utilised. The CFD software of COMSOL Multiphysics and Matlab are used in this study.

The main findings of this research can be divided into three parts. The first part evaluates the performance of the standard PV system utilising theoretical and numerical methods. This system is considered as a reference for subsequent models. The results shows that the convection currents in inclined and horizontal surfaces are weaker relative to the vertical surface. The increase of the PV length enhances heat transfer rate up to length ($2L$). However, after this length, the PV temperature increases and convective heat transfer coefficients are reduced regardless of the inclination of the PV system. In the case of the horizontal surface, the convective heat transfer rate is lower, especially at the bottom surface of the PV system. It can also be concluded that the effect of inclination appears in the laminar region (short length) and dissipates after this region.

The second part numerically and experimentally evaluates the performance of the multi-pass solar air heaters. The impacts of flow configurations on the thermal performance of a solar heater system are investigated. Recycled aluminium cans (RAC) have been utilised as turbulators with a double pass single duct solar air collector. CFD results of the models A, B, and C reveal that model C offers a greater thermal performance of 5.4% and 6.5%, respectively, compared to A and B. Furthermore, an outdoor experiment is performed based on these results. The experimental setup is examined for three configurations of model C, namely, solar air heater (SAH) without RAC model C-I, model C-II and model C-III. A good agreement between model C and the experimental data and model C-III has the best thermal efficiency of 60.2%.

The third part, the combination of the two systems from these two parts are evaluated. Firstly, a design optimisation process is performed for different multi-pass PV/T air collectors considering three steps to obtain optimal design. The steps are the selection of design parameters, preliminary parametric studies for the five models (model 1, 2, 3, 4 and 5) and employ model 4 in the optimisation process. The key results from this optimisation demonstrate explicitly the compromise that must be accepted between the conflicting objectives of thermal and electrical efficiencies or the fan power consumption and electrical power generation. It can be concluded that the use of optimisation has contributed clearly in improving both the electrical and thermal performance for finned and plain mode

TABLE OF CONTENTS

Work appearing in Jointly Authored Publications.....	i
Acknowledgements.....	ii
Abstract.....	iii
Table of Contents.....	iv
List of Figures.....	ix
List of Tables.....	xviii
Nomenclature.....	xxi
Chapter 1 INTRODUCTION.....	- 1 -
1.1 Background.....	- 1 -
1.2 Problem statement.....	- 2 -
1.3 Aim and objectives.....	- 3 -
1.4 Contributions of the research.....	- 4 -
1.5 Thesis structure.....	- 5 -
Chapter 2 LITERATURE REVIEW.....	- 7 -
2.1 Introduction.....	- 7 -
2.2 Photovoltaic systems.....	- 8 -
2.3 Types of PV technology.....	- 9 -
2.3.1 Crystalline silicon photovoltaics.....	- 10 -
2.3.2 Thin-film photovoltaics.....	- 11 -
2.3.3 Concentrator photovoltaics.....	- 11 -
2.3.4 Third-generation photovoltaics.....	- 11 -
2.4 Performance evaluation of standard PV modules.....	- 12 -
2.5 Solar thermal systems.....	- 14 -
2.6 Hybrid PV/T systems.....	- 16 -
2.7 Classification of PV/T systems.....	- 18 -
2.7.1 PV/T air collectors.....	- 19 -
2.7.2 PV/T water collectors.....	- 22 -
2.7.3 PV/T refrigerant collectors.....	- 24 -
2.7.4 PV/T heat pipe collectors.....	- 25 -
2.7.5 PV/T PCM collectors.....	- 27 -
2.7.6 Comparison between PV/T types.....	- 29 -
2.8 Early work of PV/T air collectors.....	- 32 -

2.9	Key design parameters	- 34 -
2.9.1	Geometry parameters	- 34 -
2.9.2	Material parameters	- 38 -
2.9.3	Electrical parameters	- 40 -
2.9.4	Extended surfaces	- 41 -
2.10	Solving heat transfer problems	- 44 -
2.10.1	Experimental approaches	- 45 -
2.10.2	Analytical approaches	- 45 -
2.10.3	Numerical approaches	- 46 -
2.11	Conclusions	- 46 -
Chapter 3 Mathematical Modelling		- 48 -
3.1	Introduction.....	- 48 -
3.2	Mathematical formulation.....	- 49 -
3.2.1	Glass cover	- 53 -
3.2.2	PV panel.....	- 55 -
3.2.3	Lower absorber plate	- 57 -
3.2.4	Useful heat gain	- 59 -
3.3	Heat transfer and fluid flow equations.....	- 60 -
3.3.1	Dimensionless numbers.....	- 61 -
3.3.2	Heat transfer coefficients and losses.....	- 65 -
3.3.3	Thermal and electrical performance evaluation.....	- 85 -
3.4	Numerical techniques.....	- 92 -
3.4.1	Semi-analytical.....	- 92 -
3.4.2	Numerical solution	- 97 -
3.5	Conclusions	- 101 -
Chapter 4 COMPUTATIONAL METHOD, VERIFICATION AND VALIDATION		- 102 -
4.1	Introduction.....	- 102 -
4.1.1	Discretisation approaches	- 103 -
4.1.2	Methodology of CFD modelling	- 103 -
4.1.3	Accuracy and convergence criteria	- 104 -
4.2	Mesh generation.....	- 105 -
4.3	Computational model	- 106 -
4.3.1	Governing equations.....	- 106 -

4.3.2	Conjugate heat transfer	- 110 -
4.3.3	Radiation model	- 111 -
4.4	System parameters	- 113 -
4.4.1	Description of PV/T collectors	- 113 -
4.4.2	PV physical module description	- 118 -
4.4.3	Assumptions and boundary conditions	- 120 -
4.5	Computational assumptions	- 121 -
4.5.1	Thermal radiative effects	- 121 -
4.5.2	One-way coupling approach	- 123 -
4.5.3	Symmetry boundary condition	- 126 -
4.5.4	Thin layer assumption	- 128 -
4.5.5	Representative material properties	- 131 -
4.5.6	Tolerance	- 132 -
4.6	Validation	- 133 -
4.6.1	Mesh independence test	- 133 -
4.6.2	Inter-model comparison:-model 2	- 137 -
4.6.3	Inter-model comparison:-model 3	- 140 -
4.6.4	System validation	- 143 -
4.7	Conclusions	- 148 -
Chapter 5 PERFORMANCE OF PHOTOVOLTAIC SYSTEMS WITH RESPECT TO TEMPERATURE		- 149 -
5.1	Introduction	- 149 -
5.2	Methodology	- 149 -
5.2.1	PV physical module description	- 150 -
5.2.2	PV power extraction	- 150 -
5.3	1D modelling	- 150 -
5.3.1	Energy balance equations	- 151 -
5.3.2	Numerical technique	- 156 -
5.4	CFD Modelling	- 158 -
5.4.1	Boundary conditions and governing equations	- 158 -
5.4.2	Module heat capacity	- 159 -
5.5	Meteorological data	- 160 -
5.6	Validation	- 167 -
5.6.1	Grid independence test	- 167 -

5.6.2	System validation	- 169 -
5.6.3	System verification	- 171 -
5.7	Results and discussion	- 173 -
5.8	Conclusions	- 184 -
Chapter 6 THERMO-HYDRAULIC PERFORMANCE OF MULTI-PASS SOLAR AIR HEATER		- 186 -
6.1	Introduction	- 186 -
6.2	CFD modelling	- 187 -
6.2.1	System description	- 187 -
6.2.2	Conjugate heat transfer model	- 189 -
6.2.3	Boundary conditions	- 192 -
6.2.4	Mesh independence study	- 195 -
6.3	Experimental Setup	- 197 -
6.3.1	Geometry and design considerations.....	- 199 -
6.3.2	Measurements uncertainty	- 200 -
6.4	Thermo-hydraulic performance	- 201 -
6.5	Results and discussion	- 201 -
6.5.1	Thermal performance examination of U-flow shape design.....	- 201 -
6.5.2	Experimental results.....	- 203 -
6.5.3	Comparison between numerical and experimental results	- 209 -
6.5.4	Pressure drop evaluation	- 211 -
6.6	Conclusions	- 213 -
Chapter 7 OPTIMISATION OF MULTI-PASS PV/T AIR SYSTEMS		- 215 -
7.1	Introduction.....	- 215 -
7.2	CFD approach.....	- 215 -
7.3	Thermo-hydraulic performance	- 216 -
7.4	Grid independence test.....	- 216 -
7.5	Optimum PV/T air design.....	- 218 -
7.5.1	Parameter selection	- 218 -
7.5.2	Preliminary parametric studies	- 222 -
7.5.3	Optimisation of model 4.....	- 237 -
7.5.4	Optimisation strategy.....	- 237 -
7.5.5	Optimisation analysis.....	- 242 -
7.6	Model 4-A.....	- 250 -

7.7	Conclusions.....	- 262 -
Chapter 8 CONCLUSION AND RECOMMENDATION FOR FUTURE WORK.....		- 264 -
8.1	Introduction.....	- 264 -
8.2	Main conclusions.....	- 264 -
8.3	PV module performance	- 265 -
8.4	Performance of solar air heaters	- 266 -
8.5	Design optimisation of PV/T air design.....	- 266 -
8.6	PV/T air system with off-set strip fin.....	- 267 -
8.7	Future Work.....	- 267 -
REFERENCES.....		- 268 -

LIST OF FIGURES

Fig. 1.1. Comparing finite and renewable planetary energy reserves (TW-yr)[1].	- 1 -
Fig. 1.2. Schematic of PV/T air collector	- 2 -
Fig. 2.1. Electricity generation capacity of renewable energy plant since 2000 [3].	- 7 -
Fig. 2.2. Schematic diagram of the principle of PV cells.....	- 9 -
Fig. 2.3. Schematic of the standard PV module [4].	- 9 -
Fig. 2.4. Classification of photovoltaic technologies.	- 10 -
Fig. 2.5. Types of PV modules, in (a) Mono c-Si, (b) Poly-Si and (c) Thin-film [14]. ...	- 12 -
Fig. 2.6. Flat plate PV/T water collector with the same sized separate flat plate water heater and PV module [18].	- 17 -
Fig. 2.7. Classification of the PV/T systems adapted from [127].	- 20 -
Fig. 2.8. Common parts of the flat plate PV/T collector.	- 21 -
Fig. 2.9. Cross-sections of PV/T air systems, (a) Unglazed PV/T air collector, (b) Single glazed PV/T air collector, (c) Double glazed PV/T air collector, (d) Glazed PV/T air collector double pass, inferred from [119, 122, 128].	- 21 -
Fig. 2.10. Types of water PV/T collectors adapted [110, 116, 119].	- 23 -
Fig. 2.11. Schematic diagram of the PV solar-assisted heat pump [136].	- 24 -
Fig. 2.12. Side view of conventional heat pipes adapted from [144].	- 26 -
Fig. 2.13. Cross-section of a conventional heat pipe [145].	- 26 -
Fig. 2.14. Working of PCM adapted from [149].	- 28 -
Fig. 2.15. Schematics of the different PV/T air designs side by side with heat transfer coefficients [122].	- 33 -
Fig. 2.16. Variation of overall thermal efficiency with the length of the collector [26].-	- 35 -
Fig. 2.17. Impact of duct length on the performance of collector for specific conditions, channel depth of 0.05 m and mass flux of $0.02 \text{ kg s}^{-1} \text{ m}^{-2}$ [176].	- 36 -
Fig. 2.18. Effect of duct depth on the air temperature rise and the thermal efficiency for a solar air heater with a glass cover [131].	- 37 -
Fig. 2.19. Output power of single-crystalline silicon PV cells under different operating temperatures (left) temperature dependence of the maximum output power (right) [195].	- 40 -
Fig. 2.20. Different designs of extended surfaces of PV/T air collectors [108, 118, 133, 176].	- 42 -
Fig. 2.21. PV/T air system with aluminium ∇ -grooved absorber plate [222].	- 44 -
Fig. 3.1. The representation of conservation of energy for the PV cell of model 1.	- 48 -

Fig. 3.2. Schematic of model 2.	- 49 -
Fig. 3.3. Schematic of model 3.	- 50 -
Fig. 3.4. Schematic of the energy balance equation for the top glass cover (model 3).-	54 -
Fig. 3.5. Schematic of the energy balance equation for the PV panel (model 2).	- 55 -
Fig. 3.6. Schematic of the energy balance equation for the PV module (model 3).	- 57 -
Fig. 3.7. Schematic of the energy balance equation for the lower absorber plate for models 2 and 3.	- 57 -
Fig. 3.8. Schematic of the enthalpy balance over an interval Δx and time interval Δt of the fluid flowing.....	- 60 -
Fig. 3.9. Schematic of heat transfer modes in PV/T air systems (model 3).	- 61 -
Fig. 3.10. Schematic of conjugate heat transfer between solid and fluid domains adapted from [258].	- 64 -
Fig. 3.11. Schematic of different positions of hot and cold plates, in (a) Vertical hot plate, (b) Inclined (down face of a hot plate), (c) Vertical cold plate (d) Inclined (top side of a cold plate)	- 70 -
Fig. 3.12. Schematic of buoyancy-driven flows on a horizontal position in (a) End view of flow at the top surface of the hot plate and in (b) End view of flow at the bottom surface of cold plate adapted from [241].	- 70 -
Fig. 3.13. Schematic of buoyancy-driven flows on the horizontal position in (a) Top surface of the cold plate and in (b) Bottom surface of hot plate adapted from [241].	- 71 -
Fig. 3.14. Horizontal rectangular enclosure with isothermal surfaces adapted from [272].	- 72 -
Fig. 3.15. Schematic of a horizontal rectangular enclosure with isothermal surfaces. -	77 -
Fig. 3.16. 3D temperature contour ($^{\circ}\text{C}$) for free convection in the enclosure under steady state conditions, the top surface temperature is 20°C and the bottom surface temperature is 120°C while the air gap space is 0.2 m	- 80 -
Fig. 3.17. 3D temperature contour ($^{\circ}\text{C}$) for free convection in the enclosure under steady state conditions, the top surface temperature is 90°C and the bottom surface temperature is 120°C while the air gap space is 0.2 m	- 81 -
Fig. 3.18. 3D temperature contour ($^{\circ}\text{C}$) for free convection in the enclosure under steady state conditions, the top surface temperature is 20°C and the bottom surface temperature is 120°C while the air gap space is 0.025 m	- 81 -
Fig. 3.19. 3D temperature contour ($^{\circ}\text{C}$) for free convection in the enclosure under steady state conditions, the top surface temperature is 95°C and the bottom surface temperature is 120°C while the air gap space is 0.025 m	- 82 -

Fig. 3.20. 2D modelling for free convection in the enclosure under transient conditions for two temperature differences, in (a) the lower surface temperature is 20 °C and upper surface temperature is 120 °C , Time = 300 s, surface: 2D temperature (°C), red arrow surface: velocity field, black arrow line: acceleration of gravity, (c) the lower surface temperature is 90 °C and upper surface temperature is 120 °C , Time = 300 s, surface: 2D temperature (°C), red arrow surface: velocity field, black arrow line: acceleration of gravity, (b) Time = 300 s, surface: velocity magnitude (m s⁻¹), arrow surface: velocity field, black arrow line: acceleration of gravity for temperature counter in (a), and (d) Time = 300 s, surface: velocity magnitude (m s⁻¹), arrow surface: velocity field, black arrow line: acceleration of gravity for temperature counter in (c). - 83 -

Fig. 3.21. Typical mono-crystalline and poly-crystalline silicon solar cells [306]...... - 90 -

Fig. 3.22. Flow chart of the algorithm for the semi-analytical solution of model 2.... - 96 -

Fig. 3.23. Schematic of the meshing technique used for model 2. - 100 -

Fig. 3.24. Flow chart of the algorithm for the solution of the non-linear model (model 2). - 100 -

Fig. 4.1. Overview of the different stages of a general modelling process [330, 331].- 104 -

Fig. 4.2. Mesh of PV/T air system without fins for one of the case studies: in (a) Structured mesh and in (b) Unstructured mesh..... - 105 -

Fig. 4.3. Representation of the conjugate heat transfer of air PV/T system (model 4).- 111 -

Fig. 4.4. Incoming irradiation (left), outgoing radiosity (right)...... - 112 -

Fig. 4.5. Schematics of model 2: in (a) 3D of model 2 (b) 2D cross-section front view of model 2, (c) 2D cross-section side view of model 2. - 115 -

Fig. 4.6. Schematics of model 3: in (a) 2D cross-section front view of model 3, (b) 2D cross-section side view of model 3. - 116 -

Fig. 4.7. Schematics of model 4: in (a) 2D cross-section front view of model 4, (b) 2D cross-section side view of model 4. - 116 -

Fig. 4.8. Schematics of model 5: in (a) 2D cross-section front view of model 5, (b) 2D cross-section side view of model 5. - 117 -

Fig. 4.9. Different views of model 4-A with offset strip fins..... - 118 -

Fig. 4.10. Schematic view of the main PV module components..... - 119 -

Fig. 4.11. Memory requirements with respect to degrees of freedom (DOF) for various representative cases adapted from [344]. - 122 -

Fig. 4.12. Schematic of single duct, single pass solar air thermal collector including off-set strip fins shown the symmetry planes and boundary conditions. - 123 -

Fig. 4.13. Pressure drops from one-way and fully coupled methods versus collector length under the steady state condition and laminar flow regime, $Re_{Dh} = 2550$ for model 4.- 125 -

Fig. 4.14. Pressure drops from one-way and fully coupled methods for design model 4-A (finned collector), $S_f = 10$ mm, $L = 1.2$ m, $L_f = 48$ mm $\delta_{D1} = \delta_{D2} = 25$ mm..... - 126 -

Fig. 4.15. Schematic of model 3 with offset strip fins showing the symmetrical boundary.	- 128 -
Fig. 4.16. Strip fins with 3D fins (left) or thin fins (right).....	- 128 -
Fig. 4.17. Two case studies of model 3 including offset strip fin: In (a) Thin fin model and (b) Thick fin model.	- 130 -
Fig. 4.18. Mesh used for model 3 including offset strip fin, showing the thick fin model. - 130 -	
Fig. 4.19. Velocity counter of the cross-section top view of the thin and thick models presenting in (a) Thick model, surface: velocity magnitude ($m s^{-1}$), arrow surface: velocity field, in (b) Thin model, surface: velocity magnitude ($m s^{-1}$), arrow surface: velocity field.	- 130 -
Fig. 4.20. Schematic of individual and equivalent PV module layers.....	- 131 -
Fig. 4.21. Surface temperature contour of model 1 under free convection condition, $G = 1000 W m^{-2}$, $T_{amb} = 25 ^\circ C$, in (a) Original model, (b) Equivalent model.....	- 132 -
Fig. 4.22. Mesh of the PV/T air system with fins: in (a) structured mesh and in (b) unstructured mesh.....	- 133 -
Fig. 4.23. Schematic of the single duct single pass PV/T air collector including longitudinal strip fins showing the symmetry plane and boundary conditions.	- 134 -
Fig. 4.24. Mesh element type examinations: in (a) Unstructured mesh models, (b) Structured mesh models.	- 136 -
Fig. 4.25. Skewness parameter for two cases in (a) structured mesh case and in (b) unstructured mesh case. Note: one indicates the optimal element quality and zero represents a degenerated element.....	- 137 -
Fig. 4.26. Schematic of model 2 showing the boundary conditions.	- 139 -
Fig. 4.27. Influence of the ambient and PV cell temperatures on the PV electrical efficiency using three methods for model 2, (1) Semi-analytical, (2) predictor-corrector and (3) 3D CFD.....	- 139 -
Fig. 4.28. Schematic of model 3 showing the boundary conditions.	- 140 -
Fig. 4.29. Influence of the ambient and PV cell temperatures on the PV electrical efficiency using six methods of model 3.	- 142 -
Fig. 4.30. Temperature contours ($^\circ C$) of model 3 using CFD transient method (method 6).	- 143 -
Fig. 4.31. Influence of the ambient and PV cell temperatures on the thermal efficiency of model 2 using six methods (method 1 to method 6).	- 143 -
Fig. 4.32. Schematic of the cross-sectional view of the PV/T air collector of Hegazy [122].	- 144 -
Fig. 4.33. CFD results of present work (model 2) and simulated results Amori and Al-Najjar [24] for Baghdad on 22/1/2011 for clear sky day at 12:30 PM.....	- 145 -

Fig. 4.34. CFD results of present work (model 2) and simulated results of Amori and Al-Najjar [24] for the outlet fluid temperature (T_{fout}).	- 145 -
Fig. 4.35. Schematics of the PV/T air system of Hegazy [122] (namely model II)... -	146 -
Fig. 4.36. Intensity of solar radiation versus time recorded at Egypt, Minia University on 24 June 1998.	- 146 -
Fig. 4.37. Linear solution of present work (model 3) and linear of Hegazy [122] (model II) for estimated daily thermal efficiency.	- 147 -
Fig. 4.38. Linear solution of present work (model 3) and linear of Hegazy [122] (model II) for estimated daily power fan.	- 148 -
Fig. 5.1. Schematic of the main heat transfer modes within the various layers and at the outer surfaces of the PV module.	- 152 -
Fig. 5.2. Equivalent thermal circuit of the PV laminate.	- 153 -
Fig. 5.3. Natural convection flows on the top and bottom surfaces of horizontal, vertical and inclined hot surface plates.	- 155 -
Fig. 5.4. Flow chart of the algorithm for the solution of the semi analytical model. -	157 -
Fig. 5.5. Flow chart for solar radiation estimation, in (a) estimation insolation for a whole year on a horizontal surface and in (b) estimate the maximum insolation for a day for each month.....	- 161 -
Fig. 5.6. Monthly estimated and observed insolation of PVGIS-C and PVGIS-H for Fallujah and Muscat cities.....	- 162 -
Fig. 5.7. Hourly estimated insolation with observed of PVGIS-C and PVGIS-H for Fallujah and Muscat cities for a typical day in July.	- 163 -
Fig. 5.8. Maximum incident solar radiation falling on horizontal and inclined surfaces for Fallujah and Muscat cities on 31 st of Jan.....	- 164 -
Fig. 5.9. Hourly variation of insolation and ambient temperature for Fallujah 22 nd of Jan 2011[24] and for Muscat 1 st of Oct 2013 [323].....	- 165 -
Fig. 5.10. Observed and estimated ambient temperature for Muscat 1 st of Oct 2013 [323].	- 166 -
Fig. 5.11. Estimated, PVGIS-C and PVGIS-H values of the maximum tracking angles (tilt angles) for Muscat and Fallujah cities.....	- 167 -
Fig. 5.12. Structured and unstructured mesh of standard PV unit for refinement step number (4) in Table 5.1.	- 169 -
Fig. 5.13. CFD of present work (model 1) and experimental work of Thorpe [372] for the average PV module temperature.	- 170 -
Fig. 5.14. CFD of present work (model 1) and experimental work of [121] for the average PV module temperature.	- 171 -
Fig. 5.15. CFD model and semi-analytical solution of model 1 for the average PV module temperature and electrical power, in (a) for Fallujah on a typical day in July and in (b) for Muscat on a typical day in July.....	- 172 -

Fig. 5.16. Numerical results of standard PV unit under steady and transient conditions for case study Fallujah on a typical day in July.....	- 173 -
Fig. 5.17. Hourly variation of PV module temperature, maximum insolation and ambient temperature over a year under free convection and transient conditions (time step 1 minute) in Fallujah.....	- 175 -
Fig. 5.18. Hourly variation of PV module temperature, maximum insolation and ambient temperature over a year under free convection and transient conditions (time step 1 minute) in Muscat.....	- 176 -
Fig. 5.19. 2D temperature contours ($^{\circ}\text{C}$) of standard PV module under free convection and transient conditions (time step 1 minute) in Fallujah of 1 st Aug at 13:00 and Muscat of 2 nd Jun at 11:45.....	- 177 -
Fig. 5.20. Hourly variation of module temperature and PV power generation for 12 months under free convection and transient conditions (time step 1 minute) at Fallujah.	- 178 -
Fig. 5.21. Hourly variation of module temperature and PV power generation for 12 months under free convection and transient conditions (time step 1 minute) at Muscat.	- 179 -
Fig. 5.22. 2D temperature contours ($^{\circ}\text{C}$) of standard PV module under free convection and transient conditions at Fallujah of 1 st Jun at 13:00 employing different lengths and same tilt angle (horizontal).....	- 180 -
Fig. 5.23. Impact of length of PV module on its temperature under different inclinations in Fallujah on typical 31 st Jan at 13:00.....	- 182 -
Fig. 5.24. Effect of convective heat transfer coefficients at the top and bottom surface of PV module on their temperatures under different inclinations in Fallujah 31 st of on typical day Jan at 13:00.....	- 183 -
Fig. 6.1. Schematics of the three solar air collectors (CFD models): (a) Cross-section of parallel pass double duct of co-current flow (model A); (b) Cross-section of parallel pass double duct of counter-current flow (model B); (c) Cross-section of single duct double pass of U-flow (model C).....	- 188 -
Fig. 6.2. Wind data observation for March in Ramadi city, Iraq.	- 195 -
Fig. 6.3. System meshing, using (a) unstructured, (b) structured, and (c) hybrid meshes.	- 196 -
Fig. 6.4. Schematic of single-duct double-pass (U-flow) solar air collector. (Please note that the figure is not to scale), showing: (a) The cross-section area of solar air collector including RACs; (b) SAH without RACs (model C-I); (c) Cross-section of SAH with in-line pattern (model C-II). The number of RACs is six across the width and ten along the length; and (d) Section top view of SAH with staggered configuration (model C-III). The number of RACs is seven for the first row and six for the second row across the width.....	- 198 -
Fig. 6.5. Intensity of solar radiation (G) versus time recorded in 23 February, showing the experimental [384] and estimated [50] data.....	- 201 -
Fig. 6.6. Thermal efficiency versus Reynold number under turbulent condition regime for co-current flow (model A), counter-current flow (model B) and U-flow (model C) CFD models.	- 202 -

Fig. 6.7. Pressure drop in flow duct between the inlet and the outlet for (co-current flow, model A), (counter-current flow, model B) and (U-flow, model C) CFD models. - 203 -

Fig. 6.8. Intensity of solar radiation versus time recorded on three different dates.- 204 -

Fig. 6.9. Intensity of solar radiation versus 4:30 to 18:30 hours (hrs) recorded during January–August..... - 204 -

Fig. 6.10. Collector air temperatures and incident solar radiation versus 09:00–16:00 hrs for the three models, C-I (a), C-II (b), and C-III (c)..... - 206 -

Fig. 6.11. Thermal efficiencies versus 09:00–16:00 hrs for three configurations, model C-I (plain), model C-II (in-line) and model C-III (staggered)..... - 207 -

Fig. 6.12. Thermal efficiency, the intensity of solar radiation, inlet air temperature, and inlet air velocity versus 09:00–16:00 hrs for model C-III (staggered arrangement)..... - 208 -

Fig. 6.13. Inlet and outlet air temperatures versus 09:00–16:00 hrs of the experimental (model C-I) and CFD (model C) results of the plain design..... - 210 -

Fig. 6.14. Al absorber plate temperatures versus 09:00–16:00 hrs of the experimental (model C-I) and CFD (model C) results of the plain design (without RAC)..... - 211 -

Fig. 6.15. Pressure drop profile for model C-I (single duct double pass U-flow design without cans) with $V = 1.26 \text{ m s}^{-1}$, $G = 600 \text{ W m}^{-2}$ and $T_i = 16.9 \text{ }^\circ\text{C}$ conditions; (a) 2D CFD model and (b) 3D CFD model. - 212 -

Fig. 6.16. Pressure drop from the 2D CFD, 3D CFD and empirical equations versus 09:00–16:00 hrs for design model C-I (single duct double pass U-flow design without Cans) using the data presented in Table 6.3..... - 213 -

Fig. 7.1. Velocity profile for different locations along the lower air channel for model 4 under laminar flow regime (a) $Re = 510$, $V = 0.1829 \text{ (m s}^{-1}\text{)}$, $M = 0.0041 \text{ (kg s}^{-1}\text{)}$ (b) $Re = 2550$, $V = 0.9145 \text{ (m s}^{-1}\text{)}$, $M = 0.0204 \text{ (kg s}^{-1}\text{)}$ - 218 -

Fig. 7.2. Working principle of the studied BIPV/T system: in (a) winter mode and (b) summer mode adapted from [185]. - 220 -

Fig. 7.3. Insolation and ambient temperature versus time in a typical day in July 2018.- 221 -

Fig. 7.4. Schematics of the various PV/T models along with heat transfer coefficients.- 224 -

Fig. 7.5. Pressure drop along the duct versus Re (510-2550) of the studied PV/T systems using different lengths (1.2 m and 1.6 m) and weather conditions (25 °C and 45 °C).- 228 -

Fig. 7.6. Thermal efficiencies versus Re (510-2550) of the studied PV/T systems using different lengths (1.2 m and 1.6 m) and weather conditions (25 °C and 45 °C)..... - 229 -

Fig. 7.7. PV module temperatures and the electrical efficiencies versus Re (510-2550) of the studied PV/T systems using different lengths (1.2 m and 1.6 m) and weather conditions (25 °C and 45 °C). - 230 -

Fig. 7.8. Combined efficiencies versus Re (510-2550) of the studied PV/T systems using different lengths (1.2 m and 1.6 m) and weather conditions (25 °C and 45 °C)..... - 231 -

Fig. 7.9. Side view of temperature contours for model 1 showing the temperature profile of the PV module layers using different lengths (1.2 m and 1.6 m) and weather conditions (25 °C and 45 °C) under steady state conditions.....- 232 -

Fig. 7.10. Side view of temperature contours for model 2 showing the temperature profile along the PV module and air flow channel using different lengths (1.2 m and 1.6 m) and weather conditions (25 °C and 45 °C) under steady state conditions.....- 233 -

Fig. 7.11. Side view of temperature contours for model 3 showing the temperature profile along the PV module and air flow channel using different lengths (1.2 m and 1.6 m) and weather conditions (25 °C and 45 °C) under transient conditions.- 234 -

Fig. 7.12. Side view of temperature contours for model 4 showing the temperature profile along the PV module and air flow channel using different lengths (1.2 m and 1.6 m) and weather conditions (25 °C and 45 °C) under steady state conditions.....- 235 -

Fig. 7.13. Side view of temperature contours for model 5 showing the temperature profile along the PV module and air flow channel using different lengths (1.2 m and 1.6 m) and weather conditions (25 °C and 45 °C) under steady state conditions.....- 236 -

Fig. 7.14. Temperature distribution of local temperature of model 4 and 5 along the PV module from inlet to outlet.- 237 -

Fig. 7.15. Schematic of model 4 showing the range of geometrical parameters and boundary conditions of model 4.- 239 -

Fig. 7.16. Illustration of the DOE points: (a) Lower depth of flow ($\delta D1$) versus upper depth of flow $\delta D2$, (b) Lower depth of flow ($\delta D1$) versus length of the collector (L), (c) Upper depth of flow ($\delta D2$) versus length of collector (L).....- 239 -

Fig. 7.17. Function of η_{PV} from the surrogate model at low high condition (25 °C).- 243 -

Fig. 7.18. Function of η_{th} from the surrogate model at low high condition (25 °C).- 243 -

Fig. 7.19. Pareto front showing the compromises that can be struck in maximising both η_{th} and η_{PV} together with five representative design points (e.g. P_1 - P_5) used for the PV/T performance analysis illustrated in Table 7.7 when operating at 25 °C.....- 244 -

Fig. 7.20. Pareto front showing the compromises that can be struck in maximising both η_{th} and η_{PV} together with five representative design points (e.g. P_1 - P_5) used for the PV/T performance analysis illustrated in Table 7.8 when operating at 45°C.....- 246 -

Fig. 7.21. Pareto front showing the compromises that can be struck in minimising the fan power and maximising electrical power together with five representative design points (e.g. P_1 - P_5) used for the PV performance analysis illustrated in Table 7.9 when operating at 25 °C.- 247 -

Fig. 7.22. Pareto front showing the compromises that can be struck in minimising the fan power and maximising electrical power together with five representative design points (e.g. P_1 - P_5) used for the PV/T performance analysis illustrated in Table 7.10 when operating at 45 °C.....- 248 -

Fig. 7.23. Comparison between different PV and PV/T systems showing the impact of the temperature of the PV module on electrical efficiency under similar conditions for model 1_{STC}, model 1_{PV-25}, model 1_{PV-45}, model 4_{PV/T-25}, model 4_{PV/T-25} and model 4_{PV/T-45}.- 249 -

Fig. 7.24. Sectional front (a) and side (b) views of model 4-A..... - 251 -

Fig. 7.25. Overall efficiency versus inlet air velocity for model 4-A_{non} and 4_{non}. - 252 -

Fig. 7.26. Total power generation, electrical power generation and fan power versus inlet air velocity for model 4-A_{non} and 4_{non}. - 254 -

Fig. 7.27. PV module temperature, electrical efficiency and thermal resistance versus inlet air velocity for models 4-A_{non} and 4_{non}. - 256 -

Fig. 7.28. PV module temperature, electrical efficiency and thermal efficiency versus five optimal design points (P₁ to P₅ in Table 7.7) for low temperature condition 25 °C for model 4-A_{opt} and 4_{opt}. - 257 -

Fig. 7.29. Total power generation, electrical power generation and fan power versus for the five optimal design points (P₁ to P₅ in Table 7.7 for low temperature condition 25 °C) for model 4-A and model 4. - 259 -

Fig. 7.30. Schematic of the flow behaviour in a typical offset strip fin array for design points P₁ and P₅ showing (a) the sectional top view of velocity contours for model 4-A_{opt} from a random point after the centre of the collector to the outlet. (b) The height of this sectional view is 3.1 mm from lower absorber plat to the lower tip of fins. - 260 -

LIST OF TABLES

Table 2.1. Temperature coefficient of the maximum output power for a different type of solar cell types [6, 7].	- 10 -
Table 2.2. Characteristics comparison of different circulation medium methods [119].31	
Table 3.1. Methods 1 and 2 to estimate the air gap temperature and the overall heat transfer coefficient in the enclosure.....	- 79 -
Table 3.2. Geometry factor in case of non- circular pipes under laminar flow regime condition	- 87 -
Table 4.1. Thermophysical properties of the PV/T air domains.....	- 114 -
Table 4.2. Specifications of the PV/T air systems.....	- 114 -
Table 4.3. Operating properties of the PV module BP 585 [31, 32, 35].	- 119 -
Table 4.4. Material properties of the layers of the PV module (BP 585) [31, 32, 35, 39, 342].	- 120 -
Table 4.5. Case 1 of model 4, with length, 1.24 m, 3D slice width of 15 mm, and depth of flow for the upper and lower duct of 0.025 m using the fully coupled and one-way coupled methods	- 124 -
Table 4.6. Single duct, single pass PV/T air collector within off-set fins staggered arrangement for symmetrical and original models	- 127 -
Table 4.7. Single duct single pass PV/T air collector within off-set fins staggered arrangement for the thin and thick fins.....	- 129 -
Table 4.8. Mesh parameters for thin and thick off-set fins staggered arrangement.-	129 -
Table 4.9. Equivalent thermophysical properties of the CFD domains.....	- 131 -
Table 4.10. Equivalent and original results for model 1 under free convection mode, $G = 1000 \text{ W m}^{-2}$ and $T_{amb} = 25$ and $50 \text{ }^\circ\text{C}$	- 132 -
Table 4.11. Tolerance independent tests.	- 133 -
Table 4.12. Key features of the structured and unstructured mesh models.	- 137 -
Table 4.13. Boundary conditions of [24].	- 144 -
Table 5.1. Grid independence test using structured and unstructured mesh element types for case study Fallujah on a typical day in July under transient conditions.	- 168 -
Table 5.2. Estimated maximum tracking angles (degree) values for Fallujah and Muscat cities.....	- 173 -
Table 5.3. Effect of length and tilt angle on convective heat transfer coefficient top and bottom surface of PV model in Fallujah 31 st of Jan at 13:00.	- 183 -
Table 6.1. Physical properties of the CFD domains.....	- 188 -
Table 6.2. SAH specifications for the experimental and CFD models.	- 189 -

Table 6.3. Experimental results for plain designs that are used in the validation between model C (2D CFD model) and model C-I (experimental model).....	194 -
Table 6.4. Structured mesh independent test analysis (free quad elements) for model C, using the boundary conditions $V = 2.254 \text{ m s}^{-1}$, $Re = 20000$, $G = 1000 \text{ W m}^{-2}$ and $T_{fi} = 35 \text{ }^{\circ}\text{C}$	196 -
Table 6.5. Unstructured mesh independent test analysis (free triangular elements) for model C, using the boundary conditions $V = 2.254 \text{ m s}^{-1}$, $Re = 20000$, $G = 1000 \text{ W m}^{-2}$ and $T_{fi} = 35 \text{ }^{\circ}\text{C}$	197 -
Table 6.6. Daily average of δT_{air} , T_p and η_{th}	208 -
Table 6.7. 2D CFD, 3D CFD and empirical equations predictions of the pressure drop and relative errors for design model C-I.....	213 -
Table 7.1. Boundary conditions of the grid independence test for model 4.	216 -
Table 7.2. Key features of the mesh structure for the grid independence test in Appendix B.	217 -
Table 7.3. Levels of the geometry design parameters used in the CFD design optimisation.	219 -
Table 7.4. Boundary conditions for different design parameters for models 2, 3, 4 and 5. -	223 -
Table 7.5. Fifty DOE points and their CFD results for four objective functions of model 4 for low temperature weather ($25 \text{ }^{\circ}\text{C}$).....	240 -
Table 7.6. Fifty DOE points and their CFD results for four objective functions of model 4 for high temperature weather ($45 \text{ }^{\circ}\text{C}$).	241 -
Table 7.7. PV/T design performance of model 4 at five operating conditions points located on the Pareto front together with CFD validation, as shown in Fig. 7.19 when operating at $25 \text{ }^{\circ}\text{C}$	245 -
Table 7.8. PV/T design performance of model 4 at five operating conditions points located on the Pareto front together with CFD validation, as shown in Fig. 7.20 when operating at $45 \text{ }^{\circ}\text{C}$	246 -
Table 7.9. PV/T design performance of model 4 at five operating conditions points located on the Pareto front together with CFD validation, as shown in Fig. 7.21 when operating at $25 \text{ }^{\circ}\text{C}$	248 -
Table 7.10. PV/T design performance of model 4 at five operating conditions points located on the Pareto front together with CFD validation, as shown in Fig. 7.22 when operating at $45 \text{ }^{\circ}\text{C}$	249 -
Table 7.11. Comparison between different PV and PV/T systems showing the impact of the temperature of the PV module on electrical efficiency under similar conditions for model 1_{STC} , model 1_{PV-25} , model 1_{PV-45} , model $4_{PV/T-25}$, model $4_{PV/T-45}$	250 -
Table 7.12. Dimensions and boundary conditions of model 4- A_{non} (fin gap examination). -	252 -
Table 7.13. Pressure drop and its percentage reduction for model 4- A_{non} and 4_{non} .-	253 -

Table 7.14. Total power generation, electrical power generation and fan power versus inlet air velocity for model 4-A_{non} and 4_{non}.- 255 -

Table 7.15. Total power generation, electrical power generation and fan power versus for the five optimal design points (P₁ to P₅ in Table 7.7 for low temperature condition 25 °C) for model 4-A and model 4.- 260 -

Table 7.16. A comparison between different PV and PV/T systems showing the impact of the temperature of the PV module on electrical efficiency under similar conditions for model 1_{STC}, model 1_{PV-25}, model 1_{PV-45}, model 4_{PV/T-25}, model 4_{PV/T-25} and model 4_{PV/T-45}.- 261 -

NOMENCLATURE

Symbol	Quantity	SI Unit
\dot{Q}_v	volumetric heat generation rate	$W m^{-3}$
\dot{Q}_{vd}	viscous dissipation	W
C_{th}	thermal capacity	$J ^\circ C^{-1}$
L_c	characteristic length	m
P_{er}	perimeter (wetted perimeter)	m
\dot{Q}	heat rate	W
Q_{vd}	viscous dissipation	W
\dot{S}	incident solar radiation	W
\bar{V}	mean (uniform) velocity	$m s^{-1}$
\dot{V}	flow rate	$m^3 s^{-1}$
c_p	specific heat capacity	$J kg^{-1} K^{-1}$
\dot{m}	mass flowrate	$kg s^{-1}$
q	heat transfer rate	W
δT_R	diurnal temperature range	K
P_{er}	wetted perimeter	m
A	area	m^2
D	diameter	m
E	percentage error	-
G	global solar radiation	$W m^{-2}$
h	heat transfer coefficient	$W m^{-2} K^{-1}$
hr	hour	-
L	length	m
\mathcal{L}	airflow path length from inlet to outlet	m
P	power	W
T	temperature	K or $^\circ C$
t	thickness	m
U	overall heat transfer coefficient	$W m^{-2} K^{-1}$
V	total velocity vector	$m s^{-1}$
c	specific heat capacity	$J kg^{-1} K^{-1}$
k	thermal conductivity	$W m^{-1} K^{-1}$
l	turbulence length scale	m
u	velocity component in x-direction	$m s^{-1}$
v	velocity component in y-direction	$m s^{-1}$
w	velocity component in z-direction	$m s^{-1}$
 Greek symbols		
σ	Stefan-Boltzmann constant (5.67×10^{-8})	$W m^{-2} K^{-4}$
β	tilt angle	Rad or degree
β_f	thermal expansion coefficient for fluid	-

β_{film}	thermal expansion coefficient for film layer	-
μ	dynamic viscosity	$\text{kg m}^{-1} \text{s}^{-1}$
δ	depth of flow	m
ϕ	independent fluid property	-
ρ	density	kg m^{-3}
ν	kinematic viscosity	$\text{m}^2 \text{s}^{-1}$
σ	Stefan-Boltzmann constant (5.67×10^{-8})	$\text{W m}^{-2} \text{K}^{-4}$
ρ	density	kg m^{-3}
ν	kinematic viscosity	$\text{m}^2 \text{s}^{-1}$
ε	emissivity	-
η	efficiency	-
τ	transmissivity	-

Non-dimensional Numbers

f	Fanning friction factor
gf	geometry factor
Pr	Prandtl number, $c_p \mu / k$
Re	Reynolds number, $4 \dot{m} / \mu P_{er}$
Pr	Prandtl number, $c_p \mu / k$
Ra	Rayleigh number, $\frac{g \beta_{film} \Delta T L_c^3}{\nu_{film}^2}$

Subscripts and superscripts

amb	ambient
bs	back surface of solar collector
c	cross-sectional, or characteristic value
D	depth
f	fluid domain or fan
fm	mean fluid
g	glass
h	hydraulic
fi	inlet fluid
ins	insulation
fo	outlet fluid
p	plate
s	solar or surface
th	thermal
u	useful heat gain
w	wind
ref	reference
$conv$	convection
rad	radiation

<i>g</i>	glass
<i>ted</i>	Tedlar
<i>tot</i>	total
<i>f</i>	fluid
<i>s</i>	solid

Abbreviations

AEQ	average element quality
Al	aluminium
CFD	computational fluid dynamics
Cu	copper
RMSE	root-mean-square error
PPMCC	Pearson correlation coefficient
RAC	recycled aluminium can(s)
SAH	solar air heater(s)
RT	relative tolerance
MEQ	minimum element quality
PV/T	photovoltaic/thermal
FSPM	free standing PV module
CFD	computational fluid dynamics
STC	standard conditions
EVA	ethylene-vinyl acetate
NOE	number of elements
DOF	degrees of freedom
TED	Tedlar
NOCT	nominal operating cell temperature

CHAPTER 1 INTRODUCTION

1.1 Background

The Earth is currently encountering a lot of environmental concerns and issues such as global warming and air pollution, mainly as a result of fossil fuel consumption. Energy researchers and utility companies have therefore conducted a wide range of research to find a sustainable and clean alternative approach to replace the dependence on fossil fuels. One key solution is renewable energy sources, such as solar, wind, biomass, tidal and geothermal energies. To compare the availability of fossil fuels with renewable energy sources, Fig. 1.1 shows that solar energy has the highest magnitude among all energy sources available on Earth. The power from the Sun received by the earth is approximately 1.8×10^{11} MW. This power is many thousand-folds larger than the present consumption rate on the Earth of all conventional energy sources.

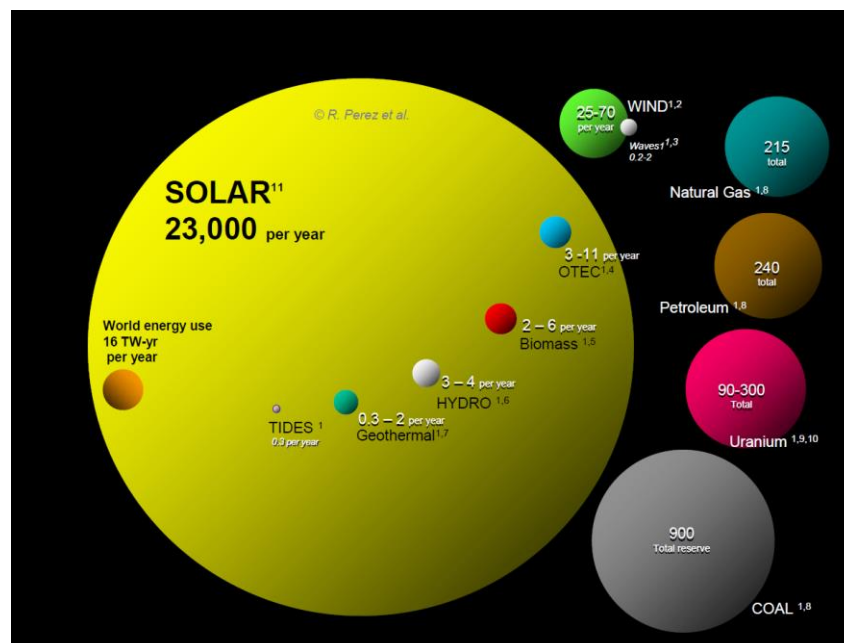


Fig. 1.1. Comparing finite and renewable planetary energy reserves (TW-yr)[1].

The applications of solar energy can be mainly divided into three categories:

- Solar energy collection systems (i.e. solar thermal collectors) which convert sunlight into thermal energy, for example, solar air/water heaters.
- Photovoltaic systems (PVs) which produce only electrical energy.
- PV/thermal (PV/T) collectors, which convert sunlight into electrical and thermal energies by coupling two systems into one hybrid PV/T solar collector. In this work, the emphasis is on PV/T air collectors in hot and cold weather conditions, see Fig. 1.2.

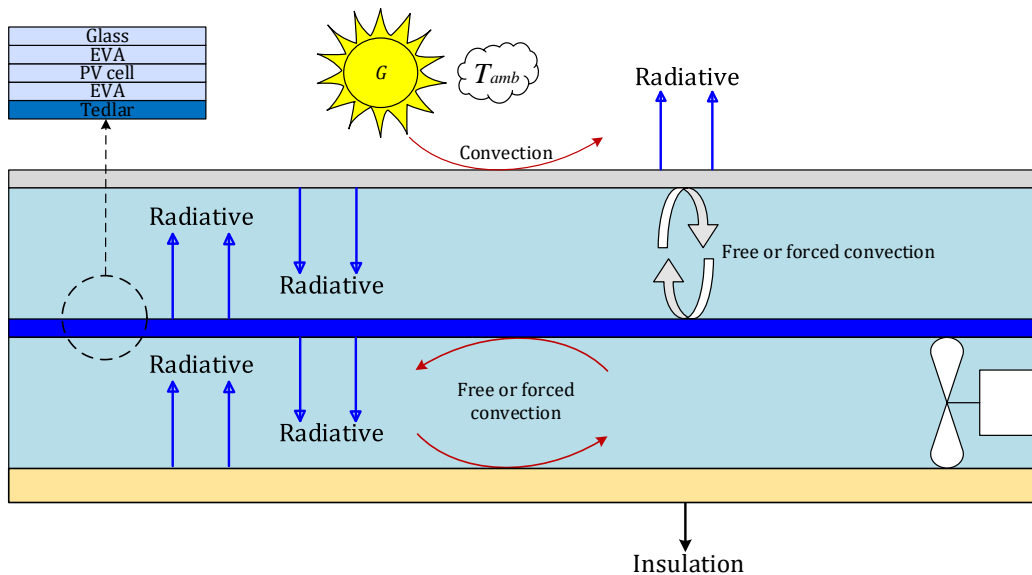


Fig. 1.2. Schematic of PV/T air collector

1.2 Problem statement

Photovoltaic systems (PVs) have witnessed exceptional development in the last two decades. PV, however, still suffer from the inherent drawback of low efficiency of between 7% and 24% at Standard Test Conditions (STC) (temperature and irradiance 25 °C and 1000 W m⁻²) compared to other solar systems, 30-75%.

The PV panel temperature is the main parameter affecting PV module efficiency. Overheating of the PV module leads to a reduction in its efficiency. This reduction can be attributed to a decline in the open-circuit voltage despite a slight increase in open-circuit current. Accordingly, reducing the temperature of the cell is necessary to enhance the electrical efficiency of PV cells.

The hybrid photovoltaic thermal (PV/T) collectors are used to control the PV cell temperature. Vast applications of PV/T technologies including solar thermal collector water/air or others coolants such as refrigerant, solar architecture technologies and integrated PV/T air systems.

Building-integrated PV/T air design is one of the most efficient techniques used to reduce the PV module temperature. This design is more efficient in low and moderate weather conditions where the ambient temperature is less than 25 °C compared to hotter weather. However, three challenges have faced PV/T air collectors. The first challenge is the fan power requirement which could consume the whole electrical generated from the PV module. The second challenge is extreme weather temperature, when well exceeding 25 °C in several parts of the world (e.g., temperature can reach 50 °C in the Middle East and South Asia). Finally, the poor heat capacity of air, which leads to poor thermal performance, compared to other coolants such as water.

1.3 Aim and objectives

This research aims to develop an efficient and affordable PV/T air collector design.

The optimisation of the PV/T air designs is first taken into consideration to minimise the fan power consumption and maximise both thermal and electrical efficiencies. Secondly, to overcome the extreme weather conditions, where the temperature reach 50 °C, by using exhausted air (precooled air) from building instead of using ambient air (hotter air). Thirdly to enhance the convective heat transfer rate of PV/T air system by suggesting a novel fin with minimum pressure penalty for PV/T air system. Consequently, the following objectives are set as milestones to achieve the research aim:

1. Develop a mathematical model to evaluate the thermal and electrical performance of a standard PV system without active cooling (model 1) using numerical methods under worst-case scenarios.
2. Develop a computational fluid dynamic (CFD) model to evaluate the thermal and electrical performance of a standard PV system without active cooling (model 1) under steady-state and transient conditions.
3. The mathematical model in point (1) is compared with the CFD models in point 2 for verification.
4. Once the CFD model is valid, this model is considered as a reference system PV/Ref (base data) to compare with the PV/T air models.

5. Develop mathematical models to evaluate the thermal, hydrodynamic and electrical performance of two PV/T air collector (models 2 and 3), in comparison with the CFD models. Analytical and numerical solution methods are used to model these two models.
6. Develop a mathematical model to estimate the weather conditions (solar radiation and ambient temperature) and validate it with commonly cited sets of data.
7. The mathematical models are solved using a script written in Matlab software.
8. Examine experimentally and numerically the effects of multi-pass configurations on the thermal and hydrodynamic performance of solar air collectors. This examination is used to ensure the accuracy of CFD solutions.
9. Examine experimentally the effect of staggered and in-line arrangements of extended surfaces to ascertain the optimum arrangement to be used in subsequent models.
10. The optimisation strategy is applied to design the best thermal, electrical and hydrodynamic PV/T air design among five models using the following steps:
 - a) Careful selection for design parameters.
 - b) Applying parametric study for five PV/T configurations.
 - c) The best PV/T air configuration in point (b) is employed in the optimisation process to maximise both thermal and electrical efficiencies and minimise the fan power consumption.
11. The optimisation model is integrated with offset strip fin in staggered arrangements to evaluate thermal and electrical performance using the optimal design parameters in point 10.

1.4 Contributions of the research

The specific contributions of this thesis can be summarised as:

1. Reduction in the computational time of CFD models using appropriate assumptions (Chapter 5).
2. Evaluate an accurate PV panel temperature for standard model without active cooling (model 1) using implicit mathematical model and steady -state and dynamic CFD models. Also, in this evaluation, include different criteria and conditions that have not been studied intensively (Chapter 6).
3. Examine the thermal performance of multipass solar air heater model including the recycle aluminium cans (RAC) with one pass double duct which has never been used before (Chapter 7).
4. Design optimisation of PV/T air collector (double pass double duct) model has never been achieved before, specifically using CFD modelling (Chapter 8).

5. Investigate the use of the off-set strip fins with optimal design (model) in staggered arrangements (Chapter 8).
6. The use of pre-cooled air from the building (exhausting air) instead of using ambient air particularly in extreme weather conditions can be considered the most significant contribution in this work, which has never exploited this technique with this type of design (Chapter 8).
7. Comparison between analytical, numerical and CFD models could contribute to enhancing the accuracy of the solution (Chapter 5).
8. Develop a novel mathematical model to estimate the free convective heat transfer coefficient and air gap temperature in the enclosure (Chapter 4).

1.5 Thesis structure

This thesis consists of nine chapters. An overview of photovoltaic, solar thermal and photovoltaic/thermal (PV/T) systems is presented in Chapter 2. This includes various categories of PV and PV/T systems. For each category, the basic concepts, advantages and limitations are discussed. The motivation of the thesis is built upon the findings of this chapter.

In Chapter 3, the mathematical formulation for two PV/T air collectors are first derived using simple heat balance technique. The first model is a single duct single pass (unglazed) PV/T air collector (model 2) while the second one is similar to model 2 but glazed (model 3). Two methods are used to solve the heat balance equations. The methods are semi-analytical and Predictor-Corrector methods. After that, the heat transfer and fluid flow equations are presented. These equations are used to estimate the heat losses and convective heat transfer coefficients to solve the heat balance equations of models 2 and 3. Mathematical formulation is then carried out to examine the free convection in the enclosure using different approaches, such as empirical and CFD approaches. While in Chapter 4, the CFD methodology used to solve the proposed PV/T air systems using COMSOL Multiphysics, including the mesh generation, comparison between two mesh types, assumptions and boundary conditions. Also, the methods used to reduce computation time are introduced. Finally, the validation and verification of different models are carried out in this chapter.

In Chapter 5, the performance evaluation of standard PV module using different approaches, including mathematical and numerical models is performed. The seasonal weather conditions, including incident solar radiation and ambient temperature are estimated and

validated. The numerical results are validated with experimental observations and verified with the current mathematical model. In Chapter 6, the numerical and experimental methods are used to examine the performance of the multi-pass solar air heaters (SAH) with and without turbulators. The CFD model has been developed using COMSOL Multiphysics v5.3a software to examine the thermal performance of three types of SAH (models A, B and C). The experimental measurement is conducted for the validation of model C. based on this examination, model C is chosen and has three design modifications, namely, model C-I, model C-II and model C-III for evaluating the different arrangements of this turbulators. The evaluation of PV/T air systems is conducted in Chapter 7. This evaluation is based on CFD design optimization of multi-pass PV/T air systems to investigate the optimum PV/T design. This optimization studies the significance of the temperature operating conditions at low and high temperatures in the geographical regions. After that, the examination of the best optimum model is coupling with off-set strip fins in staggered arrangements. The thesis findings are summarised in Chapter 8. Outlook resulting from this study and offers of recommendations for future work are also presented in this chapter.

CHAPTER 2 LITERATURE REVIEW

2.1 Introduction

Solar panels are amongst key innovations in renewable energy research during the last century [2]. Charles Fritts was the first researcher to create a PV cell in 1883 with up to 1% electrical efficiency [2]. Modern-day solar cell efficiencies reach 22%.

In recent years, there has been increasing interest in using solar PV systems [3], see Fig. 2.1. It is clear from the figure that the use of PV technology in the UK rose significantly between 2011 and 2014, where installed capacity has approximately doubled each year. Before 2000, the installed capacity was virtually non-existent, owing to the relatively low efficiency and prohibitively high cost. One reason for the low efficiency was owing to the PV cells being operated at a temperature above the design or standard conditions (STC).

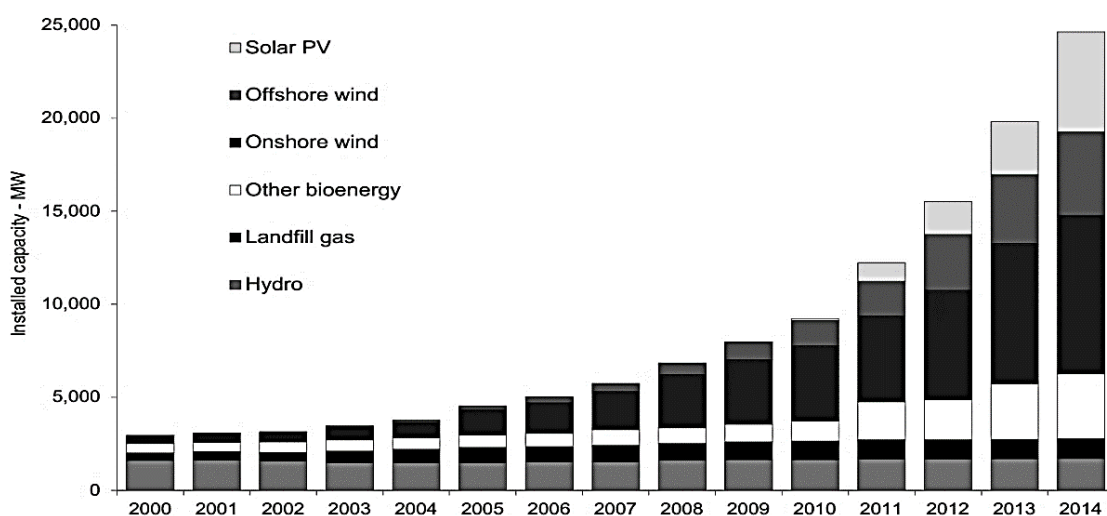


Fig. 2.1. Electricity generation capacity of renewable energy plant since 2000 [3].

In this chapter, a comprehensive review of PV and PV/thermal (PV/T) systems are presented. This includes various categories of PV and PV/T systems. For each type of PV/T system, the basic concepts, design, cooling techniques, applications, advantages and limitations of PV/T are discussed. The comparison between different PV/T types under the

same conditions is presented. After that, the emphasis on PV/T air collectors by reviewing the early work of PV/T air collector. In addition, the design parameters affecting the performance of PV/T are reviewed. Then, approaches that can be typically used to solve heat transfer problems are detailed. Furthermore, each category is discussed in detail as sub-sections using available published literature. Thus the motivation of this research is built on the findings of this chapter.

2.2 Photovoltaic systems

Solar panels are formed of photovoltaic cells. Simply broken down “Photo” implies light and “voltaic” relates to the production of electricity. Photovoltaic technology enables the production of electricity using light. PV cells typically consist of two layers of semiconductors. The layers are P-type semiconductor which has available electron-holes (+), and the N-type semiconductor has free electrons (-). When the two semiconductors are placed back-to-back, a potential difference is created in a region called the P-N junction. When the insolation or light falls on the semiconductor, the electric field across the junction between these two layers causes current to flow (see Fig. 2.2). The electricity created is multiplied by a number of cells to build panel or module. PV array comprises a number of panels, and each panel almost consists of six layers, as shown in Fig. 2.3 [4]. In the next section, the examination of different PV cell types is discussed, including the temperature coefficient and cell efficiency. Based on this examination, the PV cell type is chosen to integrate with PV/T systems in this study.

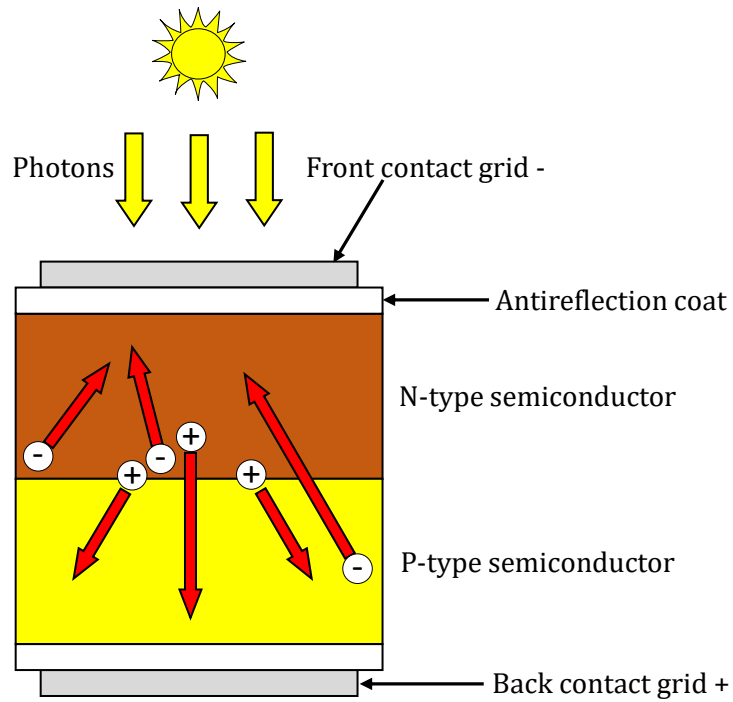


Fig. 2.2. Schematic diagram of the principle of PV cells.

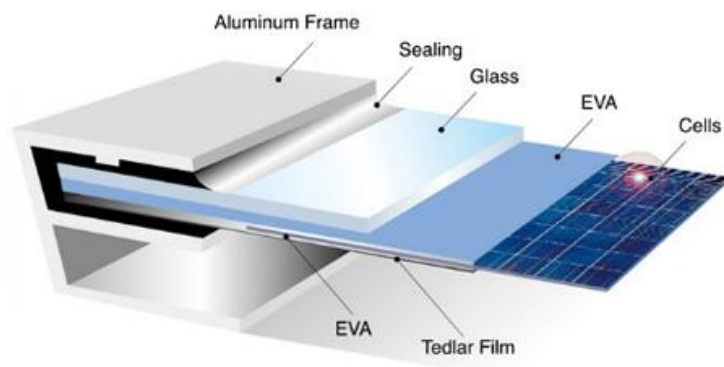


Fig. 2.3. Schematic of the standard PV module [4].

2.3 Types of PV technology

In the last three decades, there has been a rapid improvement in the field of solar PV technology. Many sorts of PV panels are available today. In this section, the general overview of the current types of PV panels is considered. The PV systems can be classified into four groups based on the type of material [5], as presented in Fig. 2.4.

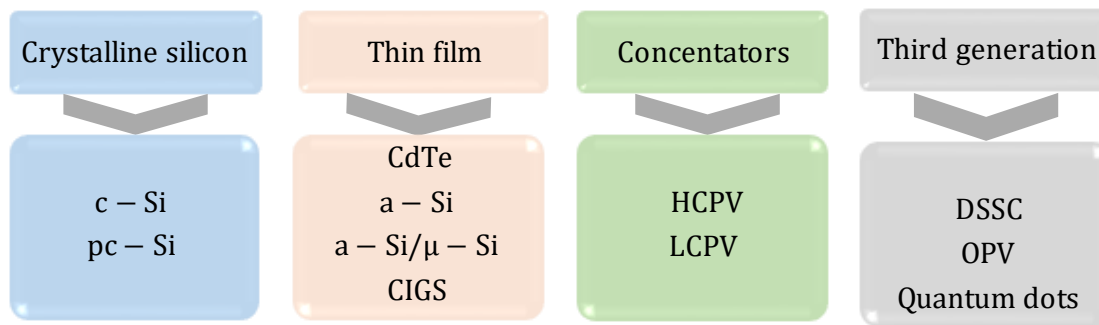


Fig. 2.4. Classification of photovoltaic technologies.

In this study, the emphasis is given to crystalline silicon cells because its temperature coefficients are higher than other types, see Table 2.1. For example, the c-Si and pc-Si, the electrical efficiencies are decreased by about 0.45 % °C⁻¹ while the a-Si, the electrical efficiency decreases about 0.25 % °C⁻¹. According to this, it is valuable to find a way to improve the Si cell efficiency by reducing the PV cell temperature, which is the bulk of the attention in this study.

Table 2.1. Temperature coefficient of the maximum output power for a different type of solar cell types [6, 7].

cell type	c-Si	c-Si	c-Si	pc-Si	pc-Si	CIS	CdTe
% °C ⁻¹	-0.469	-0.388	-0.427	-0.401	-0.431	-0.484	-0.035

2.3.1 Crystalline silicon photovoltaics

These can be divided into two main types. These types are as follows:

2.3.1.1 Polycrystalline silicon

Polycrystalline silicon, also called polysilicon or pc-Si or multi-crystalline silicon as well, or m-Si for short. The poly-Si PV is relatively cheaper product than monocrystalline silicon; owing to more straightforward manufacturing process required (see Fig. 2.5a). They are with average efficiencies about 18.5 % ± 0.4 [5, 8].

2.3.1.2 Monocrystalline silicon

It is also called single-crystal silicon, or c-Si for short. Mono c-Si cells are made from pure monocrystalline Silicon. The principal advantage is that it has relatively high efficiency. This efficiency is typically around 22.9 ± 0.6 [8]. However, the manufacturing process of these

cells needs to be more complicated compared with other technologies such as polycrystalline silicon cells; resulting slightly in a higher cost in comparison to others. Moreover, C-Si has a higher temperature coefficient, and its efficiency drops to about $0.45\% \text{ } ^\circ\text{C}^{-1}$, which means that the efficiency drops with higher temperatures more than polycrystalline silicon [5-8] (see Fig. 2.5b).

2.3.2 Thin-film photovoltaics

The thin-film technology with the most significant potential for efficiency improvement and, concerning Building-Integrated Photovoltaics (BIPV), offers attractive fields of future application [9]. Thin-film cells can be divided into four categories: Cadmium Telluride (CdTe), Amorphous Silicon (a-Si), Microcrystalline Silicon layer above the amorphous layer (a-Si/ μ -Si) and Copper Indium Gallium Selenide (CIGS) (see Fig. 2.5c) [9]. The efficiency is typically around 11.0% [10]. The temperature coefficient is lower than pc-Si and c-Si.

2.3.3 Concentrator photovoltaics

Concentrator photovoltaics (CPV) is a photovoltaic technology that produces electricity from sunlight. In contrast to traditional PVs, it utilises lenses and curved mirrors to concentrate insolation onto small, but highly efficient [11]. Two main types of CPV are high concentrator photovoltaics (HCPV) and low concentration PV (LCPV) [12]. This kind of solar technology can be thus used in smaller areas.

2.3.4 Third-generation photovoltaics

Third-generation photovoltaic cells are solar cells that are potentially able to overcome the Shockley–Queisser (SQ) limit of 31–41% power efficiency for single bandgap solar cells. SQ limit refers to “the maximum theoretical efficiency of a solar cell using a P-N junction to collect power from the cell” [13]. Dye-Sensitised Solar Cells (DSSC), Organic solar cell (OPV) and Quantum dots are the main types of third-generation PVs.

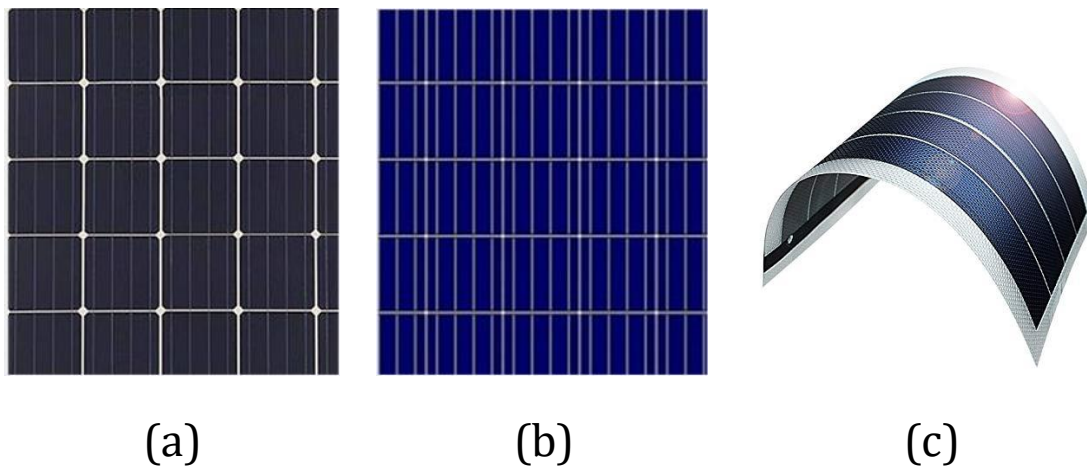


Fig. 2.5. Types of PV modules, in (a) Mono c-Si, (b) Poly-Si and (c) Thin-film [14].

According to Ling et al. [15], the maximum output power of PV modules under 1000 W m^{-2} declined from 240 to 196 W when the temperature increase from 0 to 75 °C. It is usually assumed that when the PV module temperature is above 25 °C, the efficiency of crystalline silicon drops by roughly 0.4–0.65 % [16, 17]. The utilising of the PV/T technology is used to maintain the temperature at an optimal range [18, 19].

Before proceeding to review the hybrid PV/T systems, in the next sections, firstly the examination of main methods that are used to assess the performance of standard PV module without active cooling which is subjected to ambient conditions (Section 2.4). Secondly, solar thermal air collectors are discussed, including the effect of multipass configurations and extended surfaces to the best of our knowledge (Section 2.5).

2.4 Performance evaluation of standard PV modules

The temperature of the PV module is the main parameter influencing PV efficiency. Increase the temperature of the PV module more than the standard conditions (STC, 1000 W m^{-2} and 25 °C) leads to a reduction in PV efficiency. This reduction can be attributed to a decline in the open-circuit voltage despite a slight increase in open-circuit current [20]. For a free-standing PV module (FSPM), in which the PV module is subjected to ambient conditions without active cooling, such as in a crystalline PV system, the increase in temperature is about 1.8 °C for every 100 W m^{-2} . For every 1 °C rise in temperature, the power yield decreases by around 0.5% [21]. Overheating may also cause damage to adhesive seals, delamination and non-homogeneous temperatures (hot spots)[22].

Prediction of PV cell temperature of FSPM (T_{mpv}) is essential, because this is the main parameter in Eq. 2.1 used to estimate the performance of the module [19, 23-29].

$$\eta_{PV} = \eta_{ref} [1 - \beta_{ref} (T_{mpv} - T_{ref})], \quad \text{Eq. 2.1}$$

where η_{ref} is reference efficiency and β_{ref} is the temperature coefficient of power (K^{-1}) and these are provided by the PV manufacturer at STC. This predictive equation can also be used as a reference system PV/Ref (base data) to compare with the hybrid PV/T performance.

However, STC rarely occurs in real outdoor conditions. To study behaviour under real conditions, experimental work can be employed. However, limitations of this method are that it can be complex and time-consuming particularly when undertaking for an entire year. Nevertheless, experimental work is indispensable for validation purposes.

Mathematical and CFD modelling methods are therefore considered in this study, since they are affordable, feasible and less complex than experimental work. A considerable amount of literature has been published to estimate the PV cell/module temperature using these methods [30-47].

In terms of mathematical methods, explicit and implicit numerical methods are presented here. In the explicit method, the direct solution for the dependent variable can be directly calculated using known variables. Numerous studies have attempted to formulate the PV cell temperature using this method, a list of explicit methods were reviewed by Skoplaki and Palyvos [30] to estimate the PV temperature. As an example from this list, Ingersoll [48] theoretically developed an expression to estimate module temperature under steady state conditions. The results indicated that even though the measured data used in the validation was relatively limited, a good agreement has been found under wind speed of 1 m s^{-1} . However, the main weakness of this study is that it does not consider the heat transfer which takes place in the various layers of the PV module. Another example, King et al. [49] provided new testing approaches for characterising the electrical performance of PV panels and arrays. The authors' utilise these tests to estimate the cell/ module temperature. However, this correlation does not capture some parameters such as the effect of mounting configuration, wind direction, thermal radiation and the analysis of heat transfer modes.

The implicit method is used if the dependent variables are specified by involving the unknown variable, in the left and right sides of the sets of equations. The solution, in this case, needs an iterative technique, which increases complexity, but is more accurate. A list of implicit methods was also given in Skoplaki and Palyvos [30]. For example, a simple energy balance on a unit area of a PV module is employed to implicitly predict the

temperature of the PV module [6]. The correlation is a function of local wind and ambient weather including insolation and ambient temperature under real and Nominal Operating Conditions (NOCT). These conditions occur when solar radiation of 800 W m^{-2} , ambient temperature of 20°C , tilt angle of 45° , wind speed of 1 m s^{-1} and zero electrical load [30, 33]. In design practice, the local wind speed varies and is seldom known with any certainty. Therefore, if the actual mounting is not the same as the one used in the nominal operating cell temperature test (T_{NOCT}), then estimates given by [50] are likely to be inaccurate. Also, a major problem with this kind of method is that the authors do not consider the influence of the multiple layers of the PV module.

Other methods are based on empirical correlations [51-53]. These correlations are functions of the ambient temperature (T_{amb}), type of semiconductor material and incident solar radiation (G). For example, Lasnier [52] created a formula, which is used for standard polycrystalline silicon (pc-Si) PV cell. Kalogirou and Tripanagnostopoulos [53] developed an expression for amorphous silicon (a-Si) PV cell. It should be noted that some parameters are not captured in these correlations such as wind effect and the heat loss coefficient. In terms of CFD modelling, several studies have been carried out to evaluate the PV panel performance as reported in [21, 31-33, 54-61].

2.5 Solar thermal systems

In contrast to PV technology, solar thermal systems do not produce electricity. Instead, they absorb solar radiation and produce heat. Solar air heaters (SAH) have been utilised in many industrial and domestic applications; for example, space heating and in drying processes for agricultural products, herbal medicines, and clothing [62, 63]. The performance of a SAH is influenced by the collector geometry (depth flow and length of collector), type of absorber surface (colour, roughness and material), glass cover plate (thickness, material and transparency) [64], and kind of flow regime (turbulent or laminar) [65-69]. Increasing the heat transfer rate of the SAH can be achieved by either increasing the absorber surface area or increasing the airflow [70]. While the latter will increase the heat transfer losses to the surroundings [71], they will also increase the pressure drop across the collector. A compromise approach is to use heat transfer augmentation techniques to the flat plate solar air collector, such as introducing turbulators into the air channel duct [72].

Many attempts were made to improve the performance of a double pass solar air heater by integration with extended surfaces (obstacles, fins, or turbulators) [73-75]. For example, some attempts were made to cause air turbulence in the channels using baffles or ribs [76-

78]. The presence of obstacles in the air channels had significant enhancement of the convective [79-82] heat transfers. This was attributed to the increase of heat transfer surface area along with the airflow around the fin absorbing plates. In [83], a double pass SAH with a thermal storage system was investigated, where paraffin wax was used as a thermal storage medium, resulting in higher thermal efficiency. Karwa and Srivastava [84] presented a comparison between the thermal efficiencies of a roughened and smooth duct SAH. It was found that the roughness on the airflow side of the absorber plate improved the thermal performance of the SAH by 26% higher than that of a smooth duct air heater, with the highest gain found at the lowest mass flux of $0.01 \text{ kg s}^{-1} \text{ m}^{-2}$.

In [85] a single pass SAH design was presented for improving the thermal efficiency of the system by increasing the solar intensity and flowrate and created maximum efficiencies of 40.02% and 51.50% for the flowrates 0.012 and 0.016 kg s^{-1} , respectively. Paraschiv et al. [86] tested various configurations of the absorber and airflow rates through the collector. They found that thermal efficiency increased with greater airflow rate and solar radiation. The average thermal efficiencies for typical airflow rates 0.025 and 0.045 kg s^{-1} were 47% and 63%, respectively. Chabane et al. [87] experimentally investigated the effect of longitudinally arranged fins on the thermal performance of a single pass SAH. The thermal efficiency was studied at two airflow rates, 0.012 and 0.016 kg s^{-1} , giving maximum efficiencies of 51.50% and 43.94%, respectively. Tyagi et al. [88] experimentally evaluated the performance of a flat plate SAH subject to various flow pathways (over flow, under flow and double pass) at different airflow rates of 0.014 , 0.0279 and 0.042 kg s^{-1} . For a double pass flow pattern at high flowrates, a higher thermal efficiency and heat gain by air were recorded, compared with the other two flow patterns.

In [89], a new approach was introduced for a SAH with conical springs placed on the absorber plate for airflow rates of 0.06 and 0.07 kg s^{-1} . The maximum thermal efficiencies attained were 50.4 and 65.9%, respectively, for both Type I (without conical springs) and Type II (with conical springs). The conical springs worked as turbulators, contributing to the heat transfer enhancement for Type II compared to Type I. Ramani et al. [90] carried out experimental and theoretical studies to analyse the effect of a double pass SAH with and without a porous material. The findings of this study revealed that the thermal efficiency of the system with a porous medium is up to 25% higher than that of the same system without the porous medium, and up to 35% higher than that of the system using a single pass solar air collector. Further studies used an extended surface area (ribs or a wavy configuration) with different arrangements positioned under the absorber for heat transfer enhancement [91, 92].

The comprehensive study of Alvarez et al. [93] was the first of its type for utilizing recycled aluminium cans (RAC). A comparison was made among six configurations of solar air systems, where RAC showed the highest efficiency [94-98]. Ozgen et al. [99] experimentally investigated the performance of a double pass solar air collector using RAC with different arrangements, namely: flat (without cans), corrugated (staggered) pattern and longitudinal. The authors found that the corrugated arrangement had the optimum performance among all collectors at airflow rate of 0.05 kg s^{-1} . Based on the latter study, Esen et al. [100] modelled the performance of a double pass solar air collector including RAC using dimensionless methods, called 'artificial neural network' and 'wavelet neural network' models, with fairly consistent findings [99]. It can be concluded that the thermal efficiency of multipass solar air heater is generally improved compared to the single pass, which is attributed to increasing the surface area without adding extra costs. In particular, the thermal performance of a single duct double pass solar air heater (U-flow shape) shows higher efficiency than other multi-pass types [101], particularly with staggered finned arrangements [102].

To the best of our knowledge, only limited studies are available in the literature for the impact of RAC on the SAH performance. Also, the influence of RAC with a single duct double pass solar air collector (U-flow shape) on the system performance has not been given enough attention in the past, which has motivated this study. Thus, the current study is focused on the impact of increasing turbulence in the airflow on the thermal performance of a single duct double pass solar air collector (U-flow shape) using RAC as air-flow obstacles.

2.6 Hybrid PV/T systems

PV/T system is a solar thermal collector which allows producing heat as well as electricity simultaneously. The main purpose of using PV/T is to collect waste energy from the PV module and to reduce the PV cell temperature. The waste heat can be utilised for many applications. For example, Fig. 2.6 shows a solar PV/T water collector, placed beside to a commercially available solar thermal collector and a solar photovoltaic module. The solar PV/T collector combines the solar thermal and solar photovoltaic technology in a single unit, thereby producing overall higher efficiency with less roof-space [18]. Thus, the main function of PV/T system is to keep the temperature of PV panel in the range of optimal conditions which in turn, retain the electrical efficiency an acceptable level [103, 104]. It is worth mentioning that the solar cells can withstand temperatures around $220 \text{ }^{\circ}\text{C}$ [105]. The PV panel is therefore considered as a good thermal absorber plate.



Fig. 2.6. Flat plate PV/T water collector with the same sized separate flat plate water heater and PV module [18].

Several techniques of PV/T systems can be used to reduce the PV panel temperature. Each technique has different applications, advantages, drawbacks and range of delivery temperatures. It is crucial to assess the significance of each type of PV/T system in terms of cooling capability. For example, Farahat [106] implemented experimental tests to evaluate the cooling capability of two techniques for concentrator PV cells using water and heat pipe cooling. This comparison examined the significance of real cell temperature on the performance of PV cells by monitoring the electrical characteristics of PV cells when both cooling techniques are working at the same time and conditions. The results revealed that the impact of temperature on the open-circuit voltage, which tends to drop, whereas the short circuit current increased slightly with the rise in temperature. A comparison of the annual yield of different configurations also reported that reducing the temperature of PV cells provided a more reliable thermal performance when heat pipe cooling is applied [106].

Comparatively, in the case of a standard PV panel where the PV module subject to ambient conditions without active cooling, the increase in temperature will be $1.8\text{ }^{\circ}\text{C}$ for every 100 W m^{-2} consequently, the range of PV panel efficiency could be only 8 to 9% [21]. Concerning the PV module, which is actively cooled, then the module temperature increases only $1.4\text{ }^{\circ}\text{C}$ for every 100 W m^{-2} , leading to an increase in efficiency between 12% and 14%. This increases the complexity and cost of the completed product.

Nevertheless, the energy payback period and the annual energy output per unit area have substantial improvement [21]. For a moderate insolation value 749 W m^{-2} , and an ambient

temperature of 8 to 9 °C, the average cell temperature was reduced from 52 °C to 18 °C, by cooling with cold water at 10 °C to 12 °C [107]. Another example, PV/T air system is usually used because it is less weight and design requirements and also affordable. However, the more effective is the PV/T water method because the heat capacity and density of water are thousandfold greater magnitude [18, 62, 108].

The general merits of PV/T systems can be listed as [109-113]:

1. Dual-use: the hybrid (combined) system can be used to generate electricity and heat power.
2. Efficient and practical: the overall efficiency is always higher than utilising two separate systems and is especially desired in building coupled PV (BIPV) when roof-panel spacing is finite.
3. Widespread application: the heat generated can be employed both for heating and cooling (desiccant cooling) applications which depend on of the season and substantially being convenient for domestic applications.
4. Affordable and flexible: it can be modified/installed to building without the need for any amendments. This leads to reducing the payback period. As an example, an investigation has been carried out in an Italian climate proving that the payback time for PV/T collectors is significantly lower than for individual systems [112, 114, 115].
5. Owing to the fact that merely one type of system has to be installed instead of two, a reduction of installation costs is possible [116]. Although the combined PV/T system reduces the overall efficiency because of the high solar reflectance and high infrared emission, this system saves area in roof building as well as increase the overall energy efficiency [18, 107, 117, 118].

Moreover, the comparison showed that the reduced thermal efficiency of the PV/T system was also attributed to [107].

- The available solar energy reduced by the fraction converted to electricity by the PV cells.
- Lower optical absorption of PV compared to the black thermal absorber.
- Increased heat transfer resistance introduced between the cell and absorber [18].

2.7 Classification of PV/T systems

PV/T systems can be categorised basically on two main aspects. The first aspect is the structure, and the second aspect is heat removal fluid (HRF). In terms of structure, the units could be subdivided as a flat plate, concentrated and building integrated types. According

to the HRF, the PV/T systems can be classified as air, water, refrigerant and heat-pipe [119]. The classification of PV/T systems depend on the HRF is discussed in the next section, as shown in Fig. 2.7.

2.7.1 PV/T air collectors

PV/T air collectors are similar to solar air collectors except that the thermal absorber plate is replaced with a solar PV module, as shown in Fig. 2.8. The use of PV/T air collectors can deliver different ranges of temperature through using either forced or natural technique 30-55 °C [62, 120-122]. Also, better thermal performance can offer with forced circulation than natural ones since it can enhance the convective and conductive heat transfer. However, fan power consumption decreases the net electricity output [123]. PV/T air system is not convenient and efficient if the environment temperature is above 20 °C because air could not work as a coolant but as heater and the temperature of PV panel will increase significantly [18, 53, 124]. Different design concepts have been demonstrated by researchers concerning air flow patterns, glazed and unglazed to attain high efficiency of PV modules (Fig. 2.9)[24, 27, 119, 120, 125, 126].

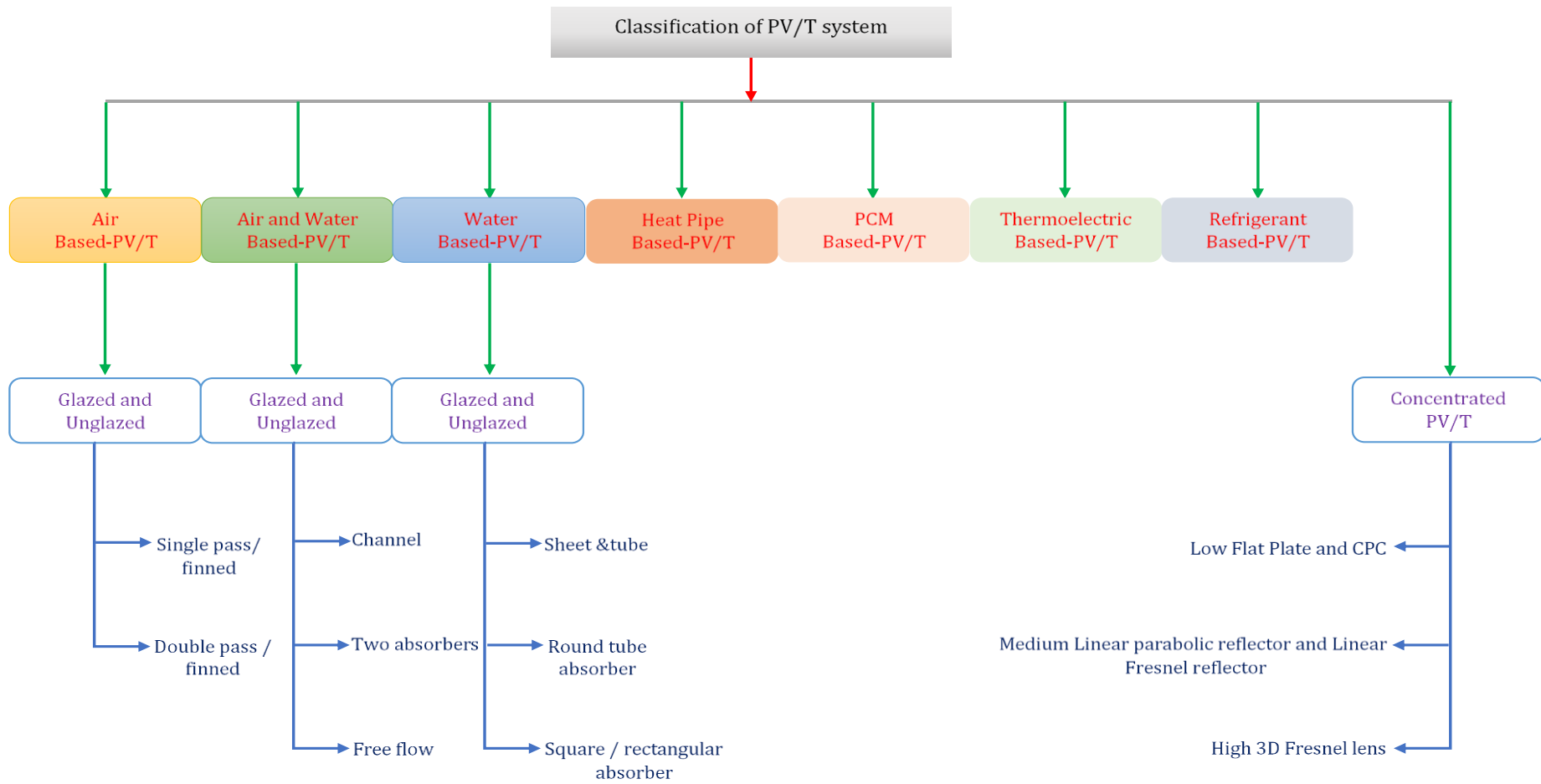
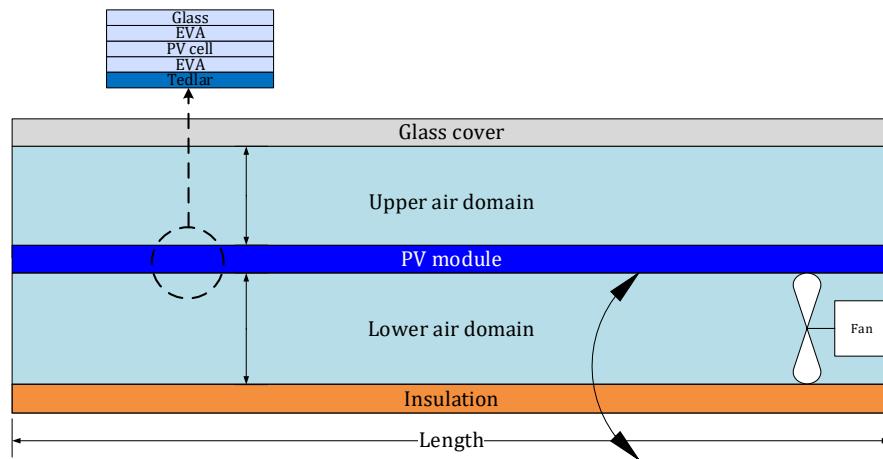


Fig. 2.7. Classification of the PV/T systems adapted from [127].



Remove the thermal absorber plate and replace it by a PV module

Fig. 2.8. Common parts of the flat plate PV/T collector.

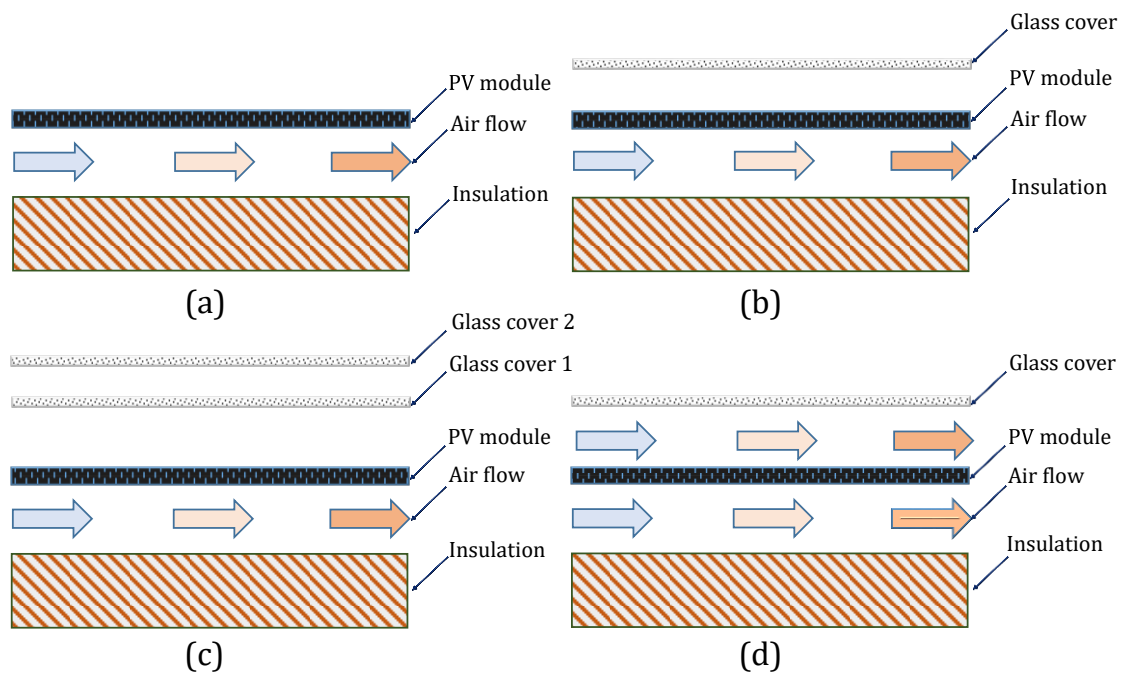


Fig. 2.9. Cross-sections of PV/T air systems, (a) Unglazed PV/T air collector, (b) Single glazed PV/T air collector, (c) Double glazed PV/T air collector, (d) Glazed PV/T air collector double pass, inferred from [119, 122, 128].

2.7.1.1 Advantages and drawbacks

In comparison with PV/T water systems. It can be highlighted a number of significant points as presented below [112, 129]:

1. The corrosion problems are serious in solar water heaters while are virtually non-existent with a solar air heater.
2. The leakage of air from the ducts or the heater connection does not present a serious problem.
3. No chemicals for antifreeze are needed, and in case of damage, they do not cause a significant loss for the building.
4. The complexity and weight are considered less than other systems such as water and refrigerant PV/T systems. This reduces the inherently high cost of systems if solar collectors are integrated into a building structure.

Besides the advantages of the solar air systems, the following limitations can be considered and should be carefully studied [62, 108, 111, 130, 131]:

1. Air has minimal heat capacity (ρcp) in comparison with water (air $\cong 1.044 \text{ kJ m}^{-3} \text{ K}^{-1}$, water $\cong 4200 \text{ kJ m}^{-3} \text{ K}^{-1}$) [132].
2. It has a relatively high power requirement and, without accurate design, the duct costs can also be high.
3. Storage of energy with solar air heating systems faces problems that are different from the storage of solar water heating
4. The cost of maintenance and noise levels are higher than natural systems
5. In low latitude regions such as Thailand, Laos, Vietnam and Indonesia with latitude between the range of $15^\circ - 23^\circ \text{ N}$, the use of PV/T air collectors in terms of effective electrical production is limited as the temperature is more than 20° C during six months of a year. In contrast to the UK with latitude $50^\circ - 57^\circ \text{ N}$ and ambient air temperature of $6 - 19^\circ \text{ C}$ making the use effective. However, the intensity of solar radiation values is low such as UK [133] (The UK's annual insolation is in the range of $750-1100 \text{ kWh m}^{-2}$).

2.7.2 PV/T water collectors

PV/T water module is a solar water collector with a new PV layer installed on the top of water heat exchanger utilising either naturally (thermosyphon operation or gravity-assisted circulation) or mechanically (gravity-circulation pumps). Fig. 2.10 presents the main types and components of the PV/T water. A wealth research has been achieved in different designs of the PV/T waters [116]. These systems are recognised from each other by differing piping systems (sheet and tube or channels), type of absorbers and number of glass covers.

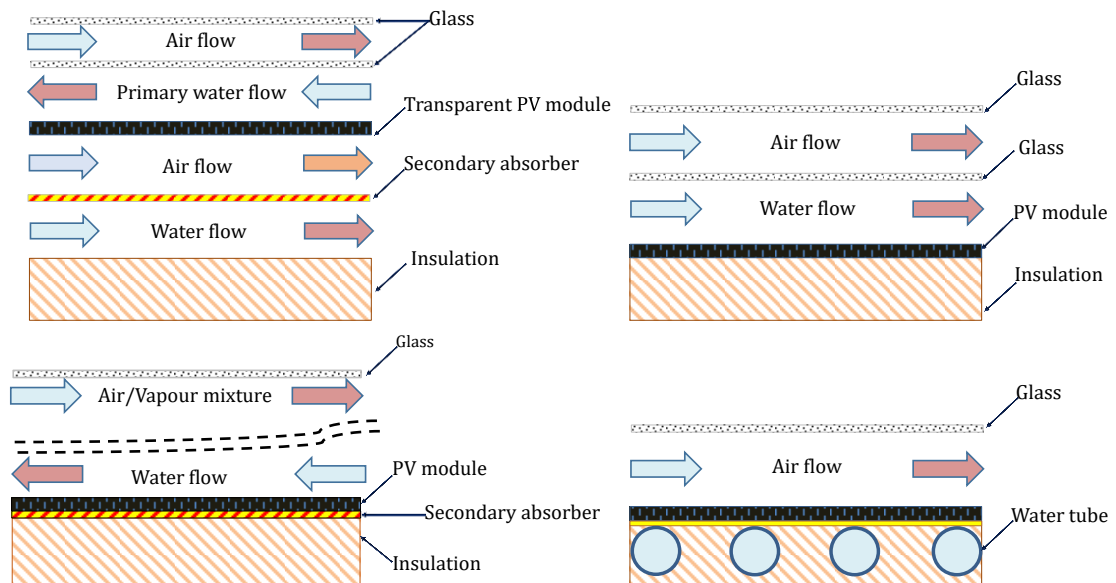


Fig. 2.10. Types of water PV/T collectors adapted [110, 116, 119].

2.7.2.1 Advantages and drawbacks

It can be listed some advantages and disadvantage of water PV/T system, as shown below: in term of advantages [111, 119, 120, 126, 134]:

- PV thermal water produces comparatively high heat transfer coefficients than natural and forced circulation of air operation.
- Higher mass flow rates compared to natural and forced circulation of air.
- Higher thermal conductivity and heat capacity of water compared to air.
- Higher temperature reduction.
- PV/T water collectors provide lower temperature fluctuations compared to PV/T air system making them more advantageous since this fluctuation offers unequal surface temperature distribution leading to an extra drop in electrical efficiency of PV panel [135].

Along with the advantages of the PV thermal water, the following can be regarded as drawbacks and should be considerably studied:

- Higher initial cost due to pumps and complexity in fabrication.
- Higher maintenance cost compared to forced air circulation.
- Higher electricity consumption compared to forced air circulation
- Leakage and pressurisation issues.

2.7.3 PV/T refrigerant collectors

In recent years, refrigerant-based PV/T heat pump systems have been investigated considerably [119] and have become a promising technology. The typical PV/T collector based refrigerant uses a PV/T evaporator in PV/T solar-assisted heat pumps (PV/T SAHP) as shown in which consists of four main parts as presented below:

- Compressor.
- Condenser.
- Evaporator.
- Refrigerant (coolant).

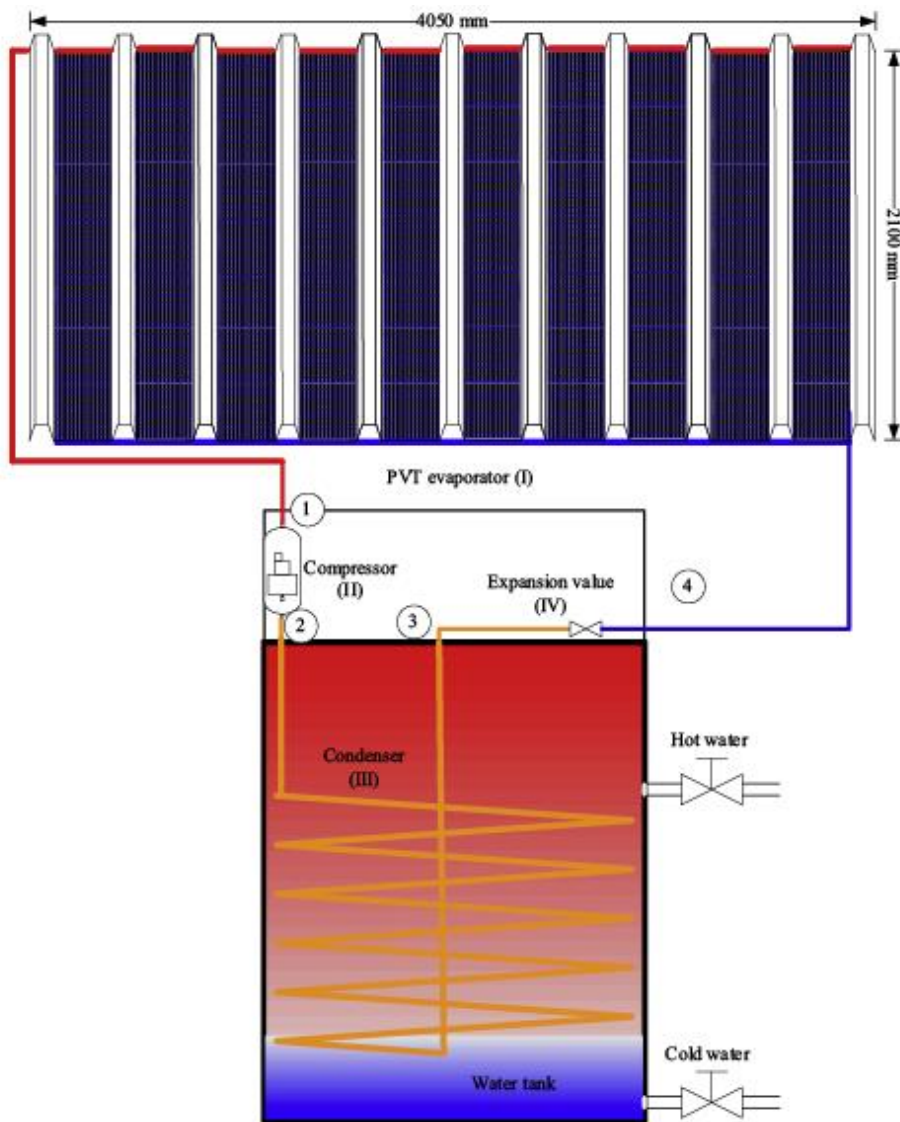


Fig. 2.11. Schematic diagram of the PV solar-assisted heat pump [136].

The basic concept is that the PV panel serves as an evaporator, where the coolant (refrigerant) absorbs thermal energy from incident solar radiation [137-139]. Also, the evaporator refrigeration effect is used to cool the solar cells, thus enhancing the performance of the PV panel. In addition, the portion of incident solar radiation is converted into electric energy by the photovoltaic effect. While, the remainder of insolation could be absorbed by the refrigerant fluid, which in turn increases the values of pressure and temperature of the coolant during the day leading to enhancement of the heat pump performance. Another function of the PV panel is to protect the evaporator from frosting at low-temperature climate.

The electrical power generated from photovoltaic units can supply to a compression vapour cycle machine achieving a direct conversion of sunlight into direct current [140]. The PV system is most appropriate for small capacity refrigeration plants used for food or medical applications in areas far from conventional energy sources [141], where a high level of solar radiation is present.

2.7.4 PV/T heat pipe collectors

The devices that merge the principles of both thermal conductivity and phase transition are called heat pipes. A standard heat pipe is shown in Fig. 2.12 and Fig. 2.13. Heat pipes offer an excellent solution for heat removal and transmission. The fundamental of design consists of two ends, the first one working as a thermal energy collector and the other end as a thermal energy discharger [120, 142]. Heat pipes consist of three sections [111, 143].

- The evaporated section (evaporator).
- The adiabatic section.
- The condensed section (condenser).

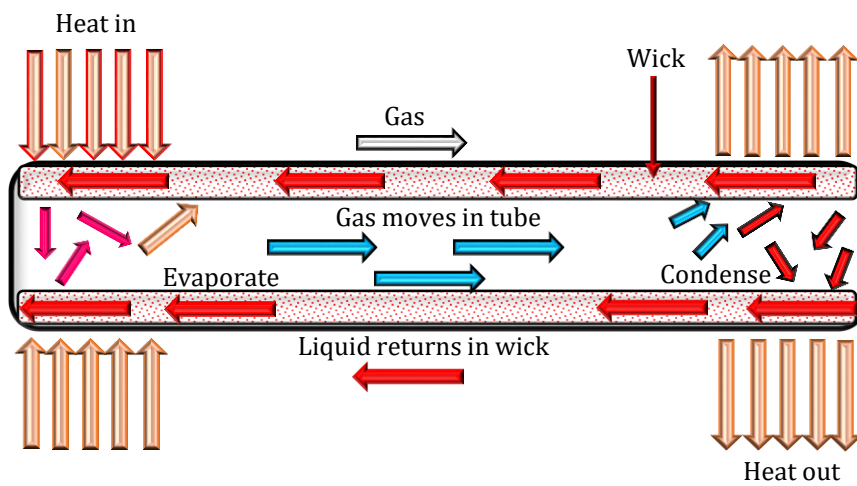


Fig. 2.12. Side view of conventional heat pipes adapted from [144].

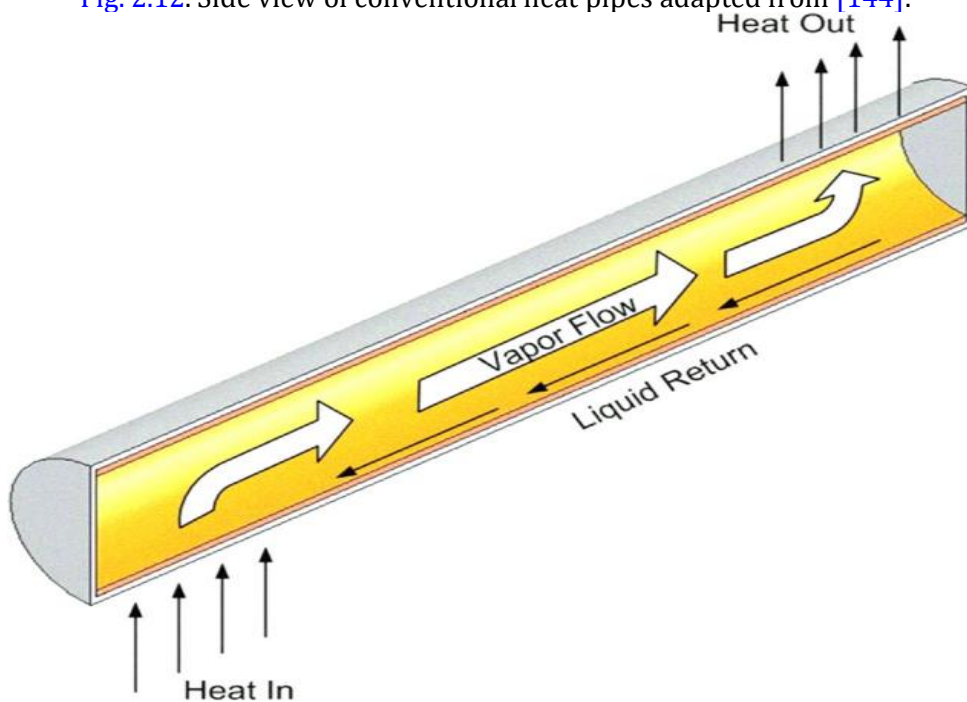


Fig. 2.13. Cross-section of a conventional heat pipe [145].

Heat pipes have been regarded for thermal management (electronic) applications specifically in a personal computer (PC) and PV technology. This is owing to the fact that heat pipes technique provides uniform temperature distribution, which, in turn, efficiently enhances the performance of PV cells [120, 144]. Avoidance of freezing that thermosyphon tube can also face from in higher latitudes, in addition to resistance to corrosion.

An example was patented by Zhao [146], this model consists of a PV layer and a flat plate heat pipe, including various microchannel arrays serving as the evaporation part of the heat

pipes. The other end of the heat pipe is the condensation part, which releases heat to the passing fluid, and the fluid within the section is condensed owing to the heat discharge [146]. The results revealed that the flat-plate design is more efficient owing to the excellent thermal contact between the PV panel and heat extraction devices, which results in a smaller thermal resistance and higher overall solar conversion efficiency. In this way, the PV efficiency could increase by 15–30% compared to the standard PVs if its surface temperature is regulated to around (40–50 °C). The overall solar conversion efficiency of the module was approximately 40% [146]. However, the design of efficient heat pipes requires a careful choice of container material, working fluid, and wick structure [120].

2.7.5 PV/T PCM collectors

Phase change materials (PCMs) latent heat storage can be obtained via four modes: liquid to solid, solid-to-liquid, solid to gas and liquid-to-gas phase change. However, only the solid-to-liquid change mode can be applied practically. Liquid to gas phase changes is unfeasible for use as thermal storage as the large volumes or high pressures needed when they are in the gas phase. Another example, liquid-to-gas changes has a higher heat of conversion than solid to liquid transitions. Finally, solid to solid phase mode is characteristically very slow and have a relatively low heat of conversion [147].

At first, the solid-to-liquid PCMs work as sensible heat storage (SHS) materials; absorbing heat will lead to an increase in temperature. Unlike typical SHS, however, when PCMs reach the temperature at which they change phase (melting points), they absorb considerable quantities of heat at an almost constant temperature. The PCM continues to absorb heat without a significant rise in temperature until all the material is transformed into the liquid phase (Fig. 2.14) [148].

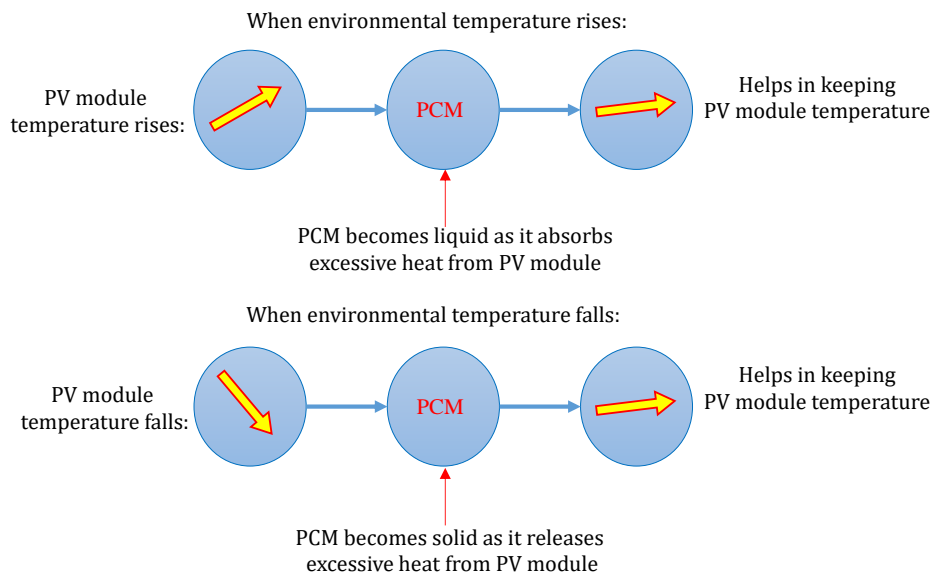


Fig. 2.14. Working of PCM adapted from [149]

Principally, to secure active and uniform cooling for PV systems and thermal management technologies, the following requirements should be taken into account [15, 150].

- Phase change temperature (PCT) (melting points) falling within the optimal range of standard operating temperature for PV thermal management technologies. Large latent heat, specific heat and thermal conductivity.
- Low volume expansion and low/no supercooling during freezing.
- Non-poisonous, non-corrosive, non-flammable, non-explosive and chemically stable.
- Low cost.

The main advantages of using this type of method are that [15, 120, 134, 142]:

- Higher heat transfer rates compared to both forced air circulation and forced water circulation.
- Higher heat absorption due to latent heating.
- Uniform cooling.
- Do not need a fan or pump in the case of the passive system while active cooling works to reduce the fan or pump consumption [15].
- Passive heat exchange.
- No maintenance cost.

The most common drawbacks of this method are that:

- High PCMs cost.

- Some PCMs are toxic.
- Some PCMs have fire safety concerns.
- Some PCMs are strongly corrosive.
- PCMs may have a disposal problem after their life cycle is complete.
- Low thermal conductivity.

2.7.6 Comparison between PV/T types

A specific comparison was made for four different types of PV/T systems by Zhang et al. [119] in terms of their technical characteristics, as demonstrated in Table 2.2. However, this comparison does not discuss PCM systems. The cooling methods are listed as follows:

1. PV/T air collectors.
2. PV/T water collectors.
3. Solar assisted heat pump (PV-SAHP).
4. Heat-pipe-based PV/T.

Four criteria are considered in this comparison, application, average efficiency, heat capacity and uniform cooling effect.

The combined efficiency for these types was evaluated based on the similar external conditions such as solar/weather conditions (i.e. typical weather condition on 22nd December in mid-east area of UK) and operational conditions (i.e. $0.01 \text{ kg m}^{-2} \text{ s}^{-1}$ of mass flow rate, 10% of initial PV efficiency). The models used in this comparison as follows:

- Indoor-simulator (IS) model for PV/T air design [151].
- Integrated PV/T system (IPVTS) model for PV/T water design [152].
- PV solar assisted heat pump (PV-SAHP) model for refrigerant-based PV/T [153].
- PV/ flat-plate heat pipe (PV/FPHP) model for heat-pipe-based PV/T [153].

It is thought that the PV/T air/water systems are more reliable and economical and therefore, considered to be more workable systems for the application. However, conventional thermal management technologies that use air or water are restricted because they have relatively low heat transfer coefficients. Thus, there is a PV temperature gradient (non-homogenous of temperature distribution) compared with PCMs and heat pipes circulation medium methods. Also, they have comparatively high capital and maintenance cost and intricacy of equipment. Moreover, Active forced air/water cooling need blowers or pumps and heat sinks, which may make the system complex and impractical [153].

The PV-SAHP systems have the advantage of lower working temperature and a more stable system which could considerably enhance the system's solar conversion efficiency. Whereas a heat pipe photovoltaic/thermal hybrid system can obtain heat from PV cells instantly and if the working temperature of the heat pipe fluid can be efficiently managed, the solar efficiency of the system could be significantly improved. While PCM principally using latent heat storage has seen much applications in thermal management technologies such as semiconductor chips. Yin et al. [154] set up PCM heat storage at the condensation section of the two heat pipes. In addition, compared with the conventional heatsink without PCM, the combination between a heatsink with PCM was capable of diminishing the peak temperature of the chip and improving the heat dissipation rate by 1.36–2.98 times [154].

Regarding applications of PV/T collectors, PV/T water system consumes 39%, and PV/T air design consumes 45%. The remaining types of PV/T collectors such as solar cooling (7%), industrial heating (6%), drying (3%) and pool heating (0.2%) [18]. The proportion aforementioned is based on mainly in the residential area with low energy (LEH) and high solar fraction SF houses, where PV/T can be coupled with a heat pump and multi-family buildings, with a restricted available roof area [18].

To conclude, these five techniques have their drawbacks that are identified in each associated sections. As referred to in earlier sections, there are various types of PV/T systems, including these materials, but more emphasis will be placed on PV/T air collectors in Section 2.8 Accordingly, this type is considered in more detail as it is the focus of this research work.

Table 2.2. Characteristics comparison of different circulation medium methods [119].

PV/T type	Average efficiency (%)	Advantage	Disadvantage
PV/T air collector	24–47	Low cost	Low heat capacity
		Plain design and construction	large air volume
			Poor thermal removal performance
			High heat loss
PV/T water collector	33–59	Relatively low cost	Non- uniform temperature distribution
		Direct contribution	Still-high PV temperature
		High thermal capacitance	Non- uniformity temperature distribution
		Low flow volume	Relatively complicated design
PV/T refrigerant collector	56–74	High reduction in PV temperature	Possible piping freezing
		Performance stability	Leakage problem
		High efficiency	Unbalanced liquid distribution
		High heat removal factor (FR)	Unfeasible for domestic application
PV/T heat pipe collectors	42–68	A promising system for thermal management technologies specifically using miniature compressors	Difficult to operate
		Homogeneous temperature distribution	Uniformity temperature distribution
		High reduction in PV temperature	High cost
		Stable performance	Risk of damage
		High solar efficiency	Complex structure
		Effective heat removal	Uniform temperature distribution

2.8 Early work of PV/T air collectors

Several works emphasised on the importance of the applications of PV/T air collectors. Therefore, the need to review some works that relate to the subject of interest. In this section, the early work of PV/T air collectors discussed. The purpose of presenting this section is to state the significance of the PV/T air system in previous decades. The initial research for the PV/T air system began in the 1970s [62, 113, 155-157]. For example, the first design of air PV/T system was created in 1978 by Wolf [113] who assessed the design and performance of PV/T air collector for a two floor structure, single family residence in Boston, U.S.A. This construction comprised a silicon solar array which merged and set up with non-concentrating thermal collector as one system. The total area was 50 m². For electricity storage purposes, a lead-acid type battery was used. For thermal storage purposes, a water tank was used [113]. Also, the author observed that although each part in hybrid system worked at an efficiency 10-20% less than which can be obtained in the case of running individually, the total output is significantly higher than a single system. Following Wolf [113], Raghuraman in 1979 [158] and also Florschuetz [159] included PV/T modelling in their works.

A relevant example, Hottel–Whillier model was modified by Florschuetz [159] to evaluate the performance of the hybrid system. The main purpose of establishing this modified system is to increase cell efficiency by decreasing the cell temperature using active and non-active cooling (free and forced convection) methods. It is found out that the use of a low thermal conductivity material such as glass in a back plate for the cells leads to reduce the heat transfer rate between the working fluid and the back surface of PV absorber; consequently, the panel is not considered as an effective fin [159].

Throughout the 1980s and 1990s, theoretical studies almost always have been a fundamental part of several investigations focused on the improvement of PV/T air collectors [160-174]. For instance, Cox and Raghuraman [175] employing modelling found a suitable combination of materials working to reduce heat emittance and enhance the solar absorptance in PV/T air systems. Bhargava et al. [161] studied the method that can be used to choose the required area to operate the fan. In other words, what is the adequate area of PV panel can provide to run the fan.

In the first years of the 2000s, Sopian et al. [128] and Hegazy [122] conducted theoretically different PV/T air collector configurations. Hegazy suggested that the model (III) exhibited better thermal and electrical efficiency than the other three models (Fig. 2.15). This is owing

to the enhanced heat removal factor from the PV panel. However, the model (IV) showed less electrical efficiency. This is because of the length of the collector is doubling, leading to an increase in the accumulation of heat and pressure drop. It can be seen that in the early work (before the 2000s), the parameters taken into considerations were limited compared to research work in PV/T systems after 2000s. Before the 2000s, the available facilities such as simulation programs and measurement devices were of limited capabilities.

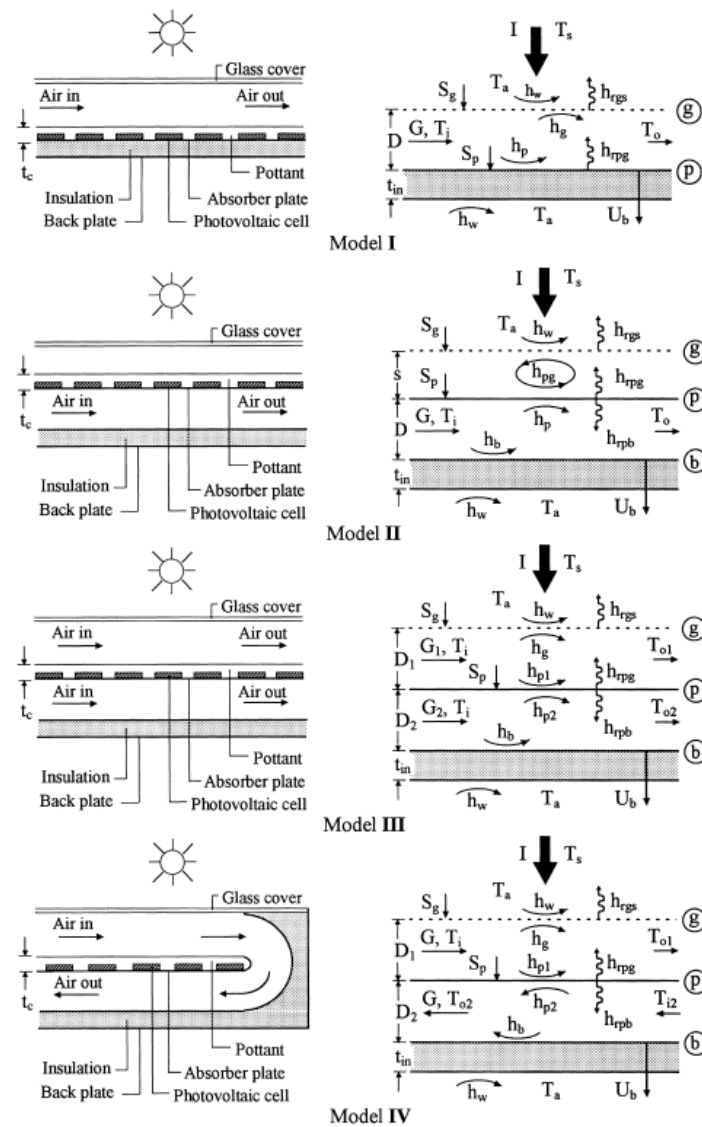


Fig. 2.15. Schematics of the different PV/T air designs side by side with heat transfer coefficients [122].

After the 2000s, impressive developments have introduced better facilities to the researchers and professionals, for example, high-performance computers and computer simulation programs such as MATLAB, EES, Comsol and ANSYS-FLUENT. As a result of the above, the research work has been specified in studying the parameters and performance.

Therefore, in the next sections, the review of air PV/T systems are based on the parameters influencing their performance.

2.9 Key design parameters

The impact of design parameters on the performance of PV/T air collectors is presented in this section. Examining these parameters provide an understanding of how they influence the design and in turn, the performance of a PV/T system. Also, this is useful for simple and optimised PV/T collectors. Several parameters have been adopted and studied over the last two decades in order to enhance the electrical and thermal performance for PV/T systems such as the geometry and operational parameters. This section will focus on the relevant parameters to the subject of interest

The design parameters can be divided into four main groups, as shown below:

- Geometry parameters, for example, duct length and depth of flow.
- Electrical parameters, such as short-circuit current and open-circuit voltage.
- Climate parameters such as ambient temperature (T_{amb}) and insolation (G).
- Operational parameters such as mass flow rate.

2.9.1 Geometry parameters

2.9.1.1 Duct length

The impact of air duct length on the performance of the PV/T air collectors is one of the vital design factors. Typically, the selection of the length of duct is affected by many factors such as mass rate, duct depth and incident solar radiation. For the specific conditions, the increase of the length of the duct means that the air takes more time to travel through the duct and subjected to hotter absorber surfaces (i.e. PV panel and lower absorber plate). Thus, this would be anticipated to a dramatic increase in the temperature at the end (saturation region).

Several studies have revealed that the effect of duct length is a crucial factor. For example, Joshi et al. [26] investigated the impact of length by comparing two PV/T air designs. The first design is glass-to-Tedlar, and the second is glass-to-glass, see Fig. 2.16. The authors deduced that thermal performance declines with increasing channel length and the increase of mass flux could enhance the thermal efficiency but only up to a certain length when saturation is attained. There is an acceptable agreement between this result and Sarhaddi et al. [25].

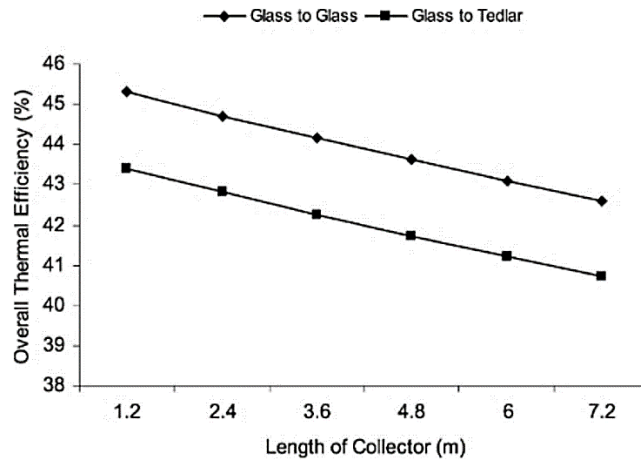


Fig. 2.16. Variation of overall thermal efficiency with the length of the collector [26].

Sopian et al. [128] revealed that there is an increase in outlet air temperatures for the given conditions (mass flux $0.028 \text{ kg s}^{-1} \text{ m}^{-2}$, insolation 1000 W m^{-2} , ambient temperature $22 \text{ }^\circ\text{C}$). The outlet fluid temperature was $44 \text{ }^\circ\text{C}$ when the length was 1 m , and it was $48 \text{ }^\circ\text{C}$ when the length was 2 m . However, this rise in fluid temperature means that the PV panels were operating at a higher temperature, and consequently, a decline in electrical efficiency was obtained for longer length [128]. A qualitative agreement is between these results and [176].

Tonui and Tripanagnostopoulos [176] theoretically examined the influence of various duct lengths on both electrical and thermal efficiency, as presented in Fig. 2.17. At specific conditions (channel depth of 0.05 m and mass flux of $0.02 \text{ kg s}^{-1} \text{ m}^{-2}$), there is a definite trend of increasing thermal efficiency. After a certain length, however, the effect of increasing the channel length is negligible. Besides, a decline in electrical efficiency occurs with increasing the channel length. These results agreed with the findings of other studies in [25, 26, 108, 172, 176-179].

In contrast, in another study, a numerical model was conducted by Garg and Adhikari [172] to evaluate the overall efficiency of PV/T air system basis on variation collector length and cell density. The results of this variation indicate that the overall efficiency and electrical efficiency increase with increasing collector length, mass rate and cell density. There is a conflict in the results shown between Garg and Adhikari [172] and other authors. Other authors kept the mass flow rate constant, while Garg and Adhikari [172] used a different approach in which varied the mass flow rate with geometry design parameters.

To conclude, a compromise should be considered between the length of duct and fan power consumption. The hydraulic fan power consumption is almost linear proportional with the duct length since the dominating parameter is the duct length. This can be seen clearly in Eq. 3.101 and Eq. 3.103 in Section 4.4.3.1.

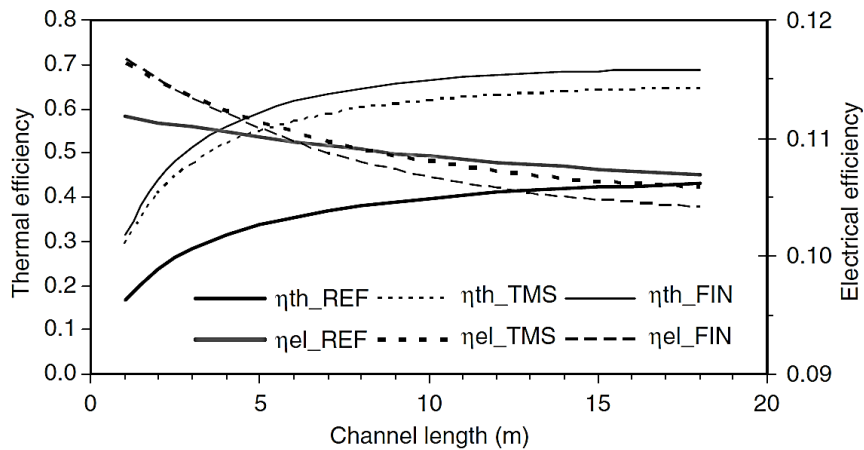


Fig. 2.17. Impact of duct length on the performance of collector for specific conditions, channel depth of 0.05 m and mass flux of $0.02 \text{ kg s}^{-1} \text{ m}^{-2}$ [176].

2.9.1.2 Duct depth

The depth of flow is considered as one of the main parameters in evaluating the forced convective heat transfer coefficient and the Reynolds number. This is precisely when the width \gg duct depth, the effect of width almost disappears, and thus, the duct depth becomes the dominating factor such as the air flows between two parallel plates [180]. An inverse proportional between the convective heat transfer coefficient and the duct of flow, meaning that if the duct flow is thinner, the heat transfer coefficient increase and the pressure drop increases.

From an experimental point of view, it is tricky to vary the duct depth or length, such as mass flow rates. Consequently, theoretical approaches are mainly used for evaluating the impact of changing the duct depth and length [181]. For example, Tonui and Tripanagnostopoulos theoretically studied the effect of depth flow on the performance of PV/T air system. The results revealed that by varying the duct depth over the range 0.05-0.5 m, the PV module temperature rises from 36 to 59 °C and the outlet fluid temperature reduces from 26 to 21 °C. The study was performed under the following conditions; 800 W m^{-2} insolation, an inlet air temperature of 20 °C, a wind speed of 1.5 m s^{-1} and mass flux of $0.05 \text{ kg s}^{-1} \text{ m}^{-2}$.

Also, there is a drop in the thermal efficiency of the PV/T air system from 30 to 5% and from 11.8 to 10.6% for electrical efficiency. The reasons behind this drop were the air velocity decrease with increasing the duct depth at the same mass rate. It can be concluded that in design PV/T air system, the depth of flow should be thinner as possible when the mass rate is constant while considering the effect of the pressure drop penalty.

Hegazy [131] and Garg and Adhikari [172] also showed that a declining of outlet fluid temperature and thermal efficiency as a function of increasing duct depth for different mass rates in a glazed solar air collector. The results of Hegazy [131] presented in Fig. 2.18. The author reported that an optimal ratio of the length of the collector to duct depth (L/δ_D) was 400 for various mass rate values [131]. Thus, a compromise should be considered when determining (L/δ_D). This compromise is between the maximizing the heat transfer rate from the PV panel to the heat transfer fluid from side minimizing the fan power needed from other side as will be considered in chapter 7.

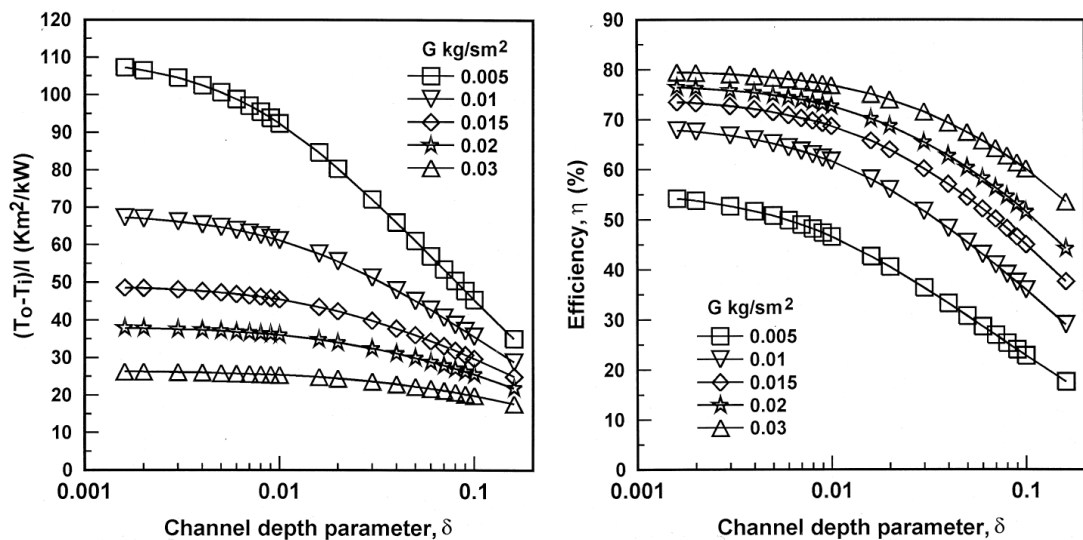


Fig. 2.18. Effect of duct depth on the air temperature rise and the thermal efficiency for a solar air heater with a glass cover [131].

In Fig. 2.18, δ the channel depth parameter as in Eq. 2.2.

$$\delta = M^{0.25} Pr^{0.83}, \quad \text{Eq. 2.2}$$

where M is air mass flow parameter.

Recently, the design of PV/T systems has been based on multi-objective design optimisation techniques. Many researchers have evaluated the performance of PV/T air systems using

optimisation process such as in [66, 67, 182-185]. The results showed that the optimisation contributed to thermal and electrical enhancement with reducing the pump or fan power consumption as a compromise action. However, few studies have examined the double duct double passes co-current flow using the optimisation process simultaneously with CFD modelling. To the best of author knowledge, only few references in the literature systematically describe the effect of design optimisation process on the performance of double duct double passes co-current flow (model 4). This was the motivation behind the present study.

To conclude, the selection of geometry parameters, i.e. depth flow and duct length rely on different conditions and criteria such as the mass rate and the weather conditions. Accordingly, in this study, the optimisation procedure is employed to choose the most compatible dimensions with specific requirements. This design optimisation is based on multi-objectives to maximise both thermal and electrical efficiencies of PV/T air collector and minimise fan power required as possible.

2.9.2 Material parameters

2.9.2.1 Frame

The collector frame must be insulated to minimise the losses resulting from heat transferred by conduction and convection to the surrounding as these losses decrease the thermal efficiency of PV/T unit. In the last two decades, insulation is usually of polyurethane foam or mineral wool, though sometimes mineral fibre insulating materials like glass wool, rock wool, glass fibre or fibreglass are used [6, 18]. Recently, the structure of collectors is now made from wood which has thicknesses ranging from 18-25 mm [26, 121], because it is lighter, more durable and affordable as well as versatile.

2.9.2.2 PV absorber

The main function of the PV panel is to absorb the incident solar radiation in which the heat exchanges between the absorber and the working fluid by convection, conduction and radiation. PV panel usually comprises three layers; glass cover, cells and Tedlar film. In case of installing or suspending fins in hybrid air PV/T collectors, it is necessary to install a sheet plate in the back surface of the PV module such as aluminium as a fin. This sheet also helps to install extended surfaces such as fins in PV/T air collectors [24]. Zakharchenko et al. [114] studied the importance of retaining better thermal conductivity between the PV panel and the absorber plate. They suggested that it should not directly use a PV module in combining

with the PV/T system without modifying using a 2 mm aluminium plate installed in the back of the PV module.

2.9.2.3 Tedlar

The Tedlar film is the back sheet installing in the back surface of the PV panel as one part to dissipate the waste heat and protect the PV panel from any water or bad conditions. The effect of Tedlar material has been evaluated by several investigations [186-188]. For instance, Tiwari and Sodha [189] studied the Tedlar-thermal conductivity in different configurations constituted by Tedlar. The results revealed that models without Tedlar are the best choice in improving system performance compared to the other designs. Koech et al. [186] tested the performance of PV/T systems utilising Tedlar layer with different values of thermal conductivity 0.0005-0.1 W m⁻¹ K⁻¹. They conclude that it is possible to create systems with higher energy yield, which in turn, allows for the released heat rapidly to the air (reduction in cell temperature).

2.9.2.4 Glass covers

The glazing has three functions; the first is avoiding the part of heat losses resulting from wind and breezes. The second one is the inherent glazing which permits the short-wave light spectrum (ultraviolet or high frequency) for entering the device and noticeably preventing infrared energy losses (low frequency and inactive) through re-radiation (greenhouse effect concept). The quality of glass should be high regarding transmissivity to the solar spectrum and extensively non-transmissivity to long-wavelength solar radiation (infrared) [62, 190]. Thirdly, the cover with the frame protects the absorber from adverse weather conditions.

Regarding of collector type, thermal losses may be minimised in PV/T collectors with the aid of a glass cover, and such collectors are termed “glazed” whereas unglazed [110, 191, 192] collectors do not possess glass covers. The glazed collectors possess smaller thermal losses practically at higher collection fluid temperatures, which leads to an increase in annual thermal yield [124, 193]. The coverless PV/T systems could provide 8% more electrical energy than a standard PV module [110, 191, 192]. It seems that there are some drawbacks of glazed PV/T collectors include overheating of bypass diodes as a result of extra insulation. Such elevated temperatures also decrease electrical yield (stagnation effect). To clarify, PV module sensitivity to hot spots and a reduction in electrical performance due to additional absorption and reflection losses which leads to reduce the total of absorbed energy by about 10% compared to glazing [124, 193]. These observations

suggest that it is essential to evaluate the benefits of glazing in terms of enhanced thermal yield as well as its disadvantage in terms of decreased electrical yield and collector quality.

2.9.3 Electrical parameters

In this section, the relationship between the electrical parameters, including voltage and current and the PV temperature, is discussed. The increase in the temperature of the PV panel is the essential parameter influencing its performance. Theoretically, the short-circuit current (I_{sc}) and the open-circuit voltage (V_{oc}) are proportional to the incident solar irradiance (G) and the ambient air temperature (T_{amb}) [194]. In reality, the open-circuit voltage is logarithmically proportional to the incident solar irradiance, and the short-circuit current increases just a little when the solar irradiance increases [19]. In other words, the parameter most influenced by a rise in temperature is V_{oc} . The effect of rising temperature is presented in Fig. 2.19 [6, 16]. It can be seen that when the temperature module increases above standard conditions (25 °C), there is a noticeable reduction in electrical power.

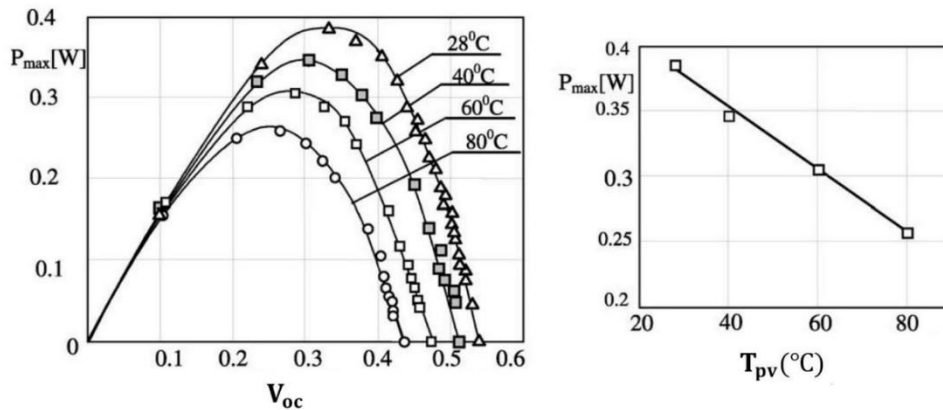


Fig. 2.19. Output power of single-crystalline silicon PV cells under different operating temperatures (left) temperature dependence of the maximum output power (right) [195].

Expressions, for the open-circuit voltage and the short-circuit current as functions of the PV module temperature, can be obtained in the literature, based on various proposed electrical models [196, 197]. Skoplaki et al. [197] studied mathematically the effect of rising of PV module temperature on open-circuit voltage and short-circuit current as shown in the set of the following equations:

$$P_{PV} = I_m V_m = FF I_{sc} V_{oc}. \tag{Eq. 2.3}$$

In this equation, the subscript m denotes to the maximum power point of the PV module power, while subscripts sc and oc refer to short circuit and open circuit values, respectively. “The fill factor is a measure of how much series resistance and how little shunt resistance there is in a solar cell and its circuit.”

$$I_{sc} = \frac{G}{G_{STCs}} I_{sc-STC} [1 + \alpha_{sc} (T_{mpv} - T_{ref})] \quad [197, 198], \quad \text{Eq. 2.4}$$

$$V_{oc} = V_{oc-STC} [1 + \beta(G) (T_{mpv} - T_{ref})] \left[1 + \delta(T) \ln \frac{G}{G_{STC}} \right] \quad [197, 198], \quad \text{Eq. 2.5}$$

where α_{sc} is short-circuit current correction coefficient for temperature, $\beta(G)$ is open-circuit voltage correction coefficient for temperature as a function of insolation, $\delta(T)$ is an open-circuit voltage correction coefficient for insolation as a function of the PV module temperature. The subscript STC refers to standard conditions [197].

2.9.4 Extended surfaces

Several configurations have been proposed in the literature regarding heat transfer augmentations. Many investigators have examined the effects of extended surfaces on improving the overall (hybrid) efficiency of PV/T systems. Extended surfaces may be divided into three main classes: 1) conventional fins [37, 67, 112, 118, 176, 190, 199-209]; 2) interposition of a thin metallic sheet (TMS) [118, 176, 210-212]; 3) obstacles (ribs) [118, 210, 213, 214] such as in Fig. 2.20.

Conventional fins can be defined as heat extraction devices attached to the PV back surface towards or against the air channel flow. Since low thermal capacity and density of air, however, this leads to the values of conductive transfer coefficients are also low. Thus, the employing of fins with PV/T air systems could enhance the performance. However, a major problem with this kind of application is that increasing the fan power consumption result in increased pressure drop, which diminishes the total electrical power. Therefore, the careful design should be taken when choosing fan in energy required terms to operate the fan, in other words, the compatibility between PV module and fan in area and power need to be taken into consideration [212, 215-217].

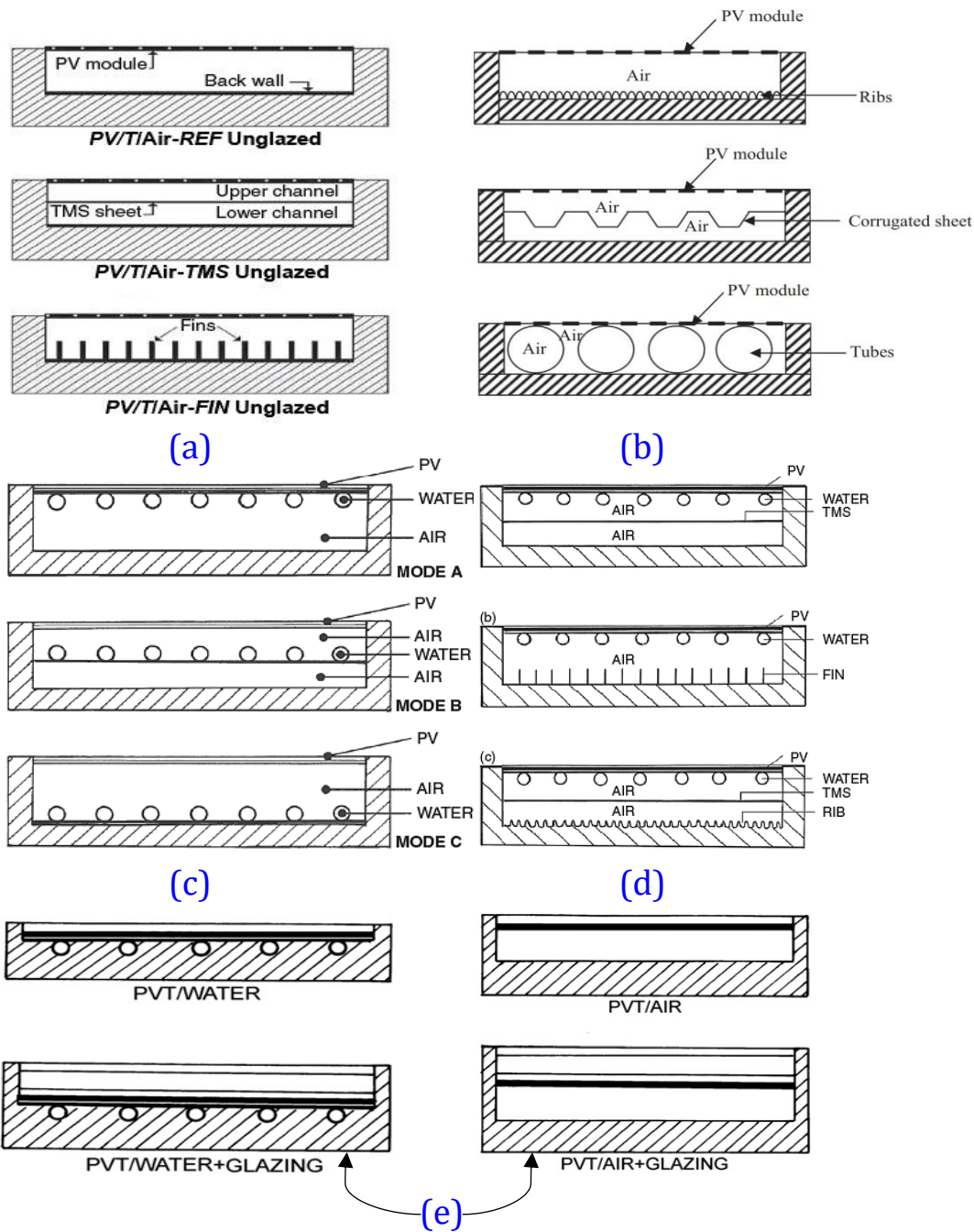


Fig. 2.20. Different designs of extended surfaces of PV/T air collectors [108, 118, 133, 176].

The second type of air heat extraction is a thin metallic sheet (TMS) suspended at the centre of the airflow passage. Thirdly is ribs (obstacles) are fixed to the opposite channel wall and also works by roughening the surface.

Comprehensive studies have been done by Tripanagnostopoulos et al. [118, 176, 211, 212, 218-220] to improve the heat transfer kinetics in the air duct of a PV/T system. The research

team modified the system by utilising two techniques. These techniques are finned rear surface or TMS installed in the centre of PV/T air system to enhance the thermal performance and to increase the extracted heat from PV panel which in turn reduce the PV panel temperature. The cross-sectional views of their models are shown in [Fig. 2.20](#). Under specific conditions, air forced convection with volume flow rate $60 \text{ m}^3 \text{ h}^{-1}$ and 0.15 m channel depth. They concluded that the use of fins produces an efficiency of 30% while TMS 28% and the typical one (without extended surface) 25% [\[211\]](#). The authors also concluded that the amended configurations provide higher thermal efficiency than the conventional system, with greater electrical production owing to the achieved PV cooling, see [Fig. 2.20a](#) [\[211\]](#).

The other research [\[118, 218\]](#) have investigated the enhancement of air heat extraction for three low-cost air and water modified systems experimentally. The results showed that the systems exhibited acceptable thermal performance at steady state test ([Fig. 2.20 d and e](#)). Another study [\[118\]](#) examined three modified systems utilising three types of extended surfaces: 1) fins; 2) tubes work as fins; 3) opposite cavity roughened (ribs). The authors conclude that fin and tubes are efficient in enhancing thermal and electrical performance, but the additional cost and pressure drop must also be taken into consideration. Whereas, opposite cavity roughened surface is an enhancement of minimum cost, which increases the total output insignificantly [Fig. 2.20b](#).

Other studies by Karim [\[221\]](#) and Othman et al. [\[222\]](#) have investigated two different designs. The first research team [\[221\]](#) examined the effect of v-groove construction, which increases the efficiency of 12% more than the conventional one while the second one [\[222\]](#) used ∇ -grooved absorber plate. The thickness of the aluminium was 0.7 mm, attached at the back of the PV module [Fig. 2.21](#). The experimental results revealed that by including the ∇ -grooved absorber plate, the electrical efficiency had been increased by 1%, and the thermal efficiency was increased by 30%.

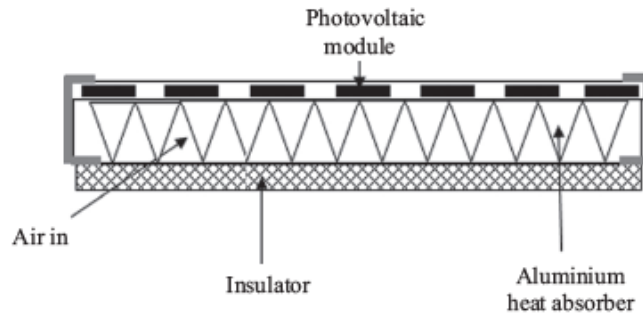


Fig. 2.21. PV/T air system with aluminium ∇ -grooved absorber plate [222].

Other amendments that have been proposed for the enhancement of heat extraction in the air duct are the utilisation of pins, matrices, porous materials, and perforated plates [118, 190, 210, 213, 214].

To sum up, a considerable effort has been carried out to improve the thermal and electrical efficiency PV/T air system by using fins, ribs, TMS, and other types of extended surfaces. However, the selection of best fin design is based on five criteria. The criteria are pressure drop, heat transfer enhancement, size, weight and cost. Of the many enhanced fin geometries described earlier, offset strip fins are widely used [223]. They have a high degree of surface compactness, and substantial heat transfer enhancement is obtained as a result of the periodic starting and development of laminar boundary layers over uninterrupted channels formed by the fins and their dissipation in the fin wakes. There is, of course, an associated increase in pressure drop due to increased friction and a form-drag contribution from the finite thickness of the fins [223]. Off-set strip fin can be considered as such fins with low-pressure drop and high contact area [182, 224-226]. In this study, to the best of the author's knowledge, no report has been found so far using off-set strip fins with multi-pass solar PV/T air collector in a staggered arrangement.

2.10 Solving heat transfer problems

There are three main approaches used to solve heat transfer problems. The first approach is experimental, as presented in Chapter 6 for validation and verification purposes. The second approach is analytical, presented in Chapter 3. Finally, CFD modelling presented extensively in this thesis as the main approach. The reason behind discussing these approaches is to show the significance of each approach.

2.10.1 Experimental approaches

Experimental approaches can be mainly classified as empirical and semi-empirical methods. Before 1939, the most general nature in solving the heat and mass transfer problems exclusively depended on the empirical methods [227]. After that, strenuous endeavours to develop the analytical methods of heat transfer problems. These efforts have been contributed now in use the experiments just for validity with theoretical or numerical models. The area of complete dependence on direct experimental data has been dramatically diminished [227]. However, direct experimental data are still a vital factor in engineering design [227].

The second approach is semi-empirical (i.e., the analogy between momentum and heat transfer (transport analogies)) [228] can also be classified as a part of experimental methods [228, 229]. This method is best defined by a statement of Reynolds theory [228]. According to this theory, the movement of heat between a surface and a fluid follows the same law as the movement of momentum between a surface and a fluid, whether by conduction or convection (radiation is neglected). These methods can be used to predict the rate of heat transfer from rates of momentum transfer and temperature profile from velocity profile in a laminar and turbulent flow. The main drawbacks of the experimental methods are:

- Cost, effort and time-consuming.
- Error of measurements (could be 20-40 %) [223, 230].
- Some experiments cannot be performed, and this includes nuclear reactors.

2.10.2 Analytical approaches

In analytical approaches, several assumptions are made to simplify and solve the governing equations. Owing to the inherent complexity of conjugate heat transfer problems, the following reasons made these methods are restricted in use and also attained only for limited classes of problem, such as laminar flow cases [227]. When the equations are in three-dimensional form; they are strongly coupled and nonlinear. Also, in practical engineering problems, the solution domains are almost always complex [231]. Therefore, when the calculation procedure becomes insurmountable, it is worthwhile to look for an alternative method of solution. As a result, the numerical model or computational fluid dynamic (CFD) is crucial for more general and complex problems [227].

2.10.3 Numerical approaches

In the recent decades, both in-house and commercial computational fluid dynamics (CFD) codes are becoming key instruments in offering a fast accurate solution at a feasible cost compared to developing an experimental setup [232]. In terms of CFD, there has been a steady increase in using CFD modelling in both academia (universities and research institutes) and industry (consultants and manufacturers). This growth is because increased availability of quality CFD models, increasing power and affordability of computing power. CFD is a branch of fluid mechanics that utilises numerical methods to examine and solve problems that include fluid flows, heat transfer and mass transport problems (with or without solid interaction) via computer-based simulation [227].

Since the 1960s, the aerospace industry has started to use the CFD technique in design [233]. This technique is powerful and spans a wide range of industrial and non-industrial application areas [233, 234] because of its ability to provide simulations with acceptable error compared to the experimental setup. For example, it can easily modify geometry design many times. Accordingly, the use of CFD technique can effectively reduce time and cost as compared to the manufacturing process [235-237]. Additionally, various phenomena can be coupled with heat transfer problems, such as the aerodynamics of aircraft, vehicles and biomedical engineering [233, 238].

2.11 Conclusions

The overall goals of this chapter are to provide an overview about, firstly, the significance of the study field, then the fundamental concept of PV/T technology and finally to understand the gaps in knowledge. A variety of literature showed that many research investigations studied the design and applications of PV/T technologies, for instance, PV/T air/water systems. The following conclusions can be drawn from this chapter:

- Care should be taken in the selection of the PV cell type when coupled with a solar thermal collector. This is because each PV cell type has a different temperature coefficient of power and melt point. In other words, the compatibility of the PV cell with solar thermal systems.
- The variety of methods used in the literature revealed that a necessity to accurately estimate the temperature of the standard PV module (PV module without active cooling exposed to ambient conditions). The methods used are mathematical, numerical and experimental. This necessity is because the temperature of the PV module is the main

parameter used to evaluate the performance of the PV panel. Also, to investigate the feasibility of hybridisation of PV/T systems.

- Various studies indicated that each PV/T technology has advantages, drawbacks and limitations. Therefore, the selection of PV cooling method is based on the weather conditions and whether the application set for industrial or residential purposes.
- Concerning the performance of solar thermal air collector, several works reported that the thermal efficiency of the multipass solar air heater is generally enhanced compared to the single pass. This can be attributed to increasing the surface area with minimum fan power consumption.
- Recently, the design of PV/T systems is based on multi-objective design optimisation. Many researchers have examined the performance of PV/T air systems using optimisation process. The results revealed that the optimisation contributed to improving the thermal and electrical efficiencies with reducing the pump or fan power consumption as a compromise action.
- Much research has been carried out to improve the thermal and electrical efficiency PV/T air system by using fins, ribs, TMS, and other types of extended surfaces. However, the selection of best fin design is based on five criteria. The criteria are; pressure drop, heat transfer enhancement, size, weight and cost.

As presented in the literature, the selection of geometry parameters, i.e. depth flow and duct length rely on different conditions and criteria such as the mass flow rate and the weather conditions. Accordingly, in this study, the optimisation procedure is employed to choose the most compatible dimensions with specific requirements. This design optimisation is based on the multi-objective method to maximise both thermal and electrical efficiencies of PV/T air collector and minimise fan power required as possible. Also, few studies have examined the double duct double passes co-current flow using the optimisation process side by the side with CFD modelling. In this study, to the best of the author's knowledge, no report has been found using off-set strip fins with multi-pass solar PV/T air collector in a staggered arrangement.

In the next chapter, the mathematical formulation for two PV/T air systems is carried out using energy balance equations. Two numerical techniques are used to solve the energy balance equations. The heat transfer and fluid flow equations related to two systems are presented. This includes relevant dimensionless numbers, the convective heat transfer coefficients in both forced and free convection modes. Moreover, the fluid and electrical equations related to evaluating thermal and electrical performance of solar air collectors are presented in the next chapter.

CHAPTER 3 MATHEMATICAL MODELLING

3.1 Introduction

In this chapter, the mathematical formulation based on the conservation of energy principle is used to describe the thermal and electrical behaviour of PV/T air collectors. For example in the PV module, which denotes as model 1, the conservation of energy principle states that the rate of energy input (i.e. the total heat generated by solar irradiation) (\dot{Q}_s) is equal to the sum of the rates of useful heat gained from the PV panel (\dot{Q}_u) and the heat losses from the PV panel (\dot{Q}_L), minus the electrical power generation (P_{PV}), which is treated as a heat sink, plus heat storage (\dot{E}_s) in the PV. The heat storage is ignored in this analysis, since it is assumed to be in the steady state condition and there is no change in the amount of energy stored in the system.

$$\dot{E}_{in} = \dot{E}_{out} + \dot{E}_g + \dot{E}_s \quad \text{Eq. 3.1}$$

$$\dot{Q}_s = (\dot{Q}_u + \dot{Q}_L) - P_{PV} + \dot{E}_s \quad \text{Eq. 3.2}$$

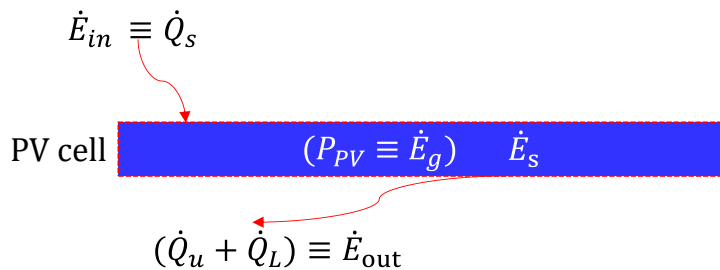


Fig. 3.1. The representation of conservation of energy for the PV cell of model 1.

Eq. 3.1 and Eq. 3.2 are equivalent, i.e. $E_{in} \equiv \dot{Q}_s$, $E_{out} \equiv (\dot{Q}_u + \dot{Q}_L)$ and $\dot{E}_g = P_{PV}$ as shown in Fig. 3.1.

PV/T air collectors consist of a certain number of components such as the PV panel device, cover glass and lower absorber plate. For each component, a simple energy balance is applied to derive the governing equation.

In this chapter, the mathematical formulation of two flat photovoltaic/thermal (PV/T) collectors based air coolant is conducted. The simple energy balance is applied to formulate

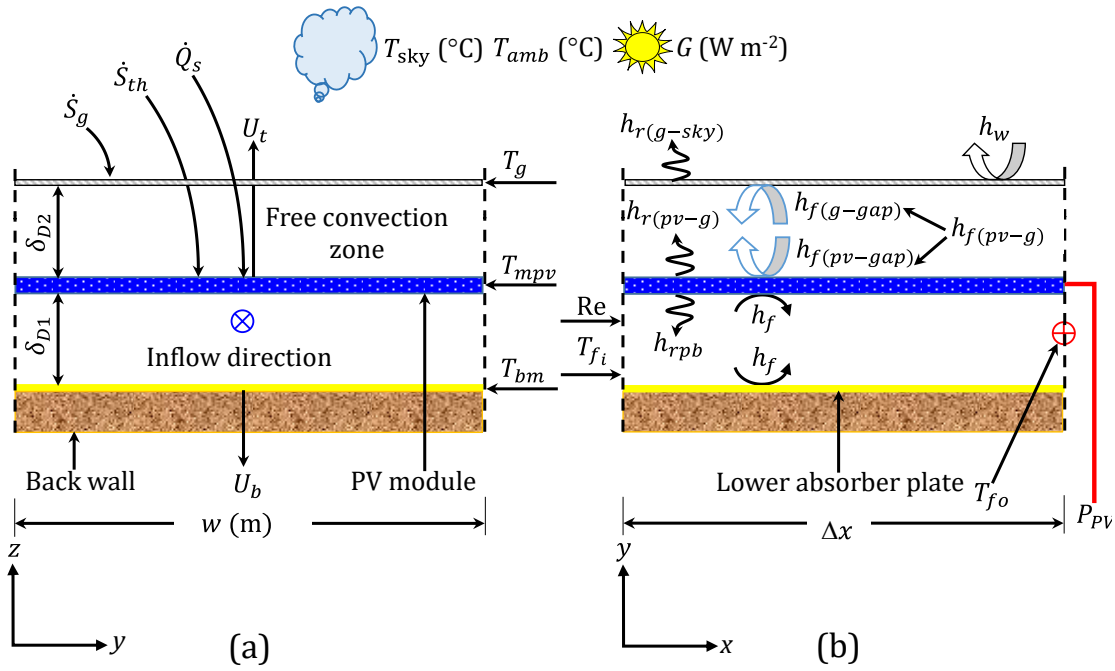


Fig. 3.3. Schematic of model 3.

In Fig. 3.2 and Fig. 3.3, T_g is the glass cover temperature ($^{\circ}\text{C}$), T_{mpv} is the PV panel temperature, T_{bm} is the temperature of the lower absorber plate ($^{\circ}\text{C}$), T_{fi} is the inlet fluid temperature ($^{\circ}\text{C}$), T_{fo} is the outlet fluid temperature ($^{\circ}\text{C}$), T_{amb} is ambient temperature ($^{\circ}\text{C}$) and T_{sky} is the sky temperature ($^{\circ}\text{C}$). The remainder abbreviations are described in the next sections.

For both models, the simple energy balance method is performed over a differential element having a width (w) and infinitesimal length Δx , resulting in surface area ($w \Delta x$). In order to derive the energy balance equation across each component of these collectors, The following assumptions are made:

- **One-Dimension:**

The thickness of the PV absorber plate (δ_{mpv}) is small compared to the other dimensions ($\delta_{mpv} \ll w \& L$). This means the temperatures at the front and the back of the PV modules are assumed to be equal. The distribution of temperature in the width direction is symmetrical. It has been experimentally proven by Al-Damook [239] that the temperature is quite similar in the width direction. In other words, it is assumed that the absorber cooled uniformly across its width.

- **The effect of longitudinal conduction:**

The heat conduction flow along the PV absorber (i.e. in the axial direction) is ignored. Several methods are used to evaluate the significance of longitudinal heat conduction term,

for example, the Peclet Number (Pe). The Pe of fluid is the ratio of the convection heat transfer rate to the conduction heat transfer rate, i.e.:

$$Pe = \frac{\text{heat transfer by convection}}{\text{heat transfer by conduction}} = Re_{D_h} Pr. \quad \text{Eq. 3.3}$$

Therefore, if Pe is small, the effect of longitudinal conduction is important and *vice versa* [240]. The second approach is that the wall conduction term (heat diffusion) may often be neglected since a thin wall of large thermal conductivity is generally used [241]. This is valid when the conducted thermal resistance (δ_{mpv}/k_{pv}) of the PV panel is relatively low compared to the value of convected thermal resistance ($1/h_f$) [241]. A comprehensive study was conducted by Bahnke and Howard [242] suggesting a non-dimensional conduction criterion to evaluate the significance of the effect of longitudinal conduction in a heat exchanger. This simply determined the results of an approximation of the actual effect of this parameter. Also, a simple analytical solution was made by Lund [243] using the perturbation technique, the results showed that the effect of longitudinal heat conduction could be a negligible, high-order effect for most practical collectors where the length is much larger than the duct half-pitch (except where the thickness-conductivity product is very high and the flow rate extremely low) [243].

However, the axial conduction in the absorber plate causes a flow of heat in the direction opposite to the flow of fluid. This results in a reduction of the fluid outlet temperature and the overall efficiency of the system. Thus, predictions made by neglecting axial conduction are optimistic [240]. In fact, the analysis which is achieved by Phillips [240] revealed that neglecting axial conduction in the performance predictions for these collectors would result in errors no larger than 12%-30% for all operating conditions [240].

- **Quasi-steady state:**

The calculations performed at every time step are assumed to have reached steady state. This is a valid assumption because, in their experiments, Amori and Abd-ALRaheem [121] and Al-Damook [239] found that the response time was approximately 15 minutes to reach steady state under new input parameters such as solar radiation, ambient temperature and airflow rate [27, 121, 122, 131, 151, 209, 244, 245].

To clarify, heat transfer is the transfer of thermal energy from a body, at a high temperature, to another at a lower temperature. The heat transfer may occur under steady or unsteady state conditions. In computational fluid dynamic (CFD), the time resource of unsteady state is massive and it is not compatible with some engineering cases [246]. A quasi steady state

model is a steady state model used by specified time span such as hour by hour energy calculations [121, 247].

Other assumptions can be summarised as below:

- Internal convective heat transfer coefficient (h_f) between wall collectors (i.e. the PV panel and lower absorber plate) and flowing air can be considered to be equal. This is because the heat capacity of air is relatively small. Also, the distance between the two absorbers is relatively small [121].
- It is assumed that the system is perfectly sealed, this means, there is no air leakage from the fluid flow through the channels.
- The solar radiation absorbed by the PV cells is converted into two types, the first one is converted to electrical energy while the remainder is converted into thermal energy.
- All thermo-physical properties of air are considered to be dependent on the temperature [122, 248, 249]. These equations work accurately in the temperature range (-73 to 127 °C).
- Heat loss from the sides of the duct is very small compared to the other heat losses and hence these losses can be neglected [250, 251].
- All material properties are supposed to be independent of temperature and equal in all directions. This is because the operating conditions of PV/T air systems do not influence the microstructural properties of the materials. More precisely, the maximum operating temperatures for these systems is around 200 °C which does not have an impact on the material properties [37].
- The thermal capacity or heat capacity ($J K^{-1}$) of the glass cover, enclosed air, PV panel absorber and lower plate are negligible at steady state. In reality, the operation of most solar energy systems is inherently transient; there is no such thing as steady state operation when one considers the transient nature of the driving forces [50]. To sum up, the temperatures of the PV module, glass, lower absorber vary only in the x-direction of the air flow [121].
- The multiple reflections and transmissions of radiation between the components of the PV module, for example, this occurs between the photovoltaic cells and the front glass can be considered as negligible. Considering these effects leads to numerous difficult terms to determine and to measure [37, 250, 252]. Krauter and Hanitsch [253] compressively studied these various effects approving this concept.
- The thermal exchanges between photovoltaic cells and the layer called encapsulant (ethyl vinyl acetate) (EVA) are ignored. This is because of the space or gap between neighbouring cells represent a tiny area. Both air fluid and glass cover do not absorb

radiant energy. This is because the transparency of these objects is very high, up to 90% [254].

- homogeneous ambient temperature is assumed [37].
- Non-isothermal surface boundary condition (constant heat flux boundary condition) is assumed.
- The thermal resistance magnitude arising from the fouling effect can be assumed as zero. This is valid for air system compared with water systems specifically for non-distilled water. That is the effect of accumulated dust, dirt and the fouling factor which is insignificant [241, 250].
- The shading effect is considered to be negligible [250].
- The airflow inside the collector has a uniform velocity (\bar{V}) which can be calculated from the known mass rate (\dot{M}) [255].
- Recirculation has not been included in this work [255].
- The top glass surface is assumed to be clean.
- The packing density of solar cells (packing factor) is unity.
- The flow is fully developed.
- The fluid is fully mixed over the cross-sectional area of flow.
- The fluid flow is transparent to thermal radiation.
- Since Δx is very small $\Delta x \rightarrow 0$, the temperature does not vary within this interval (Δx) such that $T_f(x) \cong T_f(x + \Delta x)$.

In the next section, the derivation of each energy balance equations is considered.

3.2.1 Glass cover

For model 3, the steady state energy balance equation is applied (Eq. 3.4):

$$\underbrace{[\dot{S}_g w \Delta x]}_1 + \underbrace{[h_{f(gap-g)} w dx (T_{gap}(x) - T_g(x))]}_2 + \underbrace{[h_{r(pv-g)} w \Delta x (T_{mpv}(x) - T_g(x))]}_3 - \underbrace{[h_w w \Delta x (T_g(x) - T_{amb})]}_4 - \underbrace{[h_{r(g-sky)} w \Delta x (T_g(x) - T_{sky})]}_5 = 0, \quad \text{Eq. 3.4}$$

where $h_{f(gap-g)}$ is the free convective heat transfer coefficient between the bottom surface of the glass cover and surrounding air in the enclosure ($W m^{-2} K$), $h_{r(pv-g)}$ is the radiative heat transfer coefficient between the top surface of the PV module and the bottom surface of the glass cover ($W m^{-2} K$), h_w is the wind heat transfer coefficient over the glass cover (W

m⁻² K). The heat loss owing to radiation can be expressed as the radiative heat transfer coefficient between the top surface of the glass cover and the sky ($h_{r(g-sky)}$).

$$\dot{S}_g = \alpha_g G, \quad \text{Eq. 3.5}$$

where \dot{S}_g is the rate of solar radiation absorbed by the top glass cover converting to heat (W), α_g is the absorptivity of the glass cover and G is the incident solar radiation per unit area (W m⁻²).

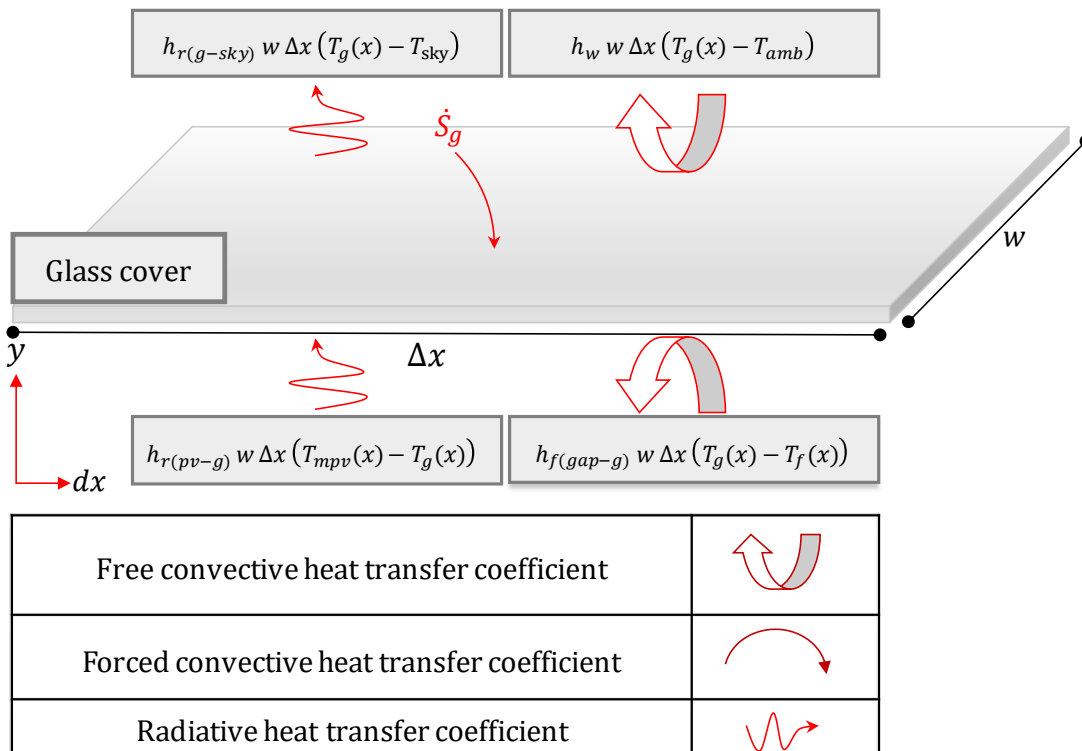


Fig. 3.4. Schematic of the energy balance equation for the top glass cover (model 3).

Each term in Eq. 3.4 can be expressed as follows:

1. The rate of solar radiation absorbed by the top glass cover converting to heat.
2. The rate of heat transfer by free convection from the air gap to the bottom surface of the glass cover.
3. The rate of heat transfer by radiation between the bottom surface of the glass cover and the top surface of the PV panel.
4. The heat transfer by free or forced convection from the top surface of glass cover to the surrounding atmosphere.

- The rate of heat transfer by radiation between the bottom surface of the glass cover and the top surface of the PV panel.

3.2.2 PV panel

For model 2, a mathematical model is developed by applying heat balance on the PV panel. Three heat transfer coefficients represented by:

- h_f , the forced convective heat transfer coefficient between the bottom surface of the PV panel and the air stream ($W m^{-2} K$).
- h_{rpb} , the radiative heat transfer coefficient between the two absorbers ($W m^{-2} K$).
- \dot{S}_{th} , the solar radiation absorbed by the PV panel converting to heat ($W m^{-2}$).
- $h_{r(pv-sky)}$, the radiative heat transfer coefficient between the PV panel and the sky ($W m^{-2} K$).

Fig. 3.5 shows the schematic description of the parameters considered here to derive the energy balance for the PV panel. Eq. 3.6 defines the energy balance of the PV panel.

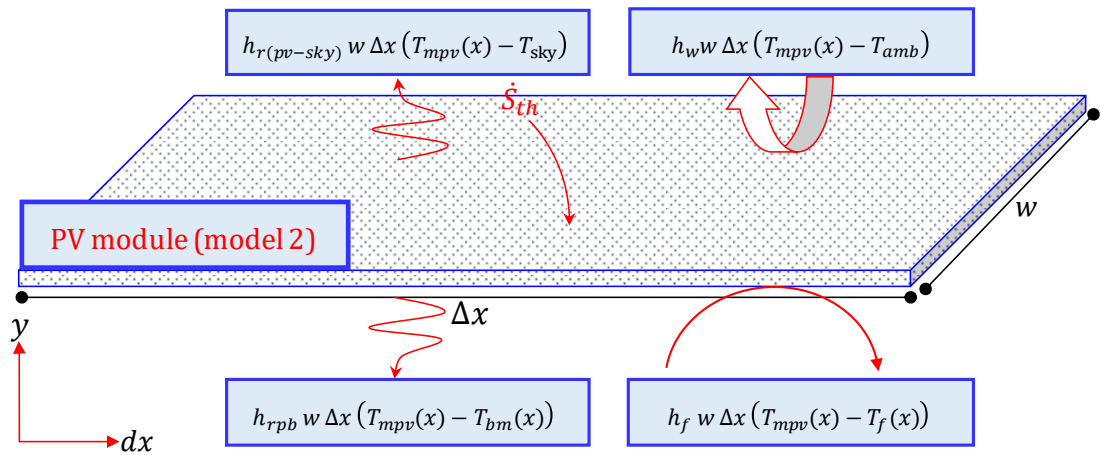


Fig. 3.5. Schematic of the energy balance equation for the PV panel (model 2).

$$\begin{aligned}
 \underbrace{[\dot{S}_{th} w \Delta x]}_1 &= \underbrace{[h_{r(pv-sky)} w \Delta x (T_{mpv}(x) - T_{sky})]}_2 + \\
 &\underbrace{[h_w w \Delta x (T_{mpv}(x) - T_{amb})]}_3 + \underbrace{[h_f w \Delta x (T_{mpv}(x) - T_f(x))]}_4 + \\
 &\underbrace{[h_{rpb} w \Delta x (T_{mpv}(x) - T_{bm}(x))]}_5.
 \end{aligned}$$

Eq. 3.6

The terms 2 and 3 in Eq. 3.6 combine to be term 2 in Eq. 3.7.

$$\underbrace{[\dot{S}_{th} w \Delta x]}_1 = \underbrace{[U_t w \Delta x (T_{mpv}(x) - T_{amb})]}_2 + \underbrace{[h_f w \Delta x (T_{mpv}(x) - T_f(x))]}_3 + \underbrace{[h_{rpb} w \Delta x (T_{mpv}(x) - T_{bm}(x))]}_4, \quad \text{Eq. 3.7}$$

where U_t is the overall top losses of the collector ($\text{W m}^{-2} \text{K}$).

$$\dot{S}_{th} = G \alpha_{pv} \tau_g (1 - \eta_{pv}). \quad \text{Eq. 3.8}$$

$$\eta_{pv} = (\eta_{ref} [1 - \beta_{ref} (T_{mpv} - T_{ref})]). \quad \text{Eq. 3.9}$$

The physical interpretation of mathematical formulation for each term in Eq. 3.7 is explained below:

1. The rate of solar radiation absorbed by the PV module converting to heat
2. The overall heat Loss from the top surface of the PV panel to the surrounding atmosphere by convection and radiation.
3. The rate of heat transfer by convection from the bottom surface of the PV module to the flowing fluid.
4. The rate of heat transfer by radiation between the two absorber plates (i.e. the bottom surface of the PV panel and the top surface of the lower absorber plate).

While for model 3, the energy balance equation for the PV panel is:

$$\underbrace{[\dot{S}_{th} w \Delta x]}_1 = \underbrace{[h_{rpb} w \Delta x (T_{mpv}(x) - T_{bm}(x))]}_2 + \underbrace{[h_f w \Delta x (T_{mpv}(x) - T_f(x))]}_3 + \underbrace{[h_{r(pv-g)} w \Delta x (T_{mpv}(x) - T_g(x))]}_4 + \underbrace{[h_{f(pv-gap)} w \Delta x (T_{mpv}(x) - T_{gap}(x))]}_5, \quad \text{Eq. 3.10}$$

where $h_{r(pv-g)}$ is the radiative heat transfer coefficient between the PV panel and the sky ($\text{W m}^{-2} \text{K}$) and $h_{f(pv-gap)}$ is the free convective heat transfer coefficient between the top surface of the PV panel and the surrounding ($\text{W m}^{-2} \text{K}$). The following are the interpretation of the heat energy balance terms in Eq. 3.10:

1. The rate of solar radiation absorbed by the PV module converting to heat.
2. The rate of heat transfer by radiation between the two absorber plates.
3. The rate of heat transfer by convection from the bottom surface of the PV module to the flowing fluid.

4. The rate of heat transfer by radiation between the bottom surface of the top glass cover and the top surface of the PV panel.
5. The rate of heat transfer by free convection from the top surface of the PV module to the air gap.

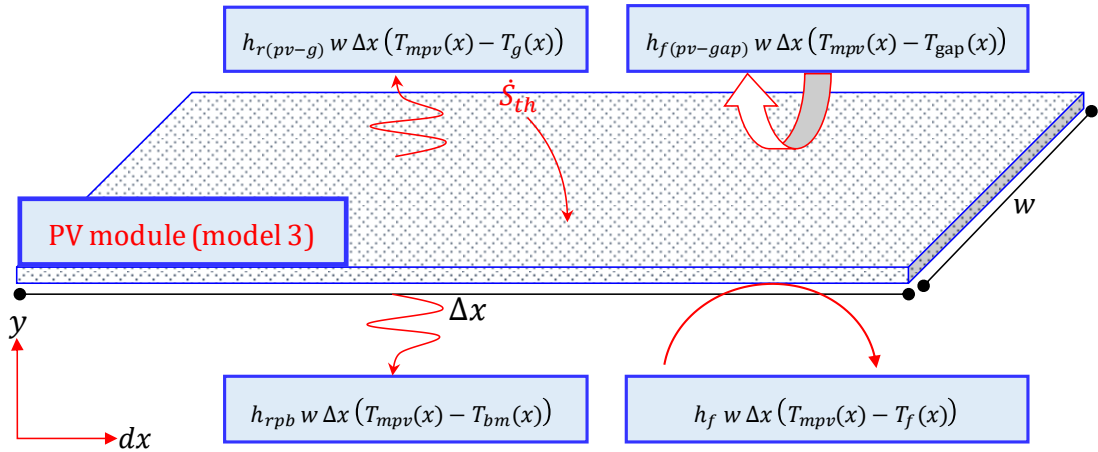


Fig. 3.6. Schematic of the energy balance equation for the PV module (model 3).

3.2.3 Lower absorber plate

In this subsection, for models 2 and 3, the energy balance equation for the lower absorber plate is developed as shown in Fig. 3.7 and Eq. 3.11. The bottom heat loss coefficient from the lower plate represented by U_b ($W m^{-2} K$).

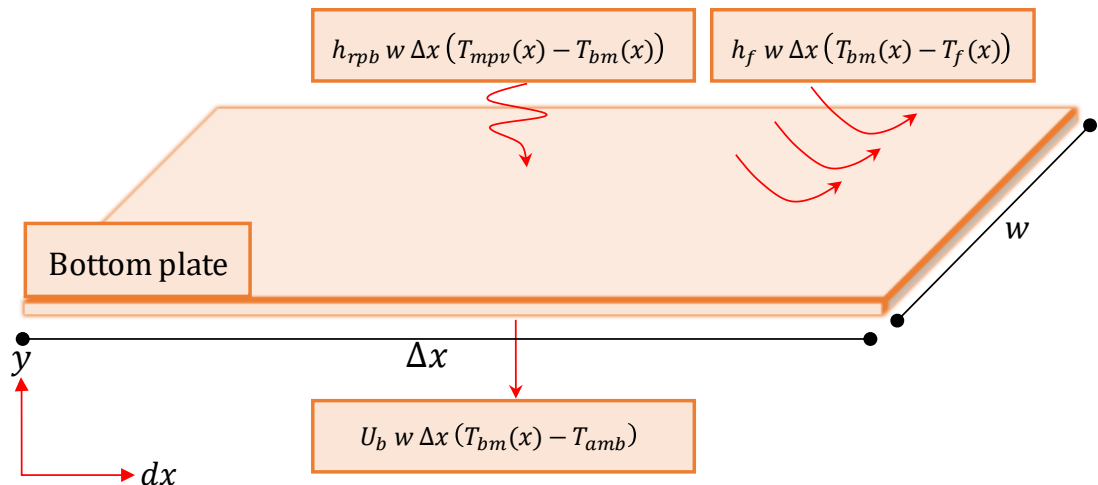


Fig. 3.7. Schematic of the energy balance equation for the lower absorber plate for models 2 and 3.

$$\underbrace{h_{rpb} (T_{mpv}(x) - T_{bm}(x)) w \Delta x}_1 = \underbrace{h_f (T_{bm}(x) - T_f(x)) w \Delta x}_2 + \underbrace{U_b (T_{bm}(x) - T_{amb}) w \Delta x}_3 \quad \text{Eq. 3.11}$$

Again, the physical interpretation of mathematical terms in Eq. 3.11 are expressed as follows;

1. The rate of heat transfer by radiation between the two absorber plates (i.e. the bottom surface of the PV panel and the top surface of the lower absorber plate)
2. The rate of heat transfer from the top surface of the lower absorber plate to the flowing fluid.
3. The rate of heat transfer by convection from the top surface of the lower absorber plate to the flowing air.
4. An overall heat loss from the bottom surface of the lower absorber plate to ambient by conduction

Rearranging Eq. 3.11 to express it in terms of the temperature of the lower absorber plate, we obtain:

$$T_{bm}(x) = \frac{h_{rpb}T_{mpv}(x) + h_f T_f(x) + U_b T_{amb}}{h_{rpb} + h_f + U_b} \quad \text{Eq. 3.12}$$

Simplifying and reformulating Eq. 3.12 by adding T_{mpv} for two sides results in:

$$T_{mpv}(x) - T_{bm}(x) = \frac{h_f (T_{mpv}(x) - T_f(x)) + U_b (T_{mpv}(x) - T_{amb})}{h_{rpb} + h_f + U_b} \quad \text{Eq. 3.13}$$

Substitute Eq. 3.13 in Eq. 3.7 to eliminate $T_{bm}(x)$.

$$S_{th} = U_t (T_{mpv}(x) - T_{amb}) + h_f (T_{mpv}(x) - T_f(x)) + h_{rpb} \left[\frac{h_f (T_{mpv}(x) - T_f(x)) + U_b (T_{mpv}(x) - T_{amb})}{h_{rpb} + h_f + U_b} \right] \quad \text{Eq. 3.7a}$$

In order to simplify Eq. 3.7a, a rearrangement is carried out to obtain the following expression:

$$S_{th} = \left[U_t + \frac{h_{rpb}U_b}{h_{rpb} + h_f + U_b} \right] (T_{mpv}(x) - T_{amb}) + \left[h_f + \frac{h_{rpb}h_f}{h_{rpb} + h_f + U_b} \right] (T_{mpv}(x) - T_f(x)). \quad \text{Eq. 3.7b}$$

Assuming \overline{U}_L and h_e terms as presented in Eq. 3.7c and Eq. 3.7d.

$$\overline{U}_L = U_t + \frac{U_b h_{rpb}}{U_b + h_{rpb} + h_f}, \quad \text{Eq. 3.7c}$$

$$h_e = h_f + \frac{h_f h_{rpb}}{U_b + h_{rpb} + h_f}, \quad \text{Eq. 3.7d}$$

where \overline{U}_L is the equivalent heat transfer coefficient between the PV panel and the ambient ($\text{W m}^{-2} \text{K}$) and h_e is the equivalent heat transfer coefficient between PV panel and fluid ($\text{W m}^{-2} \text{K}$), thus:

$$S_{th} = \overline{U}_L (T_{mpv}(x) - T_{amb}) + h_e (T_{mpv}(x) - T_f(x)). \quad \text{Eq. 3.7e}$$

From Eq. 3.7e, the mean temperature of the PV panel device is:

$$T_{mpv}(x) = \frac{S_{th} + \overline{U}_L T_{amb} + h_e T_f(x)}{\overline{U}_L + h_e}. \quad \text{Eq. 3.7f}$$

3.2.4 Useful heat gain

Once the energy balance equations of the PV/T components have been completed, the subsequent step is setting up the models to estimate the amount of heat transferred (useful heat gain) by forced convection from the two absorber plates to the flowing air. The derivation of the useful heat gain equation is valid for model 2 and model 3.

The calculation of the useful heat gain is conducted per unit flow length. The fluid enters the duct flow at temperature (T_{fi}) and the temperature of the coolant fluid increases cumulatively until at the exit of the duct (T_{fo}). Referring to Fig. 3.8, enthalpy balance over an interval Δx and time interval Δt of the fluid flowing through a single duct of length, L can be shown as follows:

$$\dot{Q}_u(x) = \dot{M}_f c p_f T_f(x), \quad \text{Eq. 3.14}$$

$$\dot{Q}_u(x + \Delta x) = \dot{M}_f c p_f T_f(x + \Delta x), \quad \text{Eq. 3.15}$$

$$\frac{\dot{Q}_u(x)}{\Delta x} = \dot{M}_f c p_f \frac{dT_f(x)}{dx}, \quad \text{Eq. 3.16}$$

$$\underbrace{\Delta t \dot{M}_f c p_f \frac{dT_f(x)}{dx} \Delta x}_1 = \underbrace{\Delta t w \Delta x h_f (T_{mpv}(x) - T_f(x))}_2 + \underbrace{\Delta t w \Delta x h_f (T_{bm}(x) - T_f(x))}_3. \quad \text{Eq. 3.17}$$

The next is the interpretation for each term of the enthalpy balance equation Eq. 3.17:

1. The total incremental useful heat transfer (enthalpy term).
2. The rate of heat transfer by convection from the bottom surface of the PV module to the flowing fluid.
3. The rate of heat transfer by convection from the top surface of the lower absorber plate to the flowing air.

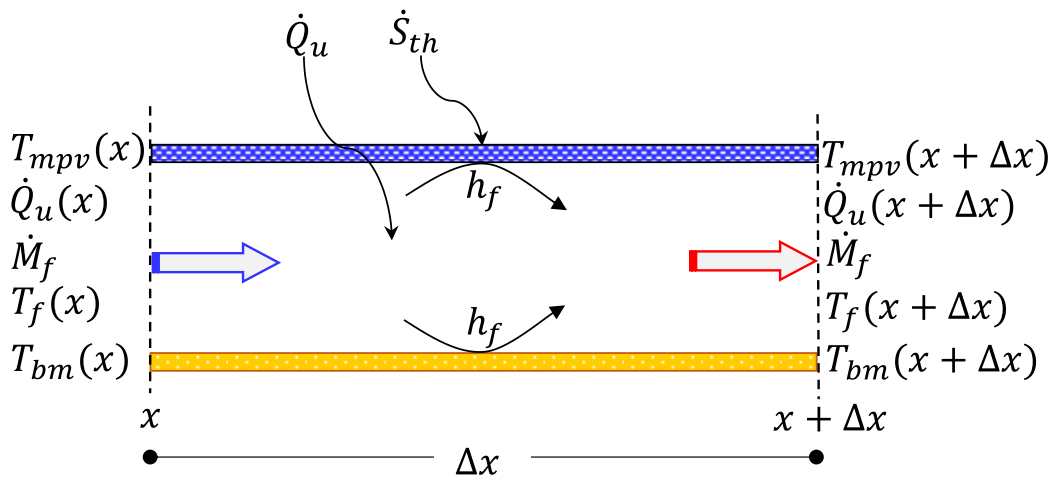


Fig. 3.8. Schematic of the enthalpy balance over an interval Δx and time interval Δt of the fluid flowing.

3.3 Heat transfer and fluid flow equations

Heat transfer is categorised into three main modes: conduction, convection and radiation. In order to describe the heat transfer behaviour in PV/T air systems, model 3 is chosen as a comprehensive example to describe this behaviour. The incidence of solar radiation on the top surface of the glass cover is reflected and is absorbed, but most of it is transmitted as illustrated in Fig. 3.9. The air gap between the glass cover and top surface of the PV module (i.e. in the upper channel) is considered a free convection zone. The fluid convection motion between the glass cover and the PV module is induced by buoyancy forces resulting from density gradients in the fluid as well as the temperature gradient between the two surfaces (see Fig. 3.9). In the lower channel, air flows by a pump or fan and is considered as forced convection. The remainder of insolation is absorbed by the PV to generate partially thermal

energy and the rest is released from the PV cells through an external circuit as electrical power. Following this, the PV layers experience conduction.

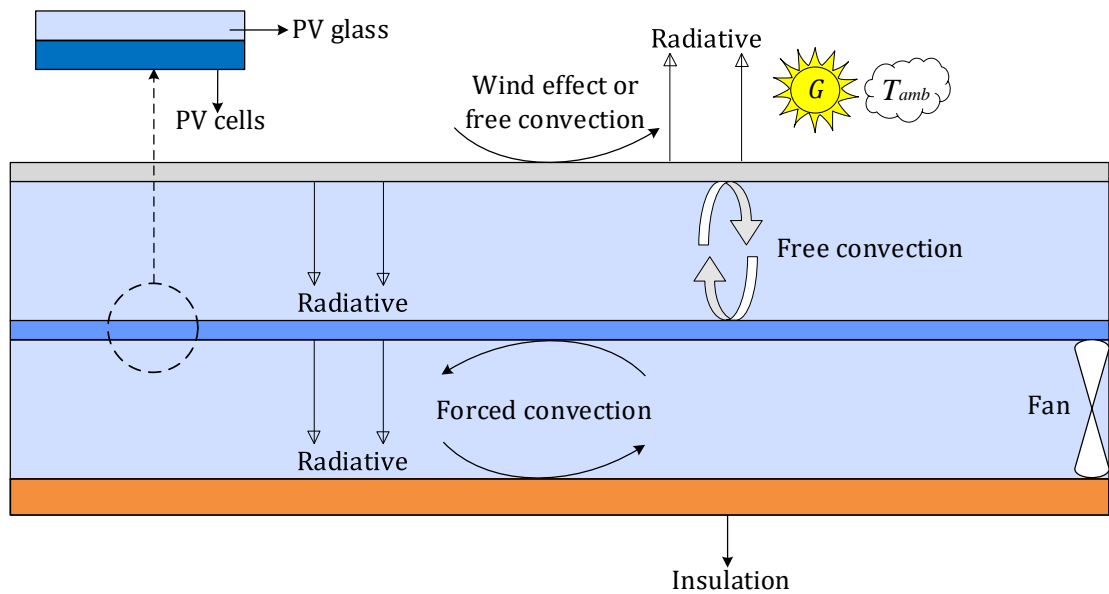


Fig. 3.9. Schematic of heat transfer modes in PV/T air systems (model 3).

In this chapter, the relevant convective and radiative heat transfer coefficients used to solve the heat balance and the fluid flow equations are presented. The examination of different approaches to solve the convection heat transfer rate in the enclosure are investigated. Finally, the thermal, hydraulic and electrical equations are introduced.

3.3.1 Dimensionless numbers

Free convection heat transfer parameters are usually formulated in terms of three dimensionless numbers: Nusslet number (Nu), Rayleigh number (Ra) and Prandtl number (Pr). Some authors correlated data in terms of the Grashof number, which is the ratio of the Ra to the Pr [250]. Meanwhile, the forced convection parameters are correlated in terms of Nusslet number, Prandtl number and Reynolds number.

3.3.1.1 Rayleigh number

The Rayleigh number (Ra) is defined as the product of Gr, which explains the relation between viscosity and buoyancy within a fluid, and the Pr, which illustrates the relationship between thermal diffusivity and momentum diffusivity [27, 121, 122].

$$\text{Ra} = \frac{\text{Buoyant force}}{\text{Viscous force}}. \quad \text{Eq. 3.18}$$

The Rayleigh number is based on the distance between the two heated plates (δ_{D2}) which is denoted as Ra_{δ_D} .

$$\text{Ra}_{\delta_D} = \text{Gr}_{\delta_D} \text{Pr} = \frac{g \beta_f (T_h - T_c) \delta_{D2}^3}{\alpha \nu_f}, \quad \text{Eq. 3.19}$$

where β_f is the thermal expansion coefficient is equal to $1/T_{\text{gap}}$ (K^{-1}), for ideal gases, where the temperature is absolute temperature. T_h is the hot side wall temperature, T_c is the cold side wall temperature, δ_{D2} is the distance between regions of high temperature and low temperature i.e., the distance between the top surface of the PV panel and bottom surface of the glass cover for model 3 as shown in Fig. 3.3. α is the thermal diffusivity of fluid ($\text{m}^2 \text{s}^{-2}$) which can be defined as a measure of the ability of a material to conduct thermal energy relative to its ability to store thermal energy [256].

$$\alpha = \frac{k_f}{\rho_f c p_f}. \quad \text{Eq. 3.20}$$

All physical properties are evaluated at the air gap temperature (T_{gap}),

$$T_{\text{gap}} = \frac{T_h + T_c}{2}. \quad \text{Eq. 3.21}$$

In this case, the Ra formulated based on characteristic length (L_c) which is denoted as Ra_{L_c}

All physical properties are evaluated at the film temperature (T_{film}).

$$T_{\text{film}} = \frac{(T_s + T_\infty)}{2}, \quad \text{Eq. 3.22}$$

$$L_c = \frac{A_s}{P_{er}} = \frac{w L}{2(w+L)}, \text{ horizontal plate} \quad \text{Eq. 3.23}$$

$$L_c = L, \text{ vertical and inclined plate} \quad \text{Eq. 3.24}$$

$$\text{Ra}_{L_c} = \frac{g \beta_{\text{film}} (T_s - T_{\text{film}}) L_c^3}{\nu_{\text{film}}^2}, \quad \text{Eq. 3.25}$$

where T_∞ is the quiescent temperature (fluid temperature far from the surface of the surface), P_{er} is the perimeter of the plate, w is the width of the plate, β_{film} is the thermal expansion coefficient is equal to $1/T_{\text{film}}$, for ideal gases, where the temperature is absolute

temperature. In case of the boundary condition is constant heat flux T_s is the uniform surface temperature.

3.3.1.2 Reynolds number

The Reynolds number (Re) can be defined as the ratio of the inertial force to the viscous force within the flow. The main function of the Reynolds number is to characterize the nature of flow (i.e. laminar, transitional or turbulent). The Reynolds number is universally used in the correlation of experimental data on frictional pressure drop and heat and mass transfer in convective flow. Re is a function of much physical modelling. For internal flow and non-circular tube (channel duct), the Reynolds number is denoted as Re_{D_h} .

$$Re_{D_h} = \frac{\text{Inertia forces}}{\text{Viscous forces}} = \frac{\rho_f \bar{V} D_h}{\mu_f} = \frac{4 \dot{M}}{\mu_f P_{er}}, \quad \text{Eq. 3.26}$$

where D_h is the hydraulic diameter or duct equivalent diameter for both circular and non-circular cross sections is:

$$D_h = \frac{4 \text{ flow area}}{\text{wetted perimeter } (P_{er})}. \quad \text{Eq. 3.27}$$

In the current study, parallel plates are considered (duct) having a width (w) and depth of flow (δ_D), the hydraulic diameter becomes:

$$D_h = \frac{4 w \delta_D}{(w + \delta_D)}. \quad \text{Eq. 3.28}$$

According to [180, 257], the critical laminar value of Reynolds number for this type of design (flow between parallel plates) is considered 2550.

$$\text{For laminar flow } Re_{D_h} < 2550, \quad \text{Eq. 3.29}$$

$$\text{for turbulent flow } Re_{D_h} > 2550. \quad \text{Eq. 3.30}$$

3.3.1.3 Nusselt number

The key criterion considered in estimating the free and forced convective heat transfer coefficients in both laminar and turbulent flow regimes is Nusselt number (Nu).

Convection heat transfer occurs at the solid-fluid interfaces (see Fig. 3.10). This heat transfer rate per unit area is expressed in terms of a heat transfer coefficient (h) and the

difference between the interface and surrounding or ambient temperatures ($T_\infty - T_{f,\Gamma}$) based on Newton's law of cooling.

$$Q_n = h(T_\infty - T_{f,\Gamma}). \quad \text{Eq. 3.31}$$

The heat transfer rate may also be expressed in terms of the thermal conductivity k_f of the fluid, according to the Fourier law of conduction, as;

$$Q_n = -k_f \frac{\partial}{\partial n} (T - T_{s,\Gamma}) \Big|_\Gamma. \quad \text{Eq. 3.32}$$

Combining Eq. 3.31 and Eq. 3.32 gives:

$$-k_f \frac{\partial}{\partial n} (T - T_{s,\Gamma}) \Big|_\Gamma = h(T_{f,\Gamma} - T_\infty). \quad \text{Eq. 3.33}$$

Rearranging Eq. 3.33 in terms of characteristic length (L_c). Thus, Nu can be defined as the ratio of the convective to the conductive heat transfer rates across the boundary as shown in Eq. 3.34.

$$\frac{h L_c}{k_f} = \frac{\frac{\partial}{\partial n} (T - T_{s,\Gamma}) \Big|_\Gamma}{(T_{f,\Gamma} - T_\infty)}, \quad \text{Eq. 3.34}$$

where Γ is the interface surface between the solid and fluid. The interface wall temperatures have the same temperature magnitude ($T_{s,\Gamma} = T_{f,\Gamma}$).

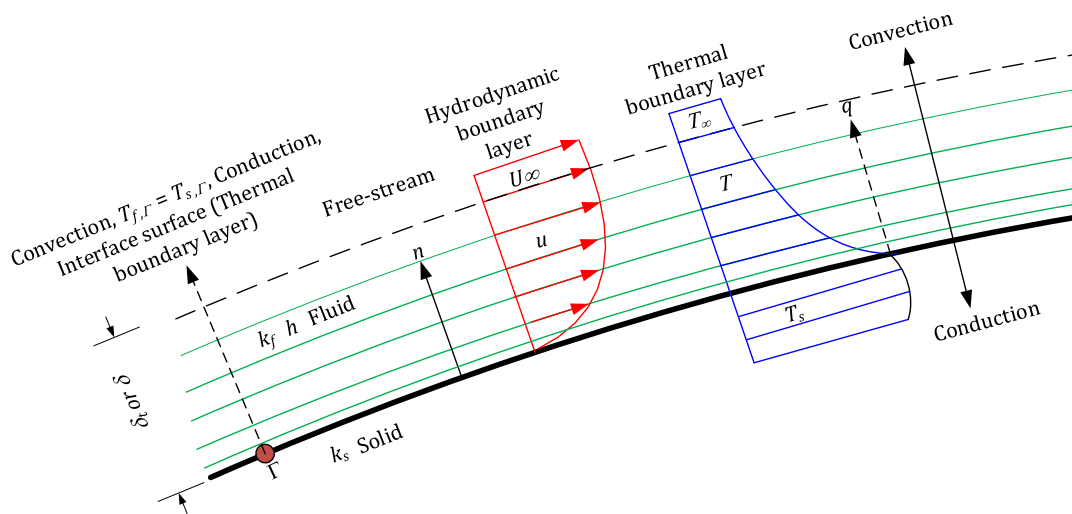


Fig. 3.10. Schematic of conjugate heat transfer between solid and fluid domains adapted from [258].

In Fig. 3.10, δ and δ_t are the thicknesses of thermal and hydrodynamic boundary layers respectively. Prandtl number is used to identify the ratio of these layers. If the Pr is 1, the two boundary layers are the same thickness.

3.3.2 Heat transfer coefficients and losses

Calculating a convective heat transfer coefficient is the key to measure the heat transfer enhancement in heat exchanger devices such as PV/T air systems. This coefficient is important in evaluating the convective heat transfer across the system. The radiative heat transfer coefficients with the relevant parameters are presented in this section.

3.3.2.1 Heat losses coefficients

In solar air collectors, there are two main heat losses. The major portion is the overall top heat loss (U_t) while the minor loss is the bottom heat loss (U_b).

For model 2, the overall top loss coefficient from the PV panel to the ambient while for model 3, the overall top loss coefficient from the PV panel to ambient via the front glazing. This coefficient (U_t) is a function of the wind velocity (V_w), the emittance of the PV panel (ε_{pv}), the emittance of the glass cover (ε_g), T_{mpv} and T_{amb} . Since the solar cell is thin, its heat capacitance is assumed as negligible [27, 122]. For model 2 and model 3, two expressions are used to evaluate top heat loss, as shown in Eq.3.35 and Eq.3.36.

$$\text{For model 2 } U_t = h_w + h_{r(pv-sky)}, \quad \text{Eq. 3.35}$$

$$\text{for model 3 } U_t = \left[\frac{1}{h_{r(pv-g)} + h_{f(pv-g)}} + \frac{1}{h_w + h_{r(g-sky)}} \right]^{-1}, \quad \text{Eq. 3.36}$$

where $h_{r(pv-sky)}$ is the radiative heat transfer coefficient between the PV absorber plate and the sky [27, 50, 122, 250, 251] which can be evaluated as in Eq. 3.37. $h_{f(pv-g)}$ is the free convective heat transfer coefficient for the bottom surface of the glass cover and the top surface of the PV module i.e. free convective heat transfer coefficient in the enclosure, see Fig. 3.3. For model 3, $h_{r(g-sky)}$ is the radiative heat transfer coefficient between the glass cover and the sky [250, 251] as shown in Eq. 3.38.

$$\text{for model 2 } h_{r(pv-sky)} = \frac{\sigma \varepsilon_{pv} (T_{mpv}^2 + T_{sky}^2)(T_{mpv} + T_{sky})(T_{mpv} - T_{sky})}{(T_{mpv} + T_{amb})}, \quad \text{Eq. 3.37}$$

$$\text{for model 3 } h_{r(g-sky)} = \frac{\sigma \varepsilon_g (T_g^2 + T_{sky}^2)(T_g + T_{sky})(T_g - T_{sky})}{(T_g - T_{amb})}. \quad \text{Eq. 3.38}$$

The measurement of the sky temperature (T_{sky}), which is called the temperature of the atmospheric filter, is complex and seldom available, several correlations are in the literature to predicting the sky temperature:

$$T_{sky} = T_{amb} \left[0.8 + \frac{T_{dp} 273}{250} \right]^{1/4} \quad [37], \quad \text{Eq. 3.39}$$

$$T_{sky} = 0.037536 T_{amb}^{1.5} + 0.32 T_{amb} \quad [32], \quad \text{Eq. 3.40}$$

$$T_{sky} = T_{amb} [0.711 + 0.0056 T_{dp} + 0.000073 T_{dp}^2 + 0.013 \cos(15t)]^{0.25} \quad [50, 259], \quad \text{Eq. 3.41}$$

$$T_{sky} = T_{amb} - 6. \quad [260], \quad \text{Eq. 3.42}$$

where T_{dp} is the dew point temperature in °C and t is the time in hours (h) from midnight. T_{dp} is measured in the range -20 °C to -30 °C. The range of the difference between the sky and air temperatures is from 5 °C in a hot-moist climate to 30 °C in a cold-dry climate. The issue with this equation is that T_{dp} is occasionally not available. Finally, a frequently used formula is given by Swinbank [261] which is used in this study. This formula has also been used by [37, 121, 250, 262].

$$T_{sky} = 0.0552 T_{amb}^{1.5}. \quad \text{Eq. 3.43}$$

A common empirical equation widely used in the calculation U_t , which secures sufficient accuracy for design purposes. This equation was correlated by Klein [263] which can also be employed to compare the results obtaining from Eq.3.35 and Eq.3.36.

$$U_t = \left[\frac{N}{\frac{C_\beta}{T_{mpv}} \left[\frac{T_{mpv} - T_{amb}}{(N+f)} \right]^e + h_{ex}} \right]^{-1} + \frac{\sigma (T_{mpv} + T_{amb})(T_{mpv}^2 + T_{amb}^2)}{\frac{1}{\varepsilon_{pv} + 0.00591 N h_{ex}} + \frac{2n_c + f - 1 + 0.133 \varepsilon_{pv}}{\varepsilon_g} - N}, \quad \text{Eq. 3.44}$$

where n_c is the number of glass covers.

$$f = (1 + 0.089 h_{ex} - 0.1166 h_{ex} \varepsilon_{pv})(1 + 0.07866 N), \quad \text{Eq. 3.45}$$

$$C_\beta = 520 (1 - 0.000051 \beta^2), \quad \text{Eq. 3.46}$$

$$e = 0.430 (1 - 100/T_{mpv}). \quad \text{Eq. 3.47}$$

For $0^\circ < \beta < 70^\circ$; for $70^\circ < \beta < 90^\circ$ use $\beta = 70^\circ$

where β is the collector tilt angle and h_{ex} is the external heat transfer coefficient either free or forced convection condition ($\text{W m}^{-2} \text{K}^{-1}$).

Assuming that there is no effect of wind or free convection and exchange radiation with surrounding from the collector back, the minor loss of the PV/T air collector can be represented by:

$$U_b = \frac{k_{ins}}{t_{ins}}, \quad \text{Eq. 3.48}$$

where k_{ins} is the back insulation and t_{ins} is the thickness of the back insulation.

Eq. 3.49 estimates the radiative heat transfer coefficients between the PV panel absorber and the glass cover $h_{r(pv-g)}$.

$$h_{r(pv-g)} = \sigma \frac{(T_{mpv} + T_g)(T_{mpv}^2 + T_g^2)}{\frac{1}{\varepsilon_{pv}} + \frac{1}{\varepsilon_g} - 1}. \quad \text{Eq. 3.49}$$

While Eq. 3.50 estimates the radiative heat transfer coefficients between two absorbers (h_{rpb}).

$$h_{rpb} = \sigma \frac{(T_{mpv} + T_{bm})(T_{mpv}^2 + T_{bm}^2)}{\frac{1}{\varepsilon_{pv}} + \frac{1}{\varepsilon_{bm}} - 1}, \quad \text{Eq. 3.50}$$

where σ is the Stefan-Boltzmann's constant which equals to $5.7 \times 10^{-8} \text{ (W m}^{-2} \text{K}^{-4}\text{)}$.

3.3.2.2 External natural convection

The main criteria that govern free convection are:

- Fluid motion induced by buoyancy forces.
- Buoyancy forces arise when there are density gradients in the fluid.
- Density gradients take place owing to temperature gradients.
- Body force takes place owing to gravity (a function of mass)

In the solar air collectors, some days there is little or no wind, the free convection mode will, therefore, dominate rather than the wind effect. This phenomenon appears clearly in a cold climate when there is a significant difference in temperature between the air and solid surface [36, 264]. The purpose of assuming the free convection phenomenon is to examine the effects of worst-case scenarios for the PV system. In this section, the Nusselt number

correlations are presented as a function of the convective heat transfer coefficient for different inclinations and conditions.

An approximated correlation equation developed to estimate the free heat transfer coefficient for the top surface of the glass cover [33, 37, 265, 266] is given in Eq. 3.51 and Eq. 3.52.

$$h_{\text{free}} = 1.78 (T_s - T_{\text{amb}})^{1/3}, \quad \text{Eq. 3.51}$$

$$h_{\text{free}} = 1.31 (T_s - T_{\text{amb}})^{1/3}, \quad \text{Eq. 3.52}$$

where T_s is the top surface temperature exposed to ambient conditions and h_{free} is the average convective heat transfer coefficient under free convection conditions.

Empirical correlations suggested by Bergman et al. [241] to estimate the convective heat transfer coefficient depending on the type of inclination and surface temperature. These correlations are valid for various engineering applications [241, 267].

$$h_{\text{free}} = \left(\frac{k_f}{L_c} \right) C \text{Ra}_{L_c}^n, \quad \text{Eq. 3.53}$$

where n is 1/4 for laminar and n is 1/3 for turbulent.

Eq. 3.53 has been developed to match with a vertical plate and presented in Eq. 3.54 and Eq. 3.55.

$$\text{For laminar flow } (10^4 \leq \text{Ra}_{L_c} \leq 10^9) \quad C = 0.59 \text{ and } n = 1/4, \quad \text{Eq. 3.54}$$

$$\text{for turbulent flow } (10^9 \leq \text{Ra}_{L_c} \leq 10^{13}) \quad C = 0.1 \text{ and } n = 1/3. \quad \text{Eq. 3.55}$$

Churchill and Chu [267] recommended a correlation equation that may be applied over the entire range of Ra_{L_c} . This is presented in Eq. 3.56, as [241, 267]:

$$h_{\text{free}} = \left(\frac{k_f}{L_c} \right) \left(0.825 + \frac{0.387 \cos(\theta) \text{Ra}_{L_c}^{1/6}}{\left(1 + \left(\frac{0.492 k_f}{cp_f \mu_f} \right)^{9/16} \right)^{8/27}} \right)^2. \quad \text{Eq. 3.56}$$

However, for the laminar regime, Churchill and Chu [267] recommend the use of Eq. 3.57 instead of Eq. 3.56 which affords greater accuracy [241, 267].

$$h_{\text{free}} = \left(\frac{k_f}{L_c} \right) \left(0.68 + \frac{0.67 \cos(\phi) \text{Ra}_{L_c}^{\frac{1}{4}}}{\left(1 + \left(\frac{0.492 k_f}{c_{p_f} \mu_f} \right)^{\frac{9}{16}} \right)^{\frac{1}{4}}} \right) \text{if } \text{Ra}_{L_c} \leq 10^9 \text{if } \text{Ra}_{L_c} \leq 10^9. \quad \text{Eq. 3.57}$$

These equations are also valid for an inclined plate in which, ϕ is the angle between the PV module and the vertical direction as shown in Fig. 3.11. These correlations are valid for $-60 < \phi < 60$ ($-30 < \beta < 30$).

where:

$$\text{for horizontal plate } L_c = \frac{A_s}{P_{er}} = \frac{w L}{2(w+L)}, \quad \text{Eq. 3.58}$$

$$\text{for vertical and inclined plate } L_c = L. \quad \text{Eq. 3.59}$$

For turbulent flow, Vliet [268] suggested that the experimental results correlated better using g instead of $g \cos(\phi)$, i.e. heat transfer in turbulent natural convection is not sensitive to the inclination angle.

According to [241, 267], the correlation equations for inclined walls (i.e. Eq. 3.56 and Eq. 3.57) are only satisfactory for the top side of a cold plate or the down face of a hot plate. Hence, these correlations are not recommended for the bottom side of a cold face nor for the top side of a hot plate. Since the application of inclined PV systems is the top and bottom sides of a hot plate which does not match the aforementioned literature cases, some deviation owing to this is thus expected. In this study, the tilt angle is in the range of $(30-90)^\circ$ and the horizontal position are both studied. Schematic representations of the free convective boundary layers for inclined, vertical and horizontal surfaces are shown in Fig. 3.11.

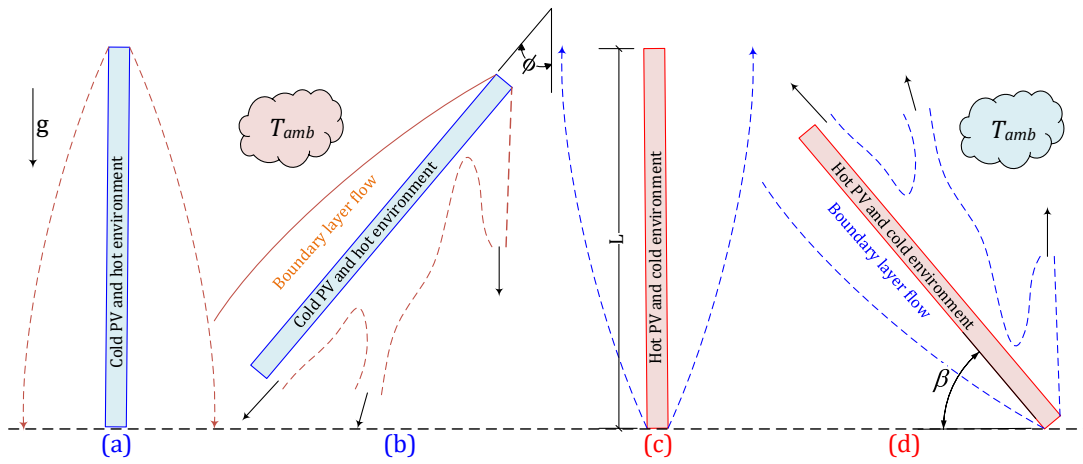


Fig. 3.11. Schematic of different positions of hot and cold plates, in (a) Vertical hot plate, (b) Inclined (down face of a hot plate), (c) Vertical cold plate (d) Inclined (top side of a cold plate)

In the case of the horizontal position (hot surface upward and hot surface downward), the set of flowing equations can be used:

1. The top surface of the hot plate or bottom surface of the cold plate [241].

Eq. 3.60 is for laminar flow and Eq. 3.61 for turbulent flow.

$$h_{\text{free}} = (k_f/L_c) 0.54 \text{Ra}_{L_c}^{1/4} (10^4 \leq \text{Ra}_{L_c} \leq 10^7), \text{Pr} \geq 0.7, \quad \text{Eq. 3.60}$$

$$h_{\text{free}} = (k_f/L_c) 0.15 \text{Ra}_{L_c}^{1/3} \cdot (10^7 \leq \text{Ra}_{L_c} \leq 10^{11}), \text{all Pr.} \quad \text{Eq. 3.61}$$

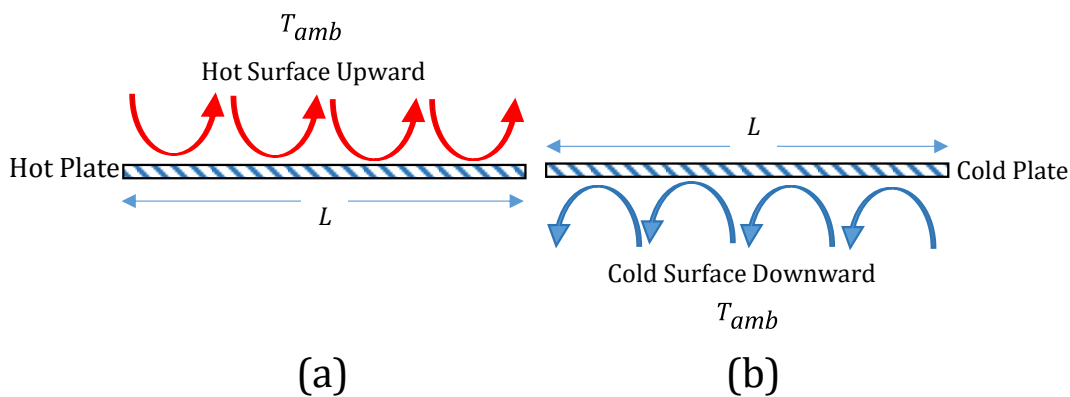


Fig. 3.12. Schematic of buoyancy-driven flows on a horizontal position in (a) End view of flow at the top surface of the hot plate and in (b) End view of flow at the bottom surface of cold plate adapted from [241].

2. The bottom surface of the hot plate or top surface of the cold plate

Either Eq. 3.62 or Eq. 3.63 can be used in case of the bottom surface of the hot plate or top surface of the cold plate as shown in Fig. 3.13.

$$h_{\text{free}} = (k_f/L_c) 0.52 \text{Ra}_{L_c}^{1/5}. (10^4 \leq \text{Ra}_{L_c} \leq 10^9), \text{Pr} \geq 0.7 \text{ [241]}, \quad \text{Eq. 3.62}$$

$$h_{\text{free}} = (k_f/L_c) 0.52 \text{Ra}_{L_c}^{1/5}. (10^5 \leq \text{Ra}_{L_c} \leq 10^{11}) \text{ [269]}. \quad \text{Eq. 3.63}$$

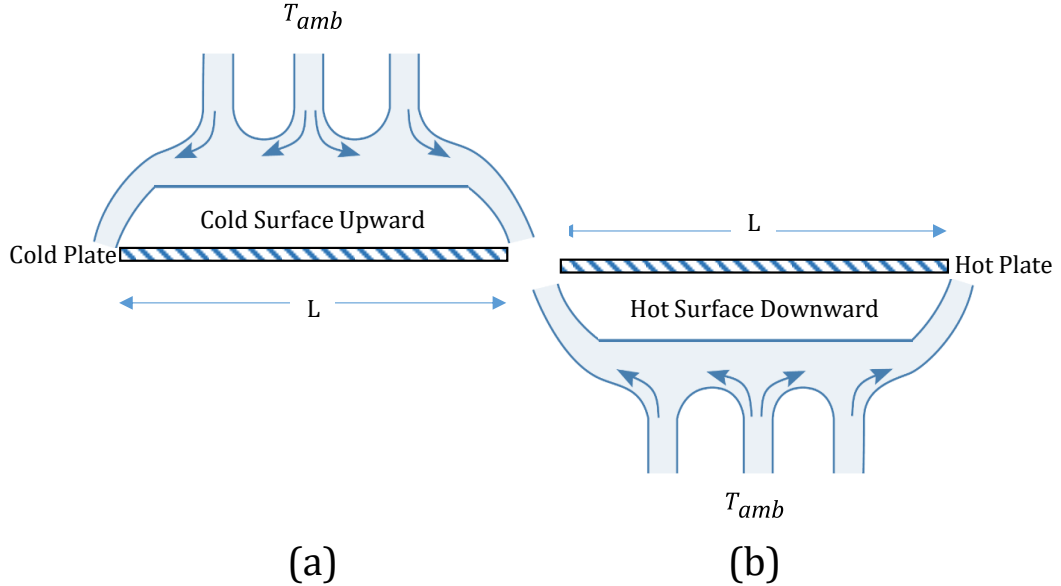


Fig. 3.13. Schematic of buoyancy-driven flows on the horizontal position in (a) Top surface of the cold plate and in (b) Bottom surface of hot plate adapted from [241].

3.3.2.3 Natural convection in enclosures

In solar air collectors, one of the major concerns is to minimize the heat losses from the hot surfaces to the colder surroundings. These heat losses result from conductive-convective and thermal radiative heat exchanges through the top surface of the absorber plate. From an energy conservation point of view, designers investigate feasible options to reduce these losses [270]. One of these options is to insulate the system by adding one or more transparent covers, which also serve as protection from weathering. However, in the case of PV/T air systems, a compromise should be considered between the rise of PV panel temperature and the reduction in heat losses. In this study, one transparent cover is therefore used to avoid this action. The recommended size of the gap between the transparent cover and the absorber plate is between 10 mm to 25 mm [270]. Empirical correlations and CFD modelling approaches are examined in this section.

3.3.2.3.1 Empirical correlations

A wide range of empirical correlations are available in the literature which have been selected based on the accuracy and the conditions of the studied systems. The conditions considered in this study are, the air gap separates the two heated surfaces. The hotter surface is located below the cooled one in the case of horizontal or tilted flat plate solar systems (β) as illustrated in Fig. 3.14a [270, 271].

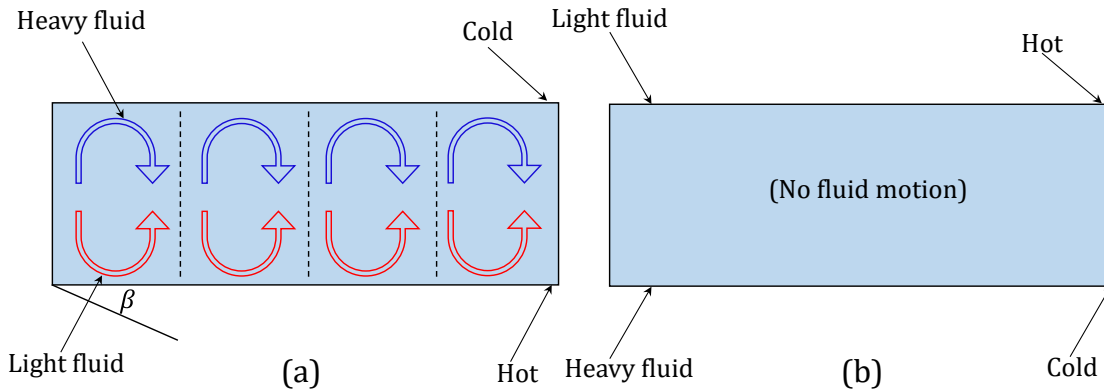


Fig. 3.14. Horizontal rectangular enclosure with isothermal surfaces adapted from [272].

For small air gap depth (δ_D) the heat transfer in the air gap can be purely conductive; this could be valid when the Rayleigh number is sufficiently small. In this case, the shape of fluid motion appears as one big cell called the base flow; the lighter fluid rises near the hot surface while the heavier fluid falls near the cold surface [252, 271]. So, the Nusselt number for the air gap becomes negligible, and it approaches unity [252, 271]. The governing equation is:

For $Ra_{\delta_D} < 1708 / \cos\beta, \beta \leq 70$

$$h_{\text{free}} = (k_f / \delta_D), \quad \text{Eq. 3.64}$$

where β the tilt angle and the critical value of Ra_{δ_D} is given by $Ra_{\delta_D} = 1708 / \cos\beta$ [271, 273].

To assume that the regime is purely conductive, the following criteria should be considered:

1. The Rayleigh number is less than the critical value [271, 273].
2. For the $Ra_{\delta_D} >$ critical value, if the depth of the air gap is relatively small, it results in a high aspect ratio (L/δ_D). The conductive heat transfer becomes the dominating mode so that the Nusselt number of unity represents pure conduction [271]. Catton et al. [274] stated that the contribution to heat transfer by the unicellular flow will always be negligible for

aspect ratios (20-200) of interest in solar collector design, however, this is not valid at the extreme ends where there is some convective heat transport associated with the fluid turning [275].

3. There are no convection currents induced while the hotter plate is at the top, as the direction of heat transfer is downwards by conduction ($Nu = 1$) as shown in Fig. 3.14b.

With increasing values of the δ_D , natural convection in the air gap becomes the dominating heat transfer mode [252]. In this case, the shape of fluid motion appears as a combination of the roll and the cellular structures [241]. The relationship between Ra and Nu is shown in Eq. 3.65 [275]. According to the results of measurements reported in [275], Eq. 3.65 is recommended for estimating heat transfer coefficient by free convection having $0 < \beta < 60$ degrees and $0 < Ra < 10^5$ with a maximum error of approx. 5% and 10% for β up to 75 degrees. From analogy with the horizontal layer, Eq. 3.65 is expected to be valid for $Ra > 10^6$. This equation has also been used by [24, 27, 121, 122, 250].

$$h_{\text{free}} = (k_f/\delta_D) \left[\{ 1 + 1.44(1 - R)^* (1 - R (\sin 1.8\beta)^{1.6}) + [0.66416 R^{-1/3} - 1]^* \} \right], \quad \text{Eq. 3.65}$$

where:

$$R = \frac{1708}{Ra_{\delta_D} \cos\beta}, \quad \text{Eq. 3.65a}$$

The meaning of the (*) exponent in Eq. 3.65 is that only positive values of the terms in the square brackets are to be used (i.e. use zero if the term is negative). All properties are evaluated at the T_{gap} .

To afford greater accuracy, a comprehensive review has been carried out by Arnold et al. [276]. They have revealed that when the heated surface lies below the cooled one, in either horizontal or tilted flat plate solar collectors, a (multi) cellular convection arises when $Ra_{\delta_D} \cos\beta \gg 1708/\cos\beta$. The authors suggest that there are three-region correlations as shown in Eq. 3.66 to Eq. 3.68:

For $1708 < Ra_{\delta_D} \cos\beta < 5900$

$$h_{\text{free}} = (k_f/\delta_D) \left(1 + 1.446 \left[\left(1 - \frac{1708}{Ra_{\delta_D} \cos\beta} \right) \right]^* \right). \quad \text{Eq. 3.66}$$

For $5900 < Ra_{\delta_D} \cos\beta < 9.23 \times 10^4$

$$h_{\text{free}} = (k_f/\delta_D) 0.229 \text{ Ra}_{\delta_D}^{0.252}. \quad \text{Eq. 3.67}$$

For $9.23 \times 10^4 < \text{Ra}_{\delta_D} \cos\beta < 10^6$

$$h_{\text{free}} = (k_f/\delta_D) 0.157 \text{ Ra}_{\delta_D}^{0.285}. \quad \text{Eq. 3.68}$$

Also, important correlations for horizontal enclosures are recommended by Jakob [277].

For $10^4 < \text{Ra}_{\delta_D} < 4 \times 10^5$

$$h_{\text{free}} = (k_f/\delta_D) 0.195 \text{ Ra}_{\delta_D}^{0.25}. \quad \text{Eq. 3.69}$$

For $4 \times 10^5 < \text{Ra}_{\delta_D} < 10^7$

$$h_{\text{free}} = (k_f/\delta_D) 0.068 \text{ Ra}_{\delta_D}^{1/3}. \quad \text{Eq. 3.70}$$

3.3.2.3.2 CFD modelling approaches

The evaluation of free convection in the enclosure is carried out using two CFD techniques. The first technique is 3D CFD modelling under transient conditions. The relevant governing equations for the air velocity $\vec{V}(x, y, z) = u, v, w$ and temperature T are based on the conservations of mass, momentum, and energy [278]. The conservations of mass and momentum are presented in detail in Section 4.3.1. Eq. 3.71 and Eq. 3.72 are the heat transfer equations for solid and fluid domains, respectively.

$$\frac{D(\rho c T)}{Dt} \cdot \nabla T = \nabla \cdot (k_s \nabla T) - \dot{Q}, \quad \text{Eq. 3.71}$$

$$\nabla \cdot (k_{x,y,z} \nabla T) = \frac{\partial}{\partial x} \left(k_x \frac{\partial T}{\partial x} \right) + \frac{\partial}{\partial y} \left(k_y \frac{\partial T}{\partial y} \right) + \frac{\partial}{\partial z} \left(k_z \frac{\partial T}{\partial z} \right), \quad \text{Eq. 3.71a}$$

$$\frac{D(\rho c T)}{Dt} = \rho c \frac{\partial T(x,y,z)}{\partial t} + \rho c u \frac{\partial T}{\partial x} + \rho c v \frac{\partial T}{\partial y} + \rho c w \frac{\partial T}{\partial z}. \quad \text{Eq. 3.71b}$$

Supposing unsteady state conditions, with internal energy conversion (i.e. electrical power generation as a heat sink), three dimensions and non-moving parts (stationary PV panel), Eq. 3.71 reduces to the following format,

$$\rho c \frac{\partial T(x, y, z)}{\partial t} = \nabla \cdot (k_{x,y,z} \nabla T) - \dot{Q}_v, \quad \text{Eq. 3.71c}$$

where ρ is the density, c is the specific heat, k_s is the thermal conductivity, \dot{Q}_v is the volume heat source or sink.

$$\rho c_{p_f} \left(\frac{\partial T(x,y,z)}{\partial t} + V \nabla T(x,y,z) \right) = \nabla \cdot (k_f \nabla T) + Q_{vd} + Q_p - \dot{Q}_v \quad [278], \quad \text{Eq. 3.72}$$

where Q_{vd} is the viscous dissipation in the fluid domain, u is the velocity vector, Q_p is the work done by pressure gradients due to heating under adiabatic compression and a thermo-acoustical phenomenon, which is relatively minor for a small Mach number.

$$Q_p = \alpha_p T \left(\frac{\partial p}{\partial t} + V \cdot \nabla p \right), \quad \text{Eq. 3.73}$$

$$\alpha_p = \frac{1}{\rho} \frac{\partial \rho}{\partial T}, \quad \text{Eq. 3.74}$$

where p is pressure, and for ideal gases, the thermal expansion coefficient α_p takes the simpler form as follows:

$$\alpha_p = \frac{1}{T}. \quad \text{Eq. 3.75}$$

This approach is considered to be accurate more than the other methods (empirical correlations) because it is more representative of real conditions. However, this method is inherently intricate because of the complexity of the transient model. For example, choosing the time step, the difficulty of solution convergence and is more expensive in terms of running time, and computer memory and RAM. For this reason, the necessity of finding an alternative method can contribute to tackling these issues.

The alternative approach is a 3D CFD model with a temperature-dependent thermal conductivity in the enclosure called effective thermal conductivity. It is usually applicable to a narrow range of Prandtl and Rayleigh numbers and aspect ratios [279]. This method is more appropriate and valid for high aspect ratio geometries, i.e. the length of the cavity (duct) to the depth of flow (height of cavity) (L/δ_D) [279].

The technique is, the thermal conductivity is increased by an empirical correlation factor that depends on the cavity dimensions and the temperature variation across the cavity. This method could be not applicable for nonrectangular geometries [280].

The difference between two methods (transient and effect thermal conductivity) is that the fluid flow domain is not modelled which implies the velocity term disappears or is neglected. The heat transfer in the interface solid-fluid (conjugate heat transfer) however,

is still modelled and considered. The increased heat transfer rate in the enclosure depends on the value of the product kNu as well as the temperature variation across the enclosure (cavity) and cavity dimension (depth flow) as shown in Eq. 3.76. Therefore, the quantity kNu is called the effective thermal conductivity of the enclosure. The term $\nabla \cdot (k_f \nabla T)$ in Eq. 3.72 becomes $\nabla \cdot (k_f Nu \nabla T)$ and the velocity term $(V \nabla T(x, y, z))$ in the same equation disappears too.

$$\rho c_{p_f} \left(\frac{\partial T(x,y,z)}{\partial t} \right) = \nabla \cdot (k_f Nu \nabla T) + Q_{vd} + Q_p - \dot{Q} \quad [278], \quad \text{Eq. 3.76}$$

$$Nu = 0.068 Ra_{\delta_D}^{1/3} Pr^{0.074}. \quad \text{Eq. 3.77}$$

For the special case of this method, the effective thermal conductivity of the enclosure becomes equal to the conductivity of the fluid ($Nu = 1$).

3.3.2.3.3 Air gap assumption

To estimate the convective heat transfer coefficient in enclosed surfaces (enclosure), it is necessary to evaluate accurate physical air properties. The physical properties of air are evaluated at air gap temperature (T_{gap}), as presented in Eq. 3.78.

$$T_{gap} = \frac{(T_{mpv} + T_g)}{2}. \quad \text{Eq. 3.78}$$

T_{gap} is the air enclosed between the bottom surface of the glass cover and the top surface of the PV panel for model 3 as shown in Fig. 3.15. In order to examine the validity of using this temperature, an investigation was conducted to justify this assumption [272]. Three methods were employed in this investigation as follows:

1. Empirical correlations (method 1) see Section 3.3.2.3.1.
2. 3D CFD modelling with a temperature-dependent thermal conductivity in the enclosure (effective thermal conductivity) (method 2). This method was explained in detail in Section 3.3.2.3.2.
3. 2D CFD modelling under transient conditions (method 3), see Section 3.3.2.3.2.

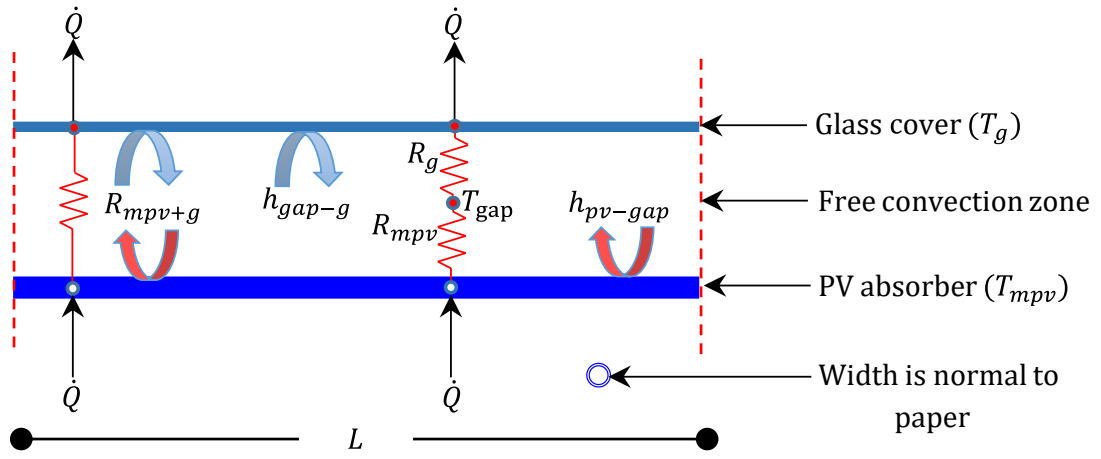


Fig. 3.15. Schematic of a horizontal rectangular enclosure with isothermal surfaces.

In enclosed surfaces, as in model 3, there are two convective heat transfer coefficients. The first one is the convective heat transfer coefficient at the top surface of the PV module (h_{pv-gap}) while the second one is at the bottom surface of the glass cover (h_{gap-g}). Instead of using the two separate convective heat transfer coefficients, it is possible to estimate an overall heat transfer coefficient in the enclosure (U_{mpv+g}). To define U_{mpv+g} , an energy balance was applied between the glass cover and the PV panel, as shown in Eq. 3.79 and Fig. 3.15.

$$\begin{aligned} \dot{Q}/A_s &= h_{pv-gap} (T_{mpv} - T_{gap}) = h_{gap-g} (T_{gap} - T_g) \\ &= U_{mpv+g} (T_{mpv} - T_g), \end{aligned} \quad \text{Eq. 3.79}$$

where A_s is the PV surface area ($L w$).

To check the reliability of Eq. 3.79, add $\mp T_{gap}$ to both sides of Eq. 3.79 which yields Eq. 3.80,

$$\begin{aligned} \frac{\dot{Q}}{A_s} &= \underbrace{(T_{mpv} - T_g)}_3 = \underbrace{(T_{mpv} - T_{gap})}_1 \underbrace{(T_{gap} - T_g)}_2 = \\ &= \underbrace{(\dot{Q}/A_s)/h_{pv-gap}}_1 + \underbrace{(\dot{Q}/A_s)/h_{gap-g}}_2 \cdot \underbrace{3}_3 \end{aligned} \quad \text{Eq. 3.80}$$

Re-arrange Eq. 3.80 to yield Eq. 3.81.

$$\frac{\dot{Q}}{A_s} = \frac{\dot{Q}}{A_s} + \frac{\dot{Q}}{A_s} \cdot \frac{1}{h_{gap-g}} \cdot h_{pv-gap} \quad \text{Eq. 3.81}$$

Thus:

$$\frac{1}{U_{pv+g}} = \frac{1}{h_{pv-gap}} + \frac{1}{h_{gap-g}}. \quad \text{Eq. 3.82}$$

Also, from Eq. 3.79, it can be concluded that:

$$T_{gap} = \frac{h_{pv-gap} T_{mpv} + h_{gap-g} T_g}{h_{pv-gap} + h_{gap-g}}. \quad \text{Eq. 3.83}$$

Concerning method 1 (Empirical correlations), two heat transfer coefficients were evaluated for the free convective heat transfer coefficients, under the glass cover and over PV panel.

The first one is the convective heat transfer coefficient between the bottom surface of the glass and surrounding (h_{gap-g}). Also, the heat transfer rate (Q_{gap-g}) was estimated. The following are the set of equations used to estimate h_{gap-g} and Q_{gap-g} :

$$Gr_{L_c} = \frac{g \beta_{filmg} (T_{gap} - T_g) L_c^3}{\nu_{filmg}^2}, \quad \text{Eq. 3.84}$$

$$Ra_{L_c} = Pr Gr_{L_c}, \quad \text{Eq. 3.85}$$

$$h_{gap-g} = (k_f / L_c) 0.54 Ra_{L_c}^{0.25}, \quad \text{Eq. 3.86}$$

$$Q_{gap-g} = h_{gap-g} A_s (T_{gap} - T_g). \quad \text{Eq. 3.87}$$

To solve the set of non-linear equations, the goal seek method was utilised [281] to estimate the air gap temperature and the results compared with the assumed T_{gap} .

The second convective heat transfer coefficient is h_{pv-gap} . The same steps were used to estimate this coefficient using the following equations:

$$Ra_{L_c} = Pr Gr_{L_c}, \quad \text{Eq. 3.88}$$

$$h_{pv-gap} = (k_f / L_c) 0.54 Ra_{L_c}^{0.25}, \quad \text{Eq. 3.89}$$

$$Q_{pv-gap} = h_{pv-gap} A_s (T_{mpv} - T_{gap}), \quad \text{Eq. 3.90}$$

$$Q_{pv+g} = A_s U_{pv+g} (T_{mpv} - T_g). \quad \text{Eq. 3.91}$$

Table 3.1 shows the estimated results of the two first methods mentioned above. Method 1 was the empirical method represented by T_{gap1} . The results of the empirical analysis revealed that there is a slight difference between T_{gap1} and T_{gap} . The second method was the CFD method (method 2) denoted by T_{gap2a} and T_{gap2b} . Referring to **Table 3.1**, the top surface temperatures are between 20 to 95 °C while the bottom surface temperature is 120 °C with an air gap space of 0.2 m and 0.025 m. The results obtained from the CFD analysis of method 2 (T_{gap2a} and T_{gap2b}) are in agreement with assumed air gap temperature, T_{gap} . The maximum and minimum temperature differences are 2 °C and 0.1°C for T_{gap2a} while the maximum and minimum temperature differences are 2.1 °C and 0.2°C for T_{gap2b} respectively. It can be concluded that there is an insignificant difference between the three temperature values (i.e., T_{gap1} , T_{gap2a} and T_{gap2b}) and T_{gap} .

In method 2 (effective thermal conductivity), the group of figures from **Fig. 3.16** to **Fig. 3.19** present the 3D temperature contour for free convection in the enclosure under steady state conditions. The boundary conditions for **Fig. 3.16** and **Fig. 3.17** are 20 °C and 90 °C respectively, while the bottom surface temperature is 120 °C with an air gap space of 0.2 m. For **Fig. 3.18** and **Fig. 3.19**, the same boundary conditions but the air space gap is 0.025 m.

Finally, 2D CFD modelling under transient conditions (method 3) is presented in **Fig. 3.20**. The average value of the air gap temperature agrees with the other two methods.

It can also be seen in **Table 3.1**, the correlation results of method 1 indicate that the heat transfer rate using individual heat transfer coefficients (h_{pv-gap} and h_{gap-g}) and overall heat transfer coefficient (U_{pv+g}) are in good agreement (Q_{gap-g} , Q_{pv-gap} and Q_{pv+g}).

Table 3.1. Methods 1 and 2 to estimate the air gap temperature and the overall heat transfer coefficient in the enclosure.

T_g	T_{mpv}	T_{gap}	T_{gap1}	T_{gap2a}	T_{gap2b}	EP%	Q_{gap-g}	h_{gap-g}	Q_{pv-gap}	h_{pv-gap}	U_{pv+g}	Q_{pv+g}
20	120	70	68.9	72.0	72.10	0.30	1605.8	3.64	1605.8	3.50	1.78	1605.8
30	120	75	74.1	76.6	76.67	0.23	1400.2	3.52	1400.2	3.40	1.73	1400.2
40	120	80	79.3	81.2	81.3	0.18	1202.2	3.39	1202.2	3.29	1.67	1202.2
50	120	85	84.5	85.9	85.98	0.13	1012.3	3.26	1012.3	3.17	1.61	1012.3
60	120	90	89.6	90.6	90.70	0.09	830.7	3.11	830.7	3.04	1.54	830.7
70	120	95	94.7	95.4	95.48	0.06	658.2	2.95	658.2	2.9	1.46	658.2
80	120	100	99.8	100.2	100.30	0.04	495.6	2.77	495.6	2.73	1.38	495.6
90	120	105	104.9	105.1	105.17	0.02	344.3	2.56	344.3	2.54	1.28	344.3
95	120	107.5	107.4	107.6	107.62	0.01	273.5	2.44	273.5	2.42	1.22	273.5

In Table 3.1, T_{gap} is the assumed air gap temperature, T_{gap1} is the air gap temperature estimated using method 1, T_{gap2a} is the air gap temperature estimated using method 2 for the air gap space is 0.2 m, T_{gap2b} is the air gap temperature estimated using method 2 where the air gap space is 0.025 m. EP is the percentage error which is compared between T_{gap2a} and T_{gap2b}

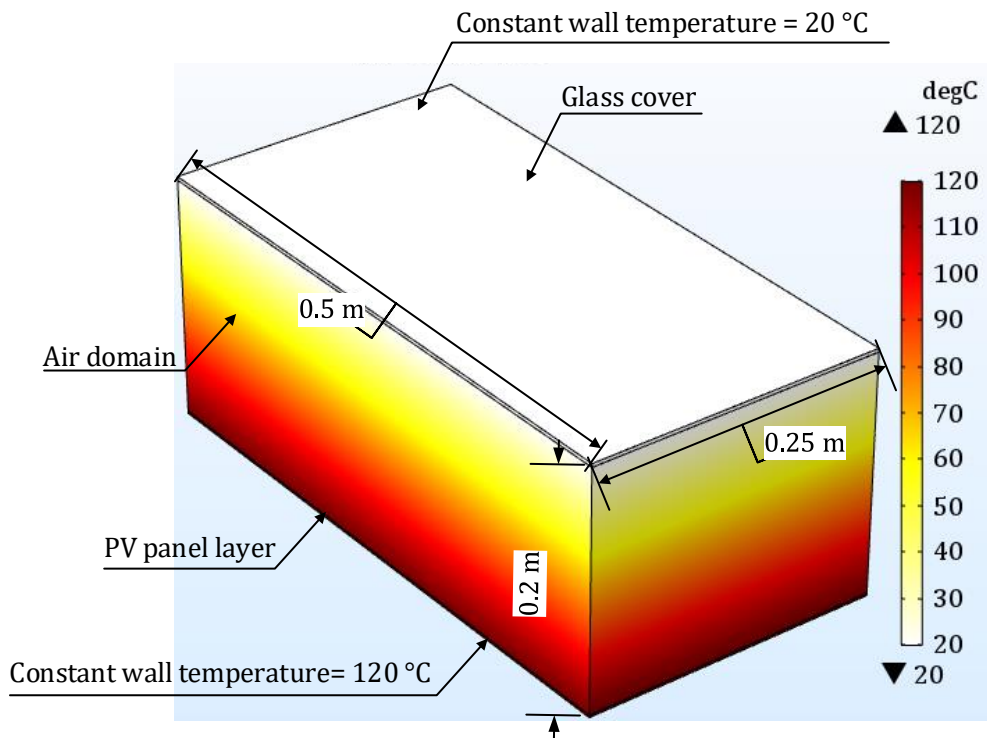


Fig. 3.16. 3D temperature contour ($^{\circ}C$) for free convection in the enclosure under steady state conditions, the top surface temperature is $20^{\circ}C$ and the bottom surface temperature is $120^{\circ}C$ while the air gap space is 0.2 m.

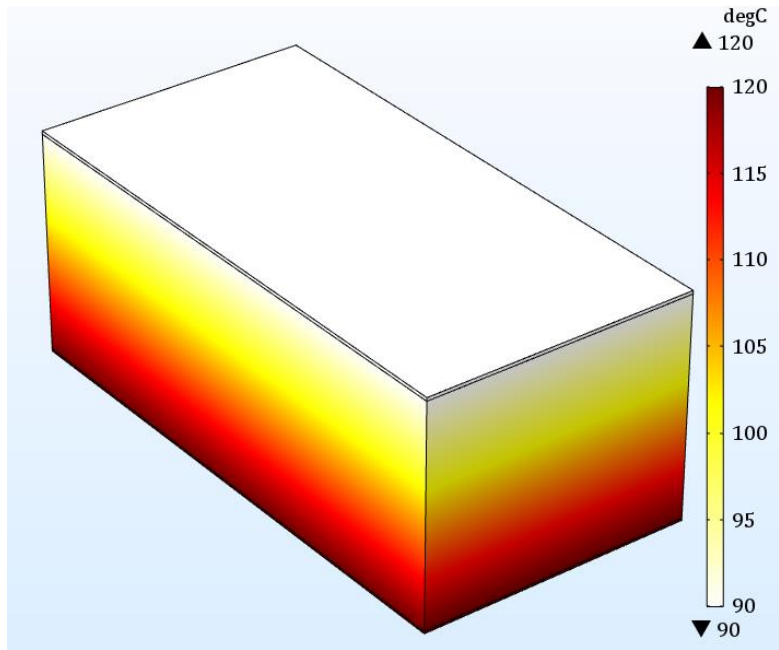


Fig. 3.17. 3D temperature contour (°C) for free convection in the enclosure under steady state conditions, the top surface temperature is 90 °C and the bottom surface temperature is 120 °C while the air gap space is 0.2 m.

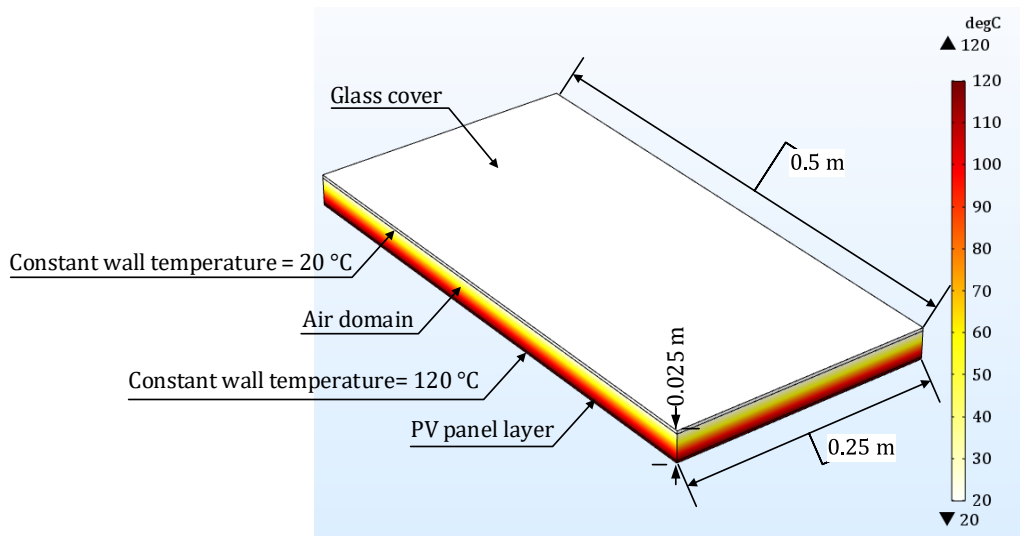


Fig. 3.18. 3D temperature contour (°C) for free convection in the enclosure under steady state conditions, the top surface temperature is 20 °C and the bottom surface temperature is 120 °C while the air gap space is 0.025 m.

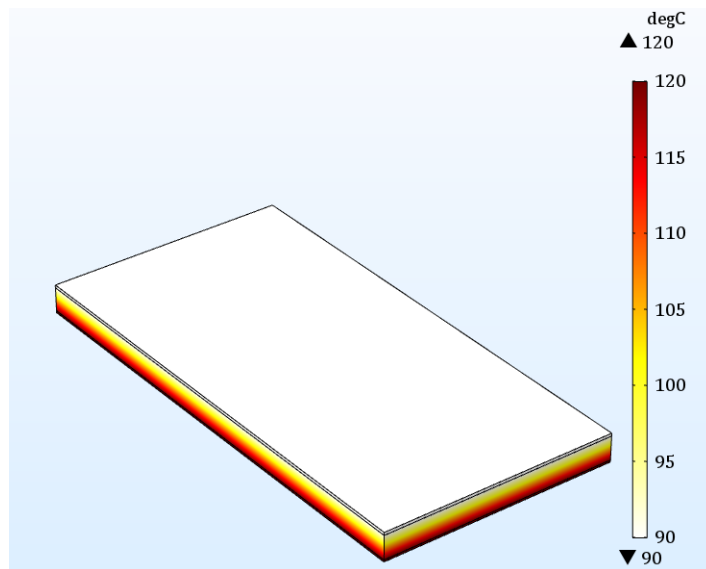


Fig. 3.19. 3D temperature contour ($^{\circ}\text{C}$) for free convection in the enclosure under steady state conditions, the top surface temperature is 95°C and the bottom surface temperature is 120°C while the air gap space is 0.025 m

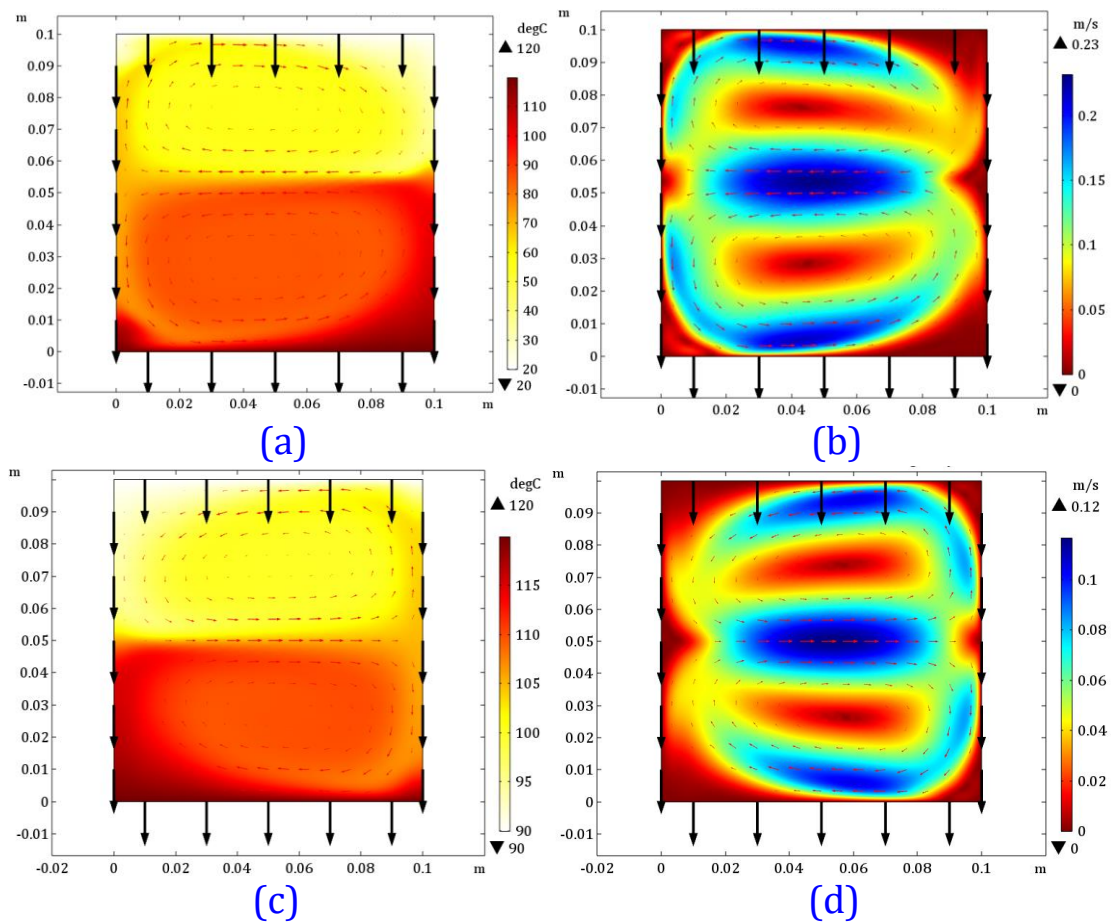


Fig. 3.20. 2D modelling for free convection in the enclosure under transient conditions for two temperature differences, in (a) the lower surface temperature is 20 °C and upper surface temperature is 120 °C , Time = 300 s, surface: 2D temperature (°C), red arrow surface: velocity field, black arrow line: acceleration of gravity, (c) the lower surface temperature is 90 °C and upper surface temperature is 120 °C , Time = 300 s, surface: 2D temperature (°C), red arrow surface: velocity field, black arrow line: acceleration of gravity, (b) Time = 300 s, surface: velocity magnitude (m s^{-1}), arrow surface: velocity field, black arrow line: acceleration of gravity for temperature counter in (a), and (d) Time = 300 s, surface: velocity magnitude (m s^{-1}), arrow surface: velocity field, black arrow line: acceleration of gravity for temperature counter in (c).

3.3.2.4 Forced convective

When the fluid is forced to flow by a pump or fan such as in model 2, evaluation of the convective heat transfer coefficients is essential, since they are directly proportional to the heat transfer rate as shown in Eq. 3.31. In the PV/T air system, the forced convective heat transfer coefficients (h_f) between the metal (solid) surfaces and air stream, (i.e. the lower and upper absorber plates and flowing air) are assumed to be equal. This is owing to the air flow depth is relatively small.

Several empirical equations have been suggested in the literature for the calculation the forced convective heat transfer coefficients in both turbulent and laminar flow regimes. It should be noted that every equation is valid for specific conditions such as the critical value of Re number and the effect of entrance length and boundary condition (constant heat flux or isothermal).

Duffie and Beckman [250] and Njomo and Dagenet [255] used a common correlation equation from the data of Kays and Crawford [282], for fully developed turbulent flow. Kays and Crawford evaluated Eq. 3.92 applying three flow situations, $L/D_h = 10$ with about 16 % percentage error and $L/D_h = 30$ with 5% percentage error and lastly, for the case of $L/D_h = 100$ the effect of the length of the entry region can be neglected.

$$h_f = (k_f/\delta_D) (0.0158 \text{Re}_{D_h}^{0.8}). \quad \text{Eq. 3.92}$$

In order to consider the effect of entrance length, Hegazy [122, 131] and Amori and Abd-AlRaheem [121] use the equation of [283] for predicting the convective heat transfer coefficient in the air stream as seen in Eq. 3.93 .

$$h_f = \left(\frac{k_f}{D_h}\right) \left(0.0158 \text{Re}_{D_h}^{0.8} + (0.00181 \text{Re}_{D_h} + 2.92) e^{\frac{-0.03795 x}{D_h}}\right), \quad \text{Eq. 3.93}$$

where x is the distance along the duct from the entrance (m).

In a different study, Tan and Charters [284] calculated the convective heat transfer coefficient in forced convection conditions using Eq. 3.94. This equation includes the effect of thermal entrance length of the air duct, which is also used by Tonui and Tripanagnostopoulos [176] and Shahsavari and Ameri [27].

$$h_f = \left(\frac{k_f}{D_h}\right) \left(0.0182 \text{Re}_{D_h}^{0.8} \text{Pr}^{0.4} \left(1 + S_D \frac{D_h}{L}\right)\right), \quad \text{Eq. 3.94}$$

where:

$$S_D = 14.3 \log(L/D_h) - 7.9 \text{ for } 0 < L/D_h \leq 60, \quad \text{Eq. 3.94a}$$

$$S_D = 17.5 \text{ for } L/D_h > 60. \quad \text{Eq. 3.94b}$$

Nu is for fully developed laminar flow, in which the fluid flows between two parallel infinite plates and is subjected to constant heat flux, this is obtained by Heaton et al. [285]. The

results were formulated in the form of Eq. 3.95. This correlation equation is also confirmed by [250, 255, 286].

$$\text{Nu} = 4.9 + \left(\frac{0.0606 (\text{Re}_{D_h} \text{Pr} D_h/L)^{1/2}}{1 + 0.0909 (\text{Re}_{D_h} \text{Pr} D_h/L)^{0.7} \text{Pr}^{0.17}} \right). \quad \text{Eq. 3.95}$$

For the same aforementioned conditions, with a high aspect ratio (w/δ_D), various studies assumed constant Nusselt number values. The values of Nusselt number falls in the range of $\text{Nu} = 5.39\text{-}8.23$ [241, 272].

3.3.3 Thermal and electrical performance evaluation

In order to assess the thermal and hydrodynamic and electrical parameters of a PV/T air collector, a number of criteria are evaluated such as pressure drop, effective thermal efficiency and fan power consumption.

3.3.3.1 Effective thermal efficiency

Estimating the effective thermal efficiency (η_{th}) is based on three main variables namely: heat benefit, pressure drop and fan power consumption. In order to represent realistic conditions in solar PV/T air collectors, the effective thermal efficiency (The first-law efficiency) is accounted with C_f ,

$$\eta_{th} = \frac{\dot{Q}_u - (P_f/C_f)}{\dot{Q}_s}. \quad \text{Eq. 3.96}$$

The following assumptions are used to simplify the energy balance for PV/T air system under steady flow condition.

1. PV/T air system is assumed as an open system.
2. The changes in potential and kinetic energies are insignificant.
3. No work interaction.

Therefore, the change in enthalpy (Δh) between the inlet and outlet can be used to estimate the heat benefit delivered by the PV/T air collectors (\dot{Q}_u) [241].

$$\dot{Q}_u = \Delta h = \dot{M}_f C_p (T_{fo} - T_{fi}), \quad \text{Eq. 3.97}$$

where \dot{M}_f is flowrate kg s^{-1} given by Eq. 3.98:

$$\dot{M}_f = \rho \bar{V} A_c, \quad \text{Eq. 3.98}$$

where ρ is the density of air (kg m^{-3}) and \bar{V} is the mean velocity at the inlet boundary (m s^{-1}), while A_c is the channel ducting cross-section area (m^2).

\dot{Q}_s is total incident solar radiation on absorber plate (W):

$$\dot{Q}_s = G A_s, \quad \text{Eq. 3.99}$$

where G is the incident solar radiation and A_s is the PV panel surface area.

The conventional method in evaluating the net thermal energy output of the solar collectors is calculated by subtracting theoretical fan power or pump power consumption (see [Eq. 3.101](#)) from the thermal output. In reality, the fan power required to drive the air in solar air collectors are affected by many factors and this method does not consider that the part of the energy will be lost and consumed in conversion and transmission losses. These losses are attributed to the efficiency of the fan $\eta_f = 0.65$, the efficiency of the electric motor used for driving the fan is $\eta_m = 0.88$, the efficiency of electrical transmission from a power plant is $\eta_{tr} = 0.92$ and the thermal conversion efficiency of the power plant is $\eta_{thc} = 0.35$. It is appropriate to combine these coefficients into one named conversion factor (C_f), which accounts for the overall efficiency of energy conversion from thermal energy to mechanical energy [\[287\]](#).

$$C_f = \eta_f \eta_m \eta_{tr} \eta_{thc} = 0.18 \text{ [288-290]}. \quad \text{Eq. 3.100}$$

The instantaneous fan power required of a particular collector is estimated by [Eq. 3.101](#).

$$P_f = \Delta p \dot{V}, \quad \text{Eq. 3.101}$$

where Δp (N m^{-2}) is the total pressure drop experienced by the air stream in passing through a channel at a flowrate, \dot{V} , ($\text{m}^3 \text{ s}^{-1}$) owing to flow friction losses (major losses) and losses at the channel entrance, exit and various fittings (minor losses).

In order to estimate accurate pressure drop values, two methods were used. The first method was numerical using COMSOL software which has a built-in pressure sub-feature, while the second method was empirical correlations as shown below.

$$\Delta p = \Delta p_f + \Delta p_{\text{dynamic}}. \quad \text{Eq. 3.102}$$

where Δp_f is the pressure drop owing to friction which is given as:

$$\Delta p_f = \frac{\rho f \bar{V}^2 L}{2 D_h}, \quad \text{Eq. 3.103}$$

where f is the Fanning friction factor for turbulent flow is calculated by [122, 291] as:

$$f = 0.079 \text{Re}_{D_h}^{-0.25} \quad 6000 < \text{Re}_{D_h} < 100000, \quad \text{Eq. 3.104}$$

The Fanning friction factor for laminar flow estimated as [292]:

$$f = \frac{g_f}{\text{Re}_{D_h}} \{ \text{Re}_{D_h} < 2550 \} \quad [180, 257], \quad \text{Eq. 3.105}$$

where g_f is the geometry factor which changes depending on the geometry type [292] which can be seen in Table 3.2.

Table 3.2. Geometry factor in case of non- circular pipes under laminar flow regime condition

Geometry	rw	g_f
Square	1	56.91
Rectangular	2:1	52.19
Rectangular	5:1	76.28
Parallel plate	∞	96.00

In Table 3.2, rw is the ratio of collector width to depth of flow δ_D .

Dynamic losses [293] ($\Delta p_{\text{dynamic}}$) in fittings that are referred to as minor losses, which result from the effects of channel entrance, exit, elbows, bends, joints, valves etc., are determined by the formula:

$$\Delta p_{\text{dynamic}} = \left(\frac{1}{2}\right) k_L \rho \bar{V}^2, \quad \text{Eq. 3.106}$$

$$k_L = k_{\text{entrance}} + k_{\text{exit}} + k_{\text{bend}}. \quad \text{Eq. 3.107}$$

The coefficients k_{entrance} and k_{exit} are set to the values of 0.5 and 1.0 for the entrance and exit losses. In the case of close return bend inside this collector, k_{bend} value is taken equal to 2.2, [294, 295]. For the sake of accuracy, the entrance and exit coefficients (minor losses) are added to the calculation of pressure drop when comparing between the CFD models and empirical correlations, since in CFD, the minor losses are not considered.

3.3.3.2 Air temperature-dependent properties

The air properties were evaluated at bulk fluid temperature using the set of equations Eq. 3.111 to Eq. 3.117 [296], verified against those presented in [248]. An analysis was performed for the internal flow mechanisms by Cengel [272] to examine a suitable expression may be used to estimate fluid properties. The average bulk temperature in the thermal fluid is a convenient reference point for evaluating properties related to convective heat transfer. This is particularly in applications related to flow in pipes and ducts such as average convective heat transfer coefficient in Newton's law of cooling [297].

Before going into detail of bulk fluid temperature, it is worthy to mention that there are two commonly known types of thermal boundary conditions used in heat transfer analyse. The first boundary is constant wall temperature (isothermal), this boundary exists in many applications, for example, 1) in case of the thickness of the absorber plate is large enough to keep its temperature uniform under high incident radiation; 2) heat capacity ($\dot{M} cp$) going to infinity [258]; 3) free convection mode such as in [298-300]; 4) phase change (boiling or condensation) [258]. The second boundary is constant heat flux which is the most commonly used in solar air systems under forced convection [301]. In this study, the heat flux boundary condition is assumed to be used, since the incident solar radiation was assumed to be uniformly distributed.

Three main expressions can be used to estimate the bulk fluid temperature under a constant surface heat flux boundary condition. The first expression is bulk fluid temperature, sometimes called adiabatic mixing cup temperature, which provides a real picture of the energy content of the fluid. This is because it characterises the average thermal energy state of the liquid. This temperature is simply measured in the lab [297]. Accordingly, in the internal flow, the general expression for bulk fluid temperature [27, 297].

$$T_{\text{bulk}} = \frac{\int \rho \bar{V} cp T dA_c}{\int \rho \bar{V} cp dA_c}. \quad \text{Eq. 3.108}$$

The numerator of Eq. 3.108 describes axial converted thermal energy whereas the denominator computes thermal capacity rate

The second expression is the average fluid temperature (\tilde{T}):

$$\tilde{T} = T_{\text{bulk}} = \frac{1}{L} \int_0^L T_f(x) dx. \quad \text{Eq. 3.109}$$

Finally, the arithmetic mean temperature expression which calculates the bulk fluid temperature by the arithmetic average of the mean temperatures at the inlet and the outlet. In analytical solution such as in mathematical modelling (Chapter 3), the use of this expression is acceptable [27, 122, 254].

$$T_{\text{bulk}} = \frac{(T_{fi} + T_{fo})}{2}. \quad \text{Eq. 3.110}$$

After identifying the appropriate bulk fluid expression, the set of empirical correlations (i.e. Eq. 3.111 to Eq. 3.117) used to estimate air properties which are a function of bulk fluid temperature and proportionally non-linear [248, 249]. These correlations may accurately work in the temperature range (-73 - 127) °C.

$$\mu = -8.39 e^{-7} + 8.36 e^{-8} T_f - 7.695 e^{-11} T_f^2 + 4.65 e^{-14} T_f^3 - 1.07 e^{-17} T_f^4, \quad \text{Eq. 3.111}$$

$$\rho = 3.9147 - 0.01608 T_f + (2.9013 e^{-5} T_f^2) - (1.9407 e^{-5} T_f^3), \quad \text{Eq. 3.112}$$

$$v = \frac{\mu}{\rho}, \quad \text{Eq. 3.113}$$

$$k = -0.0023 + 1.155 e^{-4} T_f - 7.91 e^{-8} T_f^2 + 4.118 e^{-11} T_f^3 - 7.44 e^{-15} T_f^4, \quad \text{Eq. 3.114}$$

$$cp = 1047.7 - 0.373 T_f + 9.46 e^{-4} T_f^2 - 6.03 e^{-7} T_f^3 + 1.29 e^{-10} T_f^4, \quad \text{Eq. 3.115}$$

$$\alpha = \frac{K}{\rho cp}, \quad \text{Eq. 3.116}$$

$$\text{Pr} = \frac{v}{\alpha}. \quad \text{Eq. 3.117}$$

3.3.3.3 Electrical performance evaluation

The electrical power generation in the PV module can be estimated by Eq. 3.118 [32, 67, 116, 302, 303].

$$P_{PV} = I_m V_m = FF I_{sc} V_{oc} = \eta_{PV} A_s G \alpha_{pv} \text{PF}, \quad \text{Eq. 3.118}$$

where I_m and V_m are voltage and current at the max power point, FF is the Fill factor, I_{sc} is the short circuit current and V_{oc} the open-circuit voltage [32]. The product ($G \alpha_{pv}$) is the energy absorbed by the PV laminate, where α_{pv} is the absorptivity of the silicon [302].

A_s is total surface (aperture surface) area of PV modules ($L w$) multiplied by the packing factor (PF) or packing density of solar cells which denotes the area of the module that is covered with solar cells compared to that which is blank [304]. In this study, the value of the packing factor was taken 0.83 (Poly-crystalline) [18, 191, 305]. The shape of solar cells is depending on the types of material used. mono-crystalline PV cells are semi-square or round, while poly-crystalline types are square [306] (see Fig. 3.21). The typical polycrystalline cell efficiencies fall 15–17%, roughly 1% lower than for monocrystalline cells fabricated on the same production lines. However, the efficiencies of multi-crystalline cell panels, are practically the same as those for single-crystalline cells. This is because of the greater packing factor (14%) of the square polycrystalline cells while monocrystalline cells have relatively poor packing factors [306].

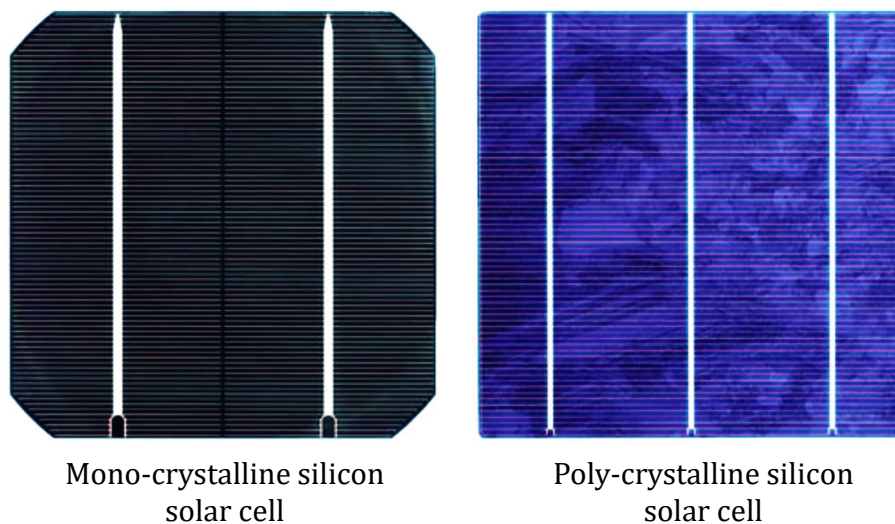


Fig. 3.21. Typical mono-crystalline and poly-crystalline silicon solar cells [306].

The electrical efficiency of the PV module, η_{PV} [19, 23-29] which represents the conventional linear expression for the PV electrical efficiency.

$$\eta_{PV} = \eta_{ref} \left(1 - \beta_{ref} (T_{mpv} - T_{ref}) \right) + \gamma \log_{10} G. \quad \text{Eq. 3.119}$$

In which $\eta_{T_{ref}}$ is the module's electrical efficiency at standard conditions ($G = 1000 \text{ W m}^{-2}$ and $T_{ref} = 25$) [307]. The temperature coefficient of the power, β_{ref} and the solar radiation coefficient, γ , are predominantly material properties which have values of around

0.0041 K^{-1} and 0.12, respectively, for crystalline silicon modules [37]. The latter, however, is commonly cancelled (zero) [308], and equation reduces to:

$$\eta_{PV} = \eta_{ref} \left(1 - \beta_{ref} (T_{mpv} - T_{ref}) \right). \quad \text{Eq. 3.120}$$

3.3.3.4 Hybrid efficiency evaluation

The total collector efficiency (hybrid or combined efficiency) of the PV/T air collector can be expressed using Eq. 3.122 [19, 260].

The equivalent electrical efficiency of PV panel can be calculated by,

$$\eta_{EPV} = \frac{\eta_{PV}}{C_{ff}}, \quad \text{Eq. 3.121}$$

$$\eta_{comb} = \eta_{th} + \eta_{EPV}, \quad \text{Eq. 3.122}$$

where C_{ff} is the conversion factor of the thermal power plant and lies between 0.29 and 0.4 [19, 24-28, 260, 309, 310], and is assumed to be 0.36 in this study.

When comparing electrical and thermal power, an equivalent electrical PV power term (P_{eq}) was also used and can be estimated by,

$$P_{eq} = \frac{P_{PV}}{C_{ff}}. \quad \text{Eq. 3.123}$$

A percentage enhancement factor (PE_{ϕ}) was used in this study such as temperature rise or thermal efficiency or electrical efficiency percentage enhancement (PE_{ϕ}) etc. This factor can be defined as [289].

$$PE_{\phi} = \frac{\phi_{finned} - \phi_{plain}}{\phi_{plain}} \times 100. \quad \text{Eq. 3.124}$$

where ϕ refers to any parameter such as electrical efficiency.

3.3.3.5 Thermal resistance

Thermal resistance criterion, R_{th} ($K W^{-1}$) is exploited here to evaluate the heat transfer enhancement of the PV/T air system. R_{th} can be physically defined as the measure of the resistance of the PV module layers to dissipating the heat, and in common use criterion

within the area of thermal management devices, because both of electronic devices and PV/T air system are similar functions.

Mathematically, it can be defined by the ratio of the temperature difference of the average temperature of PV module and the inlet fluid of the PV/T air collector to the heating power received by air in the channel duct region, see Eq. 3.125 [311, 312].

$$R_{th} = \frac{T_{mpv} - T_{fi}}{\dot{Q}_s}, \quad \text{Eq. 3.125}$$

where T_{mpv} is the average temperature on PV cells, T_{fi} is the inlet air temperature.

3.4 Numerical techniques

In this chapter, the energy balance equations for models 2 and 3 are solved using the semi-analytical and numerical methods.

3.4.1 Semi-analytical

In this method, the equations are solved analytically, but the iteration is employed to estimate the set of collector temperatures. Before solving these equations, it is necessary to re-arrange them into a form which can be integrated easily. For example, referring to Section 3.2.3 of model 2, Eq. 3.7f and Eq. 3.12 are rearranged to consider $T_f(x)$:

$$T_{bm}(x) - T_f(x) = \frac{h_{rpb}(T_{mpv}(x) - T_f(x)) - U_b(T_f(x) - T_{amb})}{h_{rpb} + h_f + U_b}, \quad \text{Eq. 3.126}$$

$$T_{mpv}(x) - T_f(x) = \frac{\dot{S}_{th} - \bar{U}_L(T_f(x) - T_{amb})}{\bar{U}_L + h_e}. \quad \text{Eq. 3.127}$$

Substituting Eq. 3.126 in Eq. 3.17 results in:

$$\frac{\dot{Q}_u(x)}{w dx} = h_f (T_{mpv}(x) - T_f(x)) + h_f \left[\frac{h_{rpb}(T_{mpv}(x) - T_f(x)) - U_b(T_f(x) - T_{amb})}{h_{rpb} + h_f + U_b} \right]. \quad \text{Eq. 3.128}$$

Simplifying and re-arranging Eq. 3.128 resulting in:

$$\frac{\dot{Q}_u(x)}{w dx} = h_e (T_{mpv}(x) - T_f(x)) - \frac{h_f U_b}{h_{rpb} + h_f + U_b} (T_f(x) - T_{amb}). \quad \text{Eq. 3.129}$$

Substituting Eq. 3.127 into Eq. 3.129 resulting in:

$$\frac{\dot{Q}_u(x)}{w dx} = \frac{h_e}{\overline{U}_L + h_e} \left[\dot{S}_{th} - \overline{U}_L (T_f(x) - T_{amb}) - \frac{h_f U_b}{h_{rpb} + h_f + U_b} \frac{\overline{U}_L + h_e}{h_e} (T_f(x) - T_{amb}) \right], \quad \text{Eq. 3.130}$$

where U_L is the heat loss transfer coefficient between air and ambient ($\text{W m}^{-2} \text{K}$).

$$U_L = \overline{U}_L + \frac{h_f U_b}{h_{rpb} + h_f + U_b} \frac{\overline{U}_L + h_e}{h_e}. \quad \text{Eq. 3.131}$$

Thus:

$$\dot{Q}_u(x) = \frac{h_e}{\overline{U}_L + h_e} [\dot{S}_{th} - U_L (T_f(x) - T_{amb})] w dx. \quad \text{Eq. 3.132}$$

In order to solve the heat balance equations, two assumptions are considered. The first assumption is that U_L and \dot{S}_{th} coefficients are distributed uniformly along the flow direction. In reality U_L and \dot{S}_{th} coefficients are local values, however, this could be valid at large aspect ratios (the thickness of the channel compared to the length) [251, 254]. The second assumption is that the radiative heat transfer coefficients are linear terms even though the rate of radiative heat transfer is nonlinear. The rate of solar radiation absorbed by an object q_{rad} which is proportional to the fourth power of temperature $q_{rad} \propto T^4$. Accordingly, Eq. 3.132 can be easily integrated as a function of (x) under specific boundary conditions as shown below. It is worth mentioning that these two assumptions are not used in solving the heat balance equations when using the Predictor-Corrector method explained in Section 3.4.2.

$$\text{Let } \theta = \dot{S}_{th} - U_L (T_f(x) - T_{amb}). \quad \text{Eq. 3.133}$$

The boundary condition is, at $\theta = \theta_i, x = 0$

$$\text{Let } \bar{F} = \frac{h_e}{\overline{U}_L + h_e}, \quad \text{Eq. 3.134}$$

$$d\theta = -U_L dT_f(x) \Rightarrow dT_f(x) = \frac{d\theta}{-U_L}. \quad \text{Eq. 3.135}$$

Hence:

$$-\frac{\dot{M}_f c p_f}{\bar{F} U_L w} d\theta = \theta dx, \quad \text{Eq. 3.136}$$

$$\int_{\theta_i}^{\theta_{\Delta x}} \frac{d\theta}{\theta} = \frac{-\bar{F} U_L A_{pv}}{\dot{M}_f c_{pf}} \int_0^{\Delta x} dx, \quad \text{Eq. 3.137}$$

$$\frac{\theta_o}{\theta_i} = e^{\frac{-\bar{F} U_L A_{pv}}{\dot{M}_f c_{pf}}}, \quad \text{Eq. 3.138}$$

$$\frac{\dot{S}_{th-U_L}(T_{fo}-T_{amb})}{\dot{S}_{th-U_L}(T_{fi}-T_{amb})} = e^{\frac{-\bar{F} U_L A_{pv}}{\dot{M}_f c_{pf}}}, \quad \text{Eq. 3.139}$$

$$1 - \frac{\dot{S}_{th-U_L}(T_{fo}-T_{amb})}{\dot{S}_{th-U_L}(T_{fi}-T_{amb})} = 1 - e^{\frac{-\bar{F} U_L A_{pv}}{\dot{M}_f c_{pf}}}, \quad \text{Eq. 3.140}$$

$$\frac{U_L(T_{fo}-T_{fi})}{\dot{S}_{th-U_L}(T_{fi}-T_{amb})} = 1 - e^{\frac{-\bar{F} U_L A_{pv}}{\dot{M}_f c_{pf}}}. \quad \text{Eq. 3.141}$$

Re-arranging Eq. 3.141 to obtain the temperature difference between the inlet and the outlet fluid:

$$T_{fo} - T_{fi} = \frac{\dot{S}_{th-U_L}(T_{fi}-T_{amb})}{U_L} \left[1 - e^{\frac{-\bar{F} U_L A_{pv}}{\dot{M}_f c_{pf}}} \right]. \quad \text{Eq. 3.142}$$

The local fluid temperature can be evaluated by using:

$$T_f(x) = \frac{\dot{S}_{th-U_L}(T_{fi}-T_{amb})}{U_L} \left[1 - e^{\frac{-\bar{F} U_L W x}{\dot{M}_f c_{pf}}} \right] + T_{fi}. \quad \text{Eq. 3.143}$$

The average fluid temperature can be attained by integrating Eq. 3.143 as shown below:

$$\tilde{T} = T_{fm} = \frac{1}{L} \int_0^L T_f(x) dx, \quad \text{Eq. 3.144}$$

$$T_f(x) = \frac{\dot{S}_{th-U_L}(T_{fi}-T_{amb})}{U_L} \left[1 - e^{\frac{-\bar{F} U_L W x}{\dot{M}_f c_{pf}}} \right] + T_{fi}. \quad \text{Eq. 3.145}$$

Assuming:

$$a_1 = \frac{-\bar{F} U_L W}{\dot{M}_f c_{pf}}, \quad \text{Eq. 3.146}$$

$$a_2 = \frac{\dot{S}_{th-U_L}(T_{fi}-T_{amb})}{U_L}. \quad \text{Eq. 3.147}$$

Substituting a_1 and a_2 in Eq. 3.145 yields:

$$T_{fm} = \frac{a_2}{a_1 L} (1 - e^{a_1 L}) + a_2 + T_{fi}. \quad \text{Eq. 3.148}$$

The useful energy gain can be expressed as:

$$\dot{Q}_u = \dot{M}_f c p_f (T_{fo} - T_{fi}). \quad \text{Eq. 3.149}$$

Two programming codes are developed to solve the set of heat balance equations for model 2 and model 3. The clarification and program instructions of the Matlab codes of model 2 are presented in Fig. 3.22. The procedure for solving model 2 is detailed below while the procedure for model 3 is the same as model 2.

The electrical and thermal parameters are dependent on each other. For example, solving the thermal model requires electrical efficiency which is directly proportional to the PV cell temperature. Under specific input data including ambient, operating and geometrical conditions (see step 1 and 2 in Fig. 3.22), the set of collector temperatures are initially assumed to be at $(T_{fo}, T_{mpv}, T_{bm}, T_{fx})$, as indicated in step 3. Using these estimated values to calculate the radiative and convective heat transfer coefficients (Eq. 3.35, Eq. 3.48, Eq. 3.50, Eq. 3.92 and/or Eq. 3.95), electrical efficiency (η_{PV}) (Eq. 3.120) and air properties (Eq. 3.111 to Eq. 3.117). These properties are evaluated at the bulk fluid temperature ($T_{bulk} = (T_{fi} + T_{fo})/2$) in the duct. After that, the energy balance equations are solved to obtain new temperatures (Eq. 3.142, Eq. 3.7f, Eq. 3.12, Eq. 3.145). These values are compared with the old values. Note that, the comparison is based on the error value which is the difference between the old and new values. The program is executed repeatedly until all collector temperature values converge. These collector temperatures are used to calculate the useful heat gain and collector efficiencies (Eq. 3.149, Eq. 3.96, Eq. 3.118, Eq. 3.122). The details of the thermal, hydraulic and electrical correlation equations of the PV/T air collector can be seen in Section 3.3.3.

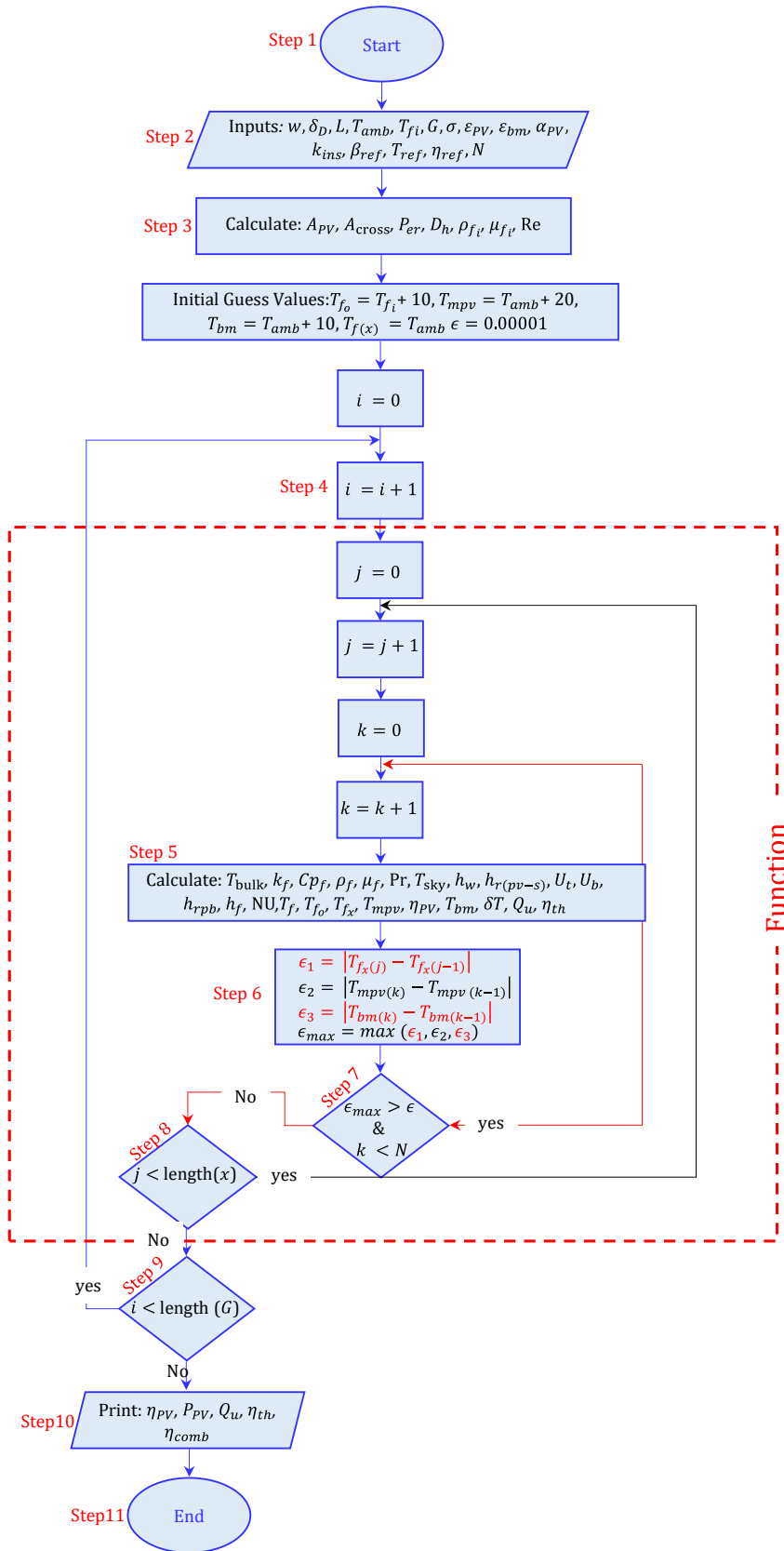


Fig. 3.22. Flow chart of the algorithm for the semi-analytical solution of model 2.

In Fig. 3.22, i, j and k refer to loop number.

3.4.2 Numerical solution

This is the second method used to solve the energy balance equation for model 2 and model 3. In this method, the equations are solved numerically and the Precedence Ordering Techniques are employed in order to reduce the number of computational steps [313]. Below are the procedural steps that are used to find the solution for model 2. These procedures are the same as for model 3.

In order to find the solution of the set of temperatures in the first node ($T_{mpv}(0), T_{bm}(0)$), we apply the boundary condition at the inlet, at $x = 0$ $T_f(x) = T_f(0) = T_{amb}$ into Eq. 3.6/Eq. 3.7 and results in:

$$S_{th} = h_{r(pv-sky)} (T_{mpv}(0) - T_{sky}) + h_{free} w dx (T_{mpv}(0) - T_{amb}) + h_f (T_{mpv}(0) - T_f(0)) + h_{rpb} (T_{mpv}(0) - T_{bm}(0)), \quad \text{Eq. 3.150}$$

$$h_{rpb} (T_{mpv}(0) - T_{bm}(0)) = h_f (T_{bm}(0) - T_f(0)) + U_b (T_{bm}(0) - T_{amb}). \quad \text{Eq. 3.151}$$

Substituting Eq. 3.8 and Eq. 3.9 yield:

$$S_{th} = G \alpha_{pv} \left(1 - (\eta_{ref} [1 - \beta_{ref} (T_{mpv}(0) - T_{ref})]) \right). \quad \text{Eq. 3.152}$$

Now, substituting Eq. 3.152, Eq. 3.35, Eq. 3.48, Eq. 3.50, Eq. 3.92/Eq. 3.95 into Eq. 3.150 results in:

$$G \alpha_{pv} \left(1 - (\eta_{ref} [1 - \beta_{ref} (T_{mpv}(0) - T_{ref})]) \right) = h_f (T_{mpv}(0) - T_f(0)) + \sigma \varepsilon_{pv} (T_{mpv}(0)^4 - T_{sky}^4) + h_{free} (T_{mpv}(0) - T_{amb}) + \sigma \frac{(T_{mpv}(0)^4 - T_{bm}(0)^4)}{\frac{1}{\varepsilon_{PV}} + \frac{1}{\varepsilon_{bm}} - 1}. \quad \text{Eq. 3.153}$$

Re-arrange Eq. 3.151 to convert it in terms of T_{bm} :

$$T_{mpv}(0) = \left(\left[\left(\frac{h_f (T_{bm}(0) - T_{fi}) + U_b (T_{bm}(0) - T_{amb})}{\sigma} \right) \left(\frac{1}{\varepsilon_{PV}} + \frac{1}{\varepsilon_{bm}} - 1 \right) \right] + (T_{bm}(0)^4) \right)^{\frac{1}{4}}. \quad \text{Eq. 3.154}$$

Now, substitute Eq. 3.154 into Eq. 3.153 to find an expression in terms of T_{bm} :

$$\begin{aligned}
G \alpha_{pv} & \left(1 - \left(\eta_{ref} \left[1 - \beta_{ref} \left(\left(\left[\left(\frac{h_f (T_{bm}(0) - T_{fi}) + U_b (T_{bm}(0) - T_{amb})}{\sigma} \right) \left(\frac{1}{\varepsilon_{pv}} + \frac{1}{\varepsilon_{bm}} - 1 \right) \right] + (T_{bm}(0)^4) \right)^{\frac{1}{4}} - T_{ref} \right] \right) \right) \right) = \\
& h_f \left(\left(\left[\left(\frac{h_f (T_{bm}(0) - T_{fi}) + U_b (T_{bm}(0) - T_{amb})}{\sigma} \right) \left(\frac{1}{\varepsilon_{pv}} + \frac{1}{\varepsilon_{bm}} - 1 \right) \right] + (T_{bm}(0)^4) \right)^{\frac{1}{4}} - T_{fi} \right) + \\
& \sigma \varepsilon_{pv} \left(\left(\left[\left(\frac{h_f (T_{bm}(0) - T_{fi}) + U_b (T_{bm}(0) - T_{amb})}{\sigma} \right) \left(\frac{1}{\varepsilon_{pv}} + \frac{1}{\varepsilon_{bm}} - 1 \right) \right] + (T_{bm}(0)^4) \right)^{\frac{4}{4}} - T_{sky}^4 \right) + \\
& h_{free} \left(\left(\left[\left(\frac{h_f (T_{bm}(0) - T_{fi}) + U_b (T_{bm}(0) - T_{amb})}{\sigma} \right) \left(\frac{1}{\varepsilon_{pv}} + \frac{1}{\varepsilon_{bm}} - 1 \right) \right] + (T_{bm}(0)^4) \right)^{\frac{1}{4}} - T_{amb} \right) + \\
& \sigma \frac{\left(\left(\left[\left(\frac{h_f (T_{bm}(0) - T_{fi}) + U_b (T_{bm}(0) - T_{amb})}{\sigma} \right) \left(\frac{1}{\varepsilon_{pv}} + \frac{1}{\varepsilon_{bm}} - 1 \right) \right] + (T_{bm}(0)^4) \right)^{\frac{4}{4}} - T_{bm}(0)^4 \right)}{\frac{1}{\varepsilon_{pv}} + \frac{1}{\varepsilon_{bm}} - 1}. \tag{Eq. 3.155}
\end{aligned}$$

To simplify Eq. 3.155 and make it easy to read, the following terms are assumed:

$$C_1 = \left[\left[\left(\frac{h_f (T_{bm}(0) - T_{fi}) + U_b (T_{bm}(0) - T_{amb})}{\sigma} \right) \left(\frac{1}{\varepsilon_{pv}} + \frac{1}{\varepsilon_{bm}} - 1 \right) \right] + (T_{bm}(0)^4) \right], \tag{Eq. 3.156}$$

$$C_2 = \left(\frac{1}{\varepsilon_{pv}} + \frac{1}{\varepsilon_{bm}} - 1 \right), \tag{Eq. 3.157}$$

$$C_3 = \eta_{ref} \left[1 - \beta_{ref} \left(C_1^{1/4} - T_{ref} \right) \right]. \tag{Eq. 3.158}$$

Substituting C_1 , C_2 and C_3 in Eq. 3.155 yields:

$$G \alpha_{pv} (1 - C_3) - h_f \left(C_1^{1/4} - T_{fi} \right) - \sigma \varepsilon_{pv} \left(C_1 - T_{sky}^4 \right) - h_{free} \left(C_1^{1/4} - T_{amb} \right) - \left(\sigma \frac{C_1}{C_2} \right) = 0. \tag{Eq. 3.159}$$

Fig. 3.23 shows the detail of the mesh while Fig. 3.24 clarifies the program algorithm for the non-linear solution of model 2. Now, using either the goal seek method, which is built-in Excel, or the Bisection method, which is built-in Matlab (fzero function), to estimate $T_{mpv(0)}, T_{bm(0)}$. The second step is to calculate the fluid temperature in the node (i) by employing Explicit/Implicit Predictor-Corrector 2nd order method. The following are the summary of the steps considered in this method:

1. Referring to Fig. 3.23 and Fig. 3.24, the calculation of fluid temperature in the node (i) was achieved using Predictor-Forward Difference as shown in Eq. 3.160.

$$T_{pred(i)} = T_f(i - 1) + \left(\frac{dT}{dx} \Big|_{(i-1)} \right) \Delta x. \quad \text{Eq. 3.160}$$

2. The Predictor-Central Difference was used to find the corrector fluid temperature ($T_{corr(i)}$) in node (i). This was achieved by firstly calculating the Predictor temperature ($T_{pred(i)}$) to calculate $\frac{dT}{dx} \Big|_{(i)}$ and $T_{mpv(i)}, T_{bm(i)}$ using the Bisection method as shown in Eq. 3.161.

$$T_{corr(i)} = T_f(i - 1) + \frac{1}{2} \left(\frac{dT}{dx} \Big|_{(i)} + \frac{dT}{dx} \Big|_{(i-1)} \right) \Delta x. \quad \text{Eq. 3.161}$$

3. The error value was set as in Eq. 3.162 and the code is run repeatedly until the solution is converged.

$$\left| \frac{T_{pred(i)} - T_{corr(i)}}{T_{pred(i)}} \right| \times 100 > 0.001. \quad \text{Eq. 3.162}$$

It should be noted that the mesh independent study was conducted to ensure the accuracy of the solution. The size of the mesh element can be calculated by:

$$\Delta x = \frac{L}{n-1}. \quad \text{Eq. 3.163}$$

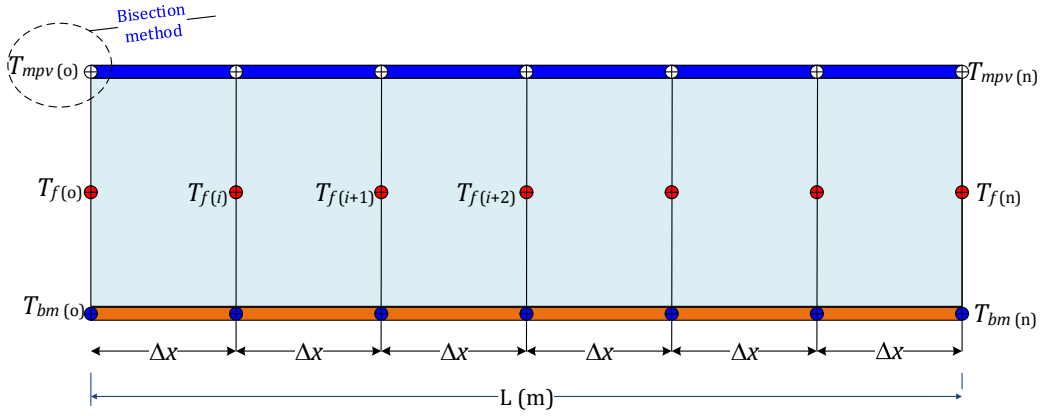


Fig. 3.23. Schematic of the meshing technique used for model 2.

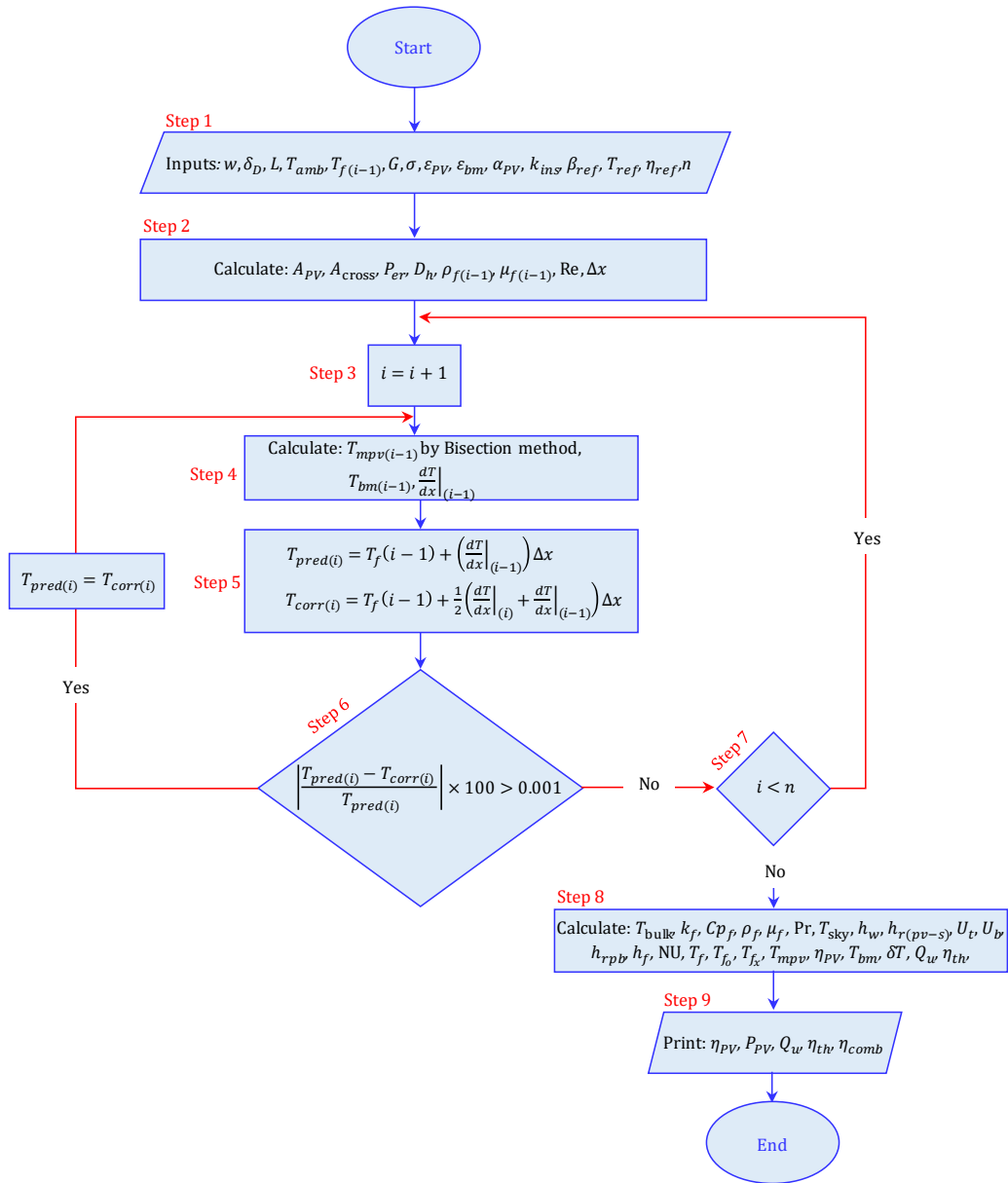


Fig. 3.24. Flow chart of the algorithm for the solution of the non-linear model (model 2).

3.5 Conclusions

In this chapter, two PV/T air systems were successfully derived. The first model is single duct single pass (model 2). While the second model is similar to model 2 but it is glazed (model 3). The heat balance method was used to derive the governing equations. Two numerical techniques were used to solve these equations. The first technique was semi-analytical, and the second was the Predictor-Corrector method.

The radiative and convective heat transfer coefficients were used to solve the energy balance equations for models 2 and 3. The relevant dimensionless numbers were also used in this analysis. Moreover, the fluid flow, thermal and electrical equations pertained to estimate the thermal and electrical performance of the PV/T air system were discussed. Finally, the air gap temperature assumption was justified by employing different approaches i.e. empirical, 3D CFD effective thermal conductivity and 3D/CFD approaches. The results revealed that the use of the overall heat transfer coefficient in the enclosure was valid regardless of the size of the air space gap.

In Chapter 4, the CFD methodology used to solve the proposed PV/T air collectors, including the mesh generation, assumptions and boundary conditions. Also, the methods used to reduce computation time are introduced. Finally, to ensure the accuracy of the solution, the validation and verification for different models are carried.

CHAPTER 4 COMPUTATIONAL METHOD, VERIFICATION AND VALIDATION

4.1 Introduction

In this work, numerical simulation is conducted for investigation into the thermal performance of photovoltaic (PV) and hybrid photovoltaic/thermal (PV/T) systems. The CFD software of COMSOL Multiphysics® is used for the analysis of heat transfer and fluid flow. COMSOL Multiphysics® uses the finite element method (FEM) [233]. In comparison among other competitive CFD software tools (e.g. STAR CCM, ANSYS Fluent, and ANSYS CFX), COMSOL is seen as a more capable of coupling Multiphysics problems of conjugate heat transfer [314-316]. The distinctive feature of COMSOL software is that it uses a built-in solar load model [317]. This model estimates the effective radiation load of the Sun based on its position relative to the earth's surface (latitude and longitude), the orientation with respect to North, the time of day, the season, and weather conditions [318]. This software also has a built-in heat transfer module that includes the main heat transfer modes (conduction, convection and radiation). COMSOL Multiphysics® v5.3a software has therefore been adopted to model the proposed PV/T air collectors.

Many research findings using COMSOL software have been validated against benchmark experimental data and numerical simulations in modelling the solar thermal collectors and PV modules [32, 237, 318-322]. However, the FEM method, used in COMSOL, is time consuming compared with the other two approaches, finite volume and finite difference methods. In order to reduce the run time, a number of assumptions are introduced, maintaining an acceptable level of accuracy. These assumptions are described in detail in Section 4.5.

In this chapter, the numerical methods used to model six PV/T air systems with different configurations are presented here. The models are standard PV (model 1), single duct single pass PV/T unglazed air collector (model 2), single duct single pass PV/T glazed air collector (model 3), parallel pass double duct with co-current flow (model 4), single duct double pass U-flow shape (model 5); and parallel pass double duct with co-current flow with off-set strip fins (model 4-A). The models are developed using COMSOL Multiphysics® v5.3a software. The governing equations, boundary conditions, and assumptions are discussed. The

examination of mesh element type and mesh verification are performed. Furthermore, validation with experimental data in literature and verification using mathematical and CFD approaches for modes 2 and 3 are examined in this chapter.

4.1.1 Discretisation approaches

Discretisation is a technique that is used to convert partial differential equations (PDEs) into algebraic equations. This allows the governing equations to be solved numerically [231, 323, 324]. This is different from the analytical solutions where the PDEs are converted to ordinary ones [231, 323]. The commonly used discretisation methods are three [314, 325-329], Finite volume method (FVM), Finite element method (FEM), and Finite difference method (FDM).

The FVM and FEM are integral forms, whereas the FDM is a differential form which is based on Taylor series [314, 329]. The mesh in FDM is comprised of rows and columns of perpendicular lines while in the FEM and FVM; each element is unique and may not necessarily be at a right angle to each other. Accordingly, FDM might not be suitable for complex geometries, particularly in meshing corners or sharp edges [236, 314].

4.1.2 Methodology of CFD modelling

The methodology can be typically divided into three stages. These stages are employed to solve CFD codes which are as follow: 1) pre-processing, 2) solver and 3) post-processing.

The first stage (i.e. pre-processing) includes the following procedures:

- Geometry creation
- Fluid properties definition
- Mesh generation
- Physical and chemical phenomena selection
- Boundary conditions identification

Numerical solution of the computational model involves solving the governing equations of fluid flow and heat transfer (continuity and energy equations). Also, the selection of the solver (iterative or direct) and monitor the convergence. Finally, the post-processing step presents the results, graphics, animations, analyses and plots (see Fig. 4.1).

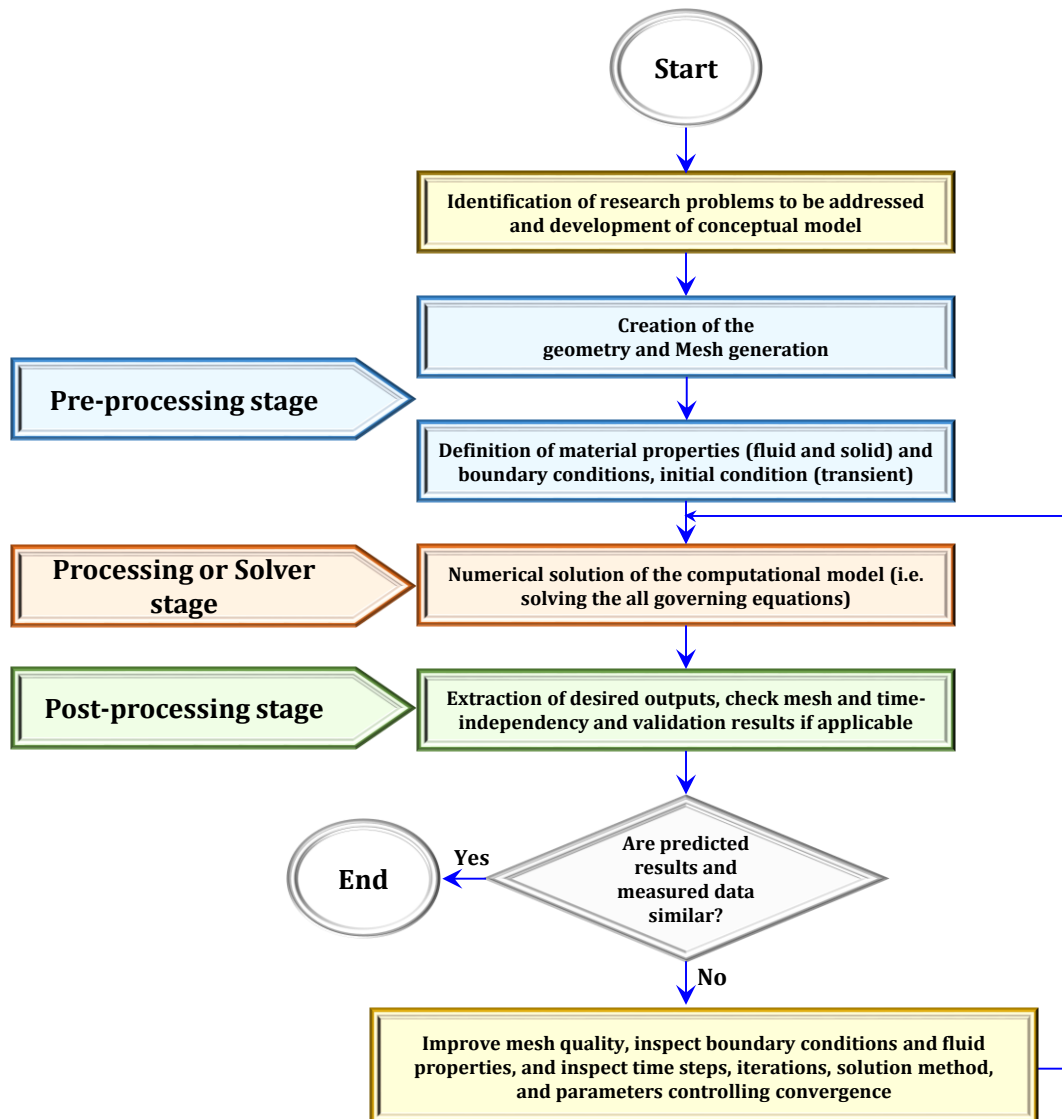


Fig. 4.1. Overview of the different stages of a general modelling process [330, 331].

4.1.3 Accuracy and convergence criteria

Several criteria are considered in order to improve the convergence and accuracy of the solution. In brief, the criteria are:

- Examining the effect of using a structured and unstructured mesh (uniform and non-uniform mesh).
- Performing a mesh independent study.
- Inspecting the mesh quality.

- Care should be taking in meshing the steep regions (i.e. edge or corner) where the solution needs to be precise, a dense mesh is required. While a lesser accuracy is required, a coarse mesh can be used.
- Inspecting the relative tolerance criteria.
- Studying the influence of the order of discretisation method in case of flow (transport) such as velocity and pressure and heat such as temperature.
- In the case of the transient condition, the inspection of the time step is crucial.
- Validation and verification.

4.2 Mesh generation

Applying a good mesh is a key to accurate computational results. Engineering judgment and experience have to be employed to generate a proper mesh since generating a mesh is not governed by an exact theoretical basis [314].

Fundamentally, the finite element method (FEM) splits the geometry into smaller sub-regions which are referred to as elements. An element comprises of a set of nodes. Over each finite element, the unknown variables (e.g., temperature, velocity, etc.) are approximated using known functions [332, 333].

Mesh elements can be classified into three types by their shape, one dimensional (lines), two dimensional (rectangles or triangles), and three dimensional (tetrahedral, hexahedral cuboid/brick, triangular prisms (prisms), and pyramids).

In this study, the 3D brick/hexahedral element type is used for meshing the PV/T air systems instead of the default option of the tetrahedral, as shown in Fig. 4.2. In Section 4.6.1, a comprehensive study was performed to examine the structured and unstructured mesh types for the proposed PV/T air model with fins.

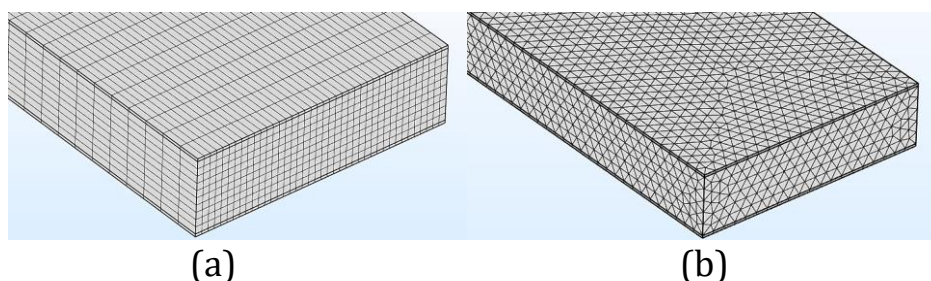


Fig. 4.2. Mesh of PV/T air system without fins for one of the case studies: in (a) Structured mesh and in (b) Unstructured mesh.

4.3 Computational model

In this section, several processes are discussed. Firstly, a numerical model of three-dimensional (3D) flow and heat transfer for five PV/T air models are developed. Secondly, the governing equations for air velocity and temperature are discussed. Thirdly, different assumptions and boundary conditions for these models are extensively explained. Then, a number of computational assumptions are used to reduce computation time. Finally, a comparison is drawn between different methods to evaluate the free convection in the enclosure.

4.3.1 Governing equations

The governing equations for the air velocity $\vec{V}(x, y, z) = u, v, w$ and temperature T are based on the conservations of mass, momentum and energy [233, 334]. These equations are solved numerically by the CFD software package COMSOL Multiphysics®. It should be noted that the three laws governing transport are as following [231]:

1. The law of conservation of mass
2. Newton's second law of motion
3. The first law of thermodynamics

4.3.1.1 Continuity equation

The continuity equation, represented by the conservation of mass, is given in a three-dimensional flow in terms of time-averaged compressible flow:

$$\frac{\partial \rho}{\partial t} + \frac{\partial}{\partial x}(\rho u) + \frac{\partial}{\partial y}(\rho v) + \frac{\partial}{\partial z}(\rho w) = 0. \quad \text{Eq. 4.1}$$

This can be re-formulated in a vector form:

$$\frac{\partial \rho}{\partial t} + \nabla \cdot \rho \vec{V} = 0, \quad \text{Eq. 4.1a}$$

where ρ is the density of air (kg m^{-3}), nabla (del), ∇ , refers to the vector gradient operator and \vec{V} is the fluid velocity vector defined as follows:

$$\nabla = \frac{\partial}{\partial x} i + \frac{\partial}{\partial y} j + \frac{\partial}{\partial z} k, \quad \text{Eq. 4.1b}$$

$$\vec{V} = ui + vj + wk. \quad \text{Eq. 4.1c}$$

Note that the Eq. 4.1a can be applied for the general case, which means transient, compressible and three-dimensional flow. In case of incompressible, ρ is constant (i.e. $\frac{\partial \rho}{\partial t} \approx 0$), Eq. 4.1a could be reduced to present in vector formula:

$$\nabla \vec{V} = 0. \quad \text{Eq. 4.1da}$$

4.3.1.2 Momentum equation

For single-phase laminar flow, a compressible Newtonian fluid including the effect of gravitational forces, under transient conditions, the general momentum equation in a three-dimensional Cartesian coordinate form as:

X-direction:

$$\rho \left(\frac{\partial u}{\partial t} + u \frac{\partial u}{\partial x} + v \frac{\partial u}{\partial y} + w \frac{\partial u}{\partial z} \right) = - \frac{\partial p}{\partial x} + \rho g_x - \left(\frac{\partial \tau_{xx}}{\partial x} + \frac{\partial \tau_{yx}}{\partial y} + \frac{\partial \tau_{zx}}{\partial z} \right), \quad \text{Eq. 4.2}$$

Y- direction:

$$\rho \left(\frac{\partial v}{\partial t} + u \frac{\partial v}{\partial x} + v \frac{\partial v}{\partial y} + w \frac{\partial v}{\partial z} \right) = - \frac{\partial p}{\partial y} + \rho g_y + - \left(\frac{\partial \tau_{xy}}{\partial x} + \frac{\partial \tau_{yy}}{\partial y} + \frac{\partial \tau_{zy}}{\partial z} \right), \quad \text{Eq. 4.3}$$

Z- direction:

$$\rho \left(\frac{\partial w}{\partial t} + u \frac{\partial w}{\partial x} + v \frac{\partial w}{\partial y} + w \frac{\partial w}{\partial z} \right) = - \frac{\partial p}{\partial z} + \rho g_z + - \left(\frac{\partial \tau_{xz}}{\partial x} + \frac{\partial \tau_{yz}}{\partial y} + \frac{\partial \tau_{zz}}{\partial z} \right), \quad \text{Eq. 4.4}$$

where:

$$\tau_{xx} = -\mu \left(2 \frac{\partial u}{\partial x} - \frac{2}{3} \nabla \cdot \vec{V} \right), \quad \text{Eq. 4.4a}$$

$$\tau_{yy} = -\mu \left(2 \frac{\partial v}{\partial y} - \frac{2}{3} \nabla \cdot \vec{V} \right), \quad \text{Eq. 4.4b}$$

$$\tau_{zz} = -\mu \left(2 \frac{\partial w}{\partial z} - \frac{2}{3} \nabla \cdot \vec{V} \right), \quad \text{Eq. 4.4c}$$

$$\tau_{xy} = \tau_{yx} = -\mu \left(\frac{\partial u}{\partial y} + \frac{\partial v}{\partial x} \right), \quad \text{Eq. 4.4d}$$

$$\tau_{xz} = \tau_{zx} = -\mu \left(\frac{\partial u}{\partial z} + \frac{\partial w}{\partial x} \right), \quad \text{Eq. 4.4e}$$

$$\tau_{yz} = \tau_{zy} = -\mu \left(\frac{\partial v}{\partial z} + \frac{\partial w}{\partial y} \right). \quad \text{Eq. 4.4f}$$

For a Newtonian incompressible fluid and under transient conditions, in cartesian coordinates:

X- direction:

$$\rho \left(\frac{\partial u}{\partial t} + u \frac{\partial u}{\partial x} + v \frac{\partial u}{\partial y} + w \frac{\partial u}{\partial z} \right) = -\frac{\partial p}{\partial x} + \rho g_x + \mu \left(\frac{\partial^2 u}{\partial x^2} + \frac{\partial^2 u}{\partial y^2} + \frac{\partial^2 u}{\partial z^2} \right), \quad \text{Eq. 4.5}$$

Y- direction:

$$\rho \left(\frac{\partial v}{\partial t} + u \frac{\partial v}{\partial x} + v \frac{\partial v}{\partial y} + w \frac{\partial v}{\partial z} \right) = -\frac{\partial p}{\partial y} + \rho g_y + \mu \left(\frac{\partial^2 v}{\partial x^2} + \frac{\partial^2 v}{\partial y^2} + \frac{\partial^2 v}{\partial z^2} \right), \quad \text{Eq. 4.6}$$

Z- direction:

$$\rho \left(\frac{\partial w}{\partial t} + u \frac{\partial w}{\partial x} + v \frac{\partial w}{\partial y} + w \frac{\partial w}{\partial z} \right) = -\frac{\partial p}{\partial z} + \rho g_z + \mu \left(\frac{\partial^2 w}{\partial x^2} + \frac{\partial^2 w}{\partial y^2} + \frac{\partial^2 w}{\partial z^2} \right). \quad \text{Eq. 4.7}$$

The set of equations from Eq. 4.5 to Eq. 4.7 are the momentum equations for an unsteady, incompressible flow which can be written in vector formula as:

$$\rho \frac{D\vec{V}}{Dt} = -\nabla p + \rho \vec{g} + \mu \cdot \nabla^2 \vec{V}, \quad \text{Eq. 4.8}$$

where:

$$\rho \frac{D\vec{V}}{Dt} = \left(\rho \frac{\partial \vec{V}}{\partial t} + \rho (\vec{V} \cdot \nabla) \vec{V} \right). \quad \text{Eq. 4.8a}$$

4.3.1.3 Energy equation

The rate of heat addition from solid to fluid particles owing to heat conduction across element boundaries is the general conductive energy equation with a heat source and translational motion between the layers.

$$\frac{D(\rho c T)}{Dt} \cdot \nabla T = \nabla \cdot (k_{x,y,z} \nabla T) + \dot{Q}_v, \quad \text{Eq. 4.9}$$

$$\nabla \cdot (k_{x,y,z} \nabla T) = \frac{\partial}{\partial x} \left(k_x \frac{\partial T}{\partial x} \right) + \frac{\partial}{\partial y} \left(k_y \frac{\partial T}{\partial y} \right) + \frac{\partial}{\partial z} \left(k_z \frac{\partial T}{\partial z} \right), \quad \text{Eq. 4.10}$$

$$\frac{D(\rho c T)}{Dt} = \rho c \frac{\partial T(x,y,z)}{\partial t} + \rho c u \frac{\partial T}{\partial x} + \rho c v \frac{\partial T}{\partial y} + \rho c w \frac{\partial T}{\partial z}, \quad \text{Eq. 4.11}$$

where ρ is the density of PV layers (kg m^{-3}), c is the heat capacity of PV layers at constant pressure ($\text{J kg}^{-1} \text{K}^{-1}$), $k_{x,y,z}$ is the thermal conductivity of the PV layers ($\text{W m}^{-1} \text{K}^{-1}$) x, y and z

directions and assumed isotropic ($k_x = k_y = k_z$). u, v and w are the velocity components in x, y and z directions, respectively, \dot{Q}_v is the volume heat source or sink.

With respect to PV cells for both PV/T air and PV systems, where the conditions are: steady state conditions, electrical power generation (heat sink) (\dot{Q}_v), stationary PV cells and 3D, Eq. 4.9 reduces to Eq. 4.12. More detail about the electrical power generation is presented in Section 3.3.3.3.

$$\nabla \cdot (k_{x,y,z} \nabla T) = \dot{Q}_v. \quad \text{Eq. 4.12}$$

In terms of other PV layers (i.e. EVA, Tedlar and glass), in which the conditions are, 3D, steady state conditions a stationary PV module layers, Eq. 4.9 reduces to Eq. 4.13.

$$\nabla \cdot (k_{x,y,z} \nabla T) = 0. \quad \text{Eq. 4.13}$$

For PV/T air system, in the fluid, the following details of fluid flow behaviour are taken into account for the solution to the heat transfer equation:

- The energy transport is due to convection, either by the convective or conductive modes of heat transfer, depending on the thermal properties.
- The viscous effects are taken into account for the production of fluid heating, which is often ignored although its impact is noticeable in viscous fluid motions.
- The compressibility effect on producing heat is considered. The pressure work term contributes to the heat equation when the fluid density becomes temperature dependent.

Taking into account the abovementioned underlying-physics of the flow, as well as conduction, generalises the transient heat equation into the following expression [278]:

$$\rho c_{p_f} \left(\frac{\partial T}{\partial t} + \vec{V} \cdot \nabla T(x, y, z) \right) + \nabla \cdot (k_f \nabla T) = Q_P + Q_{vd} + \dot{Q}_v, \quad \text{Eq. 4.14}$$

in which Q_{vd} is the viscous dissipation in the fluid domain (W m^{-3}), \vec{V} is the velocity vector (m s^{-1}) and Q_P is the work done by pressure gradients owing to heating under adiabatic compression and thermo-acoustical phenomenon (W m^{-3}), which is relatively minor for a small Mach number,

$$Q_P = \alpha_p T_f \left(\frac{\partial p}{\partial t} + V \cdot \nabla p \right), \quad \text{Eq. 4.15}$$

$$\alpha_p = \frac{1}{\rho} \frac{\partial \rho}{\partial T}, \quad \text{Eq. 4.16}$$

In which p is pressure, and for ideal gases, the thermal expansion coefficient, α_p takes the simpler form [279]:

$$\alpha_p = \frac{1}{T}. \quad \text{Eq. 4.17}$$

For a steady state problem, the temperature does not change with time and the terms with time derivatives disappear.

The final governing equation is the equation of state. In reality, the density is a function of pressure and temperature,

$$\rho = \rho(p, T). \quad \text{Eq. 4.18}$$

For ideal gas, ρ is calculated using the law of state which is valid with [248, 249].

$$\rho = \frac{p}{RT}. \quad \text{Eq. 4.19}$$

4.3.2 Conjugate heat transfer

Before computers came into extensive use, empirical correlation equations were used to model convective heat transfer problems. These equations are proportionality of heat flux to temperature difference with heat transfer coefficient (i.e. Newton's law of cooling) which was valid only in theoretical heat convection (i.e. using in simple analysis), since the time of Newton [335, 336], see Eq. 4.20.

$$-k_s \frac{\partial}{\partial n} (T - T_{s,\Gamma}) \Big|_{\Gamma} = h(T_{f,\Gamma} - T_{\infty}). \quad \text{Eq. 4.20}$$

For that reason, since the 1960s, the contemporary conjugate heat transfer module was developed to overcome this deficiency or shortage. In order to clarify, this module is used to model the coupling between conduction heat transfer in a solid domain (for example upper or lower PV surfaces) and convective heat transfer to the fluid (moving air) at the solid/fluid interface as shown in Fig. 4.3 and Eq. 4.21. This module also describes processes involving temperature variations within solid and fluid domains, as a result of the thermal interaction between these domains. This module is a built-in functionality in COMSOL software.

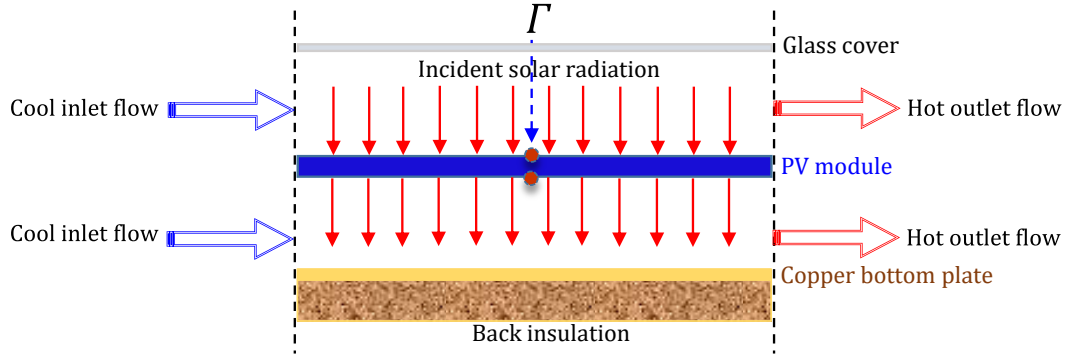


Fig. 4.3. Representation of the conjugate heat transfer of air PV/T system (model 4).

$$-k_s \frac{\partial T_s}{\partial n} \Big|_{\Gamma} = -k_f \frac{\partial T_f}{\partial n} \Big|_{\Gamma}, \quad \text{Eq. 4.21}$$

where Γ is the interface surface between the solid and fluid.

Eq. 4.21 could be valid under two conditions, the first condition is no slip (i.e. $u = v = w = 0$) and the other is when the interface wall temperatures have the same temperature magnitude ($T_s, \Gamma = T_f, \Gamma$). The energy equations in the fluid and solid domains are given by:

$$\nabla \cdot (k_s \nabla T) = 0, \quad \text{Eq. 4.22}$$

$$\rho c_{p_f} \left(\frac{\partial T_f}{\partial t} + V \nabla T_f(x, y, z) \right) + \nabla \cdot ((k_f + k_T) \nabla T_f), \quad \text{Eq. 4.23}$$

where V is the velocity of the fluid (air), T_f and T_s are the fluid and solid temperatures respectively; k_t is the turbulent thermal conductivity ($k_T = c_{p_f} \mu_T / \text{Pr}_T$), and Pr_T is the turbulent Prandtl number [232, 330, 337]. It should be noted that Eq. 4.23 is a 3D form under turbulent flow regime, however, when $\mu_T = 0$ the flow is considered to be laminar.

4.3.3 Radiation model

Thermal radiation can be defined as the stream of electromagnetic waves emitted from a body at a specific temperature. In Fig. 4.4, consider a point P located on a surface that has an emissivity (ε), reflectivity (ρ), absorptivity (α), refractive index (n), and temperature (T). The body is assumed opaque, which means that no radiation is transmitted through the body.

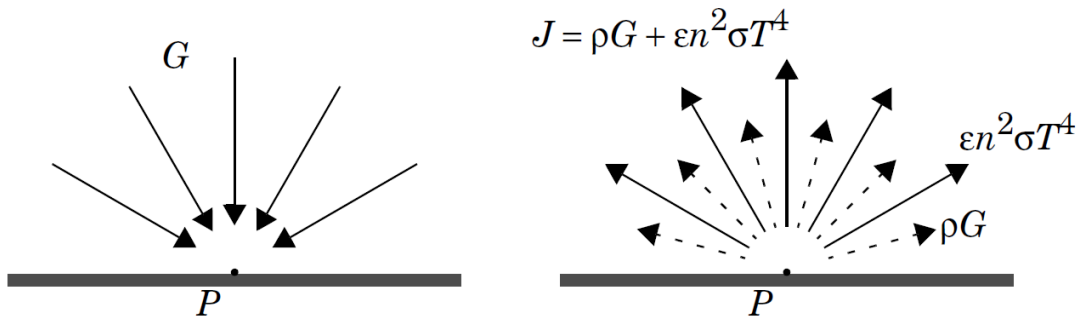


Fig. 4.4. Incoming irradiation (left), outgoing radiosity (right).

The total incoming radiative flux at P is called irradiation and denoted G . The total outgoing radiative flux at P is called radiosity and denoted J . This radiosity is the sum of reflected and emitted radiation:

$$J = \rho G + \varepsilon e_b(T). \quad \text{Eq. 4.24}$$

According to the Stefan-Boltzmann law, $e_b(T)$ is the power radiated across all wavelengths and depends on the fourth power of the temperature, $(q_r) \propto T^4$ [269, 279, 338].

$$e_b = n^2 \sigma T_s^4. \quad \text{Eq. 4.25}$$

The net inward radiative heat flux (q_r) is then given by the difference between the irradiation and the radiosity:

$$q_r = G - J. \quad \text{Eq. 4.26}$$

To eliminate J , combine Eq. 4.24 and Eq. 4.26 which yields:

$$q_r = (1 - \rho)G - \varepsilon e_b(T). \quad \text{Eq. 4.27}$$

Assuming $\alpha = \varepsilon = (1 - \rho)$ (a grey body), the net rate of radiation heat transfer from the surface, expressed per unit area of the surface, is shown in Eq. 4.29 [279].

$$q_r = (\varepsilon e_b - \varepsilon G). \quad \text{Eq. 4.28}$$

Now, substitute Eq. 4.25 in Eq. 4.28 yields:

$$q_r = \varepsilon \sigma (T_s^4 - T^4), \quad \text{Eq. 4.29}$$

where T is the surrounding temperature and T_s is the surface temperature.

It should be referred that the Surface-to-Surface Radiation interface in the Heat Transfer module implements the radiosity method that enables arbitrary temperature dependence and assumes that the emissivity and absorptivity are independent of the angle of emission and absorption. It is also possible to account for wavelength dependence on the surface emissivity and absorptivity.

4.4 System parameters

4.4.1 Description of PV/T collectors

In CFD, it is crucial to generate a geometry that sufficiently represents the physical system being studied. Four PV/T air collector designs are investigated in this study (models 2 to 5). Sketches of these designs are shown in [Fig. 4.5](#) to [Fig. 4.8](#). These designs are classified based on the direction of air flow and the number of air passes. The first design model (see [Fig. 4.5](#)) is a single duct single pass, model 2, in which air flows underneath the PV panel, whereas the upper surface of PV is subject to ambient conditions. The second design model is a single duct single pass (glazed), model 3 (see [Fig. 4.6](#)), this design is similar to model 2 but with an air gap added between the upper surface of the PV module and a glass cover. The third design is a parallel pass double duct, model 4, as can be seen in [Fig. 4.7](#), air flows under and over the surfaces of the PV module in the same direction (co-current flow). In model 5 air flows between the glass cover and the PV module and reverses in the second pass between the PV panel and the lower absorber plate, making a U-shape flow (double-pass single duct, see [Fig. 4.8](#)). Finally, the flow configuration in model 4 has been amended by including off-set strip fins in a staggered arrangement (model 4-A), as illustrated in [Fig. 4.9](#). Each geometry is comprised of four main domains. The domains are a solid domain of transparent glass cover, a PV panel, and the copper bottom plate, and the fluid domain of air. The thicknesses of the transparent glass cover, the PV panel and the copper bottom plate are 0.004 m, 0.0048 m and 0.001 m respectively, and they are all 0.8 m wide and 1.2 to 1.6 m length. [Table 4.1](#) presents the physical properties for the material of these domains, while [Table 4.2](#) reveals the specifications for PV/T air collector designs.

Table 4.1. Thermophysical properties of the PV/T air domains.

Layer	k	ρ	c_p	ε
Glass	1.4	2210	730	0.84
Aluminum	238	2700	900	0.67
Copper	400	8960	385	0.65

Table 4.2. Specifications of the PV/T air systems.

Symbol	Description	Values
Re	Reynolds number	510 and 2550 [180, 257]
T_{amb}	Ambient air temperature	45 and 25 °C [183, 185, 249, 339]
T_{in}	Fluid temperature at the collector inlet	T_{amb}
w	Collector width	0.8 m [225, 340]
w	3D slice width	0.015 m
δ_{cu-U}	Thickness of upper copper plate located on the back surface of the PV module	0.001 m
δ_{cu-L}	Thickness of the lower copper plate located in lower channel flow	0.001 m
δ_{D2}	Upper depth flow	0.025 m [50, 121, 122, 151, 172]
δ_{D1}	Lower depth flow	0.025 m [50, 151, 172]
δ_g	Thickness of glass	4 mm [122, 241, 269]
δ_{UE}	Equivalent thickness of glass and EVA	4.5 mm
δ_{LE}	Equivalent thickness of Si, Tedlar and EVA	1.3 mm
ε_{cu}	Copper (oxidized)	0.65 [241, 269]
ε_g	Average emissivity of glass	0.92 [241, 269]
β	Collector tilt angle	45 degree
G	Global solar irradiance at the collector plane	1000 W m ⁻²
L	Collector length	1.2 and 1.6 m [26, 172, 225, 340]

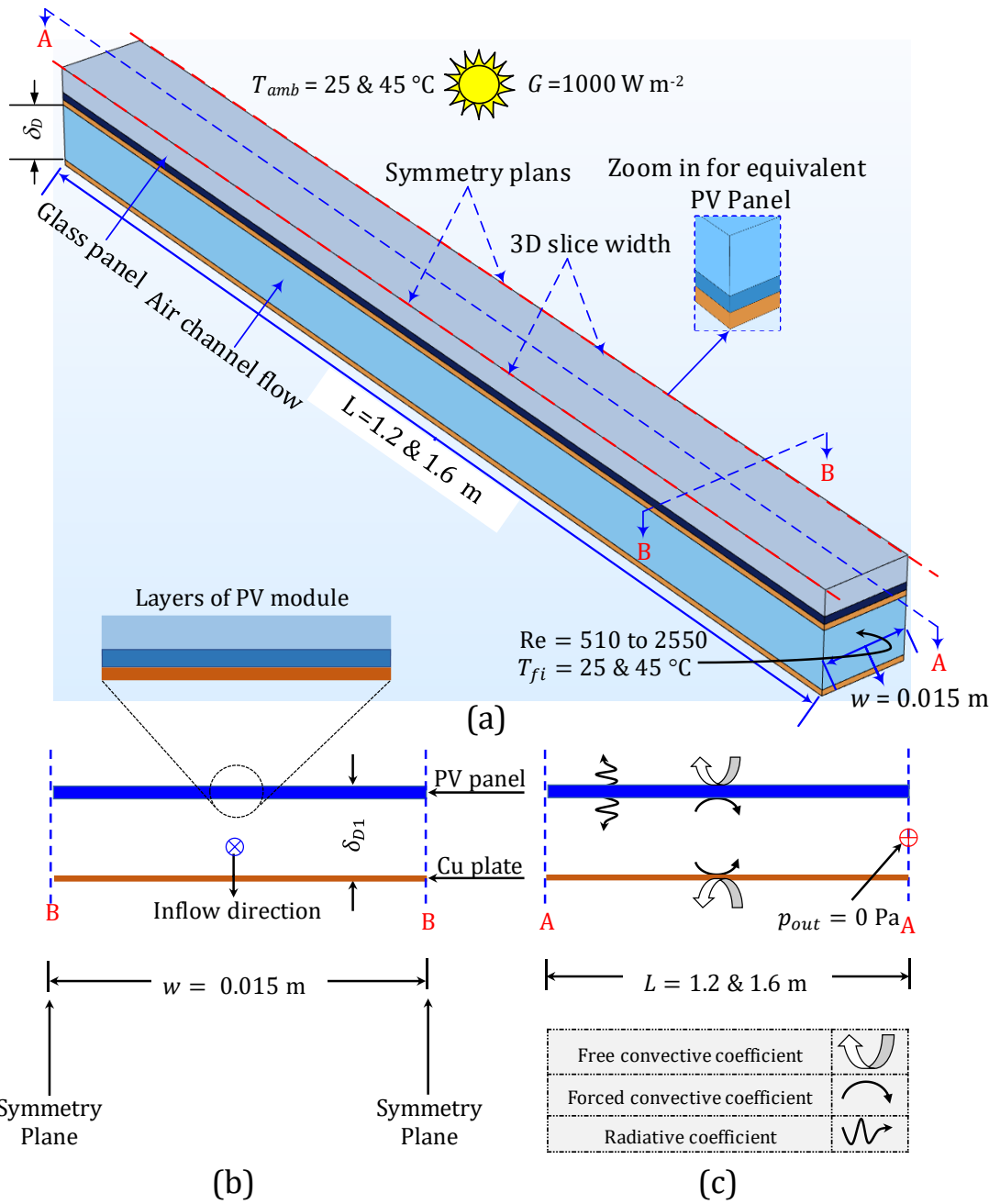


Fig. 4.5. Schematics of model 2: in (a) 3D of model 2 (b) 2D cross-section front view of model 2, (c) 2D cross-section side view of model 2.

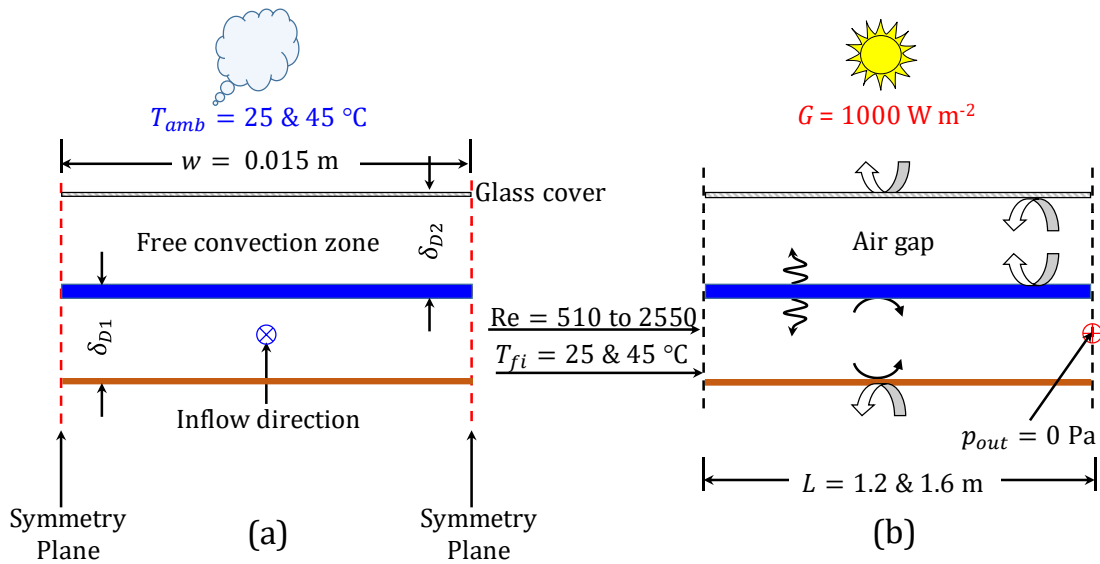


Fig. 4.6. Schematics of model 3: in (a) 2D cross-section front view of model 3, (b) 2D cross-section side view of model 3.

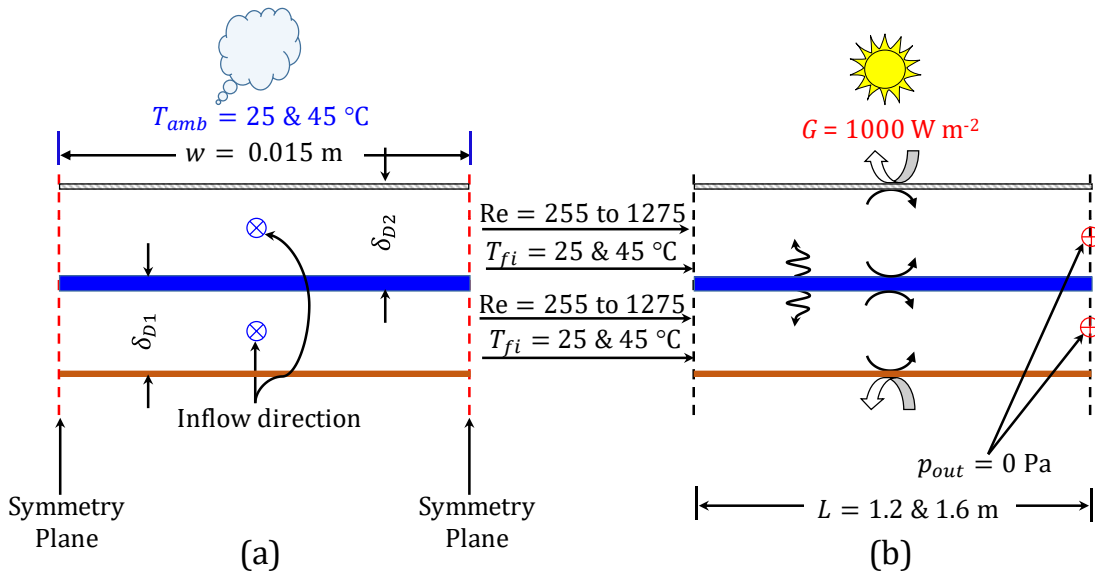


Fig. 4.7. Schematics of model 4: in (a) 2D cross-section front view of model 4, (b) 2D cross-section side view of model 4.

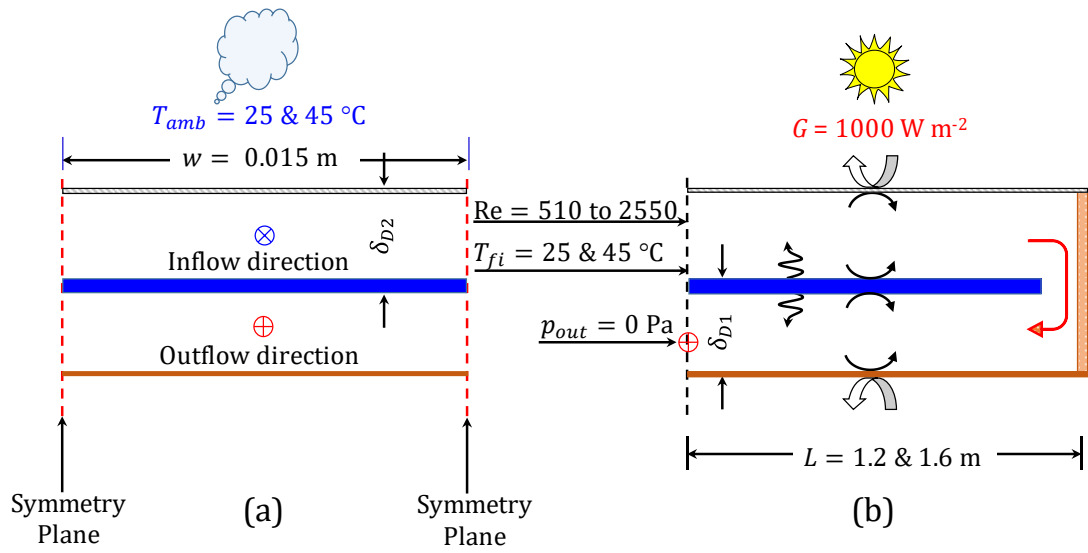
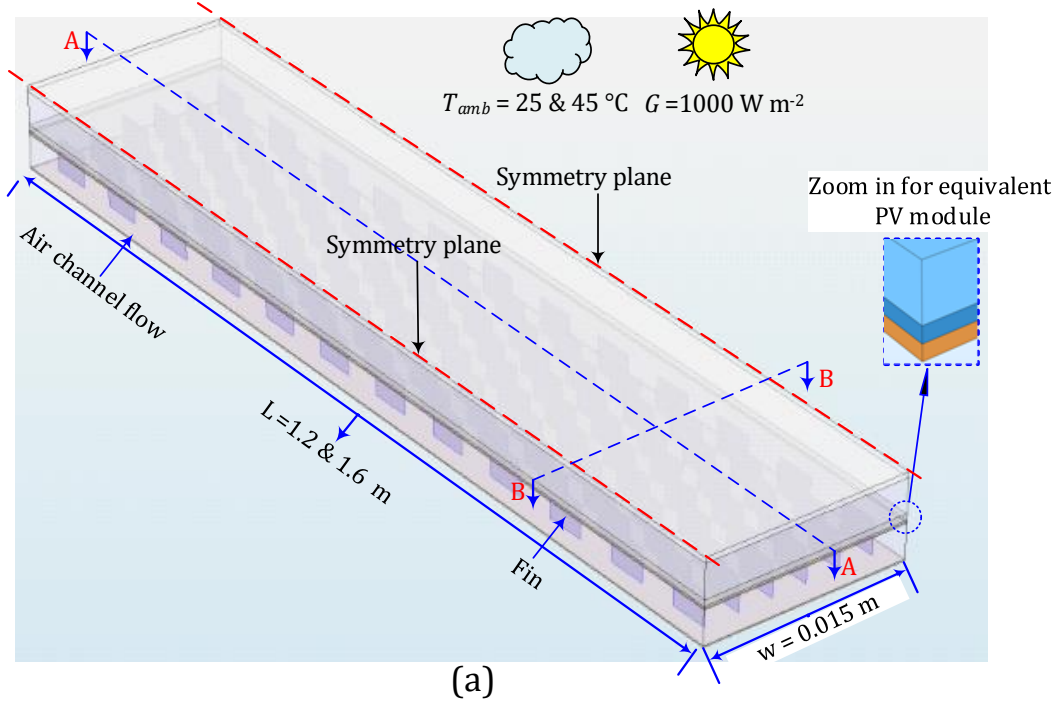


Fig. 4.8. Schematics of model 5: in (a) 2D cross-section front view of model 5, (b) 2D cross-section side view of model 5.



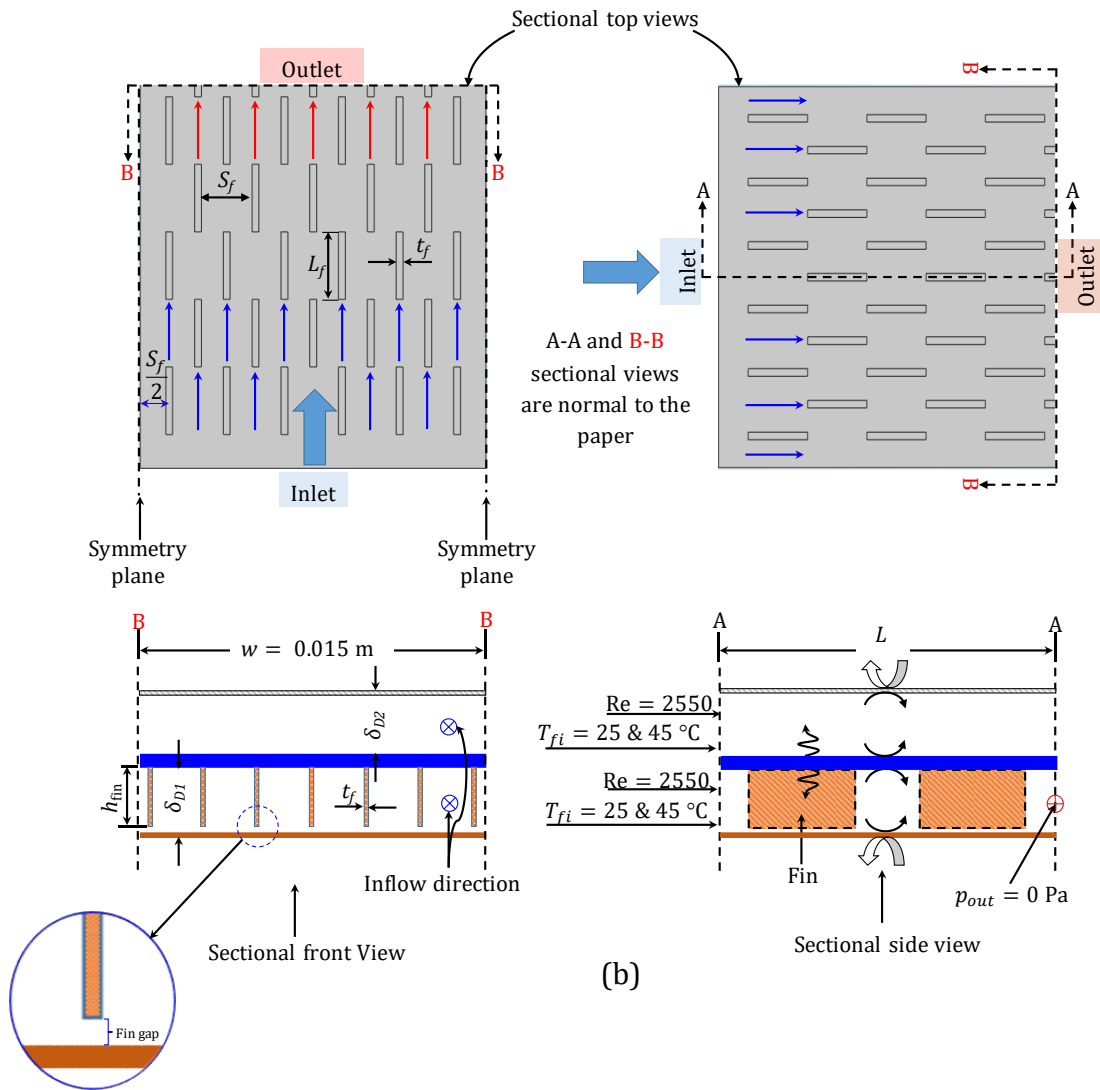


Fig. 4.9. Different views of model 4-A with offset strip fins.

4.4.2 PV physical module description

The photovoltaic technology chosen in this work is the polycrystalline BP Solar BP 585 which consists of five main components [341]: the glass cover, PV cells, encapsulation foil, a back sheet layer (Tedlar) and metal frame (see Fig. 4.10). The metal frame that encloses these components has a negligible thermal effect because of its comparatively small surface area. The properties of the PV panel materials are assumed to be independent of temperature. A brief definition of these layers is shown below [36]:

1. **Tempered glass cover:** PV module glass is built from tempered glass. The strength of this glass is better than conventional glass and its high transmittance rate (ultra-clear) and low iron content minimize optical losses [36].

2. **PV cell:** Polycrystalline silicon wafers are utilized in the BP 585 module. The electrical characteristic and physical properties of this PV is portrayed in [Table 4.3](#) and [Table 4.4](#).
3. **Cell encapsulation:** The PV cells are covered using two layers of ethylene-vinyl acetate (EVA). The front or upper layer to glue or paste the PV cells to the glass and the lower layer to protect from moisture resistance besides electrical isolation.
4. **Back sheet (Tedlar):** The polymer layer in the BP 585 is formed from polyvinyl fluoride (PVF). This layer can withstand the light and offers further insulation and moisture protection for the PV cells.

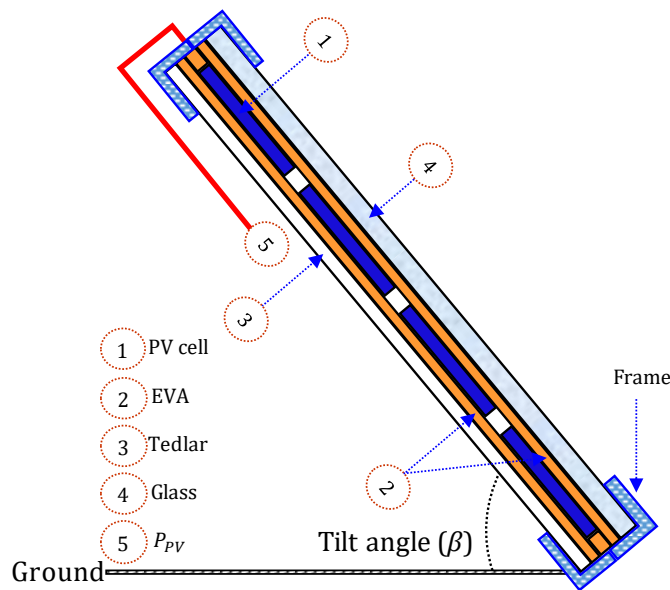


Fig. 4.10. Schematic view of the main PV module components.

Table 4.3. Operating properties of the PV module BP 585 [31, 32, 35].

Electrical data at STC		Thermal ratings		Material data	
Module maximum power (P_{max})	50 W	Operating temperature range	-40~85 °C	Panel dimensions (L w)	0.666 m × 0.606 m
Voltage at maximum power point (V_{mmp})	17.89 V	Temperature coefficient of $P_{max}, (\beta_{ref})$	-0.41%/°C	Cell type	Polycrystalline
Current at maximum power point I_{mmp}	2.8 A	Temperature coefficient of V_{oc}	-0.31%/°C	Cell number	36
Open circuit voltage (V_{oc})	21.77 V	Temperature coefficient of I_{sc}	0.058%/°C	Glass type	Tempered, high transmittance, low iron
Short circuit current (I_{sc})	3.04 A	Panel efficiency $\eta_{pv, T_{ref}}$	12.35%	Encapsulant type	EVA

Note that: All data refer to standard test conditions [AM 1.5, 1000 W m⁻², 25 °C].

Table 4.4. Material properties of the layers of the PV module (BP 585) [31, 32, 35, 39, 342].

Layer	t (mm)	k (W m ⁻¹ K ⁻¹)	ρ (kg m ⁻³)	c (J kg ⁻¹ K ⁻¹)	ϵ	τ	t/k (m ² K W ⁻¹)
PV glass	3	1.8	3000	500	0.84	0.91	1.7×10^{-3}
EVA	0.5	0.35	960	2090	-	-	1.4×10^{-3}
PV cells	0.3	148	2330	677	0.91	-	2.0×10^{-6}
Tedlar	0.5	0.2	1200	1250	0.87	-	2.5×10^{-3}

In Table 4.4, the PV thickness (t), thermal conductivity (k), density (ρ), and specific heat capacity (c).

4.4.3 Assumptions and boundary conditions

A number of assumptions and boundary conditions are considered to solve the governing equations as follows:

- The fluid is single-phase, the flow is laminar and is weakly compressible. For weakly compressible flow $\partial\rho/\partial p = 0$ and $\partial\rho/\partial\phi \neq 0$, where ϕ are other independent variables, such as time.
- All boundaries of the PV/T air collectors are subjected to ambient conditions and considered insulated (adiabatic wall condition). In other words, unless explicitly changed, boundaries are by default considered are set as insulated in the software.
- The effect of thermal radiation on a fin surface performance is negligible, this is studied in detail in Section 4.5.1.
- The solar radiation absorbed by the PV cells is converted into two types, the first one is converted to electrical energy while the remainder is converted into thermal energy.
- The fin domain is treated as a thin layer. This assumption will be discussed in Section 4.5.4.
- The solution domain of the 3D PV/T air collectors (models 2 to 5) is a rectangular duct on the x-y-z plane, bounded by the inlet, outlet and wall boundaries shown in Fig. 4.5 to Fig. 4.9.
- The properties of the air, channel duct and PV layers are temperature dependent.
- No-slip conditions.
- In order to simulate a realistic incident solar radiation:
 - a. 'External Radiation Source' sub-node is applied to the top glass surface
 - b. The glass is ultra-clear and has no absorption or emission.
 - c. This incident radiation includes the solar spectral bands U.V, visible and I.R radiation.
 - d. Uniform heat flux on the top surface of the photovoltaic [343].

- The surface-to-surface radiation model is used to simulate the thermal radiation exchange between the surfaces as discussed in detail in Section 4.3.3. This is assuming that the fluid and the glass cover are non-participating, i.e., they do not absorb, emit, or scatter any radiation as the thickness of the glass is less than 6 mm [279].
- Uniform air velocity is introduced at the inlet assuming a fully developed flow.
- At the exit, a pressure outlet boundary condition is specified with a fixed value of 101325 Pa.
- When there is little or no wind, the free convection mode will then dominate rather than the wind effect.
- The radiative exchange temperature for models 1 and 2 is ambient temperature, while the radiative exchange temperature for models 3, 4, 5 and 4-A is the upper glass cover.
- Symmetrical boundary conditions are applied on the two sides of the PV/T air collector assuming that the width $\rightarrow \infty$. The width of the 3D slice is therefore considered here rather than using the full width. This can be seen in Fig. 4.5.
- The PV layer surfaces are in perfect contact which means that thermal contact resistance between them is negligible [57].

4.5 Computational assumptions

Several assumptions have been made to reduce the computational time with minimal impact on the level of accuracy as discussed below.

4.5.1 Thermal radiative effects

The conductive heat transfer rate is dissipated from fin surfaces either by convection (Newton's law of cooling) and/or radiation from the boundaries of the fin [269, 279]. It is commonly believed that thermal radiation problems are one of the most computationally expensive [344], specifically when coupling it with turbulent models. Various representative cases simulated by Frei [344] as presented in Fig. 4.11.

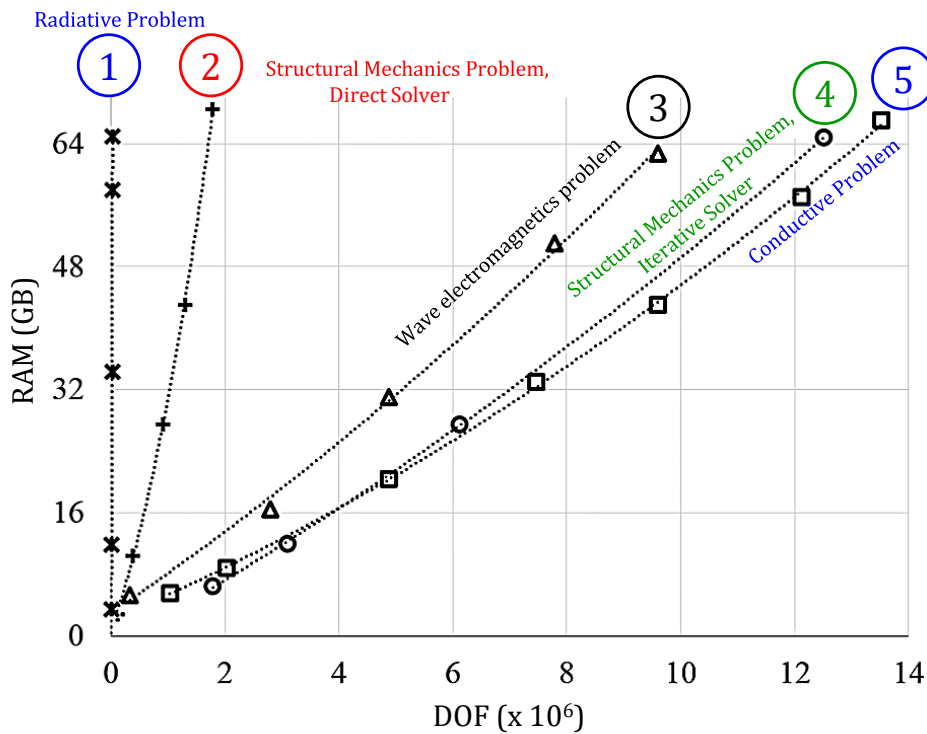


Fig. 4.11. Memory requirements with respect to degrees of freedom (DOF) for various representative cases adapted from [344].

From the data in Fig. 4.11, it is clear that the radiative heat transfer problem consumes the most physical random access memory (RAM) for the same or even lower number of degrees of freedom (DOF). In general, this is owing to the fact that the rate of radiation heat transfer is governed by a fourth-order equation, $(q_r) \propto T^4$ as mentioned in detail in Section 4.3.3.

The effect of radiation upon forced-convection heat transfer was studied by many researchers [269, 279, 322, 345, 346]. They found that the influence of thermal radiation could be negligible in the case of forced convection, specifically at high Reynolds number values, low emissivity and moderate temperatures [180, 347]. Thus, the effect of thermal radiation on fin surfaces can be neglected under these conditions. However, in free convection, there is a clear radiation effect [269, 279, 346, 348-351].

In solar air collector systems particularly where forced convection conditions apply, the neglected radiative heat transfer rate could be attributed to several reasons. Firstly, the temperature of the fin surface and collector walls are comparable [347]. This is mainly because of the fins located in the lower air duct where they are not directly subjected to incident solar radiation. Moreover, the air is assumed to be transparent to solar radiation as shown in Fig. 4.12.

A comparison between two cases with and without radiation effect is made to evaluate the effect of radiation from fin surfaces. The boundary conditions and assumptions are seen in Fig. 4.12. The results showed a 2% difference in thermal efficiency and the computation time reduced from 84.5 hours to 4.5 hours for the case with and without radiation respectively.

The second assumption is concerned with equations coupling and is discussed next.

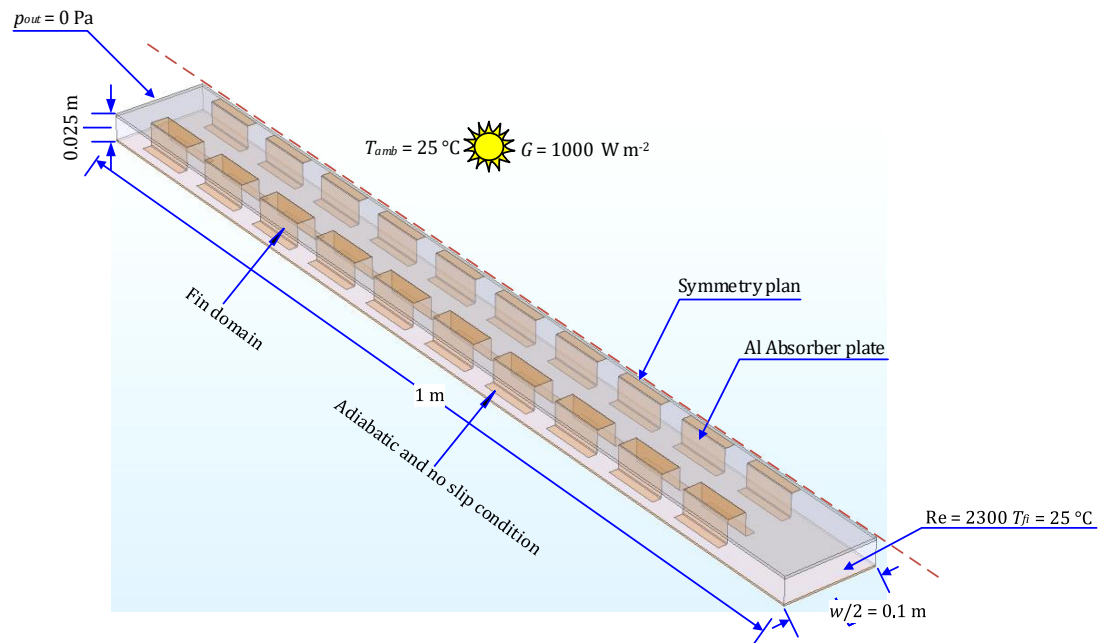


Fig. 4.12. Schematic of single duct, single pass solar air thermal collector including off-set strip fins shown the symmetry planes and boundary conditions.

4.5.2 One-way coupling approach

The fully coupled method simultaneously solves fluid flow and heat transfer. Alternatively, a one-way coupled approach can be used to solve multi-physics problems. This approach can be considered the most important assumption with respect to reducing the running time approximately by 50-70% [352]. The mechanism of this approach can be divided into two steps, firstly, the fluid flow problem is solved, the results are then used as input values for the second step to solve the heat transfer problem. This one-way coupled technique is highly versatile as it is applicable to all types of fluid flow whether it is laminar or turbulent [352, 353].

An ideal way to determine the validity of a one-way coupled approach is to compare it with a fully coupled one in a test case. Accordingly, three representative cases are examined. The first case is the PV/T air model 4 without fins, with length, 1.24 m, 3D slice width of 15 mm, and depth of flow for the upper and lower duct of 0.025 m. The fully coupled and one-way coupled methods are carried out for this system. The results are tabulated in [Table 4.5](#) showing a good level of agreement between the two methods with the computation time reduced from 275 minutes to 39 minutes.

Table 4.5. Case 1 of model 4, with length, 1.24 m, 3D slice width of 15 mm, and depth of flow for the upper and lower duct of 0.025 m using the fully coupled and one-way coupled methods.

Variable	One-way coupled	Fully coupled	Percentage error (%)
R_{th}	1.287	1.289	0.16
Δp	19.95	20.98	4.89
η_{th}	46.84	46.65	0.40
η_{pv}	11.13	11.128	0.02

In [Table 4.5](#), R_{th} represents the thermal resistance ($K W^{-1}$).

The second case is to compare the two approaches using model 4. A parametric study is undertaken here for different lengths and depths of flow. [Fig. 4.13](#) shows that the magnitude of pressure drop in the two methods exhibited good agreement. The run time is also reduced from 50 hours to 20 hours.

The third case is the PV/T air, model 4-A with fins. A parametric study is carried out here for different air velocities (0.14456, 0.1807, 0.24093, 0.3614 and 0.7228) $m s^{-1}$. The dimensions of the collector are: length of the collector is 1.2 m, depth of flow for upper and lower duct is 0.025 m, length of the fin is 0.048 m. and space between fins is 0.01 m. [Fig. 4.14](#) illustrates that the values of pressure drop in the two solution methods showed poor agreement relative to that in first and second cases. The percentage error is between 13-17% which is considered high compared to the system without fins. This increased discrepancy can be attributed to the fact that the temperature field effect on velocity is not captured in the one-way coupling method. An increase in temperature results in a decrease in the viscosity which in turn increases the average speed (see [Eq. 4.30](#)). An increase in the speed results in an increase in the pressure drop as shown [Eq. 4.31](#). This effect is captured in the fully coupled method but not in the one-way coupling one.

It has been found in this study that one-way coupling is limited to steady state and plain surface (without fins) domains. In other words, for highly temperature-dependent such air-free convection in the enclosure, which is strongly affected by temperature and can be considered inherently unsteady state condition (transient).

$$\text{Re}_{D_h} = \frac{\rho_f \bar{V} D_h}{\mu_f} = \frac{4 \dot{M}}{\mu_f P_{er}} \quad \text{Eq. 4.30}$$

$$\Delta p_f = \frac{\rho_f \bar{V}^2 L}{2 D_h}, \quad \text{Eq. 4.31}$$

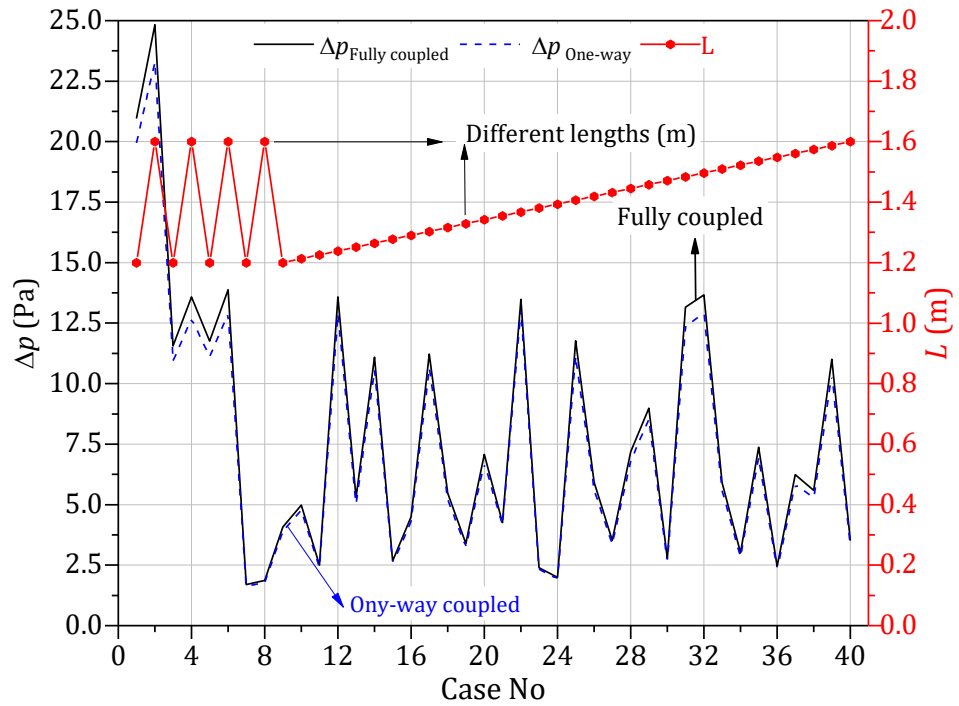


Fig. 4.13. Pressure drops from one-way and fully coupled methods versus collector length under the steady state condition and laminar flow regime, $\text{Re}_{D_h} = 2550$ for model 4.

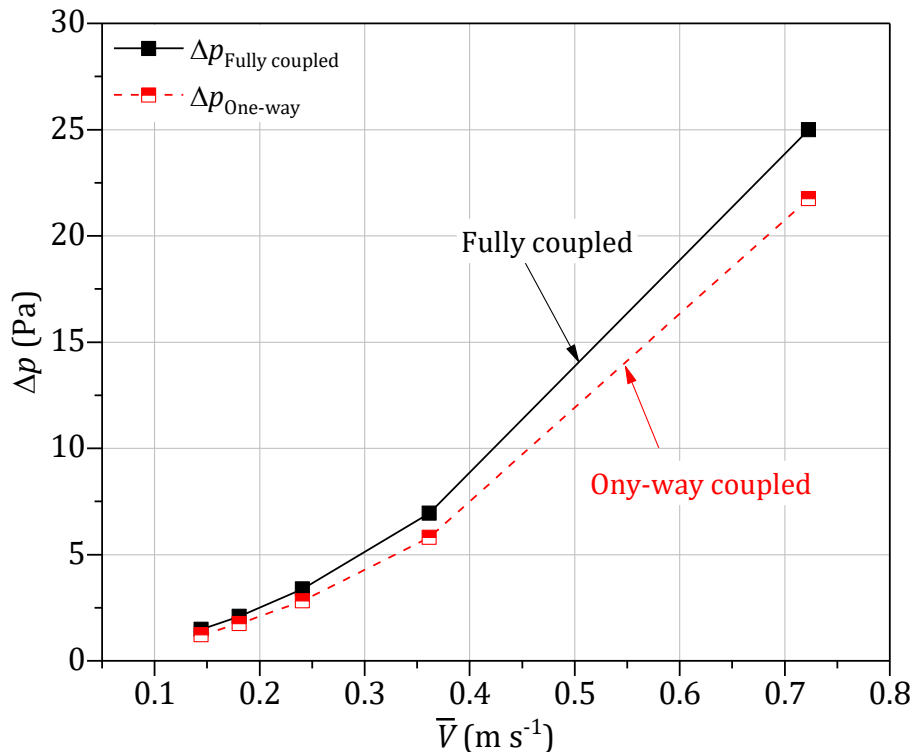


Fig. 4.14. Pressure drops from one-way and fully coupled methods for design model 4-A (finned collector), $S_f = 10$ mm, $L = 1.2$ m, $L_f = 48$ mm $\delta_{D1} = \delta_{D2} = 25$ mm.

4.5.3 Symmetry boundary condition

Symmetry boundary conditions can be applied as lines or planes in both 2D and 3D. This boundary condition contributes to reducing the computational time, by about 50%. Two symmetry boundary conditions have been applied in this work, the first one is similar to thermal insulation that there is no heat flux across the boundary as in Eq. 4.32. The second boundary condition is ‘symmetry for surface-to-surface radiation subnode’.

$$-n \cdot q = 0 \quad \text{Eq. 4.32}$$

where n is the normal direction and q is the flux (W m^{-2}).

Basically, the following constraints are considered when applying the symmetry boundary condition [279]:

- Normal gradients to the symmetry plane for the scalar quantities such as temperature are zero.
- There is no need to define the boundary conditions at symmetry boundaries.

To apply the symmetrical boundary condition, the following steps are considered:

1. Carefully selected the symmetrical plane or line (see Fig. 4.15).
2. For symmetrical model, the same air velocity and hydraulic diameter (D_h) magnitudes should be used at the inlet since the hydraulic diameter is the same for the original model (full size) and symmetrical sizes. However, the value of the mass rate is divided by two.

$$D_h = \frac{4 \left(\frac{A_c}{2} \right)}{\frac{P_{er}}{2}} = \frac{4A_c}{P_{er}} \quad \text{Eq. 4.33}$$

3. The symmetrical perimeter, cross-sectional area and mass flow rate are equal to half the magnitude of the respective parameters within the original model as shown in the symmetrical plane (see Fig. 4.15) since the symmetrical plane is zero flux and shear stress.

Table 4.6 presents the results for two selected cases of one pass PV/T air collector with upper glass, model 3. The first case is the original model without applying the symmetrical boundary condition while the second model contains the symmetrical boundary condition. It can be seen that the RAM decreased from 34.62 to 13.19 GB and the time from 194.14 to 47.49 min. The structured mesh technique type is used and the boundary conditions are presented in Fig. 4.15.

Table 4.6. Single duct, single pass PV/T air collector within off-set fins staggered arrangement for symmetrical and original models

Case type	DOF	RAM (GB)	t (min)	NOE	RT	MEQ	type of mesh
Ori	390616	34.62	194.14	102784	0.1	1	St
Sy	216056	13.19	47.49	56064	0.1	1	St
\bar{V}	\dot{M}_{ori}	\dot{M}_{sy}	Re	$T_{mpv-ori}$	T_{mpv-sy}	η_{th-ori}	η_{th-sy}
0.14227	0.00124	0.00062	400	55.52	55.14	16.71	16.13
0.28454	0.00248	0.00124	800	51.20	51.22	26.36	25.80
0.42681	0.00371	0.00186	1200	48.35	48.59	32.36	32.11
0.56908	0.00495	0.00248	1600	46.36	46.72	36.35	36.57
0.71135	0.00619	0.00309	2000	44.91	45.31	39.15	39.79

In Table 4.6, t is the solution time (min), NOE is the number of elements, RT is the relative tolerance, MEQ is the minimum element quality, Ori is the original PV/T air system (non-symmetrical), and Sy is the symmetrical PV/T air system (symmetrical).

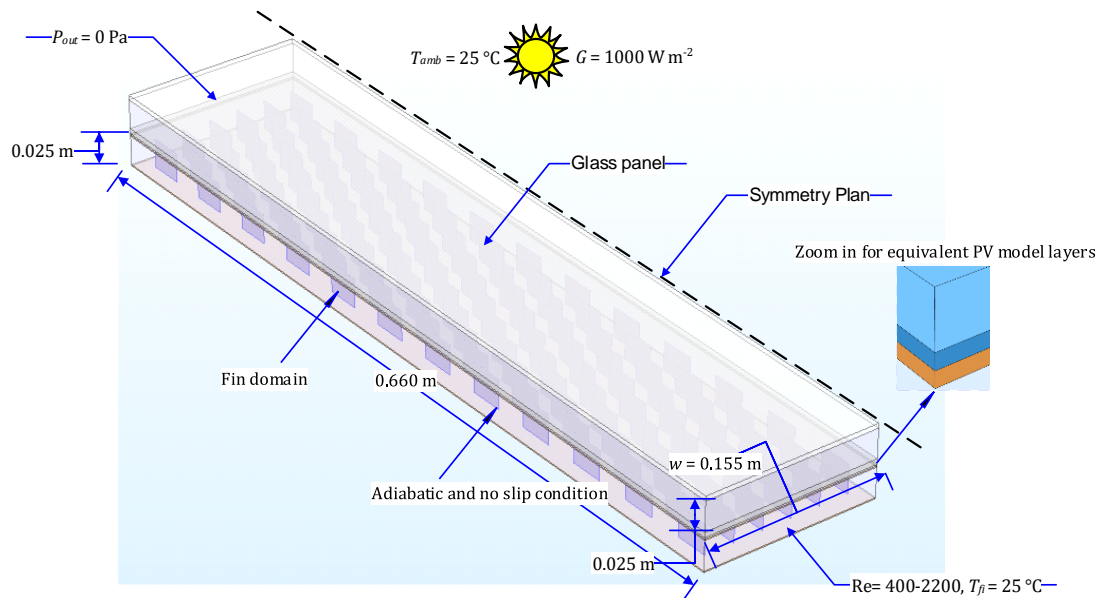


Fig. 4.15. Schematic of model 3 with offset strip fins showing the symmetrical boundary.

4.5.4 Thin layer assumption

One of the challenges in CFD modelling is a meshing of high aspect ratio components, for example, the high aspect ratio between the fin domains and fluid flow. Tackling this issue requires avoiding meshing thin layer domains which can lead to increasing the running time, potentially crashing the model and increase the number of elements.

In COMSOL Multiphysics®, 3D structure domains can be simplified as surfaces or boundaries with a high level of accurate results which depend on the thermal conductivity and thickness of materials. In order to represent realistic conditions ‘Thin Layer’ feature for heat transfer and the ‘Interior Wall’ feature for fluid flow is applied (see Fig. 4.16). This is built-in function in Comsol software.

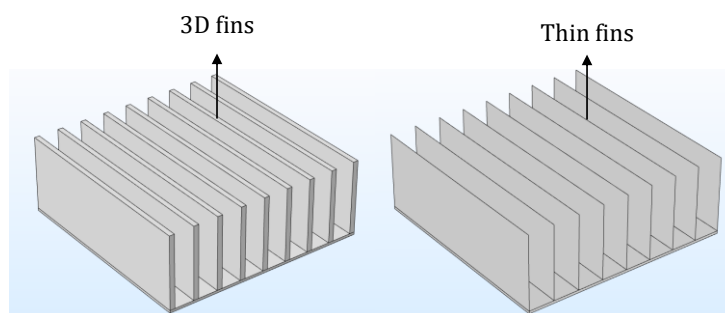


Fig. 4.16. Strip fins with 3D fins (left) or thin fins (right).

Two case studies of model 3 are considered to ensure the validity of this assumption (see Fig. 4.17). The boundary conditions, geometric and operational parameters for the selected system are shown in Fig. 4.9b and Fig. 4.15. Fin dimensions are set to 20mm in length and 3mm thickness.

Table 4.7 presents a comparison of two cases of thick and thin fins of model 3. The difference was insignificant between the two results can be attributed to:

1. The boundary layer for each fin walls for the thicker fin model shows a much faster development and thickness compared to the thin fin model (Fig. 4.19).
2. The pressure drop through the thick fin case is found greater than that of the thin fin owing to the cross-sectional surface area of resistance created by the leading edge of the fins (Fig. 4.19). Despite this difference, the thin layer assumption is still used in this work because the pressure drop in solar air thermal collector is considered a second order influence [180, 354, 355].
3. Moreover, thicker fins have larger form drag from blunt fin edges, whereas with slender fins [223].

Table 4.7. Single duct single pass PV/T air collector within off-set fins staggered arrangement for the thin and thick fins.

\bar{V}	\dot{M}	Re_{D_h}	$T_{mpv-thick}$	$T_{mpv-thin}$	η_{thick}	η_{thin}	Δp_{thick}	Δp_{thin}
0.14227	0.00062	400	55.44	55.58	16.88	16.51	0.81	0.27
0.28454	0.00124	800	51.41	51.72	27.82	26.76	2.93	0.92
0.42681	0.00186	1200	48.54	49.07	34.91	33.66	6.21	2.01
0.56908	0.00248	1600	46.47	47.14	39.65	38.58	10.56	3.59
0.71135	0.00309	2000	44.96	45.69	42.94	42.20	15.91	5.69

Owing to computational limitations, a combination of two mesh techniques (structured and unstructured) was used to mesh the thick fin system, whereas a structured mesh technique was used to mesh the thin fin as displayed in Fig. 4.18 and Table 4.8.

Table 4.8. Mesh parameters for thin and thick off-set fins staggered arrangement.

Case type	DOF	RAM (GB)	t (min)	NOE	RT	AEQ	TOM
Thick	444789	114.36	886	340901	0.1	0.7	TSt
Thin	238390	20.92	128	49368	0.1	1	St

In Table 4.8, TSt is the mesh technique that used structured and unstructured element types (hybrid mesh).

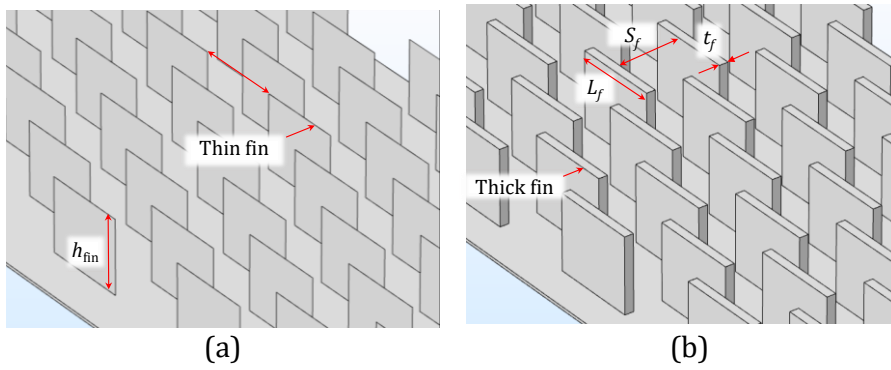


Fig. 4.17. Two case studies of model 3 including offset strip fin: In (a) Thin fin model and (b) Thick fin model.

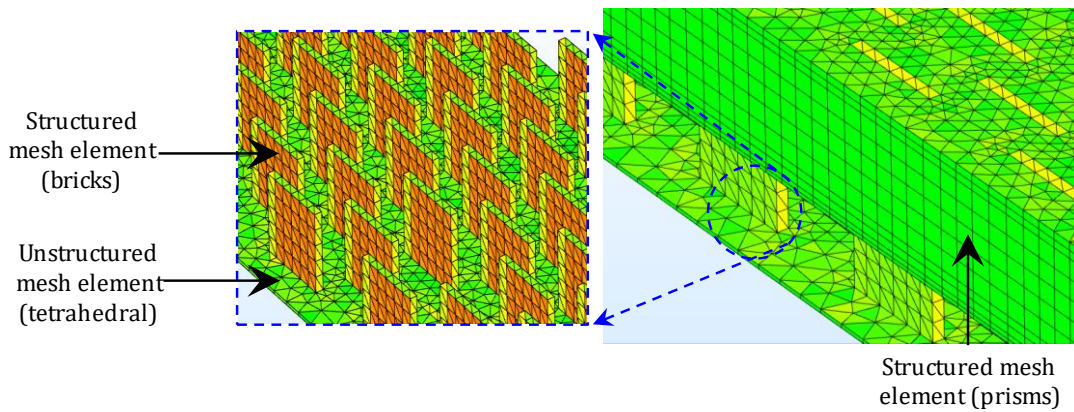


Fig. 4.18. Mesh used for model 3 including offset strip fin, showing the thick fin model.

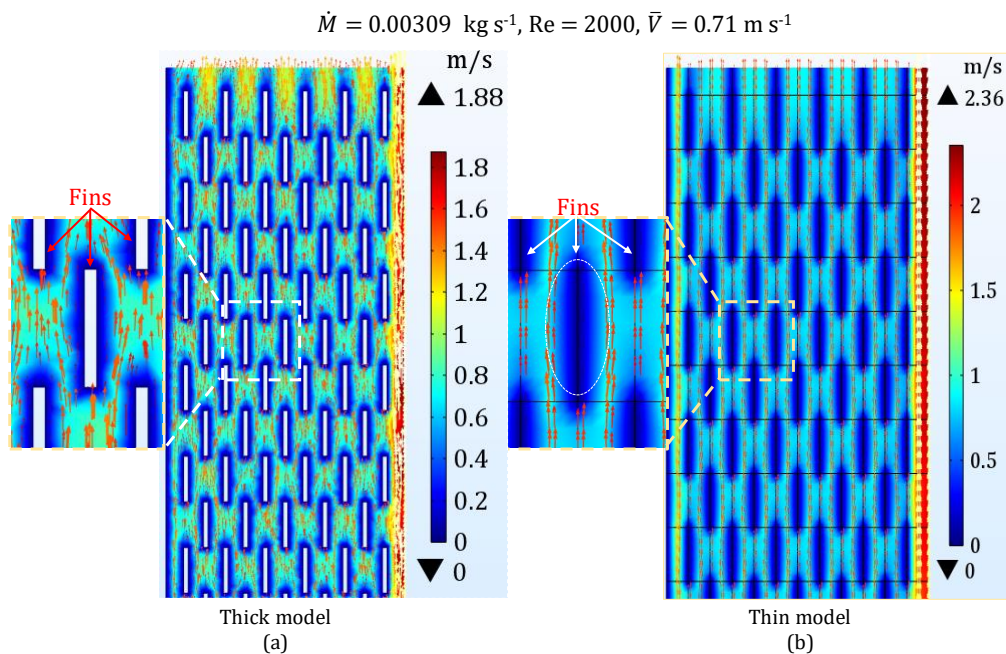


Fig. 4.19. Velocity counter of the cross-section top view of the thin and thick models presenting in (a) Thick model, surface: velocity magnitude (m s^{-1}), arrow surface: velocity field, in (b) Thin model, surface: velocity magnitude (m s^{-1}), arrow surface: velocity field.

4.5.5 Representative material properties

As mentioned in Section 4.5.4, one of the challenges in CFD modelling is meshing steep gradient regions as a result of a high aspect ratio between body components. This may lead to poor mesh quality, increasing computational time, and also lead to divergence crash the model. To reduce the impact of this effect, it is proposed in this work to combine all layers into just two. This combines the upper EVA with glass cover from the side and PV cell, lower EVA and Tedlar from the other side as shown in Fig. 4.20 and Table 4.9. The set of linear equations from Eq. 4.34 to Eq. 4.39 present the equivalent thermo-physical properties of the CFD domains.

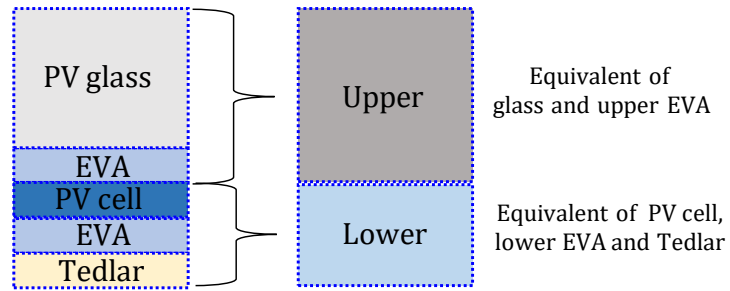


Fig. 4.20. Schematic of individual and equivalent PV module layers.

Table 4.9. Equivalent thermophysical properties of the CFD domains.

Material	Name of equivalent layers	ρ (kg m ⁻³)	k (W m ⁻¹ K ⁻¹)	c (J kg ⁻¹ K ⁻¹)	t (mm)
Glass EVA	Upper	1930.677	1.05	786.894	4.5
Silicon EVA Tedlar	Centre	1218.586	0.331	1201.798	1.3
Copper		8960	400	385	1

$$K_{g+EVA} = \frac{\delta_{glass} + \delta_{EVA}}{\frac{\delta_{EVA}}{K_{EVA}} + \frac{\delta_g}{K_g}} \quad \text{Eq. 4.34}$$

$$K_{ted+EVA+PV} = \frac{\delta_{ted} + \delta_{EVA} + \delta_{PV}}{\frac{\delta_{EVA}}{K_{EVA}} + \frac{\delta_{ted}}{K_{ted}} + \frac{\delta_{PV}}{K_{PV}}} \quad \text{Eq. 4.35}$$

$$\rho_{ted+EVA+PV} = \frac{\delta_{ted} + \delta_{EVA} + \delta_{PV}}{\frac{\delta_{EVA}}{\rho_{EVA}} + \frac{\delta_{ted}}{\rho_{ted}} + \frac{\delta_{PV}}{\rho_{PV}}} \quad \text{Eq. 4.36}$$

$$\rho_{g+EVA} = \frac{\delta_{glass} + \delta_{EVA}}{\frac{\delta_{EVA}}{\rho_{EVA}} + \frac{\delta_g}{\rho_g}} \quad \text{Eq. 4.37}$$

$$c_{ted+EVA+PV} = \frac{\delta_{ted} + \delta_{EVA} + \delta_{PV}}{\frac{\delta_{EVA}}{c_{EVA}} + \frac{\delta_{ted}}{c_{ted}} + \frac{\delta_{PV}}{c_{PV}}} \quad \text{Eq. 4.38}$$

$$c_{g+EVA} = \frac{\delta_{glass} + \delta_{EVA}}{\frac{\delta_{EVA}}{c_{EVA}} + \frac{\delta_g}{c_g}} \quad \text{Eq. 4.39}$$

where the subscripts *ted* and *g* refer to the Tedlar and glass layers respectively.

To test the validity of this assumption, an examination was carried out for the standard PV module without active cooling, model 1 under the free convection condition, $G = 1000 \text{ W m}^{-2}$ and $T_{amb} = 25$ and $50 \text{ }^\circ\text{C}$. The results revealed that the maximum percentage error is around 0.81%, as can be seen in Table 4.10 and Fig. 4.21.

Table 4.10. Equivalent and original results for model 1 under free convection mode, $G = 1000 \text{ W m}^{-2}$ and $T_{amb} = 25$ and $50 \text{ }^\circ\text{C}$

Variable	$T_{amb}, 25 \text{ }^\circ\text{C}$ (Equivalent)	$T_{amb}, 25 \text{ }^\circ\text{C}$ (Original)	Error (%)	$T_{amb}, 50 \text{ }^\circ\text{C}$ (Equivalent)	$T_{amb}, 50 \text{ }^\circ\text{C}$ (Original)	Error (%)
η_{PV}	10.96	10.94	0.18	9.71	9.69	0.21
T_{mpv}	52.32	52.75	0.81	76.95	77.43	0.61
P_{PV}	10.25	10.23	0.19	9.09	9.07	0.22

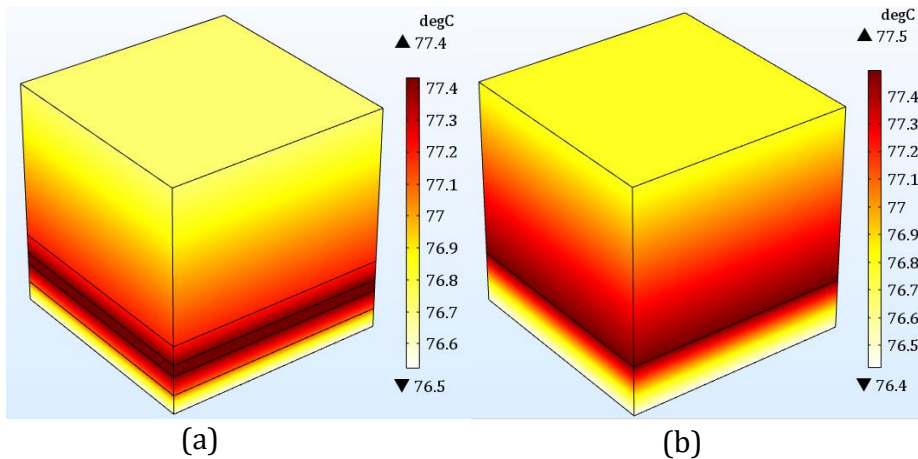


Fig. 4.21. Surface temperature contour of model 1 under free convection condition, $G = 1000 \text{ W m}^{-2}$, $T_{amb} = 25 \text{ }^\circ\text{C}$, in (a) Original model, (b) Equivalent model.

4.5.6 Tolerance

The default setting in Comsol of estimated error (i.e. relative tolerance) is 10^{-3} . A smaller value of this factor may lead to more precise results and *vice versa*. However, as the inputs to a model (for example, material properties) are typically not accurate to more than a couple of digits, tolerance independent tests should be made to ensure the accuracy of the solution. This is carried out by changing the tolerance increments of one order of magnitude

and comparing the solutions [356]. A representative case, as presented in Table 4.11, showed that the running time reduced from 39 min to 32 min when the tolerance increased from 0.001 to 0.1 with fairly consistent results.

Table 4.11. Tolerance independent tests.

Variable	Tolerance, 10^{-3}	Tolerance, 10^{-1}	Percentage error (%)
R_{th}	1.287	1.281	0.46
Δp	12.818	12.818	0
η_{th}	46.904	46.734	0.36
η_{pv}	11.130	11.135	0.04

4.6 Validation

Different approaches are adopted to validate the PV/T air models. Firstly, grid independence test using different mesh element type. Secondly, validation and verification between current mathematical models and available results in the literature.

4.6.1 Mesh independence test

In this subsection, the examination of different mesh element types is performed to evaluate the convergence speed, accuracy, computation time and mesh quality. The study is performed on a PV/T air system with longitudinal strip fins using structured and unstructured mesh element types, see Fig. 4.22.

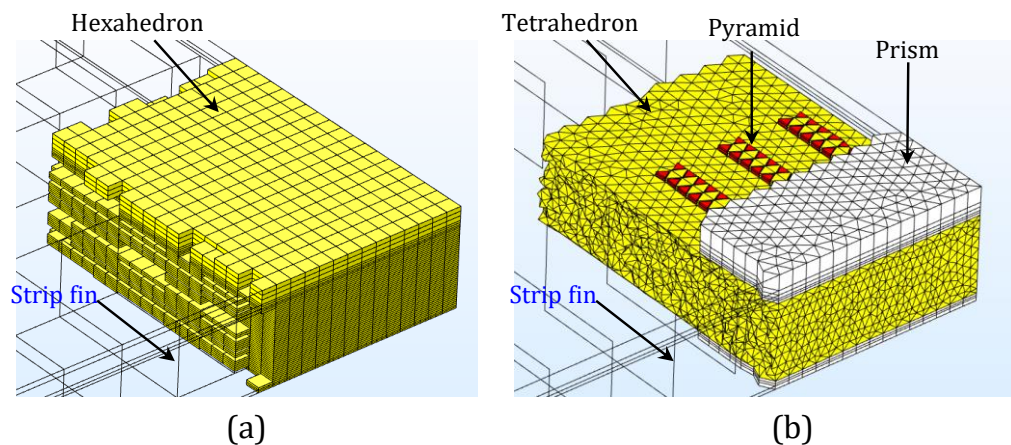


Fig. 4.22. Mesh of the PV/T air system with fins: in (a) structured mesh and in (b) unstructured mesh.

The system description and boundary conditions employed are shown in Fig. 4.23. In order to reduce computation time, the symmetry boundary condition is applied along the centre

line in the y-z plane. No-slip boundary conditions are applied on solid-fluid interface walls. In terms of weather conditions, the incident solar radiation is 1000 W m^{-2} and ambient air temperature is $50 \text{ }^\circ\text{C}$. The flow is considered to be laminar, where $Re = 2200$. Free convection conditions on the upper and lower surface of the collector are assumed.

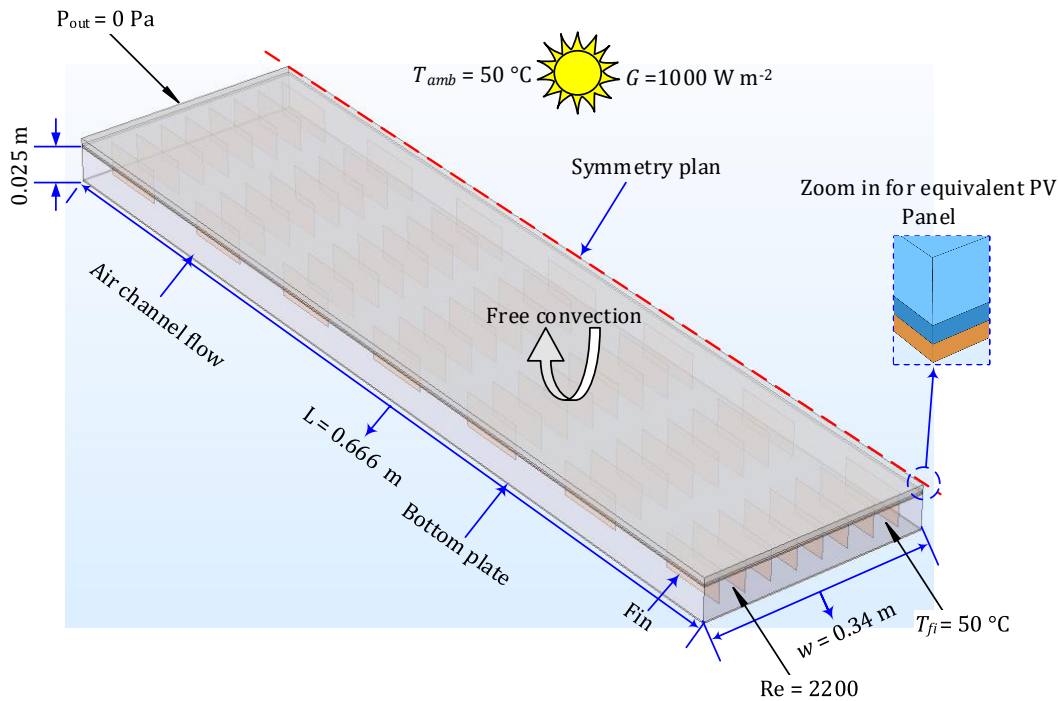


Fig. 4.23. Schematic of the single duct single pass PV/T air collector including longitudinal strip fins showing the symmetry plane and boundary conditions.

The simulated model consists of different units as listed below:

1. The PV module layers with the upper copper absorber plate.
2. The air channel duct.
3. The bottom absorber plate.
4. The lower copper absorber plate.
5. Longitudinal strip fins.

A mesh is considered to be successful or valid if any further refinement done on it does not result in a significant change to previous results. Different criteria are considered in this evaluation. Firstly, an independent mesh study is performed using structured and unstructured element types. Each surface or domain is inspected individually to evaluate the impact of this part on the rest of the system. After that, the inspection of all parts within the model has performed altogether. For example, the effect of the depth of flow is studied

with element size ranging from 1 mm to of 3 mm until convergence. The same procedure is adopted for other parts of the PV/T air system. The details of this test can be seen in [Fig. 4.24](#) and [Table 4.12](#).

Secondly, in order to inspect the quality of the mesh, two criteria are utilised which are skewness and minimum element quality (MEQ). The skewness is a criterion used to evaluate the quality of a mesh [\[357\]](#), based on equiangular skew. Elements with obtuse and acute angles are penalized when compared to ideal element angles. This criterion is used to report poor element quality within mesh generation [\[357\]](#). The skewness range is between 0 and 1 in which 1 indicates the optimal element quality while 0 represents a degenerated element.

The second criterion is the minimum element quality. The quality varies depends on the geometry and size of the physical problem. The quality is considered to be poor for most applications with a value below 0.1 [\[357\]](#).

The comparison between two mesh types revealed that the MEQ of the structured mesh is considerably higher than the unstructured mesh (see [Table 4.12](#) and [Fig. 4.25](#)). The computational time reduced from 823 minutes to 540 minutes and number of elements were significantly reduced in the structured mesh type (see [Table 4.12](#))

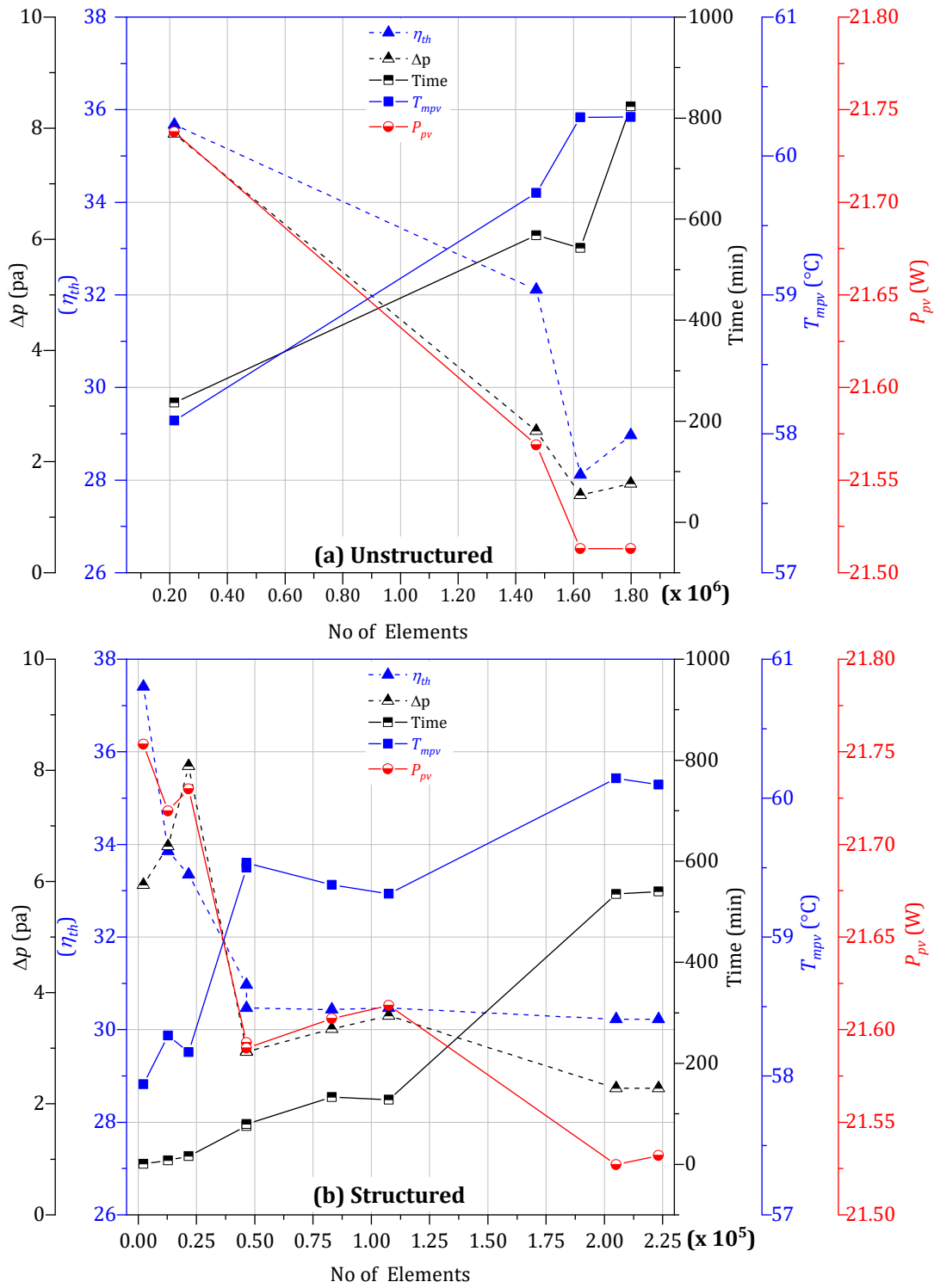


Fig. 4.24. Mesh element type examinations: in (a) Unstructured mesh models, (b) Structured mesh models.

Table 4.12. Key features of the structured and unstructured mesh models.

Structured mesh cases							
Case No	NOE	η_{th}	Δp (Pa)	P_{PV} (W)	T_{mpv}	t (min)	MEQ
1	2268	37.4	5.9	21.7	57.9	1	0.378
2	12852	33.8	6.6	21.7	58.2	8	1
3	21641	33.3	8.0	21.7	58.1	16	1
4	46436	30.9	2.9	21.5	59.4	76	1
5	46436	30.4	2.9	21.5	59.5	80	0.698
6	83096	30.4	3.3	21.6	59.3	133	0.698
7	107536	30.4	3.5	21.6	59.3	128	0.698
8	205020	30.2	2.2	21.5	60.1	535	1
9	223224	30.2	2.2	21.5	60.0	540	1
Hybrid mesh cases							
Case No	NOE	η_{th}	Δp (Pa)	P_{PV} (W)	T_{mpv}	t (min)	MEQ
1	215732	35.672	7.9	21.7	58.0	237	0.185
2	1471645	32.110	2.5	21.5	59.7	568	0.157
3	1624409	28.117	1.3	21.5	60.2	543	0.171
4	1799426	28.972	1.6	21.5	60.2	823	0.177

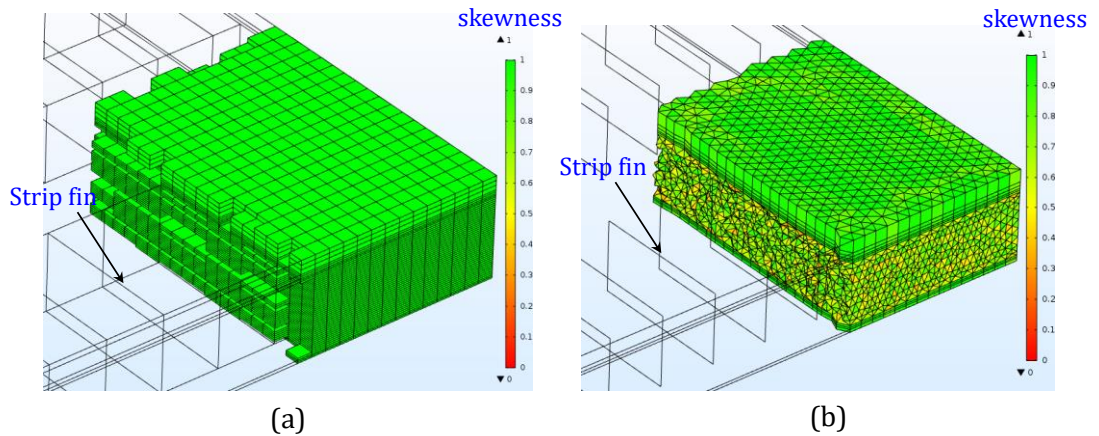


Fig. 4.25. Skewness parameter for two cases in (a) structured mesh case and in (b) unstructured mesh case. Note: one indicates the optimal element quality and zero represents a degenerated element.

4.6.2 Inter-model comparison:-model 2

Three methods are utilised to validate the single duct single pass of model 2, as listed below:

1. Semi-analytical solution (method 1)
2. Numerical model using the predictor-corrector solution (method 2)
3. 3D CFD approach under steady state conditions (method 3)

Three variables are used in this validation: the average PV cell temperature (T_{mpv}), the PV electrical efficiency (η_{pv}) and thermal efficiency (η_{th}). All of the models are modelled at different ambient temperatures (25-50 °C) and insolation (1000 W m⁻²) with a Re number of 2000 under fully developed flow condition. The model assumes a horizontal duct under the free convection condition over the top surface of the PV module and assumed an adiabatic at the bottom surface of the collector, as shown in Fig. 4.26.

The impact of PV cell and ambient temperatures on PV electrical efficiency for these three methods are presented in Fig. 4.27. As expected, Fig. 4.27 reveals a gradual decline in electrical efficiency as the ambient and PV panel temperatures increase. This is because the electrical efficiency is directly proportional to temperature. In addition, the agreement between the CFD and mathematical (semi-analytical and predictor-corrector methods) results is poor. The two mathematical models yield comparable results. The data comparison indicates that the numerical model using the predictor-corrector solution was closer to the CFD model than Semi-analytical solution. This is most likely because of the predictor-Corrector solution being more representative of real-life conditions than the semi-analytical solution. As an example:

1. In the analytical model, the mean fluid temperature of was arithmetic $\bar{T}_f = (T_i + T_o/2)$, which is less accurate compared with the predictor-corrector solution where the mean fluid temperature across the duct was calculated locally.
2. The temperature of absorber plates (i.e. T_{mpv} and T_{bm}) that are used in estimating heat transfer rate (newton law of cooling) on the upper surface of the PV panel, $Q = h (T_{mpv} - T_{amb})$ or inside the duct flow $Q = h (T_{mpv}$ or $T_{bm} - T_f)$ are local values, unlike the semi-analytical solution which takes them as average values.
3. The radiation effect is assumed linear in analytical solution but non-linear in numerical solution.

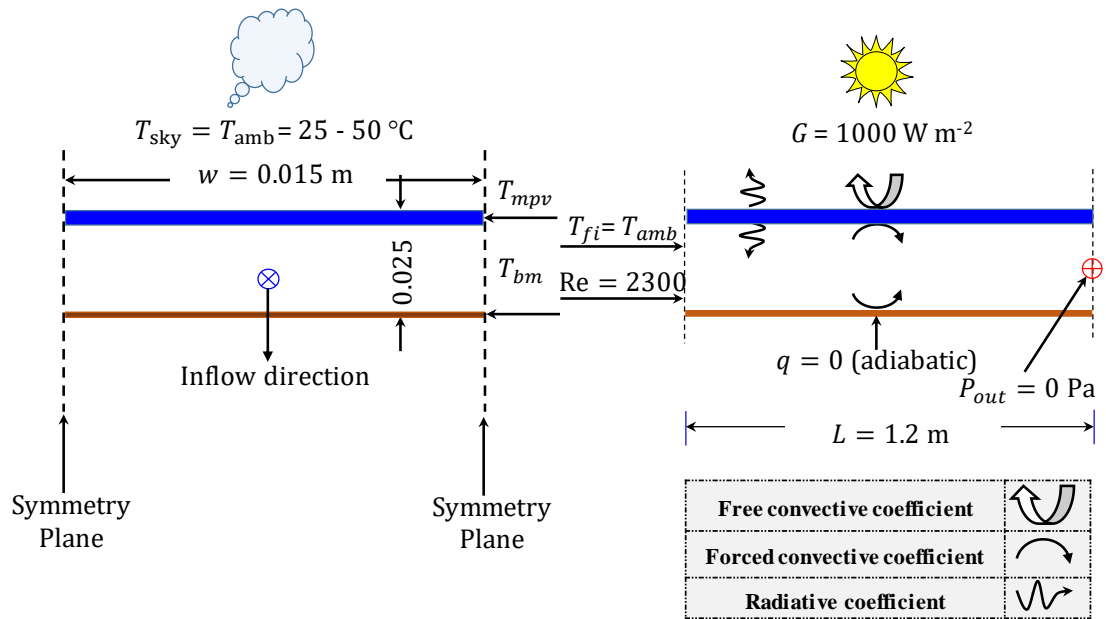


Fig. 4.26. Schematic of model 2 showing the boundary conditions.

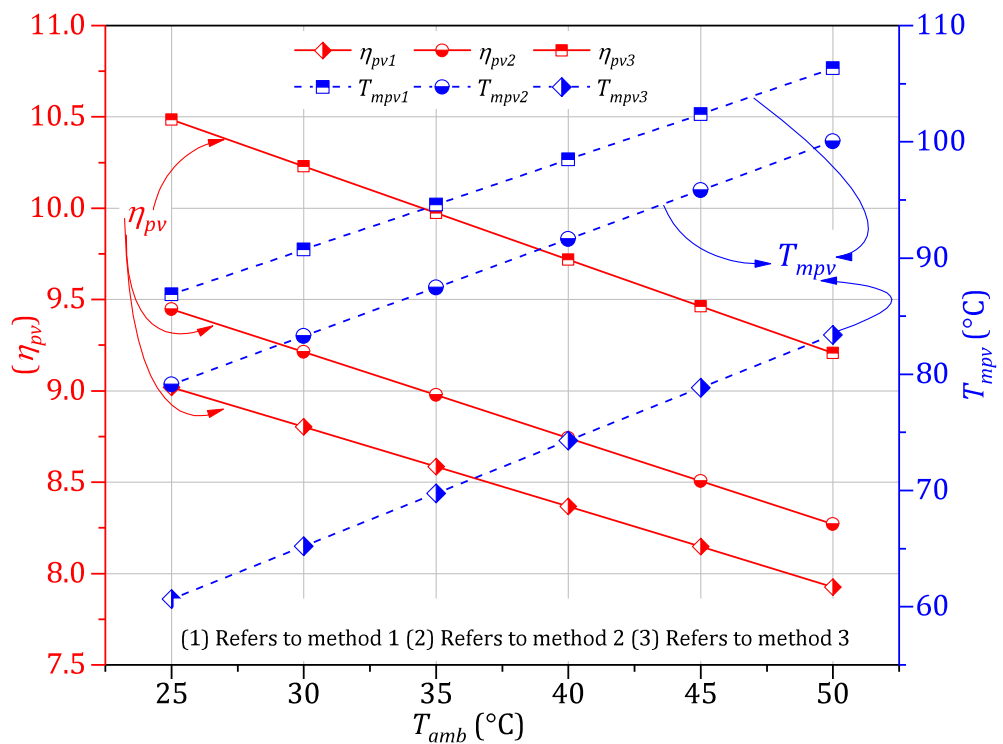


Fig. 4.27. Influence of the ambient and PV cell temperatures on the PV electrical efficiency using three methods for model 2, (1) Semi-analytical, (2) predictor-corrector and (3) 3D CFD.

4.6.3 Inter-model comparison:-model 3

Similar to model 2, various approaches were employed to validate the single duct single pass (glazed) of model 3. These approaches were explained in detail in Section 3.3.2.3, which can be listed as follows:

1. Semi-analytical solution (method 1).
2. Numerical model using the predictor-corrector solution (method 2).
3. 2D CFD approach with a temperature dependent thermal conductivity in the enclosure (effective thermal conductivity) (method 3).
4. 3D CFD approach with a temperature dependent thermal conductivity in the enclosure (effective thermal conductivity) (method 4).
5. 3D CFD approach with a temperature dependent thermal conductivity in the enclosure (effective thermal conductivity) assume that the regime is purely conductive ($Nu = 1$) (method 5).
6. CFD transient model (method 6).

The parameters are used in this validation as follows, the average PV cell temperature (T_{mpv}), the PV electrical efficiency (η_{pv}), the thermal efficiency (η_{th}) and the mean fluid temperature through the duct flow (T_{fm}). In this study, the models were examined at different metrological conditions, ambient temperatures (25-50 °C) with incident solar radiation of 1000 W m^{-2} and a Re number of 2000 under fully developed flow conditions. The model assumes a horizontal under wind effect over the top surface of the glass and assumed an adiabatic at the bottom surface of the collector as shown in Fig. 4.28.

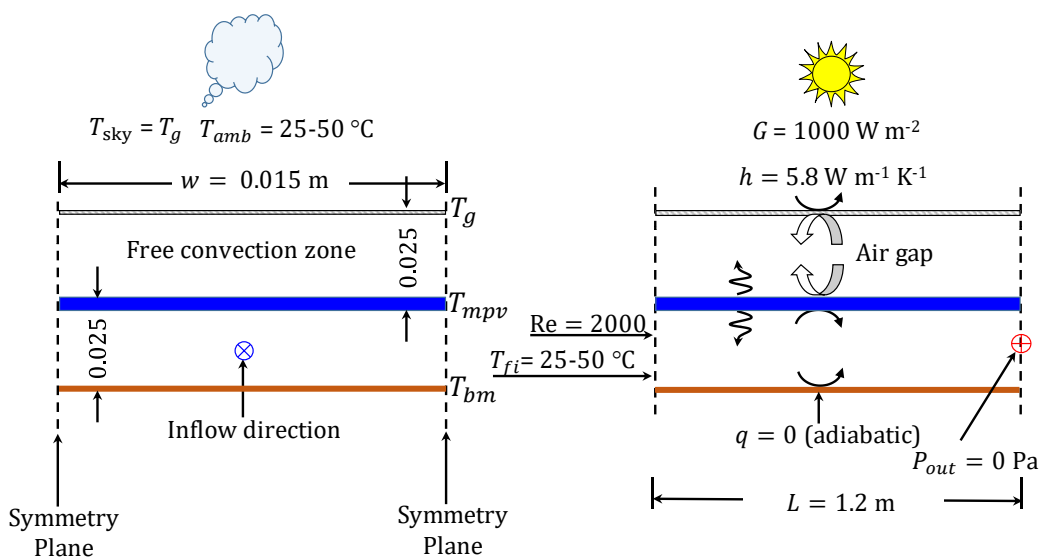


Fig. 4.28. Schematic of model 3 showing the boundary conditions.

[Fig. 4.29](#) presents the effect of PV cell temperatures on the electrical efficiency for the methods as mentioned earlier (1 to 6). As predicted, it is observed that the results of different CFD methods (method 3 to 6) are in good agreement ([Fig. 4.29 \(3 to 6\)](#)) owing to the same reasons highlighted in the validation of model 2. It can be seen from [Fig. 4.29](#) (method 6), a slight difference is found in the comparison between the transient results and the other CFD models (method 3 to 5). This can be attributed to the fact that the free convection mode is more realistic and inherently behaves transiently. The circulation of air contributes to the enhancement of the heat transfer rate (see [Fig. 4.30](#)) and consequently reduces the temperature of the upper glass. This can be clearly seen in the temperature range between 40 and 50 °C in the dashed region shown in [Fig. 4.31](#).

In conclusion, this comparison suggests that the use of method 5 ($Nu = 1$) is more applicable in terms of accuracy and running time. This comes in agreement with previous findings presented in [\[252, 271\]](#).

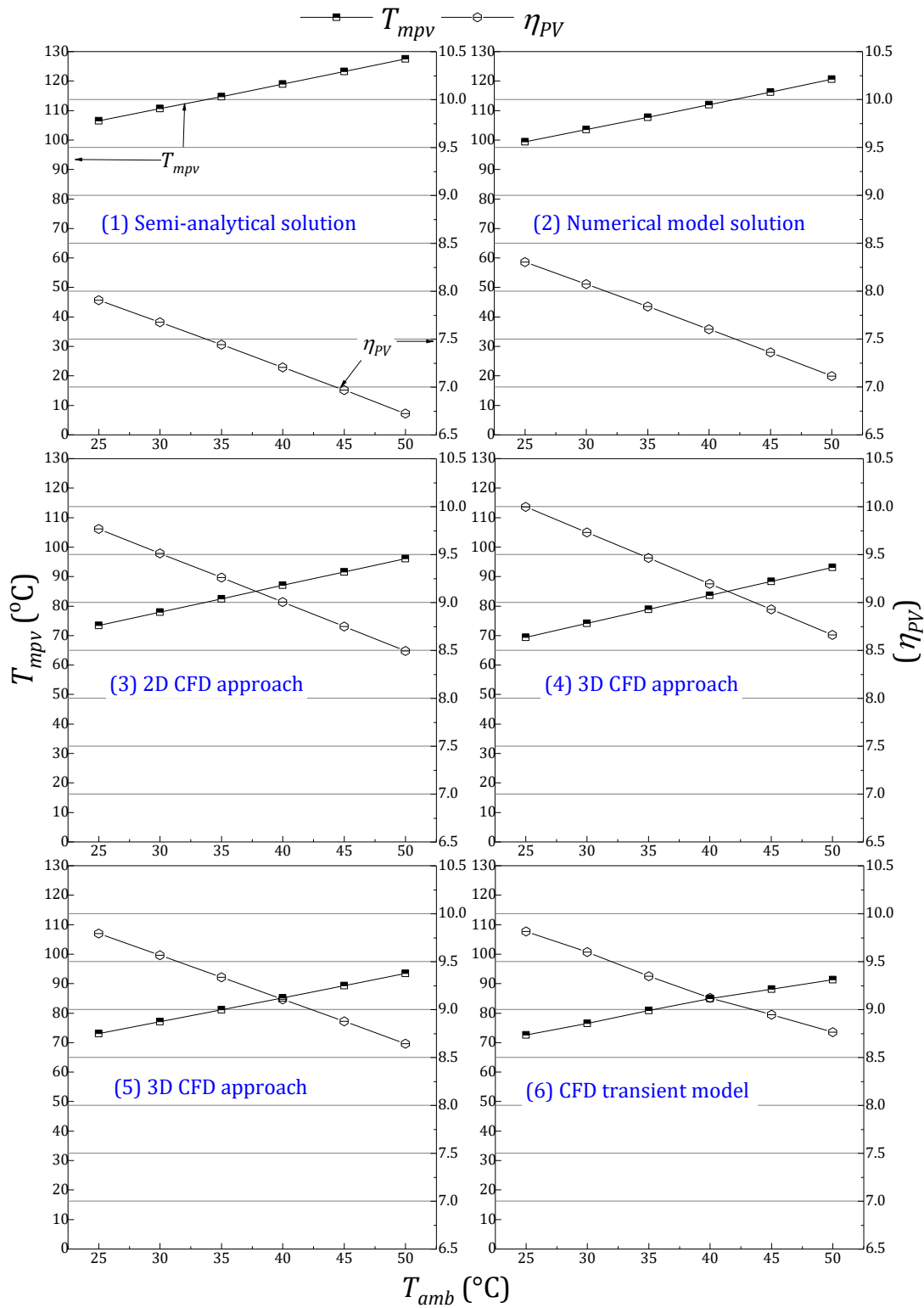


Fig. 4.29. Influence of the ambient and PV cell temperatures on the PV electrical efficiency using six methods of model 3.

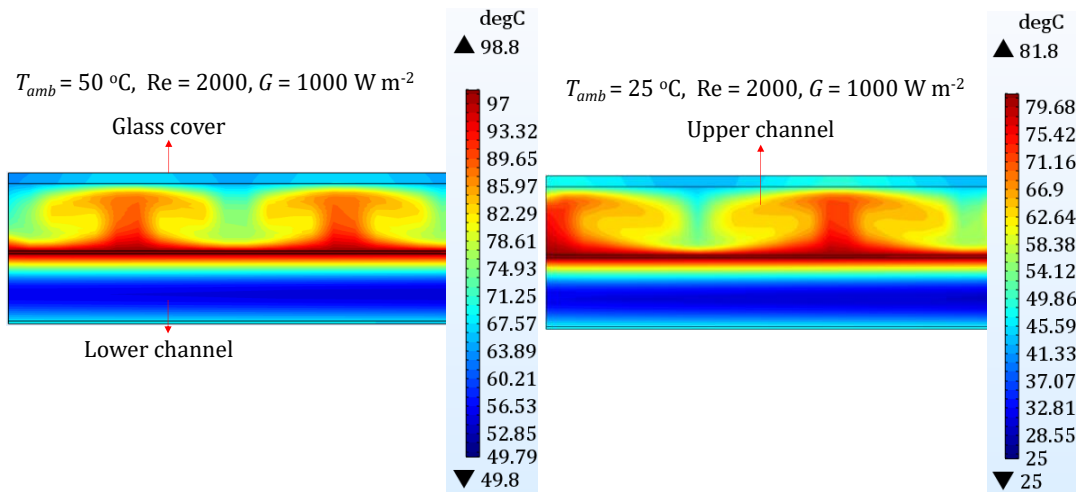


Fig. 4.30. Temperature contours (°C) of model 3 using CFD transient method (method 6).

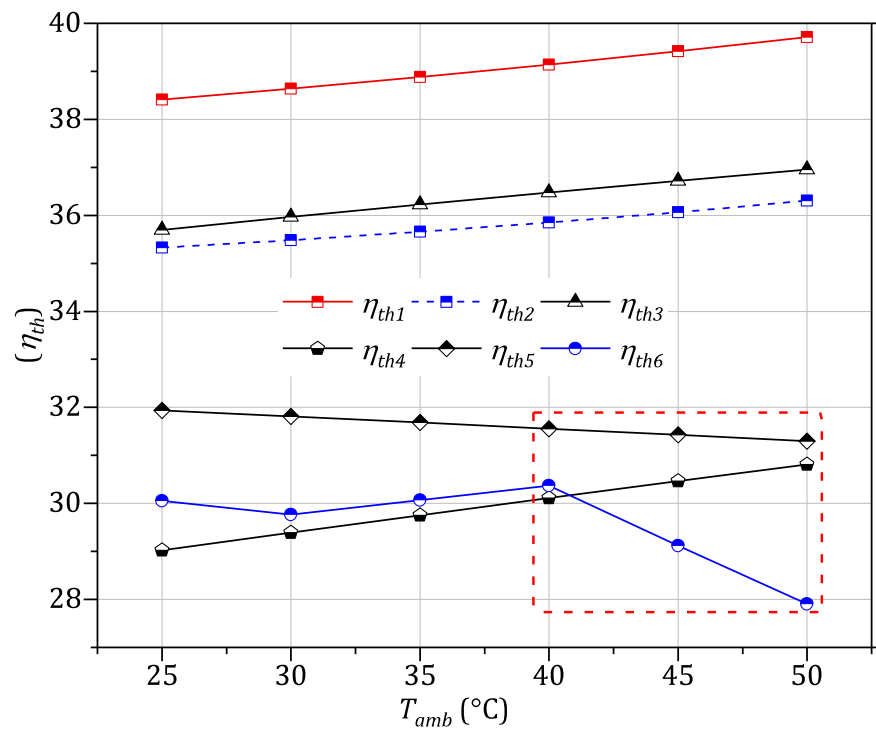


Fig. 4.31. Influence of the ambient and PV cell temperatures on the thermal efficiency of model 2 using six methods (method 1 to method 6).

4.6.4 System validation

The CFD models (models 2 and 3) were also validated against two previous studies [24, 130]. The first validation was between the CFD results of model 2 and the mathematical results of Amori and Al-Najjar [24]. The geometry of model 2 is defined as a rectangular duct

on the x-y plane, bounded by the inlet, outlet and wall boundaries as illustrated in Fig. 4.32. The flow is turbulent with $Re = 5727$. The boundary conditions and system descriptions of this validation can be seen in Fig. 4.32 and Table 4.13. The size of the structured mesh was 7050 elements with MEQ of 1.

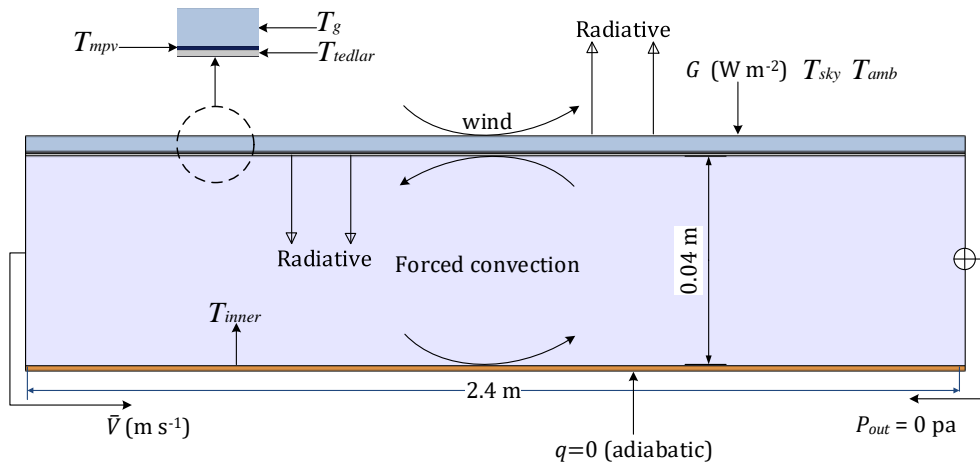


Fig. 4.32. Schematic of the cross-sectional view of the PV/T air collector of Hegazy [122].

Table 4.13. Boundary conditions of [24].

Time (h)	G ($W m^{-2}$)	T_{fi} ($^{\circ}C$)	V_w ($m s^{-1}$)	\bar{V} ($m s^{-1}$)
8:30	180.4	7.6	0.005	1.00
9:30	324.4	10.8	0.3	1.10
10:30	441.6	13.2	0.5	1.00
11:30	510.2	14.9	1.1	1.15
12:30	530.0	16.1	1.0	1.15
13:30	473.4	17.2	1.1	1.10
14:30	378.8	17.6	1.3	1.20
15:30	241.2	17.5	1.1	1.10
16:30	100.4	16.6	0.7	1.05

Fig. 4.33 compares the estimated collector body and fluid temperatures of model 2 with Amori and Al-Najjar [24]. The computed results agree well with the remarks of Amori and Al-Najjar [24] with a maximum temperature difference of 5 °C. The evaluation of the outlet fluid temperature ($T_{f,out}$) for two models is presented Fig. 4.34. The results from this figure revealed that the maximum temperature difference is about 4.5 °C between the present study and Amori and Al-Najjar [24]. The difference between the two outcomes is attributed to several reasons such as, the developed CFD model uses the conjugate heat transfer model while the mathematical model of Amori and Al-Najjar [24] used an empirical equation

(Newton's law of cooling) which is less accurate compared than the conjugate model used here. In the CFD model, the radiative heat transfer coefficients are assumed non-linear in contrast to the model developed by Amori and Al-Najjar [24].

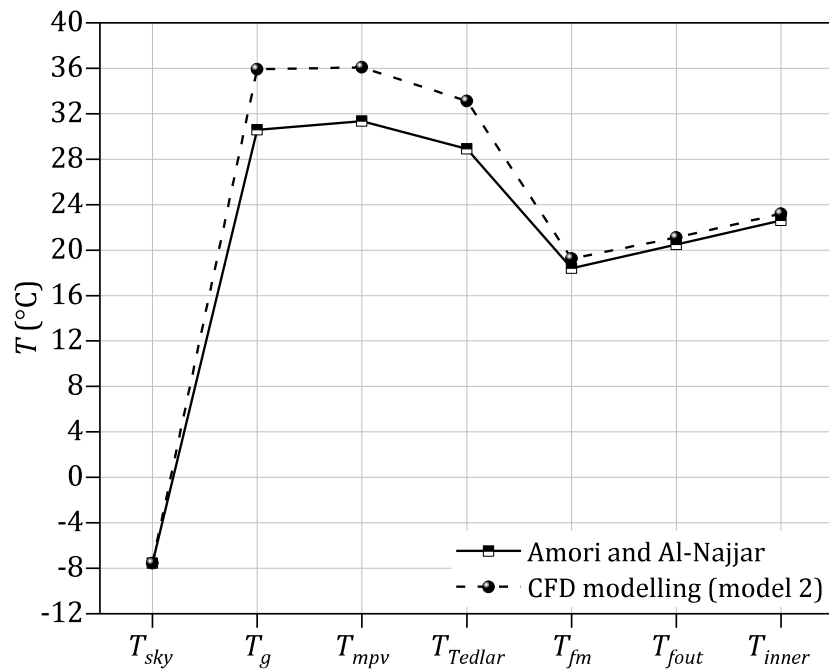


Fig. 4.33. CFD results of present work (model 2) and simulated results Amori and Al-Najjar [24] for Baghdad on 22/1/2011 for clear sky day at 12:30 PM.

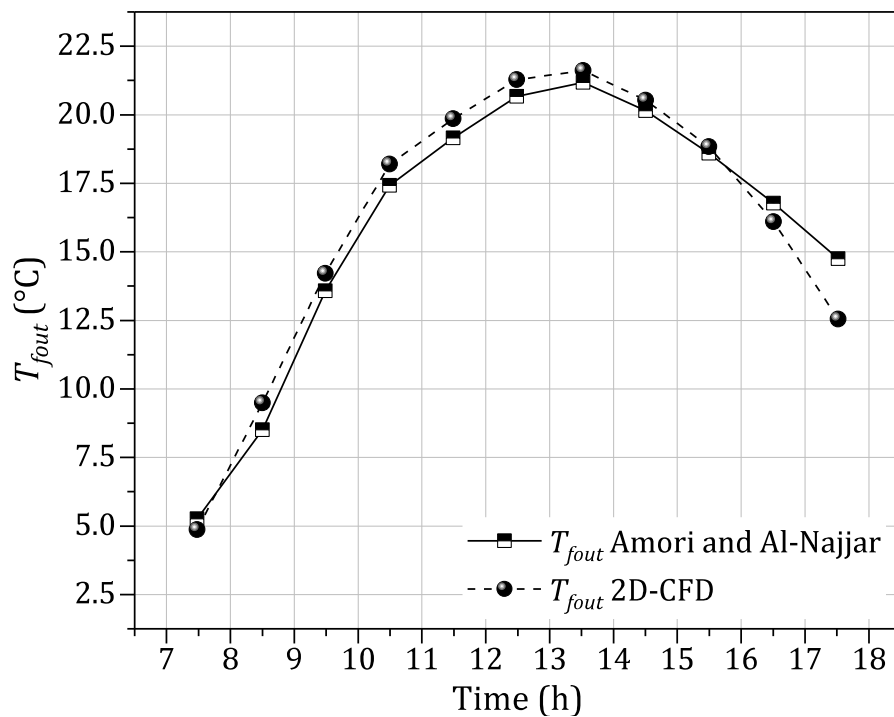


Fig. 4.34. CFD results of present work (model 2) and simulated results of Amori and Al-Najjar [24] for the outlet fluid temperature (T_{fout}).

The second validation was between the current linear solution of model 3 and the linear solution of Hegazy of model II [122]. Fig. 4.35 presents the boundary conditions and system description of this validation. The hourly weather data of the ambient temperature and insolation are displayed in Fig. 4.36. The weather data was recorded in Egypt, Minia University on 24th of June 1998, during which the wind velocity (V_w) ranged between 0.5 and 1.5 m s⁻¹.

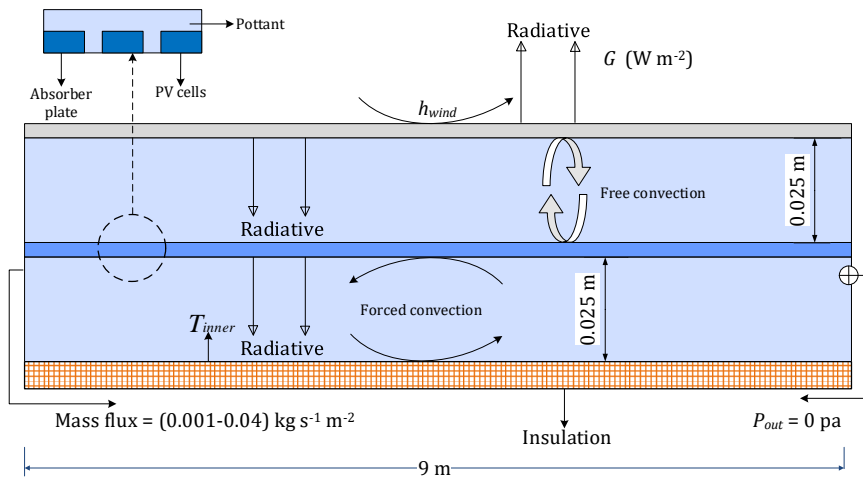


Fig. 4.35. Schematics of the PV/T air system of Hegazy [122] (namely model II).

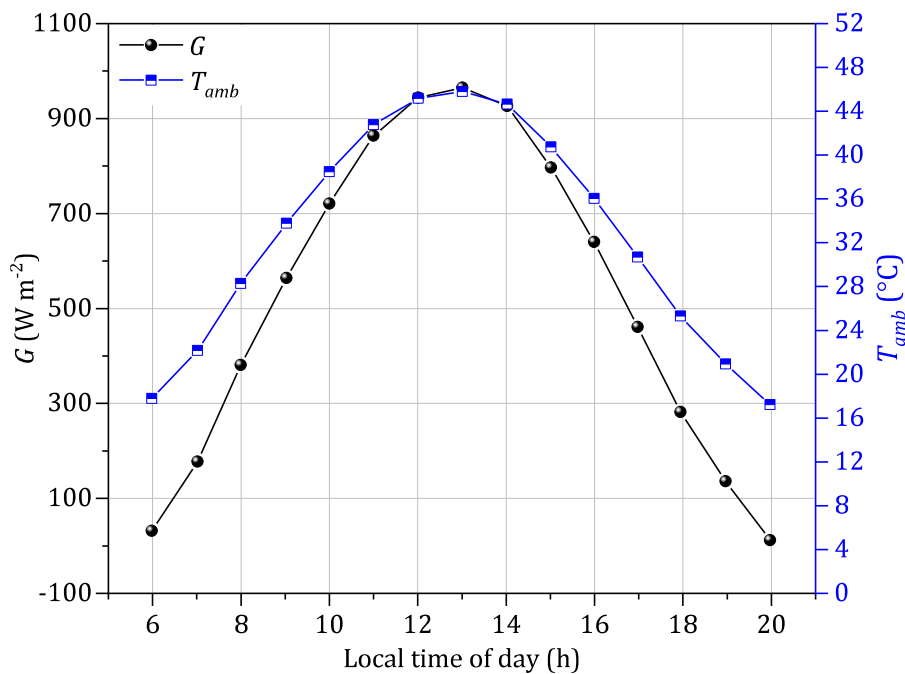


Fig. 4.36. Intensity of solar radiation versus time recorded at Egypt, Minia University on 24 June 1998.

The reliability and accuracy of the PV/T air collector are evaluated by studying the daily thermal efficiency and power fan parameters for the two models. Fig. 4.37 and Fig. 4.38 show a good agreement between the results of the models mentioned above. The slight variation between the two models is owing to a number of facts:

1. In the current study, it is assumed that the PV module is a single layer to simplify the solution. In contrast, the PV module of Hegazy [122] consists of three layers, as shown in Fig. 4.35.
2. In the present study, it is assumed that the packing factor (density of cells) is equal to 1 while Hegazy [122] used a value of 0.64 as a packing factor.

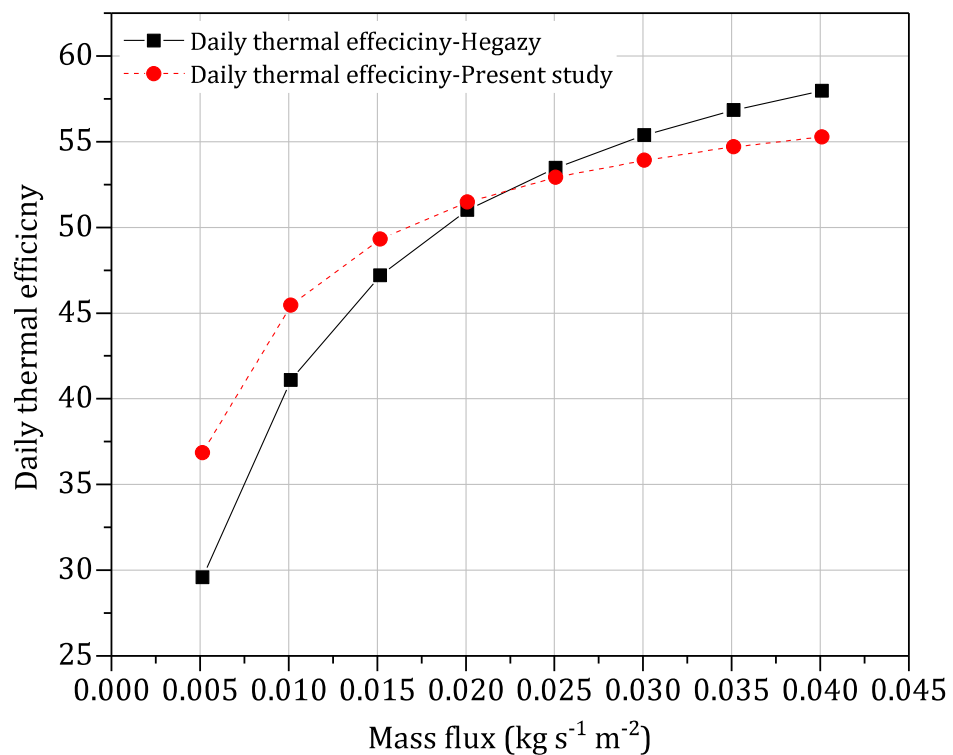


Fig. 4.37. Linear solution of present work (model 3) and linear of Hegazy [122] (model II) for estimated daily thermal efficiency.

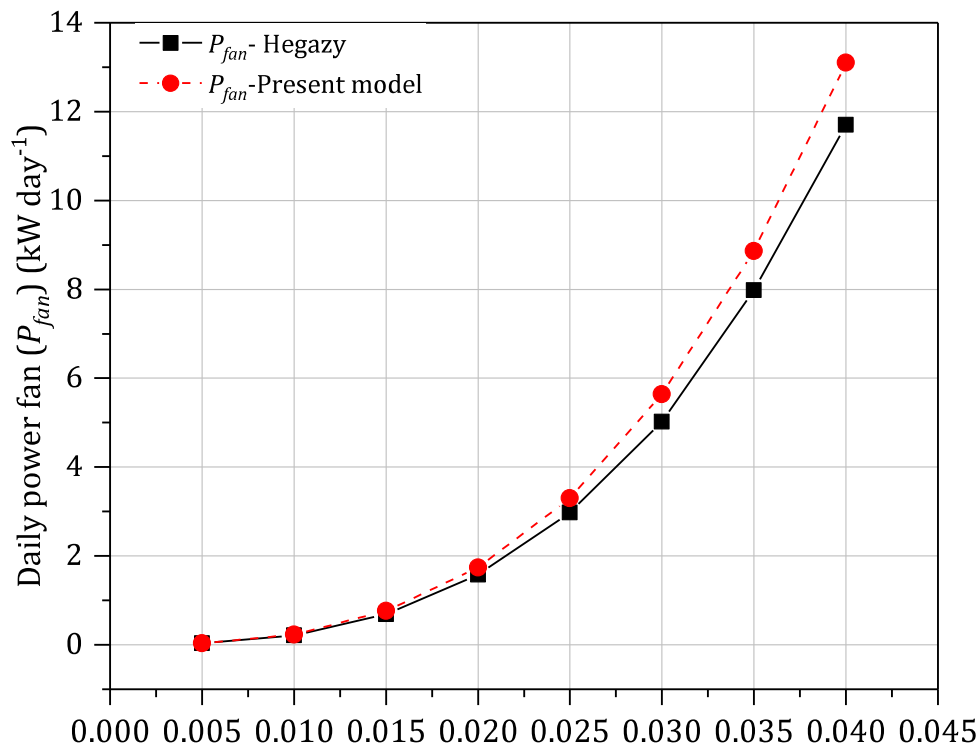


Fig. 4.38. Linear solution of present work (model 3) and linear of Hegazy [122] (model II) for estimated daily power fan.

4.7 Conclusions

COMSOL multi-physics 5.3a was used to simulate the proposed CFD models. The convective-conductive heat transfer was modelled using the conjugate heat transfer model. The radiative heat transfer model was modelled using the surface-to-surface radiation model. The system description and boundary conditions for five PV/T air system were presented. The numerical results showed that the computational assumption significantly reduced the running time, maintaining satisfactory agreement. The simulation results of the thermal, hydraulic and electrical performance (such as PV power, electrical efficiency, pressure drop and thermal efficiency) of models 2 and 3 were validated successfully against the current mathematical models and previous work reported in the literature.

In the next chapter, the evaluation of a standard PV system with respect to temperature under different conditions using different methods are introduced.

CHAPTER 5 PERFORMANCE OF PHOTOVOLTAIC SYSTEMS WITH RESPECT TO TEMPERATURE

5.1 Introduction

For two decades, there has been significant development in the production of solar PV panels. However, the efficiency of PV cells is still low compared to other solar systems such as solar thermal systems. The maximum solar cell efficiency is between 7-24% at Standard Test Conditions (STC) [62, 120]. The main factor affecting its efficiency is the PV cell temperature since it is directly proportional to the power output of the PV module. Therefore, the main aim of this chapter is to accurately predict the PV module temperature. To achieve this, several models have been examined to estimate the module temperature, including mathematical, numerical models and experimental validations. The proposed models in this discourse incorporate parameters that have not been intensively studied in the literature. The parameters are the effect of PV module length, the inclination of the PV module and the influence of the maximum possible module temperature under the worst-case scenario for two high temperature sites under free convection conditions. Moreover, to ensure accuracy, the seasonal weather conditions including incident solar radiation and ambient temperature have been estimated and validated with the standard data-set. Furthermore, the numerical results are validated with experimental observations and verified with the current mathematical model.

5.2 Methodology

Two different methods are used to model the standard PV module. The first method is a set of one dimensional (1D) non-linear energy balance equations that are solved implicitly under steady state conditions using Matlab. The second method considers steady state and transient CFD models developed using COMSOL Multiphysics v5.3a software. The CFD models are validated with measurement data reported in the literature. In order to simulate more realistic conditions, the environmental conditions are estimated and verified by comparison with standard datasets. To ensure the accuracy of the CFD models, a grid independence test is carried out.

5.2.1 PV physical module description

The photovoltaic technology used in this work is the polycrystalline BP Solar BP 585 which consists of five main components (see Fig. 4.10). The detail of this section can be seen in Section 4.4.2. This include the definition of the PV layers, the material and operating properties of the PV module (see Table 4.3 and Table 4.4).

5.2.2 PV power extraction

The electrical power generation in the PV module can be estimated by Eq. 5.1 [32, 67, 116, 302, 303].

$$P_{PV} = I_m V_m = FF I_{sc} V_{oc} = \eta_{PV} A_s \tau_{g-EVA} G \alpha_{pv}. \quad \text{Eq. 5.1}$$

where I_m and V_m are voltage and current at the max power point respectively, FF is the filling factor, I_{sc} is the short circuit current and V_{oc} the open circuit voltage [32], A_s is the total exposed surface area of PV module and the product $(\tau_{g-EVA} G \alpha_{pv})$ is the solar energy absorbed by the PV laminate, where α_{pv} is the absorptivity of the silicon and τ_{g-EVA} the combined transmissivity of the glass and the EVA layers.

5.3 1D modelling

A steady state 1D analysis is carried out to evaluate the thermal and electrical performance of the PV module. The results obtained can also be used as reference data to verify the CFD model. The short wave radiation falling on the PV module is converted into two forms - electrical and thermal. Some of this radiation is dissipated to the surroundings as thermal losses in the form of longwave radiation and by convection. The remainder is converted into electrical power. A simple energy balance method is used in this analysis. The following assumptions are taken into consideration:

- 1D heat conduction has been assumed for the current study, because the aspect ratios of the width and length of the module to the thickness of the layers lie between 200 to 2000 [358].
- There are temperature gradients across all the layers except for the PV layer itself. The equivalent thermal resistance t/k of the PV layer is three orders of magnitude less than those values of the other layers (see Table 4.4).
- The effect of accumulated dust, dirt and fouling factor is insignificant [50].
- The transmissivity of the glass and the EVA is 0.91 [59, 358].

- The ambient temperature is homogeneous [37].
- Ohmic heating (resistive heating) in the PV cells is regarded as negligible, which implies that the temperature distribution along the PV module is uniform [59].
- The ground temperature is assumed to be equal to the ambient temperature. This assumption has been widely used in many solar collector studies [32, 59, 359, 360].
- The radiative exchange from the top/front surface is to the sky (T_{sky}), which taken to be the ambient temperature. Similarly, the bottom/rear of the PV laminate is considered a radiative exchange surface to the ground.
- Both outer surfaces of the PV panel are subjected to free convection conditions [59].
- The PV system is completely sealed and bonded. This means the multiple reflections and transmissions between the components are considered negligible [37].
- The shadow effect is ignored [50].
- Perfect bonding between the layers of the PV module is assumed which means that thermal contact resistance between them is negligible [57, 342].
- The thermal conductivity of the material of the PV layers is temperature independent.
- The PV layer material are homogeneous and isotropic.
- The physical air properties are dependent on temperature.

5.3.1 Energy balance equations

The mathematical model of the PV module unit, model 1 is derived based on the work of [32, 35, 36, 38, 189, 342]. In this study, however, the temperature of the PV cell is uniform across the layer (isothermal).

Fig. 5.1 is a schematic of the PV module with the various modes of heat transfer to, within and from the module illustrated. The five temperatures are as follows: T_1 is the temperature of the top/front surface, T_2 is the temperature of the interface between the glass and EVA layers, T_3 is the temperature of the PV cell layer and is also the interface temperatures between the upper and lower EVA layers, T_4 is the temperature of the interface between the EVA and Tedlar layers and, finally, T_5 is the temperature of the bottom/rear surface. Fig. 5.2 is an equivalent thermal circuit for the heat flows through the PV laminate.

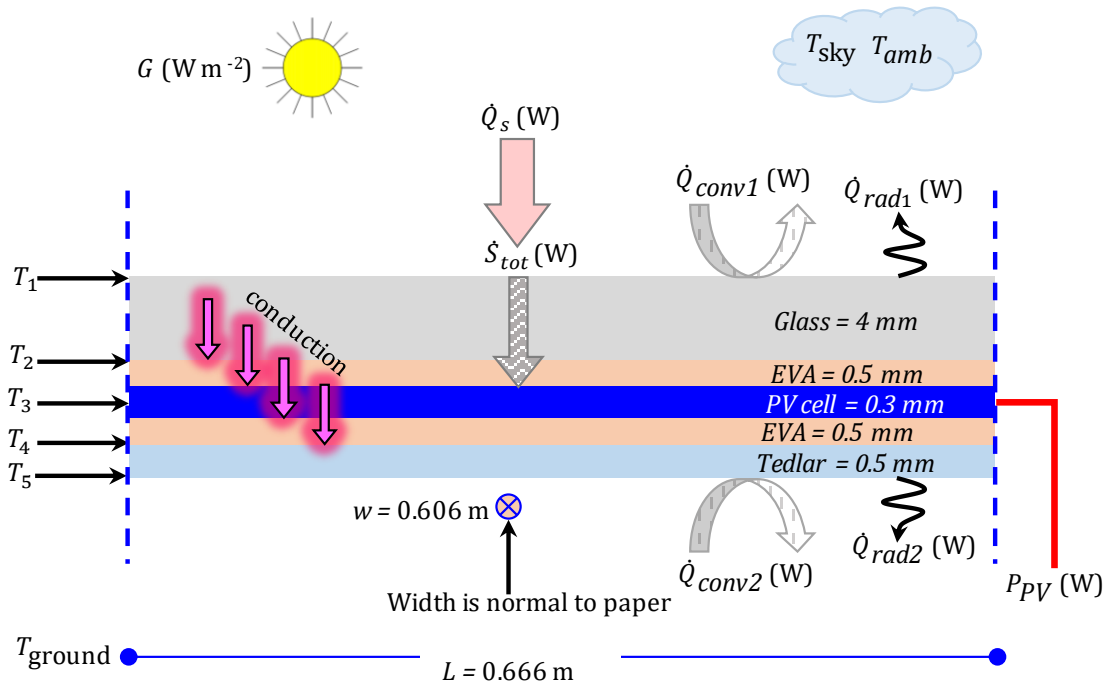


Fig. 5.1. Schematic of the main heat transfer modes within the various layers and at the outer surfaces of the PV module.

In Fig. 5.1, \dot{Q}_s is the total incident solar radiation falling on the top/front surface of the PV module. A heat balance over the PV cell layer results in the following expression:

$$\dot{S}_{tot} = P_{PV} + \dot{Q}_{top/front-loss} + \dot{Q}_{bottom/rear-loss}, \quad \text{Eq. 5.2}$$

where the total incident radiation reaching the PV cell is given as follows:

$$\dot{S}_{tot} = G A_s \tau_{g-EVA} \alpha_{pv}. \quad \text{Eq. 5.3}$$

The electrical power generated in the cell at the temperature T_3 is given by the following expression:

$$P_{PV} = \eta_{ref} [1 - \beta_{ref} (T_3 - T_{ref})] A_s \tau_{g-EVA} G \alpha_{pv}. \quad \text{Eq. 5.4}$$

The heat loss from the top/front of the cell is by conduction through the EVA and glass layers, and finally, by convection and radiation from the glass surface and is represented by the following equations:

$$\dot{Q}_{\text{top/front-loss}} = A_s \frac{T_3 - T_2}{(t_{EVA}/k_{EVA})} = A_s \frac{T_2 - T_1}{(t_g/k_g)} = \underbrace{h_{\text{free1}} A_s (T_1 - T_{\text{amb}})}_{Q_{\text{conv1}}} + \underbrace{\sigma \varepsilon_g A_s (T_1^4 - T_{\text{amb}}^4)}_{Q_{\text{rad1}}}. \quad \text{Eq. 5.5}$$

In a similar manner, the heat loss from the bottom/rear of the cell is given as follows:

$$\dot{Q}_{\text{back/rear-loss}} = A_s \frac{T_3 - T_4}{(t_{EVA}/k_{EVA})} = A_s \frac{T_4 - T_5}{(t_{ted}/k_{ted})} = \underbrace{h_{\text{free2}} A_s (T_5 - T_{\text{amb}})}_{Q_{\text{conv2}}} + \underbrace{\sigma \varepsilon_{ted} A_s (T_5^4 - T_{\text{amb}}^4)}_{Q_{\text{rad2}}}. \quad \text{Eq. 5.6}$$

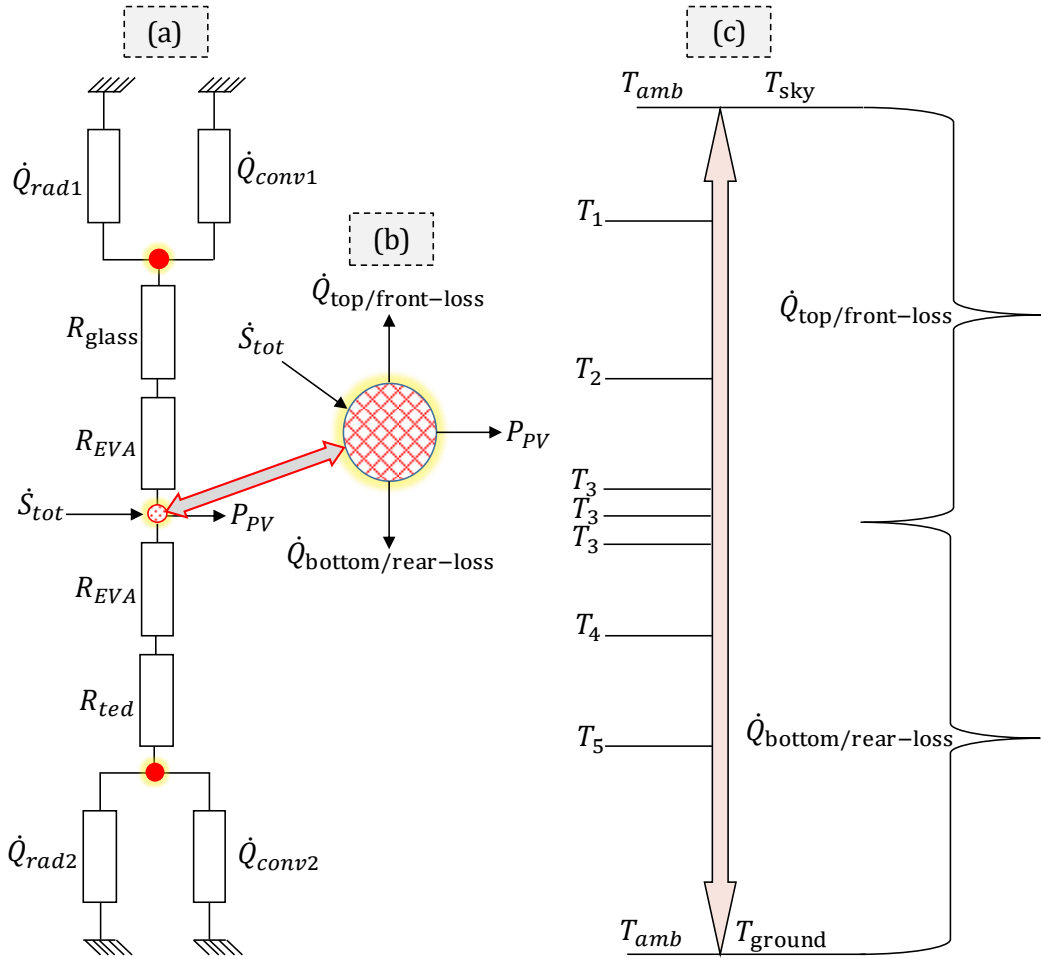


Fig. 5.2. Equivalent thermal circuit of the PV laminate.

Empirical correlations are used to estimate the free convective heat transfer coefficients on the top and bottom PV module surfaces in Eq. 5.7 and Eq. 5.8, classified based on the inclination, i.e. horizontal or inclined, the surface temperature with respect to the local surrounding temperature and type of flow regime: laminar or turbulent.

Churchill and Chu [267] recommended the following correlation that may be applied over the entire range of values of the Ra_{L_c} :

$$h_{\text{free}} = \left(\frac{k_f}{L_c} \right) \left(0.825 + \frac{0.387 \cos(\emptyset) Ra_{L_c}^{1/6}}{\left(1 + \left(\frac{0.492 k_f}{cp_f \mu_f} \right)^{9/16} \right)^{8/27}} \right)^2. \quad \text{Eq. 5.7}$$

However, for the laminar regime, Churchill and Chu [267] recommend the use of Eq. 5.8 instead of Eq. 5.7 to achieve a greater accuracy.

$$h_{\text{free}} = \left(\frac{k_f}{L_c} \right) \left(0.68 + \frac{0.67 \cos(\emptyset) Ra_{L_c}^{1/4}}{\left(1 + \left(\frac{0.492 k_f}{cp_f \mu_f} \right)^{9/16} \right)^{4/9}} \right) \text{ if } Ra_{L_c} \leq 10^9. \quad \text{Eq. 5.8}$$

These equations are also valid for an inclined plate, where L_c is the length of the PV module and \emptyset is the tilt angle (the angle between the PV module and the vertical axis, $\emptyset = 0 \rightarrow \beta = 90^\circ$ and $\emptyset = 90^\circ \rightarrow \beta = 0$). These correlations are valid for $-60^\circ < \emptyset < 60^\circ$ (or $-30^\circ < \beta < 30^\circ$).

For turbulent flow, Vliet [268] suggested that the experimental results correlated better using g instead of $g \cos(\emptyset)$, i.e. heat transfer in turbulent natural convection is not sensitive to the inclination angle.

According to [241, 267], the correlation equations for inclined walls (i.e. Eq. 5.8 and Eq. 5.7) are only satisfactory for the top side of a cold plate or the down face of a hot plate. Hence, these correlations are not recommended for the bottom side of a cold face nor for the top side of a hot plate. Since the application of inclined PV systems is the top and bottom sides of a hot plate which does not match the aforementioned literature cases, some deviation owing to this is thus expected. In this study, the tilt angles (which are in the range of $(30^\circ - 90^\circ)$ and the horizontal position are both studied. Schematic representations of the free convective boundary layers for inclined, vertical and horizontal surfaces are illustrated in Fig. 5.3. However, correlations representing these developing boundary layers and the equivalent variable heat transfer coefficients are not available, except for the vertical wall. Hence uniform heat transfer coefficients are considered in these studies and represented by the correlations Eq. 5.7 to Eq. 5.12.

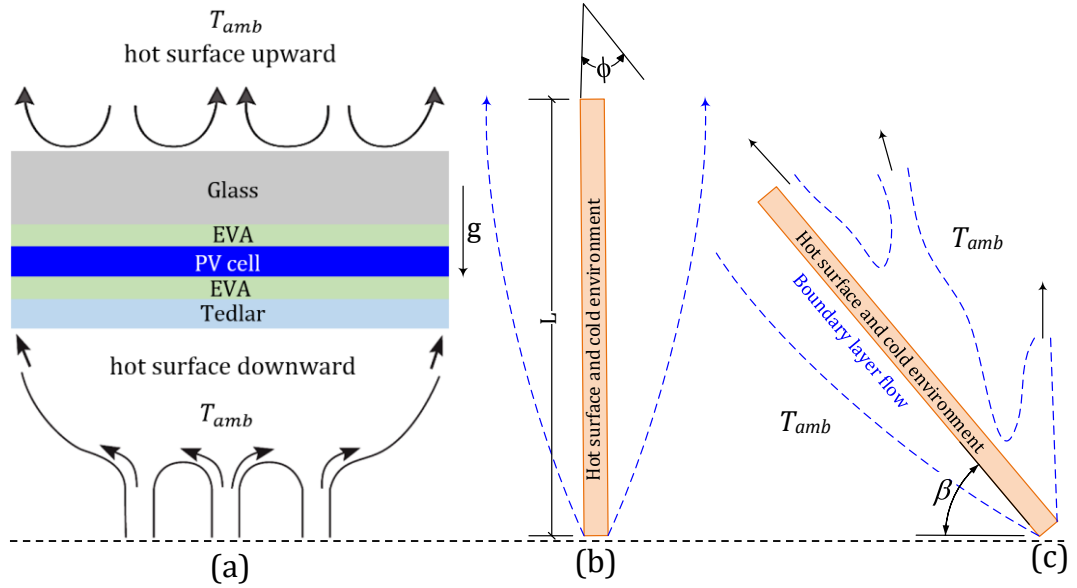


Fig. 5.3. Natural convection flows on the top and bottom surfaces of horizontal, vertical and inclined hot surface plates.

In case of the horizontal position (hot surface upward) where the top surface of the hot plate, [Eq. 5.9](#) is used for laminar flow and [Eq. 5.10](#) for turbulent flow.

$$h_{\text{free}} = (k_f/L_c) 0.54 \text{Ra}_{L_c}^{1/4} (10^4 \leq \text{Ra}_{L_c} \leq 10^7), \text{Pr} \geq 0.7. \quad \text{Eq. 5.9}$$

$$h_{\text{free}} = (k_f/L_c) 0.15 \text{Ra}_{L_c}^{1/3} (10^7 \leq \text{Ra}_{L_c} \leq 10^{11}), \text{all Pr}. \quad \text{Eq. 5.10}$$

While in the case of the bottom surface of the hot plate (hot surface downward), either [Eq. 5.11](#) or [Eq. 5.12](#) are used.

$$h_{\text{free}} = (k_f/L_c) 0.52 \text{Ra}_{L_c}^{1/5} (10^4 \leq \text{Ra}_{L_c} \leq 10^9), \text{Pr} \geq 0.7 \text{ [241]}. \quad \text{Eq. 5.11}$$

$$h_{\text{free}} = (k_f/L_c) 0.52 \text{Ra}_{L_c}^{1/5} (10^5 \leq \text{Ra}_{L_c} \leq 10^{11}) \text{ [269]}. \quad \text{Eq. 5.12}$$

where the characteristic length in the above correlations are:

$$\text{for a horizontal surface } L_c = \frac{A_s}{P_{\text{er}}} = \frac{wL}{2(w+L)}, \quad \text{Eq. 5.13}$$

$$\text{for vertical and inclined surfaces } L_c = L. \quad \text{Eq. 5.14}$$

5.3.2 Numerical technique

The non-linear algebraic equations (Eq. 5.2 to Eq. 5.12) are solved numerically using `fsolve`, which is a built-in Matlab solver. Fig. 5.4 is a logic flow diagram of the algorithm for this program. The first step is to specify the input parameters including ambient, operating and geometrical conditions (see step 1 and 2). Secondly, temperature of the PV layers were initially assumed to be at $(\hat{T}_1, \hat{T}_2, \hat{T}_3, \hat{T}_4, \hat{T}_5)$. The estimated temperature values are used to calculate the free convective heat transfer coefficients from Eq. 5.7 to Eq. 5.12 and the convective and radiative heat losses from the top/front and bottom/rear are predicted along with the electrical efficiency (η_{PV}) from Eq. 3.120.

After that, the energy balance equations are solved using `fsolve` to obtain new temperatures from Eq. 5.2 to Eq. 5.6. The new values $(T_1, T_2, T_3, T_4, T_5)$ are compared with the old values which is based on the error value i.e. the difference between the old and new values to a tolerance of 1×10^{-4} . The program is executed repeatedly until all the various temperatures converge to the set tolerance. The collector temperatures are used then to calculate the useful PV electrical power by Eq. 5.4 and the heat losses from Eq. 5.2.

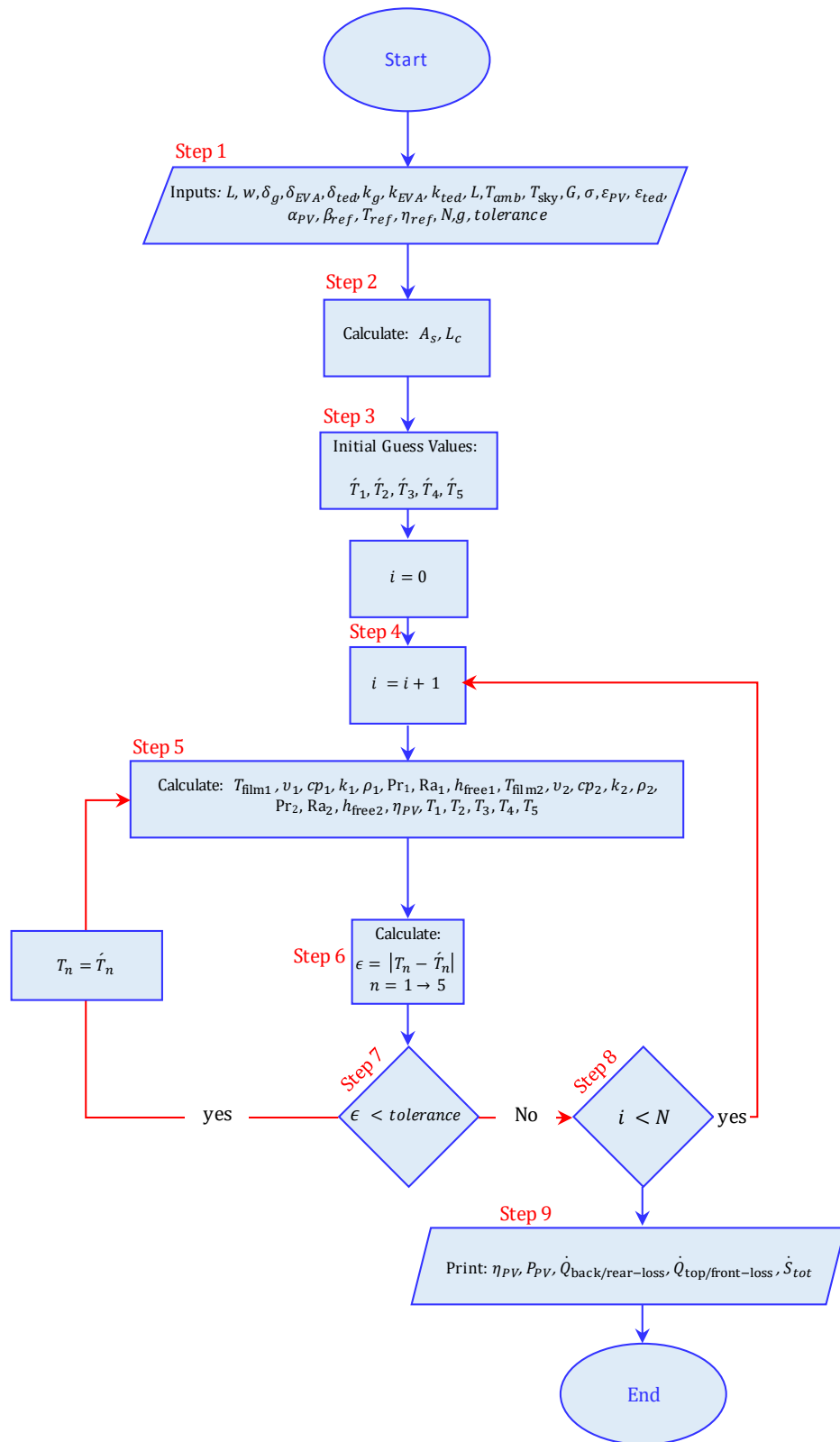


Fig. 5.4. Flow chart of the algorithm for the solution of the semi analytical model.

In Fig. 5.4, the subscripts 1 and 2 refer to top/front or back/rear surfaces of PV module. N is the number of iteration and \hat{T}_n the guess value and T_n is the calculated value.

5.4 CFD Modelling

A CFD model is developed under steady state and dynamic conditions using COMSOL Multiphysics® version 5.3a, which is based on a finite element method (FEM). The geometry of the test bench is simplified to a two 2D system. A diagram of the PV module used in this study is shown in Fig. 5.1. A one minute time step transient solver is used to enhance the accuracy of solution. To input meteorological data including ambient temperature and solar radiation, an interpolation technique (built in COMSOL) of the cubic spline function type is used. The governing equations and boundary conditions are expressed in the following sub-sections.

5.4.1 Boundary conditions and governing equations

Similar assumptions mentioned for the semi-analytical solution are considered here, however, the CFD model is 2D under transient and steady state conditions. The boundary conditions are set as close as possible to real conditions. Empirical correlations were used to estimate the free convective heat transfer coefficients on the top and bottom PV module surfaces have been presented earlier (Eq. 5.7 to Eq. 5.14). The surface-to-surface radiation module is used with an 'External Radiation' node to simulate the incoming solar radiation (COMSOL terminology are placed in quotes from here on). A 'Diffuse Surface' node is also added to model absorption and emission from the heated surfaces to the surroundings, as in Eq. 5.15 [241, 269, 338].

$$q_{rad} = \varepsilon \sigma (T_s^4 - T^4), \quad \text{Eq. 5.15}$$

where T is a surrounding temperature (K) and T_s is a surface temperature (K).

The general governing equation for the 3D conjugate heat transfer system under transient conditions with a heat generation and translational motion of the parts is Eq. 5.16.

$$\frac{D(\rho c T)}{Dt} \cdot \nabla T = \nabla \cdot (k_{x,y,z} \nabla T) + \dot{Q}_v, \quad \text{Eq. 5.16}$$

where:

$$\nabla \cdot (k_{x,y,z} \nabla T) = \frac{\partial}{\partial x} \left(k_x \frac{\partial T}{\partial x} \right) + \frac{\partial}{\partial y} \left(k_y \frac{\partial T}{\partial y} \right) + \frac{\partial}{\partial z} \left(k_z \frac{\partial T}{\partial z} \right), \quad \text{Eq. 5.16a}$$

$$\frac{D(\rho c T)}{Dt} = \rho c \frac{\partial T(x,y,z)}{\partial t} + \rho c u \frac{\partial T}{\partial x} + \rho c v \frac{\partial T}{\partial y} + \rho c w \frac{\partial T}{\partial z}, \quad \text{Eq. 5.16b}$$

where ρ is the density of PV layers (kg m^{-3}), c is the heat capacity of PV layers at constant pressure ($\text{J kg}^{-1} \text{K}^{-1}$), $k_{x,y,z}$ is the thermal conductivity of the PV layers ($\text{W m}^{-1} \text{K}^{-1}$) x, y and z directions and assumed isotropic ($k_x = k_y = k_z$). u, v and w are the velocity components in x, y and z directions, respectively, \dot{Q}_v is the volume heat source or sink.

Three cases are considered in this study as follows: In terms of PV cells where the conditions are: 2D, steady state conditions, the generated electrical power which can be treated as a heat sink (\dot{Q}_v) and a stationary PV cells, Eq. 5.16 reduces to Eq. 5.17.

$$\frac{\partial}{\partial x} \left(k_x \frac{\partial T}{\partial x} \right) + \frac{\partial}{\partial y} \left(k_y \frac{\partial T}{\partial y} \right) = \dot{Q}_v. \quad \text{Eq. 5.17}$$

Concerning other PV module layers (i.e. EVA, Tedlar and glass) in which the conditions are, 2D, steady state conditions a stationary PV layers, Eq. 5.16 converts to Eq. 5.18.

$$\frac{\partial}{\partial x} \left(k_x \frac{\partial T}{\partial x} \right) + \frac{\partial}{\partial y} \left(k_y \frac{\partial T}{\partial y} \right) = 0. \quad \text{Eq. 5.18}$$

With respect to PV cell, 2D, transient conditions where the heat generated as a heat sink, (\dot{Q}_v) and a stationary PV cells, Eq. 5.16 becomes Eq. 5.19.

$$\rho c \frac{\partial T(x,y)}{\partial t} = \frac{\partial}{\partial x} \left(k_x \frac{\partial T}{\partial x} \right) + \frac{\partial}{\partial y} \left(k_y \frac{\partial T}{\partial y} \right) - \dot{Q}_v. \quad \text{Eq. 5.19}$$

Concerning other PV layers (i.e. EVA, Tedlar and glass) the system is 2D, transient conditions a stationary PV layers, the governing equation is Eq. 5.20.

$$\rho c \frac{\partial T(x,y)}{\partial t} = \frac{\partial}{\partial x} \left(k_x \frac{\partial T}{\partial x} \right) + \frac{\partial}{\partial y} \left(k_y \frac{\partial T}{\partial y} \right). \quad \text{Eq. 5.20}$$

5.4.2 Module heat capacity

The heat capacity (C_{th}) plays a key role in identifying whether the system is under transient or steady state conditions. The heat capacity of the PV layer module materials refers to its ability to absorb and store heat. The mass of the PV layers is the main parameter in determining the amount of thermal capacity (see Eq. 5.21).

$$C_{th} = \rho c A_{pv} t, \quad \text{Eq. 5.21}$$

where C_{th} is the thermal capacity of PV module layers ($\text{J } ^\circ\text{C}^{-1}$) and t is the thickness of PV layers (m).

5.5 Meteorological data

To mimic real life conditions in our simulations, as planned in this work's objectives, relatively accurate weather parameters are estimated here. The estimated parameters are the maximum hourly global solar radiation (G_{max}) on horizontal and inclined surfaces and ambient temperature.

In terms of solar radiation estimation, the estimation is conducted using several meteorological correlations and correction factors [50, 251, 361]. These are coded using Matlab software. The correlations are functions of a number of parameters including solar time and location (latitude and longitude). The global solar radiation values during the whole year for Muscat and Fallujah cities are estimated. For each month, the selection of the day with the maximum monthly solar radiation for a horizontal surface. Then examination of the tilt angle to maximise insolation. The flow chart in Fig. 5.5 reveals the procedures taken into account to estimate the solar radiation values. The details of these equations and the calculations of solar radiation can be found in Appendix A.

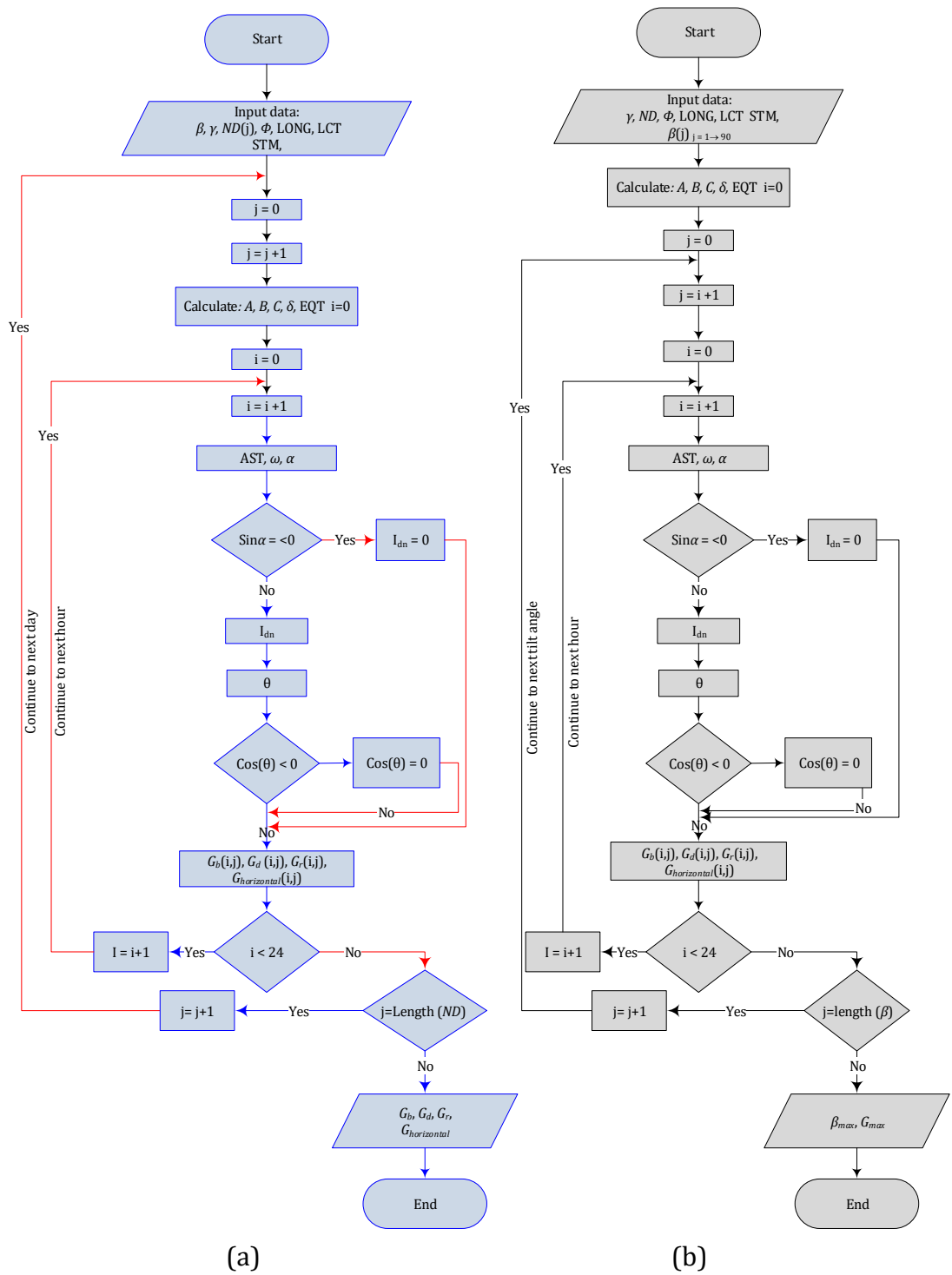


Fig. 5.5. Flow chart for solar radiation estimation, in (a) estimation insolation for a whole year on a horizontal surface and in (b) estimate the maximum insolation for a day for each month.

The estimated weather parameters are validated with two commonly cited sets of data [362, 363]. These data sets are from Photovoltaic Geographical Information System-Helioclim (PVGIS-H) and PVGIS-Climate (PVGIS-C) which are robust and widely used [364-366].

PVGIS is an online tool which provides monthly, daily and hourly global solar radiation values on horizontal and inclined surfaces.

Fig. 5.6a shows a comparison between monthly estimated and observed values of incident solar radiation for PVGIS-C and PVGIS-H for Fallujah city. The maximum absolute percentage errors are 14.6% and 26.7% for the PVGIS-C and PVGIS-H data respectively with respect to the estimated values. Similarly, Fig. 5.6b reveals that the maximum absolute percentage errors are 11.1% and 13.1% for the PVGIS-C and PVGIS-H data respectively for Muscat city.

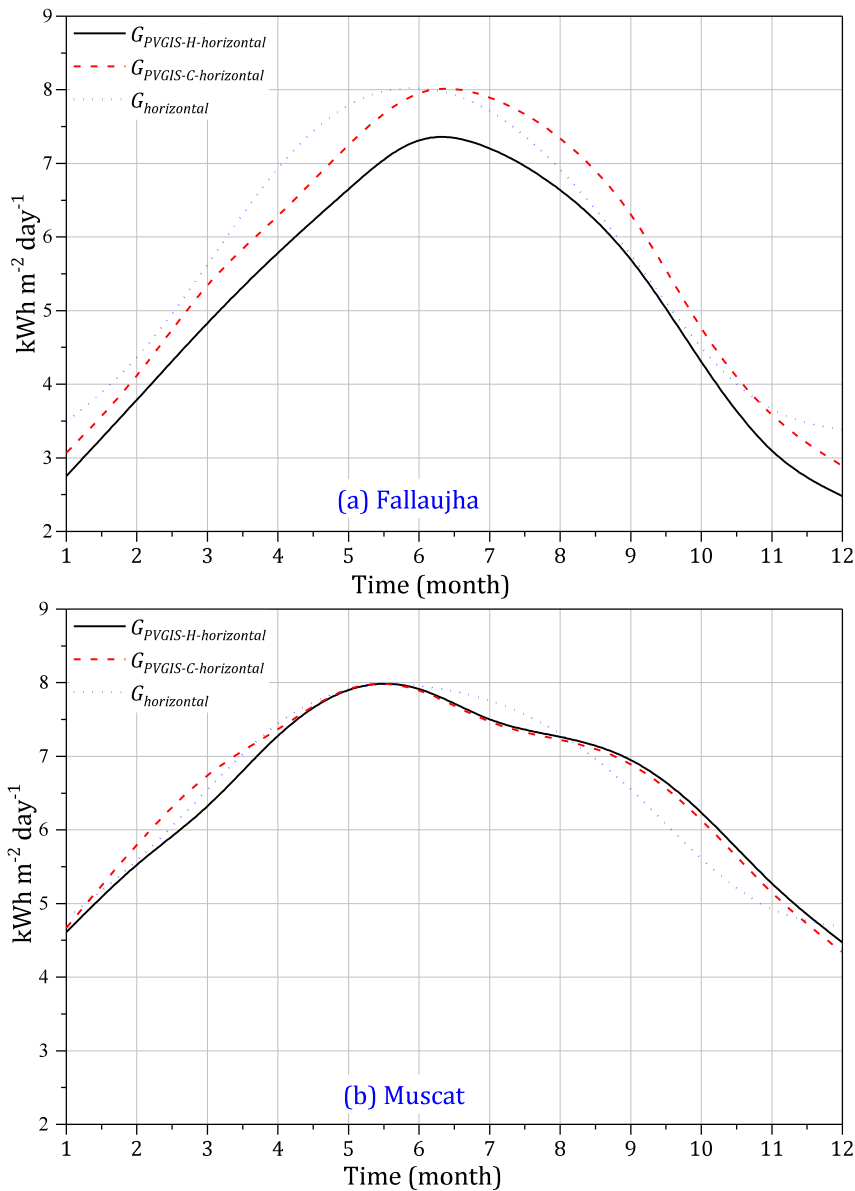


Fig. 5.6. Monthly estimated and observed insolation of PVGIS-C and PVGIS-H for Fallujah and Muscat cities.

To ensure accuracy, Fig. 5.7 (a) and (b) compare between the hourly estimated and observed insolation of PVGIS-C and PVGIS-H for Fallujah and Muscat cities for a typical day in July respectively. It can be concluded that the use of PVGIS-C and PVGIS-H data are satisfactory and confirmed by Huld et al [363], hence this confirms the validity of the estimated values.

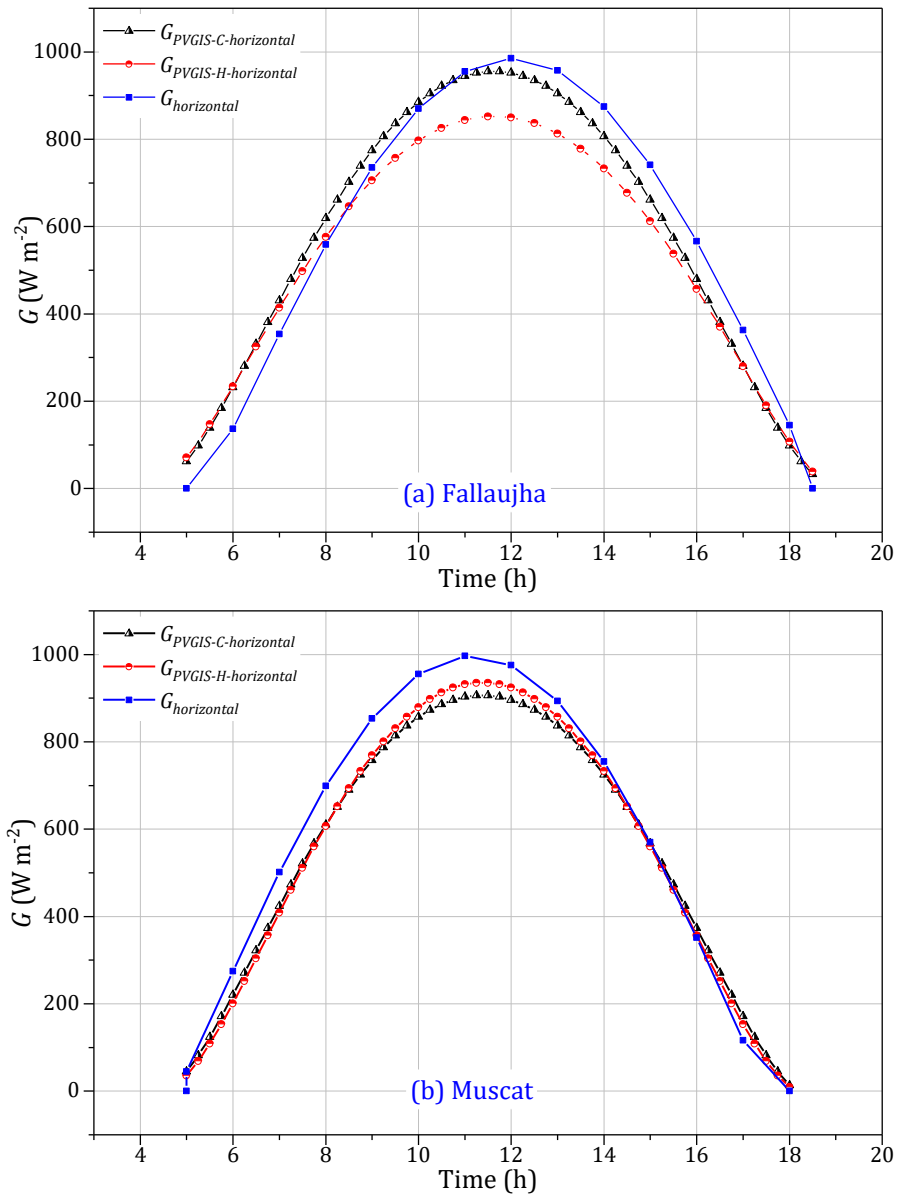


Fig. 5.7. Hourly estimated insolation with observed of PVGIS-C and PVGIS-H for Fallujah and Muscat cities for a typical day in July.

Fig. 5.8 (a) and (b) compares between the estimated incident solar radiation falling on horizontal and inclined surfaces on 31st of January for Fallujah and Muscat cities denoted by

(G) and (G_{max}) respectively. In this study, the day was chosen with the maximum possible incident solar radiation in each month with tracking angle (tilt angle) resulting in maximum solar radiation. From the graphs, it can be seen that the tracking angle contributes clearly to increasing the values of incident solar radiation.

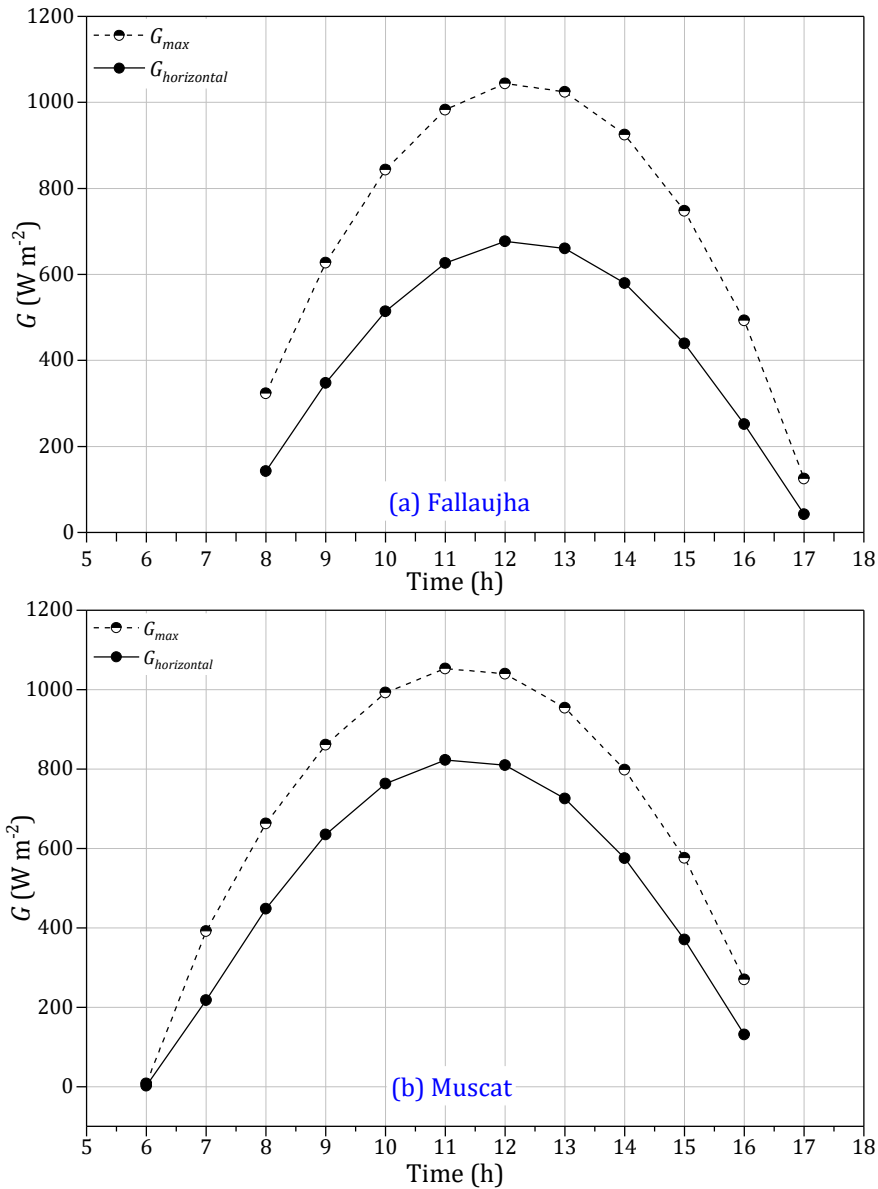


Fig. 5.8. Maximum incident solar radiation falling on horizontal and inclined surfaces for Fallujah and Muscat cities on 31st of Jan.

Fig. 5.9 presents the ambient conditions for a typical day in Muscat and Fallujah cities. As expected, the ambient temperature is proportional to the incident solar radiation values from 7:00 a.m. to the solar noon. However, after solar noon, the ambient temperatures show

a considerable deviation from the incident solar radiation. The data from these figures confirmed the trend of estimated data for the two cites used in this research.

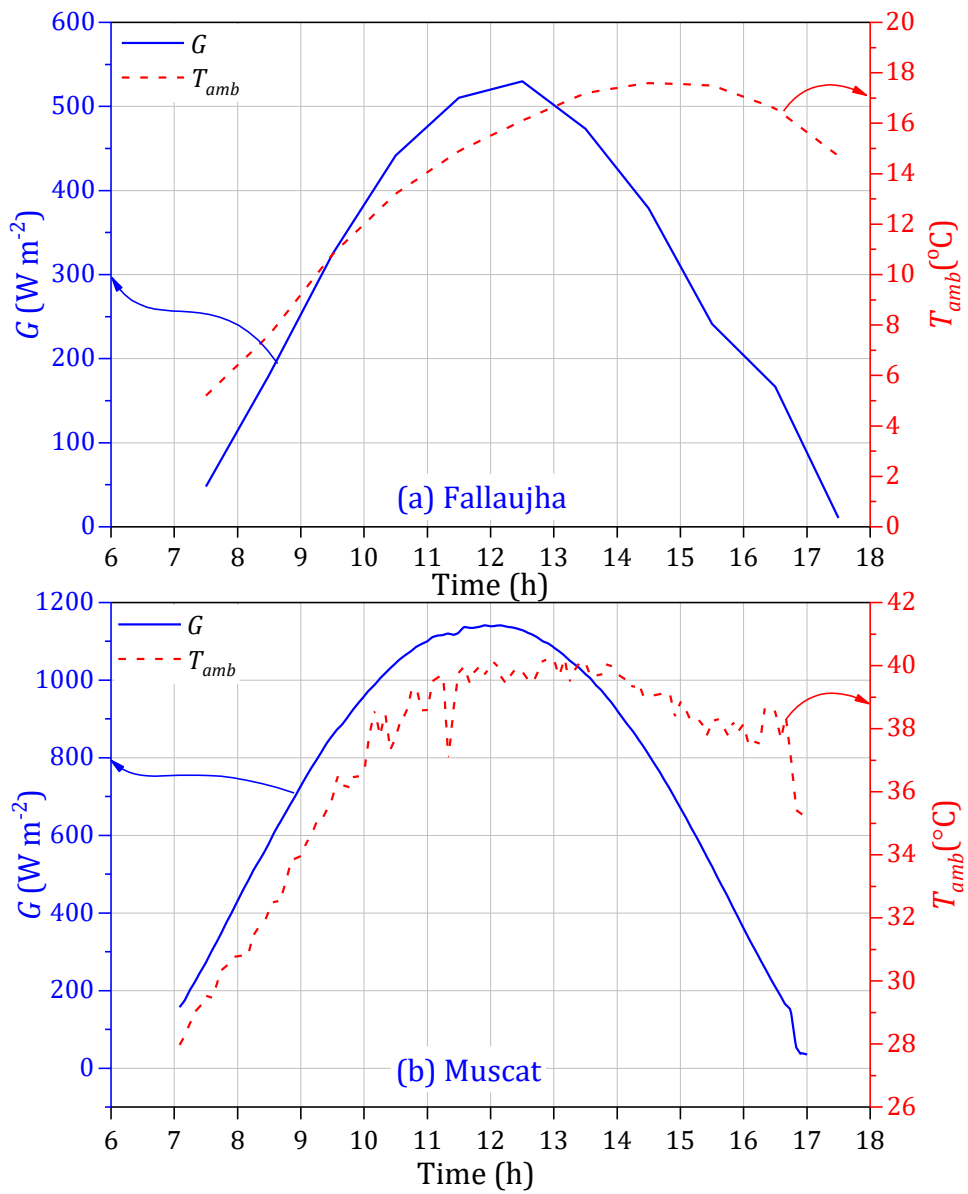


Fig. 5.9. Hourly variation of insolation and ambient temperature for Fallujah 22nd of Jan 2011 [24] and for Muscat 1st of Oct 2013 [323].

The ambient temperature is estimated and validated with real data. Diurnal air temperature range δT_R and average ambient temperature for a month (T_{avg}) parameters are used to estimate ambient temperature accurately [317, 367, 368]. The diurnal temperature range (δT_R) is the difference between the daily maximum and minimum temperature. A

correlation equation has been suggested by [317] to estimate the hourly ambient temperature as shown in Eq. 5.22.

$$T_{amb} = T_{avg} + \delta T_R \cos\left(2\pi \frac{t - 14}{24}\right), \quad \text{Eq. 5.22}$$

where t is the time in second for a 24 hour range.

Fig. 5.10 presents a comparison between the estimated and measured ambient temperature for Muscat city on 1st of October 2013 [323]. There is a qualitative and quantitative agreement between the two sets of data.

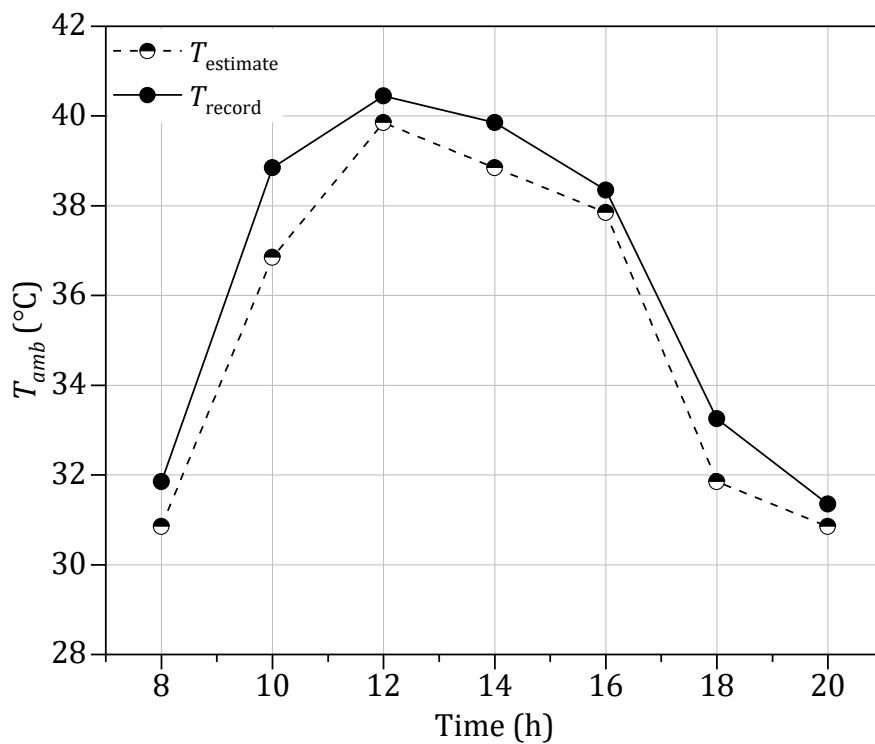


Fig. 5.10. Observed and estimated ambient temperature for Muscat 1st of Oct 2013 [323].

A comparison is made between estimated values and both PVGIS-C and PVGIS-H websites of maximum tracking angles for Muscat and Fallujah cities, which show good agreement as, explored in Fig. 5.11. This results are also in qualitative agreement with ASHRAE [369].

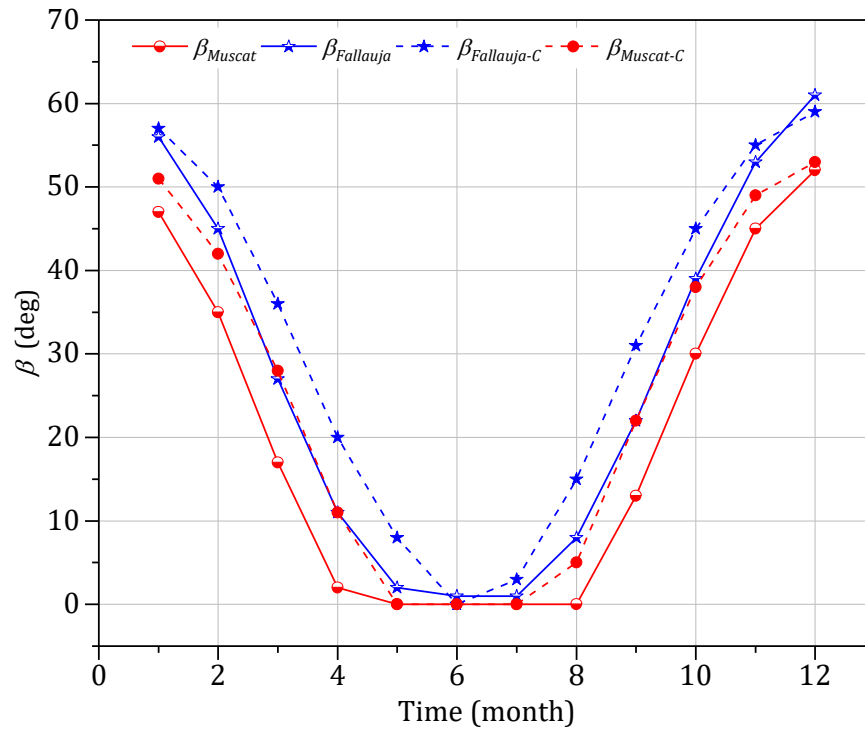


Fig. 5.11. Estimated, PVGIS-C and PVGIS-H values of the maximum tracking angles (tilt angles) for Muscat and Fallujah cities.

5.6 Validation

A grid independence test, validation with previous studies, verification between CFD and semi analytical solution as well as steady state and transient conditions were used to validate the developed model.

5.6.1 Grid independence test

In this test, two mesh element types are used, the first is simple linear free unstructured triangular mesh and the second is quadrilateral structured mesh. The mesh test analysis is conducted to obtain a proper element type and size, improve accuracy, and limit the overall computation time. Five criteria are taken into account which are physical memory (GB), solution time (s), number of elements (NOE), degrees of freedom (DOF) and minimum element quality (MEQ).

Table 5.1 demonstrates the key features of the mesh independence test analysis for standard PV system using structured and unstructured mesh elements for a case study in Fallujah on a typical day in July. As can be seen from this table, the MEQ of structured mesh is much greater than unstructured mesh. RAM, run time and NOE are noticeably reduced

using the structured mesh. Hence, using the structured mesh has significantly contributed to limiting the run time and RAM, respectively, from 1357 sec and 6.73 GB to 64 sec and 1.54 GB and will therefore be adopted.

It should be noted that even though using high mesh density such as in Trial 4 as show in [Table 5.1](#), the maximum percentage error (relative to the finest mesh) obtained is approximately 0.5%. This could be owing to:

1. The CFD model is assumed equivalent to a 1D semi-infinite solid, because of the limitation of the software to represent the solar radiation in case 1D representation using Comsol v5.3a.
2. Ignoring the thermal edges losses since the aspect ratio (length/frame thickness) is ~ 1000 . In other words , the sides of the PV module are considered to be adiabatic [\[31, 370\]](#).
3. The thickness of PV layers is comparatively small.
4. The thermal conductivity of PV layers is also relatively high.
5. The model is dominated by conduction mode.
6. We used empirical equations to calculate heat transfer coefficients by free convection for the top and bottom PV module surfaces. This means the values of these coefficients are uniform in our model , however, in reality it might change along the PV module specifically in the vertical and inclined states [\[241, 371\]](#).

Table 5.1. Grid independence test using structured and unstructured mesh element types for case study Fallujah on a typical day in July under transient conditions.

Trial No	Refinement step	RAM (GB)	Time (s)	NOE	MEQ	DOF	T_{mpv} (°C)
Unstructured mesh (triangular)							
1	Extremely coarse	6.73	1357	15765	0.345	34834	48.23
2	Very coarse	8.45	1867	21121	0.343	45954	48.31
3	less coarse	8.67	1819	20176	0.357	44163	48.30
4	Coarse	8.40	2020	22188	0.356	48249	48.32
Structured mesh (quadrilateral)							
1	Extremely coarse	1.54	64	2142	1	10011	48.32
2	Very coarse	3.12	168	4242	1	19409	48.20
3	less coarse	5.45	396	8127	1	36141	48.22
4	Coarse	8.46	678	11730	1	51635	48.27

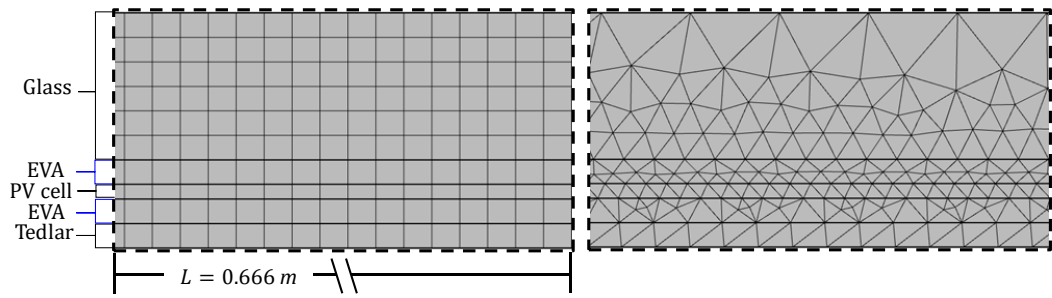


Fig. 5.12. Structured and unstructured mesh of standard PV unit for refinement step number (4) in Table 5.1.

5.6.2 System validation

The CFD developed model is validated with available experimental results from Coventry, UK [372] and Fallujah, Iraq [121].

With respect to the experimental data in Coventry, the weather station is on the roof of a building at the University of Warwick [372], a free standing monocrystalline silicon PV panel inclined at 30° and oriented to south with a dimension of 1.652 m length and 0.994 m width. The specifications of this PV module can be seen in [373]. Fig. 5.13 compares the measured and simulated PV module temperature. This figure also presents the incident solar radiation, ambient temperature and wind speed versus time 04:30–08:36 hrs on 1st August 2017. The CFD model is carried out under unsteady state conditions. It can be seen in this figure that the slope of measured PV panel temperature fluctuates because of the variation of the incident solar radiation and wind speed. The finding indicates that the CFD model is reasonably successful with a good level of conformity, approximately 3-8%. The percentage error is calculated with respect to the experimental results. This variation can be attributed to a number of factors, e.g. the effect of climate conditions such as dust and humidity, which are difficult to include in CFD calculations. Also, it is assumed that the PV panel is clean. Another reason is the accuracy of material properties values of the PV module layers.

With respect to the validation in Fallujah, the current numerical results of model 1 is validated in terms of average PV panel temperature as shown in Fig. 5.14. This figure displays the incident solar radiation, ambient temperature and PV panel temperature versus time 08:00–15:00 hrs on 24th March 2011. The CFD model was developed under steady state conditions. It can be seen that the PV panel temperature increases gradually with the solar radiation and ambient temperature from sunrise to reach a peak value at the solar noon (12:00hr) and then reduces until sunset. The results reveal that a good level of

conformity is obtained between the current CFD model and experiments with the maximum temperature difference of approximately 4 °C. This difference may be because of the following (including but not limited to) possibilities:

1. The accuracy in measuring the ambient temperature and incident solar radiation.
2. The difficulty in estimating the wind effect/wind direction accurately.
3. Dust accumulation.
4. The CFD model is simplified to a 2D problem, whereas the physical system is 3D.
5. The model used quasi-steady conditions [374], in reality, the system is inherently time-dependent.

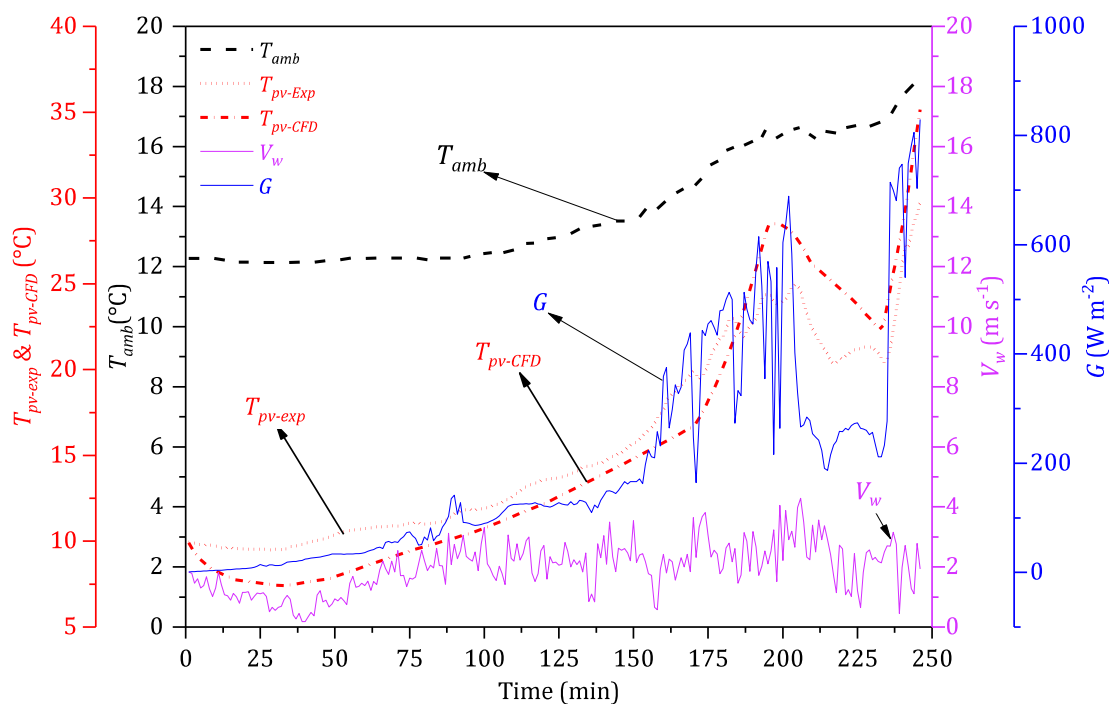


Fig. 5.13. CFD of present work (model 1) and experimental work of Thorpe [372] for the average PV module temperature.

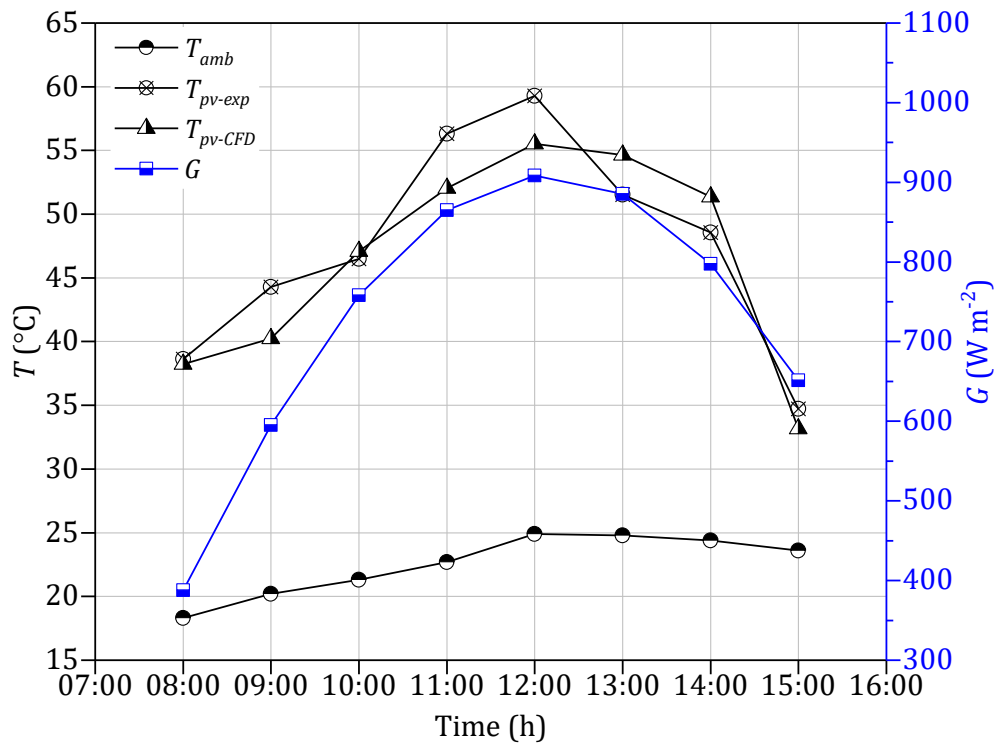


Fig. 5.14. CFD of present work (model 1) and experimental work of [121] for the average PV module temperature.

5.6.3 System verification

The first verification is between the numerical and developed steady state CFD of model 1. Two sets of weather data are considered, Fallujah and Muscat to evaluate the PV module temperature and electrical power generated for a typical day in July for Fallujah and Muscat. Even though the CFD model is 2D and the numerical model is 1D, the two models showed a close agreement as can be seen in Fig. 5.15 (a) and (b). A range of reasons may explain the results:

1. The CFD model can be assumed 1-D semi-infinite solid as justified earlier in point 1 Section 5.6.1 (grid independence test).
2. The PV layer thickness is relatively small while the thermal conductivity is comparatively high.
3. The similarity in representation of the heat transfer modes. For example, the external heat transfer by free convection is represented in the two models using the same empirical equations.

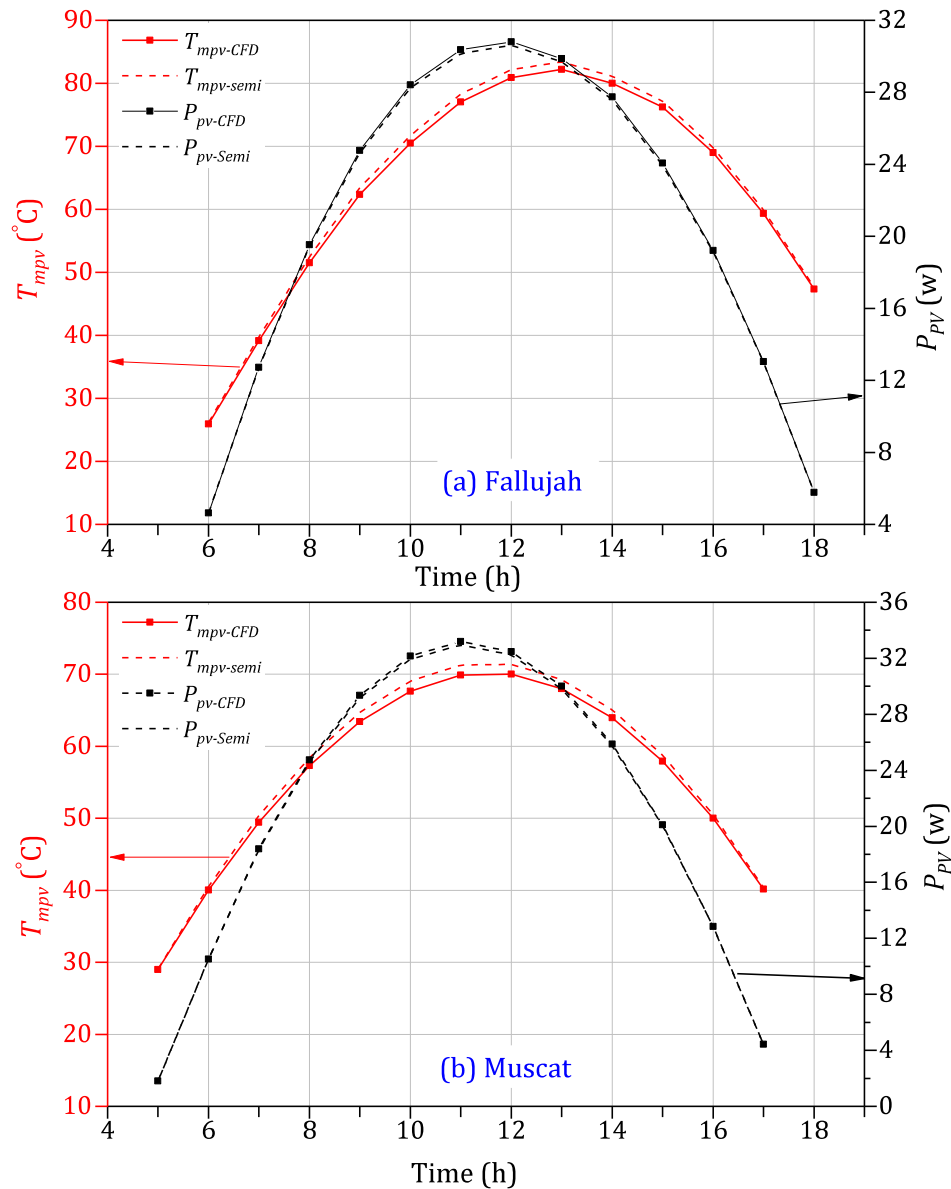


Fig. 5.15. CFD model and semi-analytical solution of model 1 for the average PV module temperature and electrical power, in (a) for Fallujah on a typical day in July and in (b) for Muscat on a typical day in July.

The second verification is an inter-model comparison between the PV unit under steady state and transient conditions for the Fallujah case study on a typical day in July as shown in Fig. 5.16. It can be seen that the two results are similar because C_{th} values are comparatively low since the thickness of the PV layers are small. It should also be mentioned that, the nature of free convective heat transfer is transient but are solved using empirical correlations not by the conjugate heat transfer models. Under this condition, the values of free convective heat transfer coefficients are uniform and do not change with time and spatial (single value). In this study, however, we still applied transient conditions to ensure accuracy, faster convergence and the inherent time dependence of PV systems.

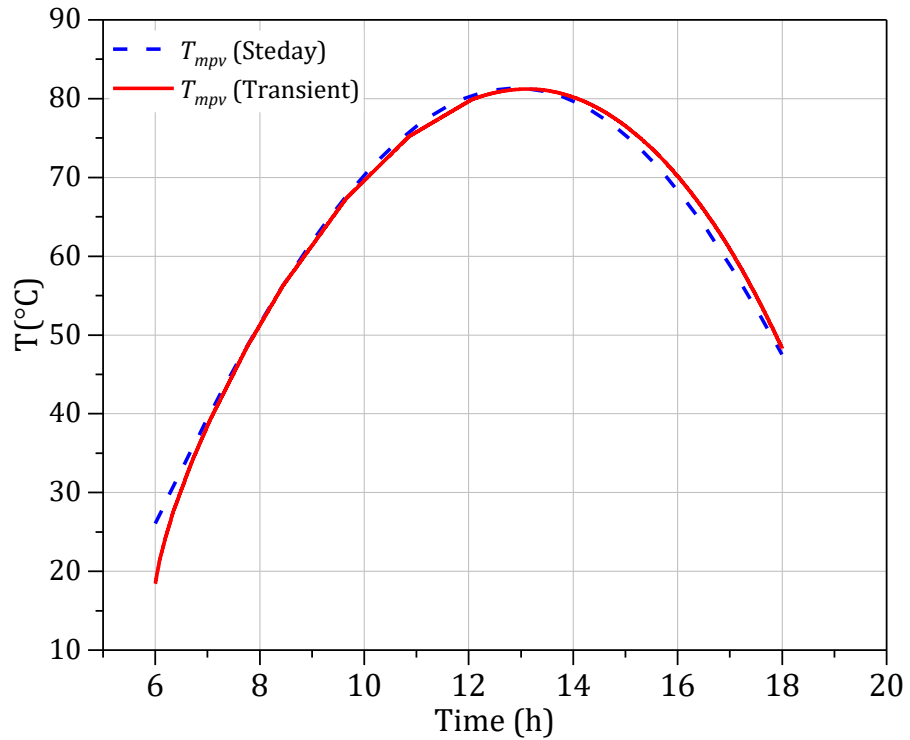


Fig. 5.16. Numerical results of standard PV unit under steady and transient conditions for case study Fallujah on a typical day in July.

5.7 Results and discussion

On the basis of the validated thermal model, the CFD simulation is carried out for two different cities as representative cases. The cities are Fallujah and Muscat, Fallujah is located in Iraq 33.34° N, 43.78° E and elevation: 47 meters above sea level (MASL). Muscat is located in Oman 23.58° N, 58.40° E and Elevation: 13 MASL. These cities are selected because they gain a relatively great amount of annual average insolation of 5.8 and 6.46 (KWh m⁻² day⁻¹) for Fallujah and Muscat respectively. Under these conditions, it can be assumed that the performance of the PV module is evaluated under worst case scenario (i.e. highest expected PV panel temperature influencing its performance).

Table 5.2 presents the maximum tracking angles, which is the angle that results in maximum solar radiation on an inclined surface, for Fallujah (β_{Fallujah}) and Muscat (β_{Muscat}).

Table 5.2. Estimated maximum tracking angles (degree) values for Fallujah and Muscat cities.

Month	Jan	Feb	March	April	May	Jun	July	Aug	Sep	Oct	Nov	Dec
β_{Fallujah}	56	45	27	11	2	1	1	8	22	39	53	61
Day	31	28	31	30	31	9	1	1	1	1	1	1
β_{Muscat}	47	35	17	2	0	0	0	0	13	30	45	52
Day	31	28	31	30	28	2	1	1	1	1	1	1

The hourly variation of PV module temperature is evaluated under maximum solar radiation and ambient temperature over a year at Fallujah and Muscat cities for original length ($L = 0.666 \text{ m}$). This is presented in Fig. 5.17 and Fig. 5.18. It is obviously seen that the PV panel temperature increases with an increase in the insolation and ambient temperature. In Fig. 5.17 the maximum module temperature is 83.4 °C in August (see also Fig. 5.19 for 2D temperature contours) in which the ambient temperature is at the maximum value throughout the year (54 °C). In Fig. 5.18, the highest module temperature is 73.72 °C in June (see Fig. 5.19) because the ambient temperature is the highest during the year (42.2 °C). Referring to Fig. 5.19, it should be noted that the maximum temperature is in the PV cell layer owing to the fact that the electrical power is generated in this layer.

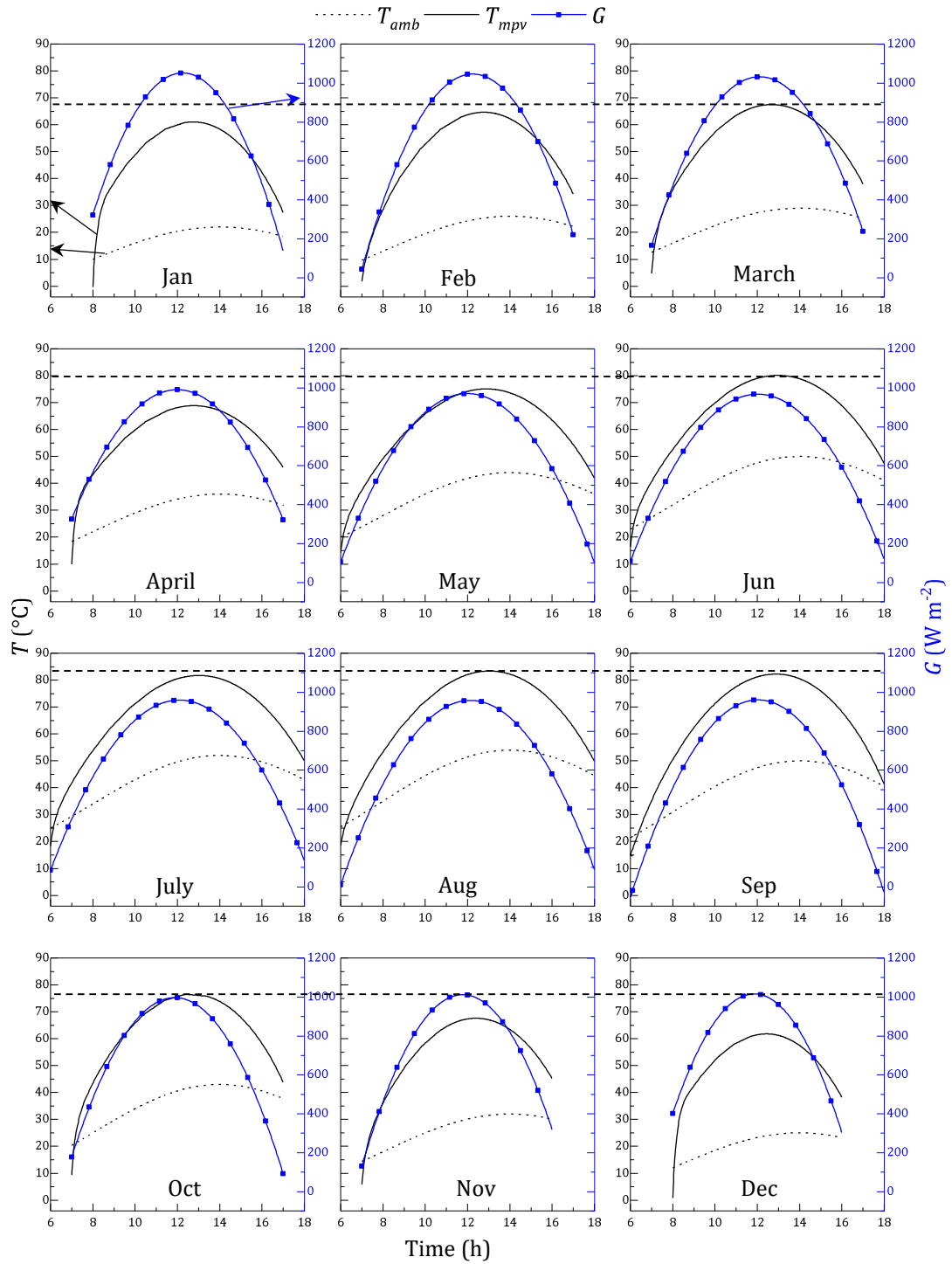


Fig. 5.17. Hourly variation of PV module temperature, maximum insolation and ambient temperature over a year under free convection and transient conditions (time step 1 minute) in Fallujah.

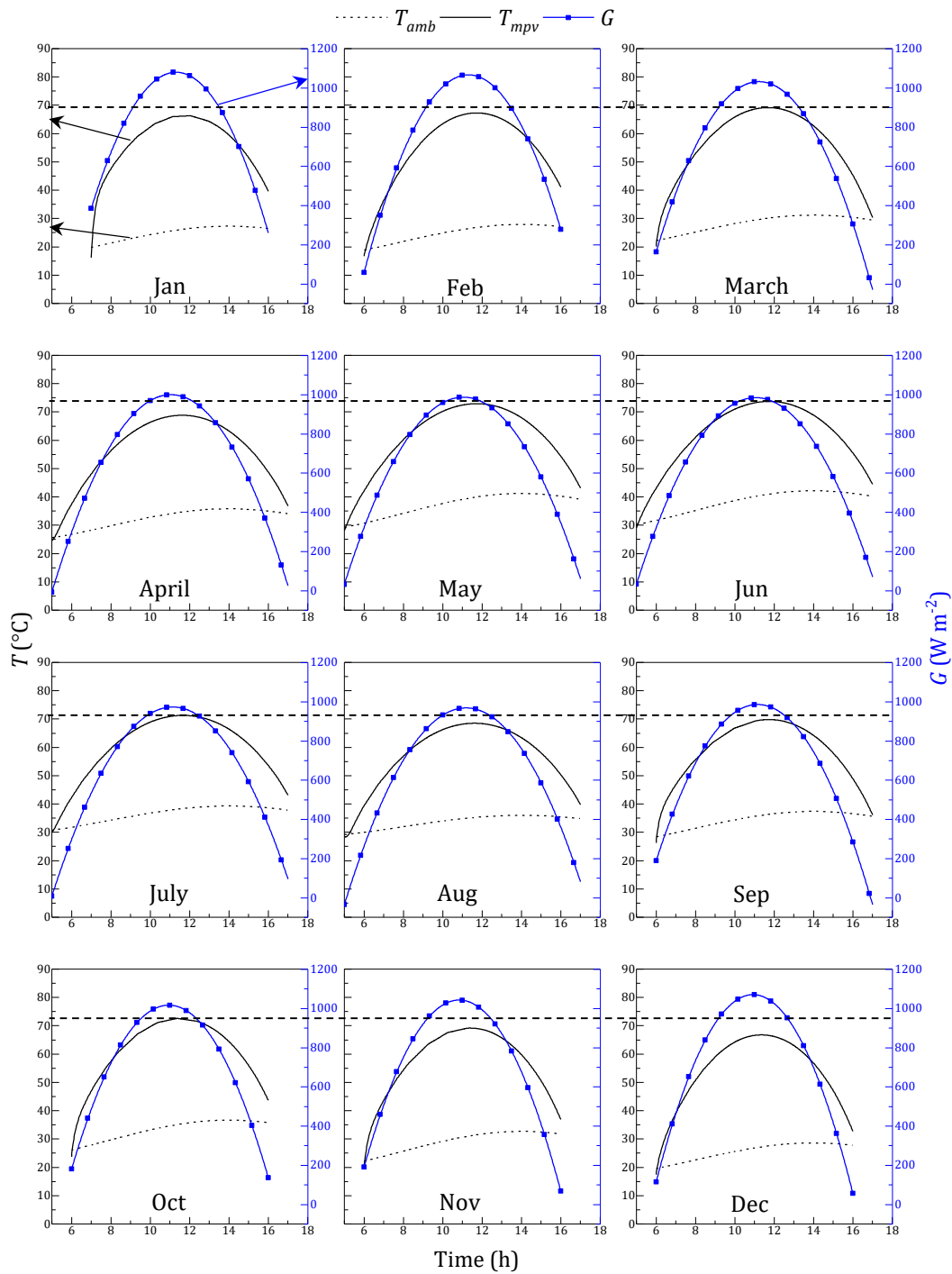


Fig. 5.18. Hourly variation of PV module temperature, maximum insolation and ambient temperature over a year under free convection and transient conditions (time step 1 minute) in Muscat.

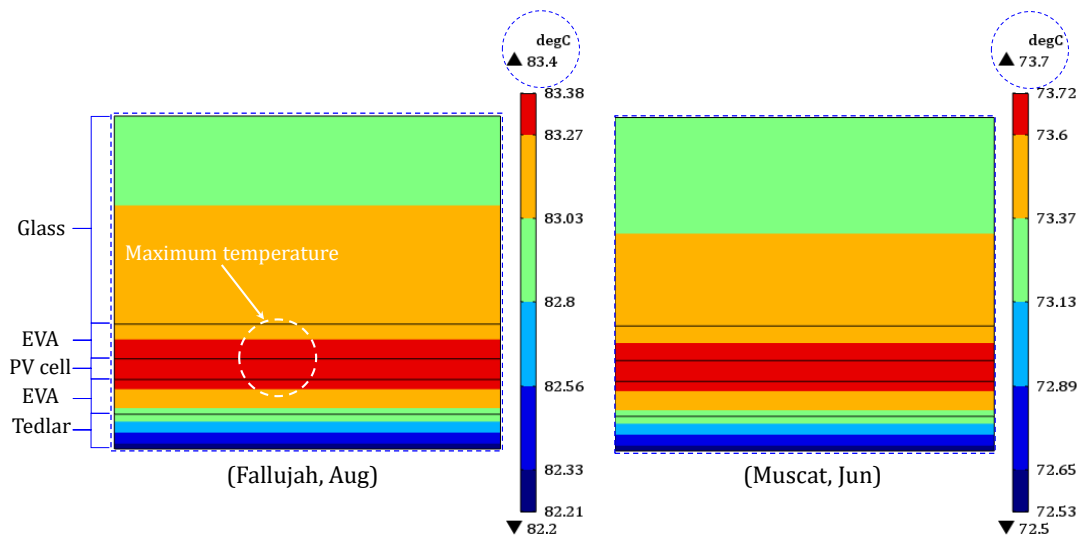


Fig. 5.19. 2D temperature contours ($^{\circ}\text{C}$) of standard PV module under free convection and transient conditions (time step 1 minute) in Fallujah of 1st Aug at 13:00 and Muscat of 2nd Jun at 11:45.

The impact of PV module temperature on its module's power output for 12 months under free convection and transient conditions at Fallujah and Muscat are demonstrated in [Fig. 5.20](#) and [Fig. 5.21](#). The trends in these figures reveal that the generation of PV power follow the PV panel temperature since the PV panel temperature and intensity of solar radiation are the main factors that influence PV power generation. Therefore, the maximum power generation is in January in Fallujah and in June in Muscat.

It can be deduced that lower ambient temperature and higher insolation values lead to better PV performance, which can be clearly seen by comparing both Muscat and Fallujah in June. Apart from the two factors mentioned above (PV panel temperature and insolation) the daylight period in Muscat is longer than Fallujah which allows for the accumulation of more solar energy per day and further increases in the solar PV power.

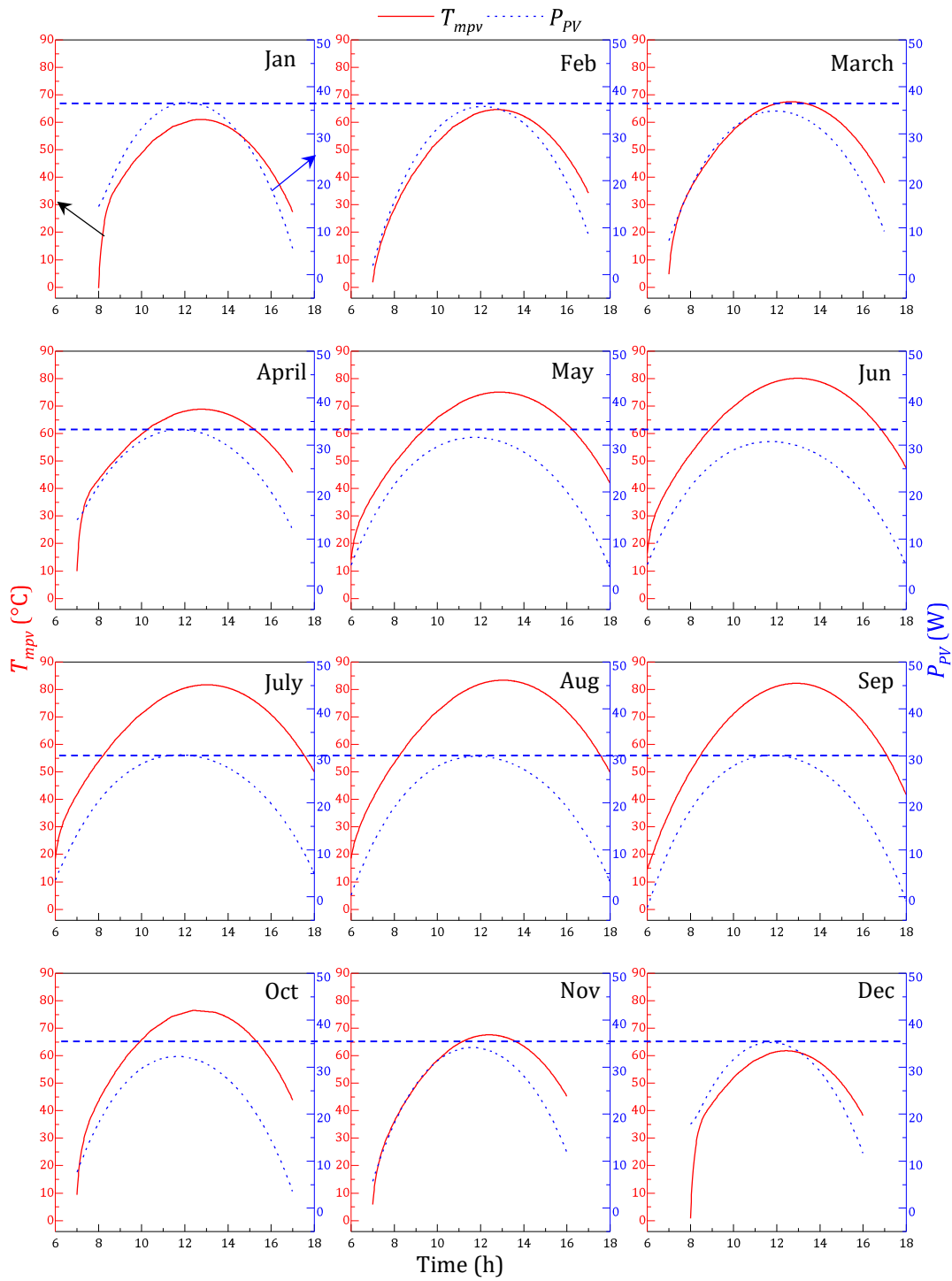


Fig. 5.20. Hourly variation of module temperature and PV power generation for 12 months under free convection and transient conditions (time step 1 minute) at Fallujah.

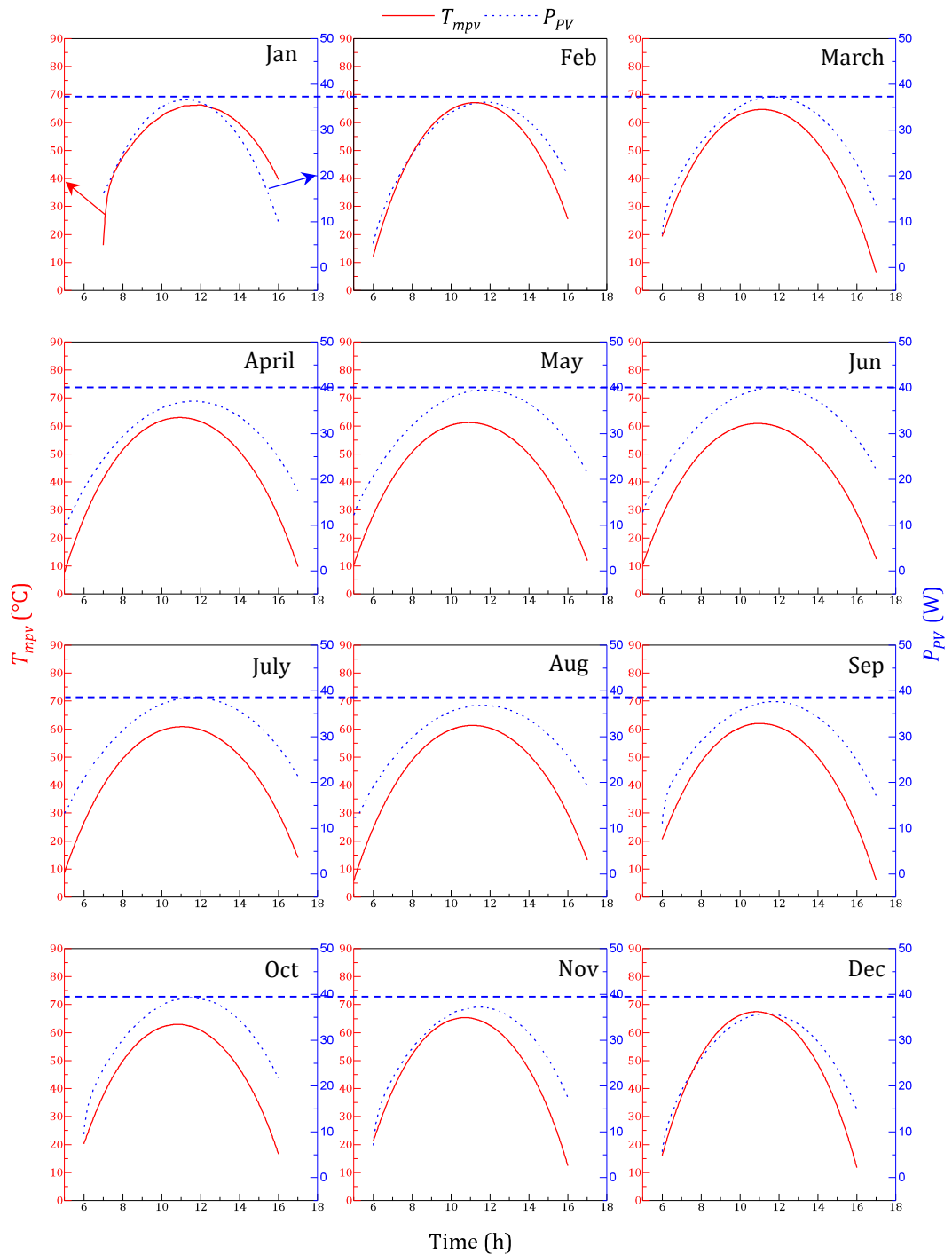


Fig. 5.21. Hourly variation of module temperature and PV power generation for 12 months under free convection and transient conditions (time step 1 minute) at Muscat.

The effect of PV length on its temperature under different inclinations and weather conditions are presented in Fig. 5.22 and Fig. 5.23.

Fig. 5.22 shows the influence of PV length (i.e. $L/8, L/4, L/2, L, 2L, 4L$) on the PV temperature in the horizontal position located in Fallujah on 1st June at 13:00. The results

demonstrate that there is a slight increase in temperature with increasing length up to $L/2$, after this length the temperature is consistent. The reason behind this is that in the entry region of the PV plate (near the PV edges) the flow is developing to be fully laminar and the convective heat transfer rate is greater than in a fully laminar region [375]. Also the edges of the PV panel allows the air flow to move easily. This can be seen clearly between $(L/8 - L/4)$. After that, the flow is laminar up to the point of transition to turbulent flow or flow separation. It can be seen that there is no enhancement in heat transfer after length L since the buoyancy force, which is normal to surface, and the convection currents are limited, as shown in Fig. 5.3. In contrast, in inclined surfaces where the temperature drops in turbulent region as expected.

To clarify, in the bottom surface of the PV module, the PV plate obstructs (blocks) airflow, apart from the PV panel edges where the flow is free to ascend. Owing to this obstruction, the flow moves horizontally, then it rises from the edges of the PV panel, and the convective heat transfer rate is inefficient. Conversely, on the top PV surface, see Fig. 5.3, the heated fluid moves freely, inducing strong natural convection currents and thus, the heat transfer rate is enhanced, see Table 5.3 which shows the upper and lower convective heat transfer coefficients

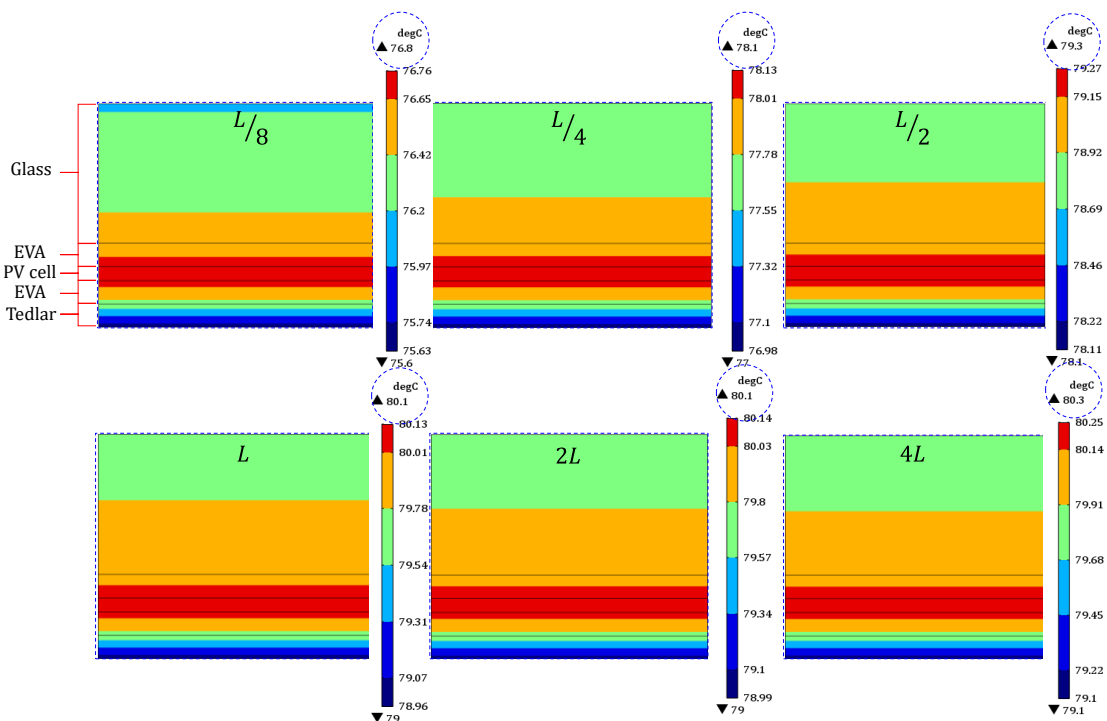


Fig. 5.22. 2D temperature contours (°C) of standard PV module under free convection and transient conditions at Fallujah of 1st Jun at 13:00 employing different lengths and same tilt angle (horizontal).

Fig. 5.23 shows the impact of the length of the PV module (i.e. $L/8, L/4, L/2, L, 2L, 4L, 6L$) on its temperature under different inclinations ($0-90^\circ$) located in Fallujah on 31st January at 13:00. In terms of horizontal position (0°), it is apparent that the trend of PV module temperature in Fig. 5.23 behaves similarly to Fig. 5.22 and owing to the same reasons highlighted in the analysis of Fig. 5.22. With respect to inclinations in the range ($30-90^\circ$), it is expected that the convection currents are weaker, and the rate of heat transfer is lower relative to the vertical position [269]. This is seen particularly in the 30° inclination because the flow is impeded by the PV, specifically in bottom surface of the PV resulting in convective heat transfer being lower.

Also, from the data in Fig. 5.23, the PV module temperatures increase with increasing length up to L for inclinations ($30-90^\circ$). This is because the flow is probably in the laminar regime and is thus sensitive to changes in length and inclination [267]. It can also be seen that the module temperatures in length $L/8$ and $L/4$ are lower than $L/2$ and L for the same inclinations. This is most likely owing to the flow in small lengths not being fully developed and the rate of heat transfer in the developing region is greater relative to longer lengths [375], see also Table 5.3. Above length L , the effect of inclination stops while that of length can be seen clearly. This was confirmed by Vliet [268] whose experimental results correlated better using g instead of $g \cos(\theta)$, i.e. heat transfer in turbulent natural convection is not sensitive to the inclination angle. In the range $2L-6L$, the temperature increase 3°C to 6°C relative to temperatures in the lower lengths' region regardless of the tilt angle. This is owing to fact that the heat transfer coefficient for bottom surfaces decrease with increase in length as can be seen in Table 5.3.

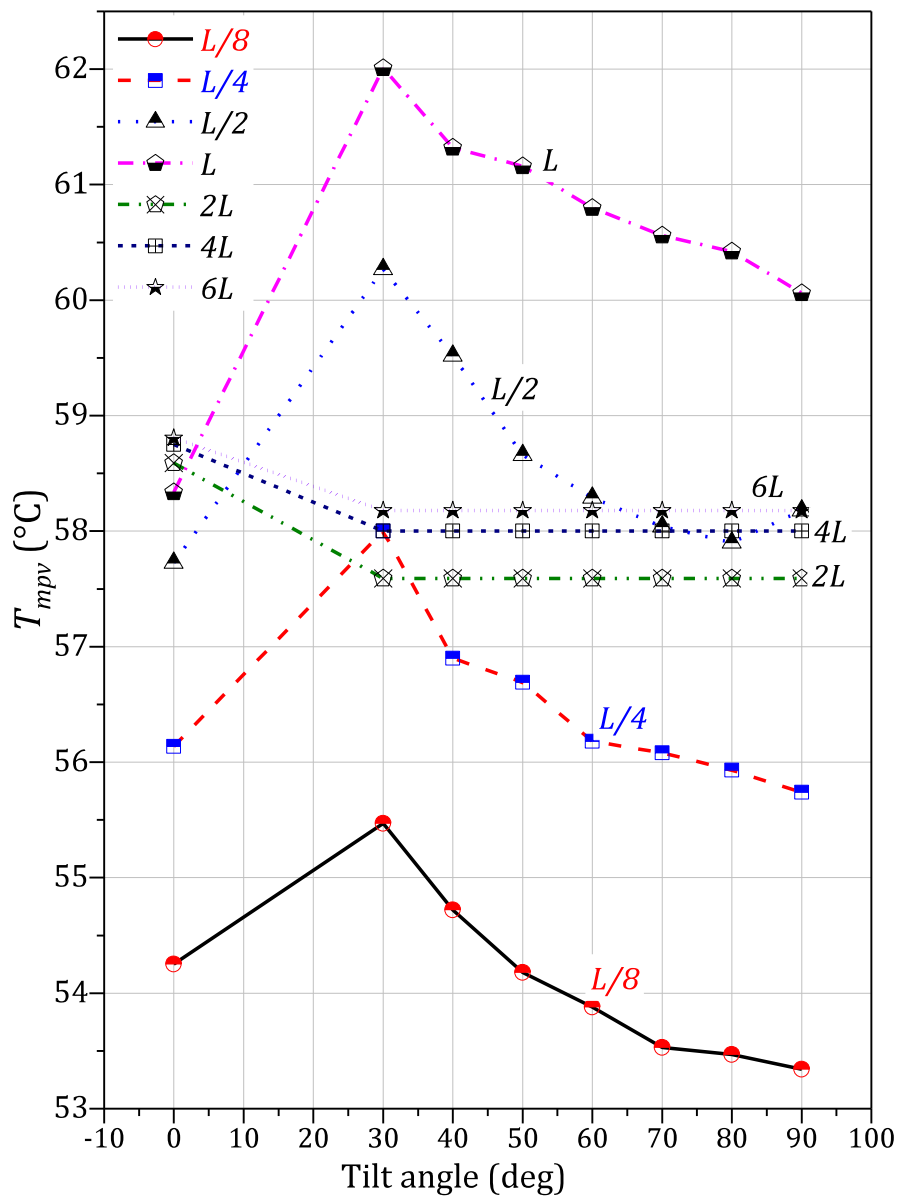


Fig. 5.23. Impact of length of PV module on its temperature under different inclinations in Fallujah on typical 31st Jan at 13:00.

In addition, Fig. 5.24 and Table 5.3 reveal the influence of the convective heat transfer coefficient at the bottom and top surfaces of the PV module on its temperature. In case of horizontal position ($\beta = 0^\circ$), the value of convective heat transfer coefficient at the top surface of the PV module (h_{top}) is greater than at bottom surface (h_{bottom}). This difference can be explained by the air flow at the bottom surface moving horizontally and being obstructed by the PV panel before ascending from their edges. While at the top surface, the flow moves freely and is driven by rising parcels of air from the top surface. This is replaced

by ascending warmer air from the ambient, and convective heat transfer coefficient is more efficient.

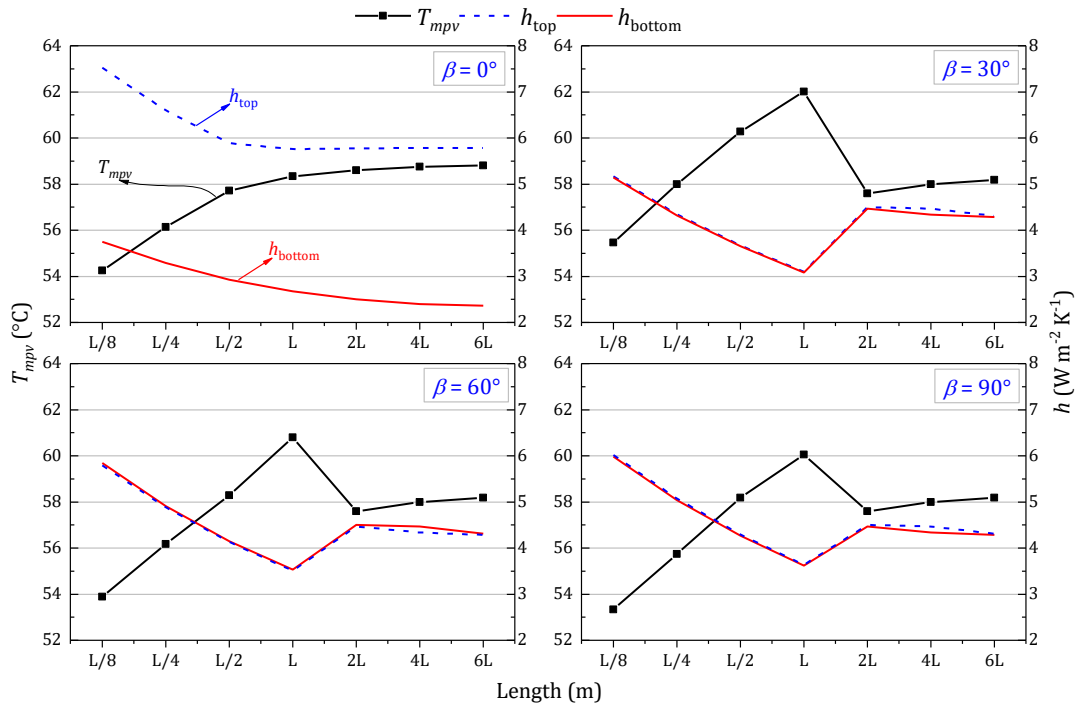


Fig. 5.24. Effect of convective heat transfer coefficients at the top and bottom surface of PV module on their temperatures under different inclinations in Fallujah 31st of on typical day Jan at 13:00.

Table 5.3. Effect of length and tilt angle on convective heat transfer coefficient top and bottom surface of PV model in Fallujah 31st of Jan at 13:00.

Tilt angle	L/8	L/4	L/2	L	2L	4L	6L
0 (h_{top})	7.52	6.6	5.89	5.76	5.773	5.78	5.783
0 (T_{mpv})	54.25	56.13	57.72	58.33	58.59	58.75	58.80
0 (h_{bottom})	3.75	3.29	2.93	2.672	2.502	2.4	2.363
30 (h_{top})	5.17	4.35	3.67	3.1	4.505	4.471	4.316
30 (T_{mpv})	55.47	58.00	60.27	62.01	57.59	58.00	58.18
30 (h_{bottom})	5.14	4.32	3.65	3.08	4.471	4.34	4.283
40 (h_{top})	5.47	4.59	3.89	3.286	4.505	4.471	4.316
40 (T_{mpv})	54.72	56.90	59.52	61.32	57.59	58.00	58.18
40 (h_{bottom})	5.43	4.56	3.86	3.265	4.471	4.34	4.283
50 (h_{top})	5.68	4.78	4.04	3.43	4.505	4.471	4.316
50 (T_{mpv})	54.18	56.69	58.66	61.16	57.59	58.00	58.18
50 (h_{bottom})	5.46	4.478	4.015	3.41	4.471	4.34	4.283
60 (h_{top})	5.84	4.91	4.15	3.53	4.505	4.471	4.316

Tilt angle	L/8	L/4	L/2	L	2L	4L	6L
60 (T_{mpv})	53.88	56.18	58.29	60.80	57.59	58.00	58.18
60 (h_{bottom})	5.79	4.88	4.13	3.505	4.471	4.34	4.283
70 (h_{top})	5.94	5.01	4.23	3.592	4.505	4.471	4.316
70 (T_{mpv})	53.53	56.08	58.04	60.56	57.59	58.00	58.18
70 (h_{bottom})	5.9	4.97	4.205	3.572	4.471	4.34	4.283
80 (h_{top})	6.00	5.06	4.277	3.632	4.505	4.471	4.316
80 (T_{mpv})	53.47	55.93	57.90	60.42	57.59	58.00	58.18
80 (h_{bottom})	5.96	5.03	4.25	3.61	4.471	4.34	4.283
90 (h_{top})	6.02	5.07	4.298	3.64	4.505	4.471	4.316
90 (T_{mpv})	53.34	55.74	58.18	60.06	57.59	58.00	58.18
90 (h_{bottom})	5.98	5.04	4.27	3.616	4.471	4.34	4.283

5.8 Conclusions

The following conclusions were from Chapter 5

- The convection currents in inclined and horizontal surfaces were weaker relative to the vertical surface thus, the rate of heat transfer is lower.
- In the case of inclined PV systems, the increase of the PV length enhances heat transfer rate up to length ($2L$). After this length, the PV temperature increase and convective heat transfer coefficients are reduced regardless of the inclination of the PV system.
- In the case of the horizontal surface, the convective heat transfer rate is lower, especially at the bottom surface of the PV system.
- The effect of inclination appears in the laminar region (short length) and dissipates after this region.
- Lower ambient temperature and higher insolation values lead to better PV performance, this can be seen by comparing both Muscat and Fallujah in June.
- The daylight period in Muscat is longer than Fallujah which allows for the accumulation of more solar energy per day and further increases in the solar PV power.
- Estimated weather condition values agree well with PVGIS-C and PVGIS-H data.
- Increasing the length of the PV panel might not be feasible or affordable because the PV array blocks and shade further arrays. Also, this might increase the cost of installation and price of base frame (in expense of cost and difficulty of installation).

In the next chapter the evaluation of solar air heaters for different configurations are carried out. Numerical and experimental methods are used in this evaluations.

CHAPTER 6 THERMO-HYDRAULIC PERFORMANCE OF MULTI-PASS SOLAR AIR HEATER

6.1 Introduction

In chapter 5, the performance of standard PV systems without active cooling was investigated. The aims of this chapter are: validate the CFD model used in this work and experimentally and numerically examine the effects of multi-pass configurations on the performance of solar air collectors. This chapter also studies the solar air heater with the PV panel removed. Removing the PV panel reduces the cost of experiments and simplifies the installation of measurement devices while still giving an indication of heat transfer enhancement owing to the multi-pass configuration. Finally, as a part of the objectives of this study, this chapter evaluates the effect of staggered and in-line arrangements of extended surfaces to ascertain the optimum arrangement to be used in the next chapter (Chapter 7).

Three different configurations are used in this study, namely, a parallel pass double duct with a co-current flow (model A), a parallel pass double duct with counter-current flow (model B), and a single duct double pass U-flow (model C). The CFD model has been developed using COMSOL Multiphysics v5.3a software to examine the thermal performance of these three types of SAH. The experimental measurement is conducted for the validation of model C (the best performing configuration, which is based on the CFD modelling results). The flow configuration in model C has three design modifications, namely: plain SAH without RAC (model C-I), SAH with RAC in-line turbulators arrangement (model C-II) and SAH with RAC in staggered turbulator arrangement (model C-III). To ensure accurate results and to evaluate pressure drop 2D and 3D CFD models are investigated and compared with empirical equations.

6.2 CFD modelling

6.2.1 System description

Sketches of the solar air collector designs used in this study are provided in [Fig. 6.1](#). The geometry comprises four main domains, namely: the solid domains of transparent glass (g) cover, aluminium (Al) and copper (Cu) absorber plates, and the fluid domain of air. The thicknesses of the transparent glass cover and absorber plates are 0.004 m and 0.001 m, respectively, and they are all 0.82 m wide and 1.92 m long. [Table 6.1](#) lists the physical properties of the material of these domains. The specifications of the CFD and experimental models are tabulated in [Table 6.2](#). Three design models are proposed and investigated in this study: firstly, a parallel pass double duct (model A), where airflows over and underneath the surfaces of Al absorber plate in the same direction (i.e. co-current flow), secondly, a parallel pass double duct (model B) is proposed but the flow pathways are in the opposite direction (i.e. counter-current flow) and thirdly, a U-flow model (model C) is proposed, where the airstream passes through the glass cover and the upper surface of Al absorber plate and reverses in the second pass through the lower surface of absorber plate and upper surface of copper bottom absorber plate (i.e. U-shape double-pass single duct flow).

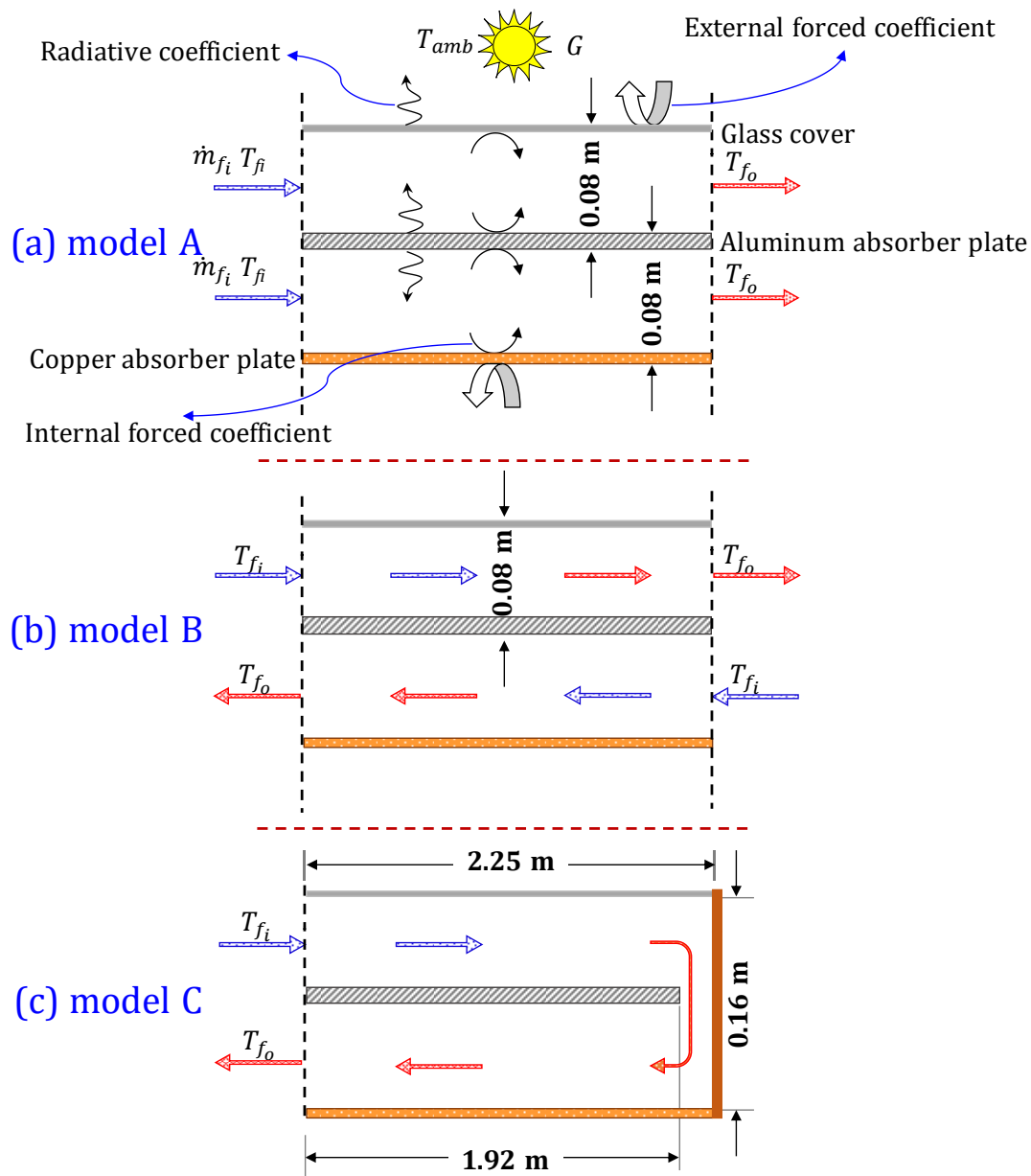


Fig. 6.1. Schematics of the three solar air collectors (CFD models): (a) Cross-section of parallel pass double duct of co-current flow (model A); (b) Cross-section of parallel pass double duct of counter-current flow (model B); (c) Cross-section of single duct double pass of U-flow (model C).

Table 6.1. Physical properties of the CFD domains.

Layer	k	ρ	c	ϵ
Glass (g)	1.4	2210	730	0.84
Aluminium (Al)	238	2700	900	0.67
Copper (Cu)	400	8960	385	0.65

Table 6.2. SAH specifications for the experimental and CFD models.

Item	Dimension	Unit
Collector length	2.25	(m)
U-turn length	0.33	(m)
Collector width	0.88	(m)
Overall depth flow	0.16	(m)
Upper depth flow	0.080	(m)
Lower depth flow	0.080	(m)
Inlet width	0.78	(m)
Inlet depth flow	0.098	(m)
Inlet area	0.07644	(m ²)
Outlet area	0.049	(m ²)
Width of absorber plate (m)	0.82	(m)
Length of absorber plate (m)	1.92	(m)
Exposed area (m ²)	1.57	(m ²)
Plate type	Flat plate	(m)

6.2.2 Conjugate heat transfer model

The governing equations for the air velocity $\vec{V}(x, y, z) = u, v, w$ and temperature T are based on the conservations of mass, momentum, and energy. In order to model the coupling between heat transfer in solid domains i.e. the absorber plates and fluid flow, the conjugate heat transfer module is used in the analysis. The turbulent flow $\kappa - \varepsilon$ model is accounted for, in relevance to its compatibility with high Reynolds numbers and weakly compressible flows [296].

The Reynolds-averaged Navier-Stokes (RANS) (temporal averaging) method is applied to solve turbulent flows. These equations were solved for the conservation of momentum for two-dimensional steady state flows, which can be written as:

$$\rho \left(\bar{u} \frac{\partial \bar{u}}{\partial x} + \bar{v} \frac{\partial \bar{u}}{\partial y} \right) = F_x - \frac{\partial \bar{p}}{\partial x} + \mu \Delta \bar{u} - \rho \left(\frac{\partial \overline{u'u'}}{\partial x} + \frac{\partial \overline{u'v'}}{\partial y} \right), \quad \text{Eq. 6.1}$$

$$\rho \left(\bar{u} \frac{\partial \bar{v}}{\partial x} + \bar{v} \frac{\partial \bar{v}}{\partial y} \right) = F_y - \frac{\partial \bar{p}}{\partial y} + \mu \Delta \bar{v} - \rho \left(\frac{\partial \overline{u'v'}}{\partial x} + \frac{\partial \overline{v'v'}}{\partial y} \right), \quad \text{Eq. 6.2}$$

where $\Delta \bar{u} = \frac{\partial^2 \bar{u}}{\partial x^2} + \frac{\partial^2 \bar{u}}{\partial y^2}$, and F_x and F_y are the external (volume) forces applied to the fluid domain. u, v and p are the momentary velocity components and pressure, respectively, \bar{u}, \bar{v}

and \bar{p} , are the time-averaged values and \acute{u} , \acute{v} and \acute{p} are the fluctuating velocities and pressure, respectively.

In turbulent flow, care should be taken with the flow adjacent to the wall, which is different from the free stream region. In order to reduce computational time, keeping within an acceptable level of accuracy, the k - ε model is used in this study. However, this model is not accurate or valid in the vicinity of walls. Therefore, flow regions in the vicinity of walls were described using wall functions [376]. The turbulence effects were modelled using the standard two-equation κ - ε model with realizability constraints. The default roughness is assumed sand roughness type with height 3.2 μm .

This model included two additional transport equations and two dependent variables: the turbulent kinetic energy (κ) and the turbulent dissipation rate (ε). The turbulent viscosity was modelled as:

$$\mu_T = \rho C_\mu \frac{\kappa^2}{\varepsilon}, \quad \text{Eq. 6.3}$$

where μ_T is the eddy viscosity. The transport equation for κ (turbulent kinetic energy) is [233]:

$$\rho \frac{\partial \kappa}{\partial t} + \rho(u \cdot \nabla)\kappa = \nabla \cdot \left(\left(\mu + \frac{\mu_T}{\sigma_\kappa} \right) \nabla \kappa \right) + P_\kappa - \rho \varepsilon. \quad \text{Eq. 6.4}$$

where u is the velocity component in the x-direction, and the production term is:

$$P_\kappa = \mu_T \left(\nabla u : (\nabla u + (\nabla u)^T) - \frac{2}{3} (\nabla u)^2 \right) - \frac{2}{3} \rho \kappa \nabla u. \quad \text{Eq. 6.5}$$

The transport equation for ε (eddy dissipation rate) [233] is:

$$\rho \frac{\partial \varepsilon}{\partial t} + \rho(V \cdot \nabla)\varepsilon = \nabla \cdot \left(\left(\mu + \frac{\mu_T}{\sigma_\varepsilon} \right) \nabla \varepsilon \right) + C_{\varepsilon 1} \frac{\varepsilon}{\kappa} P_\kappa - C_{\varepsilon 2} \rho \frac{\varepsilon^2}{\kappa}. \quad \text{Eq. 6.6}$$

In the steady state, the two time-dependent terms disappear from Eq. 6.4 and Eq. 6.6. The coefficients of the set of equations from Eq. 6.4 to Eq. 6.6 were obtained from experimental data [376]. These are $C_\mu = 0.09$, $C_{\varepsilon 1} = 1.44$, $C_{\varepsilon 2} = 1.92$, $\sigma_\kappa = 1.0$ and $\sigma_\varepsilon = 1.3$. For weakly compressible flow $\partial \rho / \partial p = 0$ and $\partial \rho / \partial \phi \neq 0$, where ϕ is other independent variable, such as time. The continuity equation, represented by the conservation of mass, is given in terms of time-averaged incompressible flow:

$$\nabla V = 0. \quad \text{Eq. 6.7}$$

The rate of heat added to the fluid particle owing to heat conduction across element boundaries is the general conduction equation with a heat source and translational motion of the parts.

$$\frac{D(\rho c T)}{Dt} \cdot \nabla T = \nabla \cdot (k_{x,y,z} \nabla T) + \dot{Q}_v, \quad \text{Eq. 6.8}$$

$$\nabla \cdot (k_{x,y,z} \nabla T) = \frac{\partial}{\partial x} \left(k_x \frac{\partial T}{\partial x} \right) + \frac{\partial}{\partial y} \left(k_y \frac{\partial T}{\partial y} \right) + \frac{\partial}{\partial z} \left(k_z \frac{\partial T}{\partial z} \right), \quad \text{Eq. 6.8a}$$

$$\frac{D(\rho c T)}{Dt} = \rho c \frac{\partial T(x,y,z)}{\partial t} + \rho c u \frac{\partial T}{\partial x} + \rho c v \frac{\partial T}{\partial y} + \rho c w \frac{\partial T}{\partial z}, \quad \text{Eq. 6.8b}$$

In these equations, ρ is the density, c is the specific heat, k is the thermal conductivity. u, v and w are the velocity components in x, y and z directions, respectively, \dot{Q}_v is the volume heat source (or sink). In the steady state with no internal energy conversion, two dimensions and non-moving parts, then Eq. 6.8 reduces to be the following expression (the Laplace equation) [353]:

$$\nabla \cdot (k_{x,y} \nabla T) = 0. \quad \text{Eq. 6.9}$$

In the fluid domain, the following details of the flow behaviour are considered for the solution to the heat transfer equation:

1. The energy transport is because of convection, either by the convective or conductive modes of heat transfer, depending on the thermal properties.
2. The viscous effects are taken into account for the production of fluid heating, which is often ignored although its impact is noticeable in viscous fluid motions.
3. The compressibility effect on producing heat is considered. The pressure work term contributes to the heat equation when the fluid density becomes temperature dependent.

Taking into account the abovementioned underlying-physics of the flow, as well as conduction, generalises the transient heat equation into the following expression [278]:

$$\rho c_{p_f} \left(\frac{\partial T}{\partial t} + V \nabla T(x, y, z) \right) + \nabla \cdot (k_f \nabla T) = Q_p + Q_{vd} + \dot{Q}_v, \quad \text{Eq. 6.10}$$

In which Q_{vd} is the viscous dissipation in the fluid domain, V is the velocity vector, Q_p is the work done by pressure gradients due to heating under adiabatic compression and thermo-acoustical phenomenon, which is relatively minor for a small Mach number,

$$Q_p = \alpha_p T \left(\frac{\partial p}{\partial t} + V \cdot \nabla p \right), \quad \text{Eq. 6.11}$$

$$\alpha_p = \frac{1}{\rho} \frac{\partial \rho}{\partial T}, \quad \text{Eq. 6.12}$$

where p is pressure, and for ideal gases, the thermal expansion coefficient α_p takes the simpler form:

$$\alpha_p = \frac{1}{T}. \quad \text{Eq. 6.13}$$

For a steady state problem, the temperature does not change with time and the terms with time derivatives disappear. The final governing equation is the equation of state. In reality, the density is a function for pressure and temperature,

$$\rho = \rho(p, T). \quad \text{Eq. 6.14}$$

For ideal gas, ρ is calculated using the law of state which is valid with Eq. 6.15.

$$\rho = p/RT. \quad \text{Eq. 6.15}$$

6.2.3 Boundary conditions

The solution domain of the 2D SAH (models A, B and C) is a rectangular duct on the x-y plane, bounded by the inlet, outlet and wall boundaries (as illustrated Fig. 6.1). The properties of the air, Al absorber plate material and Cu absorber plates are temperature dependent based on features built into the Comsol CFD software. The no-slip condition was assumed for the flow velocity at solid surfaces. The top wall boundary condition of the glass is subjected to UV and IR radiation, assuming that the glass was ultra-clear and had no absorption or emission and the insolation on the upper surface of collector is distributed uniformly across the surface [343]. The mean inlet velocity, inlet air temperature and insolation values, in comparison between model C (2D CFD model) and model C-I (experimental data), are detailed in Table 6.3. Uniform air velocity is introduced at the inlet

assuming a fully developed flow. At the exit, a pressure outlet boundary condition is specified at a fixed pressure of 101325 Pa.

According to [377] the Reynolds number was set between 10000 and 20000. In detail, the boundary conditions were as follows.

- Along the back surface of the collectors, $0 \leq x \leq L$; $y = 0$,

$$u = 0, v = 0, (-k \nabla T_{bs}) = h (T_{bs} - T_{amb}), V_w = 3 \text{ m s}^{-1}. \quad \text{Eq. 6.16}$$

- Along the upper glass surface, $0 \leq x \leq L$, $y = \delta_{D1} + \delta_{D2}$, $\delta_{D1} = \delta_{D2} = 0.08 \text{ m}$,

$$u = 0, v = 0, (-k \nabla T_g) = h (T_g - T_{amb}), V_w = 3 \text{ m s}^{-1}. \quad \text{Eq. 6.17}$$

- Along the upper surface of Al absorber plate, $0 \leq x \leq L$; $y = \delta_{D1}$,

$$u = 0, v = 0, G = 1000 \text{ W m}^{-2}. \quad \text{Eq. 6.18}$$

- At the inlet of the duct:

Model A: for lower inlet duct, $x = 0$, $0 \leq y \leq \delta_{D1}$, while for upper inlet, $x = 0$, $\delta_{D1} \leq y \leq \delta_{D2}$,

$$u = \bar{V}, v = 0, T = T_{fi}, \dot{M} = \dot{M}_{fi}. \quad \text{Eq. 6.19}$$

Model B: for lower inlet duct, $x = L$, $0 \leq y \leq \delta_{D1}$, while for upper inlet, $x = 0$, $\delta_{D1} \leq y \leq \delta_{D2}$.

$$u = \bar{V}, v = 0, T = T_{fi}, \dot{M} = \dot{M}_{fi}. \quad \text{Eq. 6.20}$$

Model C: for inlet duct, $x = 0$, $\delta_{D1} \leq y \leq \delta_{D2}$

$$u = \bar{V}, v = 0, T = T_{fi}, \dot{M} = \dot{M}_{fi} + \dot{M}_{fi} \quad \text{Eq. 6.21}$$

- At the outlet duct: for all three models $p_{out} = 0$ (gauge pressure, or 101325 Pa absolute pressure).

Table 6.3. Experimental results for plain designs that are used in the validation between model C (2D CFD model) and model C-I (experimental model).

time	T_{fi}	\bar{V}	G
9:00	16.9	1.26	600
10:00	20.9	0.96	671
11:00	21.9	0.96	886
12:00	24.4	1.03	996
13:00	23.9	0.99	1030
14:00	25.7	1.03	976
15:00	24.2	1.07	760
15:30	24.3	1.06	466

In order to simulate a realistic incident solar radiation, an External Radiation Source sub-node was applied to contribute to the incident radiative heat flux on the solar spectral bands (U.V, visible and I.R radiation). The surface-to-surface radiation model is used to simulate the thermal radiation exchange between all the surfaces which are governed by Eq. 6.22, assuming that the fluid and the glass cover were non-participating, i.e., they do not absorb, emit, or scatter any radiation. This is valid since the glass cover is ultra-clear and the thickness is less than 6 mm [279].

$$q_{rad} = A_s (\alpha G - \varepsilon E_b) = \varepsilon \sigma (T_s^4 - T^4), \quad \text{Eq. 6.22}$$

where E_b is the surface emissive power (W m^{-2}), estimated as

$$E_b = \sigma T_s^4. \quad \text{Eq. 6.23}$$

Forced convective boundary conditions were applied to the top surface of the glass cover and the bottom surface of the collector. The average wind velocity value was assumed as 2.7 m s^{-1} (see Fig. 6.2) based upon observation data agreeing with [378, 379]. To estimate the forced convective heat transfer coefficients for these two surfaces, the following empirical correlations are used [279]:

$$h_{f(g-amb)} = \frac{2k}{L} \frac{0.3387 \text{Pr}^{1/3} \text{Re}_L^{1/2}}{\left(1 + \left(\frac{0.0468}{\text{Pr}}\right)^{2/3}\right)^{1/4}} \{\text{for } \text{Re}_L \leq 5 \times 10^5\}, \quad \text{Eq. 6.24}$$

$$h_{f(g-amb)} = \frac{2k}{L} \text{Pr}^{1/3} \left(0.037 \text{Re}_L^{4/5} - 871\right) \{\text{for } \text{Re}_L > 5 \times 10^5\}, \quad \text{Eq. 6.25}$$

where $h_{f(g-amb)}$ is forced convective heat transfer coefficient at the upper and bottom surfaces of the collector, $Re_L = \frac{V_w L_c}{\nu}$ is a function of the characteristic length (L_c), which is equal to the length of the collector (L).

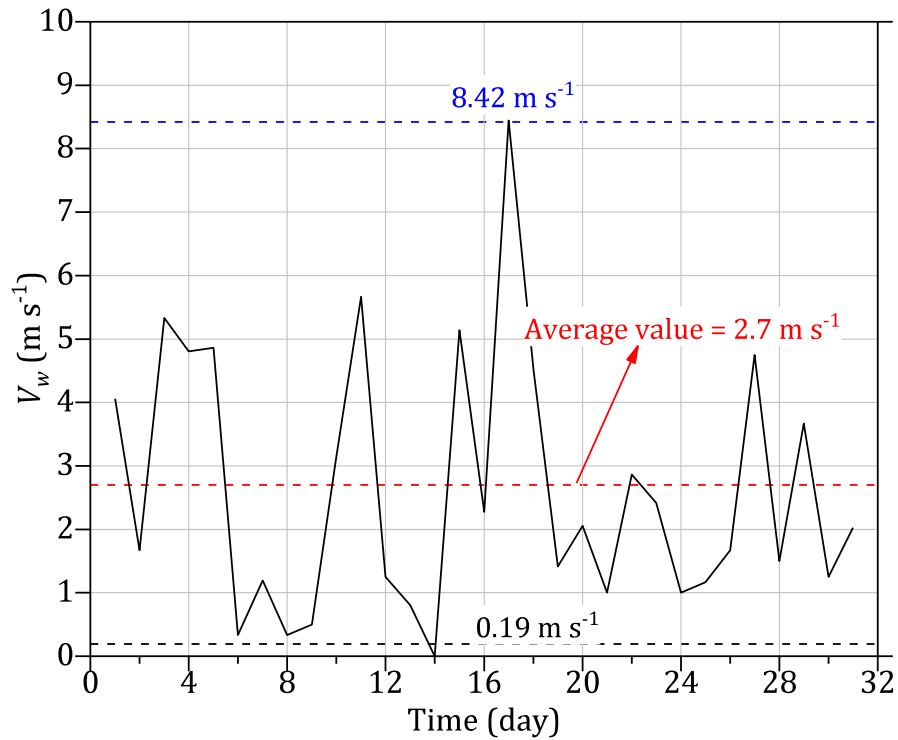


Fig. 6.2. Wind data observation for March in Ramadi city, Iraq.

6.2.4 Mesh independence study

Generally, computational domains can be meshed using structured (quad element type), unstructured (i.e. Triangular element type), or hybrid (i.e. combination of unstructured and structured) elements. The choice of mesh element type depends on the physical characteristics (e.g. turbulent or laminar flows), and the geometry of the problem (e.g. curved or straight). The examination of the impacts of mesh type and density on the solution accuracy, computational efficiency, and convergence are investigated. Three independent mesh tests were carried out for model C (see Table 5.1), starting from extremely coarse to extremely fine element sizes. The interface between solid and fluid domains (thermal and hydrodynamic boundary layers) and the U-turn region (i.e. the region when the air flows from upper channel to lower channel) was discretised for a fine mesh adjustment as listed in Fig. 6.3.

Table 6.4. Structured mesh independent test analysis (free quad elements) for model C, using the boundary conditions $\bar{V} = 2.254 \text{ m s}^{-1}$, $\text{Re} = 20000$, $G = 1000 \text{ W m}^{-2}$ and $T_{fi} = 35 \text{ }^\circ\text{C}$.

Trial No	Refinement step	No of Elements	Time (s)	RAM (GB)	η_{th}	Δp (Pa)	MEQ	RT
1	Extremely coarse (quad)	880	27	1.63	50.156	8.351	1	0.001
2	Very coarse (quad)	2024	24	1.83	51.927	10.140	1	0.001
3	less coarse (quad)	4110	38	1.96	52.116	10.390	1	0.001
4	Coarse (quad)	6764	61	2.22	52.203	10.355	1	0.001
5	Normal (quad)	13150	141	2.69	52.252	10.336	1	0.001
6	Fine (quad)	22440	250	3.33	52.238	10.339	1	0.001
7	Very Fine (quad)	35948	473	3.86	52.243	10.335	1	0.001
8	Extremely fine (quad)	112770	2907	7.07	52.271	10.344	1	0.001

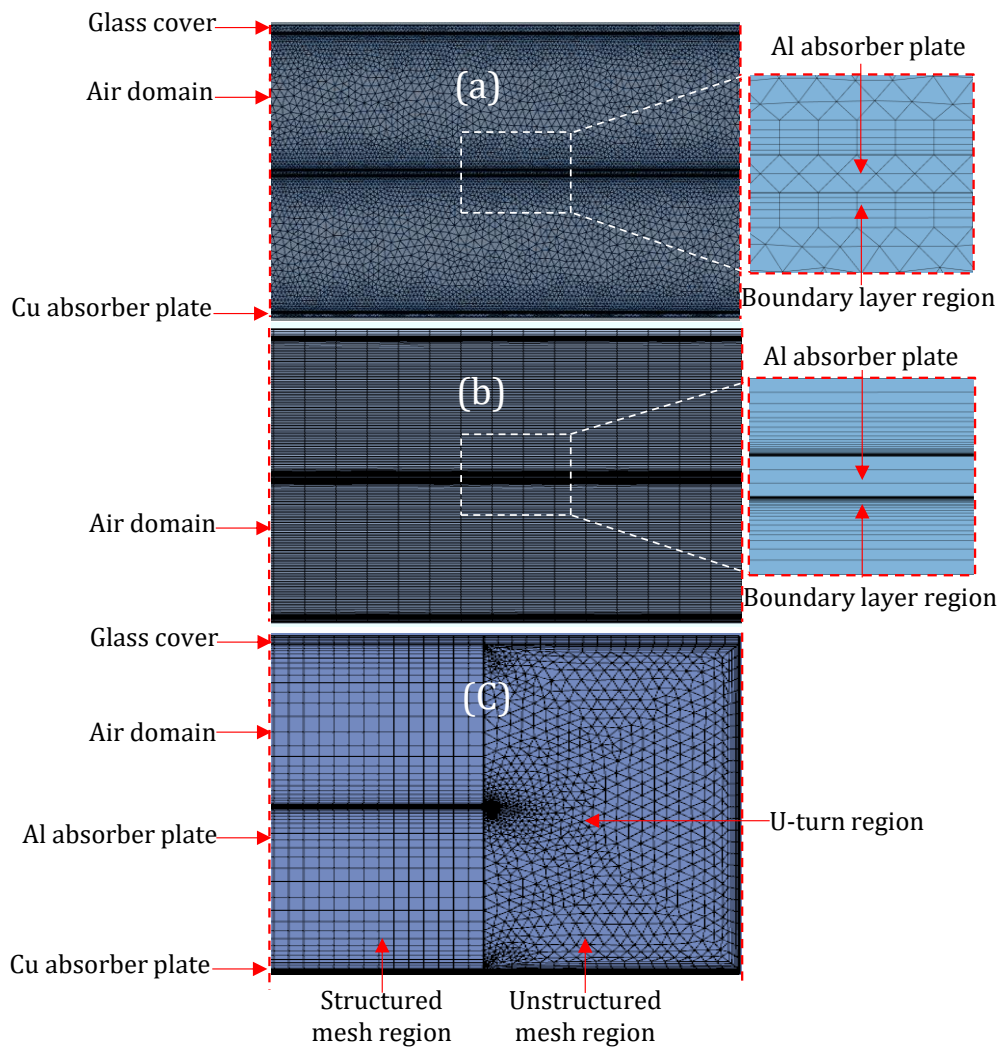


Fig. 6.3. System meshing, using (a) unstructured, (b) structured, and (c) hybrid meshes.

The third mesh provided segmentation of the system into two regions by using free triangular elements for the U-turn region and free quad elements for the other regions where the mesh could be more compatible in terms of the shape of the geometry.

As can be observed in Table 5.1 and Table 6.5, the minimum element quality (MEQ) of structured mesh is much higher than that of the unstructured mesh, while the RAM (random access memory) computational time and the number of elements are significantly reduced using the structured mesh. Thus, this test has actively contributed to reducing the running time and RAM, respectively, from 976 sec and 4.1 GB (using unstructured mesh) to 141 sec and 2.69 GB (using structured mesh).

Table 6.5. Unstructured mesh independent test analysis (free triangular elements) for model C, using the boundary conditions $\bar{V} = 2.254 \text{ m s}^{-1}$, $\text{Re} = 20000$, $G = 1000 \text{ W m}^{-2}$ and $T_{fi} = 35 \text{ }^\circ\text{C}$.

Trial No	Refinement step	No of elements	Time (s)	RAM (GB)	η_{th}	Δp (Pa)	MEQ	RT
1	Extremely coarse (Triangular)	17011	325	1.76	55.593	9.5503	0.4432	0.001
2	Very coarse (Triangular)	33649	401	3.4	55.946	10.159	0.2183	0.001
3	less coarse (Triangular)	41943	534	3.96	55.960	10.279	0.2040	0.001
4	Coarse (Triangular)	45388	845	4.05	55.929	10.260	0.1961	0.001
5	Normal (Triangular)	48756	976	4.1	55.923	10.352	0.1795	0.001
6	Fine (Triangular)	58256	796	4.2	55.907	10.362	0.1853	0.001
7	Very Fine (Triangular)	105094	2870	5.51	55.929	10.436	0.1750	0.001
8	Extremely fine (Triangular)	264432	21888	13	55.891	10.439	0.1773	0.001
Hybrid	Fine	77484	1481	2.82	55.873	10.240	0.1624	0.001

6.3 Experimental Setup

The experimental set up was designed to be tested outdoors for data collection. The flow pattern selected was a single duct double pass (U-flow). The RACs were installed on the top and bottom of the absorber plate in front of the airflow, which was completely open from two sides for direct exposure to airflow. The schematic illustration of the double-flow SAH set up is shown in Fig. 6.4 (a, b, c and d). In this study, three types of absorber plates were used in order to compare the thermal performance of SAH with and without RAC, namely, SAH without RAC (model C-I), SAH with RAC in the in-line pattern (model C-II) and SAH with RAC in a staggered pattern (model C-III).

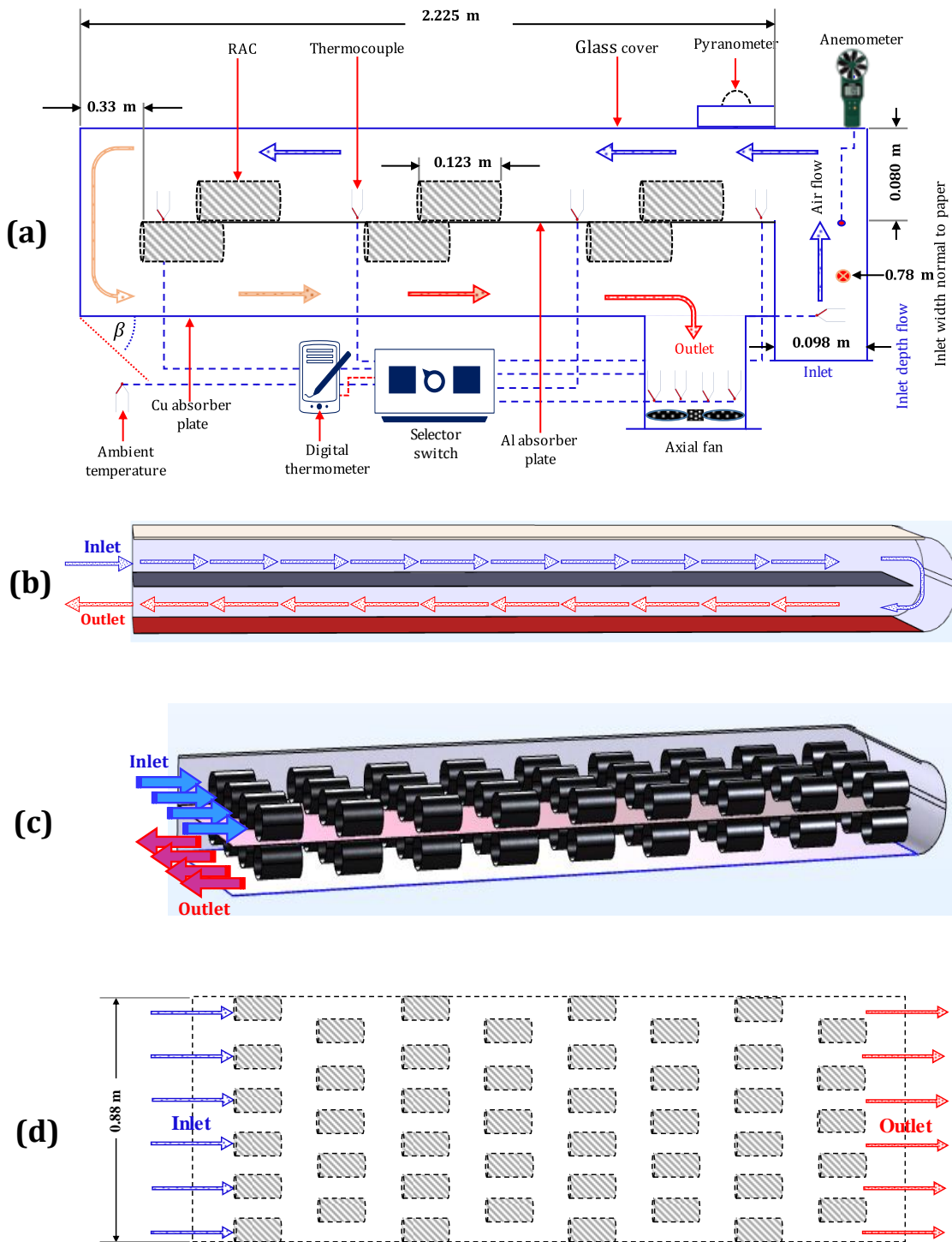


Fig. 6.4. Schematic of single-duct double-pass (U-flow) solar air collector. (Please note that the figure is not to scale), showing: (a) The cross-section area of solar air collector including RACs; (b) SAH without RACs (model C-I); (c) Cross-section of SAH with in-line pattern (model C-II). The number of RACs is six across the width and ten along the length; and (d) Section top view of SAH with staggered configuration (model C-III). The number of RACs is seven for the first row and six for the second row across the width.

6.3.1 Geometry and design considerations

The dimensions of the Al and Cu absorber plates were 1.92 m long, 0.82 m wide and 0.001m in thickness. A single glass sheet of 4 mm thickness was fixed above the Al absorber plate as a transparent glass cover, with a gap (depth flow) of 0.08 m. This solar air collector consisted of two passes; the airflow in the first pass (between the glass cover and the Al absorber plate) and the airflow reverses in the second pass (between the two absorber plates) to form a U-shape flow. The copper absorber plate was positioned on the bottom duct. All material properties and the specifications of these collectors are listed in [Table 4.2](#) and [Table 6.2](#). The ambient air was supplied by a low-pressure axial fan with a maximum power of 18 W, which was placed at the outlet of the collectors. The RAC capacity is 330 ml, with 0.123 m in length and 54 mm diameter.

- In achieving a feasible, affordable and optimal design of the solar air collector, different considerations were taken into account.
- The frame of the channel duct was fabricated from a compact wood panel (0.02 m thickness) instead of using galvanized steel that should cover with glass wool insulation or other type insulation. This potentially reduced the weight and cost of the collector, decreased the edge heat transfer losses and allowed flexibility to install instrumentations such as thermocouples.
- In order to maximize the incident solar radiation, the tilt angle ($\beta = 27^\circ$ [\[379\]](#)) was considered for this study and the solar collectors were facing the south [\[380\]](#).
- To ensure perfect contact between the RAC and Al absorber plate, two metallic washers secured with screws were placed on the contact area between the RAC and Al absorber plate.
- In order to set the system as close as to real conditions, the effect of entrance length was neglected. This is because of the difficulty in the installation, operating and architectural or structural requirements. Also, from the hydrodynamic and thermodynamic boundary layer point of views, the convective heat transfer coefficient in the developing region is higher than the developed ones [\[381\]](#).
- In order to ensure that the flow is entering in a turbulent state, the depth of flow (δ_D) was selected according to the optimisation criteria at different flowrates, suggested by [\[377\]](#) [\[50\]](#) as presented in [Eq. 6.26](#). \mathcal{L} is the airflow path length from inlet to outlet, and thus, $\mathcal{L} = 2L$ for model C-I and model C (U-flow shape) and $\mathcal{L} = L$ for other models, in the range:

$$(\mathcal{L}/D_h)_{\text{optimum}} \geq 30. \quad \text{Eq. 6.26}$$

- In order to improve the absorption and emissions, and to reduce the reflectivity (optical features) for the absorber surfaces, the Al and Cu absorber plates and RAC were roughened. This was made using coarse sandpaper measuring 40 to 60 grit and painted with black chrome nonselective coating for affordability and availability.
- In order to mount the collector, a base frame was made of Al to carry the collector and change the tilt angle for matching the maximum incident solar radiation.

6.3.2 Measurements uncertainty

For each collector, ten K-type thermocouple sensors were used; four of them were distributed equally along the flow direction on the top surface of the Al absorber plate. Five well-insulated thermocouples were installed at the inlet and the outlet collectors, one in the inlet and the rest in the outlet. Also, the air ambient temperature was measured in the shaded area using ventilated wooden Stevenson screens criteria [382], above the ground 1.5 m and behind the collector. All sensors were connected to a digital thermometer (as shown in Fig. 6.4). The thermocouples were calibrated with an average error of 1.1 °C. The inlet air velocity was measured by a multifunctional anemometer device a Testo Vane Anemometer with an uncertainty of $\pm 2\%$. The measurement range of the anemometer is 0.5-25 m s⁻¹ with a resolution of 0.1 m s⁻¹ [383].

An accurate and reliable solar meter type CMP3 pyrometer was used to measure the incident solar radiation [384]. The capability of this tracker is to measure direct, diffused and global radiation with a resolution of 0.5 Wm⁻². This meter was installed parallel to the collector, and the values were validated with estimated values in [50] with a high level of conformity (PPMCC = 0.95 and RMSE = 9.32) as shown in Fig. 6.5. Care was taken to avoid the accumulation of dirt on top of the glass surface, with regular cleaning.

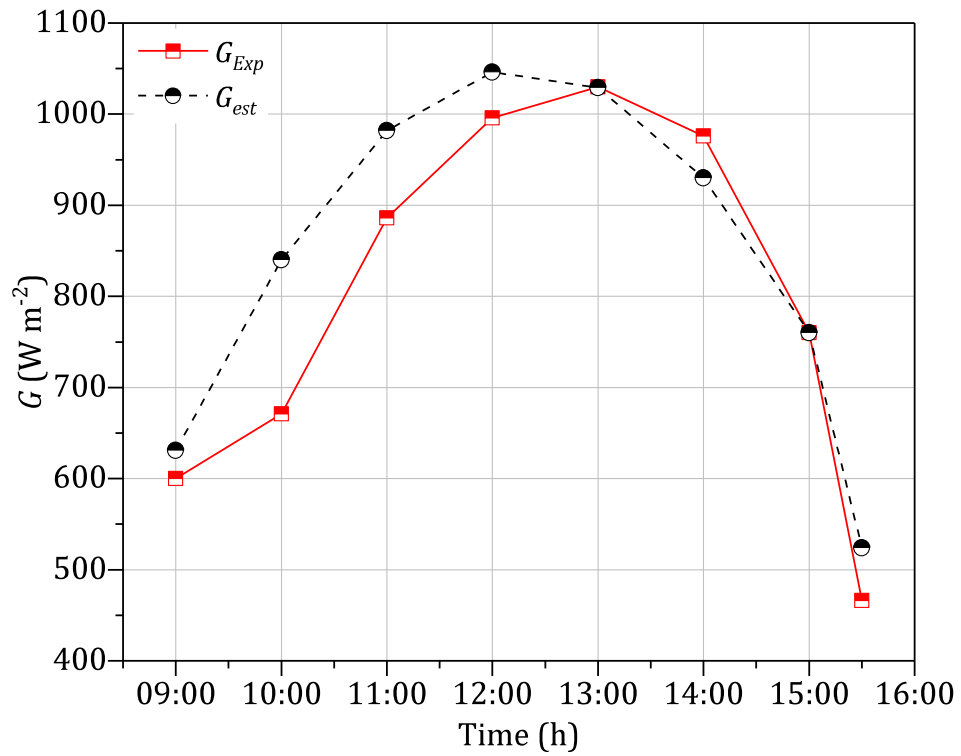


Fig. 6.5. Intensity of solar radiation (G) versus time recorded in 23 February, showing the experimental [384] and estimated [50] data.

6.4 Thermo-hydraulic performance

The evaluation of the thermo-hydraulic performance of solar air collector was presented in Section 3.3.3. This evaluation includes a number of criteria such as pressure drop, effective thermal efficiency and fan power consumption.

6.5 Results and discussion

6.5.1 Thermal performance examination of U-flow shape design

The predictions of the three models reveal that the double pass single duct solar air collector (model C) has a higher efficiency than other types of flow arrangements over the range of Re numbers investigated and these are illustrated in Fig. 6.6.

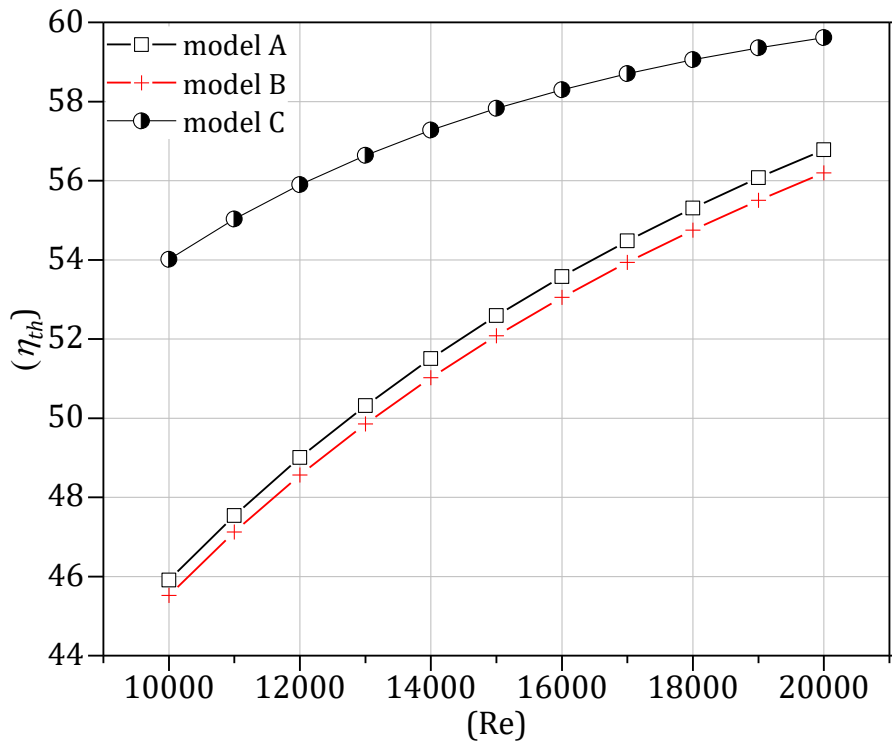


Fig. 6.6. Thermal efficiency versus Reynold number under turbulent condition regime for co-current flow (model A), counter-current flow (model B) and U-flow (model C) CFD models.

In Fig. 6.6, the average thermal efficiencies are presented for three models, namely: A the parallel pass double duct (co-current), B the parallel pass double duct (counter-current flow), and C the single duct double pass (U-flow) for the flow range $10000 \leq Re_D \leq 20000$. The average thermal effective efficiency of the U-flow model is the highest (up to 57.42 %), compared to the co-current (up to 52.1%) and counter-current (up to 51.6%) efficiencies $10^3 \leq Re_D \leq 2 \times 10^3$ over the full range of Re numbers. This is owing to the length of air path is longer than the other models, which in turn leads to accumulation of heat along the flow path increasing the outlet air temperature. It should be emphasised that improving the thermal efficiency of a certain model is made on the expense of power fan effectiveness. For instance, the U-flow model requires a fan power of about 15.7 times more than that consumed for the other two models. The average fan power consumption of models A and B is 0.364 W, each, while for model C is 6.097 W. The numerical values of pressure drop for the three models are illustrated in Fig. 6.7. In this figure, there is a marked increase in pressure drop for U-flow model (model C) compared to the other two models. This is because of the induced flow separation in the U-turn near the bend and the swirling secondary flow that occurs because of the imbalance of centripetal forces as a result of the

curvature of the duct centreline. The U-flow model (C), however, offers the highest efficiency compared to the other two models (A and B).

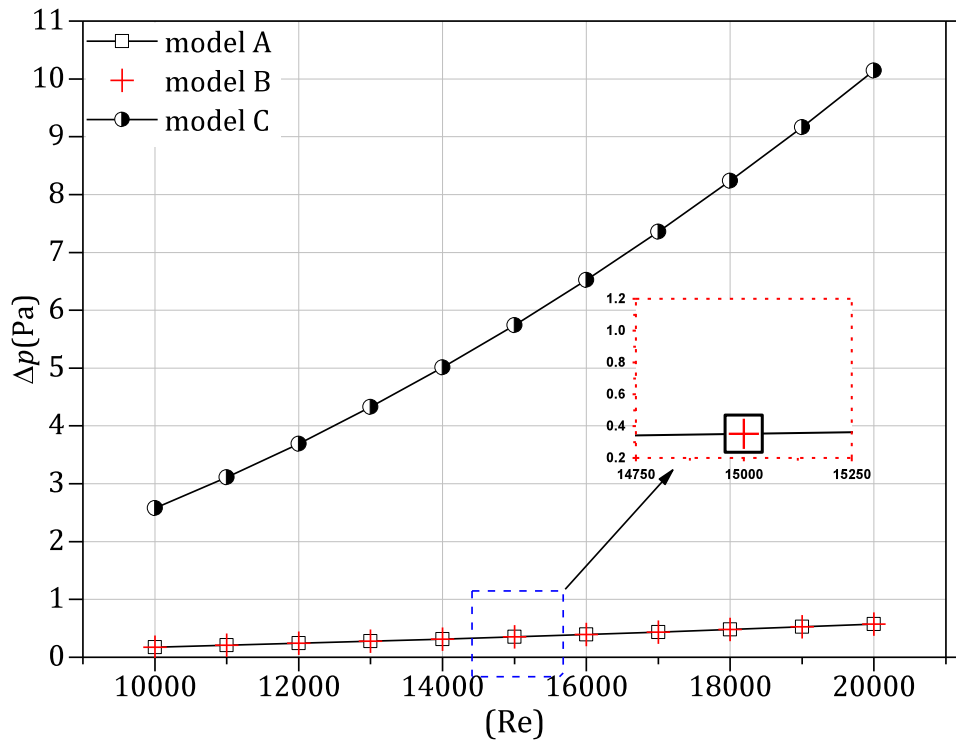


Fig. 6.7. Pressure drop in flow duct between the inlet and the outlet for (co-current flow, model A), (counter-current flow, model B) and (U-flow, model C) CFD models.

6.5.2 Experimental results

The experiments were conducted in Ar-Ramadi City, Al-Anbar province – the western region of Iraq (longitude: 33.25°N; latitude: 43.18°E) under clear sky conditions on 23rd February (model C-I) and 27th February (model C-II) and 2nd March (model C-III) between 09:00 hr and 15:30 hr. The average mass flow rates were 0.096 kg s⁻¹ for model C-I, 0.088 kg s⁻¹ for model C-II and 0.0819 kg s⁻¹ for model C-III. The solar radiation versus time for the three different dates are measured using a solar tracker device [384], and presented in Fig. 6.8. The average hourly values for the measured insolation against time during January–August are verified using data in [379] and presented in Fig. 6.9.

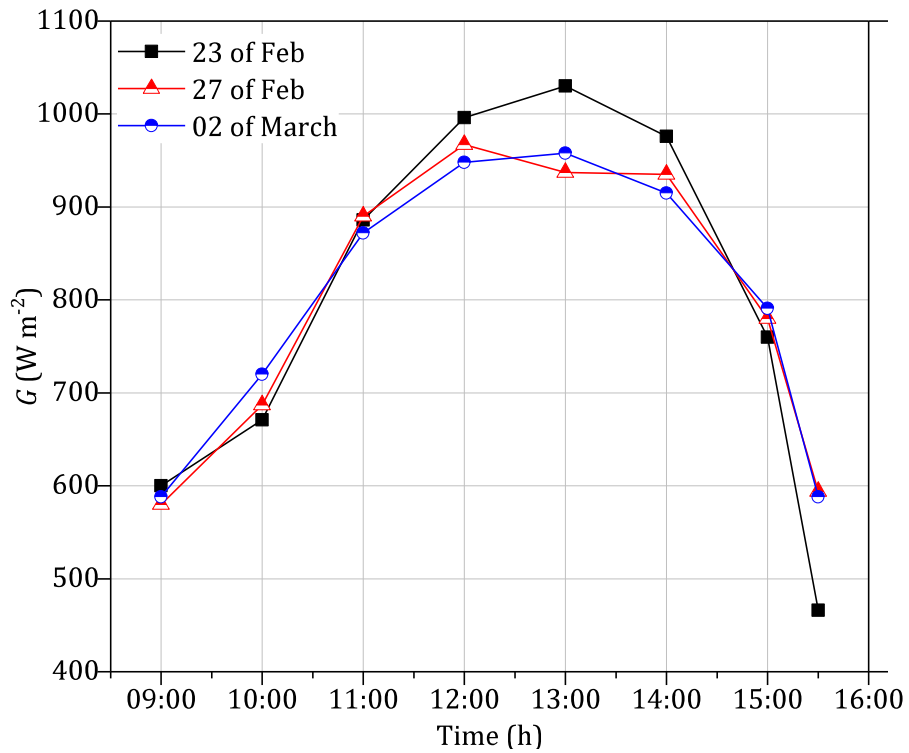


Fig. 6.8. Intensity of solar radiation versus time recorded on three different dates.

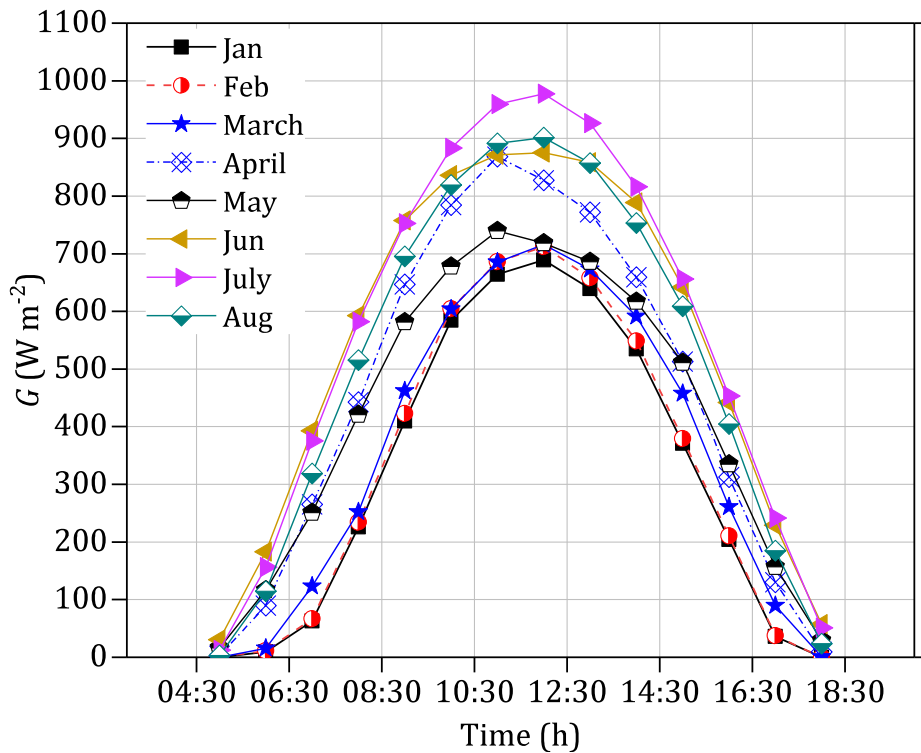


Fig. 6.9. Intensity of solar radiation versus 4:30 to 18:30 hours (hrs) recorded during January–August.

In Fig. 6.9, the intensity of solar radiation in July was the highest; while in January, it was the lowest. Also, the solar intensity increases gradually from sunrise to reach a peak value at the solar noon (12:00 hr) then reduces until sunset. However, the values of insolation were higher than the average values for the whole month. For example, the insolation values of three days at 12:00 hr (see Fig. 6.8) were in the range 948 to 996 W m⁻²; while the average insolation for the whole month was less than 700 W m⁻² (see Fig. 6.9). This is owing to the three data values being taken on an inclined collector angle (β) of 27° for that specific day; while the solar tracker device was measured on a horizontal surface [384]. This difference can also be attributed to the fact that fluctuation of weather conditions is affected by several factors, such as dust and cloud. It should be emphasised that the three tested models were exposed to almost the same weather conditions.

Fig. 6.10 presents the influence of ambient temperature and incident solar radiation on the outlet air temperature for three models: (a) Single duct double pass (solar air collector without cans) (model C-I); (b) Single duct double pass (solar air collector with in-line cans arrangement) (model C-II); and (c) Single duct double pass (solar air collector with staggered cans arrangement) (model C-III). The trends in this figure reveal that the outlet temperature generally followed the ambient temperature and incident solar radiation closely. At certain times, however, the outlet temperature acted independently from the incident solar radiation or inlet temperature. For instance, in Fig. 6.10a, the outlet temperature is slightly increased despite a dramatic decrease in the incident solar radiation value. This is because the ambient temperature at 15:30 hr remained constant and was dominant relative to the low and decreasing solar radiation intensity.

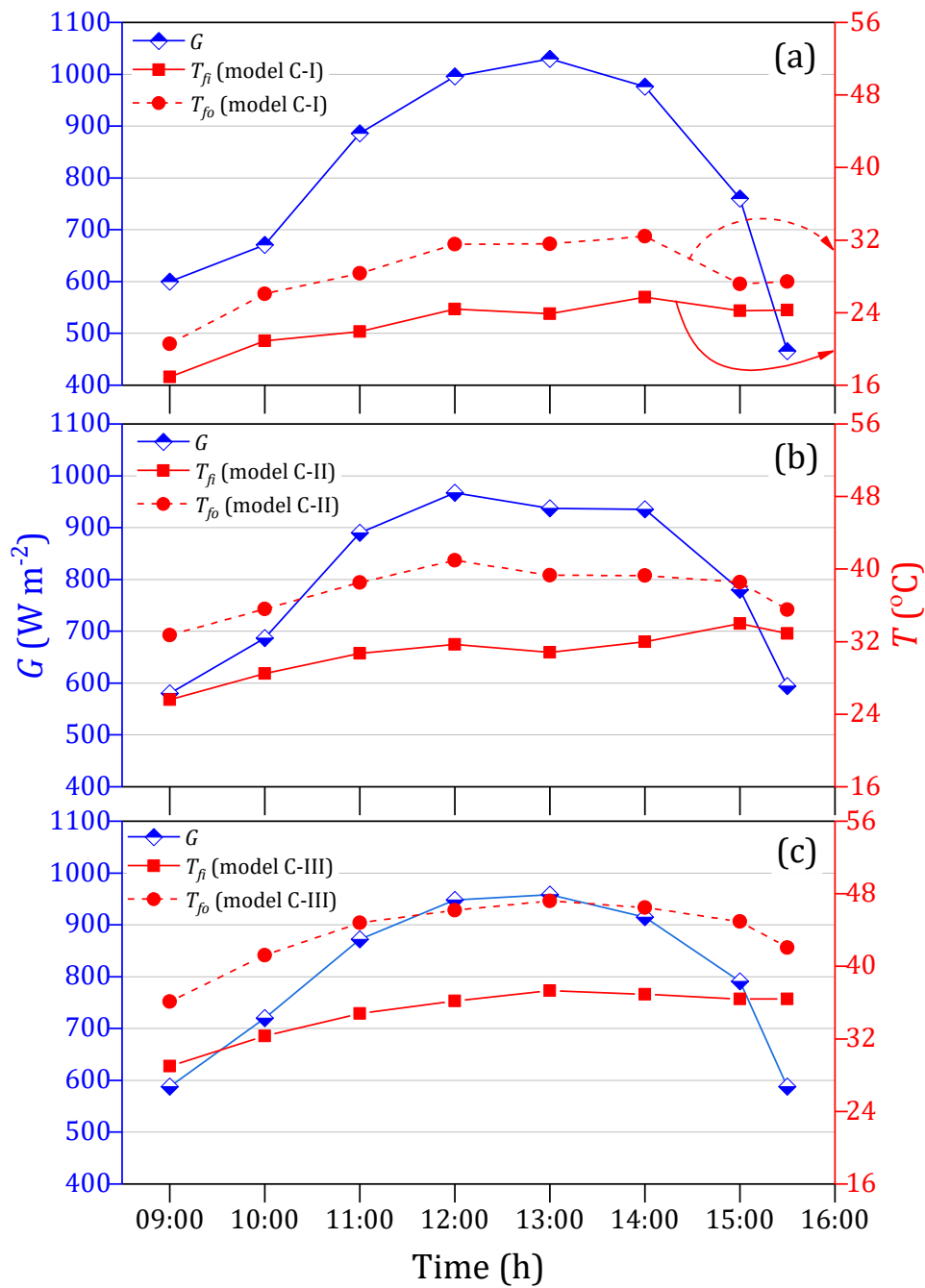


Fig. 6.10. Collector air temperatures and incident solar radiation versus 09:00–16:00 hrs for the three models, C-I (a), C-II (b), and C-III (c).

The experimentally measured thermal efficiencies of the three different models (model C-I, model C-II and model C-III) versus time are presented in Fig. 6.11. It is found that the efficiency increased with increasing contact surface area (i.e. using RACs). The average thermal efficiencies of the staggered, in-line, and plain models are 60.2%, 53.1%, and 49.4%, respectively. The staggered arrangement offers secondary flow development which has enhanced its thermal efficiency. In contrast to the latter effect, fewer vortices were found in

the less efficient in-line configuration although the number of RAC and the mass flowrate were higher than those of the staggered arrangement. No vortices were generated in the plain model; hence, the lowest thermal efficiency.

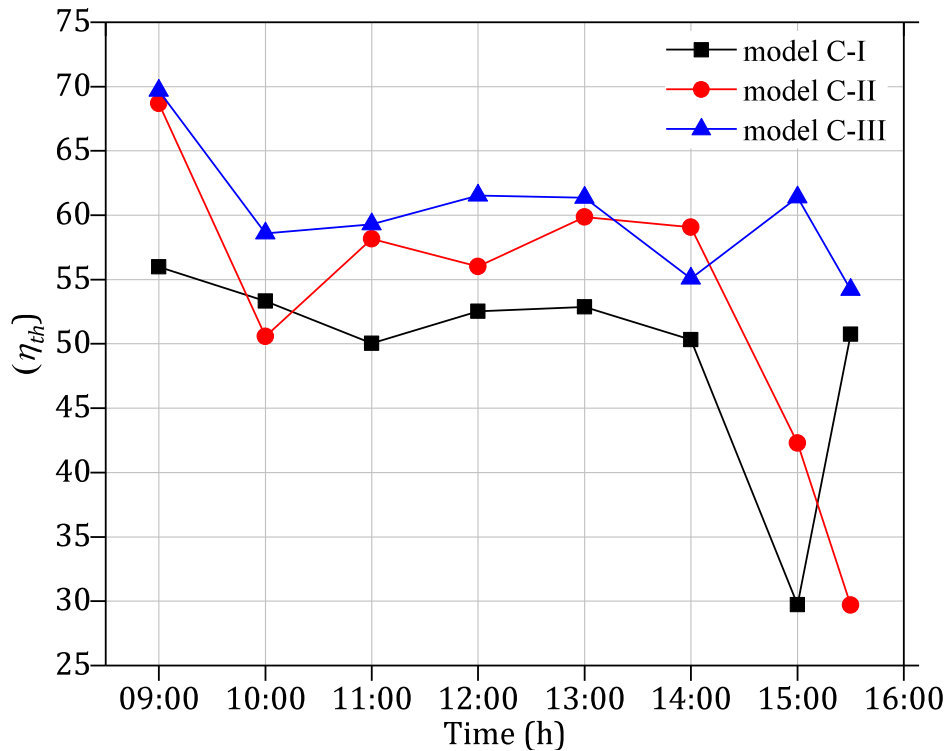


Fig. 6.11. Thermal efficiencies versus 09:00–16:00 hrs for three configurations, model C-I (plain), model C-II (in-line) and model C-III (staggered).

Fig. 6.12 presents the thermal efficiency, inlet air temperature, inlet velocity and intensity solar radiation values versus time for a double duct one pass solar air collector with the staggered RAC design (model C-III). The thermal performance of model C-III is the best. The thermal efficiency is dependent on the incident solar radiation and inlet air temperature throughout the day. Irregular behaviour occurs at 10:00 hr, when the thermal efficiency drops with increasing irradiation and inlet air temperature. This is attributed to the sudden drop in inlet air velocity which affected the thermal efficiency more than the other two parameters. Additionally, the inlet air velocity at 10:00 hr was the lowest during the day.

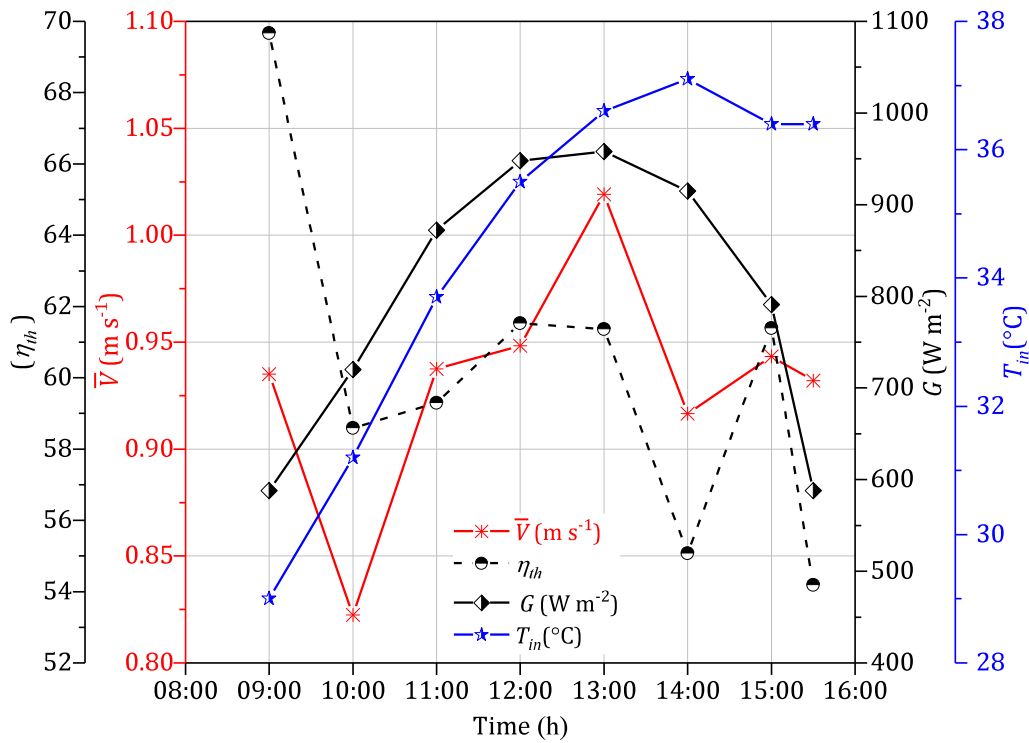


Fig. 6.12. Thermal efficiency, the intensity of solar radiation, inlet air temperature, and inlet air velocity versus 09:00–16:00 hrs for model C-III (staggered arrangement).

The daily average air temperature difference δT_{air} , Al absorber plate temperature T_p and collector thermal efficiency η_{th} are presented in Table 6.6. The maximum values of δT_{air} , T_p and η_{th} occur for the staggered model (model C-III). A higher air temperature difference of 8.68°C is achieved using the staggered model, compared to 7.24°C and 5.60°C for heaters with RACs arranged in the in-line pattern and plain plate heater, respectively. The average absorber plate temperatures are 47°C, 43.73°C and 40.94°C for the RAC staggered, in-line and plain heater configurations, respectively. Also, the thermal efficiency of SAH with the RAC arranged in a staggered pattern is about 60.2% which is the highest.

Table 6.6. Daily average of δT_{air} , T_p and η_{th} .

model	δT_{air} (K)	η_{th}	T_p (°C)	Re_{Dh}
C-I	5.3	49.4	40.9	9970
C-II	7.1	53.1	43.7	9009
C-III	8.45	60.2	47.1	8290

6.5.3 Comparison between numerical and experimental results

Statistical analysis was performed to quantify the level of conformity between the numerical (X_i) and experimental results (Y_i) of the double pass solar air heater (model C-I). The root-mean-square error (RMSE) and the Pearson product-moment correlation coefficient (linear correlation) (PPMCC) [121] were evaluated for this analysis. The RMSE can be written in the following expression:

$$\text{RMSE} = \sqrt{\frac{\sum_{i=1}^N (e_i)^2}{N}}, \quad \text{Eq. 6.27}$$

where $e_i = \frac{X_i - Y_i}{X_i} \times 100$, and the PPMCC is expressed as:

$$\text{PPMCC} = \frac{N(\sum_{i=1}^N X_i Y_i) - (\sum_{i=1}^N X_i)(\sum_{i=1}^N Y_i)}{\sqrt{N \sum_{i=1}^N (Y_i)^2 - (\sum_{i=1}^N Y_i)^2} \cdot \sqrt{N \sum_{i=1}^N (X_i)^2 - (\sum_{i=1}^N X_i)^2}}, \quad \text{Eq. 6.28}$$

where N is the number of data.

The hourly distribution of numerical and experimental results of the outlet air and the bulk fluid temperatures are displayed in Fig. 6.13 for model C-I on 23rd Feb. The average, maximum and minimum percentage error were 11.6%, 16.9% and 7.3%, respectively, which can be considered to be acceptable [385, 386]. The RMSE and PPMCC for outlet air temperature were 13.74 and 0.98, respectively. Whilst these were PPMCC = 0.98 and RMSE = 13.74 for the bulk fluid temperature. Such a noticeable deviation between experimental and numerical results can be attributed to the following factors:

- The accuracy in measuring the wind velocity, insolation and ambient temperature.
- Dust accumulation.
- The difficulty in estimating the roughness of the absorber and channel surfaces.
- The accuracy in estimating the optical properties, such as the emissivity of the absorber plates.
- The CFD models are simplified to a two-dimensional problem whereas the physical systems are three dimensional.
- Measurement uncertainty of devices.
- Despite the solar collector systems governing to quasi-steady conditions [374], in reality, the system is inherently time-dependent.
- Experimentally measured values of turbulence quantities at the inlet boundary are also required for accurate CFD simulation for turbulent flow. In the case of the $\kappa - \epsilon$

turbulence model, turbulent kinetic energy κ and turbulent dissipation rate ε are required. When these values are unavailable from experimental data, they must be predicted using the following set of equations [387].

$$\kappa = \frac{3}{2} (\bar{V}_{\text{ref}} TI)^2, \quad \text{Eq. 6.29}$$

$$\varepsilon = C_\mu^{3/4} \frac{\kappa^{3/2}}{l}, \quad \text{Eq. 6.30}$$

$$l = 0.07L, \quad \text{Eq. 6.31}$$

where \bar{V}_{ref} is the mean reference stream velocity, TI is turbulence intensity, l is the turbulence length scale, and C_μ is the $\kappa - \varepsilon$ turbulence model constant.

- The method used in estimating the experimental mean fluid temperature was arithmetic, $\bar{T}_f = (T_i + T_o)/2$ which is less accurate compared to the integration method used in CFD modelling. In other words, the thermocouples used for measuring the air flow temperature are only installed at the inlet and outlet of the collectors, which is not along the air flow direction.
- Excluding the effect of the absorption and emission (radiation effect) of glass in the numerical modelling, which is expected to be time-consuming.

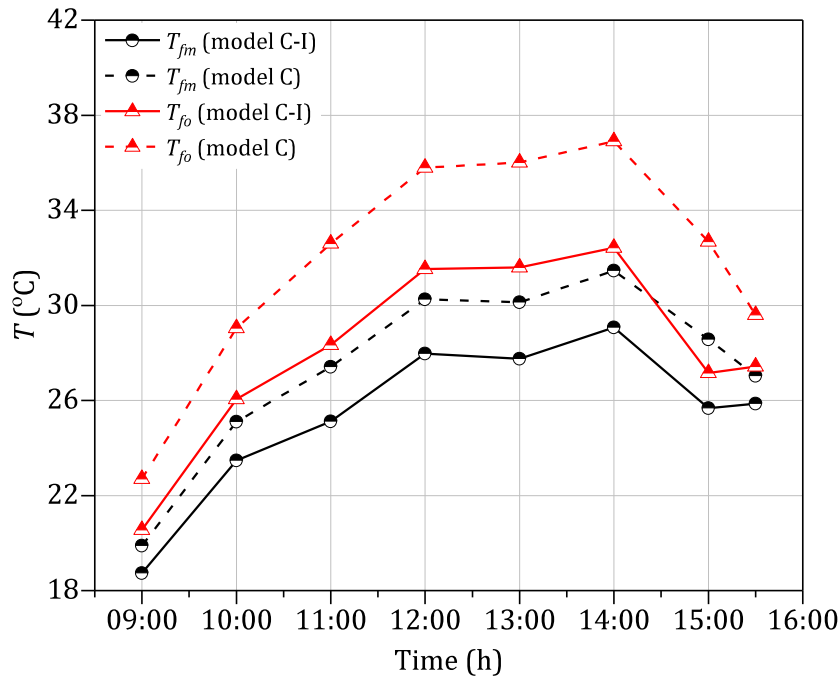


Fig. 6.13. Inlet and outlet air temperatures versus 09:00–16:00 hrs of the experimental (model C-I) and CFD (model C) results of the plain design.

Fig. 6.14 presents a comparison between the experimental (model C-I) and simulation (model C) temperatures of the absorber plate. The deviation PPMCC = 0.85 and RMSE = 9.1 of mean plate temperature \bar{T}_p was less than those seen in the measurements of fluid temperatures \bar{T}_f and T_0 . This is due to the number of thermocouples fitted along the absorber plate were higher than the two thermocouples placed at the inlet and outlet.

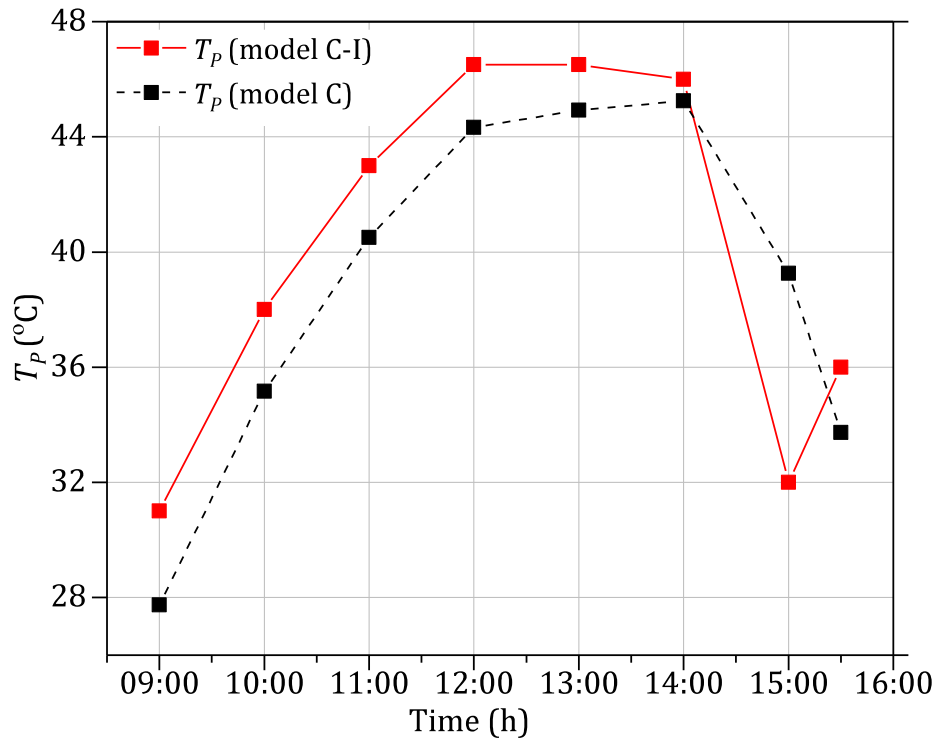


Fig. 6.14. All absorber plate temperatures versus 09:00–16:00 hrs of the experimental (model C-I) and CFD (model C) results of the plain design (without RAC).

6.5.4 Pressure drop evaluation

Estimating accurate pressure drop is crucial for the design and performance of the system [388]. Accordingly, a comparison was made between empirical equations (see Section 4.4, Subsection 3.3.3.1, Eq. 3.102) and CFD results for 2D (see Fig. 6.15a) and for 3D (see Fig. 6.15b) cases. The comparison among CFD (2D and 3D cases) and empirical results are presented in Fig. 6.15. As can be seen from Fig. 6.15 and Fig. 6.16, the highest pressure-drop was for the 3D model followed by the 2D model, with the lowest found for the empirical data. This is owing to:

- The 3D model is more representative of real-life conditions than the 2D model.

- More parameters are considered in the 3D model than those in the empirical correlations, such as the wall roughness (i.e. turbulent model), even though the default roughness wall height in Comsol could be different from real one. The default roughness is sand roughness type with height 3.2 μm . Also, the boundary layer separation in curved (U-turn) region and the effect of entry length before becoming the flow fully developed do not considered in empirical method.
- The empirical results were based on a fully developed condition unlike the other two models (i.e. 2D and 3D models) [389, 390].
- The presence of side walls is another possible explanation for the differences between 2D and 3D results, where symmetric side-planes were assumed in the 2D domain.

Additionally, the empirical correlation is subject to $\pm 25\%$ uncertainty which is valid with work made by Manglik and Bergles [223]. Table 6.7 lists the 2D CFD, 3D CFD and empirical data for the pressure drop estimated for design model C-I. The percentage of errors (E) were estimated regarding the solutions from 3D-CFD. The percentage errors of empirical equations results E_1 and the percentage error for 2D-CFD is E_2 .

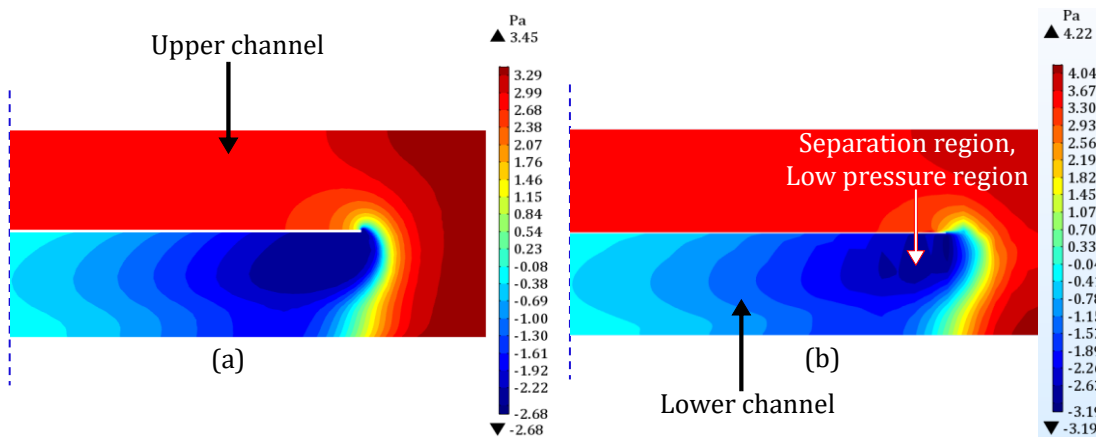


Fig. 6.15. Pressure drop profile for model C-I (single duct double pass U-flow design without cans) with $\bar{V} = 1.26 \text{ m s}^{-1}$, $G = 600 \text{ W m}^{-2}$ and $T_i = 16.9 \text{ }^\circ\text{C}$ conditions; (a) 2D CFD model and (b) 3D CFD model.

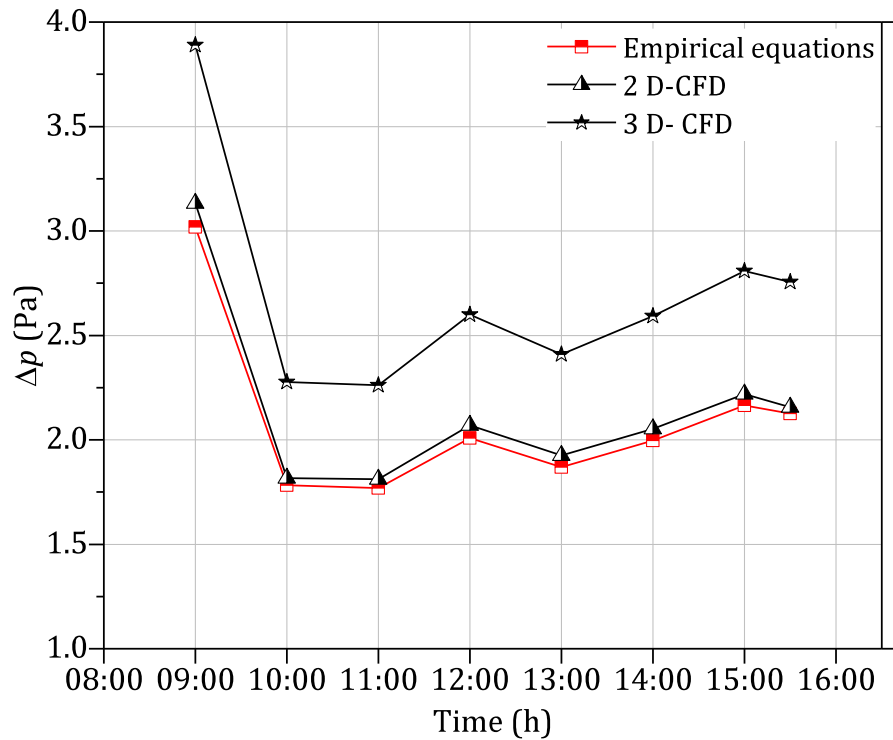


Fig. 6.16. Pressure drop from the 2D CFD, 3D CFD and empirical equations versus 09:00–16:00 hrs for design model C-I (single duct double pass U-flow design without Cans) using the data presented in Table 6.3.

Table 6.7. 2D CFD, 3D CFD and empirical equations predictions of the pressure drop and relative errors for design model C-I.

Empirical equations	2D-CFD	3D-CFD	E_1	E_2
3.01935	3.1316	3.8308	22.3578	3.58443
1.7835	1.816	2.2643	21.6354	1.789648
1.76834	1.8119	2.2505	21.81714	2.404106
2.00915	2.0695	2.5802	22.71311	2.916163
1.86987	1.925	2.3948	22.39593	2.863896
1.9968	2.053	2.5728	22.96296	2.737457
2.16472	2.2184	2.7824	22.89236	2.419762
2.1255	2.1559	2.7318	22.85777	1.410084

6.6 Conclusions

Numerical and experimental investigations were conducted to assess the performance of the double duct single pass solar air heater with recycled aluminium cans (RAC). The numerical study was built based on the finite element method provided by the COMSOL Multiphysics V5.3a software. The experiments were conducted in the western part of Iraq, Ar-Ramadi City (longitude: 33.25° N; latitude: 43.18° E) under clear skies and almost

identical weather conditions on 23rd (model C-I) and 27th (model C-II) February and 2nd (model C-III) March between 09:00 and 15:30. The average flowrates were 0.096 kg s⁻¹ for model C-I, 0.088 for model C-II kg s⁻¹ and 0.0819 kg s⁻¹. The comparative analysis of this work led to the following findings:

- Numerically, the U-flow offers better thermal performance than co-current and counter-current flow designs. Therefore, the U-flow model was chosen to be implemented in experimental studies.
- Thermal and hydrodynamic performance of numerical modelling is found to be in line with experiments (U-flow, model C-I).
- The increase in the thermal performance of U-flow model gave an increase in pressure drop, but the thermal efficiency was still higher compared to models A and B.
- The staggered arrangement (model C-III) had the highest thermal efficiency compared to the in-line (model C-II) and plain (model C-I) models.
- The in-line configuration (model C-II) had a lower efficiency compared to the staggered configuration (model C-III), even though the number of RACs and the mass flowrate were higher.

Chapter 7 is considered the main theme of this thesis since the integration of the two systems in Chapters 5 and 6 are performed. Formal optimisation design is employed to obtain optimum PV/T air collector designs with and without fins.

CHAPTER 7 OPTIMISATION OF MULTI-PASS PV/T AIR SYSTEMS

7.1 Introduction

The main applications of solar energy are thermal and electrical systems such as solar air collectors and photovoltaic systems, respectively. Hybrid photovoltaic/thermal (PV/T) system is a combination of these two systems. In Chapter 5, the evaluation of the performance of a PV system was carried out under different weather conditions, lengths and inclinations. In Chapter 6, the multi-pass solar air heaters using different configurations were evaluated. This chapter aims to optimise the hybrid PV/T air system by a three-step strategy. Firstly, the design parameters (dependent and independent) are selected carefully. Secondly, the thermo-hydraulic and electrical performances of five PV/T air systems are examined. Thirdly, the best model is utilised in a multi-objective design optimisation process. Finally, the effect of coupling/integrating the fins within the optimum PV/T air design is examined.

7.2 CFD approach

The CFD models have been developed using COMSOL Multiphysics® v5.3a software to examine the thermal and electrical performance of the PV/T air systems. Five different configurations were employed in this study, namely, single duct single pass, model 2 (Fig. 4.5), a single duct single pass (glazed), model 3 (Fig. 4.6), parallel pass double duct, model 4 (Fig. 4.7) double-pass single duct, model 5 (Fig. 4.8) and model 4-A (Fig. 4.9). The governing equations for the air velocity $\vec{V}(x, y, z) = u, v, w$ and temperature T are based on the conservations of mass, momentum and energy. These were explained in Section 4.3.1. Referring to the boundary conditions in Section 4.4.3 and Table 4.2, different temperatures were chosen as a representation of the weather conditions (i.e. 25 and 45 °C). The temperature of the fluid at the inlet was taken to be at ambient temperature ($T_{fi} = T_{amb}$). The value of the incident solar radiation was maintained at a constant 1000 W m⁻². The assumptions used in this chapter have been already mentioned in Section 4.4.3. The grid independence is discussed next.

7.3 Thermo-hydraulic performance

The evaluation of the thermo-hydraulic and electrical parameters of PV/T air collector are presented in Chapter 3, Section 3.3.3. This evaluation includes several parameters such as pressure drop, effective thermal efficiency, fan power consumption and electrical power generation.

7.4 Grid independence test

On the basis of the comparison between structured and unstructured meshes in Section 4.6.1, a structured mesh element type is adopted in the current test. Model 4 is used in this test (see Fig. 4.7). The boundary conditions of this model can be seen in Table 7.1.

Table 7.1. Boundary conditions of the grid independence test for model 4.

T_{amb}	45 °C	45 °C
G	1000 W m ⁻²	1000 W m ⁻²
δ_{D1}	0.025 m	0.025 m
δ_{D2}	0.025 m	0.025 m
L	1.2 m	1.2 m
Re	510	2550
\bar{V}	0.1829	0.9145
\dot{M}	0.0041	0.0204

Five parameters are considered in this test, which are solution time, t (s), the number of elements (NOE), degrees of freedom (DOF), physical memory, RAM (GB), and minimum element quality (MEQ). Furthermore, the PV module temperature, T_{mpv} (°C), thermal efficiency, η_{th} and pressure drop due to friction, Δp_f (W) are considered to cover the hydrodynamic and thermal parameters. The mesh is made of square elements applied on the upper glass cover in the X-Y plane varying element size step from very coarse, less coarse, normal and fine, as shown in Table 7.2. The same sizes and type of the element are used for the remaining parts of the system in the Z-direction as shown in Table 7.2. It can also be seen in Appendix B that increasing the number of elements has a small impact on the results because the model is a simple format (i.e. laminar flow and simple of geometry). For more details, the procedure is illustrated in Table 7.2 taken in performing this test.

Table 7.2. Key features of the mesh structure for the grid independence test in [Appendix B](#).

Trial No	Refinement step in the X-Y direction	Bias	Z_1 (mm)	Z_2	Z_3
1	Very coarse	0	5	5	1
2	Less coarse	0	3.6	7	1
3	Coarse	0	2.27	11	2
3a	Coarse	8	0.83	30	2
3ab	Coarse	0	0.83	30	2
3abc	Coarse	0	0.71	35	2
3abcd	Coarse	8	0.71	35	2
4	Normal	0	1.56	16	2
5	Normal	0	1.25	20	2
6	Normal	0	1	25	2
7	Normal	5	1	25	2
7a	Normal	8	0.83	30	2
7ab	Normal	0	0.83	30	2
7abc	Normal	0	0.71	35	2
7abcd	Normal	8	0.71	35	2
8	Normal	8	1	25	2
9	Normal	12	1	25	2
10	Normal	17	1	25	2
11	Fine	0	0.84	30	2
12	Fine bias	8	0.84	30	2

In [Table 7.2](#), Z_1 is the edge size in the Z direction for the upper and the lower flow channels (mm). Z_2 is the number of divisions for the upper and the lower flow channels in the Z-direction which is equal to (δ_{D1}/Z_1) and Z_3 is the number of the divisions for the PV and glass covers in the Z direction. A further examination is carried out to refine the mesh at the interface between the solid surfaces and the fluid flow to accurately estimate the field flow and temperature distribution. Bias criterion is used to refine the mesh in this region, which can be defined as the ratio of the largest edge to the smallest edge sizes. The results showed that this refinement has only a small effect, this is owing to the fact that flow under a laminar regime consists of layers as streamlines and the velocity gradient close to the wall is relatively small compared to turbulent flow. The Δp_f , however, showed a change within this particular mesh refinement when $Re = 2550$ (i.e. at higher Re). The developing region length at higher Re becomes longer under these conditions. This is because the entry length, L_{ent} (m) is a function of hydraulic diameter and Re (see [Eq. 7.1](#)) [[391](#)]. This means that the velocity profile is not fully developed at the entrance, i.e. unlike the rest of duct length where the shape of velocity is almost a parabolic profile across the collector, see [Fig. 7.1](#).

$$L_{ent} = D_h [(0.631)^{1.6} + (0.0442Re)^{1.6}]^{1/1.6}. \quad \text{Eq. 7.1}$$

In conclusion, in order to compromise between the computation time and accuracy, case 3abcd is adopted in this study for model 2 to 5.

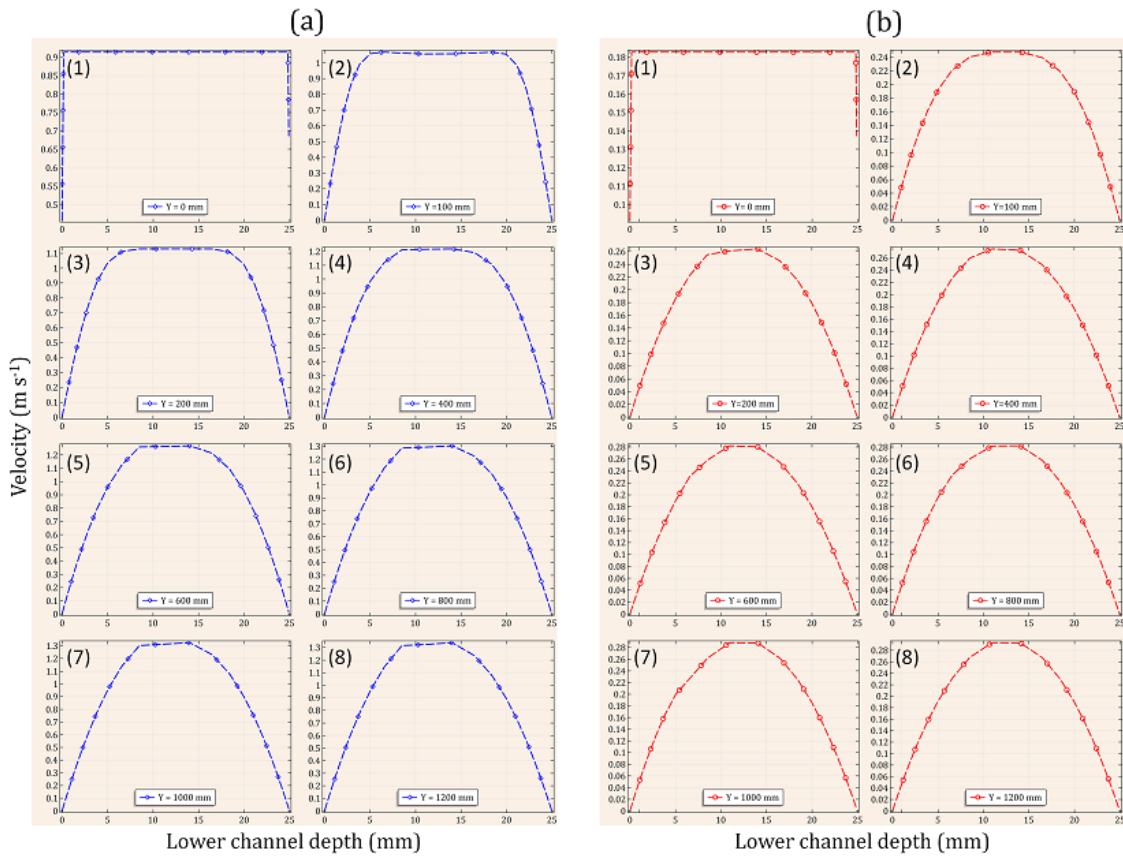


Fig. 7.1. Velocity profile for different locations along the lower air channel for model 4 under laminar flow regime (a) $Re = 510$, $\bar{V} = 0.1829$ (m s⁻¹), $\dot{M} = 0.0041$ (kg s⁻¹) (b) $Re = 2550$, $\bar{V} = 0.9145$ (m s⁻¹), $\dot{M} = 0.0204$ (kg s⁻¹).

7.5 Optimum PV/T air design

In order to obtain optimal PV/T air design and reduce the number of simulation runs, three steps are considered. The first step is to define the constant and variable parameters that are considered during this examination. Secondly, preliminary parametric studies are conducted for proposed PV/T air models (models 1, 2, 3, 4 and 5) to identify the best model. Thirdly, this best model is then employed in the design optimisation process.

7.5.1 Parameter selection

Referring to Section 2.9, the design parameters of PV/T air systems such as mass flow rate and the duct of flow are key aspects for achieving efficient and feasible PV/T air. Several authors have studied the impact of design parameters on the performance of PV/T air collectors [122, 128, 176]. The main parameters are geometrical such as length of collector, operational, for instance, mass flow rate and weather conditions, including insolation and ambient temperature. The selection of the range of design parameters needs to be

addressed as some parameters received little attention in the literature. Therefore, an investigation is conducted in the next sub-sections to identify the significance of these parameters.

7.5.1.1 Geometry parameters

In PV/T air systems, the main geometrical parameters are:

1. The width of the collector.
2. The length of the collector.
3. The lower and upper depth flows.
4. The thickness of absorber plates and glass.
5. The thickness of the back insulation.

The selection of the ranges of geometrical parameters is based on the literature. However, when the parameters are not available in the literature, the selection is determined using a large range but keeping it applicable to the real-world. [Table 7.3](#) lists the specifications of the range of geometrical parameters included in the CFD design optimisation of model 4. The optimal design ratio of the length of the collector to hydraulic diameter (L/D_h) can be found in [\[50, 122, 130, 131\]](#). This ratio is taken into consideration when selecting the depth of flow and length of the collector. The width of the collector is selected based on width, which is much greater than the depth of flow. This means that the effect of side walls can be assumed to disappear. This means the velocity profile across the width is assumed to be as a straight line.

Table 7.3. Levels of the geometry design parameters used in the CFD design optimisation.

Symbol	Description	Values
w	Collector width	0.8 m [50, 122, 225, 230, 340, 392-394]
w_{slice}	3D slice width	0.015 m
δ_{cu-U}	Thickness of upper copper plate located on the back surface of the PV module	0.001 m [394]
δ_{cu-L}	Thickness of the lower copper plate located in lower channel flow	0.001 m [394]
δ_{D2}	Upper depth flow	0.004-0.015 m [50, 121, 122, 151, 172]
δ_{D1}	Lower depth flow	0.004-0.010 m [50, 151, 172]
δ_g	Thickness of glass	4 mm [122, 241, 269]
δ_{UE}	Equivalent thickness of glass and EVA	4.5 mm
δ_{LE}	Equivalent thickness of Si, Tedlar and EVA	1.3 mm
ϵ_{cu}	Copper (oxidized)	0.65 [241, 269]
ϵ_g	Average emissivity of glass	0.92 [241, 269]
L	Collector length	0.6-1.3 m [26, 151, 172, 225, 340, 392-395]
L_f	Length of fin (see Fig. 7.24)	0.02 m [289, 290]
S_f	Space between fins (see Fig. 7.24)	0.01 m [289, 290]
h_{fin}	Height of fin (see Fig. 7.24)	$\delta_{D1} - 0.002$ m [289, 290]

7.5.1.2 Weather parameters

There are two main functions of PV/T air systems; the first function is to improve PV electrical power supply by reducing PV cell temperature. The second function is to supply dry/hot air for several applications. Both functions can, however, be used for local/domestic and industrial applications. It is also important to note that the PV/T air systems can be either integrated into the building [183] referred to as the building integrated photovoltaic/thermal (BIPV/T) system or conventional hybrid PV/T air system [396]. The BIPV/T systems reduce the cost, contribute by exploiting otherwise unused areas (i.e. walls of a building) as well as enhancing the decorated appearance (i.e. facades). In this study, it is assumed that the PV/T air systems are connected to the air handling unit (AHU) which is used for the air conditioning of the building [183, 249] as shown in Fig. 7.2.

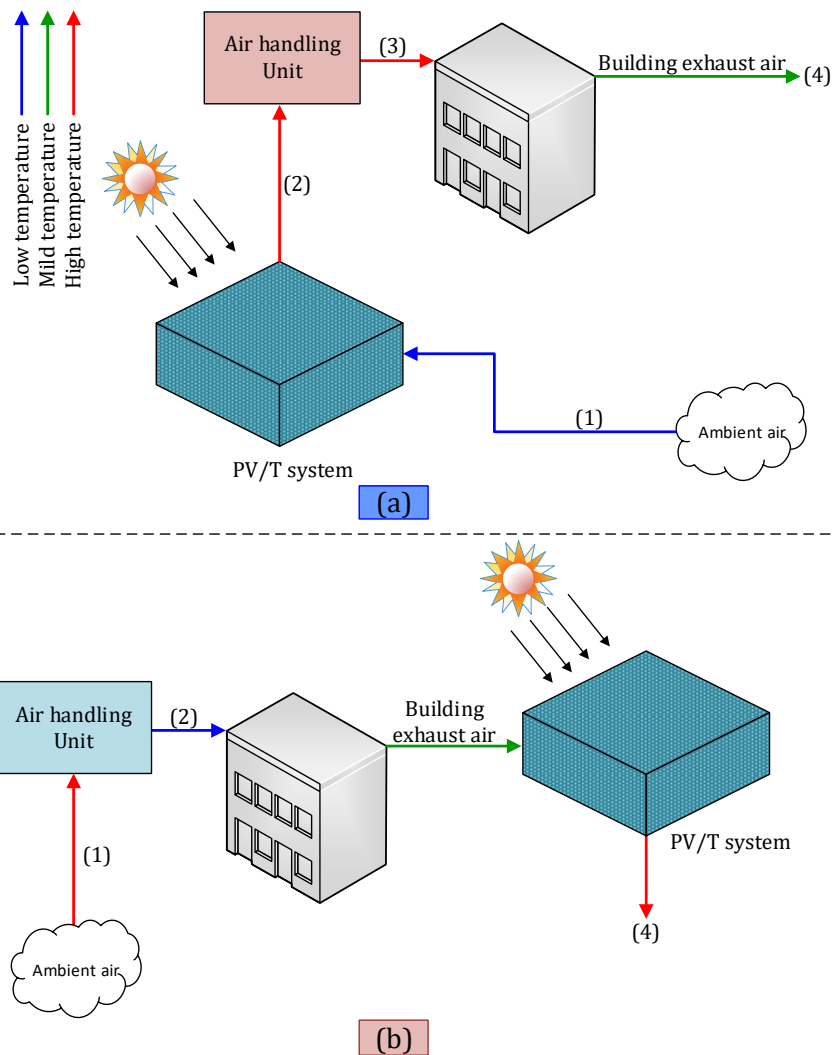


Fig. 7.2. Working principle of the studied BIPV/T system: in (a) winter mode and (b) summer mode adapted from [185].

The proposed PV/T air systems are evaluated under two operating weather conditions. The first condition examines the PV/T air systems under hot weather, mainly at 45 °C, 1000 W m⁻². This temperature is considered as the average of the hottest temperature, and it is based on the observation data for Iraq-Baghdad in July (summer of 2018), as shown in Fig. 7.3. The second condition evaluates the PV/T systems utilising pre-cooled air (typically 25 °C [183, 249, 339]), where the exhaust air from the building is used as a coolant instead of using ambient air (i.e. 45 °C). In accordance with the ASHRAE Handbook [339], the exhaust air temperature can be assumed to be between (22-24) °C. It is essential to mention that this temperature range is estimated for indoor design. However, for BIPV/T system, the temperature would be higher than this range, and it depends on different factors, e.g. duct fitting and duct insulation type. Thus, the temperature could slightly differ from the indoor temperature. As a result, in this study, the second condition is assumed 25 °C.

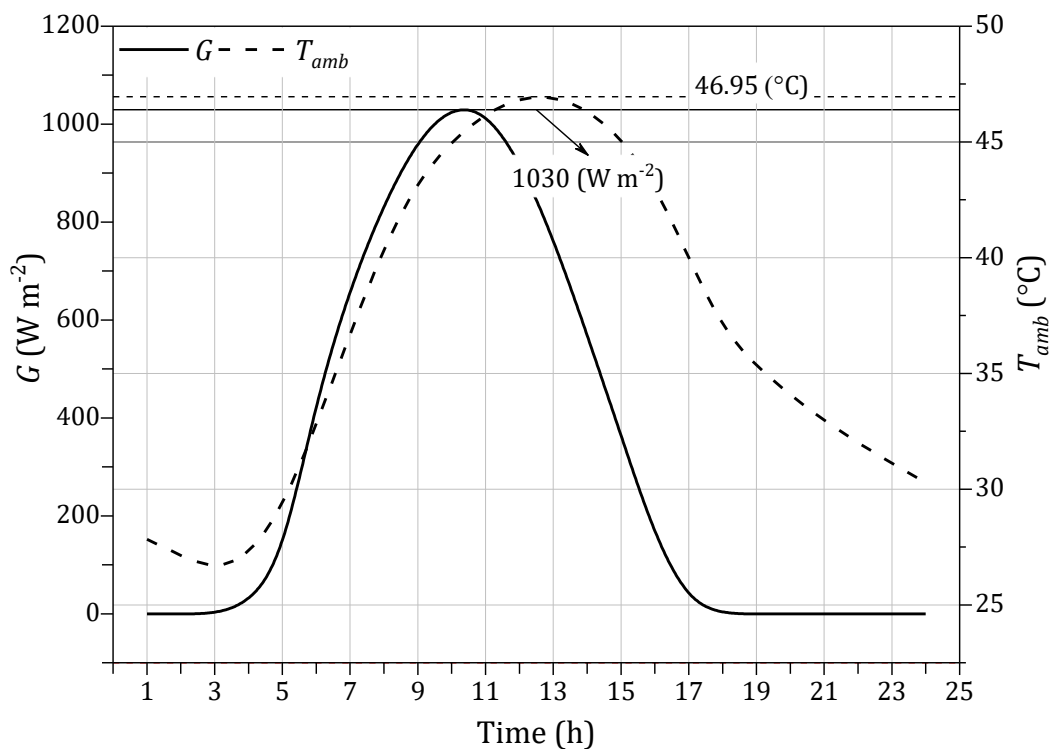


Fig. 7.3. Insolation and ambient temperature versus time in a typical day in July 2018.

7.5.1.3 Material parameters

The material parameters were predetermined by the manufacturer and remained constant throughout this study. These parameters can be divided into collector body parts and PV module parts. With respect to collector body parts (i.e. air channel frame, glass cover and

absorber plates), such as the selection of glass cover material type is based on durability, clarity and size of collector. In this study, 4 mm glass cover thickness has been chosen. The other materials can be seen in [Table 4.2](#). In terms of PV module parts, PV cell, cell encapsulation and Back sheet/Tedlar. For example, the design characteristics of the PV cells are determined by the photovoltaic reference efficiencies (η_{ref}) which are dependent on the material type, i.e. mono-crystal silicon (mono c-Si), polycrystalline silicon (poly-Si) or non-silicon based film [\[5-9\]](#). In this study, poly-Si was chosen with packing factor value 0.83, 12.35 reference efficiency and 0.0041/°C temperature coefficient of power (β_{ref}) [\[18, 191, 305\]](#). The type of material affects also the optical properties of the PV module, such as thermal emissivity (ϵ). For example, the use of mono c-Si instead of poly-Si solar cells enhances the absorption coefficient and subsequently improves the thermal efficiency of the PV/T system [\[18, 191\]](#). However, the packing factor of poly-Si is greater than mono c-Si (i.e. more aperture area subjected to incident solar radiation) ([Table 7.3](#) and [Table 4.2](#)). The poly-Si PV cells are also cheaper than mono c-Si and have a lower temperature coefficient of power, (β_{ref}) [\[306\]](#).

7.5.1.4 Operational parameters

In PV/T air systems, minimising the consumption of fan power is an essential factor. The main function of the PV panel is to provide electrical power for utilities rather than driving the PV/T air cooling fan. Accordingly, optimisation/minimisation of fan power consumption was taken into consideration, where the range of Reynolds number was determined to be in laminar flow regime (510-2550) (i.e. low mass flow rate or air velocity) [\[180, 257\]](#).

7.5.2 Preliminary parametric studies

In [Section 7.5.1](#), the parameters have defined; the second step is to run parametric studies to establish the best performance of a PV/T air collector among five models under the same conditions. This model is subsequently employed in the design optimisation process and a fin configuration effect study. The parametric study is carried out by varying different operational, geometric and weather parameters. [Table 7.4](#) tabulates the values used in this parametric study for the collector model designs (models 2 and 5). Model 1 is not a hybrid system, and it therefore does not have duct flow and thus does not include in the [Table 7.4](#).

Table 7.4. Boundary conditions for different design parameters for models 2, 3, 4 and 5.

Design parameters for models 2, 3 and 5								
T_{amb}	25 °C		45 °C		25 °C		45 °C	
G	1000 W m ⁻²							
δ_{D1}	0.025 m		0.025 m		0.025 m		0.025 m	
δ_{D2}	0.025 m		0.025 m		0.025 m		0.025 m	
L	1.2 m		1.2 m		1.6 m		1.6 m	
Re	\bar{V}	\dot{M}	\bar{V}	\dot{M}	\bar{V}	\dot{M}	\bar{V}	\dot{M}
510	0.1633	0.0039	0.1829	0.0041	0.1633	0.0039	0.1829	0.0041
1020	0.3265	0.0077	0.3658	0.0081	0.3265	0.0077	0.3658	0.0081
1530	0.4898	0.0116	0.5487	0.0122	0.4898	0.0116	0.5487	0.0122
2040	0.6530	0.0155	0.7316	0.0163	0.6530	0.0155	0.7316	0.0163
2550	0.8163	0.0193	0.9145	0.0204	0.8163	0.0193	0.9145	0.0204
Design parameters for model 4								
T_{amb}	25 °C		45 °C		25 °C		45 °C	
G	1000 W m ⁻²							
δ_{D1}	0.025 m		0.025 m		0.025 m		0.025 m	
δ_{D2}	0.025 m		0.025 m		0.025 m		0.025 m	
L	1.2 m		1.2 m		1.6 m		1.6 m	
Re	\bar{V}	\dot{M}	\bar{V}	\dot{M}	\bar{V}	\dot{M}	\bar{V}	\dot{M}
255	0.1633/2	0.0039/2	0.1829/2	0.0041/2	0.1633/2	0.0039/2	0.1829/2	0.0041/2
318.75	0.3265/2	0.0077/2	0.3658/2	0.0081/2	0.3265/2	0.0077/2	0.3658/2	0.0081/2
425	0.4898/2	0.0116/2	0.5487/2	0.0122/2	0.4898/2	0.0116/2	0.5487/2	0.0122/2
637.5	0.6530/2	0.0155/2	0.7316/2	0.0163/2	0.6530/2	0.0155/2	0.7316/2	0.0163/2
1275	0.8163/2	0.0193/2	0.9145/2	0.0204/2	0.8163/2	0.0193/2	0.9145/2	0.0204/2

The full explanation of models 1 to 5 is in Section 4.4.1. Sketches of these configurations are Fig. 7.4 below. For more detailed sketches, refer to Fig.4.5 to Fig.4.8 and Fig.4.10. In brief, model 1 is a standard PV module without active cooling where it is exposed to ambient conditions. Model 2 is a single duct single pass PV/T air collector. Model 3 is similar to model 2 but with an air gap added between the top surface of the PV module and a glass cover. Model 4 is a parallel pass double duct where air flows under and over the surfaces of the PV module in the same direction (co-current flow). In the fifth configuration, air flows between the glass cover and the PV module and reverses in the second pass between the PV panel and lower absorber plate, making a U-shape flow (double-pass single duct).

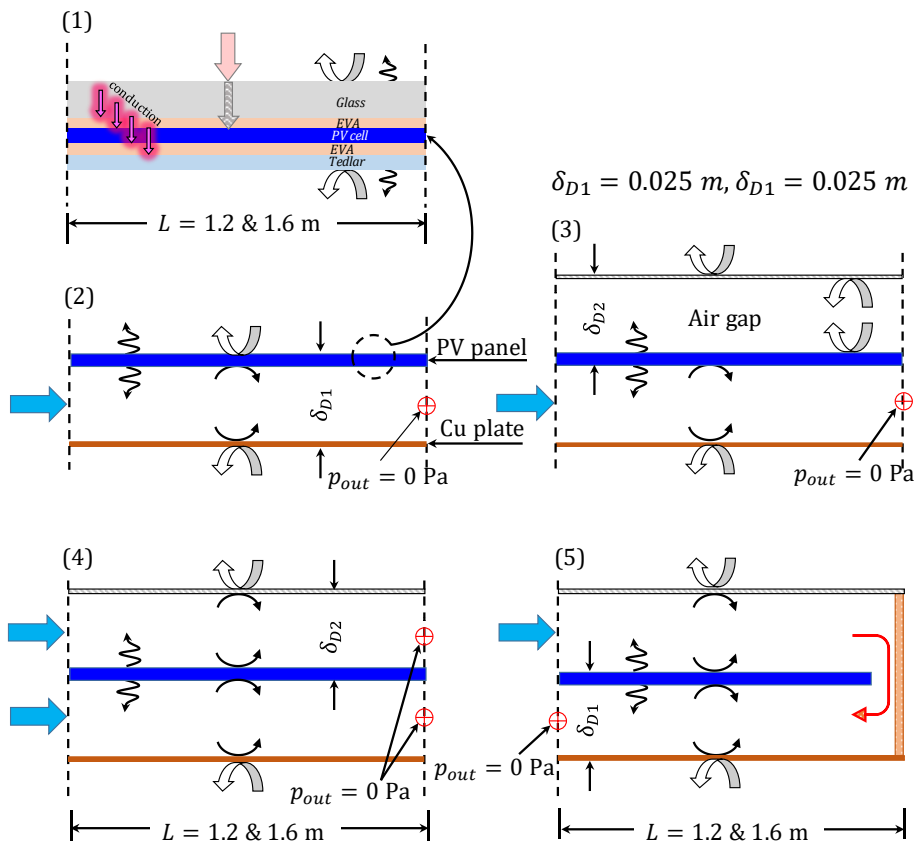


Fig. 7.4. Schematics of the various PV/T models along with heat transfer coefficients.

Using MATLAB, the operational parameters (mass flow rate and Reynolds number) are varied with respect to air temperatures at the inlet (i.e. 25 and 45 °C), as seen in Table 7.4. The Reynolds number is maintained between 510-2550. The same depth of flow is used for the upper and lower channels (0.025 m) [50, 121, 122, 151]. The original width is 0.8 m, but the symmetry boundary condition is applied on two sides of the collector with a 3D slice width of 0.015 m as seen in Fig. 4.5. For the sake of realistic comparison, all the models use the same mass flow rate at the inlet ducts. Models 2, 3, 5 have one air pass inlet, but model 4 has two passes (see Fig. 4.7), in which the mass flow rates in the upper and lower channels are taken as half of those in the air flow channel of model 2, 3 and 5, as shown in Fig. 4.5, Fig. 4.6 and Fig. 4.8. This can also be seen clearly in Table 7.4.

In order to make a realistic comparison between the proposed PV/T designs, in this parametric study, the thermal, hydrodynamic and electrical parameters of five PV/T air collectors are evaluated. Four of them are hybrid systems (PV/T air system, models 2 to 5) while model 1 is just a standard PV system without active cooling. The reason behind adding model 1 to this comparison is to show the effect of hybridisation of PV/T systems.

Accordingly, all models are named as PV/T air systems for the sake of simplicity. Five parameters are evaluated in this comparison as follows:

The first parameter is pressure drop along the flow channel for the PV/T air systems. The pressure drop versus the Re for the five PV/T air designs under different lengths, operational and weather conditions are shown in [Fig. 7.5](#). It can be seen that pressure drop values rise with increasing Re, length of collector and the ambient temperature for all PV/T air configurations. In terms of length of the collector, it is predicted that with increasing length, the pressure drop also increases since it is the main parameters affecting the pressure drop in the air channel system. With respect to ambient temperature, the increase in the ambient temperature could lead to an increase in the kinematic viscosity of air and hence increase the velocity in the duct for the same Re value.

It can be noted in [Fig. 7.5](#) that models 2 and 3 have almost similar pressure drop values because they have only a single pass where the air flows underneath the PV module, as shown in [Fig. 7.4](#). On the other hand, model 4 shows the minimum pressure drop value, while model 5 has the maximum value. The reason that the pressure drop of model 4 is the lowest is that it has two flow channels where the velocity is half that of the other designs (models 2, 3 and 5). To clarify based on the Bernoulli and empirical equations used to estimate pressure drop and friction factors such as in [Chapter 3](#), the pressure drop is governed by a second-order equation, $\Delta p \propto V^2$. This means when the value of velocity is 3 m s⁻¹ for model 4 and the value of velocity is 6 m s⁻¹ for other models, the pressure drop is proportional with (3)² for model 4 and (6)² for others. On the other hand, model 4 has a higher number of walls than model 2 and 3, this will lead to an increase in pressure drop (friction factor).

Model 5 has the maximum pressure drop owing to the U-turn shape, and there is extra pressure head in U-flow region where the air moves from the upper to lower channel. In other words, there is a significant increase in pressure drop for U-flow model (model 5) compared to the other models. This is owing to the induced flow separation in the U-turn near the bend and the swirling secondary flow that occurs because of the imbalance of centripetal forces as a result of the curvature of the duct centreline [\[230\]](#).

The second parameter is thermal efficiency. [Fig. 7.6](#) presents the influence of Re on thermal efficiencies for all proposed PV/T air designs under different lengths, operational and weather conditions. From the figure, it is seen that as the Re rises, the thermal efficiency increases logarithmically owing to increasing in convective heat transfer coefficient. This is because the convective heat transfer coefficient is directly proportional to Re. Also,

increasing Re leads to an increase in the heat gain (enthalpy) of collectors, which in turn increases the thermal efficiency, as shown in Eq. 3.97. Observation of Fig. 7.6 shows that model 4 and 5 have almost identical thermal efficiencies specifically at length 1.2 m. While at length 1.6 m at either 25 °C or 45 °C, model 4 has higher thermal efficiency than model 5. This observation can be attributed to the fact that at larger length (1.6 m) model 4 has lower local fluid temperature along the PV absorber. Therefore, model 4 cools the PV module more efficiently. This means that the temperature difference between the fluid and solid becomes smaller and smaller until it becomes negligible. This reduces heat transfer dramatically according to Newton's law of cooling. Another reason is that the cooling occurs from lower and upper surfaces simultaneously where fresh air is fed to the upper and lower ducts at the same time rather than one side such as in model 5. This can be seen clearly in Fig. 7.12, Fig. 7.13 and Fig. 7.14.

Moreover, it is clearly seen that the thermal efficiency for model 3 is higher than model 2 because model 3 is covered with glass and this contributes to capturing more heat and the glass works as an insulator (enclosure). Finally, in all models, the increase in length reduces their thermal efficiency. This is because the mass flow rate is relatively small (laminar regime) and after 1.2 m, a saturation in temperature leads to a reduction in the convective heat transfer rate as can be seen clearly in Fig. 7.10 and Fig. 7.11 in dashed lines. These results confirmed by the findings of [176, 189, 397]. This reduction is owing to the fact that the temperature difference (local temperature difference between fluid and solid) and hence the convective heat transfer coefficient is reduced.

The effect of the temperature of the PV module on electrical efficiency under different Re , length of PV modules and ambient conditions for five PV/T systems, are shown in Fig. 7.7. In general, all models exhibit an increase in electrical efficiency with a decrease in temperature of the PV module regardless of the type of model, ambient temperature and the length of the collector. Examination of Fig. 7.7 reveals that model 2 has the lowest PV module temperature and thus the maximum electrical efficiency. This happens, since the top surface of the PV module is subjected to ambient conditions (unglazed) while model 3, 4 and 5 are glazed. However, in connection with Fig. 7.6, it is obvious that the thermal efficiency of model 2 is the lowest, and this is the reason behind the lowest PV module temperature. It can also be observed that the second best electrical efficiency is model 4 regardless of the weather conditions and length of the collector.

Finally, a comparison between different models to evaluate the combined efficiencies (electrical plus thermal) for the PV / T air systems are shown in Fig. 7.8. This figure presents the variation of combined efficiencies of the studied models with Re under different weather

conditions and lengths. Considering Fig. 7.6 and Fig. 7.7, it can be seen that the maximum thermal efficiency is model 4, while the maximum electrical efficiency is model 2, but the maximum combined efficiency is model 4. Overall, model 4 has the maximum combined efficiency with minimum fan power consumption (minimum pressure drop).

The group of figures from Fig. 7.9 to Fig. 7.13 present the temperature contours of the studied models. Fig. 7.9 shows a side view of the temperature contour of model 1. It is clear that the temperature of the PV cell is the highest region, which is rational since the solar radiation falls directly on PV cells, and the electrical power is generated in this region. Also, there is no effect of changing the length of the PV module on its temperature. This was explained in detail in Chapter 5 where the impact of length disappeared after a length of 1.2 m Fig. 5.24.

Fig. 7.10 displays a side view of the temperature contour of model 2. It can be seen that the temperature increases gradually from inlet to the outlet. In addition, the effect of length on the temperature distribution of model 2 can be observed. For example, the maximum temperature is 55.2 °C for 1.6 m and it is 54.6 °C for 1.2 m at ambient temperature of 25 °C. Similarly, Fig. 7.11 presents the same behaviour of model 2 in terms of gradual increase in temperature from inlet to outlet. However, the temperature values are higher than in model 2 because the upper channel is an enclosure in which the air is in free convection mode (enclosure) and the effect of convection currents can be seen. Finally, Fig. 7.12 and Fig. 7.13 demonstrate the effect of the PV length, ambient temperature and the direction of flow for models 4 and 5, respectively. It is similar to models 2 and 3 (gradual increase in temperature from inlet to outlet), however, model 4 shows the least local fluid temperature since the cooling takes place at the lower and upper surfaces of the PV panel at the same time. Fig. 7.14 confirms this concept as can be seen the temperature trend of model 4 is lower than of model 5 and after length 1.2 m the two trend nearly matches.

Some important observations are noted in the foregoing paragraphs and can be summarized. Firstly, model 4 has the best thermal performance compared with those of models 2, 3 and 5. Furthermore, model 4 has the lowest fan power consumption among all models unlike model 5 has the maximum fan power consumption. Model 2 has a lower PV module temperature and thus the maximum electrical efficiency. Finally, model 4 has the best total efficiency with lowest pressure drop, thus this model is selected to include for the next step of optimisation. These findings are confirmed by [122, 398].

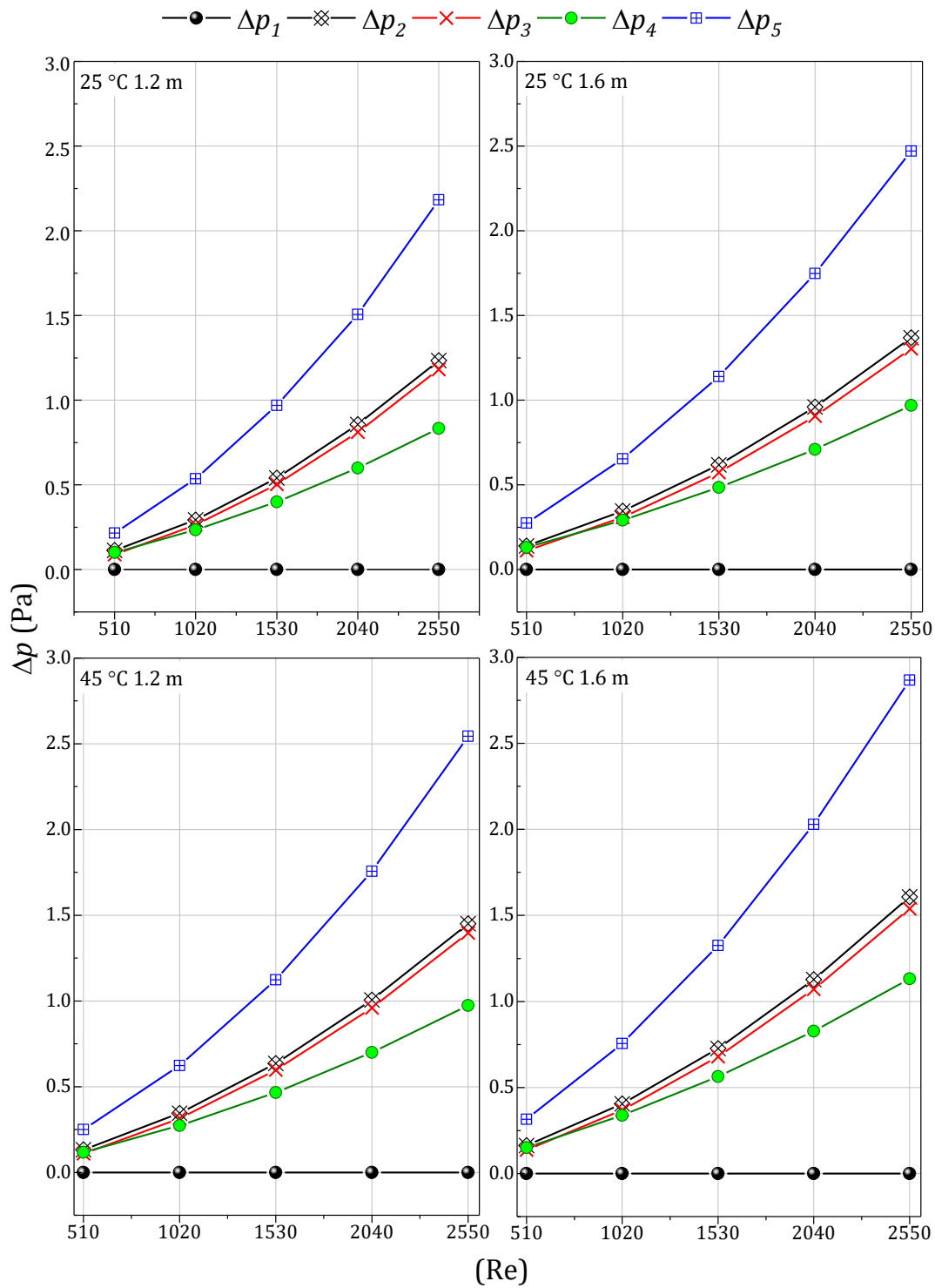


Fig. 7.5. Pressure drop along the duct versus Re (510-2550) of the studied PV/T systems using different lengths (1.2 m and 1.6 m) and weather conditions (25 °C and 45 °C).

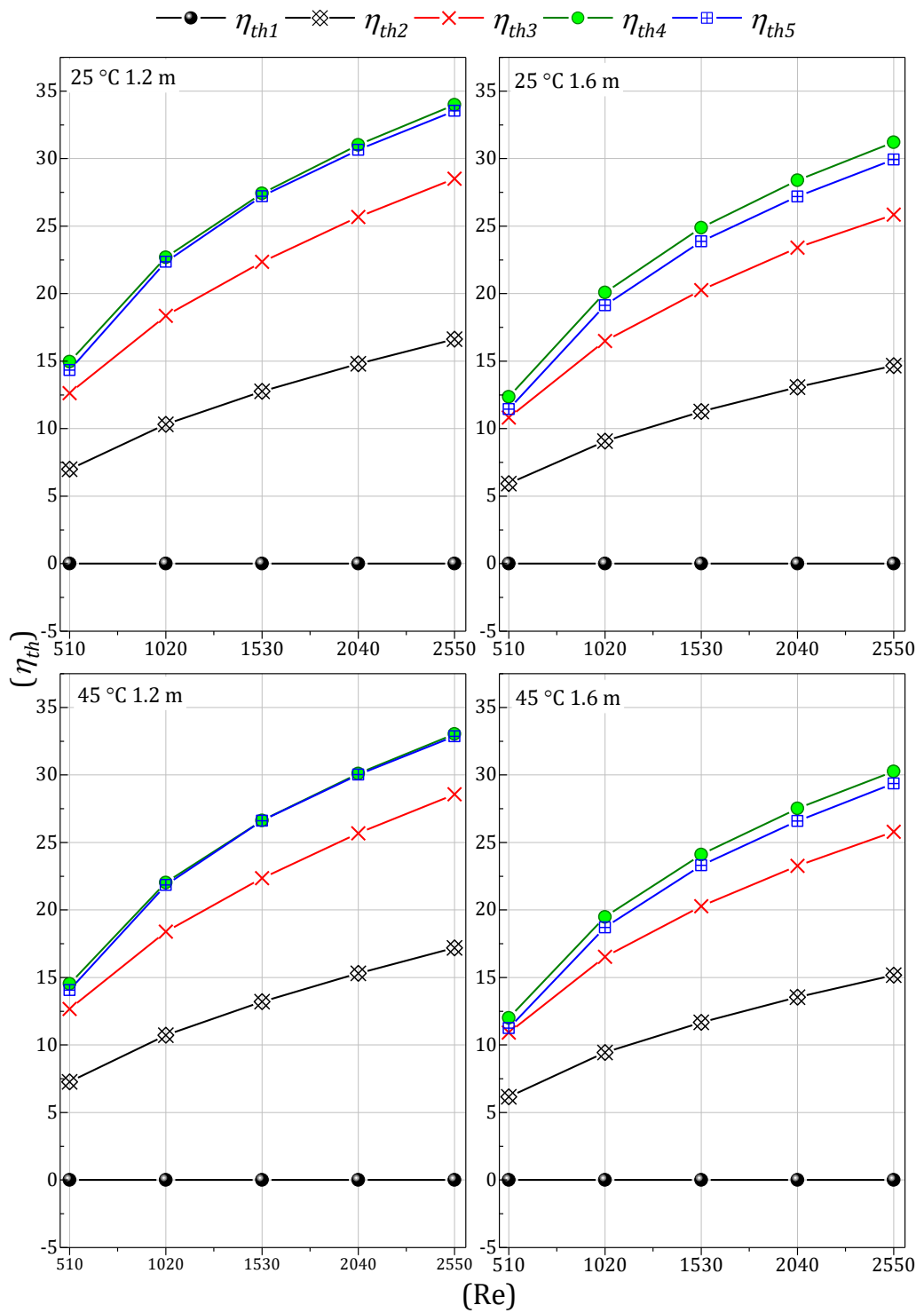


Fig. 7.6. Thermal efficiencies versus Re (510-2550) of the studied PV/T systems using different lengths (1.2 m and 1.6 m) and weather conditions (25 °C and 45 °C).

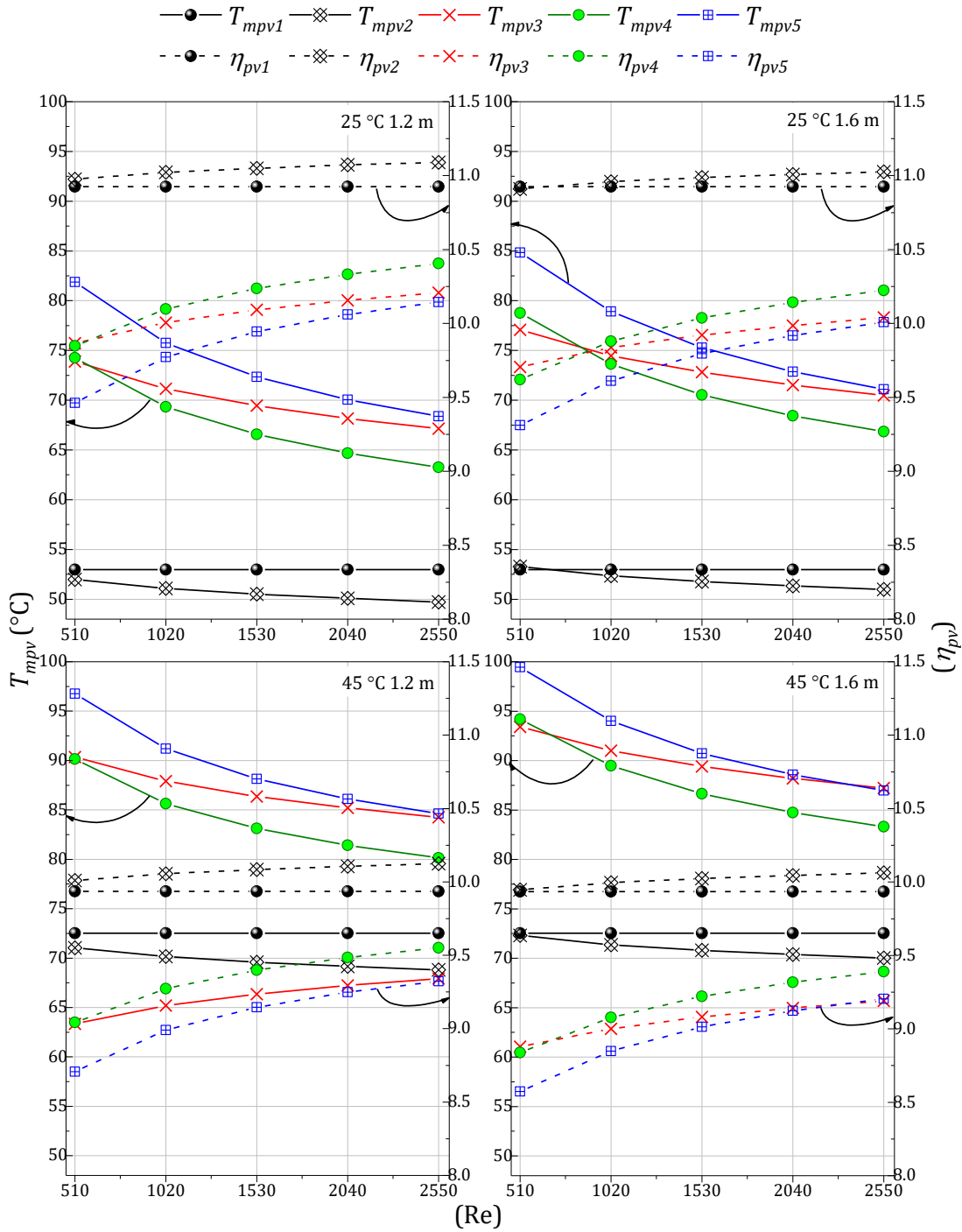


Fig. 7.7. PV module temperatures and the electrical efficiencies versus Re (510-2550) of the studied PV/T systems using different lengths (1.2 m and 1.6 m) and weather conditions (25 °C and 45 °C).

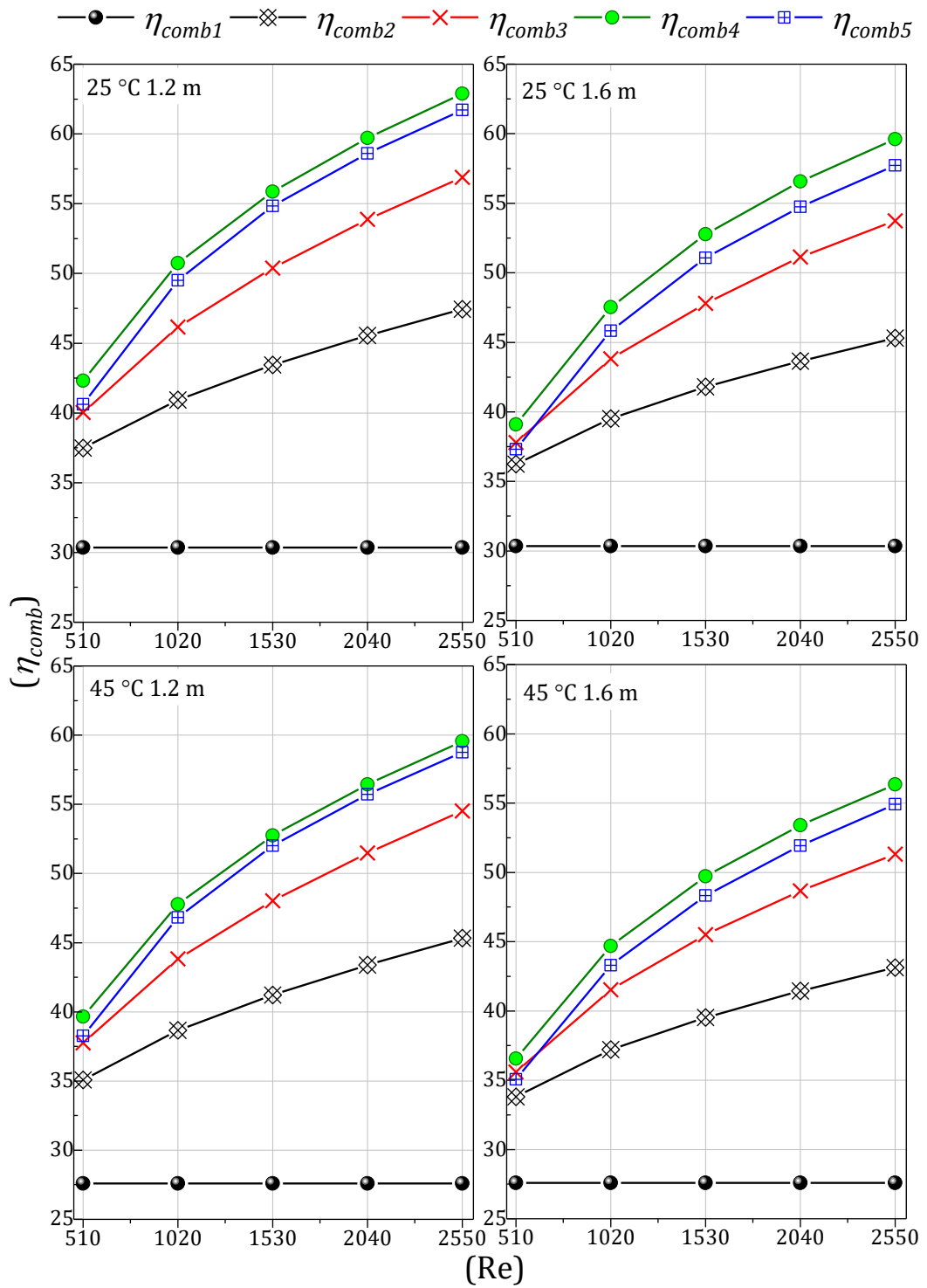


Fig. 7.8. Combined efficiencies versus Re (510-2550) of the studied PV/T systems using different lengths (1.2 m and 1.6 m) and weather conditions (25 °C and 45 °C).

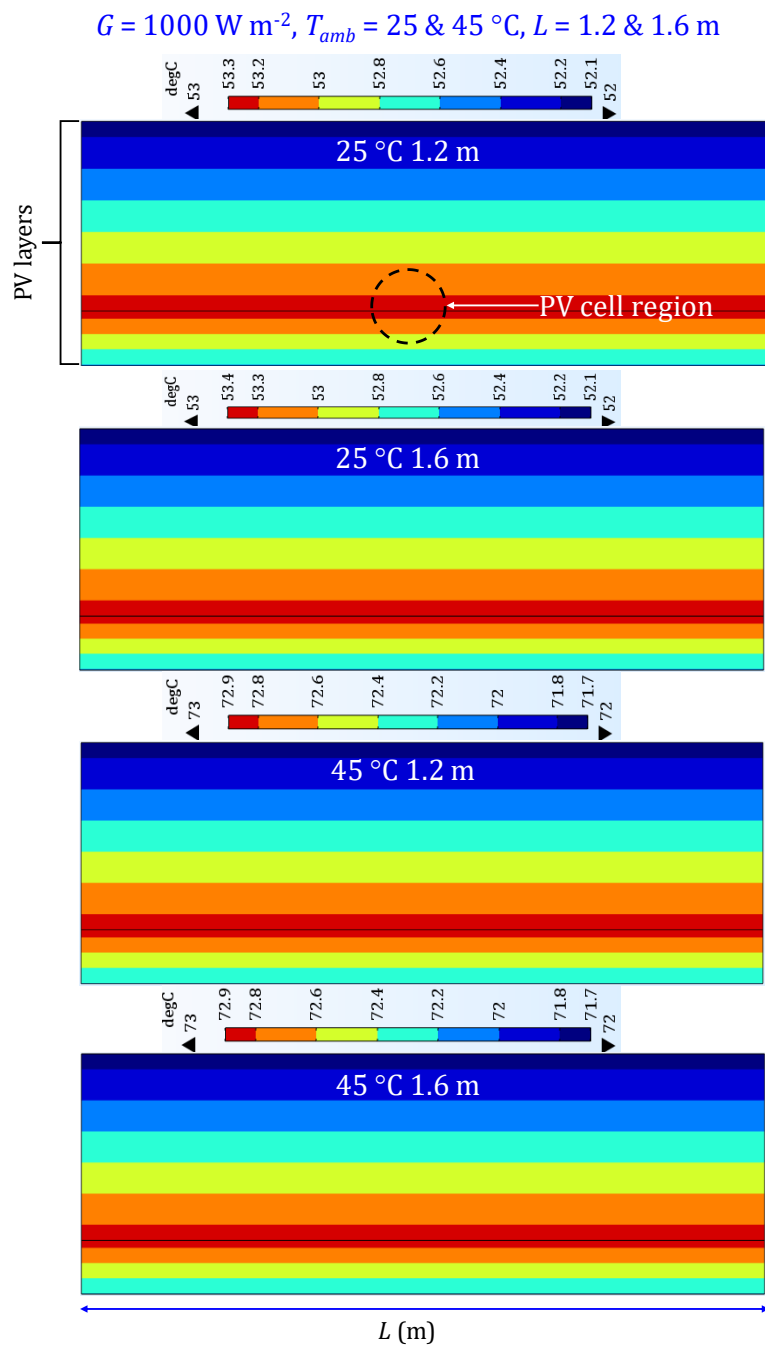


Fig. 7.9. Side view of temperature contours for model 1 showing the temperature profile of the PV module layers using different lengths (1.2 m and 1.6 m) and weather conditions (25 °C and 45 °C) under steady state conditions.

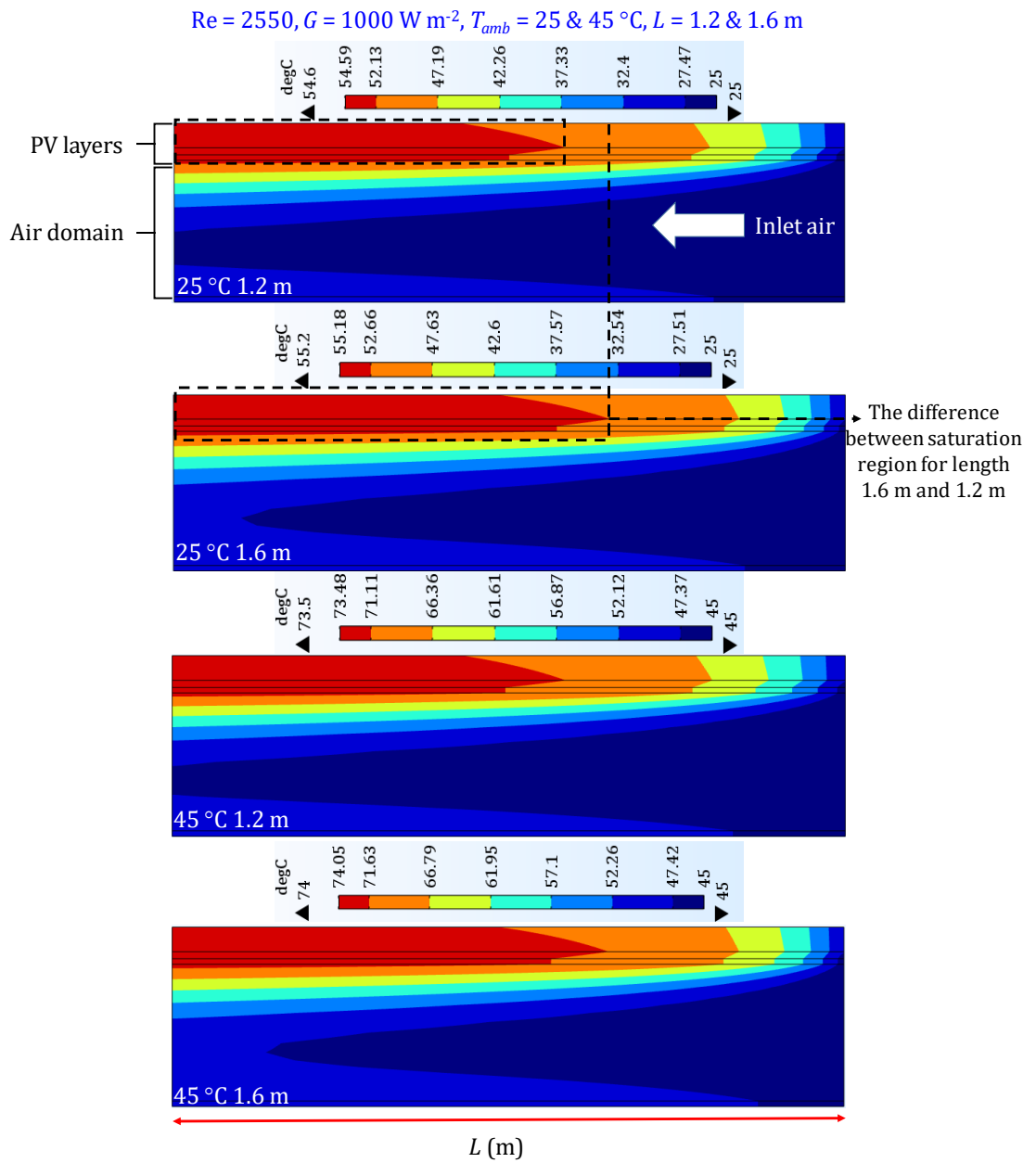


Fig. 7.10. Side view of temperature contours for model 2 showing the temperature profile along the PV module and air flow channel using different lengths (1.2 m and 1.6 m) and weather conditions (25 °C and 45 °C) under steady state conditions.

Time = 7000 sec, $Re = 2550$, $G = 1000 \text{ W m}^{-2}$, $T_{amb} = 25 \text{ \& } 45 \text{ }^\circ\text{C}$, $L = 1.2 \text{ \& } 1.6 \text{ m}$

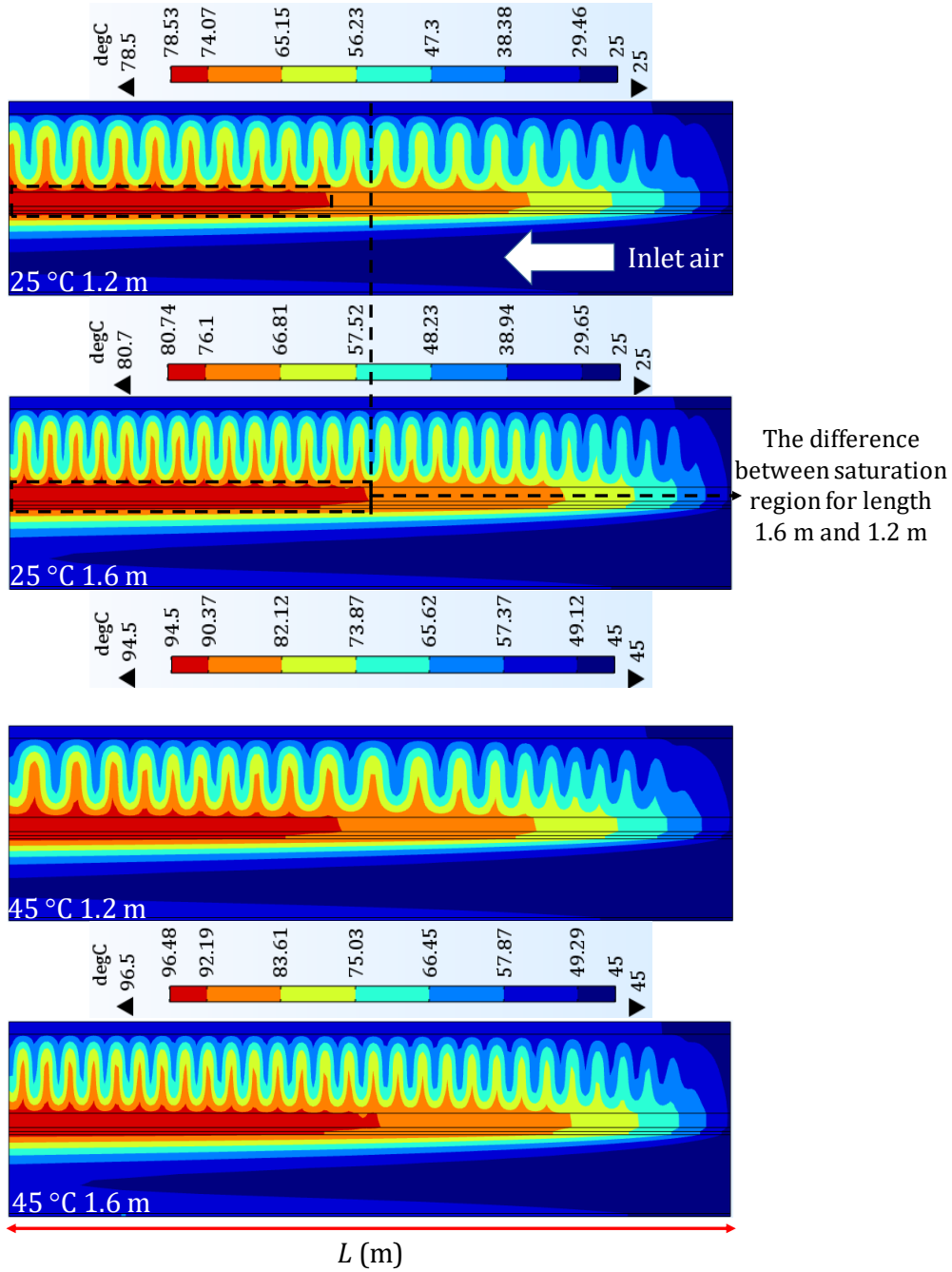


Fig. 7.11. Side view of temperature contours for model 3 showing the temperature profile along the PV module and air flow channel using different lengths (1.2 m and 1.6 m) and weather conditions (25 °C and 45 °C) under transient conditions.

$Re = 2550, G = 1000 \text{ W m}^{-2}, T_{amb} = 25 \text{ \& } 45 \text{ }^\circ\text{C}, L = 1.2 \text{ \& } 1.6 \text{ m}$

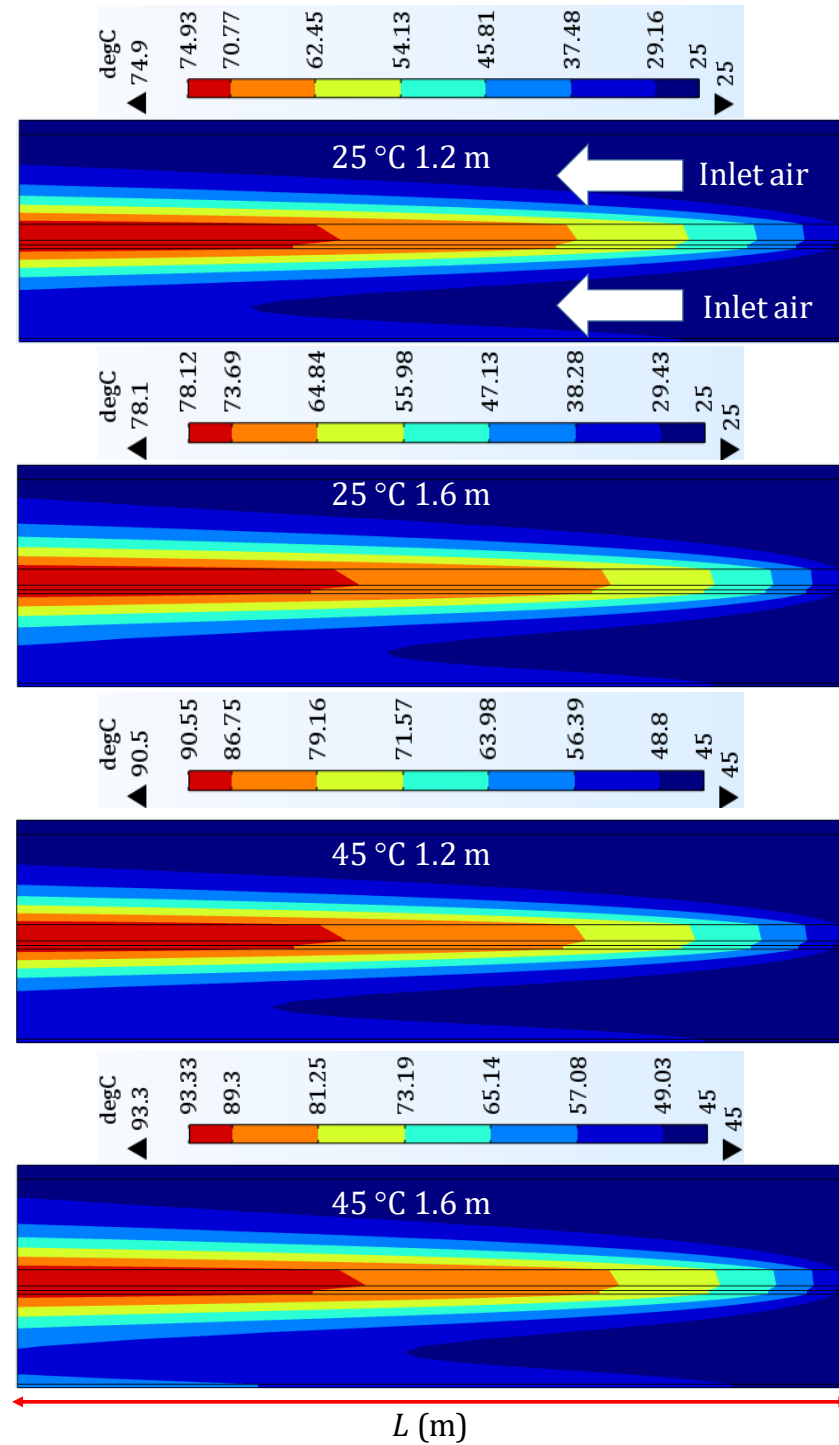


Fig. 7.12. Side view of temperature contours for model 4 showing the temperature profile along the PV module and air flow channel using different lengths (1.2 m and 1.6 m) and weather conditions (25 °C and 45 °C) under steady state conditions.

$Re = 2550, G = 1000 \text{ W m}^{-2}, T_{amb} = 25 \text{ \& } 45 \text{ }^\circ\text{C}, L = 1.2 \text{ \& } 1.6 \text{ m}$

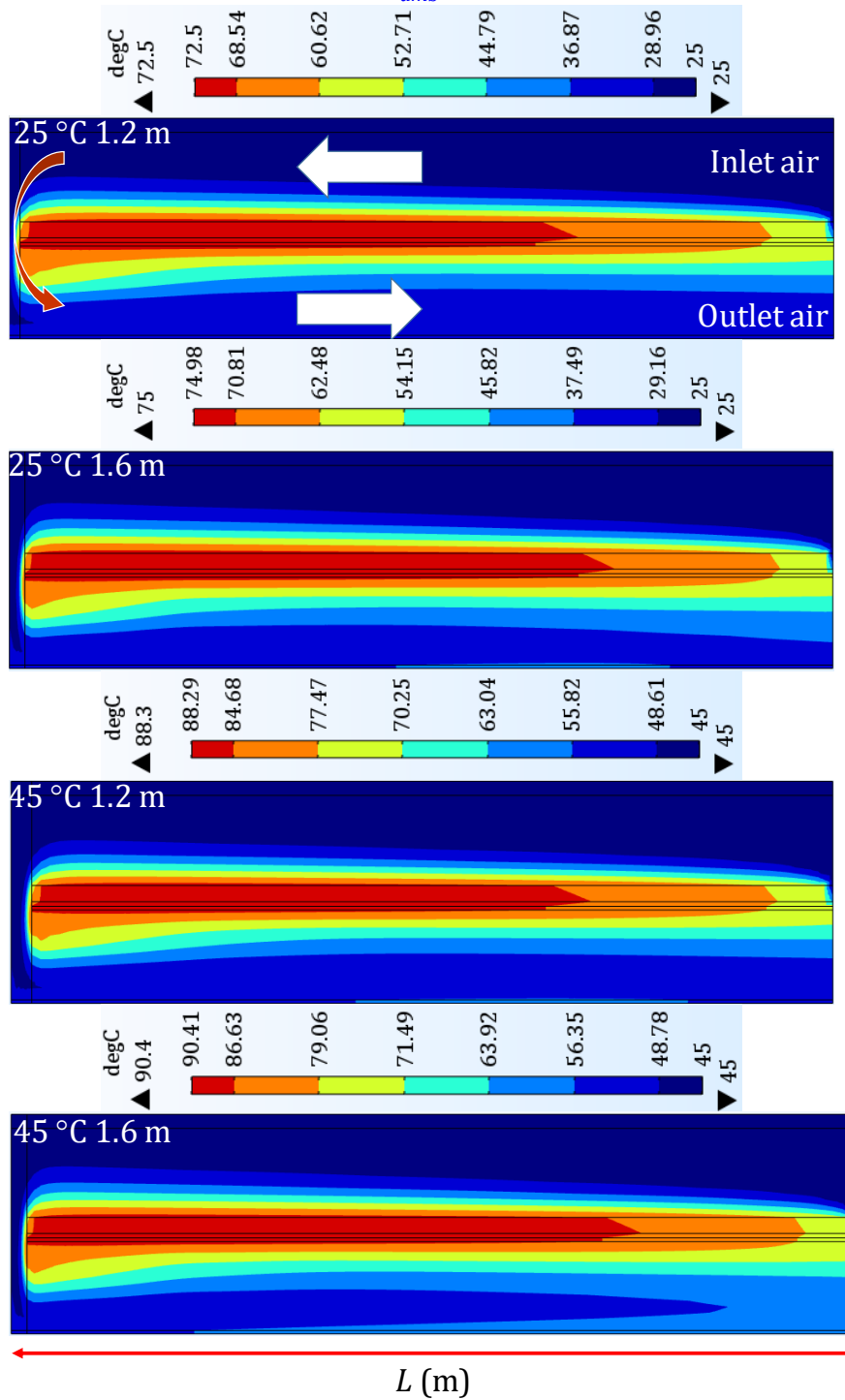


Fig. 7.13. Side view of temperature contours for model 5 showing the temperature profile along the PV module and air flow channel using different lengths (1.2 m and 1.6 m) and weather conditions (25 °C and 45 °C) under steady state conditions.

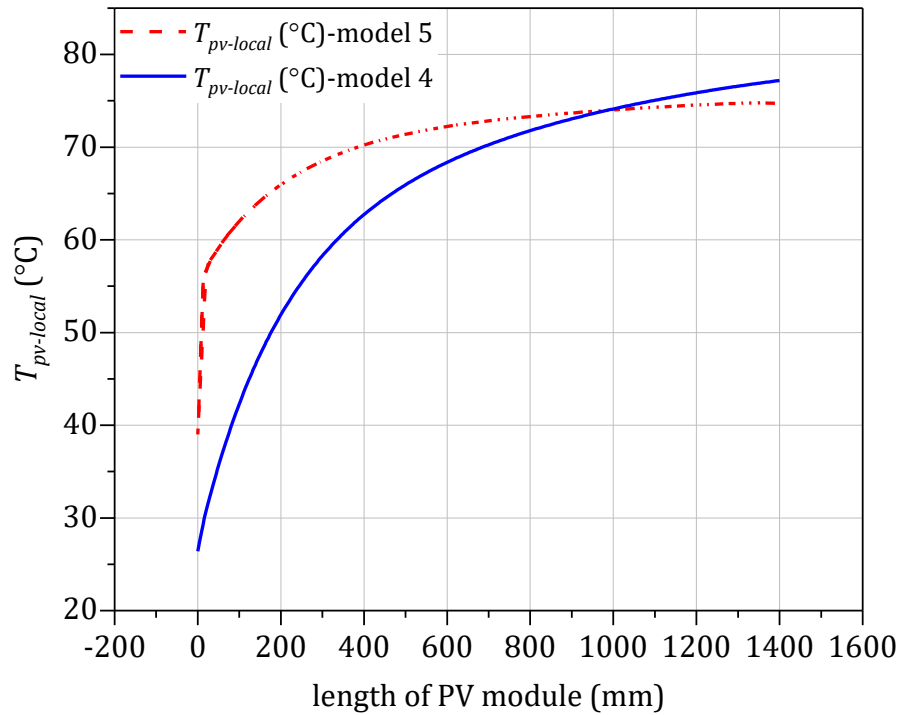


Fig. 7.14. Temperature distribution of local temperature of model 4 and 5 along the PV module from inlet to outlet.

7.5.3 Optimisation of model 4

The results from the parametric study show that model 4 has the best performance with minimum fan power consumption. Therefore, model 4 has been selected to employ in the optimisation process. The thermal, electrical and hydrodynamic analyses performed in the parametric study section are now extended to carry out a formal optimisation study of model 4. Integrating optimisation techniques with the CFD methodology to find the optimal design could efficiently contribute in providing great benefits. The emphasis, then, of this section is on the formulation of an optimisation problem.

7.5.4 Optimisation strategy

To perform optimisation for the PV/T air system design a number of steps are considered. Firstly, multi-objective functions are formulated, with the goal to minimise the fan power and maximise the electrical power for one case, and to maximise both the electric and the thermal efficiencies for the second case. Secondly, the objectives are parameterised in terms of length of a collector (L), the depth of the lower air flow channel (δ_{D1}) and the upper air flow channel (δ_{D2}). Since the range of geometry parameters has already been selected in Section 7.5.1.1 (Table 7.3), now, the next step is to use this range to generate the design of experiments (DOE). To obtain the DOE, an Optimal Latin Hypercube (OLH) is employed,

which uses a permutation genetic algorithm, to ensure a uniform distribution of the points within the design space using combinations of the parameters δ_{D1} , δ_{D2} , and L , see Fig. 7.16 [399]. Fig. 7.15 shows the sketch of model 4 illustrating the range of geometry parameters and boundary conditions including the operational and weather conditions.

Thirdly, a 3D CFD simulation is employed at the generated DOE points to obtain the corresponding responses and the results can be seen in Table 7.5 and Table 7.6. In design optimisation, A surrogate model can be defined as an engineering method utilised in which an outcome of interest is not straightforwardly directly measured; a model of the outcome is adopted instead. Most engineering design problems need experiments and/or simulations to evaluate design objective and constraint functions as a function of design variables. The use of Surrogate models are crucial since they mimic the behaviour of the CFD model as close as possible while being computationally cheaper to evaluate compared to the computational time of the CFD modelling. These models have been proven successful for a range of engineering applications, e.g. the design optimisation of fluid flow and heat transfer problems [400, 401]. Surrogate models (response surface functions) are generated using a Radial Basis Function (RBF) method from a set of known values at specified DOE points [332, 400, 402]. After that, the Pareto front is obtained using the genetic algorithm technique to provide designers with the opportunity to select the most convenient compromise point among the optimum designs. In the next section, the analysis of optimisation results for different Pareto front curves is discussed. The Pareto frontier is the set of all Pareto efficient allocations, conventionally shown graphically. It also is commonly known as the Pareto front or Pareto set. Also, Genetic algorithms are a type of optimization algorithm, meaning they are used to find the optimal solution(s) to a given computational problem that maximizes or minimizes a particular function.

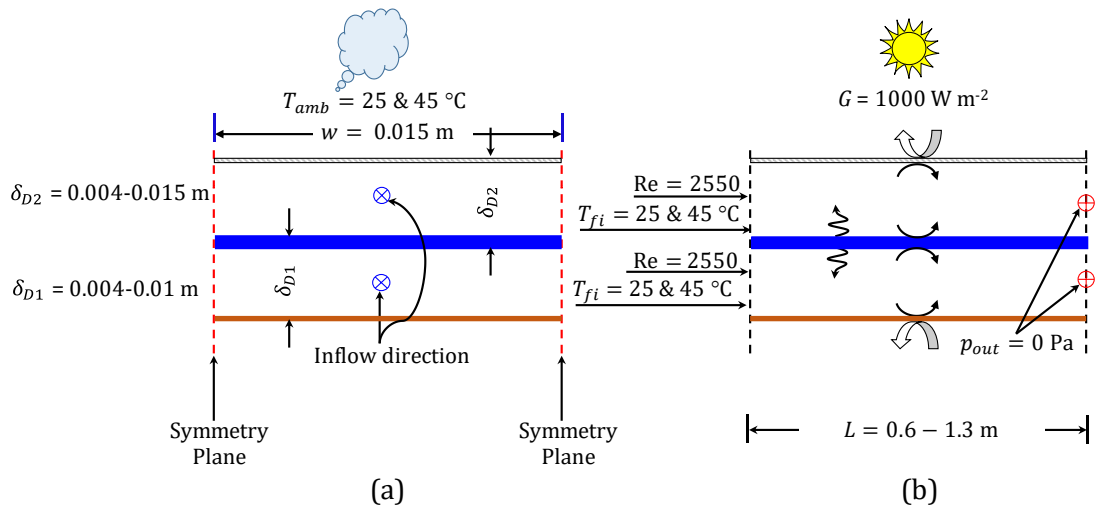


Fig. 7.15. Schematic of model 4 showing the range of geometrical parameters and boundary conditions of model 4.

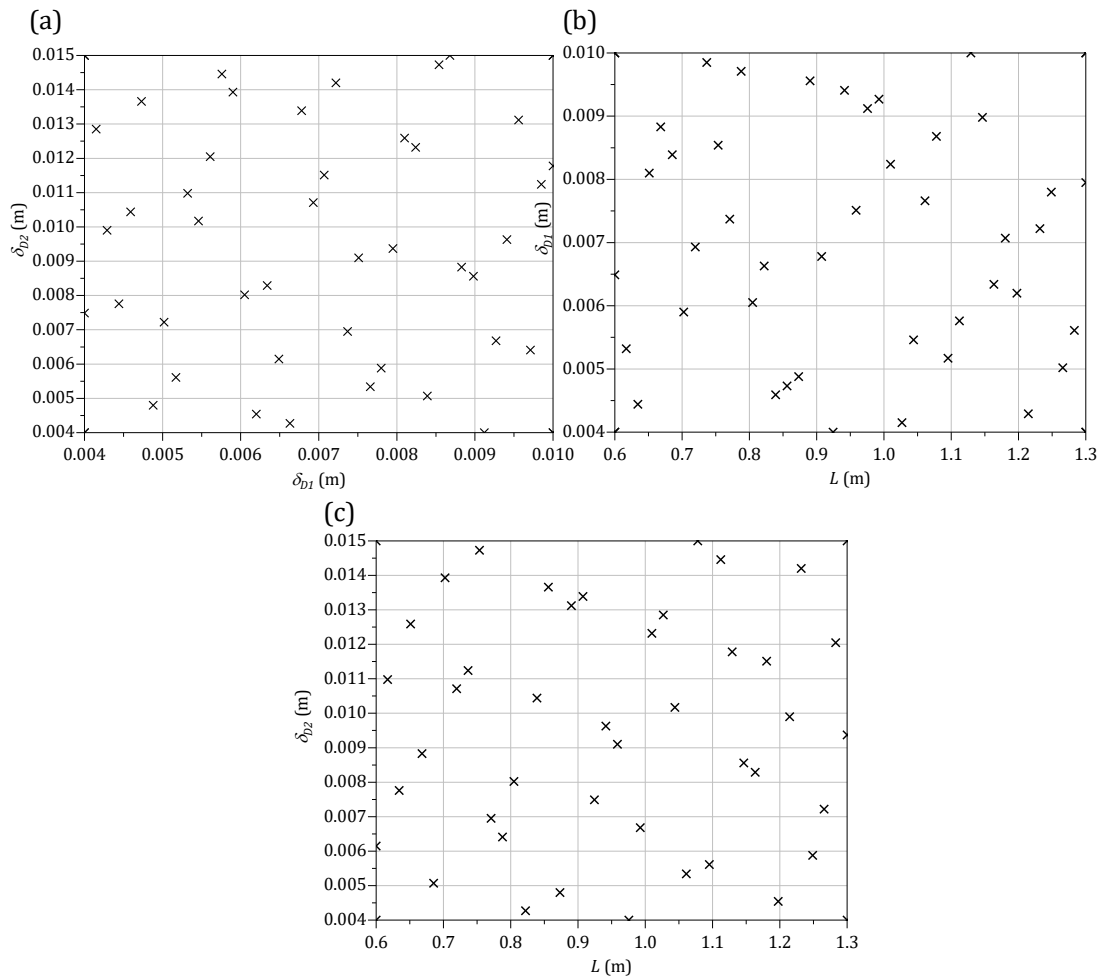


Fig. 7.16. Illustration of the DOE points: (a) Lower depth of flow (δ_{D1}) versus upper depth of flow δ_{D2} , (b) Lower depth of flow (δ_{D1}) versus length of the collector (L), (c) Upper depth of flow (δ_{D2}) versus length of collector (L)

Table 7.5. Fifty DOE points and their CFD results for four objective functions of model 4 for low temperature weather (25 °C).

L (m)	δ_{D1} (m)	δ_{D2} (m)	\bar{V}_L (m s ⁻¹)	\bar{V}_U (m s ⁻¹)	\dot{M} (kg s ⁻¹)	η_{th}	η_{PV}	P_f (W)	P_{PV} (W)
0.6	0.004	0.004	4.97	4.97	0.0377	47.10	11.74	13.34	42.09
0.6	0.01	0.004	2.00	4.97	0.0378	45.84	11.61	7.37	41.63
0.6	0.004	0.015	4.97	1.34	0.0380	40.12	11.58	7.05	41.52
0.6	0.01	0.015	2.00	1.34	0.0381	49.89	11.37	0.99	40.77
1.3	0.004	0.004	4.97	4.97	0.0377	45.56	11.48	22.92	89.16
1.3	0.01	0.004	2.00	4.97	0.0378	43.36	11.31	12.44	87.84
1.3	0.004	0.015	4.97	1.34	0.0380	36.26	11.27	12.14	87.54
1.3	0.01	0.015	2.00	1.34	0.0381	43.83	11.00	1.40	85.45
0.92439	0.004	0.00749	4.97	2.67	0.0378	44.35	11.51	10.72	63.55
1.0268	0.00415	0.01285	4.79	1.57	0.0379	39.61	11.38	9.36	69.83
1.2146	0.00429	0.0099	4.64	2.02	0.0378	41.50	11.34	10.04	82.30
0.63415	0.00444	0.00776	4.48	2.58	0.0378	46.34	11.61	6.56	44.00
0.83902	0.00459	0.01044	4.34	1.92	0.0379	43.54	11.46	6.52	57.47
0.8561	0.00473	0.01366	4.21	1.47	0.0379	41.47	11.41	5.82	58.37
0.87317	0.00488	0.0048	4.08	4.15	0.0377	47.42	11.56	10.22	60.30
1.2659	0.00502	0.00722	3.97	2.77	0.0378	44.84	11.34	8.32	85.76
1.0951	0.00517	0.00561	3.85	3.55	0.0378	46.86	11.44	9.01	74.83
0.61707	0.00532	0.01098	3.74	1.83	0.0379	46.17	11.54	3.85	42.55
1.0439	0.00546	0.01017	3.65	1.97	0.0379	44.35	11.34	5.10	70.73
1.2829	0.00561	0.01205	3.55	1.67	0.0379	41.77	11.22	5.21	85.98
1.1122	0.00576	0.01446	3.46	1.39	0.0380	41.42	11.24	4.25	74.70
0.70244	0.0059	0.01393	3.38	1.45	0.0380	44.95	11.43	3.05	47.99
0.80488	0.00605	0.00802	3.30	2.49	0.0378	47.66	11.46	4.09	55.10
1.1976	0.0062	0.00454	3.22	4.38	0.0378	46.47	11.40	10.81	81.61
1.1634	0.00634	0.00829	3.15	2.41	0.0378	45.75	11.29	4.60	78.51
0.6	0.00649	0.00615	3.07	3.24	0.0378	49.39	11.60	4.20	41.58
0.82195	0.00663	0.00427	3.01	4.66	0.0378	47.43	11.54	8.98	56.70
0.90732	0.00678	0.01339	2.94	1.50	0.0380	45.00	11.30	2.64	61.24
0.71951	0.00693	0.01071	2.88	1.87	0.0379	47.93	11.42	2.48	49.12
1.1805	0.00707	0.01151	2.82	1.74	0.0379	44.45	11.20	3.01	78.98
1.2317	0.00722	0.0142	2.77	1.42	0.0380	42.64	11.13	2.69	81.93
0.77073	0.00737	0.00695	2.71	2.87	0.0378	48.93	11.46	3.51	52.77
0.95854	0.00751	0.0091	2.66	2.20	0.0379	47.45	11.31	2.84	64.81
1.061	0.00766	0.00534	2.61	3.73	0.0378	47.39	11.38	6.21	72.13
1.2488	0.0078	0.00588	2.56	3.39	0.0378	46.43	11.29	5.73	84.21
1.3	0.00795	0.00937	2.51	2.14	0.0379	45.33	11.16	3.02	86.72
0.65122	0.0081	0.01259	2.47	1.60	0.0380	48.87	11.41	1.63	44.39
1.0098	0.00824	0.01232	2.43	1.63	0.0380	46.17	11.21	1.97	67.65
0.68537	0.00839	0.00507	2.38	3.93	0.0378	48.46	11.54	5.00	47.26
0.75366	0.00854	0.01473	2.34	1.37	0.0381	47.51	11.30	1.45	50.90
1.0781	0.00868	0.015	2.31	1.34	0.0381	44.89	11.13	1.65	71.70
0.66829	0.00883	0.00883	2.27	2.27	0.0379	50.04	11.44	1.97	45.67

L (m)	δ_{D1} (m)	δ_{D2} (m)	\bar{V}_L (m s ⁻¹)	\bar{V}_U (m s ⁻¹)	\dot{M} (kg s ⁻¹)	η_{th}	η_{PV}	P_f (W)	P_{PV} (W)
1.1463	0.00898	0.00856	2.23	2.34	0.0379	46.97	11.21	2.63	76.77
0.97561	0.00912	0.004	2.20	4.97	0.0378	45.27	11.44	10.28	66.71
0.99268	0.00927	0.00668	2.16	2.99	0.0379	47.85	11.32	3.45	67.13
0.94146	0.00941	0.00963	2.13	2.08	0.0380	48.19	11.26	1.93	63.33
0.89024	0.00956	0.01312	2.10	1.53	0.0380	47.68	11.22	1.37	59.67
0.7878	0.00971	0.00641	2.06	3.11	0.0379	48.75	11.41	3.17	53.72
0.73659	0.00985	0.01124	2.03	1.79	0.0380	49.61	11.33	1.38	49.85
1.1293	0.01	0.01178	2.00	1.71	0.0380	46.38	11.12	1.57	75.02

In Table 8.6, L is the length of the channel, δ_{D1} and δ_{D2} are the lower and upper depth of flows (m) and, \bar{V}_L and \bar{V}_U are the lower and upper mean inlet velocity (m s⁻¹).

Table 7.6. Fifty DOE points and their CFD results for four objective functions of model 4 for high temperature weather (45 °C).

L (m)	δ_{D1} (m)	δ_{D2} (m)	\bar{V}_L (m s ⁻¹)	\bar{V}_U (m s ⁻¹)	\dot{M} (kg s ⁻¹)	η_{th}	η_{PV}	P_f (W)	P_{PV} (W)
0.6	0.004	0.004	5.57	5.57	0.0397	46.45	10.76	17.55	38.57
0.6	0.01	0.004	2.24	5.57	0.0398	45.59	10.64	9.69	38.14
0.6	0.004	0.015	5.57	1.51	0.0399	39.49	10.61	9.26	38.04
0.6	0.01	0.015	2.24	1.51	0.0401	49.44	10.42	1.30	37.35
1.3	0.004	0.004	5.57	5.57	0.0397	45.10	10.51	30.05	81.67
1.3	0.01	0.004	2.24	5.57	0.0398	43.27	10.36	16.32	80.45
1.3	0.004	0.015	5.57	1.51	0.0399	35.50	10.32	15.86	80.20
1.3	0.01	0.015	2.24	1.51	0.0401	43.12	10.08	1.83	78.33
0.92439	0.004	0.00749	5.57	2.99	0.0398	43.73	10.54	14.06	58.23
1.0268	0.00415	0.01285	5.37	1.75	0.0399	38.90	10.43	12.26	63.98
1.2146	0.00429	0.0099	5.20	2.27	0.0398	40.90	10.39	13.35	75.41
0.63415	0.00444	0.00776	5.02	2.88	0.0398	45.77	10.64	8.65	40.33
0.83902	0.00459	0.01044	4.86	2.15	0.0398	42.95	10.51	8.61	52.68
0.8561	0.00473	0.01366	4.71	1.65	0.0399	40.82	10.46	7.70	53.51
0.87317	0.00488	0.0048	4.57	4.65	0.0397	47.11	10.59	13.44	55.28
1.2659	0.00502	0.00722	4.44	3.10	0.0398	44.37	10.39	10.97	78.57
1.0951	0.00517	0.00561	4.32	3.98	0.0397	46.40	10.48	11.85	68.56
0.61707	0.00532	0.01098	4.19	2.05	0.0399	45.79	10.57	5.08	38.99
1.0439	0.00546	0.01017	4.09	2.21	0.0399	43.77	10.39	6.70	64.81
1.2829	0.00561	0.01205	3.98	1.87	0.0399	41.19	10.28	6.83	78.78
1.1122	0.00576	0.01446	3.88	1.56	0.0400	40.89	10.30	5.58	68.46
0.70244	0.0059	0.01393	3.79	1.62	0.0400	44.36	10.48	4.03	43.98
0.80488	0.00605	0.00802	3.69	2.79	0.0398	47.28	10.50	5.37	50.49
1.1976	0.0062	0.00454	3.60	4.91	0.0397	46.32	10.45	14.15	74.77
1.1634	0.00634	0.00829	3.52	2.70	0.0398	45.40	10.35	6.02	71.93
0.6	0.00649	0.00615	3.44	3.63	0.0398	49.15	10.63	5.54	38.10
0.82195	0.00663	0.00427	3.37	5.22	0.0397	47.10	10.58	11.90	51.96

L (m)	δ_{D1} (m)	δ_{D2} (m)	\bar{V}_I (m s ⁻¹)	\bar{V}_{II} (m s ⁻¹)	\dot{M} (kg s ⁻¹)	η_{th}	η_{PV}	P_f (W)	P_{PV} (W)
0.90732	0.00678	0.01339	3.30	1.68	0.0400	44.39	10.35	3.46	56.12
0.71951	0.00693	0.01071	3.23	2.10	0.0399	47.47	10.47	3.26	45.01
1.1805	0.00707	0.01151	3.16	1.95	0.0399	43.97	10.26	3.96	72.37
1.2317	0.00722	0.0142	3.10	1.59	0.0400	42.03	10.20	3.54	75.09
0.77073	0.00737	0.00695	3.04	3.22	0.0398	48.63	10.50	4.61	48.35
0.95854	0.00751	0.0091	2.98	2.46	0.0399	46.91	10.37	3.72	59.39
1.061	0.00766	0.00534	2.92	4.18	0.0398	46.98	10.42	8.20	66.09
1.2488	0.0078	0.00588	2.87	3.80	0.0398	46.29	10.34	7.51	77.16
1.3	0.00795	0.00937	2.82	2.39	0.0399	44.88	10.23	3.96	79.46
0.65122	0.0081	0.01259	2.76	1.79	0.0400	48.41	10.45	2.14	40.67
1.0098	0.00824	0.01232	2.72	1.83	0.0400	45.56	10.27	2.59	61.99
0.68537	0.00839	0.00507	2.67	4.40	0.0398	48.18	10.57	6.61	43.30
0.75366	0.00854	0.01473	2.62	1.53	0.0400	46.96	10.36	1.90	46.64
1.0781	0.00868	0.015	2.58	1.51	0.0401	44.12	10.20	2.17	65.71
0.66829	0.00883	0.00883	2.54	2.54	0.0399	49.70	10.48	2.59	41.84
1.1463	0.00898	0.00856	2.50	2.62	0.0399	46.48	10.27	3.46	70.35
0.97561	0.00912	0.004	2.46	5.57	0.0398	44.93	10.48	13.51	61.11
0.99268	0.00927	0.00668	2.42	3.35	0.0399	47.44	10.37	4.53	61.51
0.94146	0.00941	0.00963	2.38	2.33	0.0399	47.62	10.32	2.54	58.04
0.89024	0.00956	0.01312	2.35	1.72	0.0400	47.04	10.28	1.80	54.68
0.7878	0.00971	0.00641	2.31	3.49	0.0399	48.47	10.46	4.18	49.23
0.73659	0.00985	0.01124	2.28	2.00	0.0400	49.13	10.38	1.81	45.68
1.1293	0.01	0.01178	2.24	1.91	0.0400	45.83	10.19	2.07	68.75

7.5.5 Optimisation analysis

Firstly, a surrogate-based optimisation is carried out with the goal to maximise both the electric and the thermal efficiencies as previously undertaken by previous authors [67]. This will then be followed by reformulating the design optimisation problem in order to minimise the fan power consumption and maximise electrical power. The current design optimisation studies are also performed to investigate the significance of the temperature operating conditions, low temperature (25 °C) and high temperature (45 °C). These two temperatures are found to be an appropriate representation for low and high temperatures in the geographical regions under investigations. Illustrative examples of functions η_{PV} and η_{th} in terms of the design variables δ_{D1} and δ_{D2} and L are shown in Fig. 7.17 and Fig. 7.18 respectively. The multi-objective genetic algorithm (GA) technique, which is founded in [403, 404], is utilised to obtain the Pareto front curves for the four objectives i.e. the fan power (P_f) and the electrical power (P_{PV}) on one hand, the electric efficiency (η_{PV}) and the thermal efficiency (η_{th}) on the other hand.

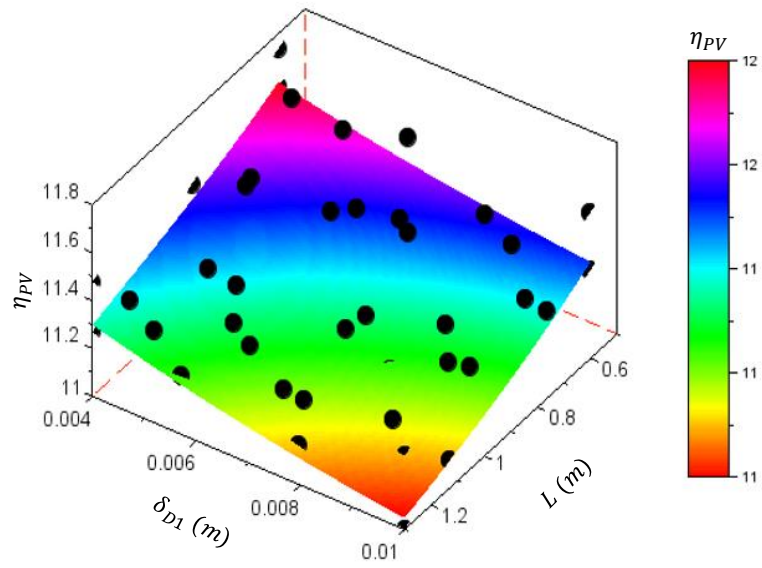


Fig. 7.17. Function of η_{PV} from the surrogate model at low high condition (25 °C).

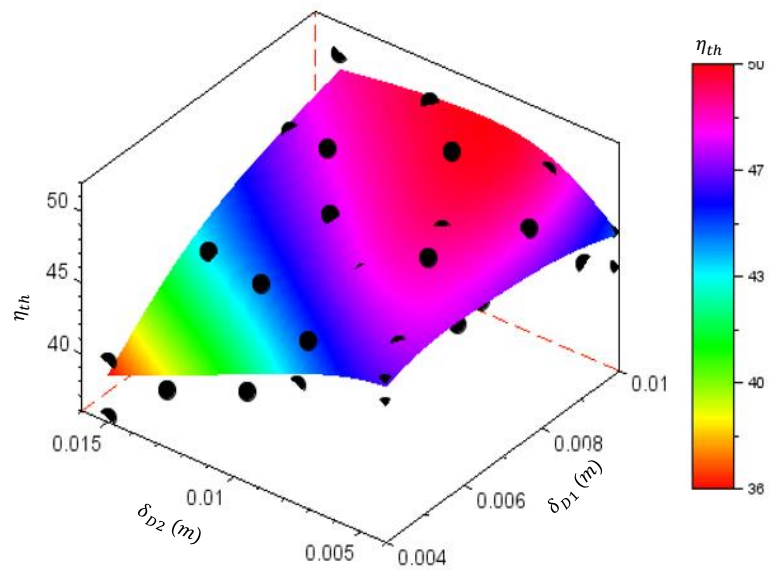


Fig. 7.18. Function of η_{th} from the surrogate model at low high condition (25 °C).

The first Pareto front curve represents the design optimisation analysis in terms of thermal and electrical efficiencies at low temperature (25 °C) as presented in Fig. 7.19. Inspection of

Fig. 7.19 reveals that it cannot move along the optimised design points lying on the Pareto front to reduce thermal efficiency without increasing the electrical efficiency. One of the compromise points is P_3 in which the thermal and electrical efficiencies are 49.1889 and 11.6064. The geometry parameters of this point are $L = 0.6080$, $\delta_{D1} = 0.0064$ m and $\delta_{D2} = 0.0057$ m. Referring to Fig. 7.19 and Table 7.7, it can be seen that there are five design points, which lying on the Pareto front, are highlighted. In order to ensure the accuracy of results, the validation of the five points is performed as detailed in Table 7.7 and Fig. 7.19. The results exhibit very good agreement between the estimated and CFD results.

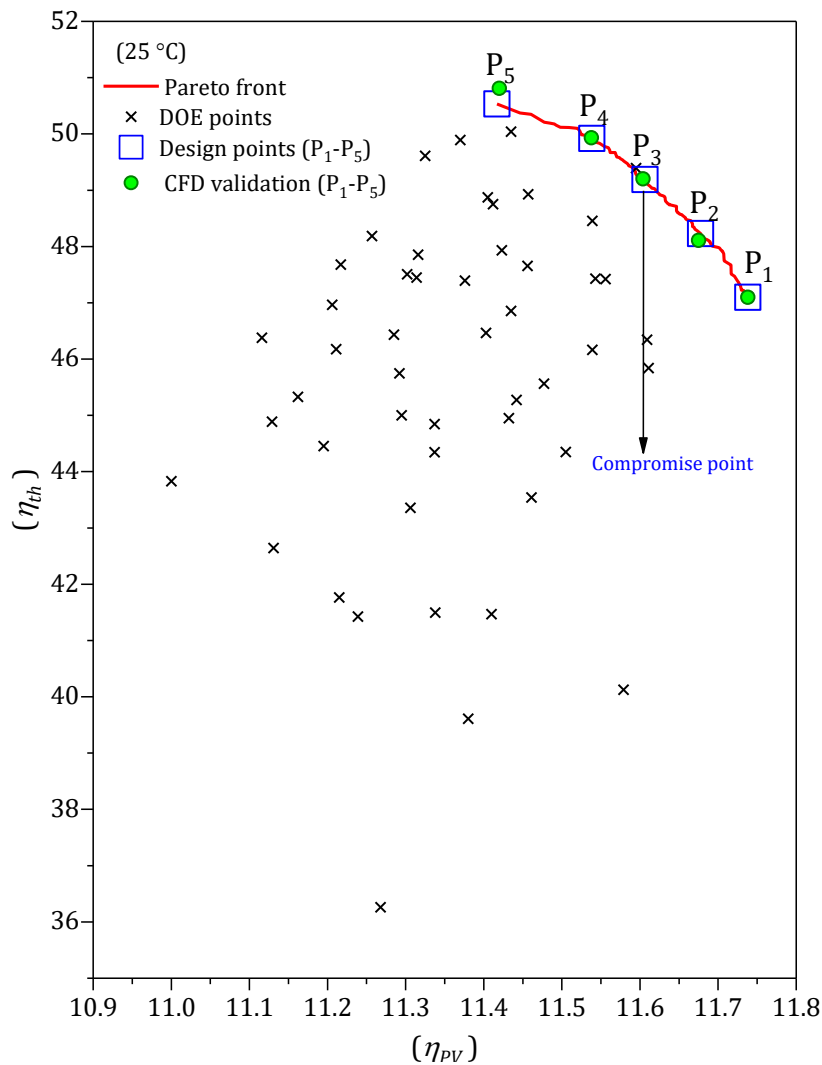


Fig. 7.19. Pareto front showing the compromises that can be struck in maximising both η_{th} and η_{pv} together with five representative design points (e.g. P₁-P₅) used for the PV/T performance analysis illustrated in Table 7.7 when operating at 25 °C.

Table 7.7. PV/T design performance of model 4 at five operating conditions points located on the Pareto front together with CFD validation, as shown in Fig. 7.19 when operating at 25 °C.

Design points for Pareto front				Metamodels		CFD validation		Relative error	
Case	L (m)	δ_{D1} (m)	δ_{D2} (m)	η_{th}	η_{PV}	η_{th}	η_{PV}	η_{th} (%)	η_{PV} (%)
P ₁	0.6000	0.0100	0.0110	50.5326	11.4169	50.8080	11.4200	0.5420	0.0268
P ₂	0.6089	0.0076	0.0071	49.9194	11.5383	49.9310	11.5380	0.0231	0.0023
P ₃	0.6080	0.0064	0.0057	49.1889	11.6064	49.2010	11.6040	0.0246	0.0206
P ₄	0.6074	0.0053	0.0044	48.2299	11.6777	48.1070	11.6750	0.2555	0.0229
P ₅	0.6000	0.0040	0.0040	47.0980	11.7380	47.0970	11.7380	0.0022	0.0000

The second Pareto front curve is the design optimisation analysis of model 4 in terms of thermal and electrical efficiencies at high temperature (45 °C), as shown in Fig. 7.20. Similarly to low-temperature design optimisation case, Fig. 7.20 indicates that no dominated point gives both maximum values for two objectives. A selected compromise point is P₃, where the thermal and electrical efficiencies are 48.9896 and 10.6273. The geometry parameters of this point are $L = 0.6131$, $\delta_{D1} = 0.0065$ m and $\delta_{D2} = 0.0058$ m.

Five candidate optimum designs have been selected from the Pareto front, as shown in Fig. 7.20 and Table 7.8. Similarly to the low-temperature case, the validation of the five points is performed which shown in Fig. 7.20 and Table 7.8. The results indicate that there is very good agreement between the predicted and CFD results.

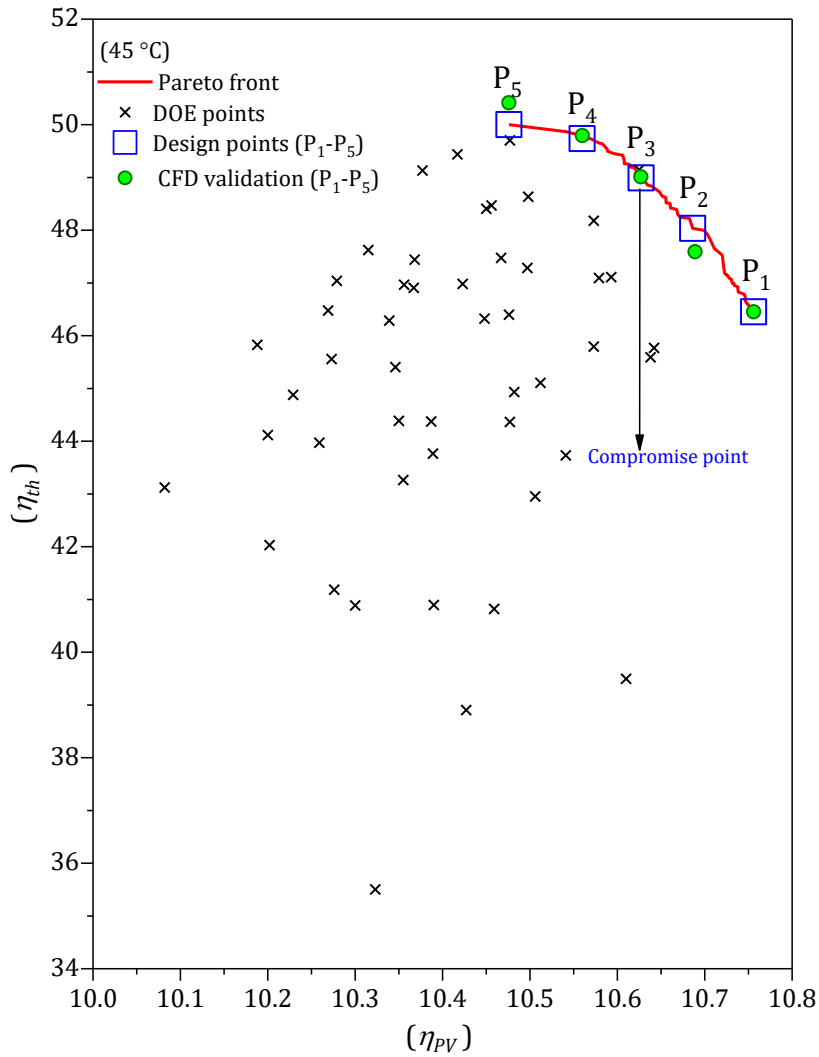


Fig. 7.20. Pareto front showing the compromises that can be struck in maximising both η_{th} and η_{PV} together with five representative design points (e.g. P₁-P₅) used for the PV/T performance analysis illustrated in Table 7.8 when operating at 45°C.

Table 7.8. PV/T design performance of model 4 at five operating conditions points located on the Pareto front together with CFD validation, as shown in Fig. 7.20 when operating at 45 °C.

Case	Design points for Pareto front			Metamodels		CFD validation		Relative Error	
	L (m)	δ_{D1} (m)	δ_{D2} (m)	η_{th}	η_{PV}	η_{th}	η_{PV}	η_{th} (%)	η_{PV} (%)
P ₁	0.6171	0.0100	0.0094	50.0005	10.4761	50.4130	10.4760	0.8183	0.0006
P ₂	0.6134	0.0081	0.0071	49.7368	10.5598	49.7930	10.5600	0.1129	0.0021
P ₃	0.6131	0.0065	0.0058	48.9896	10.6273	49.0110	10.6270	0.0436	0.0026
P ₄	0.6181	0.0059	0.0042	48.0327	10.6863	47.5910	10.6890	0.9281	0.0257
P ₅	0.6000	0.0040	0.0040	46.4510	10.7560	46.4510	10.7560	0.0000	0.0000

On the other hand, in terms of design optimisation of power fan and electrical power, Fig. 7.21 and Fig. 7.22 present the design of experiments, the Pareto front curves and the validation points of model 4 at a low and high temperature, 25 °C and 45 °C respectively. Furthermore, the impact of the two objective functions of interest is shown in these figures. The most significant result in these figures is that the impact of increasing the fan power on

PV power generation almost disappeared after the compromise point (P_3), see Fig. 7.21 and Fig. 7.22. In other words, in Fig. 7.21 and Fig. 7.22, there is a clear trend of a slight increase in electrical power generation compared to huge increase in fan power consumption after P_3 . It should be mentioned that the main variables affect the electrical power generation are the collector dimensions (length, depth of flows); however, this study offers the best compromise point (P_3) for this range of collector dimensions. Finally, two validations are performed for Pareto front curves for low and high temperatures, as illustrated in Table 7.9, Table 7.10, Fig. 7.21 and Fig. 7.22. The predicted results are in agreement with CFD results.

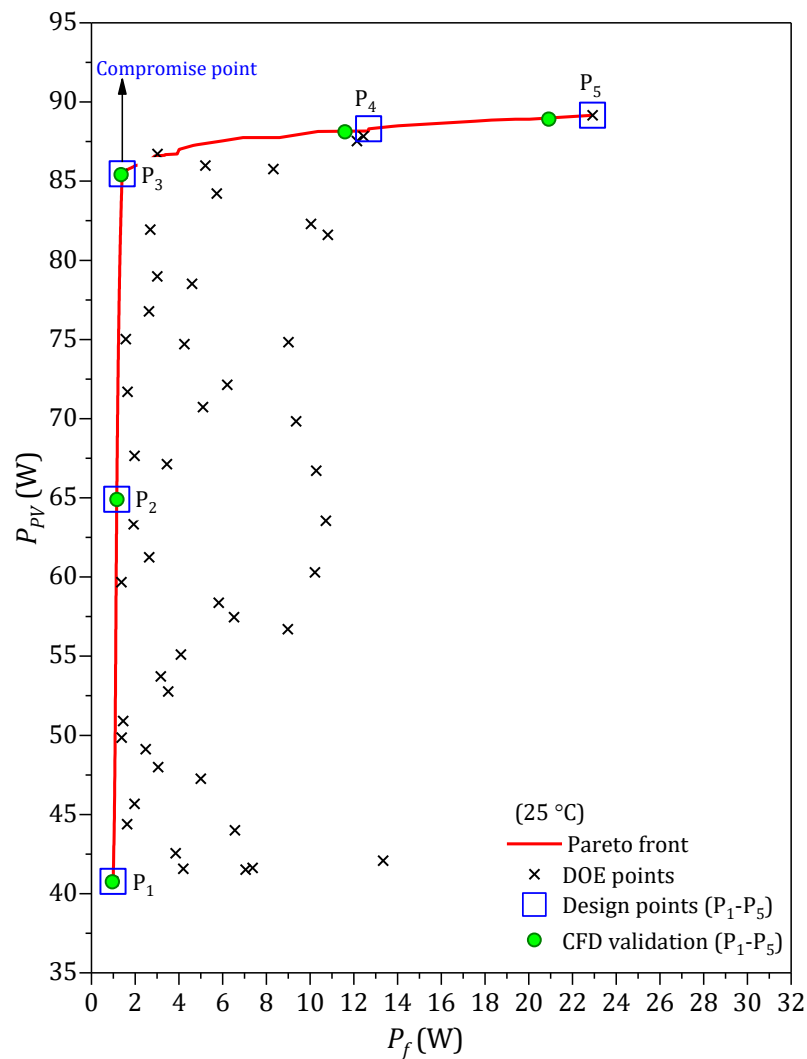


Fig. 7.21. Pareto front showing the compromises that can be struck in minimising the fan power and maximising electrical power together with five representative design points (e.g. P_1 - P_5) used for the PV performance analysis illustrated in Table 7.9 when operating at 25 °C.

Table 7.9. PV/T design performance of model 4 at five operating conditions points located on the Pareto front together with CFD validation, as shown in Fig. 7.21 when operating at 25 °C.

Design points for Pareto front				Metamodels		CFD validation		Relative Error	
Case	L (m)	δ_{D1} (m)	δ_{D2} (m)	P_f (W)	P_{PV} (W)	P_f (W)	P_{PV} (W)	P_f (%)	P_{PV} (%)
P ₁	0.6000	0.0100	0.0150	0.9904	40.7680	0.9566	40.7480	0.0491	3.5312
P ₂	0.9756	0.0100	0.0150	1.1578	64.9089	1.1697	64.8840	0.0384	1.0162
P ₃	1.3000	0.0100	0.0149	1.4056	85.4630	1.3588	85.4010	0.0726	3.4471
P ₄	1.2987	0.0059	0.0046	12.6832	88.3088	11.6000	88.1170	0.2177	9.3380
P ₅	1.3000	0.0040	0.0040	22.9220	89.1630	20.9160	88.9070	0.2879	9.5907

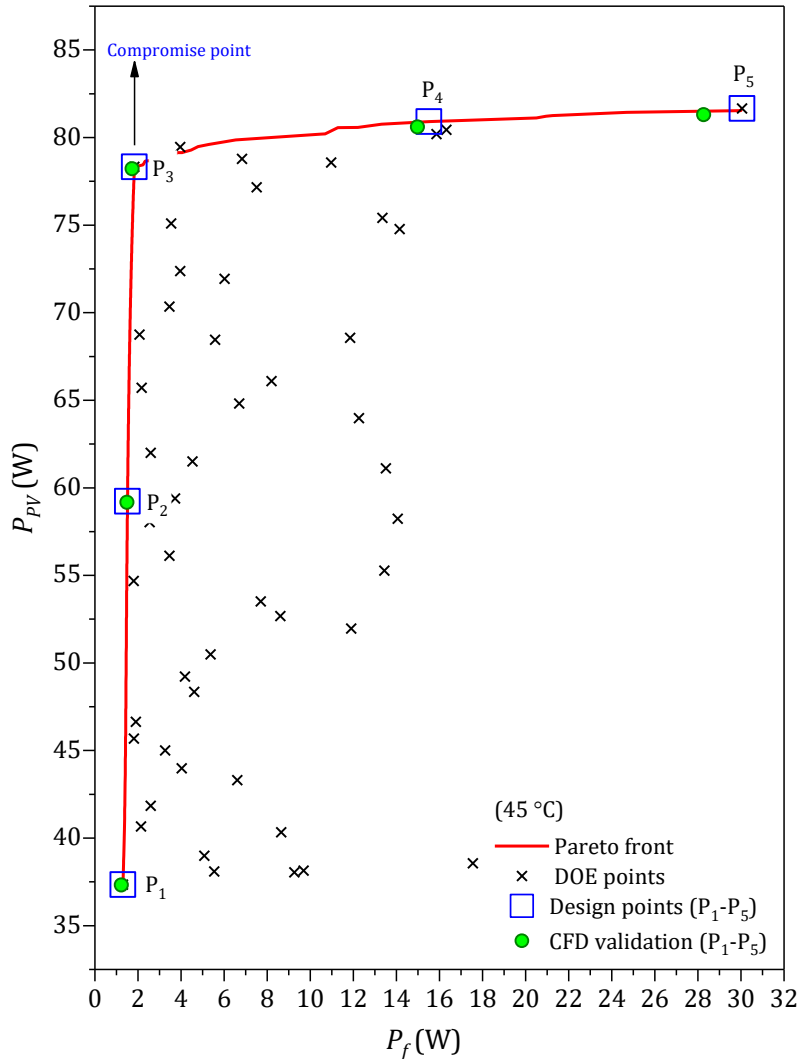


Fig. 7.22. Pareto front showing the compromises that can be struck in minimising the fan power and maximising electrical power together with five representative design points (e.g. P₁-P₅) used for the PV/T performance analysis illustrated in Table 7.10 when operating at 45 °C.

Table 7.10. PV/T design performance of model 4 at five operating conditions points located on the Pareto front together with CFD validation, as shown in Fig. 7.22 when operating at 45 °C.

Design points for Pareto front				Metamodels		CFD validation		Relative Error	
Case	L (m)	δ_{D1} (m)	δ_{D2} (m)	P_f (W)	P_{PV} (W)	P_f (W)	P_{PV} (W)	P_f (%)	P_{PV} (%)
P ₁	0.6000	0.0100	0.0150	1.3023	37.3500	1.2268	37.3160	0.0911	6.1542
P ₂	0.9712	0.0100	0.0150	1.5125	59.2303	1.4887	59.1710	0.1003	1.5963
P ₃	1.3000	0.0100	0.0150	1.8333	78.3270	1.7297	78.2150	0.1432	5.9895
P ₄	1.2996	0.0052	0.0055	15.5108	80.9034	14.9800	80.5970	0.3801	3.5432
P ₅	1.3000	0.0040	0.0040	30.0530	81.6650	28.2670	81.2990	0.4502	6.3183

Finally, Fig. 7.23 and Table 7.11 present the main findings of this chapter for five PV systems under similar conditions. It can be observed that the use of pre-cooled air effectively contributes to improving electrical performance by 15% to 18%. For example, when the electrical efficiency of model 1_{PV-45} is 9.93%, while, model 4_{PV/T-25} with pre-cooled air has an electrical efficiency of 11.74%. This is an improvement by 18% compared to model 1_{PV-45}. In addition, the PV module temperature decreased from 72.28 °C in model 1_{PV-45} to 36.94 °C in model 4_{PV/T-25} with pre-cooled air.

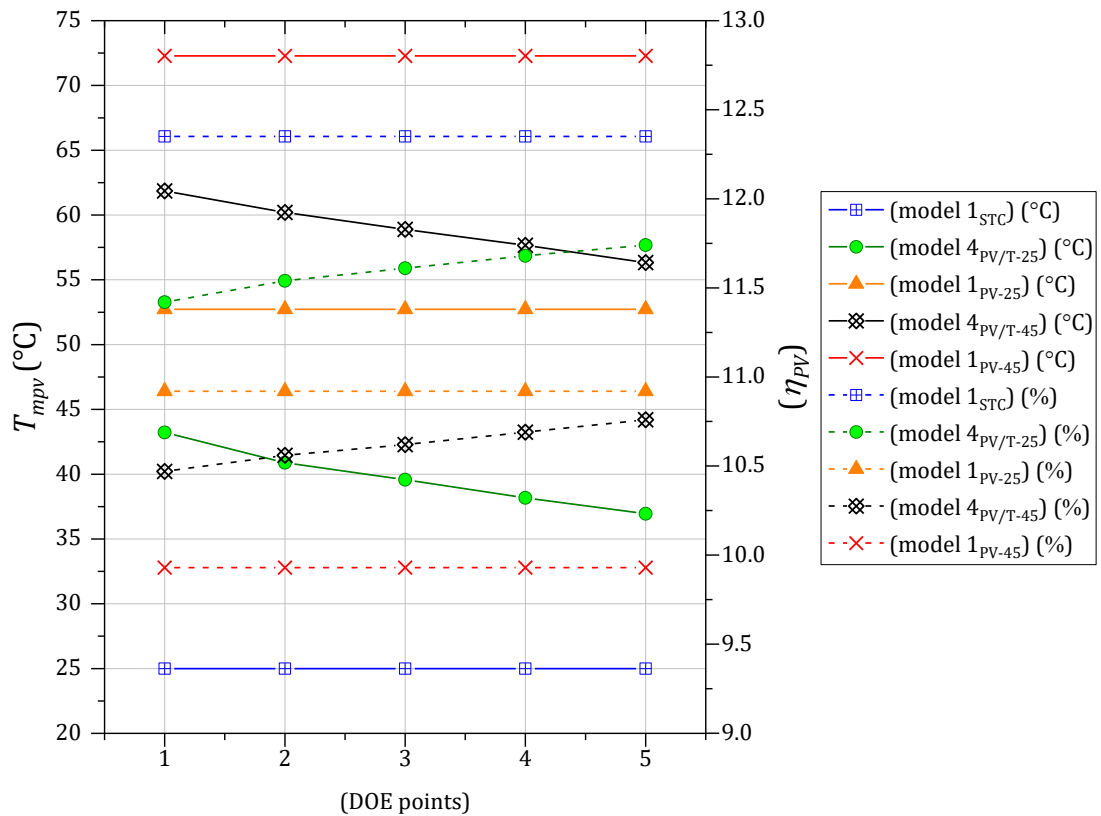


Fig. 7.23. Comparison between different PV and PV/T systems showing the impact of the temperature of the PV module on electrical efficiency under similar conditions for model 1_{STC}, model 1_{PV-25}, model 1_{PV-45}, model 4_{PV/T-25}, model 4_{PV/T-25} and model 4_{PV/T-45}.

In Fig. 7.23 and Table 7.11, η_{ref} and T_{ref} are the reference electrical efficiency and the temperature of the PV module at standard conditions (STC) respectively (model 1_{STC}). T_{PV-25} and η_{PV-25} are the electrical efficiency and the temperature of the PV module at low temperature (25 °C) (model 1_{PV-25}). In this model, the system is exposed to ambient conditions without cooling. T_{PV-45} and η_{PV-45} are similar to model 1_{PV-25} but the electrical efficiency and the temperature of the PV module are evaluated at high temperature (45 °C) (model 1_{PV-45}). $\eta_{PV/T-25}$ and $T_{PV/T-25}$ are the electrical efficiency and the temperature of the PV module at low temperature (25 °C) of the hybrid PV/T air system (model 4_{PV/T-25}). In model 4_{PV/T-25}, the PV/T air system uses precooled air the exhaust air of the building as a coolant instead of using ambient air (i.e. 45 °C). $T_{PV/T-45}$ and $\eta_{PV/T-25}$ are similar to model 4_{PV/T-25} however, the electrical efficiency and the temperature of the PV module are evaluated at high temperature (45 °C) (model 4_{PV/T-45}). $PE_{T_{mpv}}$ is the percentage reduction of the PV module temperature between T_{PV-45} and $T_{PV/T-25}$. $PE_{\eta_{PV}}$ is the percentage enhancement of the PV module efficiency between η_{PV-45} and $\eta_{PV/T-25}$.

Table 7.11. Comparison between different PV and PV/T systems showing the impact of the temperature of the PV module on electrical efficiency under similar conditions for model 1_{STC}, model 1_{PV-25}, model 1_{PV-45}, model 4_{PV/T-25}, model 4_{PV/T-25} and model 4_{PV/T-45}.

PV temperatures, T_{mpv} (°C)				
T_{ref}	$T_{PV/T-25}$	T_{PV-25}	$T_{PV/T-45}$	T_{PV-45}
25.00	43.224	52.73	61.86	72.28
25.00	40.888	52.73	60.20	72.28
25.00	39.577	52.73	58.89	72.28
25.00	38.173	52.73	57.66	72.28
25.00	36.943	52.73	56.33	72.28
Electrical Efficiencies, η_{PV} (%)				
η_{ref}	$\eta_{PV/T-25}$	η_{PV-25}	$\eta_{PV/T-45}$	η_{PV-45}
12.35	11.42	10.92	10.47	9.93
12.35	11.54	10.92	10.56	9.93
12.35	11.61	10.92	10.62	9.93
12.35	11.68	10.92	10.69	9.93
12.35	11.74	10.92	10.76	9.93
$PE_{T_{mpv}}$, percentage reduction of the PV module temperature between T_{PV-45} and $T_{PV/T-25}$ (%)				
40.20	43.43	45.24	47.19	48.89
$PE_{\eta_{PV}}$, percentage enhancement of the PV module efficiency between η_{PV-45} and $\eta_{PV/T-25}$ (%)				
15.01	16.21	16.92	17.62	18.23

7.6 Model 4-A

In this section, the flow configuration in model 4 is modified to include a staggered off-set strip fin arrangement (model 4-A). The mesh independence study, boundary conditions, assumptions, numerical methods and validation were detailed in Chapter 4. For a full

description of model 4-A, see Fig. 4.9 while For a brief description, see Fig. 7.24. The dimensions of fins are chosen based on [289, 290]. The thermal, electrical and hydrodynamic parameters of this system are examined in three stages. Before starting the stages, it should be noted that the names of models in this section are as follows: model 4_{non} , model $4-A_{non}$, model 4_{opt} and model $4-A_{opt}$. Model 4_{non} and model $4-A_{non}$ are model 4 (with and without fins, respectively, using the common dimensions from literature (non-optimised models). Model 4_{opt} is similar to Model 4_{non} , but this model is optimised model under low condition (i.e. Table 7.7 (P₁-P₅)). Model $4-A_{opt}$ is also similar to model $4-A_{non}$ but using the optimal dimensions that result from the optimisation process of model 4 (i.e. Table 7.7 (P₁-P₅)). The first stage is to evaluate the effect of fin gap (see Fig. 7.24) on the performance of model 4-A. Secondly, the examination of model $4-A_{non}$ and model 4_{non} . Finally, a comparison is conducted using the optimal dimensions that result from the optimisation process of model 4_{opt} (i.e. Table 7.7 (P₁-P₅)) to evaluate the finned model (model $4-A_{opt}$).

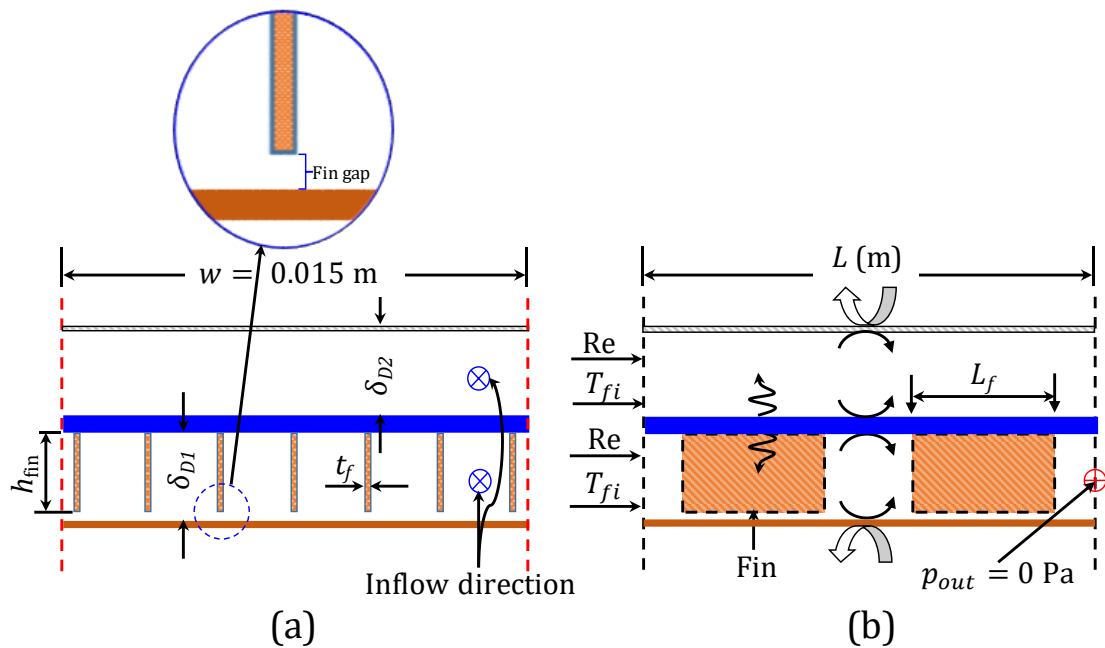


Fig. 7.24. Sectional front (a) and side (b) views of model 4-A.

Firstly, the fin gap is that between the top surface of the lower absorber plate and the lower surface of fins, as shown in Fig. 7.24. The effect of the fin gap on the overall PV/T performance is investigated. The weather conditions are constant during this examination. Incident solar radiation is 1000 W m^{-2} ambient temperature is $40 \text{ }^\circ\text{C}$. The ambient temperature is assumed to equal to the fluid inlet temperature. The other boundary

conditions and dimensions can be seen in Table 7.12. Four different fin gaps are considered, 2 mm, 1.5 mm, 1 mm and 0 mm.

Table 7.12. Dimensions and boundary conditions of model 4-A_{non} (fin gap examination).

Case	L (m)	δ_{D1} (m)	δ_{D2} (m)	L_f (m)	S_f (m)	w (m)	Re	\bar{V} (m s ⁻¹)	\dot{M} (kg s ⁻¹)
1	1.2	0.025	0.025	0.048	0.01	0.6	410.56	0.145	0.0052
2	1.2	0.025	0.025	0.048	0.01	0.6	513.20	0.181	0.0065
3	1.2	0.025	0.025	0.048	0.01	0.6	684.27	0.241	0.0087
4	1.2	0.025	0.025	0.048	0.01	0.6	1026.41	0.361	0.0130
5	1.2	0.025	0.025	0.048	0.01	0.6	2052.81	0.723	0.0261

The impact of various fin gaps on the overall performance of model 4-A_{non} is shown in Fig. 7.25. It is seen that when the fin gap increases the overall efficiency of PV/T air system increases, particularly at the 2 mm fin gap. This enhancement can be attributed to the fact that the fin gap allows the air to flow underneath the fins which enables the flow of heat from the lower surface of the fins (from the upper to the lower direction of the fins). This means that there is an interaction between the air and the solid face in this region by convection-conduction. Another advantage from this investigation is that the pressure drop along the duct is decreased by up to a 10.5% decrease, as shown in Table 7.13.

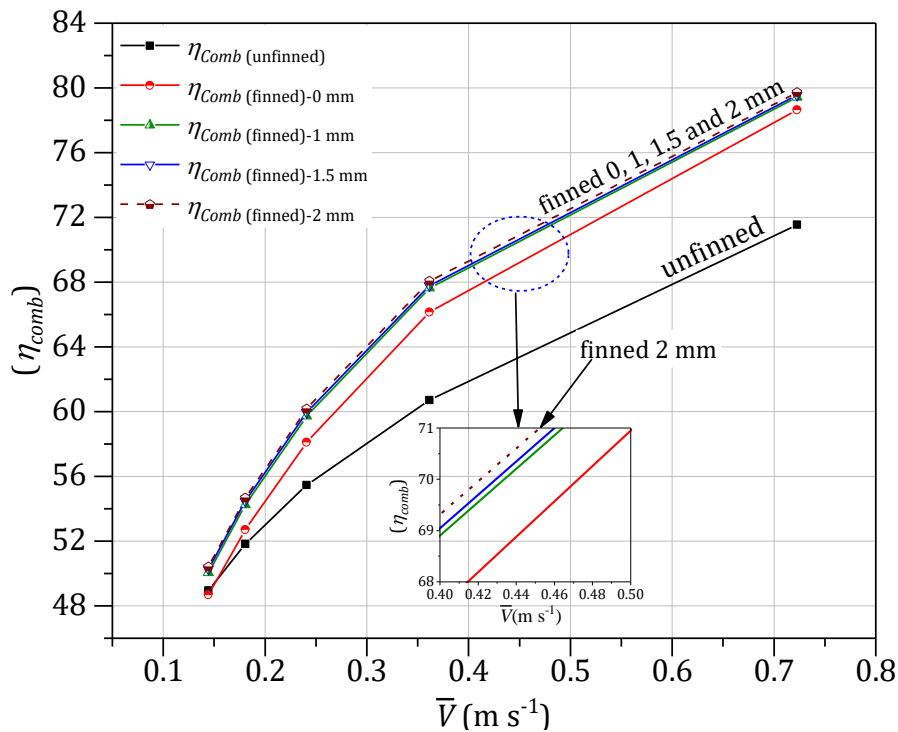


Fig. 7.25. Overall efficiency versus inlet air velocity for model 4-A_{non} and 4_{non}.

Table 7.13. Pressure drop and its percentage reduction for model 4-A_{non} and 4_{non}.

Re	410.56	513.2	684.27	1026.41	2052.81
$\Delta p_{-0\text{ mm}}$	1.47	2.09	3.38	6.97	26.10
$\Delta p_{-2\text{ mm}}$	1.44	2.03	3.22	6.47	23.34
$PE_{\Delta p}$ (%)	2.04	2.87	4.73	7.17	10.57

In [Table 7.13](#), $PE_{\Delta p}$ is the percentage reduction of pressure drop between model 4-A_{non} with fin gap 2 mm and model 4-A_{non} with fin gap 0 mm.

The second stage is to compare the performance of model 4_{non} with model 4-A_{non}. The boundary and weather conditions are similar to the first step (examination of the fin gap).

[Fig. 7.25](#) also shows the impact of a range of velocities on the overall efficiency for both with and without fins systems. The overall efficiency is seen to be directly proportional to the velocity of the air. This is expected because of the convective heat transfer coefficient being directly proportional to the Re and inlet air velocity. However, at velocities less than 0.15 m s⁻¹ (Re = 410) the efficiency of model 4_{non} is higher than that of model 4-A_{non}. This effect is owing to the fin effectiveness at this range working as a conductive resistance layer to heat transfer rather than a dissipater of heat.

[Fig. 7.26](#) and [Table 7.14](#) illustrate the effect of fan power consumption on the total and electrical power generation using various inlet air velocities for model 4-A_{non} (fin gap 2 mm) and model 4_{non}. The total power generation, P_{total} (W) is the summation of the electrical power generation plus the thermal heat gain. It can be observed from the data that there is a clear trend of increasing fan power increases the total power. Although typically, increasing fan power reduces total power, the presence of a better cooling PV leads to an increase in total power generation. It can be said that increasing fan power leads to increasing electrical efficiency. Therefore, there is a need for careful selection of fan. This can be achieved by optimising the fan consumption for maximising the electrical efficiency. In addition, it is found that the highest fan power is required for the finned model (model 4-A_{non}) with the lowest found for the plain model (model 4_{non}). The maximum percentage enhancement in electrical power generation between the last and first velocities (0.14456 and 0.14456 m s⁻¹) ([Table 7.14](#)) is 8.79% for model 4-A_{non} and 6.68% for model 4_{non}.

In connection to [Fig. 7.21](#) and [Fig. 7.22](#) also indicate how significant the effect of the fan power selection to optimise its consumption for model 4_{opt}. For example, when the fan power is about 1.3 W the electrical power generation is 85.4 W, whereas when the fan power 20.9 W the electrical power generation is 88.9 W. This means, fan power increases about 15.5 times to increase the power by 4.1% ([Table 7.9](#)). It could be not valid to use the

optimal dimensions of model 4_{opt} to build the model 4-A_{opt}; thus, motivation is to carry out a new optimisation process for model 4-A for future work.

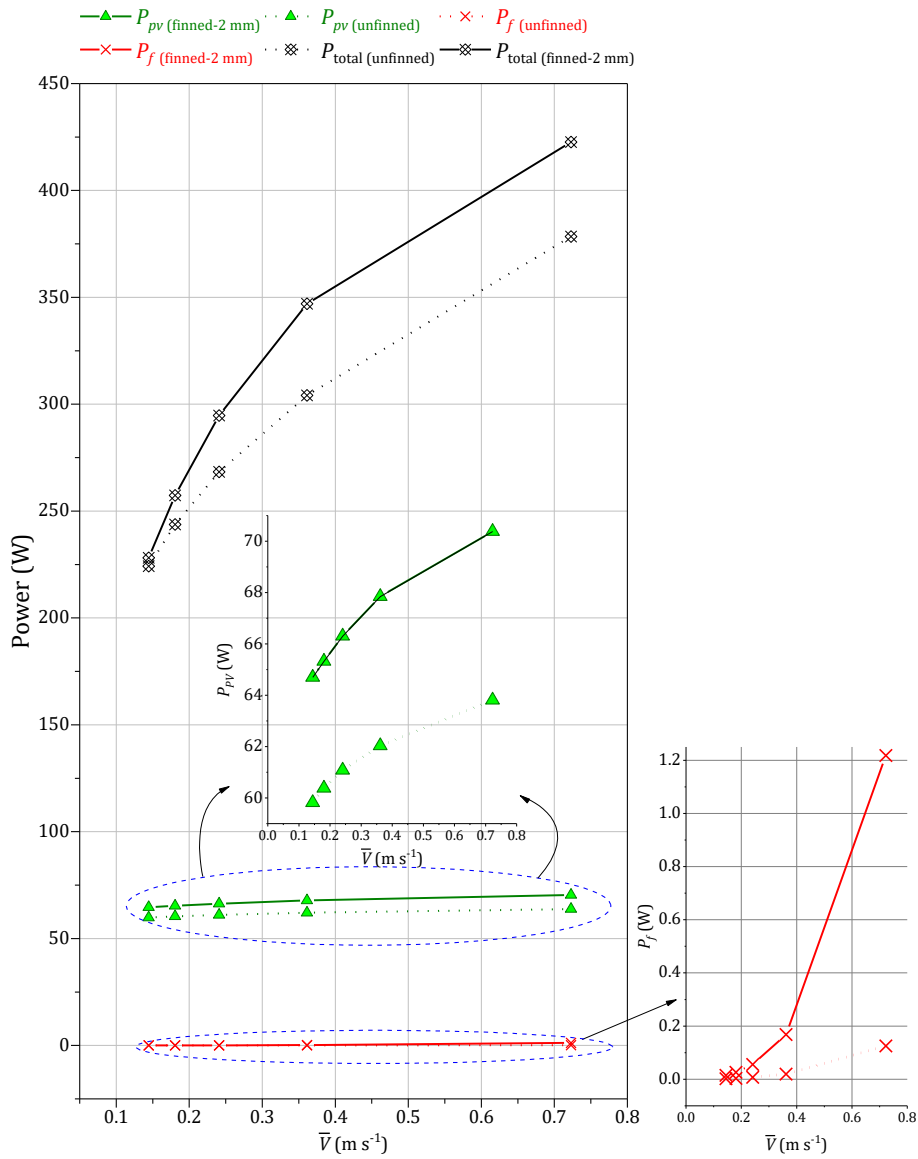


Fig. 7.26. Total power generation, electrical power generation and fan power versus inlet air velocity for model 4-A_{non} and 4_{non}.

Table 7.14. Total power generation, electrical power generation and fan power versus inlet air velocity for model 4- A_{non} and 4_{non} .

\bar{v} (m s ⁻¹)	Model 4- A_{non} (finned-2 mm)			Model 4_{non}			Percentage enhancement	
	P_{PV} (W)	P_f (W)	P_{total} (W)	P_{PV} (W)	P_f (W)	P_{total} (W)	$PE_{P_{PV}}$ (%)	$PE_{P_{total}}$ (%)
0.14456	64.700	0.0149	228.12	59.816	0.00210	224.260	8.165	1.721
0.18070	65.328	0.0262	257.32	60.380	0.00354	243.760	8.195	5.563
0.24093	66.308	0.0556	294.68	61.084	0.00705	268.340	8.552	9.816
0.36140	67.848	0.1679	346.96	62.036	0.01943	304.084	9.369	14.100
0.72280	70.384	1.2181	422.64	63.812	0.12554	378.476	10.299	11.669

In [Table 7.14](#), $PE_{P_{PV}}$ and $PE_{P_{total}}$ are the percentage enhancement of the electrical and total power generation for model 4- A_{non} with respect to model 4_{non} , respectively.

A comparison of the electrical efficiency of models 4- A_{non} and 4_{non} is presented in [Fig. 7.27](#). In this figure, thermal resistance and PV module temperature parameters are considered for a range of Re (410-2052)/air velocities 0.145-0.723 m s⁻¹, see [Table 7.12](#). The temperature of the PV module is inversely proportional to the rise of air velocity. This is expected because the convective heat transfer coefficient is directly proportional to the air velocity. This reduction in temperature results in a similar rise in electrical efficiency as seen by [Eq. 3.120](#).

It can also be seen that thermal resistance and temperature of the PV module are similar trends since temperature of the PV module is the main parameter to calculate the thermal resistance ([Eq. 3.125](#)) while other parameters in this equation are kept constant during this examination.

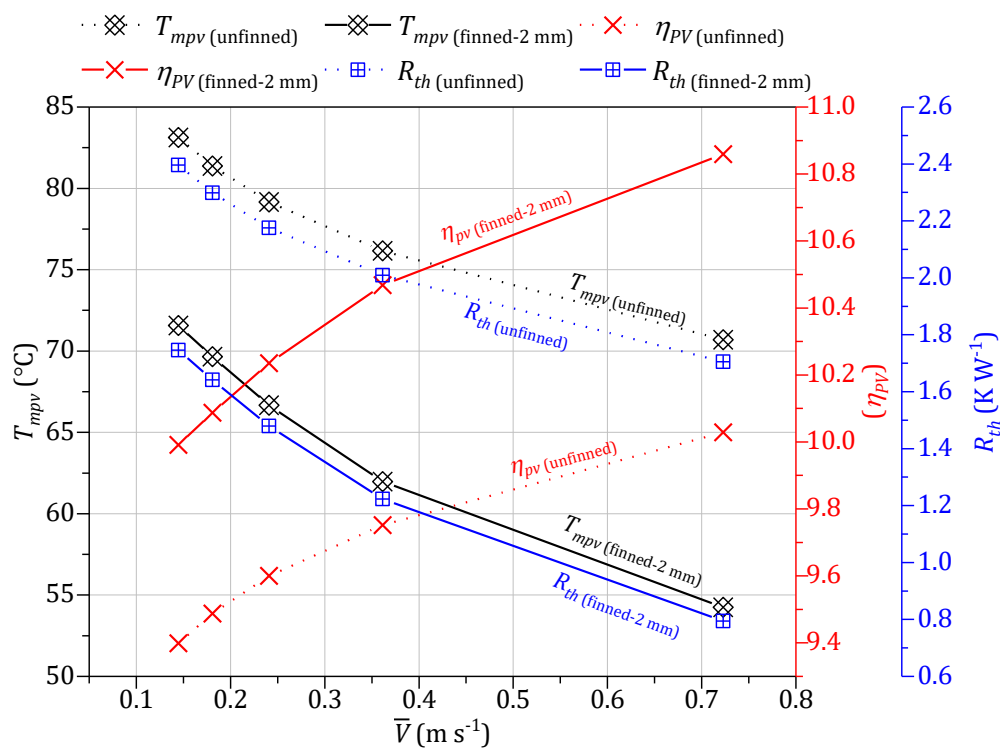


Fig. 7.27. PV module temperature, electrical efficiency and thermal resistance versus inlet air velocity for models 4-A_{non} and 4_{non}.

The final step is to investigate the effect of addition off-set strip fins (staggered arrangements) for model 4-A_{opt} using the dimensions and boundary conditions of model 4 (Table 7.7 (P₁-P₅)).

A comparison between the thermal efficiency, electrical efficiency and PV module temperature for model 4_{opt} and model 4-A_{opt} is shown in Fig. 7.28. In this comparison, the optimal dimensions are used in Table 7.7, (P₁-P₅) for low temperature condition 25 °C. Similarly to Fig. 7.27, the PV module efficiency is inversely proportional to the temperature of the PV module. Although model 4-A_{opt} shows better PV cooling i.e. lower PV temperature and higher electrical efficiency, the impact of varying dimensions of the collector is clearly seen in the plain model in which there is a gradual decrease in temperature and increase in electrical efficiency that offers flexibility for designers to choose the compromise design point among them. While in model 4-A_{opt} the trend of the curves is nearly straight. This means the use of optimal dimensions may not be suitable for model 4-A and new optimisation process should be applied to achieve better thermal and electrical enhancement for model 4-A. This figure also shows the thermal efficiency for the two models. It is apparent that thermal efficiency for model 4_{opt} also reveals a significant effect when using optimal dimensions. In contrast, model 4-A_{opt} specifically at P₅, when the thermal efficiency decrease dramatically compared to model 4_{opt}. This is because the air

temperature difference between the inlet and outlet in is lower for model 4-A_{opt} than model 4_{opt} at P₅, confirming the significance of the optimisation process to optimise the fan power consumption.

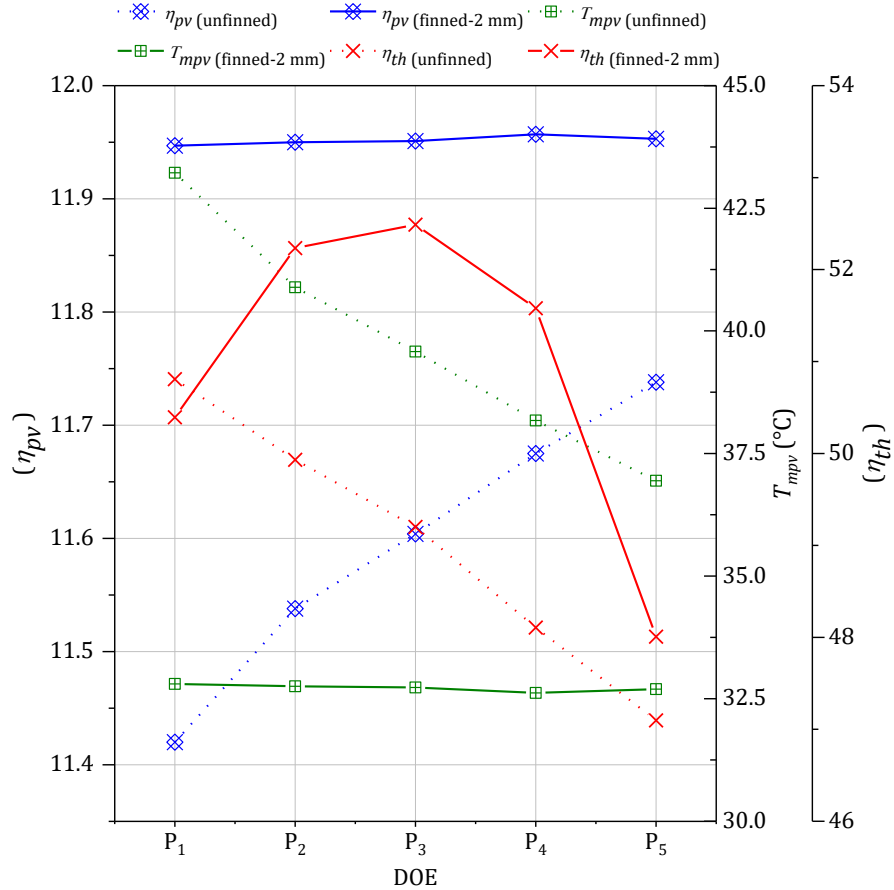


Fig. 7.28. PV module temperature, electrical efficiency and thermal efficiency versus five optimal design points (P₁ to P₅ in Table 7.7) for low temperature condition 25 °C for model 4-A_{opt} and 4_{opt}.

An overall comparison is performed to evaluate the thermal and hydrodynamic performance for model 4_{opt} and model 4-A_{opt}, as shown in Fig. 7.29 and Table 7.15. It is similar to Fig. 7.26 and Table 7.14, The total power generation is the total of the electrical and thermal power generation, P_{total} (W). It is worth mentioning that each design point is an individual case in which it has different conditions. This means the inspection is carried out at each point separately as well as between the design points (P₁-P₅) to evaluate the performance of two models (model 4-A_{opt} and 4_{opt}). Firstly, as expected the highest fan power is required for the finned model (model 4-A_{opt}) with the lowest found for the plain model (model 4_{opt}).

Secondly, the maximum and minimum $PE_{P_{total}}$ are 13.30% at P_4 and 1.93% at P_1 respectively. Whereas the maximum and minimum $PE_{P_{PV}}$ are 4.62% at P_1 and 1.83% at P_5 respectively. It can be seen that the trends of PV power and total power generation are similar to [Fig. 7.19](#) since this graph is built on the data extracted from this figure. For that, the P_3 is considered as also a compromise point since this point offer both acceptable electrical and total power generation with lower fan power consumption compared to other points. For example, the $PE_{P_{total}}$ and $PE_{P_{PV}}$ are 10.32% and 3% at P_3 respectively with lower fan power consumption compared to P_5 when the fan consumes almost the whole electrical power generation; this can be seen clearly in P_5 in [Table 7.15](#) and [Fig. 7.29](#).

The single most salient observation to emerge from the data comparison at P_5 is that even though fan power consumption is the maximum at this point, the percentage enhancement for both magnitudes ($PE_{P_{total}}$ and $PE_{P_{PV}}$) are the minimum compared to P_4 . This is a motivation for future work to optimise the model 4-A.

In addition, data from examination of model 4_{non} can be compared with the data in [Table 7.8](#) model 4_{opt} , which shows that both electrical and thermal performance is enhanced. For example, the thermal efficiencies for model 4_{opt} and model 4_{non} are 50.1 and 44.5 respectively while the electrical efficiency is 10.5% for model 4_{opt} and 9.98 for model 4_{non} .

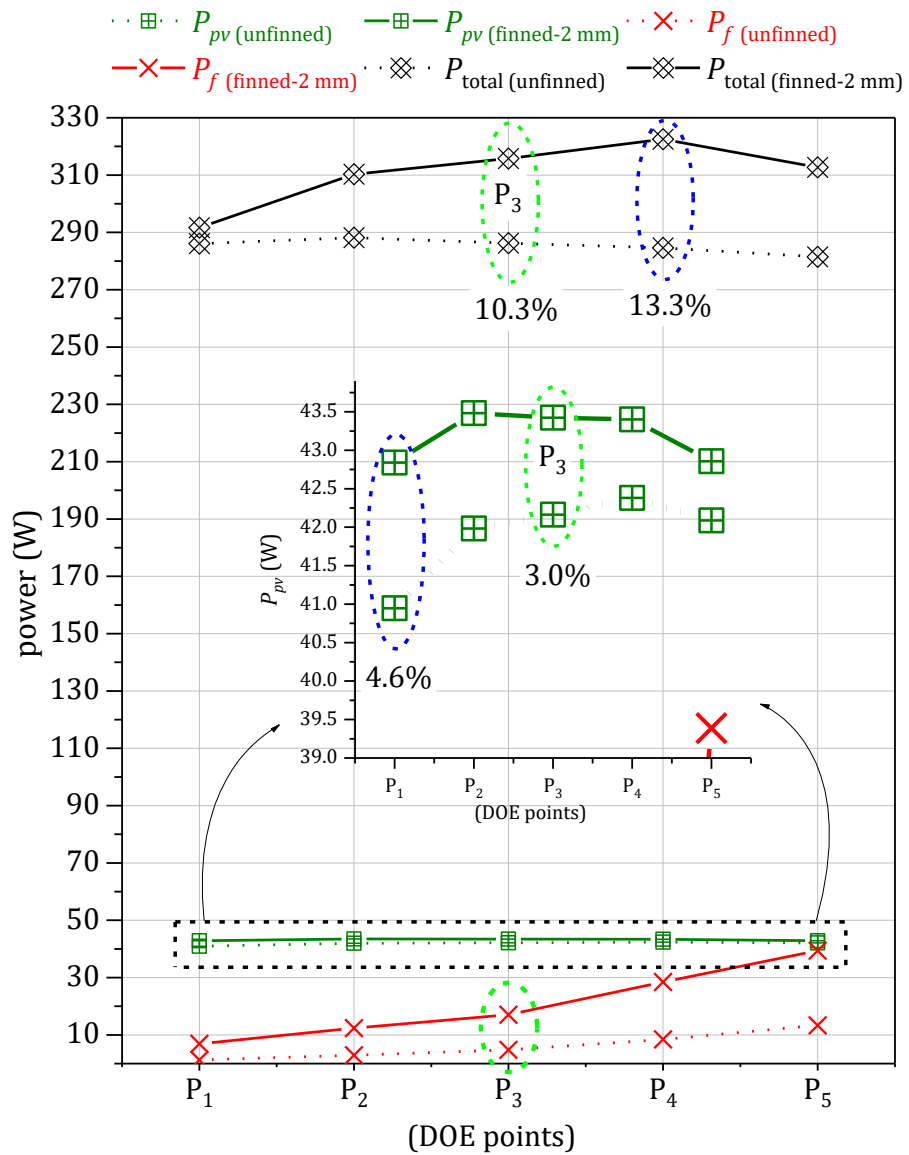


Fig. 7.29. Total power generation, electrical power generation and fan power versus for the five optimal design points (P₁ to P₅ in Table 7.7 for low temperature condition 25 °C) for model 4-A and model 4.

Fig. 7.30 shows the sectional top view of the velocity profile for model 4-A_{opt} at P₁ and P₅. This view is selected from a random point after the centre of the collector to the outlet. The height of this sectional view is 3.1 mm from lower absorber plat to fins as shown in Fig. 7.30b. It can be seen that the velocity adjacent to the wall of fins is close to zero. Also, there is an outward displacement near the leading edge, followed by a local acceleration near the trailing edge and the eventual dissipation of the boundary layer in the fin wakes [223, 375].

Table 7.15. Total power generation, electrical power generation and fan power versus for the five optimal design points (P_1 to P_5 in Table 7.7 for low temperature condition 25 °C) for model 4-A and model 4.

DOE Points	Model 4-A (finned-2 mm)			Model 4 (unfinned)			Percentage enhancement	
	P_{PV} (W)	P_f (W)	P_{total} (W)	P_{PV} (W)	P_f (W)	P_{total} (W)	$PE_{P_{PV}}$ (%)	$PE_{P_{total}}$ (%)
P_1	42.839	6.9118	291.64	40.946	1.274	286.10	4.623	1.936
P_2	43.483	12.360	310.28	41.984	2.941	288.15	3.570	7.680
P_3	43.423	17.055	315.78	42.163	4.762	286.24	3.000	10.320
P_4	43.401	28.453	322.49	42.380	8.462	284.61	2.409	13.309
P_5	42.858	39.387	312.68	42.087	13.336	281.49	1.832	11.080

In Table 7.15, $PE_{P_{PV}}$ and $PE_{P_{total}}$ are the percentage enhancement of the electrical and total power generation for model 4-A with respect to model 4 using the optimal dimensions in Table 7.7 for low temperature condition 25 °C, respectively.

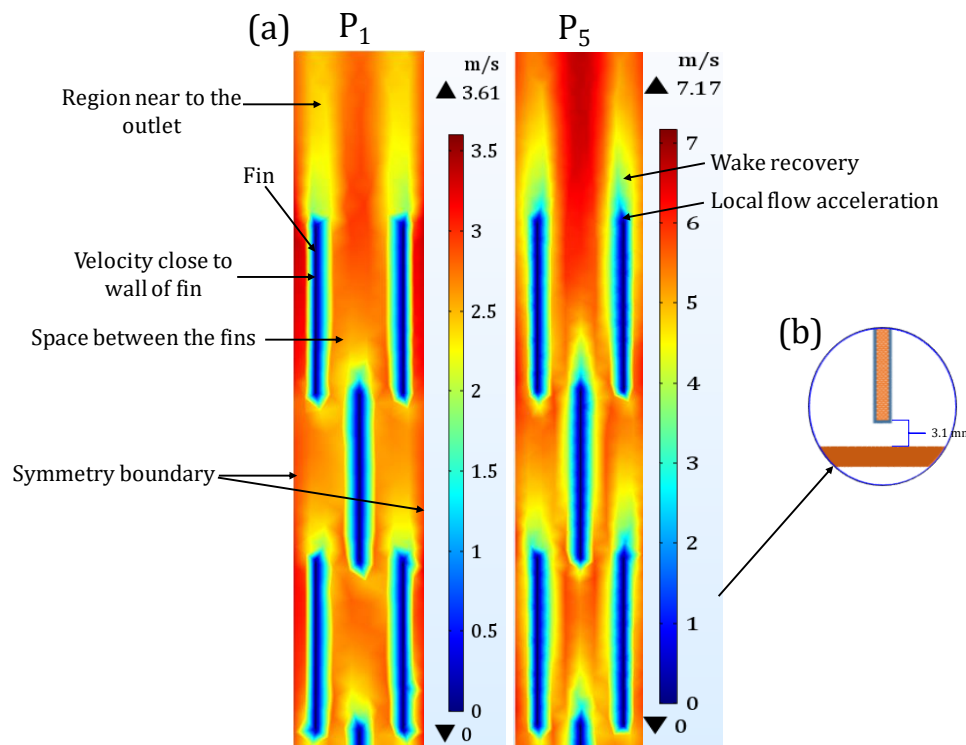


Fig. 7.30. Schematic of the flow behaviour in a typical offset strip fin array for design points P_1 and P_5 showing (a) the sectional top view of velocity contours for model 4-A_{opt} from a random point after the centre of the collector to the outlet. (b) The height of this sectional view is 3.1 mm from lower absorber plat to the lower tip of fins.

Finally, referring to Fig. 7.23 and Table 7.11, where the overall comparison between different PV/T air systems are carried out apart from the model 4-A (with fins). In this comparison, the effect of fins on the PV/T air system (model 4) is presented in Table 7.16.

This table is built on [Table 7.11](#) however; an additional column has been incorporated to show the effect of fins on the overall performance of model 4 ($T_{PV/T-fin}$ and $\eta_{PV/T-fin}$).

The maximum percentage enhancement of the PV module efficiency between η_{PV-45} and $\eta_{PV/T-fin}$ is 20.37%. The maximum percentage reduction of the PV module temperature between T_{PV-45} and $T_{PV/T-fin}$ is 54.88% respectively. This table also shows the comparison between model 4_{opt} (optimal model) and model 4-A_{opt} (finned model). For example, the maximum and minimum percentage enhancement of the PV module efficiency between $\eta_{PV/T-25}$ and $\eta_{PV/T-fin}$ are 4.61% and 1.81% respectively. The maximum and minimum percentage reduction of the PV module temperature between $T_{PV/T-25}$ and $T_{PV/T-fin}$ are 24.12% and 11.50% respectively.

Table 7.16. A comparison between different PV and PV/T systems showing the impact of the temperature of the PV module on electrical efficiency under similar conditions for model 1_{STC}, model 1_{PV-25}, model 1_{PV-45}, model 4_{PV/T-25}, model 4_{PV/T-25} and model 4_{PV/T-45}.

PV temperatures, T_{mpv} (°C)					
T_{ref}	$T_{PV/T-25}$	T_{PV-25}	$T_{PV/T-45}$	T_{PV-45}	$T_{PV/T-fin}$
25.00	43.22	52.73	61.86	72.28	32.80
25.00	40.88	52.73	60.20	72.28	32.75
25.00	39.57	52.73	58.89	72.28	32.72
25.00	38.17	52.73	57.66	72.28	32.61
25.00	36.94	52.73	56.33	72.28	32.69
Electrical Efficiencies, η_{PV} (%)					
η_{ref}	$\eta_{PV/T-25}$	η_{PV-25}	$\eta_{PV/T-45}$	η_{PV-45}	$\eta_{PV/T-fin}$
12.35	11.42	10.92	10.47	9.93	11.94
12.35	11.54	10.92	10.56	9.93	11.95
12.35	11.61	10.92	10.62	9.93	11.95
12.35	11.68	10.92	10.69	9.93	11.95
12.35	11.74	10.92	10.76	9.93	11.95
$PE_{T_{mpv}}$, percentage reduction of the PV module temperature between $T_{PV/T-25}$ and $T_{PV/T-fin}$ (%)					
24.12	19.90	17.31	14.56	11.50	-
$PE_{\eta_{PV}}$, percentage enhancement of the PV module efficiency between $\eta_{PV/T-25}$ and $\eta_{PV/T-fin}$ (%)					
4.61	3.55	2.94	2.37	1.81	-
$PE_{T_{mpv}}$, percentage reduction of the PV module temperature between T_{PV-45} and $T_{PV/T-fin}$ (%)					
54.62	54.69	54.73	54.88	54.77	-
$PE_{\eta_{PV}}$, percentage enhancement of the PV module efficiency between η_{PV-45} and $\eta_{PV/T-fin}$ (%)					
20.31	20.34	20.35	20.41	20.37	-

$\eta_{PV/T-fin}$ and $T_{PV/T-fin}$ are the electrical efficiency and the temperature of the PV module at low temperature (25 °C) of the hybrid PV/T air system (model 4-A_{PV/T-25}). In model 4_{PV/T-fin}, the PV/T air system uses precooled air the exhaust air of the building as a coolant instead of using ambient air (i.e. 45 °C). $PE_{T_{mpv}}$ is the percentage reduction of the PV module temperature between T_{PV-45} and $T_{PV/T-fin}$. $PE_{\eta_{PV}}$ is the percentage enhancement of the PV module efficiency between η_{PV-45} and $\eta_{PV/T-fin}$.

7.7 Conclusions

In this chapter, CFD analysis has been used to model the PV/T air collectors under laminar flow regime. Three steps are considered to obtain an optimal design. The first step is the selection of design parameters, while the second one is to perform preliminary parametric studies for the five models (models 1, 2, 3, 4 and 5). In brief, the five models are a standard PV system without active cooling, model 1, single duct single pass, model 2, a single duct single pass (glazed), model 3, parallel pass double duct, model 4 and double-pass single duct, model 5. The parametric study comparing the five models revealed that model 4 has the best performance. The last step is to employ model 4 in an optimisation process. Five main steps have been considered in the optimisation of model 4. Firstly, the formulation of the objective functions with the goal to minimise fan power and maximise electrical power for one case, and to maximise both electric and thermal efficiencies for the second case. Secondly, the objective functions are parameterised in terms of three variables ($L, \delta_{D1}, \delta_{D2}$). A design of experiments (DOE) has been produced using Optimal Latin Hypercube (OLH) method to be input in the CFD simulation to obtain the corresponding responses. After that, the metamodels have been generated from DOE points.

Finally, the genetic algorithm method has been used to obtain Pareto front curves. For each two objectives and conditions, a Pareto front curve is obtained. Four Pareto front curves are presented. The first two curves are the design optimisation analysis in terms of thermal and electrical efficiencies at low and high temperatures (25 °C and 45 °C). The second two curves are in terms of design optimisation of power fan and electrical power at low and high temperatures (25 °C and 45 °C). The Pareto front curves demonstrate explicitly the compromise that must be accepted between the conflicting objectives of thermal and electrical efficiencies or the fan power consumption and electrical power generation. Finally, model 4 has been modified by integrating it with off-set strip fins in the lower duct namely model 4-A. The evaluation of this model has been performed at two stages. The first stage is to evaluate the system using the common dimensions from literature (non-optimised models) and compare it with the plain model for the same conditions (model 4_{non} and model 4-A_{non}). The second stage is evaluating model 4-A using the optimal dimensions that result from the design optimisation process of model 4, see [Table 7.7](#) (P₁-P₅), and comparing it with the optimised model 4 without fins (model 4_{opt} and model 4-A_{opt}). It can be concluded from the data of the two evaluations that both electrical and thermal performances of model 4 and model 4-A are enhanced. For example, the thermal efficiencies for model 4_{opt} and model 4_{non} are 50.1 and 44.5 respectively while the electrical efficiencies are 10.5% and 9.98 respectively. It, therefore, can be concluded that the use of optimisation

has contributed significantly in improving both the electrical and thermal performances for the finned and plain models (model 4 and model 4-A).

CHAPTER 8 CONCLUSION AND RECOMMENDATION FOR FUTURE WORK

8.1 Introduction

As highlighted in Chapter 1, there were three main challenges to overcome with PV/T air systems; 1) the fan power requirement, 2) extreme weather temperature which could reach 50 °C in the Middle East, 3), and the poor heat capacity of air, which leads to poor thermal performance, compared to other coolants such as water. The aim of this research was, therefore, to address these challenges developing an efficient and affordable PV/T air system. To achieve this, eleven objectives have been suggested where appropriate several different solution methods are utilised. The methods can be divided mainly into three types. The first is the mathematical formulation for two PV/T systems using semi-analytical and numerical techniques (as described in Chapter 3 and part from Chapter 5). The second is experimental work examining the performance of multi-pass solar air heaters with and without turbulators and to ensure the accuracy of CFD solutions (Chapter 6). The last method is CFD analysis using COMSOL Multiphysics®, including different approaches such as mesh sensitivity analysis, assumptions to reduce the run time, validation and verification (composing the majority of thesis).

8.2 Main conclusions

In brief, the main findings of this research can be divided into three parts. The first part evaluates the performance of the PV system model 1 using heat balance as well as CFD modelling under steady state and transient conditions. This system is considered as a reference for subsequent models, as detailed in Chapter 5. The second part numerically and experimentally evaluates the performance of the multi-pass solar air heaters, as demonstrated in Chapter 6. After that, the combination of the two systems from these two parts are evaluated (Chapter 7). This includes performing a design optimisation process for different multi-pass PV/T air collectors. Finally, the examination of the PV/T enhancement of the optimal design (model 4) has been carried out by coupling with off-set strip fins. Consequently, the following sections summarise the main conclusions of these three parts

8.3 PV module performance

The examination of the performance of the PV module requires an accurate prediction of its temperature. This is owing to the fact that PV module efficiency is directly proportional to its temperature. Three methods have been employed in this evaluation, including mathematical, numerical models and experimental validations. The proposed models in this discourse incorporate parameters that have not been intensively studied in the literature. The parameters are: the effect of PV module length, the inclination of the PV module and the influence of the maximum possible module temperature under the worst case scenario for two high temperature sites under free convection conditions. Moreover, to ensure accuracy, the seasonal weather conditions including incident solar radiation and ambient temperature have been estimated and validated with the standard data-set. Furthermore, the numerical results are validated with experimental observations and verified with the current mathematical model.

The main findings can be summarized as follows:

Firstly, the convection currents in inclined and horizontal surfaces are weaker relative to the vertical surface thus, the rate of heat transfer is lower. With respect to inclined PV systems, the increase of the PV length enhances heat transfer rate up to length $(2L)$. After this length, the PV temperature increase and convective heat transfer coefficients are reduced regardless of the inclination of the PV system. In the case of the horizontal surface, the convective heat transfer rate is lower, especially at the bottom surface of the PV system. It can also be concluded that the effect of inclination appears in the laminar region (short length) and dissipates after this region. It should be noted that increasing the length of the PV panel might not be feasible/affordable because the PV array blocks and shade further arrays. In addition, this might increase the cost of installation and price of the base frame (in the expense of cost and difficulty of installation).

Concerning the effect of geographical region, lower ambient temperature and higher insolation values lead to better PV performance. This can be seen by comparing both Muscat and Fallujah in June. The daylight period in Muscat is also longer than Fallujah which allows for the accumulation of more solar energy per day and further increases in the solar PV power.

8.4 Performance of solar air heaters

Numerical and experimental investigations are conducted to assess the performance of the multi-pass solar air heaters with and without recycled aluminium cans (RAC). The numerical study is built based on the finite element method provided by the COMSOL Multiphysics V5.3a software. The experiments are conducted in the western part of Iraq, Ar-Ramadi City (longitude: 33.25° N; latitude: 43.18° E) under clear skies and almost identical weather conditions on 23rd (model C-I) and 27th (model C-II) February and 2nd (model C-III) March between 09:00 and 15:30. The average flowrates were 0.096 kg s⁻¹ for model C-I, 0.088 for model C-II kg s⁻¹ and 0.0819 kg s⁻¹.

The following conclusions can be made from this analysis:

- Numerically, the U-flow offers better thermal performance than co-current and counter-current flow designs. Therefore, the U-flow model was chosen to be implemented in experimental studies.
- Thermal and hydrodynamic performance of numerical modelling is found to be in line with experiments (U-flow, model C-I).
- The increase in the thermal performance of U-flow model gave an increase in pressure drop, but the thermal efficiency is still higher compared to models A and B.
- The staggered arrangement (model C-III) had the highest thermal efficiency compared to the in-line (model C-II) and plain (model C-I) models.
- The in-line configuration (model C-II) has a lower efficiency compared to the staggered configuration (model C-III), even though the number of RACs and the mass flowrate are higher.

8.5 Design optimisation of PV/T air design

In this section, CFD analysis has been used to model the PV/T air collectors under laminar flow regime. Three steps are considered to obtain optimal PV/T air design. The first step is the selection of design parameters while the second one is to perform preliminary parametric studies for the five models (models 1, 2, 3, 4 and 5) which revealed that model 4 has the best performance. The last step is to employ model 4 in the optimisation process. Five main steps have been considered to conduct the optimisation of model 4. Firstly, the formulation of the objective functions with the goal to minimise the fan power and maximise the electrical power for the first case, and to maximise both electric and the thermal efficiencies for the second case. Secondly, the objective functions are parameterised in terms of three variables ($L, \delta_{D1}, \delta_{D2}$). Design of experiments (DOE) has been generated to

be used later in the CFD simulation to obtain the corresponding responses. After that, the metamodels have been produced from DOE points. Finally, the genetic algorithm method has been used to obtain Pareto front curves. The Pareto front curves demonstrate explicitly the compromise that must be accepted between the conflicting objectives of thermal and electrical efficiencies or the fan power consumption and electrical power generation.

8.6 PV/T air system with off-set strip fin

The optimal model from the previous section (model 4) has been modified by coupling with off-set strip fins in lower duct namely model 4-A. The evaluation of this model has been performed at two stages. The first stage is to evaluate the system using the common dimensions from literature (non-optimised models) and compared with the plain model for the same conditions. The second stage is to evaluate model 4-A using the optimal dimensions that result from the design optimisation process of model 4 and compared with model 4 optimised model. It can be concluded from the data of two evaluations that both electrical and thermal performance of model 4 and model 4-A are enhanced. For example, the thermal efficiencies for model 4_{opt} and model 4_{non} are 50.1 and 44.5 respectively while the electrical efficiency is 10.5% for model 4_{opt} and 9.98 for model 4_{non}. It, therefore, can be concluded that the use of optimisation has contributed clearly in improving both the electrical and thermal performance for finned and plain mode (model 4 and model 4-A).

8.7 Future Work

In this section, further work possibilities are listed:

- This study has not been done entirely experimentally, therefore, there can be a new experimental study which can further test the conclusions made in the work.
- The optimisation objectives can be extended to be five design variables by including the impact of mass flow rate and length of fins and space between them while keeping the length of collector constant since it is not easy to change the length of photovoltaic. The optimisation study can be achieved by further including the effect of fan power consumption with both thermal and electrical efficiencies simultaneously in multi-objective process.
- To investigate the possibility to combine a PV/T air system with appropriate phase change material to secure uniform cooling. This could contribute to reduce the mismatch effect and increase the life span for the PV panels.

REFERENCES

- [1] R. Perez and M. Perez, "A fundamental look at energy reserves for the planet," *The IEA SHC Solar Update*, vol. 50, no. 2, 2009.
- [2] L. Y. Bronicki and D. Berger, "Telecommunications: Paving the way for PV and ORC wide spread use of electricity production," in *Electrical & Electronics Engineers in Israel (IEEEI), 2014 IEEE 28th Convention of*, 2014: IEEE, pp. 1-5.
- [3] J. Twidell and T. Weir, *Renewable energy resources*. Routledge, 2015.
- [4] T. T. Chow, "A review on photovoltaic/thermal hybrid solar technology," *Applied energy*, vol. 87, no. 2, pp. 365-379, 2010.
- [5] H.-U. Bernard, R. D. Burk, Z. Chen, K. van Doorslaer, H. zur Hausen, and E.-M. de Villiers, "Classification of papillomaviruses (PVs) based on 189 PV types and proposal of taxonomic amendments," *Virology*, vol. 401, no. 1, pp. 70-79, 2010.
- [6] M. Mattei, G. Notton, C. Cristofari, M. Muselli, and P. Poggi, "Calculation of the polycrystalline PV module temperature using a simple method of energy balance," *Renewable Energy*, vol. 31, no. 4, pp. 553-567, 4// 2006, doi: <http://dx.doi.org/10.1016/j.renene.2005.03.010>.
- [7] J. Del Cueto, "Comparison of energy production and performance from flat-plate photovoltaic module technologies deployed at fixed tilt," in *Photovoltaic Specialists Conference, 2002. Conference Record of the Twenty-Ninth IEEE*, 2002: IEEE, pp. 1523-1526.
- [8] M. A. Green, K. Emery, Y. Hishikawa, W. Warta, and E. D. Dunlop, "Solar cell efficiency tables (Version 45)," *Progress in photovoltaics: research and applications*, vol. 23, no. 1, pp. 1-9, 2015.
- [9] Y. Hamakawa, *Thin-film solar cells: next generation photovoltaics and its applications*. Springer Science & Business Media, 2013.
- [10] J. Allan, "The development and characterisation of enhanced hybrid solar photovoltaic thermal systems," Brunel University London., 2015.
- [11] N. Tanaka, "Technology roadmap-solar photovoltaic energy," *International energy agency report. Paris/France*, 2010.
- [12] W. C. Sinke *et al.*, "A strategic research agenda for photovoltaic solar energy technology," 2007.
- [13] W. Shockley and H. J. Queisser, "Detailed balance limit of efficiency of p - n junction solar cells," *Journal of applied physics*, vol. 32, no. 3, pp. 510-519, 1961.
- [14] n. s. energy. "PV Solar Thin Film vs. Polycrystalline." <https://www.newssouthernenergy.com/pv-solar-thin-film-vs-polycrystalline/> (accessed).
- [15] Z. Ling *et al.*, "Review on thermal management systems using phase change materials for electronic components, Li-ion batteries and photovoltaic modules," *Renewable and Sustainable Energy Reviews*, vol. 31, pp. 427-438, 2014.

- [16] E. Radziemska, "The effect of temperature on the power drop in crystalline silicon solar cells," *Renewable Energy*, vol. 28, no. 1, pp. 1-12, 1// 2003, doi: [http://dx.doi.org/10.1016/S0960-1481\(02\)00015-0](http://dx.doi.org/10.1016/S0960-1481(02)00015-0).
- [17] H. A. Weakliem and D. Redfield, "Temperature dependence of the optical properties of silicon," *Journal of Applied Physics*, vol. 50, no. 3, pp. 1491-1493, 1979, doi: <http://dx.doi.org/10.1063/1.326135>.
- [18] J. J. Michael, S. Iniyan, and R. Goic, "Flat plate solar photovoltaic-thermal (PV/T) systems: a reference guide," *Renewable and Sustainable Energy Reviews*, vol. 51, pp. 62-88, 2015.
- [19] N. Aste, C. del Pero, and F. Leonforte, "Water flat plate PV-thermal collectors: A review," *Solar Energy*, vol. 102, pp. 98-115, 2014.
- [20] J. K. Kaldellis, M. Kapsali, and K. A. Kavadias, "Temperature and wind speed impact on the efficiency of PV installations. Experience obtained from outdoor measurements in Greece," *Renewable Energy*, vol. 66, pp. 612-624, 2014.
- [21] H. G. Teo, P. S. Lee, and M. N. A. Hawlader, "An active cooling system for photovoltaic modules," *Applied Energy*, vol. 90, no. 1, pp. 309-315, 2// 2012, doi: <http://dx.doi.org/10.1016/j.apenergy.2011.01.017>.
- [22] H. J. Solheim, H. G. Fjær, E. A. Sørheim, and S. E. Foss, "Measurement and simulation of hot spots in solar cells," *Energy Procedia*, vol. 38, pp. 183-189, 2013.
- [23] D. Evans and L. Florschuetz, "Cost studies on terrestrial photovoltaic power systems with sunlight concentration," *Solar Energy*, vol. 19, no. 3, pp. 255-262, 1977.
- [24] K. E. Amori and H. M. T. Al-Najjar, "Analysis of thermal and electrical performance of a hybrid (PV/T) air based solar collector for Iraq," *Applied Energy*, vol. 98, pp. 384-395, 2012.
- [25] F. Sarhaddi, S. Farahat, H. Ajam, A. Behzadmehr, and M. Mahdavi Adeli, "An improved thermal and electrical model for a solar photovoltaic thermal (PV/T) air collector," *Applied Energy*, vol. 87, no. 7, pp. 2328-2339, 7// 2010, doi: <http://dx.doi.org/10.1016/j.apenergy.2010.01.001>.
- [26] A. S. Joshi, A. Tiwari, G. N. Tiwari, I. Dincer, and B. V. Reddy, "Performance evaluation of a hybrid photovoltaic thermal (PV/T) (glass-to-glass) system," *International Journal of Thermal Sciences*, vol. 48, no. 1, pp. 154-164, 1// 2009, doi: <http://dx.doi.org/10.1016/j.ijthermalsci.2008.05.001>.
- [27] A. Shahsavari and M. Ameri, "Experimental investigation and modeling of a direct-coupled PV/T air collector," *Solar Energy*, vol. 84, no. 11, pp. 1938-1958, 2010.
- [28] B. Huang, T. Lin, W. Hung, and F. Sun, "Performance evaluation of solar photovoltaic/thermal systems," *Solar energy*, vol. 70, no. 5, pp. 443-448, 2000.
- [29] S. Dubey, J. N. Sarvaiya, and B. Seshadri, "Temperature dependent photovoltaic (PV) efficiency and its effect on PV production in the world—a review," *Energy Procedia*, vol. 33, pp. 311-321, 2013.
- [30] E. Skoplaki and J. Palyvos, "Operating temperature of photovoltaic modules: A survey of pertinent correlations," *Renewable Energy*, vol. 34, no. 1, pp. 23-29, 2009.
- [31] I.-R. Caluianu and F. Băltărețu, "Thermal modelling of a photovoltaic module under variable free convection conditions," *Applied Thermal Engineering*, vol. 33, pp. 86-91, 2012.

- [32] K. Kant, A. Shukla, A. Sharma, and P. H. Biwole, "Thermal response of poly-crystalline silicon photovoltaic panels: Numerical simulation and experimental study," *Solar Energy*, vol. 134, pp. 147-155, 2016.
- [33] Y. B. Assoa *et al.*, "Thermal analysis of a BIPV system by various modelling approaches," *Solar Energy*, vol. 155, pp. 1289-1299, 2017.
- [34] G. A. Barron-Gafford, R. L. Minor, N. A. Allen, A. D. Cronin, A. E. Brooks, and M. A. Pavao-Zuckerman, "The Photovoltaic Heat Island Effect: Larger solar power plants increase local temperatures," *Scientific reports*, vol. 6, p. 35070, 2016.
- [35] K. Kant, A. Shukla, A. Sharma, and P. H. Biwole, "Heat transfer studies of photovoltaic panel coupled with phase change material," *Solar Energy*, vol. 140, pp. 151-161, 2016.
- [36] S. Armstrong and W. Hurley, "A thermal model for photovoltaic panels under varying atmospheric conditions," *Applied Thermal Engineering*, vol. 30, no. 11-12, pp. 1488-1495, 2010.
- [37] G. Notton, C. Cristofari, M. Mattei, and P. Poggi, "Modelling of a double-glass photovoltaic module using finite differences," *Applied Thermal Engineering*, vol. 25, no. 17-18, pp. 2854-2877, 2005.
- [38] K. Touafek, M. Haddadi, and A. Malek, "Design and modeling of a photovoltaic thermal collector for domestic air heating and electricity production," *Energy and Buildings*, vol. 59, pp. 21-28, 2013.
- [39] A. Jones and C. Underwood, "A thermal model for photovoltaic systems," *Solar energy*, vol. 70, no. 4, pp. 349-359, 2001.
- [40] Y. B. Assoa, L. Gaillard, C. Ménézo, N. Negri, and F. Sauzedde, "Dynamic prediction of a building integrated photovoltaic system thermal behaviour," *Applied Energy*, vol. 214, pp. 73-82, 2018.
- [41] S. Kaplanis and E. Kaplani, "A new dynamic model to predict transient and steady state PV temperatures taking into account the environmental conditions," *Energies*, vol. 12, no. 1, p. 2, 2019.
- [42] S. P. Aly, S. Ahzi, and N. Barth, "An adaptive modelling technique for parameters extraction of photovoltaic devices under varying sunlight and temperature conditions," *Applied Energy*, vol. 236, pp. 728-742, 2019.
- [43] H. Brahma, L. Baruah, and N. Sarmah, "Electrical and thermal modelling to evaluate photovoltaic module performance in varying outdoor condition," in *2018 2nd International Conference on Power, Energy and Environment: Towards Smart Technology (ICEPE)*, 2018: IEEE, pp. 1-6.
- [44] R. A. Agathokleous and S. A. Kalogirou, "Part II: Thermal analysis of naturally ventilated BIPV system: Modeling and Simulation," *Solar Energy*, vol. 169, pp. 682-691, 2018.
- [45] Y. Du, W. Tao, Y. Liu, J. Jiang, and H. Huang, "Heat transfer modeling and temperature experiments of crystalline silicon photovoltaic modules," *Solar Energy*, vol. 146, pp. 257-263, 2017.
- [46] F. Grubišić-Čabo, S. Nižetić, D. Čoko, I. M. Kragić, and A. Papadopoulos, "Experimental investigation of the passive cooled free-standing photovoltaic panel with fixed aluminum fins on the backside surface," *Journal of cleaner production*, vol. 176, pp. 119-129, 2018.

- [47] D. Torres-Lobera and S. Valkealahti, "Inclusive dynamic thermal and electric simulation model of solar PV systems under varying atmospheric conditions," *Solar Energy*, vol. 105, pp. 632-647, 2014.
- [48] J. Ingersoll, "Simplified calculation of solar cell temperatures in terrestrial photovoltaic arrays," *Journal of solar energy engineering*, vol. 108, no. 2, pp. 95-101, 1986.
- [49] D. L. King, C. E. Witt, M. Al-Jassim, and J. M. Gee, "Photovoltaic module and array performance characterization methods for all system operating conditions," in *AIP Conference Proceedings*, 1997, vol. 394, no. 1: AIP, pp. 347-368.
- [50] J. A. Duffie and W. A. Beckman, *Solar engineering of thermal processes*. Hoboken, New Jersey: John Wiley & Sons, 2013.
- [51] D. L. King, J. A. Kratochvil, and W. E. Boyson, *Photovoltaic array performance model*. United States. Department of Energy, 2004.
- [52] F. Lasnier, *Photovoltaic engineering handbook*. Routledge, 2017.
- [53] S. A. Kalogirou and Y. Tripanagnostopoulos, "Hybrid PV/T solar systems for domestic hot water and electricity production," *Energy Conversion and Management*, vol. 47, no. 18, pp. 3368-3382, 2006.
- [54] R. Zhang, P. A. Mirzaei, and J. Carmeliet, "Prediction of the surface temperature of building-integrated photovoltaics: Development of a high accuracy correlation using computational fluid dynamics," *Solar Energy*, vol. 147, pp. 151-163, 2017.
- [55] E. Ruiz-Reina and M. Sidrach-de-Cardona, "Simulation of the Convective Heat Transfer and Working Temperature Field of a Photovoltaic Module using COMSOL Multiphysics," in *Proceedings of the COMSOL Conference 2009 Milan*.
- [56] G. Acciani, O. Falcone, and S. Vergura, "Analysis of the thermal heating of poly-Si and a-Si photovoltaic cell by means of FEM," *cell*, vol. 4, no. 4, 2010.
- [57] M. U. Siddiqui, A. F. Arif, L. Kelley, and S. Dubowsky, "Three-dimensional thermal modeling of a photovoltaic module under varying conditions," *Solar energy*, vol. 86, no. 9, pp. 2620-2631, 2012.
- [58] J.-c. Zhou, Z. Zhang, H.-j. Liu, and Q. Yi, "Temperature distribution and back sheet role of polycrystalline silicon photovoltaic modules," *Applied Thermal Engineering*, vol. 111, pp. 1296-1303, 2017.
- [59] Y. Lee and A. A. Tay, "Finite element thermal analysis of a solar photovoltaic module," *Energy Procedia*, vol. 15, pp. 413-420, 2012.
- [60] G. Gan and S. B. Riffat, "CFD modelling of air flow and thermal performance of an atrium integrated with photovoltaics," *Building and Environment*, vol. 39, no. 7, pp. 735-748, 2004.
- [61] R. Edgar, S. Cochard, and Z. Stachurski, "A computational fluid dynamic study of PV cell temperatures in novel platform and standard arrangements," *Solar Energy*, vol. 144, pp. 203-214, 2017.
- [62] A. Saxena and A. El-Sebaai, "A thermodynamic review of solar air heaters," *Renewable and Sustainable Energy Reviews*, vol. 43, pp. 863-890, 2015, doi: <https://doi.org/10.1016/j.rser.2014.11.059>.
- [63] M. Aktaş, A. Sözen, A. D. Tuncer, E. Arslan, M. Koşan, and O. Çürük, "Energy-Exergy Analysis of A Novel Multi-Pass Solar Air Collector With Perforated Fins," *International Journal of Renewable Energy Development*, vol. 8, no. 1, pp. 47-55, 2019.

- [64] B. A. Zvirin, Y, "A novel algorithm to investigate conjugate heat transfer in transparent insulation: application to solar collectors," *Numerical Heat Transfer: Part A: Applications*, vol. 35, no. 7, pp. 757-777, 1999.
- [65] A. S. Yadav and J. Bhagoria, "A numerical investigation of square sectioned transverse rib roughened solar air heater," *International Journal of Thermal Sciences*, vol. 79, pp. 111-131, 2014.
- [66] M. Farshchimonfared, J. Bilbao, and A. Sproul, "Channel depth, air mass flow rate and air distribution duct diameter optimization of photovoltaic thermal (PV/T) air collectors linked to residential buildings," *Renewable Energy*, vol. 76, pp. 27-35, 2015.
- [67] W. Fan, G. Kokogiannakis, and Z. Ma, "A multi-objective design optimisation strategy for hybrid photovoltaic thermal collector (PVT)-solar air heater (SAH) systems with fins," *Solar Energy*, vol. 163, pp. 315-328, 2018.
- [68] İ. T. Toğrul and D. Pehlivan, "The performance of a solar air heater with conical concentrator under forced convection," *International journal of thermal sciences*, vol. 42, no. 6, pp. 571-581, 2003.
- [69] S. Rhee and D. Edwards, "Laminar entrance flow in a flat plate duct with asymmetric suction and heating," *Numerical heat transfer*, vol. 4, no. 1, pp. 85-100, 1981.
- [70] A. Kabeel, M. H. Hamed, Z. Omara, and A. Kandeal, "Influence of fin height on the performance of a glazed and bladed entrance single-pass solar air heater," *Solar Energy*, vol. 162, pp. 410-419, 2018.
- [71] H. K. Ghritlahre and R. K. Prasad, "Investigation of thermal performance of unidirectional flow porous bed solar air heater using MLP, GRNN, and RBF models of ANN technique," *Thermal Science and Engineering Progress*, vol. 6, pp. 226-235, 2018.
- [72] N. Moumami, S. Youcef-Ali, A. Moumami, and J. Desmons, "Energy analysis of a solar air collector with rows of fins," *Renewable Energy*, vol. 29, no. 13, pp. 2053-2064, 2004.
- [73] Z. a. H. Obaid, A. Al - damook, and W. H. Khalil, "The thermal and economic characteristics of solar air collectors with different delta turbulators arrangement," *Heat Transfer—Asian Research*, pp. 1-23, 2019, doi: <https://doi.org/10.1002/htj.21472>.
- [74] A. Saravanan. and S. Jaisankar, "Heat transfer augmentation techniques in forced flow V-trough solar collector equipped with V-cut and square cut twisted tape," *International Journal of Thermal Sciences*, vol. 140, no. 1, pp. 59-70, 1// 2019, doi: <http://www.sciencedirect.com/science/article/pii/S1290072916317331>.
- [75] H. Fugmann, L. Schnabel, and B. Frohnafel, "Heat transfer and pressure drop correlations for laminar flow in an in-line and staggered array of circular cylinders," *Numerical Heat Transfer, Part A: Applications*, vol. 75, no. 1, pp. 1-20, 2019.
- [76] B. S. Romdhane, "The air solar collectors: comparative study, introduction of baffles to favor the heat transfer," *Solar Energy*, vol. 81, no. 1, pp. 139-149, 2007.
- [77] A. S. Yadav and J. Bhagoria, "A numerical investigation of turbulent flows through an artificially roughened solar air heater," *Numerical Heat Transfer, Part A: Applications*, vol. 65, no. 7, pp. 679-698, 2014.
- [78] H. Benzenine, R. Saim, S. Abboudi, O. Imine, H. F. Oztop, and N. Abu-Hamdeh, "Numerical study of a three-dimensional forced laminar flow in a channel equipped

- with a perforated baffle," *Numerical Heat Transfer, Part A: Applications*, vol. 73, no. 12, pp. 881-894, 2018.
- [79] G. Xie, S. Zheng, and B. Sundén, "Heat transfer and flow characteristics in Rib-/deflector-roughened cooling channels with various configuration parameters," *Numerical Heat Transfer, Part A: Applications*, vol. 67, no. 2, pp. 140-169, 2015.
- [80] S. Biswas, P. Sharma, B. Mondal, and G. Biswas, "Analysis of mixed convective heat transfer in a ribbed channel using the lattice Boltzmann method," *Numerical Heat Transfer, Part A: Applications*, vol. 68, no. 1, pp. 75-98, 2015.
- [81] M. T. Al-Asadi, F. Alkasmoul, and M. Wilson, "Heat transfer enhancement in a micro-channel cooling system using cylindrical vortex generators," *International Communications in Heat and Mass Transfer*, vol. 74, pp. 40-47, 2016.
- [82] M. T. Al-Asadi, A. Al-damook, and M. Wilson, "Assessment of vortex generator shapes and pin fin perforations for enhancing water-based heat sink performance," *International Communications in Heat and Mass Transfer*, vol. 91, pp. 1-10, 2018.
- [83] S. Krishnananth and K. K. Murugavel, "Experimental study on double pass solar air heater with thermal energy storage," *Journal of King Saud University-Engineering Sciences*, vol. 25, no. 2, pp. 135-140, 2013.
- [84] R. Karwa and V. Srivastava, "Thermal performance of solar air heater having absorber plate with v-down discrete rib roughness for space-heating applications," *Journal of Renewable Energy*, vol. 2013, 2013.
- [85] F. Chabane, N. Moumami, S. Benramache, D. Bensahal, and O. Belahssen, "Collector efficiency by single pass of solar air heaters with and without using fins," *Engineering Journal (Eng. J.)*, vol. 17, no. 3, pp. 43-55, 2013.
- [86] L. S. Paraschiv, S. Paraschiv, and I. V. Ion, "Experimental and theoretical analyses on thermal performance of a solar air collector," *Environmental Engineering & Management Journal (EEMJ)*, vol. 13, no. 8, pp. 1965-1970 2014, doi: <http://omicron.ch.tuiasi.ro/EEMJ/>
- [87] F. Chabane, N. Moumami, and S. Benramache, "Experimental study of heat transfer and thermal performance with longitudinal fins of solar air heater," *Journal of advanced research*, vol. 5, no. 2, pp. 183-192, 2014.
- [88] R. Tyagi, R. Ranjan, and K. Kishore, "Performance studies on flat plate solar air heater subjected to various flow patterns," *Applied Solar Energy*, vol. 50, no. 2, pp. 98-102, 2014.
- [89] M. Abuşka and M. B. Akgül, "Experimental study on thermal performance of a novel solar air collector having conical springs on absorber plate," *Arabian Journal for Science and Engineering*, vol. 41, no. 11, pp. 4509-4516, 2016.
- [90] B. Ramani, A. Gupta, and R. Kumar, "Performance of a double pass solar air collector," *Solar Energy*, vol. 84, no. 11, pp. 1929-1937, 2010.
- [91] A. Priyam and P. Chand, "Thermal and thermohydraulic performance of wavy finned absorber solar air heater," *Solar Energy*, vol. 130, pp. 250-259, 2016.
- [92] R. K. Ravi and R. Saini, "Experimental investigation on performance of a double pass artificial roughened solar air heater duct having roughness elements of the combination of discrete multi V shaped and staggered ribs," *Energy*, vol. 116, pp. 507-516, 2016.

- [93] G. Alvarez, J. Arce, L. Lira, and M. Heras, "Thermal performance of an air solar collector with an absorber plate made of recyclable aluminum cans," *Solar Energy*, vol. 77, no. 1, pp. 107-113, 2004.
- [94] A. Mohamad, "High efficiency solar air heater," *Solar energy*, vol. 60, no. 2, pp. 71-76, 1997.
- [95] B. Parker, M. Lindley, D. Colliver, and W. Murphy, "Thermal performance of three solar air heaters," *Solar Energy*, vol. 51, no. 6, pp. 467-479, 1993.
- [96] M. Sodha and R. Chandra, "Solar drying systems and their testing procedures: a review," *Energy Conversion and Management*, vol. 35, no. 3, pp. 219-267, 1994.
- [97] S. J. B. Hale, *Methods of testing to determine the thermal performance of solar collectors*. Atlanta: ASHRAE, 1986.
- [98] K. Altfeld, W. Leiner, and M. Fiebig, "Second law optimization of flat-plate solar air heaters Part I: The concept of net exergy flow and the modeling of solar air heaters," *Solar Energy*, vol. 41, no. 2, pp. 127-132, 1988.
- [99] F. Ozgen, M. Esen, and H. Esen, "Experimental investigation of thermal performance of a double-flow solar air heater having aluminium cans," *Renewable Energy*, vol. 34, no. 11, pp. 2391-2398, 2009.
- [100] H. Esen, F. Ozgen, M. Esen, and A. Sengur, "Artificial neural network and wavelet neural network approaches for modelling of a solar air heater," *Expert systems with applications*, vol. 36, no. 8, pp. 11240-11248, 2009.
- [101] S. Chamoli, R. Chauhan, N. Thakur, and J. Saini, "A review of the performance of double pass solar air heater," *Renewable and Sustainable Energy Reviews*, vol. 16, no. 1, pp. 481-492, 2012.
- [102] L. Perão, P. Zdanski, and M. Vaz Jr, "Conjugate heat transfer in channels with heat-conducting inclined fins," *Numerical Heat Transfer, Part A: Applications*, vol. 73, no. 2, pp. 75-93, 2018.
- [103] G. Tiwari, R. Mishra, and S. Solanki, "Photovoltaic modules and their applications: a review on thermal modelling," *Applied Energy*, vol. 88, no. 7, pp. 2287-2304, 2011.
- [104] J. Yazdanpanahi, F. Sarhaddi, and M. M. Adeli, "Experimental investigation of exergy efficiency of a solar photovoltaic thermal (PVT) water collector based on exergy losses," *Solar Energy*, vol. 118, pp. 197-208, 2015.
- [105] H. Zondag *et al.*, "PVT roadmap. A European guide for the development and market introduction of PVT technology," Energy research Centre of the Netherlands ECN, 2005.
- [106] M. Farahat, "Improvement the thermal electric performance of a photovoltaic cells by cooling and concentration techniques," in *39th International Universities Power Engineering Conference, 2004. UPEC 2004.*, 2004, vol. 2: IEEE, pp. 623-628.
- [107] B. Sandnes and J. Rekstad, "A photovoltaic/thermal (PV/T) collector with a polymer absorber plate. Experimental study and analytical model," *Solar Energy*, vol. 72, no. 1, pp. 63-73, 1// 2002, doi: [http://dx.doi.org/10.1016/S0038-092X\(01\)00091-3](http://dx.doi.org/10.1016/S0038-092X(01)00091-3).
- [108] F. Hussain, M. Othman, K. Sopian, B. Yatim, H. Ruslan, and H. Othman, "Design development and performance evaluation of photovoltaic/thermal (PV/T) air base solar collector," *Renewable and Sustainable Energy Reviews*, vol. 25, pp. 431-441, 2013.

- [109] V. Tyagi, S. Kaushik, and S. Tyagi, "Advancement in solar photovoltaic/thermal (PV/T) hybrid collector technology," *Renewable and Sustainable Energy Reviews*, vol. 16, no. 3, pp. 1383-1398, 2012.
- [110] M. A. Hasan and K. Sumathy, "Photovoltaic thermal module concepts and their performance analysis: a review," *Renewable and Sustainable Energy Reviews*, vol. 14, no. 7, pp. 1845-1859, 2010.
- [111] A. Kumar, P. Baredar, and U. Qureshi, "Historical and recent development of photovoltaic thermal (PVT) technologies," *Renewable and Sustainable Energy Reviews*, vol. 42, pp. 1428-1436, 2015.
- [112] R. Kumar and M. A. Rosen, "A critical review of photovoltaic-thermal solar collectors for air heating," *Applied Energy*, vol. 88, no. 11, pp. 3603-3614, 2011.
- [113] M. Wolf, "Performance analyses of combined heating and photovoltaic power systems for residences," *Energy Conversion*, vol. 16, no. 1, pp. 79-90, 1976.
- [114] P. Frankl, M. Gamberale, and R. Battisti, "Life cycle assessment of a PV cogenerative system: comparison with a solar thermal collector and a PV system," in *Proceedings of the 16th European photovoltaic solar energy conference, Glasgow*, 2000, pp. 1-5.
- [115] S. Tselepis and Y. Tripanagnostopoulos, "Economic analysis of hybrid photovoltaic/thermal solar systems and comparison with standard PV modules," in *Proceedings of the international conference PV in Europe*, 2002, pp. 7-11.
- [116] H. Zondag, D. De Vries, W. Van Helden, R. Van Zolingen, and A. Van Steenhoven, "The yield of different combined PV-thermal collector designs," *Solar energy*, vol. 74, no. 3, pp. 253-269, 2003.
- [117] P. Affolter, D. Ruoss, P. Toggweiler, and A. Haller, "New generation of Hybrid Solar PV/T collectors," 2000.
- [118] Y. Tripanagnostopoulos, "Aspects and improvements of hybrid photovoltaic/thermal solar energy systems," *Solar energy*, vol. 81, no. 9, pp. 1117-1131, 2007.
- [119] X. Zhang, X. Zhao, S. Smith, J. Xu, and X. Yu, "Review of R&D progress and practical application of the solar photovoltaic/thermal (PV/T) technologies," *Renewable and Sustainable Energy Reviews*, vol. 16, no. 1, pp. 599-617, 2012.
- [120] A. Makki, S. Omer, and H. Sabir, "Advancements in hybrid photovoltaic systems for enhanced solar cells performance," *Renewable and Sustainable Energy Reviews*, vol. 41, pp. 658-684, 2015.
- [121] K. E. Amori and M. A. Abd-AlRaheem, "Field study of various air based photovoltaic/thermal hybrid solar collectors," *Renewable Energy*, vol. 63, pp. 402-414, 2014.
- [122] A. A. Hegazy, "Comparative study of the performances of four photovoltaic/thermal solar air collectors," *Energy Conversion and Management*, vol. 41, no. 8, pp. 861-881, 2000.
- [123] B. Robles-Ocampo *et al.*, "Photovoltaic/thermal solar hybrid system with bifacial PV module and transparent plane collector," *Solar Energy Materials and Solar Cells*, vol. 91, no. 20, pp. 1966-1971, 2007.
- [124] Y. Tripanagnostopoulos, M. Souliotis, R. Battisti, and A. Corrado, "Application aspects of hybrid PV/T solar systems," *Physics Department, University of Patras, Patras*, vol. 26500, 2003.

- [125] T. T. Chow, G. Tiwari, and C. Menezo, "Hybrid solar: a review on photovoltaic and thermal power integration," *International Journal of Photoenergy*, vol. 2012, 2012.
- [126] R. Avezov, J. Akhatov, and N. Avezova, "A review on photovoltaic-thermal (PV-T) air and water collectors," *Applied Solar Energy*, vol. 47, no. 3, pp. 169-183, 2011.
- [127] A. Elbreki *et al.*, "The role of climatic-design-operational parameters on combined PV/T collector performance: A critical review," *Renewable and Sustainable Energy Reviews*, vol. 57, pp. 602-647, 2016.
- [128] K. Sopian, K. Yigit, H. Liu, S. Kakac, and T. Veziroglu, "Performance analysis of photovoltaic thermal air heaters," *Energy Conversion and Management*, vol. 37, no. 11, pp. 1657-1670, 1996.
- [129] G. Tiwari and M. Ghosal, *Renewable energy resources: basic principles and applications*. Alpha Science Int'l Ltd., 2005.
- [130] A. A. Hegazy, "Performance of flat plate solar air heaters with optimum channel geometry for constant/variable flow operation," *Energy Conversion and Management*, vol. 41, no. 4, pp. 401-417, 2000.
- [131] A. A. Hegazy, "Optimum channel geometry for solar air heaters of conventional design and constant flow operation," *Energy conversion and management*, vol. 40, no. 7, pp. 757-774, 1999.
- [132] W. M. Kays, M. E. Crawford, and B. Weigand, *Convective heat and mass transfer*. Tata McGraw-Hill Education, 2012.
- [133] S. Kalogirou and Y. Tripanagnostopoulos, "Industrial application of PV/T solar energy systems," *Applied Thermal Engineering*, vol. 27, no. 8, pp. 1259-1270, 2007.
- [134] A. Hasan, S. McCormack, M. Huang, and B. Norton, "Evaluation of phase change materials for thermal regulation enhancement of building integrated photovoltaics," *Solar Energy*, vol. 84, no. 9, pp. 1601-1612, 2010.
- [135] M. Y. H. Othman, F. Hussain, K. Sopian, B. Yatim, and H. Ruslan, "Performance study of air-based photovoltaic-thermal (PV/T) collector with different designs of heat exchanger," *Sains Malaysiana*, vol. 42, no. 9, pp. 1319-1325, 2013.
- [136] H.-L. Tsai, "Modeling and validation of refrigerant-based PVT-assisted heat pump water heating (PVTa-HPWH) system," *Solar Energy*, vol. 122, pp. 36-47, 2015.
- [137] R. Mastrullo and C. Renno, "A thermoeconomic model of a photovoltaic heat pump," *Applied Thermal Engineering*, vol. 30, no. 14, pp. 1959-1966, 2010.
- [138] R. Daghigh, M. H. Ruslan, and K. Sopian, "Advances in liquid based photovoltaic/thermal (PV/T) collectors," *Renewable and Sustainable Energy Reviews*, vol. 15, no. 8, pp. 4156-4170, 2011.
- [139] J. Ji, H. He, T. Chow, G. Pei, W. He, and K. Liu, "Distributed dynamic modeling and experimental study of PV evaporator in a PV/T solar-assisted heat pump," *International Journal of Heat and Mass Transfer*, vol. 52, no. 5, pp. 1365-1373, 2009.
- [140] T. A. Kattakayam and K. Srinivasan, "Thermal performance characterization of a photovoltaic driven domestic refrigerator," *International Journal of Refrigeration*, vol. 23, no. 3, pp. 190-196, 2000.
- [141] A. Cherif and A. Dhoubib, "Dynamic modelling and simulation of a photovoltaic refrigeration plant," *Renewable Energy*, vol. 26, no. 1, pp. 143-153, 2002.

- [142] D. Du, J. Darkwa, and G. Kokogiannakis, "Thermal management systems for Photovoltaics (PV) installations: A critical review," *Solar Energy*, vol. 97, pp. 238-254, 2013.
- [143] X. Zhao, X. Zhang, S. B. Riffat, and Y. Su, "Theoretical study of the performance of a novel PV/e roof module for heat pump operation," *Energy conversion and Management*, vol. 52, no. 1, pp. 603-614, 2011.
- [144] S.-Y. Wu, Q.-L. Zhang, L. Xiao, and F.-H. Guo, "A heat pipe photovoltaic/thermal (PV/T) hybrid system and its performance evaluation," *Energy and buildings*, vol. 43, no. 12, pp. 3558-3567, 2011.
- [145] M. Browne, B. Norton, and S. McCormack, "Phase change materials for photovoltaic thermal management," *Renewable and Sustainable Energy Reviews*, vol. 47, pp. 762-782, 2015.
- [146] Y. Zhao, "Photovoltaic cell radiating and combined heat and power system," *Patent CN 200820123998 U*, vol. 4, no. 08, 2008.
- [147] M. Kenisarin and K. Mahkamov, "Solar energy storage using phase change materials," *Renewable and Sustainable Energy Reviews*, vol. 11, no. 9, pp. 1913-1965, 2007.
- [148] A. Sharma, V. Tyagi, C. Chen, and D. Buddhi, "Review on thermal energy storage with phase change materials and applications," *Renewable and Sustainable energy reviews*, vol. 13, no. 2, pp. 318-345, 2009.
- [149] S. S. Konjare, R. Shrivastava, R. Chadge, and V. Kumar, "Efficiency improvement of PV module by way of effective cooling-a review," in *Industrial Instrumentation and Control (ICIC), 2015 International Conference on*, 2015: IEEE, pp. 1008-1011.
- [150] Z. Rao and S. Wang, "A review of power battery thermal energy management," *Renewable and Sustainable Energy Reviews*, vol. 15, no. 9, pp. 4554-4571, 2011.
- [151] S. Solanki, S. Dubey, and A. Tiwari, "Indoor simulation and testing of photovoltaic thermal (PV/T) air collectors," *Applied energy*, vol. 86, no. 11, pp. 2421-2428, 2009.
- [152] B. Huang, T. Lin, W. Hung, and F. Sun, "Performance evaluation of solar photovoltaic/thermal systems," *Solar energy*, vol. 70, no. 5, pp. 443-448, 2001.
- [153] J. Ji *et al.*, "Experimental study of photovoltaic solar assisted heat pump system," *Solar Energy*, vol. 82, no. 1, pp. 43-52, 2008.
- [154] H. Yin, X. Gao, J. Ding, and Z. Zhang, "Experimental research on heat transfer mechanism of heat sink with composite phase change materials," *Energy Conversion and Management*, vol. 49, no. 6, pp. 1740-1746, 2008.
- [155] N. S. Kapany, "High efficiency solar panel," ed: Google Patents, 1976.
- [156] P. Hughes, J. Duffie, and W. Beckman, "Simulation study of several solar heating systems with offpeak auxiliary," *Solar Energy*, vol. 19, no. 3, pp. 317-319, 1977.
- [157] S. Rahman, M. Khallat, and B. H. Chowdhury, "A discussion on the diversity in the applications of photovoltaic systems," *Energy Conversion, IEEE Transactions on*, vol. 3, no. 4, pp. 738-746, 1988.
- [158] P. Raghuraman, "Analytical predictions of liquid and air photovoltaic/thermal, flat-plate collector performance," *Journal of solar energy engineering*, vol. 103, no. 4, pp. 291-298, 1981.

- [159] L. Florschuetz, "Extension of the Hottel-Whillier model to the analysis of combined photovoltaic/thermal flat plate collectors," *Solar energy*, vol. 22, no. 4, pp. 361-366, 1979.
- [160] T. Takada, K. Fukae, T. Mimura, M. Mori, and S. Shiomi, "Solar cell module and hybrid roof panel using the same," ed: Google Patents, 2000.
- [161] A. K. Bhargava, H. Garg, and R. K. Agarwal, "Study of a hybrid solar system—solar air heater combined with solar cells," *Energy Conversion and Management*, vol. 31, no. 5, pp. 471-479, 1991.
- [162] H. Garg and R. Adhikari, "System performance studies on a photovoltaic/thermal (PV/T) air heating collector," 1999.
- [163] K. Altfeld, W. Leiner, and M. Fiebig, "Second law optimization of flat-plate solar air heaters. Part 2: Results of optimization and analysis of sensibility to variations of operating conditions," *Solar Energy*, vol. 41, no. 4, pp. 309-317, 1988.
- [164] J. P. Forsström and P. Lund, "Optimization of operating strategies in a community solar heating system," *Applied mathematical modelling*, vol. 9, no. 2, pp. 117-124, 1985.
- [165] M. S. Sodha, S. K. Bharadwaj, and A. Kumar, "Technoeconomic optimization of a hybrid solar air-heating system," *International Journal of Energy Research*, vol. 12, no. 4, pp. 739-750, 1988, doi: [10.1002/er.4440120412](https://doi.org/10.1002/er.4440120412).
- [166] H.-M. Yeh and Y.-C. Ting, "Efficiency of solar air heaters packed with iron filings," *Energy*, vol. 13, no. 7, pp. 543-547, 1988/07/01 1988, doi: [http://dx.doi.org/10.1016/0360-5442\(88\)90009-6](http://dx.doi.org/10.1016/0360-5442(88)90009-6).
- [167] A. K. Bhargava, H. P. Garg, and R. K. Agarwal, "Study of a hybrid solar system—solar air heater combined with solar cells," *Energy Conversion and Management*, vol. 31, no. 5, pp. 471-479, // 1991, doi: [http://dx.doi.org/10.1016/0196-8904\(91\)90028-H](http://dx.doi.org/10.1016/0196-8904(91)90028-H).
- [168] H. P. Garg, C. Choudhury, R. Jha, and Z. H. Zaidi, "Performance prediction of a hybrid air-to-water solar heater," *Renewable Energy*, vol. 2, no. 3, pp. 211-218, 6// 1992, doi: [http://dx.doi.org/10.1016/0960-1481\(92\)90034-Z](http://dx.doi.org/10.1016/0960-1481(92)90034-Z).
- [169] C. Choudhury and H. Garg, "Performance calculations for closed-loop air-to-water solar hybrid heating systems with and without a rock bed in the solar air heater," *Renewable energy*, vol. 3, no. 8, pp. 897-905, 1993.
- [170] R. S. Misra, "Evaluation of economic and thermal performance of closed loop solar hybrid air and water heating systems for Indian climates," *Energy Conversion and Management*, vol. 34, no. 5, pp. 363-372, 5// 1993, doi: [http://dx.doi.org/10.1016/0196-8904\(93\)90087-Q](http://dx.doi.org/10.1016/0196-8904(93)90087-Q).
- [171] K. Sopian, K. S. Yigit, H. T. Liu, S. Kakaç, and T. N. Veziroglu, "Performance analysis of photovoltaic thermal air heaters," *Energy Conversion and Management*, vol. 37, no. 11, pp. 1657-1670, 11// 1996, doi: [http://dx.doi.org/10.1016/0196-8904\(96\)00010-6](http://dx.doi.org/10.1016/0196-8904(96)00010-6).
- [172] H. P. Garg and R. S. Adhikari, "Conventional hybrid photovoltaic/thermal (PV/T) air heating collectors: steady-state simulation," *Renewable Energy*, vol. 11, no. 3, pp. 363-385, 7// 1997, doi: [http://dx.doi.org/10.1016/S0960-1481\(97\)00007-4](http://dx.doi.org/10.1016/S0960-1481(97)00007-4).
- [173] H. P. Garg and R. S. Adhikari, "System performance studies on a photovoltaic/thermal (PV/T) air heating collector," *Renewable Energy*, vol. 16, no. 1-4, pp. 725-730, 1// 1999, doi: [http://dx.doi.org/10.1016/S0960-1481\(98\)00263-8](http://dx.doi.org/10.1016/S0960-1481(98)00263-8).

- [174] M. Y. H. Othman, B. Yatim, K. Sopian, and M. N. A. Bakar, "Performance analysis of a double-pass photovoltaic/thermal (PV/T) solar collector with CPC and fins," *Renewable energy*, vol. 30, no. 13, 2005.
- [175] C. Cox and P. Raghuraman, "Design considerations for flat-plate-photovoltaic/thermal collectors," *Solar energy*, vol. 35, no. 3, pp. 227-241, 1985.
- [176] J. Tonui and Y. Tripanagnostopoulos, "Air-cooled PV/T solar collectors with low cost performance improvements," *Solar energy*, vol. 81, no. 4, pp. 498-511, 2007.
- [177] K. Moradi, M. Ali Ebadian, and C.-X. Lin, "A review of PV/T technologies: Effects of control parameters," *International Journal of Heat and Mass Transfer*, vol. 64, pp. 483-500, 9// 2013, doi: <http://dx.doi.org/10.1016/j.ijheatmasstransfer.2013.04.044>.
- [178] B. Yousef and N. Adam, "Performance analysis for flat plate collector with and without porous media," *Journal of Energy in Southern Africa*, vol. 19, no. 4, p. 33, 2008.
- [179] D. Bahrehmand and M. Ameri, "Energy and exergy analysis of different solar air collector systems with natural convection," *Renewable Energy*, vol. 74, pp. 357-368, 2// 2015, doi: <http://dx.doi.org/10.1016/j.renene.2014.08.028>.
- [180] K. Hollands and E. Shewen, "Optimization of flow passage geometry for air-heating, plate-type solar collectors," *Journal of Solar Energy Engineering*, vol. 103, no. 4, pp. 323-330, 1981.
- [181] E. Znouda, N. Ghrab-Morcos, and A. Hadj-Alouane, "Optimization of Mediterranean building design using genetic algorithms," *Energy and Buildings*, vol. 39, no. 2, pp. 148-153, 2007.
- [182] M. Yang, X. Yang, X. Li, Z. Wang, and P. Wang, "Design and optimization of a solar air heater with offset strip fin absorber plate," *Applied Energy*, vol. 113, pp. 1349-1362, 2014.
- [183] M. Khaki, A. Shahsavari, S. Khanmohammadi, and M. Salmazadeh, "Energy and exergy analysis and multi-objective optimization of an air based building integrated photovoltaic/thermal (BIPV/T) system," *Solar Energy*, vol. 158, pp. 380-395, 2017.
- [184] M. Farshchimonfared, J. Bilbao, and A. Sproul, "Full optimisation and sensitivity analysis of a photovoltaic-thermal (PV/T) air system linked to a typical residential building," *Solar Energy*, vol. 136, pp. 15-22, 2016.
- [185] A. Shahsavari and S. Khanmohammadi, "Feasibility of a hybrid BIPV/T and thermal wheel system for exhaust air heat recovery: energy and exergy assessment and multi-objective optimization," *Applied Thermal Engineering*, vol. 146, pp. 104-122, 2019.
- [186] R. K. Koech, H. O. Ondieki, J. K. Tonui, and S. K. Rotich, "A steady state thermal model for photovoltaic/thermal (PV/T) system under various conditions," *International Journal of Energy and Environmental Engineering (IJEE)*, 2012.
- [187] M. I. Sohel, Z. Ma, P. Cooper, J. Adams, and R. Scott, "A theoretical investigation of a solar photovoltaic thermal system integrated with phase change materials," 2013.
- [188] R. Zakharchenko *et al.*, "Photovoltaic solar panel for a hybrid PV/thermal system," *Solar Energy Materials and Solar Cells*, vol. 82, no. 1-2, pp. 253-261, 5/1/ 2004, doi: <http://dx.doi.org/10.1016/j.solmat.2004.01.022>.
- [189] A. Tiwari and M. S. Sodha, "Parametric study of various configurations of hybrid PV/thermal air collector: Experimental validation of theoretical model," *Solar*

- Energy Materials and Solar Cells*, vol. 91, no. 1, pp. 17-28, 1/5/ 2007, doi: <http://dx.doi.org/10.1016/j.solmat.2006.06.061>.
- [190] F. E. Edlin, "Plastic glazings for solar energy absorption collectors," *Solar Energy*, vol. 2, no. 2, pp. 3-6, 1958.
- [191] P. Dupeyrat, C. Ménézo, M. Rommel, and H.-M. Henning, "Efficient single glazed flat plate photovoltaic-thermal hybrid collector for domestic hot water system," *Solar Energy*, vol. 85, no. 7, pp. 1457-1468, 2011.
- [192] S. Dubey and G. Tiwari, "Thermal modeling of a combined system of photovoltaic thermal (PV/T) solar water heater," *Solar Energy*, vol. 82, no. 7, pp. 602-612, 2008.
- [193] S. A. Kalogirou and Y. Tripanagnostopoulos, "Hybrid PV/T solar systems for domestic hot water and electricity production," *Energy Conversion and Management*, vol. 47, no. 18-19, pp. 3368-3382, 11// 2006, doi: <http://dx.doi.org/10.1016/j.enconman.2006.01.012>.
- [194] E. Radziemska, "Thermal performance of Si and GaAs based solar cells and modules: a review," *Progress in Energy and Combustion Science*, vol. 29, no. 5, pp. 407-424, // 2003, doi: [http://dx.doi.org/10.1016/S0360-1285\(03\)00032-7](http://dx.doi.org/10.1016/S0360-1285(03)00032-7).
- [195] B. J. Huang *et al.*, "Solar cell junction temperature measurement of PV module," *Solar Energy*, vol. 85, no. 2, pp. 388-392, 2// 2011, doi: <http://dx.doi.org/10.1016/j.solener.2010.11.006>.
- [196] W. De Soto, S. Klein, and W. Beckman, "Improvement and validation of a model for photovoltaic array performance," *Solar energy*, vol. 80, no. 1, pp. 78-88, 2006.
- [197] E. Skoplaki, A. G. Boudouvis, and J. A. Palyvos, "A simple correlation for the operating temperature of photovoltaic modules of arbitrary mounting," *Solar Energy Materials and Solar Cells*, vol. 92, no. 11, pp. 1393-1402, 11// 2008, doi: <http://dx.doi.org/10.1016/j.solmat.2008.05.016>.
- [198] A. Luque and S. Hegedus, *Handbook of photovoltaic science and engineering*. John Wiley & Sons, 2011.
- [199] M. A. Karim and M. Hawlader, "Performance investigation of flat plate, v-corrugated and finned air collectors," *Energy*, vol. 31, no. 4, pp. 452-470, 2006.
- [200] M. Tabatabaian, W. Tivy, and C. Bibby, "Design and Development of a Hybrid Photovoltaic-Thermal/PVT System," in *ASME 2012 6th International Conference on Energy Sustainability collocated with the ASME 2012 10th International Conference on Fuel Cell Science, Engineering and Technology*, 2012: American Society of Mechanical Engineers, pp. 919-930.
- [201] M. E. A. Alfegi, K. Sopian, M. Y. H. Othman, and B. B. Yatim, "Experimental investigation of single pass, double duct photovoltaic thermal (PV/T) air collector with CPC and fins," *American Journal of applied sciences*, vol. 5, no. 7, pp. 866-871, 2008.
- [202] M. Y. Othman, B. Yatim, K. Sopian, and M. N. A. Bakar, "Performance studies on a finned double-pass photovoltaic-thermal (PV/T) solar collector," *Desalination*, vol. 209, no. 1, pp. 43-49, 2007.
- [203] K. Branker and J. M. Pearce, "Financial return for government support of large-scale thin-film solar photovoltaic manufacturing in Canada," *Energy Policy*, vol. 38, no. 8, pp. 4291-4303, 2010.
- [204] H. Garg, G. Datta, and A. K. Bhargava, "Performance studies on a finned-air heater," *Energy*, vol. 14, no. 2, pp. 87-92, 1989.

- [205] H. Garg, R. Jha, C. Choudhury, and G. Datta, "Theoretical analysis on a new finned type solar air heater," *Energy*, vol. 16, no. 10, pp. 1231-1238, 1991.
- [206] K. Pottler, C. M. Sippel, A. Beck, and J. Fricke, "Optimized finned absorber geometries for solar air heating collectors," *Solar Energy*, vol. 67, no. 1, pp. 35-52, 1999.
- [207] P. Naphon, "On the performance and entropy generation of the double-pass solar air heater with longitudinal fins," *Renewable Energy*, vol. 30, no. 9, pp. 1345-1357, 2005.
- [208] A. N. Özakin and F. Kaya, "Effect on the exergy of the PVT system of fins added to an air-cooled channel: A study on temperature and air velocity with ANSYS Fluent," *Solar Energy*, vol. 184, pp. 561-569, 2019.
- [209] A. M. Elsafi and P. Gandhidasan, "Comparative study of double-pass flat and compound parabolic concentrated photovoltaic-thermal systems with and without fins," *Energy conversion and management*, vol. 98, pp. 59-68, 2015.
- [210] D. Gupta, S. Solanki, and J. Saini, "Heat and fluid flow in rectangular solar air heater ducts having transverse rib roughness on absorber plates," *Solar Energy*, vol. 51, no. 1, pp. 31-37, 1993.
- [211] J. Tonui and Y. Tripanagnostopoulos, "Improved PV/T solar collectors with heat extraction by forced or natural air circulation," *Renewable energy*, vol. 32, no. 4, pp. 623-637, 2007.
- [212] J. Tonui and Y. Tripanagnostopoulos, "Performance improvement of PV/T solar collectors with natural air flow operation," *Solar Energy*, vol. 82, no. 1, pp. 1-12, 2008.
- [213] J. Zhu, M. Fiebig, and N. Mitra, "Numerical investigation of turbulent flows and heat transfer in a rib-roughened channel with longitudinal vortex generators," *International journal of heat and mass transfer*, vol. 38, no. 3, pp. 495-501, 1995.
- [214] J. Han and J. S. Park, "Developing heat transfer in rectangular channels with rib turbulators," *International Journal of Heat and Mass Transfer*, vol. 31, no. 1, pp. 183-195, 1988.
- [215] G. Gan, "Numerical determination of adequate air gaps for building-integrated photovoltaics," *Solar Energy*, vol. 83, no. 8, pp. 1253-1273, 2009.
- [216] E. Dascalaki *et al.*, "On the combination of air velocity and flow measurements in single sided natural ventilation configurations," *Energy and Buildings*, vol. 24, no. 2, pp. 155-165, 1996.
- [217] S. A. Kalogirou, G. Florides, and S. Tassou, "Energy analysis of buildings employing thermal mass in Cyprus," *Renewable Energy*, vol. 27, no. 3, pp. 353-368, 2002.
- [218] Y. Tripanagnostopoulos, D. Tzavellas, I. Zoulia, and M. Chortatou, "Hybrid PV/T systems with dual heat extraction operation," in *Proceedings of the 17th PV solar energy conference, Munich, 2001*, pp. 22-26.
- [219] Y. Tripanagnostopoulos, T. Nousia, and M. Souliotis, "Test results of air cooled modified PV modules," in *proceedings of 17th European Photovoltaic Solar Conference, Munich, 2001*.
- [220] Y. Tripanagnostopoulos, T. Nousia, and M. Souliotis, "Low cost improvements to building integrated air cooled hybrid PV-Thermal systems," in *Proceedings of 16th European PV solar energy conference, 2000*, vol. 2, pp. 1874-99.
- [221] M. A. Karim and M. Hawlader, "Performance evaluation of a v-groove solar air collector for drying applications," *Applied Thermal Engineering*, vol. 26, no. 1, pp. 121-130, 2006.

- [222] M. Y. Othman, H. Ruslan, K. Sopian, and G. L. Jin, "Performance Study of Photovoltaic-Thermal (Pv/T) Solar Collector with Grooved Absorber Plate," 2009.
- [223] R. M. Manglik and A. E. Bergles, "Heat transfer and pressure drop correlations for the rectangular offset strip fin compact heat exchanger," *Experimental Thermal and Fluid Science*, vol. 10, no. 2, pp. 171-180, 1995.
- [224] L. A. Tagliafico, F. Scarpa, and M. De Rosa, "Dynamic thermal models and CFD analysis for flat-plate thermal solar collectors—A review," *Renewable and Sustainable Energy Reviews*, vol. 30, pp. 526-537, 2014.
- [225] S. Youcef-Ali and J. Desmons, "Numerical and experimental study of a solar equipped with offset rectangular plate fin absorber plate," *Renewable Energy*, vol. 31, no. 13, pp. 2063-2075, 2006.
- [226] A. Handbook, "ASHRAE handbook—fundamentals," Atlanta, GA, 2009.
- [227] W. M. Kays, *Convective heat and mass transfer*. Tata McGraw-Hill Education, 2012.
- [228] O. MOLNAR and Z. ZSIGMOND, "Application of analogy of momentum and heat transfer at shell and tube condenser," *EXPRES 2017*, vol. 1, no. 2, p. 21, 2017.
- [229] E.-U. Schlünder, "Analogy between heat and momentum transfer1," *Chemical Engineering and Processing: Process Intensification*, vol. 37, no. 1, pp. 103-107, 1998.
- [230] M. Al-Damook, Z. A. H. Obaid, M. Al Qubeissi, D. Dixon-Hardy, J. Cottom, and P. J. Heggs, "CFD modeling and performance evaluation of multipass solar air heaters," *Numerical Heat Transfer, Part A: Applications*, pp. 1-27, 2019.
- [231] A. W. Date, *Introduction to computational fluid dynamics*. Cambridge University Press, 2005.
- [232] A. J. S. Al-damook, "Design optimisation and analysis of heat sinks for electronic cooling," University of Leeds, 2016.
- [233] H. K. Versteeg and W. Malalasekera, *An introduction to computational fluid dynamics: the finite volume method*. United Kingdom: Pearson Education, 2007.
- [234] B. Xia and D.-W. Sun, "Applications of computational fluid dynamics (CFD) in the food industry: a review," *Computers and electronics in agriculture*, vol. 34, no. 1, pp. 5-24, 2002.
- [235] J. Tu, G. H. Yeoh, and C. Liu, *Computational fluid dynamics: a practical approach*. Butterworth-Heinemann, 2012.
- [236] S. Patankar, *Numerical heat transfer and fluid flow*. CRC press, 1980.
- [237] A. Chialastri and M. Isaacson, "Performance and optimization of a BIPV/T solar air collector for building fenestration applications," *Energy and Buildings*, vol. 150, pp. 200-210, 2017.
- [238] C. E. Baukal Jr, V. Gershtein, and X. J. Li, *Computational fluid dynamics in industrial combustion*. CRC press, 2000.
- [239] M. A. A. Al-Damook, "Performance analysis of various conceptual design for the air based photovoltaic /thermal collectors," University of Baghdad, 2011.
- [240] W. F. Phillips, "The effects of axial conduction on collector heat removal factor," *Solar Energy*, vol. 23, no. 3, pp. 187-191, 1979.
- [241] T. L. Bergman, F. P. Incropera, D. P. DeWitt, and A. S. Lavine, *Fundamentals of heat and mass transfer*. John Wiley & Sons, 2011.

- [242] G. Bahnke and C. Howard, "The effect of longitudinal heat conduction on periodic-flow heat exchanger performance," *Journal of Engineering for Power*, vol. 86, no. 2, pp. 105-117, 1964.
- [243] K. O. F. Lund, "General thermal analysis of parallel-flow flat-plate solar collector absorbers," *Solar Energy*, vol. 36, no. 5, pp. 443-450, 1986.
- [244] I. Guarracino, C. N. Markides, A. Mellor, and N. J. Ekins-Daukes, "Dynamic coupled thermal-and-electrical modelling of sheet-and-tube hybrid photovoltaic/thermal (PVT) collectors," *Applied Thermal Engineering*, doi: <http://dx.doi.org/10.1016/j.applthermaleng.2016.02.056>.
- [245] S. Fischer, W. Heidemann, H. Müller-Steinhagen, B. Perers, P. Bergquist, and B. Hellström, "Collector test method under quasi-dynamic conditions according to the European Standard EN 12975-2," *Solar Energy*, vol. 76, no. 1, pp. 117-123, 2004.
- [246] H. Xiao, Z.-Z. Xu, and S.-K. Lyu, "Quasi-Steady-State scheme and application on prewhirl flow and heat transfer in aeroengine," *International Journal of Precision Engineering and Manufacturing*, vol. 16, no. 2, pp. 343-350, 2015.
- [247] M. Medina, "A quasi-steady-state heat balance model of residential walls," *Mathematical and computer modelling*, vol. 30, no. 7-8, pp. 103-112, 1999.
- [248] E. M. Alfegi, K. Sopian, M. Y. Othman, and B. B. Yatim, "Mathematical model of double pass photovoltaic thermal air collector with fins," *American Journal of Environmental Sciences*, vol. 5, no. 5, p. 592, 2009.
- [249] M. Ahmed-Dahmane and A. Z. Malek, Tahar "Design and analysis of a BIPV/T system with two applications controlled by an air handling unit," *Energy Conversion and Management*, vol. 175, pp. 49-66, 2018.
- [250] J. A. Duffie and W. A. Beckman, "Solar energy thermal processes," University of Wisconsin-Madison, Solar Energy Laboratory, Madison, WI, 1974.
- [251] S. A. Kalogirou, *Solar energy engineering: processes and systems*. United States of America: Academic Press, 2013.
- [252] C. Cox III and P. Raghuraman, "Design considerations for flat-plate-photovoltaic/thermal collectors," *Solar energy*, vol. 35, no. 3, pp. 227-241, 1985.
- [253] S. Krauter and R. Hanitsch, "Actual optical and thermal performance of PV-modules," *Solar energy materials and solar cells*, vol. 41, pp. 557-574, 1996.
- [254] H.-M. Yeh and C.-D. Ho, "Collector efficiency in downward-type internal-recycle solar air heaters with attached fins," *Energies*, vol. 6, no. 10, pp. 5130-5144, 2013.
- [255] D. Njomo and M. Dagueuet, "Sensitivity analysis of thermal performances of flat plate solar air heaters," *Heat and mass transfer*, vol. 42, no. 12, pp. 1065-1081, 2006.
- [256] J. H. Lienhard, *A heat transfer textbook*. Courier Corporation, 2013.
- [257] I. Tosun, D. Uner, and C. Ozgen, "Critical Reynolds number for Newtonian flow in rectangular ducts," *Industrial & engineering chemistry research*, vol. 27, no. 10, pp. 1955-1957, 1988.
- [258] I. Y. Hussain, "Advanced Heat Transfer / II - Convection and Mass Transfer, University of Baghdad -College of Engineering, Delivered 09 November 2017," 2016, pp. 10-11.
- [259] S. Li, P. Karava, S. Currie, W. E. Lin, and E. Savory, "Energy modeling of photovoltaic thermal systems with corrugated unglazed transpired solar collectors-Part 1: Model development and validation," *Solar Energy*, vol. 102, pp. 282-296, 2014.

- [260] F. Sarhaddi, S. Farahat, H. Ajam, A. Behzadmehr, and M. M. Adeli, "An improved thermal and electrical model for a solar photovoltaic thermal (PV/T) air collector," *Applied Energy*, vol. 87, no. 7, pp. 2328-2339, 2010.
- [261] W. C. Swinbank, "Long - wave radiation from clear skies," *Quarterly Journal of the Royal Meteorological Society*, vol. 89, no. 381, pp. 339-348, 1963.
- [262] A. S. Mujumdar, *Handbook of industrial drying*. CRC press, 2014.
- [263] S. Klein, "Calculation of flat-plate collector loss coefficients," *Solar energy*, vol. 17, p. 79, 1975.
- [264] O. Turgut and N. Onur, "Three dimensional numerical and experimental study of forced convection heat transfer on solar collector surface," *International Communications in Heat and Mass Transfer*, vol. 36, no. 3, pp. 274-279, 3// 2009, doi: <http://dx.doi.org/10.1016/j.icheatmasstransfer.2008.10.017>.
- [265] E. Skoplaki, A. Boudouvis, and J. Palyvos, "A simple correlation for the operating temperature of photovoltaic modules of arbitrary mounting," *Solar Energy Materials and Solar Cells*, vol. 92, no. 11, pp. 1393-1402, 2008.
- [266] U. Eicker, *Solar technologies for buildings*. John Wiley & Sons, 2006.
- [267] S. W. Churchill and H. H. Chu, "Correlating equations for laminar and turbulent free convection from a vertical plate," *International journal of heat and mass transfer*, vol. 18, no. 11, pp. 1323-1329, 1975.
- [268] G. C. Vliet, "Natural convection local heat transfer on constant-heat-flux inclined surfaces," 1969: ASME.
- [269] Y. A. Cengel and A. Ghajar, "Heat and mass transfer (a practical approach, SI version)," ed: McGraw-Hill Education, 2011.
- [270] H. Buchberg, I. Catton, and D. Edwards, "Natural convection in enclosed spaces—a review of application to solar energy collection," *Journal of Heat Transfer*, vol. 98, no. 2, pp. 182-188, 1976.
- [271] T. Unny, G. Raithby, and L. Konicek, "Free Convective Heat Transfer Across Inclined Air Layers," *Journal of Heat Transfer*, p. 189, 1976.
- [272] Y. A. Cengel, *Heat and mass transfer*. Tata McGraw-Hill Education, 2007.
- [273] J. E. Hart, "Stability of the flow in a differentially heated inclined box," *Journal of Fluid Mechanics*, vol. 47, no. 3, pp. 547-576, 1971.
- [274] I. Catton, P. Ayyaswamy, and R. Clever, "Natural convection flow in a finite, rectangular slot arbitrarily oriented with respect to the gravity vector," *International Journal of Heat and Mass Transfer*, vol. 17, no. 2, pp. 173-184, 1974.
- [275] K. Hollands, T. Unny, G. Raithby, and L. Konicek, "Free convective heat transfer across inclined air layers," *Journal of Heat Transfer*, vol. 98, no. 2, pp. 189-193, 1976.
- [276] J. N. Arnold, "Experimental Investigation of Natural Convection in Finite Rectangular Regions Inclined at Various Angles from 0 to 180," University of California, Los Angeles--Engineering, 1974.
- [277] M. Jakob, *Heat Transfer*. Wiley, New York, 1949.
- [278] R. B. Bird, "Transport phenomena," *Applied Mechanics Reviews*, vol. 55, no. 1, pp. R1-R4, 2002.
- [279] T. L. Bergman, F. P. Incropera, and A. S. Lavine, *Fundamentals of heat and mass transfer*. United States of America: John Wiley & Sons, 2011.

- [280] W. Frei. "Modeling Natural and Forced Convection in COMSOL Multiphysics®." <https://uk.comsol.com/blogs/modeling-natural-and-forced-convection-in-comsol-multiphysics/> (accessed).
- [281] Y.-j. Chu, R. J. Oswald, J.-f. Puget, and J.-y. Shyr, "SYSTEM AND METHOD FOR COMBINING WHAT-IF AND GOAL SEEKING ANALYSES FOR PRESCRIPTIVE TIME SERIES FORECASTING," ed: US Patent App. 15/367,818, 2018.
- [282] W. M. Kays and M. E. Crawford, *Convective heat and mass transfer*. Tata McGraw-Hill Education, 2012.
- [283] F. A. Biehl, "Test results and analysis of a convective loop solar air collector," Los Alamos National Lab., NM (USA), 1981.
- [284] H. Tan and W. Charters, "Effect of thermal entrance region on turbulent forced-convective heat transfer for an asymmetrically heated rectangular duct with uniform heat flux," *Solar Energy*, vol. 12, no. 4, pp. 513-516, 1969.
- [285] H. Heaton, W. Reynolds, and W. Kays, "Heat transfer in annular passages. Simultaneous development of velocity and temperature fields in laminar flow," *International Journal of Heat and Mass Transfer*, vol. 7, no. 7, pp. 763-781, 1964.
- [286] W. Mercer, W. Pearce, and J. Hitchcock, "Laminar forced convection in the entrance region between parallel flat plates," *Journal of Heat Transfer*, vol. 89, no. 3, pp. 251-256, 1967.
- [287] M. Mittal and L. Varshney, "Optimal thermohydraulic performance of a wire mesh packed solar air heater," *Solar Energy*, vol. 80, no. 9, pp. 1112-1120, 2006.
- [288] A. Cortes and R. Piacentini, "Improvement of the efficiency of a bare solar collector by means of turbulence promoters," *Applied Energy*, vol. 36, no. 4, pp. 253-261, 1990.
- [289] S. Rai, P. Chand, and S. Sharma, "Evaluation of thermo hydraulic effect on offset finned absorber solar air heater," *Renewable Energy*, vol. 125, pp. 39-54, 2018.
- [290] S. Rai, P. Chand, and S. Sharma, "An analytical investigations on thermal and thermohydraulic performance of offset finned absorber solar air heater," *Solar Energy*, vol. 153, pp. 25-40, 2017.
- [291] J. Hartnett, J. Koh, and S. McComas, "A comparison of predicted and measured friction factors for turbulent flow through rectangular ducts," *Journal of Heat Transfer*, vol. 84, no. 1, pp. 82-88, 1962.
- [292] "Friction Factor for Laminar Flow." <https://www.nuclear-power.net/nuclear-engineering/fluid-dynamics/major-head-loss-friction-loss/friction-factor-for-laminar-flow/> (accessed).
- [293] Z. Ai and C. Mak, "Pressure losses across multiple fittings in ventilation ducts," *The Scientific World Journal*, vol. 2013, 2013.
- [294] R. L. Daugherty, *Fluid mechanics with engineering applications*. New York: Tata McGraw-Hill Education, 1989.
- [295] D. F. Young, B. R. Munson, T. H. Okiishi, and W. W. Huebsch, *A brief introduction to fluid mechanics*. United States of America: John Wiley & Sons, 2010.
- [296] *CFD Module Users Guide*, COMSOL Multiphysics Modeling Software 5.3a, 2018.
- [297] F. Kreith, R. M. Manglik, and M. S. Bohn, *Principles of heat transfer*. Cengage learning, 2012.

- [298] W. Gao, W. Lin, and E. Lu, "Numerical study on natural convection inside the channel between the flat-plate cover and sine-wave absorber of a cross-corrugated solar air heater," *Energy Conversion and Management*, vol. 41, no. 2, pp. 145-151, 2000.
- [299] Y. Varol and H. F. Oztop, "Buoyancy induced heat transfer and fluid flow inside a tilted wavy solar collector," *building and environment*, vol. 42, no. 5, pp. 2062-2071, 2007.
- [300] Y. Varol and H. F. Oztop, "A comparative numerical study on natural convection in inclined wavy and flat-plate solar collectors," *Building and Environment*, vol. 43, no. 9, pp. 1535-1544, 2008.
- [301] L. Abhay, V. Chandramohan, and V. Raju, "Numerical analysis on solar air collector provided with artificial square shaped roughness for indirect type solar dryer," *Journal of Cleaner Production*, vol. 190, pp. 353-367, 2018.
- [302] S. Dubey, G. Sandhu, and G. Tiwari, "Analytical expression for electrical efficiency of PV/T hybrid air collector," *Applied energy*, vol. 86, no. 5, pp. 697-705, 2009.
- [303] R. Wang and T. Ge, *Advances in Solar Heating and Cooling*. Woodhead Publishing, 2016.
- [304] J. Ji *et al.*, "Effect of fluid flow and packing factor on energy performance of a wall-mounted hybrid photovoltaic/water-heating collector system," *Energy and Buildings*, vol. 38, no. 12, pp. 1380-1387, 2006.
- [305] C. Rajoria, P. K. Gupta, S. Agrawal, G. Tiwari, and D. Singh, "Effect of Different Photovoltaic Materials on Energetic and Exergetic Performance of Photovoltaic Thermal Arrays," in *MATEC Web of Conferences*, 2017, vol. 95: EDP Sciences, p. 01006.
- [306] T. Saga, "Advances in crystalline silicon solar cell technology for industrial mass production," *npg asia materials*, vol. 2, no. 3, p. 96, 2010.
- [307] D. Evans, "Simplified method for predicting photovoltaic array output," *Solar energy*, vol. 27, no. 6, pp. 555-560, 1981.
- [308] E. Skoplaki and J. Palyvos, "On the temperature dependence of photovoltaic module electrical performance: A review of efficiency/power correlations," *Solar energy*, vol. 83, no. 5, pp. 614-624, 2009.
- [309] A. S. Joshi and A. Tiwari, "Energy and exergy efficiencies of a hybrid photovoltaic-thermal (PV/T) air collector," *Renewable Energy*, vol. 32, no. 13, pp. 2223-2241, 2007.
- [310] W. Fan, G. Kokogiannakis, Z. Ma, and P. Cooper, "Development of a dynamic model for a hybrid photovoltaic thermal collector-Solar air heater with fins," *Renewable Energy*, vol. 101, pp. 816-834, 2017.
- [311] Y. Chen, B. Peng, X. Hao, and G. Xie, "Fast approach of Pareto-optimal solution recommendation to multi-objective optimal design of serpentine-channel heat sink," *Applied Thermal Engineering*, vol. 70, no. 1, pp. 263-273, 2014.
- [312] A. F. Al-Neama, N. Kapur, J. Summers, and H. M. Thompson, "An experimental and numerical investigation of the use of liquid flow in serpentine microchannels for microelectronics cooling," *Applied Thermal Engineering*, vol. 116, pp. 709-723, 2017.
- [313] A. L. Myers, "Introduction to chemical engineering and computer calculations," 1976.
- [314] D. W. Pepper and J. C. Heinrich, *The Finite Element Method: Basic Concepts and Applications with MATLAB, MAPLE, and COMSOL*. CRC Press, 2017.

- [315] M. Design. "What's The Difference Between FEM, FDM, and FVM?" <https://www.machinedesign.com/fea-and-simulation/what-s-difference-between-fem-fdm-and-fvm> (accessed).
- [316] S. Bagwell, P. D. Ledger, A. J. Gil, M. Mallett, and M. Kruip, "A linearised hp - finite element framework for acousto - magneto - mechanical coupling in axisymmetric MRI scanners," *International Journal for Numerical Methods in Engineering*, vol. 112, no. 10, pp. 1323-1352, 2017.
- [317] *Heat Transfer Module User's Guide*, COMSOL Multiphysics Modeling Software 5.3a, 2018.
- [318] A. Alvarez, O. Cabeza, M. Muñiz, and L. Varela, "Experimental and numerical investigation of a flat-plate solar collector," *Energy*, vol. 35, no. 9, pp. 3707-3716, 2010.
- [319] J. Basheer Sheeba and A. Krishnan Rohini, "Structural and thermal analysis of asphalt solar collector using finite element method," *Journal of Energy*, vol. 2014, 2014.
- [320] J. Jeon, S. Park, and B. J. Lee, "Analysis on the performance of a flat-plate volumetric solar collector using blended plasmonic nanofluid," *Solar Energy*, vol. 132, pp. 247-256, 2016.
- [321] A. Álvarez, M. Muñiz, L. Varela, and O. Cabeza, "Finite element modelling of a solar collector," in *Int. Conf. on Renew. Energies and Power Quality, Granada (Spain)*, 2010.
- [322] H. Teo, P. Lee, and M. Hawlader, "An active cooling system for photovoltaic modules," *Applied Energy*, vol. 90, no. 1, pp. 309-315, 2012.
- [323] A. Hashmi and S. S. Abdullah, "Design, Fabrication and Testing of Hybrid Parabolic Dish Concentrator, Stirling Engine & PCM-Storage in Oman," University of Leeds, 2015.
- [324] P. Nithiarasu, R. W. Lewis, and K. N. Seetharamu, *Fundamentals of the finite element method for heat and mass transfer*. John Wiley & Sons, 2016.
- [325] J. Peiró and S. Sherwin, "Finite difference, finite element and finite volume methods for partial differential equations," in *Handbook of materials modeling*: Springer, 2005, pp. 2415-2446.
- [326] A. T. Patera, "A spectral element method for fluid dynamics: laminar flow in a channel expansion," *Journal of computational Physics*, vol. 54, no. 3, pp. 468-488, 1984.
- [327] R. Pohrt and Q. Li, "Complete boundary element formulation for normal and tangential contact problems," *Physical Mesomechanics*, vol. 17, no. 4, pp. 334-340, 2014.
- [328] A. Kurganov and E. Tadmor, "New high-resolution central schemes for nonlinear conservation laws and convection-diffusion equations," *Journal of Computational Physics*, vol. 160, no. 1, pp. 241-282, 2000.
- [329] D. Salvi, D. Boldor, J. Ortego, G. Aita, and C. Sabliov, "Numerical modeling of continuous flow microwave heating: a critical comparison of COMSOL and ANSYS," *Journal of Microwave Power and Electromagnetic Energy*, vol. 44, no. 4, pp. 187-197, 2010.
- [330] A. F. M. Al-Neama, "Serpentine minichannel liquid-cooled heat sinks for electronics cooling applications," University of Leeds, 2018.

- [331] E. Wicklein *et al.*, "Good modelling practice in applying computational fluid dynamics for WWTP modelling," *Water Science and Technology*, vol. 73, no. 5, pp. 969-982, 2016.
- [332] M. T. K. Al-Asadi, "Heat transfer, fluid flow analysis and energy management of micro-channel heat sinks using vortex generators and nanofluids," University of Leeds, 2018.
- [333] J. Zhu, *The finite element method: its basis and fundamentals*. Elsevier, 2013.
- [334] J. A. Jr, "Governing equations of fluid dynamics," in *Computational fluid dynamics*. Springer, 2009, pp. 15-51.
- [335] A. S. Dorfman, *Conjugate problems in convective heat transfer*. CRC Press, 2009.
- [336] A. Zebib and Y. Wo, "A two-dimensional conjugate heat transfer model for forced air cooling of an electronic device," *Journal of Electronic Packaging*, vol. 111, no. 1, pp. 41-45, 1989.
- [337] W. M. Kays, "Turbulent Prandtl number—where are we?," *Journal of Heat Transfer*, vol. 116, no. 2, pp. 284-295, 1994.
- [338] A. Al-Damook, N. Kapur, J. Summers, and H. Thompson, "An experimental and computational investigation of thermal air flows through perforated pin heat sinks," *Applied thermal engineering*, vol. 89, pp. 365-376, 2015.
- [339] A. Handbook, "Heating, ventilating, and air-conditioning applications," *Atlanta (GA): ASHRAE*, 2011.
- [340] S. Youcef-Ali, "Study and optimization of the thermal performances of the offset rectangular plate fin absorber plates, with various glazing," *Renewable Energy*, vol. 30, no. 2, pp. 271-280, 2005.
- [341] A. Tiwari and M. J. S. E. Sodha, "Performance evaluation of solar PV/T system: an experimental validation," vol. 80, no. 7, pp. 751-759, 2006.
- [342] F. Calise, R. D. Figaj, and L. Vanoli, "Experimental and Numerical Analyses of a Flat Plate Photovoltaic/Thermal Solar Collector," *Energies*, vol. 10, no. 4, p. 491, 2017.
- [343] S. Khanna, K. Reddy, and T. K. Mallick, "Optimization of finned solar photovoltaic phase change material (finned pv pcm) system," *International Journal of Thermal Sciences*, vol. 130, pp. 313-322, 2018.
- [344] W. Frei. "COMSOL Blog,How Much Memory Is Needed to Solve Large COMSOL Models?" <https://www.comsol.com/blogs/much-memory-needed-solve-large-comsol-models/> (accessed).
- [345] R. Cess, "The effect of radiation upon forced-convection heat transfer," *Applied scientific research*, vol. 10, no. 1, p. 430, 1961.
- [346] R. Cess, "The interaction of thermal radiation with conduction and convection heat transfer," *Advances in Heat Transfer*, vol. 1, no. 1, 1964.
- [347] M. Asadi and R. H. Khoshkho, "Temperature distribution along a constant cross sectional area fin," *International Journal of Mechanics and Applications*, vol. 3, no. 5, pp. 131-137, 2013.
- [348] R. Cess, "The interaction of thermal radiation with free convection heat transfer," *International Journal of Heat and mass transfer*, vol. 9, no. 11, pp. 1269-1277, 1966.
- [349] W. England and A. Emery, "Thermal radiation effects on the laminar free convection boundary layer of an absorbing gas," *Journal of Heat transfer*, vol. 91, no. 1, pp. 37-44, 1969.

- [350] R. Li, M. Bousetta, E. Chénier, and G. Lauriat, "Effect of surface radiation on natural convective flows and onset of flow reversal in asymmetrically heated vertical channels," *International journal of thermal sciences*, vol. 65, pp. 9-27, 2013.
- [351] D. Bhanja and B. Kundu, "Thermal analysis of a constructal T-shaped porous fin with radiation effects," *International journal of refrigeration*, vol. 34, no. 6, pp. 1483-1496, 2011.
- [352] P. Oberdorfer. "How to Save Computational Time with a One-Way Coupling Approach." <https://uk.comsol.com/model/cross-flow-heat-exchanger-173> (accessed).
- [353] M. Al Hamdani, M. Al Qubeissi, M. Al-Damook, D. Dixon-Hardy, and P. J. Heggs, "Thermal Optimisation of Fin Clusters for Heat Sink Purposes," in *11th ICTEA: International Conference on Thermal Engineering*, in Doha Qatar in collaboration with Texas A&M Doha campus and Hamad Bin Khalifa University, 2018, vol. 2018.
- [354] H. Ammari, "A mathematical model of thermal performance of a solar air heater with slats," *Renewable Energy*, vol. 28, no. 10, pp. 1597-1615, 2003.
- [355] V. Dabra and A. Yadav, "Effect of pressure drop and air mass flow rate on the performance of concentric coaxial glass tube solar air collector: A theoretical approach," *Arabian Journal for Science and Engineering*, vol. 43, no. 9, pp. 4549-4559, 2018.
- [356] "Solutions to Linear Systems of Equations: Direct and Iterative Solvers." <https://uk.comsol.com/blogs/solutions-linear-systems-equations-direct-iterative-solvers/> (accessed).
- [357] H. Gothäll. "COMSOL BLOG, How to Inspect Your Mesh in COMSOL Multiphysics." <https://uk.comsol.com/blogs/how-to-inspect-your-mesh-in-comsol-multiphysics/> (accessed).
- [358] A. Tiwari and M. Sodha, "Performance evaluation of solar PV/T system: an experimental validation," *Solar Energy*, vol. 80, no. 7, pp. 751-759, 2006.
- [359] W. Anis, R. Mertens, and R. Van Overstraeten, "Calculation of solar cell operating temperature in a flat plate PV array," in *Photovoltaic solar energy conference. 5*, 1984, pp. 520-524.
- [360] A. I. Kudish, E. G. Evseev, G. Walter, and T. Leukefeld, "Simulation study of a solar collector with a selectively coated polymeric double walled absorber plate," *Energy Conversion and Management*, vol. 43, no. 5, pp. 651-671, 2002.
- [361] M. Adil, O. Ibrahim, Z. Hussein, and K. Waleed, "Experimental Investigation of SAHs Solar Dryers with Zigzag Aluminum Cans," 2015.
- [362] PVGIS, <http://photovoltaic-software.com/pvgis.php>, Jun, 2017 2017. [Online]. Available: <http://photovoltaic-software.com/pvgis.php>.
- [363] T. Huld, R. Müller, and A. Gambardella, "A new solar radiation database for estimating PV performance in Europe and Africa," *Solar Energy*, vol. 86, no. 6, pp. 1803-1815, 2012.
- [364] A. Bocca, L. Bottaccioli, E. Chiavazzo, M. Fasano, A. Macii, and P. Asinari, "Estimating photovoltaic energy potential from a minimal set of randomly sampled data," *Renewable Energy*, vol. 97, pp. 457-467, 2016.
- [365] R. Zorer, C. Volschenk, and J. Hunter, "Integrating Geographic Information Systems and hemispherical photography in the assessment of canopy light profiles in a vineyard," *Agricultural and Forest Meteorology*, vol. 232, pp. 672-681, 2017.

- [366] D. Palmer, I. Cole, T. Betts, and R. Gottschalg, "Interpolating and Estimating Horizontal Diffuse Solar Irradiation to Provide UK-Wide Coverage: Selection of the Best Performing Models," *Energies*, vol. 10, no. 2, p. 181, 2017.
- [367] M. Qu, J. Wan, and X. Hao, "Analysis of diurnal air temperature range change in the continental United States," *Weather and Climate Extremes*, vol. 4, pp. 86-95, 2014.
- [368] D. R. Easterling *et al.*, "Maximum and minimum temperature trends for the globe," *Science*, vol. 277, no. 5324, pp. 364-367, 1997.
- [369] H. A. S. H. ASHRAE, "Hvac applications handbook," *IP Edition*, 2011.
- [370] A. Radwan and M. Ahmed, "The influence of microchannel heat sink configurations on the performance of low concentrator photovoltaic systems," *Applied energy*, vol. 206, pp. 594-611, 2017.
- [371] W. M. Deen, *Analysis of Transport Phenomena, Topics in Chemical Engineering*. Oxford University Press, New York, 1998.
- [372] R. Thorpe. "weather Data, University of Warwick" <https://files.warwick.ac.uk/rthorpe/browse#Weather+Data> (accessed).
- [373] Datasheet Sharp solar module NU-E245 (J5) 245 Wp [Online] Available: <http://www.solaruk.com/pdf/DS%20-%20Sharp%20NU%20Series%20235W-245W%20-%20Data%20Sheet.pdf>
- [374] I. Guarracino, A. Mellor, N. J. Ekins-Daukes, and C. N. Markides, "Dynamic coupled thermal-and-electrical modelling of sheet-and-tube hybrid photovoltaic/thermal (PVT) collectors," *Applied Thermal Engineering*, vol. 101, pp. 778-795, 2016.
- [375] W. M. Kays and A. L. London, "Compact heat exchangers," 1984.
- [376] D. C. Wilcox, *Turbulence modeling for CFD*. DCW industries La Canada, CA, 1993.
- [377] K. Sukhatme and S. P. Sukhatme, *Solar energy: principles of thermal collection and storage*. Hoboken, New Jersey: Tata McGraw-Hill Education, 1996.
- [378] OGIMET. "Professional information about meteorological conditions in the world." <http://www.ogimet.com/gsynres.phtml.en> (accessed).
- [379] S. s. s. radiation. "data-helioclim-3 archives for free feb." <http://www.soda-pro.com/web-services/radiation/helioclim-3-archives-for-free> (accessed).
- [380] *HVAC Applications Handbook*, H. A. S. H. ASHRAE, Atlanta, 2011.
- [381] A. Schack, "Industrial heat transfer," *Verlag Stahleisen M B H, Dusseldorf. 1970, 464 P*, 1970.
- [382] S. T. Buisan, C. Azorin - Molina, and Y. Jimenez, "Impact of two different sized Stevenson screens on air temperature measurements," *International Journal of Climatology*, vol. 35, no. 14, pp. 4408-4416, 2015.
- [383] "LUTRON EM-9000 ENVIRONMENT METER, + Humidity, Anemometer, Light, type K/J." <http://www.lutronmalaysia.com/index.php/item/1085-thermometers-thermocouple/5065-lutron-em-9000-environment-meter-humidity-anemometer-light-type-k-j> (accessed).
- [384] Renewable Energy Research Center. "Install a solar tracking system the first of its kind in Iraq," <http://www.uoanbar.edu.iq/RERCenter/English/CMS.php?ID=33> (accessed).
- [385] D. N. Moriasi, J. G. Arnold, M. W. Van Liew, R. L. Bingner, R. D. Harmel, and T. L. Veith, "Model evaluation guidelines for systematic quantification of accuracy in watershed

- simulations," *Transactions of the ASABE*, vol. 50, no. 3, pp. 885-900, 2007, doi: 10.13031/2013.23153.
- [386] Z. Zhang, W. Zhang, Z. J. Zhai, and Q. Y. Chen, "Evaluation of various turbulence models in predicting airflow and turbulence in enclosed environments by CFD: Part 2—Comparison with experimental data from literature," *Hvac&R Research*, vol. 13, no. 6, pp. 871-886, 2007.
- [387] *ASHRAE handbook: fundamentals*, M. S. Owen and H. E. Kennedy, Atlanta, 2009. [Online]. Available: <http://www.uoanbar.edu.iq/RERCenter/English/CMS.php?ID=33>
- [388] M. Gupta and S. Kaushik, "Performance evaluation of solar air heater having expanded metal mesh as artificial roughness on absorber plate," *International Journal of Thermal Sciences*, vol. 48, no. 5, pp. 1007-1016, 2009.
- [389] B. Brinkworth, "Estimation of flow and heat transfer for the design of PV cooling ducts," *Solar Energy*, vol. 69, no. 5, pp. 413-420, 2000.
- [390] M. Ansari and M. Bazargan, "Optimization of flat plate solar air heaters with ribbed surfaces," *Applied Thermal Engineering*, vol. 136, pp. 356-363, 2018.
- [391] F. Durst, S. Ray, B. Ünsal, and O. Bayoumi, "The development lengths of laminar pipe and channel flows," *Journal of fluids engineering*, vol. 127, no. 6, pp. 1154-1160, 2005.
- [392] O. K. Ahmed and Z. A. Mohammed, "Dust effect on the performance of the hybrid PV/Thermal collector," *Thermal Science and Engineering Progress*, vol. 3, pp. 114-122, 2017.
- [393] O. K. Ahmed and Z. A. Mohammed, "Influence of porous media on the performance of hybrid PV/Thermal collector," *Renewable energy*, vol. 112, pp. 378-387, 2017.
- [394] T. Rajaseenivasan, S. Srinivasan, and K. Srithar, "Comprehensive study on solar air heater with circular and V-type turbulators attached on absorber plate," *Energy*, vol. 88, pp. 863-873, 2015.
- [395] J. C. Mojumder, W. T. Chong, H. C. Ong, and K. Leong, "An experimental investigation on performance analysis of air type photovoltaic thermal collector system integrated with cooling fins design," *Energy and buildings*, vol. 130, pp. 272-285, 2016.
- [396] H. Garg and R. S. Adhikari, "Conventional hybrid photovoltaic/thermal (PV/T) air heating collectors: steady-state simulation," *Renewable energy*, vol. 11, no. 3, pp. 363-385, 1997.
- [397] K. Sopian, H. Liu, S. Kakac, and T. Veziroglu, "Performance of a double pass photovoltaic thermal solar collector suitable for solar drying systems," *Energy Conversion and Management*, vol. 41, no. 4, pp. 353-365, 2000.
- [398] K. E. Amori and M. Al-Damook, "Performance Analysis of Four Conceptual Designs for the Air Based Photovoltaic/Thermal Collectors," *Journal of Engineering*, vol. 20, no. 6, pp. 28-45, 2014.
- [399] A. Narayanan, V. Toropov, A. Wood, and I. Campean, "Simultaneous model building and validation with uniform designs of experiments," *Engineering Optimization*, vol. 39, no. 5, pp. 497-512, 2007.
- [400] A. F. Al-Neama, Z. Khatir, N. Kapur, J. Summers, and H. M. Thompson, "An experimental and numerical investigation of chevron fin structures in serpentine

minichannel heat sinks," *International Journal of Heat and Mass Transfer*, vol. 120, pp. 1213-1228, 2018.

- [401] Z. Khatir, A. Taherkhani, J. Paton, H. Thompson, N. Kapur, and V. Toropov, "Energy thermal management in commercial bread-baking using a multi-objective optimisation framework," *Applied Thermal Engineering*, vol. 80, pp. 141-149, 2015.
- [402] Z. Khatir, K. Kubiak, P. Jimack, and T. Mathia, "Dropwise condensation heat transfer process optimisation on superhydrophobic surfaces using a multi-disciplinary approach," *Applied Thermal Engineering*, vol. 106, pp. 1337-1344, 2016.
- [403] C. M. Fonseca and P. J. Fleming, "Genetic Algorithms for Multiobjective Optimization: Formulation Discussion and Generalization," in *Icga*, 1993, vol. 93, no. July: Citeseer, pp. 416-423.
- [404] K. Deb, S. Agrawal, A. Pratap, and T. Meyarivan, "A fast elitist non-dominated sorting genetic algorithm for multi-objective optimization: NSGA-II," in *International conference on parallel problem solving from nature*, 2000: Springer, pp. 849-858.
- [405] K. A. Joudi, "Some aspects of solar irradiance calculation," in *Proceeding of the third Arab international solar energy conference*, Baghdad, N. S. A. edited by Al-Hamdani N.I., Aliwi S.M., Saman W.Y., and Akrawi A.A, Ed., Feb. 1988: EDP Sciences.
- [406] P. J. Lunde, "Solar thermal engineering: space heating and hot water systems," *New York, John Wiley and Sons, Inc., 1980. 635 p.*, 1980.
- [407] L. Lamm, "A new analytic expression for the equation of time," *Solar Energy*, vol. 26, pp. 465-474, 1981.

APPENDIX A SOLAR RADIATION EQUATIONS

In order to estimate the global solar radiation on the surface, three components should be determined which are the beam, reflected, and diffuse radiation. A few variables should be evaluated for any day of the month to use in next calculation. The variables are solar intensity (A) the atmospheric extinction coefficient (B) and sky diffuse factor (C) [405]:

$$A = 1158[1 + 0.066 \cos(360 ND/370)], \quad \text{Eq.A. 1}$$

$$B = 0.175[1 - 0.2 \cos(0.93 ND)] - 0.0045[1 - \cos(1.86 ND)], \quad \text{Eq.A. 2}$$

$$C = 0.0956[1 - 0.42 \cos(360 ND/370)] - 0.0075[1 - \cos(1.95 ND)]. \quad \text{Eq.A. 3}$$

The declination angle δ and sun altitude angle α are given by Lunde [406] as:

$$\delta = 23.45 \sin\left(\frac{360(ND-80)}{370}\right), \quad \text{Eq.A. 4}$$

$$\sin\alpha = \cos\phi \cos\delta \cos\omega + \sin\delta \sin\phi, \quad \text{Eq.A. 5}$$

where ϕ is the latitude angle which equals 33.3° N for Fallujah and 23.58° N for Muscat and ω is the hour angle [406]:

$$\omega = 15(\text{AST} - 12), \quad \text{Eq.A. 6}$$

where AST is the apparent solar time.

$$\text{AST} = \text{LCT} - \frac{(\text{STM}-\text{LONG})}{15} + \frac{\text{EQT}}{60}, \quad \text{Eq.A. 7}$$

where LCT is the local time in hours, STM is the standard meridian of local time zone which equals 45° E for Iraq and Oman using the following equation:

$$\text{STM} = \frac{360}{24} \Delta t, \quad \text{Eq.A. 8}$$

where Δt is the difference between the time London (i.e. Greenwich Mean Time not summer time) and the time in time Iraq or Oman, LONG is the longitude of the location concerned and equals 43.78° E for Fallujah and 58.40° E for Muscat.

EQT is the equation of time given by Lamm [407] as:

$$EQT = \sum_{k=0}^5 A_k \sin\left(\frac{2\pi kND}{365.25}\right) + B_k \sin\left(\frac{2\pi kND}{365.25}\right), \quad \text{Eq.A. 9}$$

where ND is the number of day in a 4-year cycle and A_k and B_k are constant given in Table A.1. Duffie and Beckman[50] introduced a general definition of incident angle for any surface orientation as:

$$\begin{aligned} \cos \theta = & \sin \delta \sin \phi \cos \beta - \sin \delta \cos \phi \sin \beta \cos \gamma + \\ & \cos \delta \cos \phi \cos \beta \cos \omega + \cos \delta \sin \phi \sin \beta \cos \gamma \cos \omega + \\ & \cos \delta \sin \beta \sin \gamma \sin \omega, \end{aligned} \quad \text{Eq.A. 10}$$

where γ is the surface azimuth angle which values 0° for south orientation, west is positive and east is negative ($-180 \leq \gamma \leq 180$).

For a collector oriented to south $\gamma = 0$ and the incident angle calculation reduces to:

$$\cos \theta = \cos(\phi - \beta) \cos \delta \cos \omega + \sin(\phi - \beta) \sin \delta. \quad \text{Eq.A. 11}$$

The direct normal irradiance is calculated as [406]:

$$I_{DN} = A e^{\left(\frac{-P_L}{P_o} B\right)}, \quad \text{Eq.A. 12}$$

where $\frac{-P_L}{P_o}$ is the pressure at the altitude concerned relative to the standard atmospheric pressure at sea level and is given as [406]:

$$\frac{-P_L}{P_o} = e^{(-0.0001148 H_{alt})}, \quad \text{Eq.A. 13}$$

where H_{alt} is the altitude in meters above sea level. The beam irradiance can be computed as:

$$G_b = I_{DN} \cos \theta. \quad \text{Eq.A. 14}$$

The diffuse and the ground-reflected components of radiation are computed as:

$$G_b = I_{DN} C \left(\frac{1+\cos\beta}{2} \right), \quad \text{Eq.A. 15}$$

$$G_r = \rho_g (C + \sin\alpha) \left(\frac{1+\cos\beta}{2} \right). \quad \text{Eq.A. 16}$$

where ρ_g is the ground reflectivity which equals (0.2) for ordinary ground or vegetation, (0.8) for snow cover and (0.15) for gravel surface [50]. For the present work the value was taken at 0.2. The total incident radiation on a surface is then:

$$G = G_b + G_d + G_r. \quad \text{Eq.A. 17}$$

Table A.1 A_k and B_k coefficients for Eq. A.9.

k	A_k	B_k
0	$2.087e^{-4}$	0
1	$9.2869 e^{-3}$	$-1.2229 e^{-1}$
2	$-5.2258 e^{-2}$	$-1.5698 e^{-1}$
3	$-1.3077 e^{-3}$	$-5.1602 e^{-3}$
4	$-2.1867 e^{-3}$	$-2.9823 e^{-3}$
5	$-1.51 e^{-4}$	$-2.3463 e^{-4}$

APPENDIX B GRID INDEPENDENCE CHECK

Table B.1. Mesh independent test analysis for two conditions ($Re = 510, \bar{V} = 0.1829 \text{ (m s}^{-1}\text{)}, \dot{M} = 0.0041 \text{ (kg s}^{-1}\text{)}$) and ($Re = 2550, \bar{V} = 0.9145 \text{ (m s}^{-1}\text{)}, \dot{M} = 0.0204 \text{ (kg s}^{-1}\text{)}$).

Trial No	NOE	RAM	t	DOF	MEQ	T_{mpv}	η_{th}	Δp_f	T_{fo}
$Re = 510, \bar{V} = 0.1829 \text{ (m s}^{-1}\text{)}, \dot{M} = 0.0041 \text{ (kg s}^{-1}\text{)}$									
1	3360	1.81	41	22713	1	86.48	24.08	0.207	73.85
2	9804	3.30	277	60204	1	86.31	23.54	0.207	73.28
3	19401	5.45	265	115584	1	86.11	23.08	0.207	72.74
4	64935	21.56	1759	358716	1	86.02	22.90	0.211	72.52
5	78225	23.67	1706	438876	1	86.00	22.91	0.213	72.53
6	94905	24.30	1792	539076	1	85.97	22.84	0.214	72.45
7	94905	24.48	1752	539076	1	85.88	22.70	0.220	72.28
8	94905	25.97	1787	539076	1	85.86	22.67	0.222	72.25
9	94905	26.81	1755	539076	1	85.84	22.66	0.223	72.23
10	94905	27.03	1759	539076	1	85.82	22.65	0.224	72.22
11	169242	60.80	6397	942326	1	85.95	22.80	0.216	72.40
12	169242	64.61	8866	942326	1	85.85	22.66	0.222	72.23
$Re = 2550, \bar{V} = 0.9145 \text{ (m s}^{-1}\text{)}, \dot{M} = 0.0204 \text{ (kg s}^{-1}\text{)}$									
1	3360	1.85	44	22713	1	75.90	46.36	1.408	56.20
2	9804	3.4	295	60204	1	75.96	45.35	1.403	55.96
3	19401	5.59	264	115584	1	75.97	44.37	1.429	55.72
3a	44823	8.09	352	285824	1	75.74	43.11	1.56	55.42
3ab	44823	8.84	346	285824	1	75.83	43.43	1.50	55.50
3abc	51513	9.49	382	330624	1	75.81	43.36	1.51	55.48
3abcd	51513	9.49	385	330624	1	75.75	43.10	1.57	55.42
4	64935	20.97	1586	358716	1	75.90	43.87	1.46	55.60
5	78225	22.23	1642	438876	1	75.87	43.65	1.48	55.55
6	94905	25.98	1827	539076	1	75.84	43.52	1.49	55.51
7	94905	27.18	1780	539076	1	75.75	43.20	1.54	55.44
7a	111555	27.21	2014	639276	1	75.74	43.12	1.56	55.42
7ab	111555	27.32	1969	639276	1	75.83	43.43	1.50	55.50
7abc	128205	28.87	2128	739476	1	75.81	43.37	1.51	55.48
7abcd	128205	27.97	2290	739476	1	75.74	43.11	1.56	55.42
8	94905	26.36	1757	539076	1	75.73	43.15	1.55	55.43
9	94905	23.85	1746	539076	1	75.71	43.10	1.557	55.42
10	94905	25.66	1807	539076	1	75.69	43.07	1.563	55.41
11	169242	61.51	7368	942326	1	75.83	43.44	1.504	55.50
12	169242	63.74	8378	942326	1	75.73	43.12	1.558	55.42

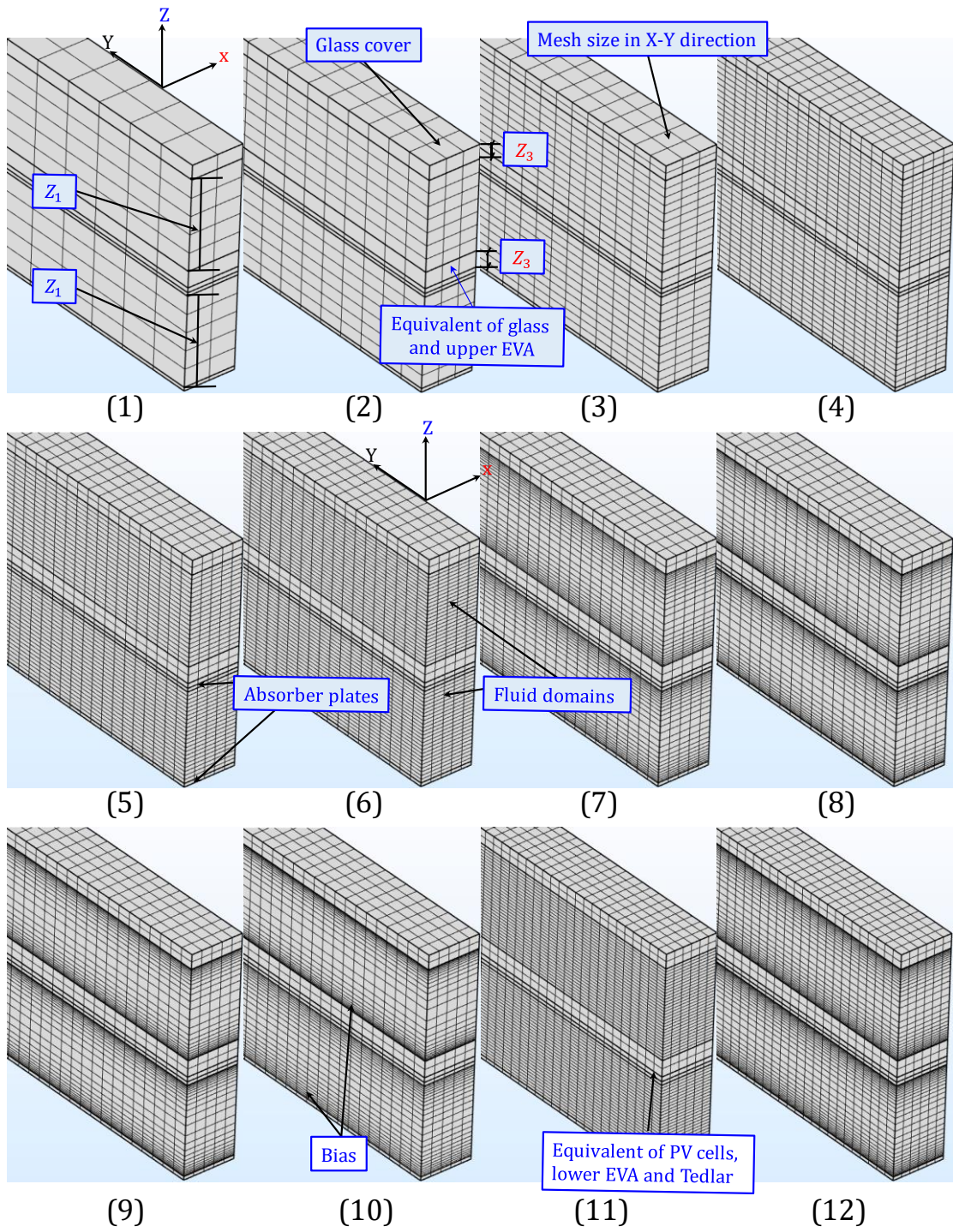


Fig. B.1. Grid independence test for model 4 using hexahedral mesh element type.